5-2014

Ab Initio Studies of Proton Transport in Proton Exchange Membranes

Jeffrey Keith Clark
University of Tennessee - Knoxville, jclark51@utk.edu

To the Graduate Council:

I am submitting herewith a dissertation written by Jeffrey Keith Clark entitled "*Ab Initio* Studies of Proton Transport in Proton Exchange Membranes." I have examined the final electronic copy of this dissertation for form and content and recommend that it be accepted in partial fulfillment of the requirements for the degree of Doctor of Philosophy, with a major in Chemical Engineering.

Stephen J. Paddison, Major Professor

We have read this dissertation and recommend its acceptance:

Brian J. Edwards, Siris O. Laursen, Robert J. Hinde

Accepted for the Council:
Dixie L. Thompson

Vice Provost and Dean of the Graduate School

(Original signatures are on file with official student records.)

Ab Initio Studies of Proton Transport in Proton Exchange Membranes

A Dissertation Presented for the

Doctor of Philosophy

Degree

The University of Tennessee, Knoxville

Jeffrey Keith Clark

May 2014

DEDICATION

This dissertation is dedicated to my wife, Lindsey, who has supported and encouraged me throughout my academic career.

ACKNOWLEDGEMENTS

I would like to express sincere gratitude to my advisor, Dr. Stephen J. Paddison, for his support and encouragement throughout my graduate studies at the University of Tennessee. His guidance played a pivotal role in my research as well as my professional and personal growth. I would also like to extend thanks to Dr. Bradley Habenicht who served as a mentor and introduced me to *ab initio* molecular dynamics techniques and methods. Further appreciation goes out to the other past and present members of our research group: Dr. Dongsheng Wu, Dr. Chen Wang, Dr. Milan Kumar, Dr. Jun He, and Mrs. Fatemeh Sphehr. Special thanks goes out to the National Science Foundation which supported this work and provided me the opportunity to be a part of the "Sustainable Technology through Advanced Interdisciplinary Research" (STAIR) program at UT.

ABSTRACT

A molecular-level understanding of factors that contribute to transport properties of proton exchange membranes (PEMs) for fuel cell applications is needed to aid in the development of superior membrane materials. *Ab initio* electronic structure calculations were undertaken on various PEM ionomer fragments to explore the effects of local hydration, side chain connectivity, protogenic group separation, and specific side chain chemistry on proton dissociation and transfer at low hydration. Cooperative interactions between both intra- and inter-molecular acidic groups and hydrogen bond connectivity were found to enhance proton dissociation at very low degrees of hydration. The energetics associated with proton transfer were highly dependent on the disruption of the hydrogen bond network where bond breaking, without an accompanying formation of a new bond, was strongly resisted. The effects of nanoscale confinement within different hydrophobic environments on structural and dynamical properties in PEMs were studied using *ab initio* molecular dynamics simulations on idealized systems of water molecules, slightly acidic water, and acid molecules confined in bare and fluorinated single-walled carbon nanotubes (CNTs) with different diameters. Inclusion of the fluorine atoms led to considerably different hydrogen bond structuring within the nanotube than in the bare CNTs. The water molecules in the fluorinated CNTs exhibited hydrogen bond-like interactions with the fluorine atoms resulting in a preferential, well-structured arrangement near the CNT surface. This was also observed with the addition of an excess proton where the proton shuttled between water molecules near the fluorinated walls

rather than along the tube axis, as found in the bare CNTs. For aqueous triflic acid, proton dissociation depended on the level of hydration, the degree of confinement, and the surrounding environment. At the lowest hydration level, dissociation was most pronounced in the bare CNTs with little dissociation in the fluorinated systems regardless of the diameter. However, at the highest hydration level, the least amount of dissociation was observed in the larger diameter bare tube due to direct hydrogen bonding between triflic acid molecules with nearly complete dissociation in each of the others indicating an influence of the confinement and the fluorinated surface on hydrogen bonding and proton transfer properties.

Table of Contents

LIST OF TABLES

LIST OF FIGURES

Chapter 1 Introduction

The increasing global demand for energy coupled with the pressure towards reducing emissions from conventional energy systems based on the combustion of fossil fuels has propelled efforts in development of viable alternative energy sources. Among the promising candidates are hydrogen fuel cells due to their wide range of applicability and minimal environmental impact.[1-3] These devices provide energy through electrochemical conversion of hydrogen into electricity, and efficient fuel cell performance relies heavily on the choice of electrolyte material. Among the most commonly used electrolytes are proton exchange (or polymer electrolyte) membranes (PEMs). In a PEM fuel cell, the solid polymer membrane not only acts as the electrolyte, but also as the internal ion-conducting medium and the separator of the electrodes and reactant gases.[4] PEM fuel cells offer high power density, fast startup time, and are light weight which makes them promising candidates for stationary, portable, and automotive use.[5]

1.1 Proton Exchange Membranes

The wide variety of applications for PEM fuel cells places demands on the membrane including high proton conductivity ($\geq 10^{-1}$ Scm^{-1}), sustained mechanical durability over several operating cycles, and high chemical and thermal stability in an oxidative environment at temperatures as high as 120°C.[6-8] Currently, the most widely used PEMs are perfluorosulfonic acid (PFSA) ionomers, such as Nafion™, as they exhibit high proton conductivity ($\sim 10^{-1}$ Scm^{-1}) and good chemical and mechanical stability.[9] A PFSA membrane consists of a hydrophobic poly(tetrafluoroethylene) (PTFE) backbone functionalized with hydrophilic sulfonic acid-terminated perfluoroether pendant side chains. The hydrophobic portion provides the mechanical stability and the hydrophilic terminal acidic groups, when hydrated, provide high proton conductivity. However, currently available PFSA membranes only exhibit high proton conductivity under conditions of high degrees of hydration (>95% relative humidity) which leads to significant water 'cross-over' due to electro-osmotic drag and permeation and restricts the operating temperature to below the boiling point of water

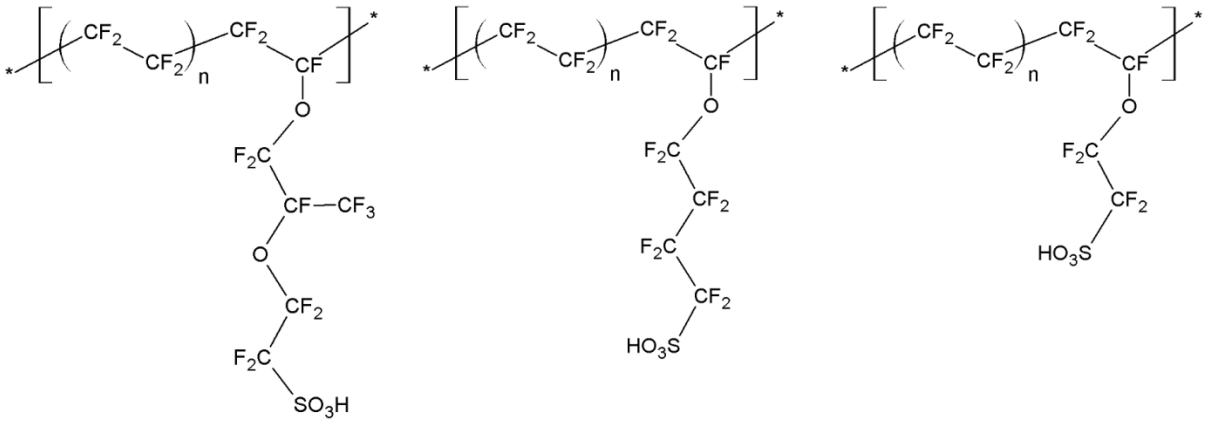

(a) (b) (c)

Figure 1.1. Chemical structures of the PFSA membranes: (a) Nafion, (b) the 3M PFSA membrane, and (c) the short side chain Aquivion.

(100°C at 1 atm) to prevent drying of the membrane.[10] Low temperature operation necessitates the use of expensive platinum or platinum alloy catalysts due to poor electrode reaction kinetics at low temperatures. Furthermore, at temperatures below 120°C the platinum-based catalysts are more susceptible to poisoning from trace amounts of carbon monoxide in the hydrogen feed stream, which preferentially adsorbs onto the platinum surface blocking the reaction sites.[8]

These complications have led to considerable effort in the development of membrane materials that exhibit high proton conductivity at low hydration levels allowing for higher temperature operation and removal of the issues associated with water management and carbon monoxide poisoning.[7, 11-15] These include changing the side chain acidic group or incorporation of multiple acid groups per side chain, the use of sulfonated aryl main chain polymers and heterocyclic polymers, and modification of the backbone and/or side chain chemistry of currently available materials.[8, 14, 16, 17] It remains, however, that the majority of the readily available PEM materials are PFSA derivatives of Nafion. Proton conductivity in PEMs can be improved by reducing the ionomer equivalent weight (EW ≡ grams ionomers per mole of acid) resulting in a higher ion exchange capacity (IEC).[18] This allows for

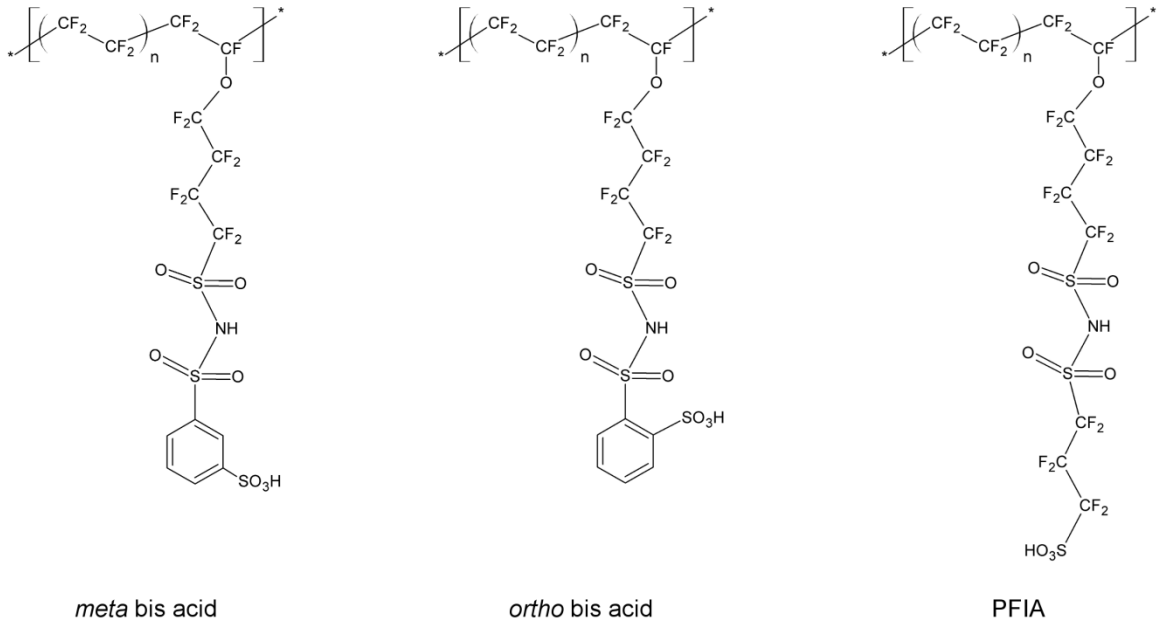

Figure 1.2. Chemical structures of the MASC membranes.

improved performance in both fully hydrated membranes, as well as under drier conditions at higher temperatures.[14] However, too low of an EW can compromise the mechanical integrity of the system as the polymer can become water soluble. Reduction in the EW is commonly done by shortening the Nafion side chain as in the Aquivion™ short side chain (SSC) PFSA membrane[16] from Solvay and the 3M PFSA membrane,[14] whose chemical structures are shown in Figure 1.1. These materials have been shown to exhibit higher proton conductivity than Nafion while still maintaining good mechanical properties.[14, 19-23] The improved performance of these lower EW ionomers is primarily due to the increased IEC as the shorter side chain membranes exhibit similar proton conductivities to Nafion at the same EW.[18]

Bis[(perfluoroalkyl)sulfonyl] imide analogues of Nafion have also been shown to have greater thermal stability,[24] stronger gas phase acidity,[25] and higher proton conductivity at low hydration levels when compared to typical PFSA ionomers.[24, 26] A new class of ionomers constructed from the 3M PFSA membrane use a bis sulfonyl imide functional group as both a protogenic group and a link to a sulfonic acid containing aromatic or

perfluorinated functional group (Figure 1.2). The incorporation of multiple acid groups per side chain results in lower EW ionomers then the PFSA counterparts without loss of backbone tetrafluoroethylene units important to the mechanical integrity of the membrane.[17, 23] These multi-acid side chain (MASC) ionomers contain side chains that are either fully fluorinated or partially fluorinated which all exhibit higher proton conductivities than the 3M PFSA membrane made from the same ionomer precursors at high relative humidity. The proton conductivity in the partially fluorinated ionomers drops at low hydration levels, but the fully fluorinated ionomer maintains a higher proton conductivity than the PFSA precursor at all hydration levels.[17, 23]

There are also classes of widely available non-fluorinated hydrocarbon-based PEMs. Aromatic hydrocarbons are typically incorporated into the hydrocarbon polymer to enhance stability at elevated temperatures and offer the possibility for electrophilic and nucleophilic substitutions.[27] Since most polymers do not inherently possess proton conducting properties, these materials typically undergo a sulfonation process to add functional sulfonic acid groups that are relatively easy to introduce onto aromatic rings. In fact, the first PEMs used for actual fuel cell applications were developed by General Electric for the NASA Gemini space program in the early 1960s based on sulfonated polystyrene; however, the materials suffered from poor long-term durability and chemical degradation.[28] Over the years several other sulfonated hydrocarbons have emerged as promising candidates for PEM fuel cells due to potential lower cost than PFSA membranes, widely available in various forms, freedom for chemical modification, and ease of recyclability.[29] Some aryl polymers that have been used as a base for post-sulfonation include poly(aryl ether)s, poly(ether ether ketone)s, poly(ether ether sulfone)s, poly(phenylene)s, polyimides, and others. These materials, however, currently cannot compete with PFSA membranes due to lower proton conductivity at low hydration levels and issues regarding durability associated with high degrees of sulfonation.[30]

Another group of PEM materials are acid–base complexes which can exhibit high proton conductivity without humidification. In general, these involve incorporation of an acid into

a basic polymer to promote proton conductivity. Several basic polymers have been examined including poly(ethylene oxide), poly(vinyl alcohol), poly(acryl amide), and poly(ethylene imine) in combination with sulfuric, phosphoric, and various halide acids.[9] Of the combinations, phosphoric acid-doped polybenzimidazole (PBI/H_3PO_4) has received a great deal of attention due to its high proton conductivity and good oxidative and thermal stability at elevated operating temperatures.[1] An issue associated with the use of PBI/H_3PO_4 in fuel cells is gradual phosphoric acid loss through the water formed at the cathode during long-term fuel cell operation.[31, 32] To address this problem, hydrophobic phosphoric acid derivatives have been proposed as dopants to replace H_3PO_4 that exhibit higher acid retention; however the proton conductivities of these membranes are too low for practical applications.[32] An alternative method to eliminate the need for water in the membrane is to replace water with heterocyclic amines such as imidazole and benzimidazole.[33] This has been shown to lead to proton conductivities comparable to hydrated polymers at temperatures between 150 and 250°C.[30] However, the volatility of the heterocyclic liquids prevents them from being used in actual fuel cell systems. This can be circumvented by immobilizing the imidazole through direct incorporation into the polymer backbone. In this manner, long-range proton transport requires intermolecular proton transfer events only, and appropriate tethering ensures that the heterocyclic groups can aggregate allowing for proton transfer.[30]

1.2 Proton Transfer Properties

Proton transfer and transport in aqueous systems play fundamental roles in many chemical and biological systems and processes.[4, 34-36] The transport of protons through the aqueous domain of the ionomer membrane is the essential feature for functionality of PEM fuel cells. Many studies have shown that protons diffuse through the membrane bearing resemblance to some features observed in bulk water.[35, 37-42] Water and aqueous solutions exhibit unusually high proton mobility. As such, proton transport in aqueous media has been an area of immense research for many years. In bulk water, protons are not isolated species but instead exist as solvated cations, such as a hydronium ion (H_3O^+). The protons

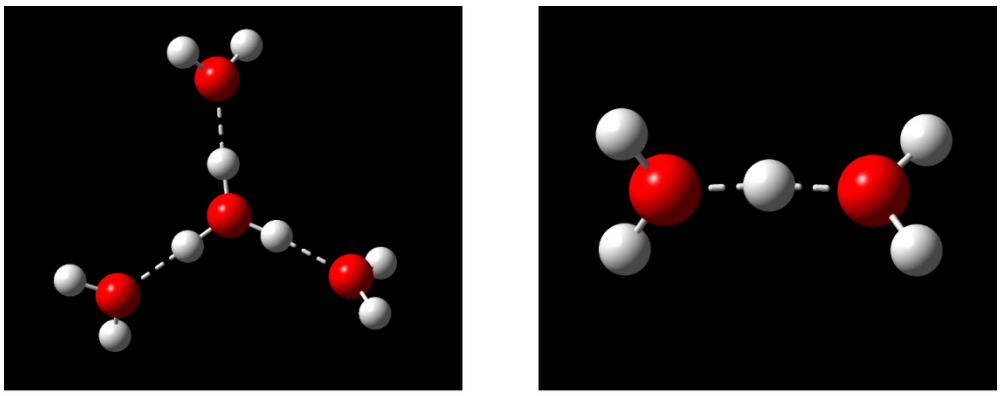

(a) (b)

Figure 1.3. (a) The solvated hydronium ion or Eigen cation ($H_9O_4^+$) and (b) a proton shared between two water molecules termed the Zundel cation ($H_5O_2^+$). Hydrogen bonds are denoted by dashed lines.

can diffuse via translational dynamics as a hydrated cation which is termed vehicular diffusion.[4] Alternatively, the protonic charge can propagate through the hydrogen bond network via successive proton hops from one oxygen site to the next. Amazingly, the basic idea behind proton hopping through 'water wires' was envisioned in 1806 by von Grotthuss when water was believed to be OH and not H_2O.[43] Over a century later, two major complexes were independently proposed to describe the region containing the excess proton: a solvated hydronium ion termed the Eigen cation[44, 45] ($H_9O_4^+$) and a Zundel cation[46] ($H_5O_2^+$) where the excess proton is shared between two water molecules, shown in Figure 1.3a and b, respectively. These complexes were traditionally considered to be mutually exclusive in the explanation of the proton hopping mechanism. However, the current understanding of this process comes from independent Car–Parrinello molecular dynamics (CPMD) simulations[38, 39] and NMR data.[37] The data revealed that this proton conduction mechanism occurs through a series of interconversions between Eigen cations and Zundel cations through changes in the hydrogen bond pattern without net motion of the cation itself, this type of mechanism is known as the 'Grotthuss mechanism' or 'structural diffusion' and is schematically shown in Figure 1.4. An underlying feature of this mechanism is the concept of 'presolvation' where the proton accepting species must first exhibit a coordination structure that corresponds to the species it will transform into upon

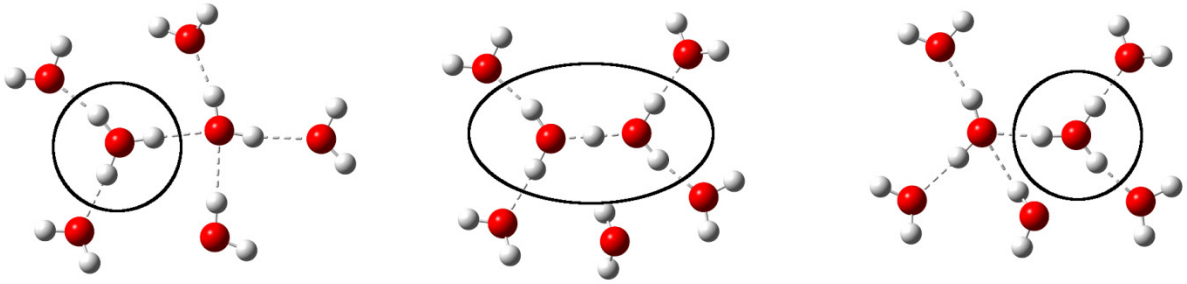

Figure 1.4. Schematic representation of the mechanism of structural diffusion of an excess proton in water going from (a) and Eigen cation to (b) a Zundel cation to (c) an Eigen cation.

the proton transfer reaction.[35, 47, 48] In bulk water this corresponds to the breaking of a hydrogen bond between a four-fold coordinated water molecule in the first solvation shell of the central hydronium ion in $H_9O_4^+$ and a water molecule in the second solvation shell reducing the coordination number of the proton receiving water molecules to three. This results in the proton receiving water molecule having a coordination pattern similar to $H_9O_4^+$ and proton transfer can occur through the interconversion process mentioned above. Proton transfer, thus, requires dynamical changes in the hydrogen bond network beyond the first hydration shell.[37, 38, 40, 41, 48-50]

The mechanisms of proton conduction in bulk water provide a framework for understanding proton transport in PEMs. However, the transport of protons in a hydrated PEM ionomer is considerably more complicated due to the heterogeneous nature of the polymer and the nanoconfinement of the water around the acid groups and hydrated protons. Nevertheless, the water-based proton conduction mechanisms have also been studied on proton-conducting PFSA membranes. Currently available PFSA materials must be sufficiently hydrated to conduct protons at high rates as the presence of water plays a critical role in the formation of free protonic charge carriers and overall proton mobility in these materials. When hydrated, these ionomers phase separate into hydrophilic and hydrophobic domains through solvation and subsequent aggregation of the sulfonic acid groups.[4, 30, 51] This leads to proton dissociation from the sulfonic acid groups into the

aqueous domain allowing for long-range proton transport through the membrane[4, 52] by means of both vehicular and structural diffusion[43, 53-56] with mechanisms and rates bearing characteristics comparable to those observed in bulk water.[35, 37-41] A complete understanding of this requires insight into the formation and breaking of hydrogen bonds in highly complex systems. As there are few experimental techniques that can achieve this level of resolution, *ab initio* (i.e. from first principles of quantum mechanics) molecular modeling techniques have been extensively employed in attempts to uncover the fundamental characteristics of proton transfer properties in these materials.

Proton dissociation and subsequent separation from the acid groups is a fundamental component of proton transfer in PEMS. As such, a great deal of work has focused on how these properties are influenced by the hydrogen bond structure and water content, particularly at low hydration levels where interactions between water molecules and the acidic groups dominate. The water content in PEMs is typically denoted by λ which is defined as the number of water molecules per sulfonic acid group. Due to the significant computational cost of electronic structure calculations, early investigations on PFSA ionomers were limited to small fragments representative of the terminal portion of the side chain, such as triflic acid (CF_3SO_3H), with a single water molecule.[57, 58] Increased computational capabilities allowed for later studies to explore the effects of higher hydration levels on proton dissociation in triflic acid and larger side chain fragments.[59-63] These studies indicated that spontaneous proton dissociation occurred after the addition of three water molecules (i.e. $\lambda = 3$), and that the proton fully separated into the second hydration shell at either $\lambda = 5$ or 6, depending on the study, as shown in Figure 1.5. In addition to PFSA ionomers, electronic structure calculations have been used to explore local hydration and proton dissociation in other fragments of various PEM ionomers and acidic moieties including: aryl main-chain sulfonic acids,[59] sulfonyl imides,[64] imidazole,[65] phosphonic acid,[65, 66] phosphoric acid,[67] and carboxylic acid.[68] Many of the studies also went beyond solely the choice of protogenic group by exploring how the side

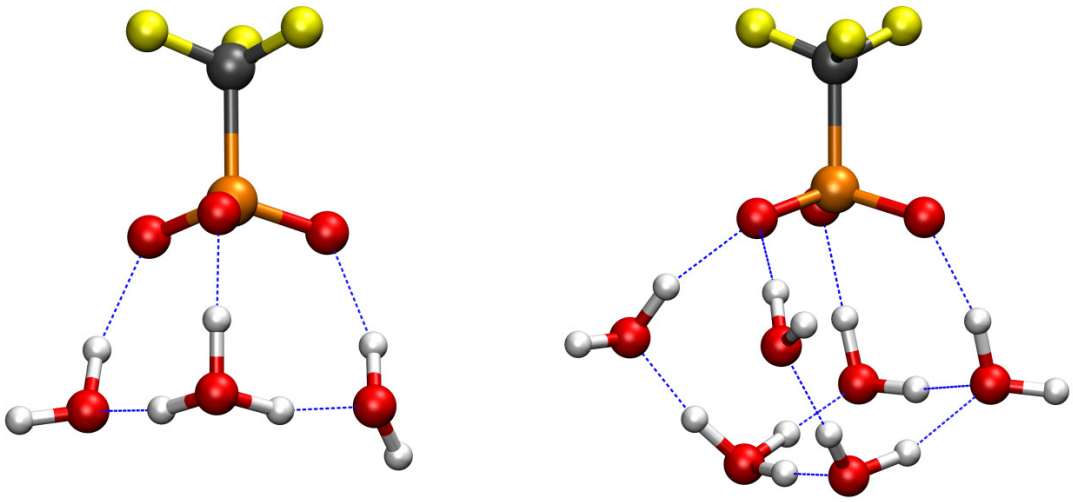

(a) (b)

Figure 1.5. Optimized conformation of triflic acid with the addition of (a) 3 H_2O and (b) 6 H_2O molecules.

chain chemistry governs proton dissociation in a variety of ionomer fragments with different substituent groups.[59, 63, 64, 66] The effects multiple pendant perfluorinated sulfonic acid side chains located on the same PTFE backbone have on local hydration and proton dissociation have also been investigated on the short side chain (SSC) PFSA membrane[69-72] and the 3M PFSA membrane.[73, 74] These studies revealed the importance that protogenic group separation and side chain connectivity through hydrogen bonding have on proton dissociation and the state of the dissociated proton(s) in these materials under conditions of low hydration. Specifically, cooperative interactions between the acidic groups through either direct hydrogen bonds or via a hydrogen bond bridge through a single water molecule or hydronium ion enhanced proton dissociation at hydration levels below $\lambda = 3$. These interactions were observed when the side chains were separated by a small number of CF_2 backbone units and were not present as the side chain separation increased without forcing conformational changes to the backbone indicating there may be some influence on the flexibility of the side chains and backbone on proton dissociation.

Though not technically an *ab initio* technique, empirical valence bond (EVB) schemes[75-77] designed to allow for dynamic proton shuttling have been utilized to study proton mobility and solvation in PFSA systems.[78-81] These simulations revealed that the sulfonate ions can effectively trap hydronium ions from diffusing away preventing full solvation of the hydronium by other water molecules. Instead, structural diffusion was found to be the dominant mechanism for contact ion pair to solvent-separated ion pair transitions important in proton transport. Evidence of structural diffusion has also been observed in *ab initio* molecular dynamics (AIMD) simulations employed to study proton transport in model PFSA systems,[82-88] as well as other PEMs,[89, 90] at various levels of hydration and protogenic group density. The importance of an extended hydrogen bond network in the facilitation of long-range proton transfer was revealed by first principles Car–Parrinello molecular dynamics simulations on hydrates of triflic acid ($CF_3SO_3H(H_2O)_n$, n = 1-3,5).[84, 85] These studies also demonstrated the formation of stable defect structures where a proton is shared between neighboring sulfonic acid groups which promoted formation of a Zundel cation under conditions of limited water. AIMD simulations on proton dynamics in a model Nafion® pore revealed distinctly different hydrogen bond patterns between systems at low and high hydration levels.[83] At higher water content the hydrogen bond network was more continuous which gave rise to structural diffusion that contributed to net proton transport. Proton shuttling was also observed in systems at lower water content. However, the hydrogen bond network was found to be fragmented leading to proton hopping events that shuttled between neighboring water molecules and did not contribute to net diffusion. This is consistent with the observation that structural diffusion is the major contributor to proton conduction a high degrees of hydration, while the vehicular mechanism is more prevalent at low hydration levels due to suppression of intermolecular proton transfer.[4]

1.3 Nanoscale Confinement

Fluids in confined environments exhibit considerably different structural and dynamic properties than those observed in bulk.[91] Water is among the most widely studied confined fluids as it is found in a wide variety of important systems in chemistry, biology, and

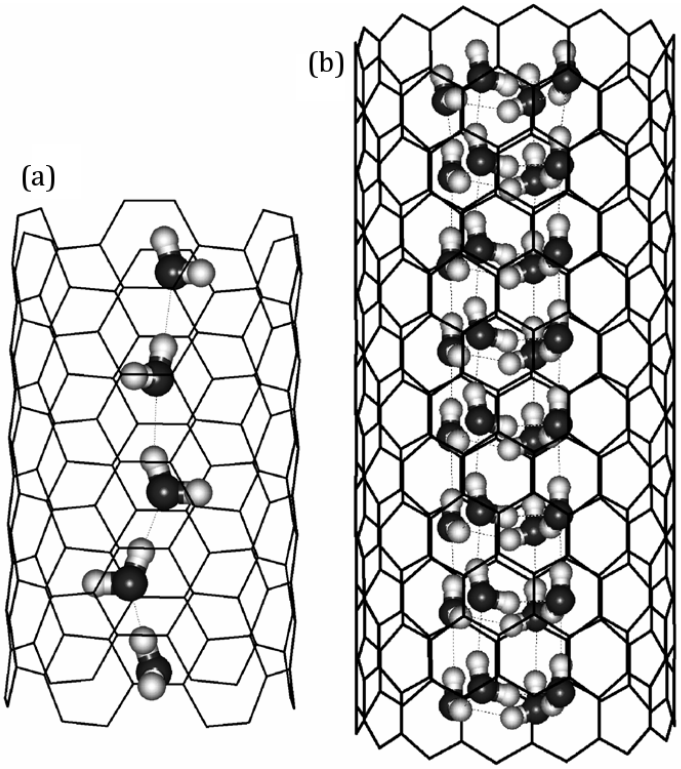

Figure 1.6. A one-dimensional water wire within a narrow CNT of diameter 8.1 Å where each water molecule is involved in two hydrogen bonds; (b) a highly structured multi-layered configuration of water molecules within a CNT of diameter 11.1 Å where each water molecule is involved in four hydrogen bonds.

technological applications, including PEMs.[92, 93] When water is confined, there is a conflict between the optimal hydrogen bond network, interactions with the surface, and the fit within the space available.[92] There have been many studies on water confined in a variety of environments including fullerenes,[94] between graphene sheets,[95] and other nanostructures.[91, 93, 96-101] Carbon nanotubes (CNTs) have also been used to study confinement effects on water.[92, 95, 102-117] While these nanostructures are hydrophobic in bulk water,[118, 119] both simulations[93, 108, 119, 120] and experiments[121-125] have shown that water molecules can readily fill open-ended carbon nanotubes. Deep inelastic neutron scattering experiments revealed that the proton momentum distribution in water confined in CNTs is vastly different from that observed in bulk water indicating a significant impact confinement has on the state of water.[126, 127] The water structure in carbon nanotubes

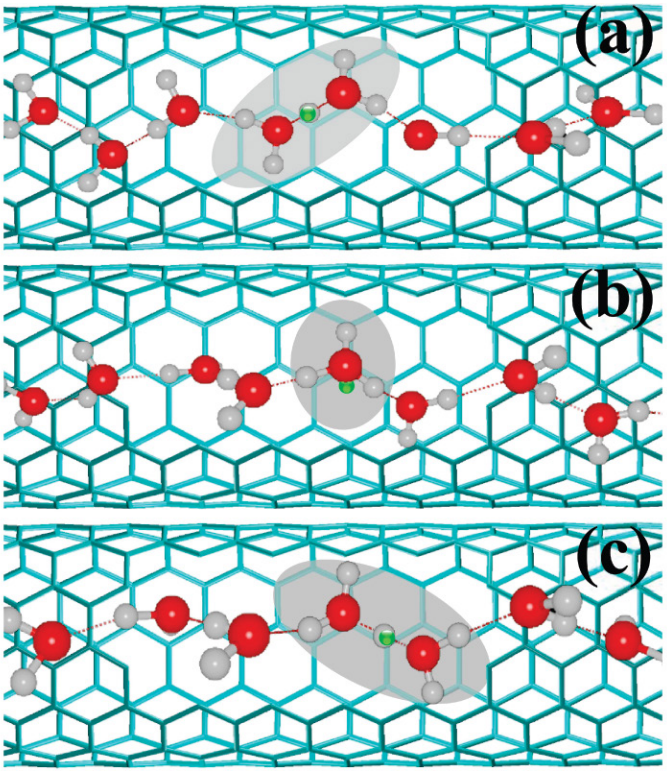

Figure 1.7. Snapshots from a simulation revealing a proton transfer event along a one-dimensional water wire going from (a) a Zundel cation to (b) $H_3O_7^+$ to (c) a Zundel cation.

exhibits a great deal of diversity depending on several properties, including channel diameter.[119] In small diameter CNTs (< 10 Å), simulations reveal that the water molecules inside the tube exhibit a one-dimensional, single-file hydrogen bonding pattern (Figure 1.6a).[93, 108] With increasing diameter there is a greater region in which the water molecules can access the interior, and a layered, well-structured arrangement of water molecules forms (Figure 1.6b).[92] Though a variety of arrangements has been reported dependent on CNT chirality and simulation parameters, they each exhibit considerably different characteristics than bulk water revealing a solid-like symmetric structure with a liquid-like degree of hydrogen bonding.[128] The nature of the surfaces between which the water is confined may also have an effect on the properties of water, and the exact nature of the surface–water interaction has been shown to be important.[120] Simulations have revealed that even slight changes in the carbon–water interaction parameters considerably

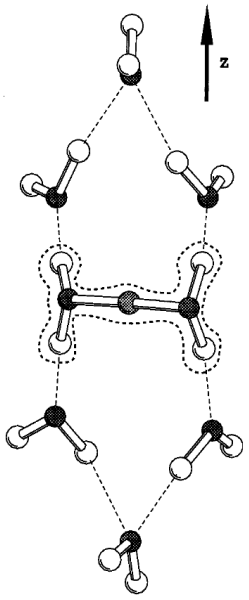

Figure 1.8. An example of a configuration of water inside a narrow CNT that impedes proton transfer. The solvated Zundel cation in the center lies perpendicular to the CNT axis.

affect the results.[120] Furthermore, water molecules near the CNT walls can potentially hydrogen bond to it depending on the surface composition which also affects the structural and dynamical properties.[92]

The structure of water formed within confined hydrophobic surfaces offers an effective proton-conducting medium, especially in the one-dimensional water wires.[93] Proton transport, both in bulk water and in PEM membranes, is highly dependent on the structural dynamics of hydrogen bonding. Water absorbed in PEM membranes experiences a high degree of confinement with a range of environments. The highly aligned structure of confined water allows for rapid proton transport via the Grotthuss mechanism. Molecular dynamics simulations have shown that the proton conductivity in the confined environment of a very narrow CNT can exceed that of bulk water by over an order of magnitude.[129] The rationale behind the increased proton conductivity is the formation of quasi-one dimensional water wires where proton transfer is essentially a local hopping event that does not require hydrogen bond rearrangements beyond the first solvation shell. This has been shown to resemble a 'Zundel–Zundel' mechanism with an intermediate state

of $H_7O_3^+$, as shown in Figure 1.7.[110] With increasing diameter, however, the hydrogen bonding becomes more three dimensional in nature allowing for the formation of Eigen cations and the protons no longer are restricted to transfer solely along the CNT axis. This also allows for certain configurations to be formed that impede proton transfer through the CNT, such as proton transfer perpendicular to the tube axis shown in Figure 1.8.[130] This suggests that proton conductivity in CNTs is highly dependent on the influence the geometric confinement has on the hydrogen bonding.

As previously mentioned, PFSA membranes phase separate into hydrophobic domains containing the PTFE backbone and hydrophilic domains that contain the acidic side chains, water molecules, and protons.[30] This phase separation occurs at the nanometer scale and is influenced by the amount of absorbed water and the specific ionomer chemistry.[52, 131] An immense amount of research has focused on the structure of these domains and their influence on proton mobility. While a number of models have been proposed for their shape and dependency on water content,[132-136] a precise understanding of the nature of these domains remains to be elucidated. As such, the structural and dynamical properties are typically probed though simulations using simple, model systems. Simulations on transport properties and confinement effects in PEMs have been performed in idealized cylindrical and slab-like pores.[83, 86, 87, 137, 138] Similar to proton transport in water confined in CNTs, the effects of the confined environment and dimensions on proton transport and hydrogen bonding in PEMs can be studied. However, proton and water transport in PEMs has increased complexity due to the presence of the acidic groups.

AIMD simulations have been performed on model sulfonated perfluoroalkane pores of different diameters (~17.0 and 20.6 Å) but with the same accessible surface area containing four sulfonic acid groups at hydration levels from $\lambda = 2.5 - 4.5$.[138] It was found that near complete dissociation occurred in the narrower pore at the lowest hydration level which was not the case in the wider channel. This was attributed to a more uniform solvation of the sulfonic acid groups by the water molecules in the narrow channel due to shorter sulfonic acid group separation and less free volume for the water to occupy. The

protons in narrow channels also had a greater propensity to form Zundel cations and exhibit structural diffusion at the highest hydration level resulting in greater overall proton mobility even with the higher sulfonate group density. Isolated clustering of the water molecules around individual sulfonic acid groups was observed in the larger pore at all hydration levels. This led to the formation of trapped hydronium ion–sulfonate group contact ion pairs with little evidence of Grotthuss shuttling and overall lower mobility.[138] Other studies have used CNTs functionalized with $-CF_2SO_3H$ groups to explore the factors that contribute to proton dynamics in a confined environment using AIMD.[86, 87, 137] While true PFSA membranes are considerably less homogeneous than the well-structured CNTs, the use of CNTs provided an idealized model for investigation on the channel size and environment, the spacing of acid groups, and the hydration level on proton transport properties. Three different diameter CNTs (11.2, 13.2, and 14.1 Å) were chosen to explore the effect of nanoscale confinement. Furthermore, the inner walls of the CNT were either left bare to provide a delocalized negative charge or functionalized with fluorine atoms to provide a localized negative charge to investigate the influence of different hydrophobic surfaces. As with the study mentioned above, the systems with less separation between sulfonic acid groups led to a greater propensity for proton dissociation and increasing the distance between sulfonic acid groups led to less hydrogen bond connectivity where the water molecules formed isolated clusters around the sulfonate groups.[137] However, shorter sulfonic acid group separation here led to an increase in 'trap states' that hinder proton mobility which may be influenced by the greater confinement within the CNTs.[86] When the CNT walls were fluorinated, the fluorine atoms provided a localized negative charge that could accept weak hydrogen bonds from water molecules and hydrated cations which increased proton dissociation and stabilized the hydrogen bond network.[87] The effects of nanoscale confinement were found to be most pronounced in the smallest diameter CNTs indicating that only slight increases in the channel diameter can influence the hydrogen bonding and proton mobility in these systems.[137]**Equation Section 2**

1.4 Research Overview

The body of work encompassing this dissertation focuses primarily on probing structural and dynamical properties of PEMs and nanoconfined fluids via *ab initio* molecular modeling techniques. Electronic structure calculations were performed to study the impact side chain length in PFSA ionomers has on conformational freedom (flexibility) as well as the dependence on the level of theory used on the determined properties. Calculations were also performed to study the roles local hydration, side chain separation, and hydrogen bond connectivity have on proton dissociation and the energetics of proton transfer in fragments of the 3M PFSA membrane containing two pendant side chains with different separation along a PTFE backbone. Similar work was carried out on single side chain fragments of the 3M MASC ionomers to study the influence of protogenic group separation and side chain chemistry on proton dissociation and transfer. *Ab initio* molecular dynamics simulations were used to explore confinement effects on water, slightly acidic water, and aqueous triflic acid using single-walled CNTs with diameters ranging from 11 – 14 Å as confinement vessels. The influence of the nature of the confined surface on hydrogen bonding and proton transfer properties was also studied by comparing systems with bare or fluorinated inner CNT walls. The following section outlines the theoretical background of the methods used which is followed by the results of these studies.

Chapter 2 Theoretical Background

2.1 *Ab initio* Electronic Structure

The properties of a system in quantum mechanics are entirely described by a function of the particles' coordinates known as the wave function. Associated with every measurable property in a system is a quantum mechanical operator which, when operating upon the wave function, will yield the observable value times the wave function.[139, 140] For example, the Schrödinger equation is an eigenvalue equation for the Hamiltonian (energy) operator whose eigenvalue provides the total energy, *E*, of the system. *Ab initio* electronic structure theory aims to obtain solutions to the time-independent Schrödinger equation:

$$\hat{\mathcal{H}}(\mathbf{r},\mathbf{R})\psi(\mathbf{r},\mathbf{R}) = E\psi(\mathbf{r},\mathbf{R}) \tag{2.1}$$

where the time independent many-body molecular wave function, $\psi(\mathbf{r},\mathbf{R})$, is explicitly dependent on the 3*N* coordinates of all *N* electrons, $\mathbf{r} \equiv \{\mathbf{r}_i\}$, and the coordinates of all nuclei, $\mathbf{R} \equiv \{\mathbf{R}_I\}$. The molecular Hamiltonian, $\hat{\mathcal{H}}(\mathbf{r},\mathbf{R})$, is an operator which consists of the kinetic energy of all electrons and nuclei and the potential energy due to electron-nuclear attraction, electron-electron repulsion, and nuclear-nuclear repulsion. In atomic units, it is of the form

$$\hat{\mathcal{H}}(\mathbf{r},\mathbf{R}) = -\frac{1}{2}\sum_i \nabla_i^2 - \sum_I \frac{1}{2M_I}\nabla_I^2 - \sum_i \sum_I \frac{Z_I}{|\mathbf{r}_i - \mathbf{R}_I|} + \sum_j \sum_{i>j} \frac{1}{|\mathbf{r}_i - \mathbf{r}_j|} + \sum_I \sum_{J>I} \frac{Z_I Z_J}{|\mathbf{R}_I - \mathbf{R}_J|} \tag{2.2}$$

where *i* and *j* refer to electrons, *I* and *J* refer to nuclei, M_I is the ratio of the mass of nucleus *I* to the mass of an electron, and Z_I and Z_J are the atomic numbers of the nuclei. In principle, Equation 2.1 can be solved to yield the energy and molecular wave function for any quantum system. The wave function itself has no direct physical analog or connection to experiment; however, the square of the wave function $|\psi|^2$ represents the particle probability density with the normalization condition

$$\int_{-\infty}^{\infty}\int_{-\infty}^{\infty}\cdots\int_{-\infty}^{\infty}\int_{-\infty}^{\infty}\psi(\mathbf{r},\mathbf{R})^{*}\psi(\mathbf{r},\mathbf{R})d\mathbf{r}d\mathbf{R}=\int|\psi|^{2}d\tau=1 \tag{2.3}$$

where $\int d\tau$ denotes integration over the full range of all the coordinates in the system.

The Hamiltonian for a system of electrons and nuclei (Equation 2.2) is exceedingly complex due to the interdependency of nuclear and electronic motion. Fortunately, an approximation exists that greatly simplifies this aspect of solving the Schrödinger equation. It rests on the fact that the electrons move much faster than the nuclei due to their greatly smaller mass, and the electrons can be thought to respond instantaneously to the nuclear coordinates. Classically this implies that the change in the nuclear configuration is negligible during the time cycle of electron motion; thus the nuclei can be regarded as fixed as the electrons carry out their motion. This is the Born–Oppenheimer (BO) or adiabatic approximation,[141] which allows for removal of the nuclear kinetic energy term in Equation 2.2, and the electron-nuclear attraction becomes only parametrically dependent on the 'fixed' nuclear positions. The Schrödinger equation for electronic motion then becomes

$$\left(\hat{\mathcal{H}}_{el}+V_{NN}\right)\psi_{el}=U\psi_{el}\,. \tag{2.4}$$

Here, ψ_{el} is the electronic wave function, U is the electronic energy including nuclear repulsion, and the electronic Hamiltonian, $\hat{\mathcal{H}}_{el}$, and nuclear-repulsion, V_{NN}, terms are given by

$$\hat{\mathcal{H}}_{el}(\mathbf{r};\mathbf{R})=-\frac{1}{2}\sum_{i}\nabla_{i}^{2}-\sum_{i}\sum_{I}\frac{Z_{I}}{|\mathbf{r}_{i}-\mathbf{R}_{I}|}+\sum_{j}\sum_{i>j}\frac{1}{|\mathbf{r}_{i}-\mathbf{r}_{j}|} \tag{2.5}$$

$$V_{NN}(\mathbf{R})=\sum_{I}\sum_{J>I}\frac{Z_{I}Z_{J}}{|\mathbf{R}_{I}-\mathbf{R}_{J}|}\,. \tag{2.6}$$

The electronic coordinates are the variables in Equation 2.4, and the nuclear coordinates are parameters. The subscript *el* will henceforth be dropped unless necessary. The

electronic energy at each 'fixed' nuclear configuration is the effective potential that the nuclei feel, thus solving the electronic Schrödinger equation for various nuclear configurations defines the potential energy surface (PES). From a computational point of view, even with the BO approximation, this partial differential equation containing $3N$ unknowns is impossible to solve explicitly (beyond the case of the hydrogen atom). This has led to the development of additional methods and approximations aiming to reduce the complexity of the problem.

Several methods make use of the variational principle which states that the ground state energy, E_0, is always less than or equal to the energy determined with a trial wave function, ψ_{trial}, i.e.,

$$\frac{\int \psi_{trial}^{*} \hat{\mathcal{H}} \psi_{trial} d\tau}{\int \psi_{trial}^{*} \psi_{trial} d\tau} = E_{trial} \geq E_0 . \tag{2.7}$$

The energy from any trial wave function is always an upper bound to the ground state energy unless the wave function is exact. Thus, by minimizing E_{trial} by varying the trial wave function, an approximation for the ground state energy and wave function can be obtained.

2.1.1 Hartree–Fock Method

The electron-electron repulsion term in Equation 2.5 makes it impossible to separate the Schrödinger equation into single-electron equations preventing an analytic solution for any multi-electron system. However, if the electrons were independent, then the Hamiltonian could be broken into single-electron Hamiltonians, and the wave function would be a product of individual electron wave functions (spatial orbitals), $\phi_i(\mathbf{r}_i)$, called a Hartree product

$$\psi^{HP}(\mathbf{r}_1, \mathbf{r}_2 ..., \mathbf{r}_N) = \phi_1(\mathbf{r}_1)\phi_2(\mathbf{r}_2)\cdots\phi_N(\mathbf{r}_N). \tag{2.8}$$

This form of the wave function, however, does not include the spin coordinate associated

with electrons and does not satisfy the antisymmetry principle (Pauli principle), which states that the wave function describing fermions must be antisymmetric with respect to interchange of space-spin coordinates between any two particles. Spin is included by introducing a generic α or β spin function, $\sigma(\omega)$, with spin variable, ω. The product of a spatial orbital and a spin function yields what is known as a spin orbital, $\chi(\mathbf{x}) \equiv \phi(\mathbf{r})\sigma(\omega)$, with the set of space-spin coordinates, $\mathbf{x} \equiv \{\mathbf{r}, \omega\}$, including the spatial and spin coordinates for the electrons. Although spin has now been accounted for, replacing the spatial orbitals of Equation 2.8 with spin orbitals still results in a wave function that does not satisfy the antisymmetry principle. This is overcome by the use of Slater determinants.

The trial wave function cast as a Slater determinant of orthonormal one-electron spin orbitals takes the form

$$\psi^{SD}(\mathbf{x}_1, \mathbf{x}_2, \ldots, \mathbf{x}_N) = \frac{1}{\sqrt{N!}} \begin{vmatrix} \chi_1(\mathbf{x}_1) & \chi_2(\mathbf{x}_1) & \cdots & \chi_N(\mathbf{x}_1) \\ \chi_1(\mathbf{x}_2) & \chi_2(\mathbf{x}_2) & \cdots & \chi_N(\mathbf{x}_2) \\ \vdots & \vdots & \ddots & \vdots \\ \chi_1(\mathbf{x}_N) & \chi_2(\mathbf{x}_N) & \cdots & \chi_N(\mathbf{x}_N) \end{vmatrix} \tag{2.9}$$

where the $1/\sqrt{N!}$ term ensures normalization of the wave function. The mathematical properties of the Slater determinant inherently satisfy the antisymmetry requirement and the Pauli exclusion principle. Specifically, for the former, interchanging the space-spin coordinates of two electrons (i.e., swapping two rows of Equation 2.9) changes the sign of the determinant. For the latter, if two electrons were occupying the same spin orbital, two rows would be equal, and the value of the determinant would be zero (i.e., the probability of this happening is zero).

The Slater determinant is a summation of the *N*! permutations of arranging the electrons into the different spin orbitals, whose terms are multiplied by ±1 depending on the parity of the permutation. This allows for a simplified notation for the Slater determinant by use of the antisymmetrizer, $\hat{\mathcal{A}}$, defined by

$$\hat{\mathcal{A}} = \frac{1}{\sqrt{N!}} \sum_{p} (-1)^{\mu(p)} \hat{\mathcal{P}}_p \tag{2.10}$$

where the summation is over all p permutations carried out by the permutation operator, $\hat{\mathcal{P}}$, and $\mu(p)$ is the parity of the permutation, which is the least number of interchanges needed to put the permuted indices back into the original order. The antisymmetrizer is an hermitian operator ($\hat{\mathcal{A}} = \hat{\mathcal{A}}^{\dagger}$) that commutes with the Hamiltonian ($\hat{\mathcal{A}}\hat{\mathcal{H}} = \hat{\mathcal{H}}\hat{\mathcal{A}}$) and its square is proportional to itself, $\hat{\mathcal{A}}^2 = \sqrt{N!}\,\hat{\mathcal{A}}$. The summation in Equation 2.10 carries out all possible one-electron, two-electon,..., *N*-electron permutations, and can be expanded as

$$\sum_{p} (-1)^{\mu(p)} \hat{\mathcal{P}}_p = 1 - \sum_{ij} \hat{\mathcal{P}}_{ij} + \sum_{ijk} \hat{\mathcal{P}}_{ijk} - \cdots \tag{2.11}$$

For a system of *N* electrons, the trial Hartree–Fock wave function in Equation 2.9 can now be written as

$$\psi^{SD} = \hat{\mathcal{A}} \left(\prod_{i=1}^{N} \chi_i(\mathbf{x}_i) \right) = \hat{\mathcal{A}} \prod_{i=1}^{N} \chi_i(i). \tag{2.12}$$

Having the functional form of the Hartree–Fock wave function, the next step is to simplify the Hamiltonian in Equation 2.5 into a more compact form with a one-electron operator, $\hat{f}_i$, dependent only on the coordinates of particle *i* and a two-electron operator, $\hat{v}_{ij}$,

$$\hat{f}_i = -\frac{1}{2}\nabla_i^2 - \sum_{I} \frac{Z_I}{|\mathbf{r}_i - \mathbf{R}_I|} \tag{2.13}$$

$$\hat{v}_{ij} = \frac{1}{|\mathbf{r}_i - \mathbf{r}_j|}. \tag{2.14}$$

The Hamiltonian can now be written as

$$\hat{\mathcal{H}}_{el} = \sum_{i} \hat{f}_i + \sum_{i} \sum_{j>i} \hat{v}_{ij}\,. \tag{2.15}$$

Dirac 'bra-ket' notation will be used for the remainder of this discussion where integration over all coordinates is denoted by closed brackets; for example,

$$E = \frac{\int \psi^* \hat{\mathcal{H}} \psi \, d\tau}{\int \psi^* \psi \, d\tau} = \frac{\langle \psi | \hat{\mathcal{H}} | \psi \rangle}{\langle \psi | \psi \rangle} \tag{2.16}$$

and for orthonormal wave functions

$$\int \psi_i^* \psi_j d\tau = \langle \psi_i | \psi_j \rangle = \delta_{ij} \qquad \delta_{ij} \equiv \begin{cases} 0 \text{ for i} \neq \text{j} \\ 1 \text{ for i} = \text{j} \end{cases}. \tag{2.17}$$

Assuming that the wave function is normalized, the Hartree–Fock energy can be determined via

$$E^{HF} = \langle \psi^{SD} | \hat{\mathcal{H}}_{el} + V_{NN} | \psi^{SD} \rangle = \langle \psi^{SD} | \sum_i \hat{f}_i | \psi^{SD} \rangle + \langle \psi^{SD} | \sum_i \sum_{j>i} \hat{v}_{ij} | \psi^{SD} \rangle + V_{NN} . \tag{2.18}$$

The nuclear repulsion term does not depend on the electron coordinates and can immediately be integrated out to yield a constant; this term can be ignored for now and added in later. Substituting the wave function in Equation 2.12 into Equation 2.18 and using the aforementioned properties of the antisymmetrizer yields

$$\begin{aligned} \langle \psi^{SD} | \hat{\mathcal{H}}_{el} | \psi^{SD} \rangle &= \left\langle \hat{\mathcal{A}} \prod_{j=1}^{N} \chi_j(j) \middle| \hat{\mathcal{H}}_{el} \middle| \hat{\mathcal{A}} \prod_{k=1}^{N} \chi_k(k) \right\rangle \\ &= \left\langle \prod_{j=1}^{N} \chi_j(j) \middle| \hat{\mathcal{H}}_{el} \hat{\mathcal{A}}^{\dagger} \middle| \hat{\mathcal{A}} \prod_{k=1}^{N} \chi_k(k) \right\rangle \\ &= \left\langle \prod_{j=1}^{N} \chi_j(j) \middle| \hat{\mathcal{H}}_{el} \middle| \hat{\mathcal{A}}^2 \prod_{k=1}^{N} \chi_k(k) \right\rangle \\ &= \sum_{p=1}^{N!} (-1)^{\mu(p)} \left\langle \prod_{j=1}^{N} \chi_j(j) \middle| \hat{\mathcal{H}}_{el} \middle| \hat{\mathcal{P}}_p \prod_{k=1}^{N} \chi_k(k) \right\rangle \end{aligned} \tag{2.19}$$

For the one-electron operator, the only permutation that yields a non-zero result is the

identity permutation as any others would lead to a $\left\langle \chi_j \middle| \chi_k \right\rangle_{j\neq k} = 0$ term in the product due to orthonormal spin orbitals. For arbitrary electron *i* this results in

$$\begin{aligned}\sum_{p=1}^{N!}(-1)^{\mu(p)}\left\langle \prod_{j=1}^{N}\chi_j(j)\middle|\hat{f}_i\middle|\hat{\mathcal{P}}_p\prod_{k=1}^{N}\chi_k(k)\right\rangle &= \left\langle \chi_i(i)\middle|\hat{f}_i\middle|\chi_i(i)\right\rangle\prod_{\substack{j=1\\ j\neq i}}^{N}\left\langle \chi_j(j)\middle|\chi_j(j)\right\rangle \\ &= \left\langle \chi_i(i)\middle|\hat{f}_i\middle|\chi_i(i)\right\rangle = f_{ii}\end{aligned} . \qquad (2.20)$$

The two electron operator, $\hat{v}_{ij}$, only acts on the coordinates of electrons *i* and *j*, and only the identity permutation and the permutation $\hat{\mathcal{P}}_{ij}$ have non-zero contributions. Considering arbitrary electrons *i* and *j*,

$$\sum_{p=1}^{N!}(-1)^{\mu(p)}\left\langle \prod_{k=1}^{N}\chi_k(k)\middle|\hat{v}_{ij}\middle|\hat{\mathcal{P}}_p\prod_{n=1}^{N}\chi_n(n)\right\rangle = \left\langle \prod_{k=1}^{N}\chi_k(k)\middle|\hat{v}_{ij}\middle|\left(1-\hat{\mathcal{P}}_{ij}\right)\prod_{n=1}^{N}\chi_n(n)\right\rangle. \qquad (2.21)$$

The term associated with the identity permutation for electrons *i* and *j* is

$$\begin{aligned}\left\langle \prod_{k=1}^{N}\chi_k(k)\middle|\hat{v}_{ij}\middle|\prod_{n=1}^{N}\chi_n(n)\right\rangle &= \left\langle \chi_i(i)\chi_j(j)\middle|\hat{v}_{ij}\middle|\chi_i(i)\chi_j(j)\right\rangle\prod_{\substack{k=1\\ k\neq i,j}}^{N}\left\langle \chi_k(k)\middle|\chi_k(k)\right\rangle \\ &= \left\langle \chi_i(i)\chi_j(j)\middle|\hat{v}_{ij}\middle|\chi_i(i)\chi_j(j)\right\rangle = J_{ij}\end{aligned} \qquad (2.22)$$

and is termed the Coulomb integral because it represents the electrostatic energy of repulsion between two electrons with probability densities $|\chi_i|^2$ and $|\chi_j|^2$. The term arising from the $\hat{\mathcal{P}}_{ij}$ operator is

$$\begin{aligned}\left\langle \prod_{k=1}^{N}\chi_k(k)\middle|\hat{v}_{ij}\middle|-\hat{\mathcal{P}}_{ij}\prod_{n=1}^{N}\chi_n(n)\right\rangle &= \left\langle \chi_i(i)\chi_j(j)\middle|\hat{v}_{ij}\middle|\chi_j(i)\chi_i(j)\right\rangle\prod_{\substack{k=1\\ k\neq i,j}}^{N}\left\langle \chi_k(k)\middle|\chi_k(k)\right\rangle \\ &= \left\langle \chi_i(i)\chi_j(j)\middle|\hat{v}_{ij}\middle|\chi_j(i)\chi_i(j)\right\rangle = K_{ij}\end{aligned} \qquad (2.23)$$

which is the exchange integral. This term has no classical analog and is a consequence of the antisymmetry property of the wave function. Note, the integration variables labeled (*i*)

and (j) are dummy variables and will, as a convention, either be suppressed or replaced when needed with the coordinates of electron 1 and 2 in the one- and two-electron integrals and the corresponding operators. The energy can now be written as (omitting the nuclear-nuclear repulsion)

$$E^{HF} = \sum_{i=1}^{N} f_{ii} + \frac{1}{2}\sum_{i,j=1}^{N}\left(J_{ij} - K_{ij}\right). \tag{2.24}$$

The Hartree–Fock method applies the variational principle to determine the spin orbitals that minimize the energy. To apply this, the Coulomb and exchange integrals are written as operators in the energy expression such that

$$\hat{J}_i(1)\left|\chi_j(2)\right\rangle = \left\langle\chi_i(1)\left|\hat{v}_{12}\right|\chi_i(1)\right\rangle\chi_j(2)\rangle \tag{2.25}$$

$$\hat{K}_i(1)\left|\chi_j(2)\right\rangle = \left\langle\chi_i(1)\left|\hat{v}_{12}\right|\chi_j(1)\right\rangle\chi_i(2)\rangle \tag{2.26}$$

$$E^{HF} = \sum_{i}^{N}\left\langle\chi_i\left|\hat{f}_1\right|\chi_i\right\rangle + \frac{1}{2}\sum_{i,j}^{N}\left(\left\langle\chi_j\left|\hat{J}_i\right|\chi_j\right\rangle - \left\langle\chi_j\left|\hat{K}_i\right|\chi_j\right\rangle\right) + V_{NN}. \tag{2.27}$$

Equation 2.27 can now be minimized using the Lagrange method of undetermined multipliers under the constraint of orthonormal orbitals.

$$\mathcal{L} = E^{HF} - \sum_{i,j}^{N}\lambda_{ij}\left(\left\langle\chi_i\left|\chi_j\right\rangle - \delta_{ij}\right)\right. \tag{2.28}$$

$$\delta\mathcal{L} = \delta E^{HF} - \sum_{i,j}^{N}\left(\left\langle\delta\chi_i\left|\chi_j\right\rangle + \left\langle\chi_i\left|\delta\chi_j\right\rangle\right)\right. = 0 \tag{2.29}$$

Substituting Equation 2.27 into Equation 2.29, after some algebra and rearranging yields

$$\begin{aligned}\delta\mathcal{L} &= \sum_{i}^{N}\left\langle\delta\chi_i(1)\right|\left[\hat{f}_1\left|\chi_i(1)\right\rangle + \sum_{j}^{N}\left(\hat{J}_j(1) - \hat{K}_j(1)\right)\left|\chi_i(1)\right\rangle - \sum_{j}^{N}\lambda_{ij}\left|\chi_j(1)\right\rangle\right] + c.c. \\ &= \sum_{i}^{N}\left\langle\delta\chi_i(1)\right|\left[\hat{\mathcal{F}}(1)\left|\chi_i(1)\right\rangle - \sum_{j}^{N}\lambda_{ij}\left|\chi_j(1)\right\rangle\right] + c.c = 0\end{aligned} \tag{2.30}$$

where *c.c.* denotes the complex conjugate and $\hat{F}$ is the Fock operator, $\hat{\mathcal{F}} = \hat{f}_1 + \sum_j \left(\hat{J}_j - \hat{K}_j \right)$.

The variation in the orbital, $\delta\chi_i$, is completely arbitrary, so in order for the equation to always equal zero, the term in brackets must be zero for all values of *i*. Hence,

$$\hat{\mathcal{F}}(1)\chi_i(1) = \sum_j^N \lambda_{ij}\chi_j(1). \tag{2.31}$$

The Slater determinant wave function is invariant to any unitary transformation of spin orbitals, and Equation 2.31 can be simplified by choosing a transformation that diagonalizes the matrix of Lagrange multipliers (i.e., $\lambda_{ij} = 0$ and $\lambda_{ii} = \varepsilon_i$). This leads to the canonical Hartree–Fock equations[142, 143]

$$\hat{\mathcal{F}}(1)\chi_i'(1) = \varepsilon_i'\chi_i'(1). \tag{2.32}$$

Taking the sum over the occupied "orbital energies" and dropping the primes yields

$$\sum_i \varepsilon_i = \sum_i \left\{ f_{ii} + \sum_j \left(J_{ij} - K_{ij} \right) \right\} \tag{2.33}$$

which is not the same as the total energy from Equation 2.24. Hence, the total energy is not the sum of the individual "orbital energies" due to double counting of the Coulomb minus exchange energies. Solving for f_{ii} in Equation 2.33 and substituting into Equation 2.24 gives for the total Hartree–Fock energy

$$E^{HF} = \sum_i \varepsilon_i - \frac{1}{2}\sum_i \sum_j \left(J_{ij} - K_{ij} \right), \tag{2.34}$$

which for a closed-shell system where all occupied orbitals contain two electrons has the form

$$E^{HF} = 2\sum_{i=1}^{N/2} \varepsilon_i - \sum_i^{N/2} \sum_j^{N/2} \left(2J_{ij} - K_{ij} \right). \tag{2.35}$$

The Fock operator is a one electron operator where each electron moves in an average field of all other electrons arising from the Coulomb and exchange operators. It is, therefore, a mean-field approach to the many-body problem which neglects electron correlation. Since the Fock operator both operates on the orbitals and is dependent on the set of orbitals, each orbital Fock operator can only be determined if all of the other occupied orbitals are known. This necessitates iterative methods for solving the Hartree–Fock equations with an initial guess of the orbitals. These orbitals are used to construct the Fock operator which generates a new set of orbitals and the procedure is repeated until self-consistency is reached. The orbitals that are a solution to the Hartree–Fock equations are commonly referred to as self-consistent field (SCF) orbitals. In practice, numerical solutions are typically obtained by approximating the unknown orbitals as a linear expansion of *M* known basis functions, φ_k,

$$\chi_i' = \sum_k^M c_{ik}\varphi_k \tag{2.36}$$

where the c_{ik} are expansion coefficients to be determined. The basis functions are commonly atomic orbital functions centered on atoms, and this technique is referred to as the linear combination of atomic orbitals (LCAO) approximation. Substituting Equation 2.36 into the canonical Hartree–Fock equation, left multiplying by φ_υ^* and integrating gives

$$\sum_k^M c_{ik} \underbrace{\left\langle \varphi_\upsilon \middle| \hat{\mathcal{F}}(1) \middle| \varphi_k \right\rangle}_{\equiv F_{\upsilon k}} = \varepsilon_i \sum_k^M c_{ik} \underbrace{\left\langle \varphi_\upsilon \middle| \varphi_k \right\rangle}_{\equiv S_{\upsilon k}} \tag{2.37}$$

$$\mathbf{FC} = \mathbf{SC}\varepsilon \tag{2.38}$$

where **F**, **C**, and **S** are the Fock, coefficient, and basis function overlap matrices and ε is a diagonal matrix of the orbital energies. The Hartree–Fock equations cast in matrix form under the LCAO approximation are the Hartree–Fock–Roothaan equations. Introducing the finite set of basis functions reforms the set of coupled integro-differential equations into a generalized matrix eigenvalue equation that is solved self-consistently for the expansion

coefficients.

2.1.2 Post Hartree–Fock

The Hartree–Fock approximation is a simplified theory that does not include the details of instantaneous electron–electron correlations. Post-HF methods have been developed to include such correlations including Møller–Plesset perturbation theory[144] and configuration interaction (CI).[145] In Møller–Plesset perturbation theory, the exact Hamiltonian (under the Born–Oppenheimer approximation) is treated as a small perturbation to the sum over single electron Fock operator introduced earlier:

$$\hat{\mathcal{H}} = \sum_{i=1}^{N} \hat{\mathcal{F}}_i + \lambda \hat{\mathcal{V}} = \hat{\mathcal{H}}_0 + \lambda \hat{\mathcal{V}} \tag{2.39}$$

where λ is a perturbation parameter and $\hat{\mathcal{V}}$ is the perturbation operator defined by the difference between the exact Hamiltonian (under the Born–Oppenheimer approximation) and $\hat{\mathcal{H}}_0$ above

$$\hat{\mathcal{V}} = \hat{\mathcal{H}} - \hat{\mathcal{H}}_0 = \sum_i \sum_{j>i} \hat{v}_{ij} - \sum_j \sum_n \left[\hat{J}_n(j) - \hat{K}_n(j) \right] \tag{2.40}$$

The perturbed energy and wave function are then written out as a Taylor series expansion in λ, i.e.,

$$\begin{aligned} \left|\psi_i\right\rangle &= \left|\psi_i^{(0)}\right\rangle + \left|\lambda\psi_i^{(1)}\right\rangle + \left|\lambda^2\psi_i^{(2)}\right\rangle + \cdots = \sum_n \left|\lambda^n \psi_i^{(n)}\right\rangle \\ E_i &= E_i^{(0)} + \lambda E_i^{(1)} + \lambda^2 E_i^{(2)} + \cdots = \sum_n \lambda^n E_i^{(n)} \end{aligned} . \tag{2.41}$$

By convention, the perturbed wave function is chosen to be intermediately normalized, i.e., $\left\langle \psi_i^{(0)} \middle| \psi_i \right\rangle = 1$ and $\left\langle \psi_i^{(0)} \middle| \psi_i^{(n)} \right\rangle = 0$. Substitution of the Hamiltonian, the wave function, and the energy expressions into the Schrödinger equation gives

$$\left(\hat{\mathcal{H}} - \lambda\hat{\mathcal{V}}\right) \left| \sum_n \lambda^n \psi_i^{(n)} \right\rangle = \sum_n \lambda^n E_i^{(n)} \left| \sum_n \lambda^n \psi_i^{(n)} \right\rangle . \tag{2.42}$$

Expanding out terms and collecting values in equal powers of λ gives

$$\begin{aligned}
&\lambda^0 : \hat{\mathcal{H}}_0 \left|\psi_i^{(0)}\right\rangle = E_i^{(0)} \left|\psi_i^{(0)}\right\rangle \\
&\lambda^1 : \hat{\mathcal{H}}_0 \left|\psi_i^{(1)}\right\rangle + \hat{\mathcal{V}} \left|\psi_i^{(0)}\right\rangle = E_i^{(0)} \left|\psi_i^{(1)}\right\rangle + E_i^{(1)} \left|\psi_i^{(0)}\right\rangle \\
&\lambda^2 : \hat{\mathcal{H}}_0 \left|\psi_i^{(2)}\right\rangle + \hat{\mathcal{V}} \left|\psi_i^{(1)}\right\rangle = E_i^{(0)} \left|\psi_i^{(2)}\right\rangle + E_i^{(1)} \left|\psi_i^{(1)}\right\rangle + E_i^{(2)} \left|\psi_i^{(0)}\right\rangle
\end{aligned} \tag{2.43}$$

and so forth. Left multiplying by $\left\langle\psi_i^{(0)}\right|$ and using the normalization convention leads to the expressions for the n^{th}-order energies

$$\begin{aligned}
E_i^{(0)} &= \left\langle\psi_i^{(0)}\right| \hat{\mathcal{H}}_0 \left|\psi_i^{(0)}\right\rangle \\
E_i^{(1)} &= \left\langle\psi_i^{(0)}\right| \hat{\mathcal{V}} \left|\psi_i^{(0)}\right\rangle \\
E_i^{(2)} &= \left\langle\psi_i^{(0)}\right| \hat{\mathcal{V}} \left|\psi_i^{(1)}\right\rangle
\end{aligned} \quad . \tag{2.44}$$

CI was not used in this work, so it is only mentioned in passing. The general concept is that electron correlation is treated self-consistently through the assumption that the wave function is a linear combination of excited state determinants generated by exciting orbitals in the reference SCF determinant, Φ_0, from occupied orbitals to unoccupied (virtual) orbitals.

$$\left|\psi\right\rangle = c_0 \left|\Phi_0\right\rangle + \sum_{ra} c_a^r \left|\Phi_a^r\right\rangle + \sum_{\substack{a<b \\ r<s}} c_{ab}^{rs} \left|\Phi_{ab}^{rs}\right\rangle + \cdots \tag{2.45}$$

Here, $\left|\Phi_a^r\right\rangle$ refers to the Slater determinant formed by exciting spin orbital *a* in $\left|\Phi_0\right\rangle$ to unoccupied spin orbital *r*. The expansion coefficients are optimized based on the variational principle. In practice, the expansion of Equation 2.45 must be truncated to some order of excitations. Truncation at the zeroth-order is, of course, the Hartree–Fock method. First-order truncation gives 'configuration interaction with single excitations' (CIS), and second-order gives 'configuration interaction with single and double excitations' (CISD),

and so forth. If all *N*-electron wave functions are taken into account, the calculation is called full configuration interaction (FCI) which is exact within the specified one-electron basis.

2.1.3 Density Functional Theory

A commonly used alternative to the post-Hartree–Fock methods used to account for electron correlation is density functional theory (DFT).[146] DFT provides the framework to determine all the properties of a system through the electron probability density, $\rho(\mathbf{r})$. Unlike the many-electron wave function, which is dependent on 3*N* spatial variables, the electron probability density is a function of only three spatial variables irrespective of the number of electrons for a given set of nuclear positions and is experimentally observable, for instance, via X-ray diffraction. As mentioned earlier, the square of the wave function is a measure of the electron probability density. The total electron density arising from *N* electrons is *N* times the integral of the squared wave function over the spin coordinates of all electrons and over all but one of the spatial coordinates

$$\rho(\mathbf{r}_1) = N\int\cdots\int \left|\psi(\mathbf{x}_1,\mathbf{x}_2,...,\mathbf{x}_N)\right|^2 d\sigma_1 d\mathbf{x}_2\cdots d\mathbf{x}_N . \tag{2.46}$$

This represents the probability of finding any of the *N* electrons with arbitrary spin in volume element $d\mathbf{r}_1$.

Density functional theory relies on two fundamental theorems proposed by Hohenberg and Kohn.[147] The first theorem states that for any system of electrons in an external potential $v_{ext}(\mathbf{r})$, the ground state molecular energy, wave function, and all other molecular electronic properties are uniquely determined by the ground state electron density, $\rho_0(\mathbf{r})$, alone. The ground state electronic energy, E_0, is a functional of the ground state electron density, i.e.,

$$E_0 = E_{v(\mathbf{r})}\left[\rho_0(\mathbf{r})\right] \equiv F^{HK}\left[\rho_0(\mathbf{r})\right] + \int v_{ext}(\mathbf{r})\rho_0(\mathbf{r})d\mathbf{r} \tag{2.47}$$

$$F^{HK}\left[\rho_0(\mathbf{r})\right] \equiv T_e\left[\rho_0(\mathbf{r})\right] + V_{ee}\left[\rho_0(\mathbf{r})\right]. \tag{2.48}$$

Here, $F^{HK}\left[\rho_0(\mathbf{r})\right]$ is the desired universal functional, which is independent of the external potential, containing the kinetic energy of electrons, $T_e\left[\rho_0(\mathbf{r})\right]$, and the electron-electron interaction, $V_{ee}\left[\rho_0(\mathbf{r})\right]$. The trivial $E_{NN}(\mathbf{R})$ component arising from static nuclear repulsion has been ignored for now. The second theorem is nothing more than the variational principle formulated for electron densities. It states that the electron density that minimizes the exact energy functional is the true ground state density, thus, providing a variational method to determine the density, i.e.,

$$E_{v(\mathbf{r})}\left[\rho_{trial}(\mathbf{r})\right] \geq E_{v(\mathbf{r})}\left[\rho_0(\mathbf{r})\right] \equiv E_0 \tag{2.49}$$

where for an *N*-electron system the trial density must satisfy $\int \rho_{trial}(\mathbf{r}) d\mathbf{r} = N$ and $\rho_{trial}(\mathbf{r}) \geq 0$.

In principle, Hohenberg–Kohn formalism allows for all ground state properties to be obtained exactly from ρ_0 without having to determine the molecular wave function. Unfortunately, the theorems neither explain how to find ρ_0 without first finding the wave function nor describe what the universal functional is, and its exact form remains unknown. However, in 1965, Kohn and Sham (KS) devised an approach to handle the unknown $F^{HK}\left[\rho_0(\mathbf{r})\right]$.[148] In their scheme, the system of *N* interacting electrons is replaced by a fictitious reference system of *N* non-interacting electrons which has the exact ground state electron density as the real molecular system of interacting electrons. For a system of non-interacting electrons the electron density can be constructed as a sum over one-electron Kohn–Sham spatial orbitals $\phi_i^{KS}(\mathbf{r})$

$$\rho = \rho_s = \sum_{i=1}^{N} \left| \phi_i^{KS} \right|^2 \tag{2.50}$$

The energy functional can be recast as

$$E_{v(\mathbf{r})}[\rho] = T_s[\rho] + E_H[\rho] + E_{xc}[\rho] + \int v_{ext}(\mathbf{r})\rho(\mathbf{r})d\mathbf{r} \tag{2.51}$$

where $T_s[\rho]$ is the kinetic energy of non-interacting electrons

$$T_s[\rho] = -\frac{1}{2}\sum_{i=1}^{N}\left\langle \phi_i^{KS} \middle| \nabla_i^2 \middle| \phi_i^{KS} \right\rangle \tag{2.52}$$

$E_H[\rho]$ is the Hartree (or Coulomb) energy

$$E_H[\rho] = \frac{1}{2}\int\int \frac{\rho(\mathbf{r})\rho(\mathbf{r}')}{|\mathbf{r}-\mathbf{r}'|}d\mathbf{r}d\mathbf{r}' \tag{2.53}$$

and $E_{xc}[\rho]$ is the unknown exchange-correlation energy functional

$$E_{xc}[\rho] = \left(T_e[\rho] - T_s[\rho]\right) + \left(V_{ee}[\rho] - E_H[\rho]\right) \tag{2.54}$$

which contains all the corrections between the between the exact and the non-interacting kinetic energy and the non-classical part of the electron-electron interaction.

Analogous to the Hartree–Fock method, Equation 2.51 can minimized using the Lagrange method of undetermined multipliers with the constraint $\int \rho(\mathbf{r})d\mathbf{r} = N$ to obtain the central equation in Kohn-Sham DFT

$$\left[-\frac{1}{2}\nabla_i^2 + V^{eff}\right]\phi_i^{KS} = \varepsilon_i^{KS}\phi_i^{KS} \tag{2.55}$$

where the ε_i^{KS} are the Kohn–Sham orbital energies and

$$V^{eff} = -\sum_{\alpha}\frac{Z_{\alpha}}{|\mathbf{R}-\mathbf{r}|} + \int \frac{\rho(\mathbf{r}')}{|\mathbf{r}-\mathbf{r}'|}d\mathbf{r}' + \upsilon_{xc}(\mathbf{r})$$
$$\upsilon_{xc} = \frac{\delta E_{xc}[\rho]}{\delta\rho(\mathbf{r})} \tag{2.56}$$

where $E_{xc}[\rho]$ is the chosen exchange-correlation functional.

The Kohn–Sham DFT equations are similar to the Hartree–Fock eigenvalue equations. Since V^{eff} depends on $\rho(\mathbf{r})$, ϕ_i^{KS} depend on V^{eff}, and $\rho(\mathbf{r})$ depends on ϕ_i^{KS}, the Kohn–Sham equations must be solved iteratively until self-consistency is reached. In solving Equation 2.55, the Kohn–Sham orbitals are usually expanded in terms of a set of basis functions similar to the Hartree–Fock–Roothaan formalism. If the form of the exchange-correlation term $E_{xc}[\rho]$ was known, the Kohn-Sham energy (Equation 2.51) would be exact. However, the explicit expression for it has not been found, and approximations must be made.

The simplest approximation to $E_{xc}[\rho]$ is the local density approximation (LDA) which assumes that E_{xc} depends only on the value of the density at that point,[148]

$$E_{xc}^{LDA}[\rho] \equiv \int \rho(\mathbf{r})\varepsilon_{xc}(\rho)d\mathbf{r} \tag{2.57}$$

where $\varepsilon_{xc}(\rho)$ is the exchange-correlation energy per electron in a homogeneous electron gas with electron density ρ and can be split into exchange and correlation terms

$$\varepsilon_{xc}(\rho) = \varepsilon_x(\rho) + \varepsilon_c(\rho) \tag{2.58}$$

The exchange energy term has the exact form

$$E_x^{LDA} = \int \rho\varepsilon_x d\mathbf{r} = -\frac{3}{4}\left(\frac{3}{\pi}\right)^{1/3}\int\left[\rho(\mathbf{r})\right]^{4/3}d\mathbf{r} \tag{2.59}$$

and numerical forms for the correlation part have been determined and are available from highly accurate quantum Monte Carlo calculations.[149] The LDA can be generalized to treat

the electron spin in the homogeneous electron gas where $E_{xc} = E_{xc}\left[\rho^{\alpha}, \rho^{\beta}\right]$ and

$$E_x^{LSDA} = -\frac{3}{4}\left(\frac{6}{\pi}\right)^{1/3} \int \left[\left(\rho^{\alpha}\right)^{4/3} + \left(\rho^{\beta}\right)^{4/3}\right] d\mathbf{r} \tag{2.60}$$

This is useful for open-shell molecules and molecular geometries near dissociation, and for closed-shell molecules reverts back to LDA. The accuracy of the L(S)DA approximation depends on the system being studied, and it fails to give accurate results for highly inhomogeneous systems.

An improvement to the LDA which takes into account the spatial variation of the density is the generalized gradient approximation (GGA):[150]

$$E_{xc}^{GGA}[\rho] \equiv \int f\left(\rho(\mathbf{r}), \left|\nabla\rho(\mathbf{r})\right|\right) d\mathbf{r} \tag{2.61}$$

where $f\left(\rho(\mathbf{r}), \left|\nabla\rho(\mathbf{r})\right|\right)$ is a suitably chosen function of the two variables. As with the LDA, the exchange and correlation energies are split up to parameterize separately. A variety of GGA functionals has been developed including the Perdew and Wang (PW91)[151] and Perdew–Burke–Ernzerhof (PBE)[150, 152] functionals. Among the most popular gradient-corrected exchange functionals is Becke's (B88),[153]

$$E_x^{B88} = E_x^{LSDA} - b \sum_{\sigma=\alpha,\beta} \int \frac{\left(\rho^{\sigma}\right)^{4/3} \chi_{\sigma}^2}{1 + 6b\chi_{\sigma} \sinh^{-1} \chi_{\sigma}} d\mathbf{r} \tag{2.62}$$

where $\chi_{\sigma} \equiv \left|\nabla\rho^{\sigma}\right| \left(\rho^{\sigma}\right)^{-4/3}$ and b is an empirical parameter with value 0.0042 atomic units determined through fitting known Hartree–Fock exchange energies of several atoms. Commonly used gradient-corrected correlation functionals include those of Lee, Yang, and Parr (LYP),[154] Perdew (P86),[155, 156] and Vosko, Wilk, and Nusair (VWN).[157] The exchange and correlation functions are combined to produce a mixed functional, for example, Becke's GGA exchange with the GGA correlation of Lee, Yang, and Parr is BLYP.

Perhaps the most popular choice of exchange-correlation functionals are hybrid functionals, introduced by Becke,[158] which mix exact (HF) exchange of the occupied Kohn–Sham orbitals with approximate DFT exchange and correlation functionals having the simplest form

$$E_{xc} = aE_x^{HF} + (1-a)E_x^{DFT} + E_c^{DFT} \tag{2.63}$$

with the mixing parameter *a*. Functionals of this type are not limited to a single parameter, and one of the most popular hybrid functionals is B3LYP (Becke, three-parameter, Lee-Yang-Parr) defined by

$$E_{xc}^{B3LYP} = (1-a)E_x^{LSDA} + aE_x^{HF} + b\Delta E_x^{B88} + (1-c)E_c^{LSDA} + cE_c^{LYP} \tag{2.64}$$

where a = 0.20, b = 0.72, and c = 0.81, which were determined from fits of thermochemical data. Several other hybrid functionals are available that are defined in a similar way with various exchange and correlation functionals and different amounts of HF exchange. Hybrid functionals are considered the most accurate density functionals for energy calculations, and are the typical method of choice in DFT calculations.

2.1.4 Basis Sets

As mentioned in the discussion of Hartree–Fock theory, the orbitals are typically treated as a linear combination of mathematical functions known as basis functions. In fact, most modern quantum chemistry methods use a form of basis set expansion which can be atom centered or not atom centered.

$$\phi_i(\mathbf{r}) = \sum_k c_{ik} f_k \tag{2.65}$$

Slater type orbitals (STO) are hydrogen-atom-like exponential functions of the form

$$f_i^{STO} = Nr^{n-1}e^{-\zeta r}Y_{lm}(\theta,\phi) \tag{2.66}$$

N is a normalization constant, Y_{lm} are spherical harmonic functions, n, l, and m are the

quantum numbers, and ζ controls the width of the orbital (large ζ gives tight function, small ζ gives diffuse function). Unfortunately, functions of this type are computationally expensive when calculating the two-electron orbitals, and they are not often used in quantum chemical calculations. Instead, Gaussian-type orbitals (GTO) are commonly used.

$$f_{abc}^{GTO}(x,y,z) = Nx^a y^b z^c e^{-\alpha r^2} . \tag{2.67}$$

Here, *N* is a normalization constant, α is a positive orbital exponent, and *a*, *b*, *c* are positive integers that dictate the nature of the orbital. STOs and GTOs are in general taken as atom-centered functions. Though GTOs are computationally convenient,[159] real hydrogen atomic orbitals have a cusp at the nucleus and have a radial decay that is exponential in *r*, which GTOs lack.

A strategy to improve upon this is to take a linear combination of GTOs fit to approximate better the proper radial shape of STOs, i.e.,

$$f_{\tau}^{CG} = \sum_{j} d_{j\tau} f_{j}^{GTO} \tag{2.68}$$

The basis function f_{τ}^{CG} is referred to as a contracted Gaussian (CG) basis function with contraction coefficients $d_{j\tau}$, and the individual Gaussians forming it are called primitive Gaussians. The molecular orbitals are then a linear combination of contracted Gaussian-type orbitals with coefficients to be determined in the calculation. The exponents of the primitive Gaussians and the coefficients $d_{j\tau}$ defining each CG, however, are not modified during the calculation and are chosen to represent the optimal shape of the basis function.

A wide variety of basis sets composed of CGs are available for electronic structure calculations. A 'minimal' or single-zeta basis set consists of one CG for each inner-shell and valence-shell atomic orbital of each atom. These have the designation STO-*n*G (Slater-type orbitals approximated by *n* primitive Gaussians). Basis sets of this type provide a computationally inexpensive means for performing electronic structure calculations at the

cost of typically poor accuracy in the results. Higher *n*-zeta basis sets are also available where *n* represents the number of CGs for each inner- and valence-shell, but this obviously results in a higher computational cost as *n* is increased. A key in reducing the computational cost is in realizing that the core electrons are less affected by the chemical environment than the valence electrons, and they can be treated separately. This observation led to the development of 'split-valence' basis sets. A split-valence basis set uses a minimal basis for the core orbitals and *n*-zeta basis sets for the valence electrons. Among the most widely used split-valence basis sets are Pople basis sets with nomenclature that indicates the number of Gaussians used to describe core and valence orbitals.[160, 161] For example, a 6-31G basis set uses a single CG constructed of six primitive Gaussians for the core orbitals and two CGs for the valence orbitals, the first consisting of three primitives and the second with one.

The use of multiple basis functions for orbitals allows for the size of the orbitals to change. However, in molecular environments, the shapes of the orbitals are also distorted (polarized) for optimal bonding. This effect is accounted for by adding polarization functions to the basis set which represent higher angular momentum than what is found in the atomic valence orbitals. For example, the distortion of *s* and *p* orbitals can be incorporated by including *p* and *d* functions in the basis set, respectively. Two common notations are used for indicating inclusion of polarization functions to a basis set. One uses asterisks (*) at the end of the basis set, such as 6-31G* or 6-31G**. The single asterisk denotes that a set of *d*-type polarization functions are added to heavy atoms, and two asterisks denote that *p*-type functions are added to first row elements as well. These are also known as the 6-31G(d) and 6-31G(d,p) basis sets. When dealing with anions, excited states, and weakly bonded systems, there is significant electron density at large distances from the nuclei, and the basis sets are often augmented with diffuse functions. These are very shallow Gaussian functions that better resolve the tail-end of the atomic orbitals. In Pople notation they are designated by a plus sign, for example 6-31++G is the 6-31G basis set plus diffuse *s* and *p* functions for heavy atoms and a diffuse *s* function for first row atoms.

Computational expense is a major concern in performing HF and post-HF calculations as the required time scales rapidly with the number of basis functions in the calculation. In Hartree–Fock, the size of the Hamiltonian to be diagonalized for N atomic orbitals (basis functions) grows as N^4. Similarly, MP2 scales as N^5 and CI scales roughly as N^{2m+2}, where m is the excitation level. Density functional theory scales as N^3. Therefore, while increasing the size of the basis set greatly improves accuracy for most calculations, it also vastly increases the computational cost. There are also basis sets that are not atom-centered, including plane wave basis sets, which will be discussed in the section on *ab initio* molecular dynamics.

As a final note for this section, localized basis sets suffer from what is known as basis set superposition error (BSSE). When atoms of interacting molecules approach each other, their basis functions overlap, effectively increasing the size of the basis set from what it would be for isolated molecules. The improved descriptions of the interacting species resulting from the increased size of the basis set is not, in itself, an error. The error associated with BSSE comes from the inconsistent treatment of the individual molecules as the intermolecular distance is varied resulting in different basis set overlap for different separations. A common method to remove approximately BSSE is the Boys and Bernardi counterpoise correction (CP).[162] Consider the binding energy, $\Delta E_{bind}\left(AB\right)$ of two species A and B

$$\Delta E_{bind}\left(AB\right) = E_{AB}^{AB}\left(AB\right) - E_{A}^{A}\left(A\right) - E_{B}^{B}\left(B\right). \tag{2.69}$$

Here the superscripts correspond to the basis set, the subscripts denote the geometry, and the terms in parentheses represent the considered system. For example, $E_{AB}^{AB}\left(AB\right)$ is the energy of the interacting *AB* species evaluated in the union of basis sets for *A* and *B* with the geometry associated with the interacting species. In the CP method, the BSSE corrected binding energy is evaluated as

$$\Delta E_{bind}^{CP}(AB) = \left[E_{AB}^{AB}(AB) - E_{AB}^{AB}(A) - E_{AB}^{AB}(B)\right] + \left[E_{AB}^{A}(A) - E_{A}^{A}(A)\right] + \left[E_{AB}^{B}(B) - E_{B}^{B}(B)\right] \quad (2.70)$$

where $E_{AB}^{AB}(A)$ and $E_{AB}^{AB}(B)$ are the energies of species *A* and *B*, respectively, evaluated using the full *AB* basis set with the geometry they adopt when interacting and $E_{AB}^{A}(A)$ and $E_{AB}^{B}(B)$ are the energies of *A* and *B* using their individual basis functions but with the geometry adopted when interacting. The first term in brackets in Equation 2.70 is the energy of bringing species *A* and *B* together with the interacting geometry computed using the full basis set. The basis functions used in the individual energy expression $E_{AB}^{AB}(A)$ include those from *B*, and vice versa, even though the nuclei on which they are centered are not actually there. These are typically called ghost functions. The terms in the second line of Equation 2.70 accounts for the energy required to distort the individual equilibrium structure to the structure adopted when interacting. The errors are susceptible to the size of the basis set. Minimal basis sets have small BBSE as the basis functions are not diffuse enough to substantially impact surrounding atoms. However, exceedingly small basis sets provide less accuracy and BSSE corrections are necessary for accurate interaction energies when using moderate to large basis sets. If the basis set was complete, which is never the case, BSSE would not be an issue.

2.2 *Ab initio* Molecular Dynamics

The basic concept underlying *ab initio* molecular dynamics (AIMD) methods is the generation of finite-temperature trajectories from the forces acting on the nuclei obtained via 'on the fly' electronic structure calculations. The electronic variables are, thus, active and explicit degrees of freedom throughout the simulation rather than being integrated out and represented by fixed interaction potentials. This implies that, given a suitable approximate solution of the many-electron problem, 'chemically complex' systems (i.e. systems in which the electronic structure significantly changes during the dynamics) can be treated with AIMD. This also leads to a shift in the approximation from the level of

selecting the appropriate interaction potentials to the level of choosing a particular approximation for solving the Schrödinger equation. Despite the advantages of AIMD and the constantly increasing computational power, problems still exist with AIMD simulations. Namely, due to the cost of treating the electronic degrees of freedom, the simulations are limited to much smaller time and length scales than what is typically accessible through classical MD. Nevertheless, AIMD methods have the advantage of being capable of treating systems in which the breaking and forming of bonds occurs without the need for any empirical parameterization. In principle, any of the quantum mechanical methods for computing electronic structure mentioned previously can be used in AIMD simulations. However, the overwhelming majority of simulations employ Hohenberg–Kohn–Sham DFT.[147, 148] Though a variety of AIMD techniques are available, this discussion will be restricted to two widely used methods: Born–Oppenheimer (BO) molecular dynamics and Car–Parrinello (CP) molecular dynamics.

2.2.1 Car–Parrinello Molecular Dynamics

Car–Parrinello molecular dynamics[163] takes advantage of the quantum mechanical adiabatic time-scale separation of fast electronic and slow nuclear motion by transforming that into classical-mechanical adiabatic energy-scale separation in the framework of dynamical systems theory. To achieve this, the two-component quantum/classical problem is mapped onto a two-component purely classical problem with two separate energy scales by considering the extended Kohn–Sham energy functional to be dependent on $\left\{\phi_i^{KS}\right\}$ and **R**. In doing this, the explicit time dependence of the quantum subsystem dynamics is lost. The CPMD method uses the Lagrangian, in KS formalism,

$$\mathcal{L}_{CP} = \frac{1}{2}\left(\sum_I M_I \dot{\mathbf{R}}_I^2 + \sum_i \mu \left\langle \dot{\phi}_i^{KS} \middle| \dot{\phi}_i^{KS} \right\rangle\right) - \left\langle \psi_0 \middle| \hat{\mathcal{H}} \middle| \psi_0 \right\rangle + \sum_{i,j} \Lambda_{ij} \left(\left\langle \phi_i^{KS} \middle| \phi_j^{KS} \right\rangle - \delta_{ij} \right) \qquad (2.71)$$

where proper orbital orthonormality, $\left\langle \phi_i^{KS} \middle| \phi_j^{KS} \right\rangle = \delta_{ij}$, is imposed by the Lagrange multipliers, Λ_{ij}. The Lagrangian is used to generate trajectories for the ionic and electronic degrees of freedom through the coupled set of equations of motion

$$M_I \ddot{\mathbf{R}}_I = -\nabla_I \left\langle \psi_0 \middle| \hat{\mathcal{H}}^{KS} \middle| \psi_0 \right\rangle \tag{2.72}$$

$$\mu \ddot{\phi}_i^{KS} = -\hat{\mathcal{H}}^{KS} \phi_i^{KS} + \sum_j \Lambda_{ij} \phi_j^{KS} \tag{2.73}$$

where M_I and $\mathbf{R}_I$ are the mass and position of nuclei *I*, respectively; ϕ_i^{KS} are the KS orbitals, which are allowed to evolve classically with fictitious inertial parameter μ. According to the CP equations of motion, the nuclei evolve in time at a certain (instantaneous) physical temperature $\propto \sum_I M_I \dot{\mathbf{R}}_i^2$, while a 'fictitious temperature' $\propto \sum_i \mu \left\langle \dot{\phi}_i^{KS} \middle| \dot{\phi}_i^{KS} \right\rangle$ is associated with the electronic degrees of freedom. If the 'fictitious temperature' corresponds to 'cold electrons', the electronic subsystem is close to its instantaneous minimum energy, $\min_{\left\{\phi_i^{KS}\right\}} E^{KS}$, i.e., close to the exact Born–Oppenheimer surface. Thus, an optimized ground-state initial configuration will stay close to its ground-state during time evolution if it is kept at sufficiently low temperature. The electronic orbitals should adiabatically follow the motion of the ions, performing only small oscillations about the electronic ground state.

2.2.2 Born–Oppenheimer Molecular Dynamics

The electronic structure is included in BOMD simulations by computing the electronic structure according to the static coordinates of the nuclei at each molecular dynamics time step. The *ab initio* dynamics are reduced to solving the time-independent Schrödinger equation at each step followed by propagation of the nuclei via Newton's equations of motion based on the computed forces. Hence, the time dependence of the electronic structure is dictated by its parametric dependence on the classical dynamics of the nuclei.[164] The BOMD method is, thus, defined by

$$M_I \ddot{\mathbf{R}}_I(t) = -\nabla_I \min_{\psi_0} \left\{ \left\langle \psi_0 \middle| \hat{\mathcal{H}} \middle| \psi_0 \right\rangle \right\} \tag{2.74}$$

$$\hat{\mathcal{H}} \psi_0 = E_0 \psi_0 \tag{2.75}$$

for the electronic ground state. The minimum energy must be reached for the nuclear configuration at every time step of in BOMD simulations under the constraint of orthonormal single-particle wave functions. In KS formalism, the corresponding constrained minimization of the energy is expressed as

$$\min_{\left\{\phi_i^{KS}\right\}}\left\{\left\langle\psi_0\middle|\hat{\mathcal{H}}\middle|\psi_0\right\rangle\right\}\Big|_{\left\{\left\langle\phi_i^{KS}\middle|\phi_j^{KS}\right\rangle=\delta_{ij}\right\}} \tag{2.76}$$

which can be cast as the Lagrangian

$$\mathcal{L}^{BO}=-\left\langle\psi_0\middle|\hat{\mathcal{H}}\middle|\psi_0\right\rangle+\sum_{i,j}\Lambda_{ij}\left(\left\langle\phi_i^{KS}\middle|\phi_j^{KS}\right\rangle-\delta_{ij}\right) \tag{2.77}$$

where, again, Λ_{ij} are Lagrange multipliers imposing orthonormality of orbitals. Variation of the Lagrangian with respect to the KS orbitals results in the BOMD equations of motion

$$M_I\ddot{\mathbf{R}}_I=-\nabla_I\min_{\left\{\phi_i^{KS}\right\}}\left\{\left\langle\psi_0\middle|\hat{\mathcal{H}}^{KS}\middle|\psi_0\right\rangle\right\} \tag{2.78}$$

$$0=-\hat{\mathcal{H}}^{KS}\phi_i^{KS}+\sum_j\Lambda_{ij}\phi_j^{KS}\,. \tag{2.79}$$

A commonly used package implementing KS–DFT is the Vienna *Ab initio* simulation package (VASP)[165-167] which is employed in this work.

An important component of AIMD methods is the determination of forces acting on the nuclei. The force acting on ion *I* is given by

$$\mathbf{F}_I=-\nabla_I\left\langle\psi_0\middle|\hat{\mathcal{H}}\middle|\psi_0\right\rangle \tag{2.80}$$

with derivative

$$\nabla_I\left\langle\psi_0\middle|\hat{\mathcal{H}}\middle|\psi_0\right\rangle=\left\langle\psi_0\middle|\nabla_I\hat{\mathcal{H}}\middle|\psi_0\right\rangle+\left\langle\nabla_I\psi_0\middle|\hat{\mathcal{H}}\middle|\psi_0\right\rangle+\left\langle\psi_0\middle|\hat{\mathcal{H}}\middle|\nabla_I\psi_0\right\rangle. \tag{2.81}$$

If the wave function is an exact eigenfunction of the Hamiltonian, the last two terms on the

right-hand side of Equation 2.81 vanish leaving the form from the Hellmann–Feynman theorem[168, 169]

$$\mathbf{F}_I^{HFT} = -\left\langle \psi_0 \middle| \nabla_I \hat{\mathcal{H}} \middle| \psi_0 \right\rangle . \tag{2.82}$$

This is also valid for variational wave functions provided that complete basis sets are used.[164] Unfortunately, in practice the wave functions are expanded on a set of finite basis functions, and the contributions from variations in the wave function with respect to the nuclear positions have to be evaluated. In general, two additional forces are present: the Pulay force and the non-self-consistency correction

$$\mathbf{F}_I = \mathbf{F}_I^{HFT} + \mathbf{F}_I^{P} + \mathbf{F}_I^{NSC} . \tag{2.83}$$

The Pulay force comprises of the nuclear gradients of the basis functions which vanishes if the basis functions do not depend on atomic positions, as with plane waves. The non-self-consistency correction arises from the difference between the exact self-consistent potential and the numerical approximate potential and is always present in BOMD simulations as exact self-consistency is never fully reached; estimation techniques are available that approximately correct for this error.[164]

2.2.3 Plane Waves and Pseudopotentials

Plane wave basis sets are commonly employed in *ab initio* molecular dynamics simulations with periodic boundary conditions as they are intrinsically periodic and orthogonal. According to Bloch's theorem, the Kohn–Sham orbitals for a periodic system can be written as a product of a periodic function $u_{j,\mathbf{k}}(\mathbf{r})$ and a wave-like term $e^{i\mathbf{k}\cdot\mathbf{r}}$, i.e.,

$$\phi_{j,\mathbf{k}}^{KS}(\mathbf{r}) = e^{i\mathbf{k}\cdot\mathbf{r}} u_{j,\mathbf{k}}(\mathbf{r}) . \tag{2.84}$$

where $\mathbf{k}$ is a wave vector within the first Brillouin zone.[164] The function $u_{i,\mathbf{k}}$ contains the periodicity of the system, $u_{j,\mathbf{k}}(\mathbf{r}) = u_{j,\mathbf{k}}(\mathbf{r}+\mathbf{L})$, with direct lattice vectors $\mathbf{L}$, and can be expanded as a set of plane waves:

$$u_{j,\mathbf{k}}(\mathbf{r}) = \Omega^{-1/2} \sum_{\mathbf{G}} c_{j,\mathbf{k}}(\mathbf{G}) e^{i\mathbf{G}\cdot\mathbf{r}} \tag{2.85}$$

with reciprocal lattice vectors $\mathbf{G}$, complex expansion coefficients $c_{j,\mathbf{k}}(\mathbf{G})$, and volume of the periodic cell Ω. Inserting Equation 2.85 into Equation 2.84 gives

$$\phi_{j,\mathbf{k}}^{KS}(\mathbf{r}) = \Omega^{-1/2} \sum_{\mathbf{G}} c_{j,\mathbf{k}}(\mathbf{G}) e^{i(\mathbf{G}+\mathbf{k})\cdot\mathbf{r}} \tag{2.86}$$

for the KS orbitals. Generally, to describe correctly the properties of a periodic system, a sufficient sampling of the Brillouin zone is required. However, in many applications, particularly with nonmetallic systems, it is often justifiable to consider a single **k**-point corresponding to **k** = (0,0,0) known as the Γ-point.[170] In this manner, the orbital expansion reduces to

$$\phi_{j}^{KS}(\mathbf{r}) = \Omega^{-1/2} \sum_{\mathbf{G}} c_{j}(\mathbf{G}) e^{i\mathbf{G}\cdot\mathbf{r}} . \tag{2.87}$$

Plane waves are eigenvectors of the kinetic energy operator

$$-\frac{1}{2}\nabla^2 e^{i\mathbf{G}\cdot\mathbf{r}} = \frac{1}{2}\left|\mathbf{G}\right|^2 e^{i\mathbf{G}\cdot\mathbf{r}} . \tag{2.88}$$

In practice, the summations over the **G**-vectors in Equation 2.87 are truncated, and only the plane waves with kinetic energy below a given cut-off are kept:

$$\frac{1}{2}\left|\mathbf{G}\right|^2 \le E_{cut} . \tag{2.89}$$

Plane wave basis sets have the advantage over atom-centered basis sets in that there is no basis set superposition error or Pulay corrections to the Hellmann–Feynman force. Furthermore, the quality of the calculations, within the DFT approximations, can be tuned by E_{cut} alone. Unfortunately, the number of plane waves needed to describe accurately the rapidly oscillating wave functions in the core region exceeds practical limits. One approach to address this problem is to treat the valence electrons explicitly and replace the core

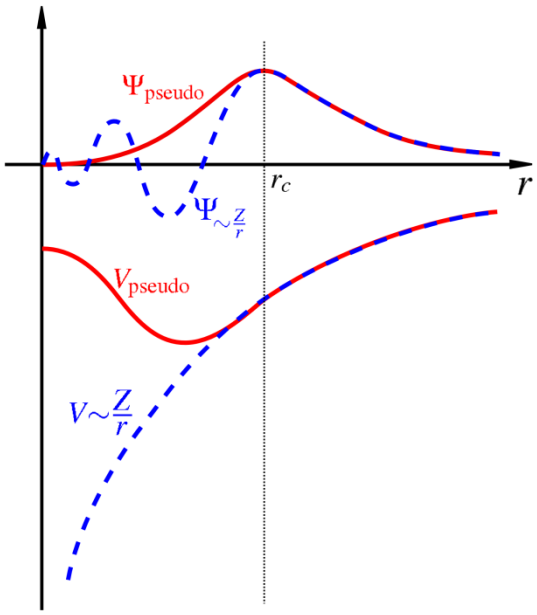

Figure 2.1. Schematic representation of the all-electron and pseudopotential and their corresponding wave functions.

electrons with pseudopotentials to combine their impact on the valence electrons with that of the nuclei as an effective, smooth potential. Within the core region, pseudopotentials are weaker than the exact potential and the pseudo wave function contains no radial nodes, as schematically shown in Figure 2.1, to allow for a small plane wave cut-off. Outside the core region, the pseudopotential and the pseudo wave function match those of the corresponding all-electron ones. One critical feature is that pseudopotentials be transferrable for each element in different chemical environments. The use of pseudopotentials, thus, reduces the number of electrons and allows for reduction of basis set size. Another approach is the class of augmented plane wave (APW) methods which, in the simplest form, partition space into two regions: atom-centered spheres and interstitial regions away from the nuclei. In the interstitial regions, the electrons are treated on a plane wave basis while the electrons within the spheres are treated on a local atomic basis in which the wave functions match at the spherical boundary. A more general approach as an extension to these is the projector augmented wave (PAW) method, which is used in this work and described in further detail.

2.2.4 Projector Augmented Wave Method

The PAW method attempts to combine the computational efficiency of using pseudopotentials with the accuracy of all-electron calculations. As with the APW method, the PAW method divides space into distinct regions: non-overlapping spherical regions around each atom, $\bigcup_a \Omega_a$, termed augmentation spheres centered at $\mathbf{R}_a$ with cutoff radii r_c^a and the interstitial regions, Ω_{I}, such that $\Omega = \Omega_{\mathrm{I}} + \bigcup_a \Omega_a$. The difficulties in using a plane wave basis set lie in the atomic spherical regions. To address this problem, a linear transformation $\hat{\mathcal{T}}$ is introduced that maps the true all-electron KS single-particle wave function onto computationally convenient auxiliary wave functions,

$$\left|\psi_n\right\rangle = \hat{\mathcal{T}}\left|\tilde{\psi}_n\right\rangle, \tag{2.90}$$

where *n* is a quantum state label. From this transformation, the transformed equations to be solved are

$$\hat{\mathcal{T}}^{\dagger}\hat{\mathcal{H}}\hat{\mathcal{T}}\left|\tilde{\psi}_n\right\rangle = \varepsilon_n \hat{\mathcal{T}}^{\dagger}\hat{\mathcal{T}}\left|\tilde{\psi}_n\right\rangle. \tag{2.91}$$

Since the true all-electron wave functions are smooth beyond a certain distance from the core, the transformation operator is constructed to modify only the wave function inside the atom-specific augmentation spheres. Hence, $\hat{\mathcal{T}}$ is written as

$$\hat{\mathcal{T}} = 1 + \sum_a \hat{\mathcal{T}}^a, \tag{2.92}$$

where the subscript *a* runs over all augmentation spheres (atoms) in the unit cell, and the atom-centered transformation, $\hat{\mathcal{T}}^a$, has no effect outside the augmentation sphere. For every atom, the operator $\hat{\mathcal{T}}^a$ adds the difference between the true and auxiliary wave functions. Inside each augmentation sphere, the true wave function is expanded in a set of defined local basis functions, $\left\{\phi_i^a\right\}$, termed partial waves, that aim to describe correctly the

oscillating behavior of the wave function inside the sphere. For each partial wave, a corresponding smooth auxiliary partial wave, $\tilde{\phi}_i^a$, is defined such that

$$\left|\phi_i^a\right\rangle = \hat{\mathcal{T}}\left|\tilde{\phi}_i^a\right\rangle = \left(1 + \sum_{a'} \hat{\mathcal{T}}^{a'}\right)\left|\tilde{\phi}_i^a\right\rangle = \left(1 + \hat{\mathcal{T}}^a\right)\left|\tilde{\phi}_i^a\right\rangle \tag{2.93}$$

and

$$\hat{\mathcal{T}}^a\left|\tilde{\phi}_i^a\right\rangle = \left|\phi_i^a\right\rangle - \left|\tilde{\phi}_i^a\right\rangle. \tag{2.94}$$

Since $\hat{\mathcal{T}}^a$ will only change the wave function within the augmentation spheres; the partial waves and their corresponding auxiliary partial waves must be identical outside of the augmentation spheres, i.e.,

$$\forall a,\ \phi_i^a(\mathbf{r}) = \tilde{\phi}_i^a(\mathbf{r}) \ \text{ for } \ \left|\mathbf{r} - \mathbf{R}_a\right| > r_c^a \tag{2.95}$$

with $\phi_i^a(\mathbf{r}) = \left\langle \mathbf{r}\middle|\phi_i^a\right\rangle$ and the same for $\tilde{\phi}_i^a(\mathbf{r})$. Within the augmentation sphere the auxiliary partial waves are chosen so that they form a complete basis for the auxiliary wave function

$$\left|\tilde{\psi}_n\right\rangle = \sum_i \left|\tilde{\phi}_i^a\right\rangle c_{ni}^a \quad \text{within } \Omega_a. \tag{2.96}$$

Left multiplying both sides by $\hat{\mathcal{T}}$ gives

$$\begin{aligned} \hat{\mathcal{T}}\left|\tilde{\psi}_n\right\rangle &= \sum_i \hat{\mathcal{T}}\left|\tilde{\phi}_i^a\right\rangle c_{ni}^a \\ \psi_n &= \sum_i \left|\phi_i^a\right\rangle c_{ni}^a \qquad \text{within } \Omega_a \end{aligned} \tag{2.97}$$

indicating that both the true and auxiliary wave functions have the same expansion coefficients. A set of projector functions, $\left\{\tilde{p}_i^a\right\}$, can be chosen that are orthonormal to the auxiliary partial waves, $\left\langle \tilde{p}_i^a\middle|\tilde{\phi}_j^a\right\rangle = \delta_{ij}$, and left multiplying Equation 2.96 by $\left\langle \tilde{p}_i^a\right|$ gives the relation

$$\left\langle \tilde{p}_i^a \middle| \tilde{\psi}_n \right\rangle = \sum_j \left\langle \tilde{p}_i^a \middle| \tilde{\phi}_j^a \right\rangle c_{nj}^a = \sum_j c_{nj}^a \delta_{ij} = c_{ni}^a . \tag{2.98}$$

Equation 2.96 can then be written

$$\left| \tilde{\psi}_n \right\rangle = \sum_i \left| \tilde{\phi}_i^a \right\rangle \left\langle \tilde{p}_i^a \middle| \tilde{\psi}_n \right\rangle \quad \text{within } \Omega_a \tag{2.99}$$

and since there is no overlap between augmentation spheres, the projector function must satisfy $\sum_i \left| \tilde{\phi}_i^a \right\rangle \left\langle \tilde{p}_i^a \right| = 1$ inside each augmentation sphere. Using this relation and Equation 2.94, $\hat{\mathcal{T}}^a$ is shown to be

$$\hat{\mathcal{T}}^a = \sum_i \hat{\mathcal{T}}^a \left| \tilde{\phi}_i^a \right\rangle \left\langle \tilde{p}_i^a \right| = \sum_i \left(\left| \phi_i^a \right\rangle - \left| \tilde{\phi}_i^a \right\rangle \right) \left\langle \tilde{p}_i^a \right| \tag{2.100}$$

and the transformation operator is thus

$$\hat{\mathcal{T}} = 1 + \sum_a \hat{\mathcal{T}}^a = 1 + \sum_a \sum_i \left(\left| \phi_i^a \right\rangle - \left| \tilde{\phi}_i^a \right\rangle \right) \left\langle \tilde{p}_i^a \right| . \tag{2.101}$$

Using the definition of the transformation operator, the all-electron wave function becomes

$$\begin{aligned} \left| \psi_n \right\rangle &= \left| \tilde{\psi}_n \right\rangle + \sum_a \sum_i \left(\left| \phi_i^a \right\rangle - \left| \tilde{\phi}_i^a \right\rangle \right) \left\langle \tilde{p}_i^a \middle| \tilde{\psi}_n \right\rangle \\ &= \left| \tilde{\psi}_n \right\rangle + \sum_a \left(\left| \psi_n^a \right\rangle - \left| \tilde{\psi}_n^a \right\rangle \right) \end{aligned} , \tag{2.102}$$

where

$$\begin{aligned} \left| \psi_n^a \right\rangle &= \sum_i \left| \phi_i^a \right\rangle \left\langle \tilde{p}_i^a \middle| \tilde{\psi}_n \right\rangle \\ \left| \tilde{\psi}_n^a \right\rangle &= \sum_i \left| \tilde{\phi}_i^a \right\rangle \left\langle \tilde{p}_i^a \middle| \tilde{\psi}_n \right\rangle \end{aligned} , \tag{2.103}$$

which separates the atom-centered and interstitial contributions to the wave function. The frozen core approximation is used which assumes that the core states are not affected by the chemical environment. Thus, the core states $\left| \psi_n^c \right\rangle$ are identical to the atomic core states,

i.e., $\left|\psi_n^c\right\rangle = \left|\phi_\alpha^{a,c}\right\rangle$ where *n* refers to a specific atom, *a*, and atomic state, *α*. Expectation values, $\left\langle\hat{\mathcal{O}}\right\rangle$, under the frozen core approximation can be obtained by

$$\left\langle\hat{\mathcal{O}}\right\rangle = \sum_n^{N_v} f_n \left\langle\psi_n\middle|\hat{\mathcal{O}}\middle|\psi_n\right\rangle + \sum_{\alpha=1}^{N_c}\left\langle\phi_\alpha^{a,c}\middle|\hat{\mathcal{O}}\middle|\phi_\alpha^{a,c}\right\rangle, \tag{2.104}$$

where f_n is the occupancy a the valence state, N_v is the number of valence states, and N_c is the number of core states. Using Equation 2.102 and dropping the state index here for convenience yields

$$\begin{aligned}\left\langle\psi\middle|\hat{\mathcal{O}}\middle|\psi\right\rangle &= \left\langle\tilde{\psi} + \sum_a\left(\psi^a - \tilde{\psi}^a\right)\middle|\hat{\mathcal{O}}\middle|\tilde{\psi} + \sum_{a'}\left(\psi^{a'} - \tilde{\psi}^{a'}\right)\right\rangle \\ &= \left\langle\tilde{\psi}\middle|\hat{\mathcal{O}}\middle|\tilde{\psi}\right\rangle + \sum_a\left(\left\langle\psi^a\middle|\hat{\mathcal{O}}\middle|\psi^a\right\rangle - \left\langle\tilde{\psi}^a\middle|\hat{\mathcal{O}}\middle|\tilde{\psi}^a\right\rangle\right) \\ &+ \sum_a\left(\left\langle\psi^a - \tilde{\psi}^a\middle|\hat{\mathcal{O}}\middle|\tilde{\psi} - \tilde{\psi}^a\right\rangle + \left\langle\tilde{\psi} - \tilde{\psi}^a\middle|\hat{\mathcal{O}}\middle|\psi^a - \tilde{\psi}^a\right\rangle\right) \\ &+ \sum_{a\neq a'}\left\langle\psi^a - \tilde{\psi}^a\middle|\hat{\mathcal{O}}\middle|\psi^{a'} - \tilde{\psi}^{a'}\right\rangle\end{aligned}. \tag{2.105}$$

For local operators, the last two lines vanish, as long as the partial wave expansion is converged. Combining this and Equation 2.104 gives for the expectation value of local operators

$$\left\langle\hat{\mathcal{O}}\right\rangle = \sum_n^{N_v} f_n \left\langle\tilde{\psi}_n\middle|\hat{\mathcal{O}}\middle|\tilde{\psi}_n\right\rangle + \sum_a\sum_{i,j}\left(\left\langle\phi_i^a\middle|\hat{\mathcal{O}}\middle|\phi_j^a\right\rangle - \left\langle\tilde{\phi}_i^a\middle|\hat{\mathcal{O}}\middle|\tilde{\phi}_j^a\right\rangle\right)D_{ij}^a + \sum_a\sum_\alpha^{N_c}\left\langle\phi_\alpha^{a,c}\middle|\hat{\mathcal{O}}\middle|\phi_\alpha^{a,c}\right\rangle, \tag{2.106}$$

where the matrix, D_{ij}, is defined as

$$D_{ij}^a = \sum_n f_n \left\langle\tilde{\psi}_n\middle|\tilde{p}_i^a\right\rangle\left\langle\tilde{p}_j^a\middle|\tilde{\psi}_n\right\rangle. \tag{2.107}$$

In a similar manner, the electron density is given by

$$\rho(\mathbf{r}) = \tilde{\rho}(\mathbf{r}) + \sum_a\left(\rho^a(\mathbf{r}) - \tilde{\rho}^a(\mathbf{r})\right) \tag{2.108}$$

with

$$\begin{aligned}\tilde{\rho}(\mathbf{r}) &= \sum_n f_n \left\langle \tilde{\psi}_n \middle| \mathbf{r} \right\rangle \left\langle \mathbf{r} \middle| \tilde{\psi}_n \right\rangle + \tilde{\rho}_c \\ \rho^a(\mathbf{r}) &= \sum_{ij} D_{ij}^a \left\langle \phi_i^a \middle| \mathbf{r} \right\rangle \left\langle \mathbf{r} \middle| \phi_j^a \right\rangle + \rho_c^a \\ \tilde{\rho}^a(\mathbf{r}) &= \sum_{ij} D_{ij}^a \left\langle \tilde{\phi}_i^a \middle| \mathbf{r} \right\rangle \left\langle \mathbf{r} \middle| \tilde{\phi}_j^a \right\rangle + \tilde{\rho}_c^a\end{aligned}, \tag{2.109}$$

where ρ_c^a is the core density of atom *a* and $\tilde{\rho}_c^a$ is the auxiliary core density, which equals the core density in the interstitial region but is smooth in the augmentation sphere. Like the density, the total KS energy is divided into three terms,

$$E^{KS} = \tilde{E} + \sum_a E^a - \sum_a \tilde{E}^a , \tag{2.110}$$

in which the first term contains only smooth functions and extends over space while the remaining terms are atom-centered. The three energy expressions are given as

$$\tilde{E} = \sum_n f_n \left\langle \tilde{\psi}_n \middle| -\frac{1}{2}\nabla^2 \middle| \tilde{\psi}_n \right\rangle + \int V_{loc}(\mathbf{r}) \tilde{\rho}(\mathbf{r}) d\mathbf{r} + E_H\left[\tilde{\rho} + \hat{\rho}\right] + E_{xc}\left[\tilde{\rho}\right] \tag{2.111}$$

$$E^a = \sum_n f_n \sum_{ij} \left\langle \tilde{\psi}_n \middle| \tilde{p}_i^a \right\rangle \left\langle \phi_i^a \middle| -\frac{1}{2}\nabla^2 \middle| \phi_j^a \right\rangle \left\langle \tilde{p}_j^a \middle| \tilde{\psi}_n \right\rangle + E_H\left[\rho^a + \rho^{Za}\right] + E_{xc}\left[\rho^a\right] \tag{2.112}$$

$$\begin{aligned}\tilde{E}^a = &\sum_n f_n \sum_{ij} \left\langle \tilde{\psi}_n \middle| \tilde{p}_i^a \right\rangle \left\langle \tilde{\phi}_i^a \middle| -\frac{1}{2}\nabla^2 \middle| \tilde{\phi}_j^a \right\rangle \left\langle \tilde{p}_j^a \middle| \tilde{\psi}_n \right\rangle + \int V_{loc}(\mathbf{r}) \tilde{\rho}^a(\mathbf{r}) d\mathbf{r} \\ &+ E_H\left[\tilde{\rho}^a + \hat{\rho}\right] + E_{xc}\left[\tilde{\rho}^a\right]\end{aligned} . \tag{2.113}$$

Here, V_{loc} is an arbitrary potential inside the augmentation spheres which would vanish if the partial wave expansion were complete, ρ^{Za} is the point charge density of the nuclei, and $\hat{\rho}$ is a compensation charge density added to reproduce the correct multipole moments of the all-electron charge density located in each augmentation sphere. The $\tilde{E}$ term is evaluated on a regular grid while E^a and $\tilde{E}^a$ are evaluated on radial grids centered around each ion.

2.3 Additional Terminology and Applications

As previously mentioned, solving the Schrödinger equation for various nuclear configurations defines the potential energy surface (PES), a central concept in computational chemistry used within the Born–Oppenheimer approximation. These surfaces are important in understanding the relationship between the potential energy and the molecular geometry as well as in studying reaction paths. There are 3*N* total coordinates for any molecule corresponding to the Cartesian coordinates of each of the *N* atoms; however, the potential energy of a molecule is invariant to overall translations and rotations. Thus, the potential energy depends only on the position of the nuclei relative to each other, the internal coordinates. Subtracting the three translations and three (two for linear molecules) rotations that do not change the energy leaves 3*N*-6 (3*N*-5 for linear molecules) internal degrees of freedom, which completely define the molecular geometry. These can be represented by, for example, bond lengths, bond angles, and torsion angles. The energy as a function of these coordinates defines the potential energy surface. The points of interest on PESs are stationary points where the gradient of the energy with respect to the generalized coordinates $\{q_i\}$ are zero; i.e.,

$$\frac{\partial E}{\partial q_1} = \frac{\partial E}{\partial q_2} = \cdots \frac{\partial E}{\partial q_n} = 0. \tag{2.114}$$

where $n = 3N - 6$ (or $3N - 5$) if working in internal coordinates and $n = 3N$ in Cartesian. The positions of the stationary points are independent of the choice of coordinates. Stationary points can be minima, transition states, and higher-order saddle points. Local minima correspond to the lowest-energy points within a region of the PES where any small change in the geometry increases the energy, and the lowest of all of these on the entire PES is the global minimum. These can represent different stable conformations of molecules, structural isomers, and reactants and products of a reaction. Transition states are first-order saddle points that are minima in all directions on the PES except for one in which it is a maximum. Higher-order saddle points correspond to points that are minima in all

dimensions except for n, where $n > 1$, where it is a maximum. The first derivative determines whether or not the configuration is a stationary point but it does not distinguish between the different types. In order to determine this, the second derivatives with respect to the coordinates must be taken. These are typically cast as a matrix known as the Hessian.

$$\mathbf{H} = \begin{bmatrix} \dfrac{\partial^2 E}{\partial q_1^2} & \dfrac{\partial^2 E}{\partial q_1 \partial q_2} & \cdots & \dfrac{\partial^2 E}{\partial q_1 \partial q_n} \\ \dfrac{\partial^2 E}{\partial q_2 \partial q_1} & \dfrac{\partial^2 E}{\partial q_2^2} & \cdots & \dfrac{\partial^2 E}{\partial q_2 \partial q_n} \\ \vdots & \vdots & \ddots & \vdots \\ \dfrac{\partial^2 E}{\partial q_n \partial q_1} & \cdots & \cdots & \dfrac{\partial^2 E}{\partial q_n^2} \end{bmatrix} \tag{2.115}$$

For a minimum, all of the eigenvalues of the Hessian matrix are positive, while for a transition state all eigenvalues are positive except one, and only one, negative eigenvalue. While internal coordinates involving bond lengths and angles are conceptually convenient, it is often difficult to determine the independent coordinates without redundancies for large molecular systems and gradients and Hessians are generally easier to calculate in Cartesian coordinates. It is common to use mass-weighted Cartesian coordinates $\tilde{q}_i = \sqrt{m_N}\Delta x_i$ when constructing the Hessian, where Δx_i is the displacement of the i^{th} coordinate from the stationary point and m_N is the mass of the associated atom. The subscript i runs over the $3N$ coordinates while the subscript N goes over the number of atoms. For example, the coordinates $(\Delta x_1, \Delta x_2, \Delta x_3)$ correspond to the displacements of the x, y, z Cartesian coordinates from the stationary point of atom 1, each with the mass m_1. Diagonalization of the Hessian based on the mass-weighted Cartesians yields $3N$ eigenvectors and eigenvalues. Six (five for linear molecules) of the eigenvectors correspond to the translation and rotational motion of the molecule whose eigenvalues are (in principle) zero. The remaining $3N$-6 ($3N$-5 for linear) correspond to the internal vibrations connected to the vibrational spectra whose eigenvectors correspond to the normal mode

unit vectors containing the directions of the normal modes of vibration and the eigenvalues are the corresponding force constants. The vibrational frequencies are proportional to the square root of the force constant and, as such, minima contain all real vibrational frequencies while transition states contain a single imaginary frequency. The eigenvector corresponding to the imaginary frequency at a transition state is the so-called intrinsic reaction coordinate (IRC), which is the minimum-energy path (path of steepest descent from the transition state) connecting minima in mass-weighted coordinates. The geometric parameter associated with the IRC is typically a combination of several parameters, though in some cases the primary component(s) can be determined.

Locating stationary points requires a geometry optimization. Geometry optimizations are performed by using an input geometry, which is ideally close to the desired stationary point, as an initial structure for an algorithm that systematically changes the geometry until a stationary point is found. The most widely used algorithms for geometry optimization use the first and second derivatives of the energy and transform back and forth between Cartesian and internal coordinates.[139] If one is interested in how the energy of a system responds to changes in a particular geometric parameter, for example the asymmetric stretch coordinate involved in proton transfer or the rotation of a dihedral angle in a polymer, rigid or relaxed PES scans can be performed. Rigid PES scans start from an optimized geometry and stepwise vary the chosen geometric parameter (internal coordinate) while keeping all other degrees of freedom fixed at their equilibrium values performing a single point energy calculation at each step. Relaxed PES scans also systematically vary the chosen internal coordinate fixing it at each step but all other degrees of freedom are fully optimized at each step. If the scan results in a curve containing maxima and minima, a normal mode analysis can be performed at geometries corresponding to the maxima to determine if they correspond to transition states (i.e., one and only one imaginary frequency associated with the coordinate). Relaxed PES scans are used exclusively in this work. In addition to normal mode analysis providing the vibrational frequencies to characterize stationary points and obtain the IR spectra, the frequencies also are used to determine the zero-point energy (ZPE). The ZPE is the vibrational energy that a

molecule retains even at absolute zero as the molecule is never truly stationary and is given by $E_{ZPE} = \sum_{i=1}^{3N-6(5)} \frac{1}{2} h\nu_i$, where h is Planck's constant and ν_i is the frequency of normal mode *i*. For accurate calculations, the ZPE is added to the total energy.

Another commonly employed method in computational chemistry regards determination of the distribution of charge within a molecule by determining partial atomic charges on individual atoms through what is known as a population analysis. There are several available population analysis techniques used to estimate the partial atomic charges; the simplest method is the Mulliken population analysis which is based on the population of LCAO basis sets. If the coefficients of the basis functions φ_α and φ_β are $c_{\alpha i}$ and $c_{\beta i}$ and the occupancy of each orbital is f_i the total number of electrons can be defined as

$$\begin{aligned} N &= \sum_{\alpha\beta}^{M_{basis}} D_{\alpha\beta} S_{\alpha\beta} = \sum_{\alpha\beta}^{M_{basis}} P_{\alpha\beta} \\ D_{\alpha\beta} &= \sum_{i}^{N_{orb}} f_i c_{\alpha i}^* c_{\beta i} \\ S_{\alpha\beta} &= \int \varphi_\alpha^* \varphi_\beta d\mathbf{r} \end{aligned} \qquad (2.116)$$

where $D_{\alpha\beta}$ and $S_{\alpha\beta}$ are the density and overlap matrices, respectively, and $P_{\alpha\beta}$ is the population matrix constructed by multiplying each corresponding element of the density and overlap matrices. In the Mulliken analysis, the electrons are distributed into the atomic orbital basis functions. The diagonal element $P_{\alpha\alpha}$ gives the number of electrons in atomic orbital α and the off-diagonal element $P_{\alpha\beta}$ gives half the number of electrons shared by orbitals α and β (there is an equivalent $P_{\beta\alpha}$). With each orbital there is, thus, a gross orbital population obtained by a sum over a row, $GOP_\alpha = \sum_{\beta}^{M_{basis}} P_{\alpha\beta}$, and $\sum_{\alpha}^{M_{basis}} GOP_\alpha = N$. The total number of electrons assigned to a given atom, *A*, is the summation of GOP_α over all orbitals α belonging to atom *A*, the gross atom population $GAP_A = \sum_{\alpha \in A} GOP_\alpha$. The charge on

an atom, Q_A, is then defined as the difference of the gross atom population and the atomic number Z_A for this atom:

$$Q_A = Z_A - GAP_A. \tag{2.117}$$

The equal partitioning of the electrons from the off-diagonal terms is problematic because it does not account for differences in electronegativity of the atoms. Furthermore, the method is entirely dependent on the basis set used so computations with different basis sets cannot be compared and, unlike other properties, larger basis sets do not always increase that accuracy of the charge analysis.

Other techniques to compute partial atomic charges use the molecular electrostatic potential (MESP) which is the potential energy of a positive test charge at a particular location near a molecule. Two popular schemes utilizing this are the Merz–Singh–Kollman (MK)[171, 172] and the Charges from Electrostatic Potentials Using a Grid-Based (ChelpG)[173] methods. In each case, partial atomic charges are derived from a least-squares fit to the electrostatic potential calculated at a large number of points around the molecule to reproduce the MESP as closely as possible under the constraint that the sum of all atomic charges is equal to the overall charge of the system. The methods primarily in the points used to electrostatic potential. In MK, the grid points are located on four layers around the molecule constructed as an overlay of the van der Waals spheres around each atom. The best results are obtained by sampling points that are not too close to the van der Waals surface so the layers are constructed based on the van der Waals radii scaled up by factors of 1.4, 1.6, 1.8, and 2.0.[171, 172] In ChelpG, the MESP is calculated at a number of evenly spaced grid points regularly distributed in a cube. The cube is chosen such that the molecule is located at its center with 2.8 Å of space added between the molecule and the cube boundaries. Each of these methods discard points falling within the van der Waals radius of the molecule from the fitting procedure. The techniques using the MESP also provide a framework for generating electrostatic potential surfaces. For visualization, these are typically mapped onto the molecular electron density, which retains the underlying

shape of the chemical structure, based on a color-coded scheme that indicates electron-rich and electron-deficient regions of a molecule. The resulting model, thus, simultaneously depicts information about the size and shape of the molecule and the distribution and delocalization of charge.

Lastly, the concept of solvation is briefly addressed. Electronic structure calculations are carried out in the gas phase *in vacuo* at 0 K. However, most chemical processes take place in solvent. One method to include solvent effects is to introduce an implicit solvation model. Implicit solvation models quantify the solvent as a polarizable continuum with constant dielectric permittivity. The molecule (solute) is placed into a cavity in the continuum solvent medium. The charge distribution of the solute polarizes the solvent producing a solvent reaction potential which is added to the Hamiltonian. A common implicit solvation model is the polarizable continuum model (PCM) and its derivatives. The solvation free energy is given by

$$\Delta G_{sol} = \Delta G_{es} + \Delta G_{dr} + \Delta G_{cav}. \tag{2.118}$$

The terms ΔG_{es} and ΔG_{dr} are the electrostatic and dispersion-repulsion contributions to the free energy, and ΔG_{cav} is the energy required to make the cavity. These terms all depend on the definition of the cavity. The cavity in this method is generally constructed in three different ways depicted in Figure 2.2: (1) as a set of overlapping van der Waals spheres centered on the solute atoms which is used in calculating ΔG_{cav}, (2) the solvent accessible surface (SAS) is defined as the set of points corresponding to the center of a spherical solvent molecule as it rolls on the van der Waals surface used to calculate ΔG_{dr}, and (3) the solvent excluded surface (SES) defined as the surface of the tangent points as a spherical solvent molecule rolls on the van der Waals surface used to calculate ΔG_{es}.[139] The reaction field is represented through point charges located on the surface of the cavity which are localized through division of the spherical surface into small regions of known area.

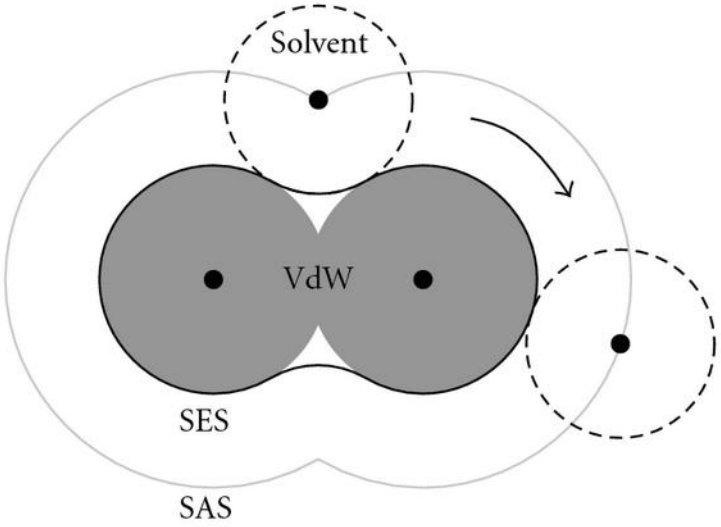

Figure 2.2. Illustration of the polarizable continuum model cavity surfaces.

2.4 Computational Methods and Models

2.4.1 Electronic structure calculations

All electronic structure calculations in this work were performed using the Gaussian 03 and 09 suites of programs.[174, 175] The final results presented in each study used the Kohn–Sham formalism of density functional theory (DFT) [147, 148] with optimizations carried out without symmetry constraints. However, not all studies used exactly the same level of theory, methodology, and systems. In all cases, collective effects of the extended environment have been neglected, and the results should be regarded as relative comparisons between the studied systems and not absolute values pertaining to a full, hydrated membrane. This section provides the computational details.

***Side chain flexibility in PFSA ionomers*.** Three single PFSA fragments were considered each consisting of a CF_3CFCF_3 backbone representation corresponding to: Nafion ($-OCF_2CF(CF_3)O(CF_2)_2SO_3H$), Aquivion or the short side chain (SSC) ($-O(CF_2)_2SO_3H$), and the 3M PFSA ($-O(CF_2)_4SO_3H$). Full optimizations (i.e., over all degrees of freedom) of the all *trans* conformation of the single side chain fragments were carried out using DFT invoking

Becke's 3-parameter Lee-Yang-Parr exchange-correlation functional (B3LYP)[154, 158, 176] and Grimme's B97D[177] functional, which includes empirical dispersion corrections, using the 6-31G** split-valence basis set.[160, 161, 178] Potential energy surface (PES) scans for rotation about the bonds along the side chains were then performed on the optimized structures to obtain relative energy profiles for these events. The scans were carried out by systematically rotating the chosen bond in 5° increments. The dihedral angle of the bond was the only fixed parameter with geometry optimizations performed over all other degrees of freedom at each step. Scans were also performed with each functional using the integral equation formalism (IEF) polarizable continuum model (PCM)[179] with water as the solvent to assess the solvation effect on the relative energy profiles. Test calculations were also performed for one of the SSC profiles using B97D with the larger 6-311++G(2d,2p) basis set and second-order Møller–Plesset theory (MP2) with the 6-31G** basis set to compare the results. Due to the computational cost, the calculations were performed without inclusion of the solvation model. The profiles using MP2/6-31G** and B97D/6-311++G(2d,2p)[180-183] follow the same trend as the B97D results with the smaller basis set and differ considerably from the B3LYP results. The energy maxima for the B97D scan with the larger basis set were only marginally higher than those obtained with the smaller basis set, and the MP2 maxima were found to be only slightly lower. The differences obtained did not merit the significantly greater computational cost of these calculations.

***Equivalent weight and side chain connectivity/Protogenic group separation and side chain chemistry*.** The systems in these two studies were quite different, but the same methodology was used in each case. The first study involved two fragments of the 3M PFSA membrane each with two pendant side chains ($-O(CF_2)_4SO_3H$) separated along a PTFE backbone by either five or seven CF_2 units corresponding to membrane equivalent weights of 590 and 690 g mol^{-1}. In the second study, single side chain fragments of three 3M MASC ionomers with a small backbone representation were used. Two of these are structural isomers with protogenic group separation determined by the location of a sulfonic acid group on an aromatic ring ($-O(CF_2)_4SO_2(NH)SO_2C_6H_4SO_3H$ where the sulfonic acid group is located in either the *meta* or the *ortho* position) and the third, termed the PFIA, has

protogenic groups separated by CF_2 units ($-O(CF_2)_4SO_2(NH)SO_2(CF_2)_3SO_3H$). Full optimizations were initially carried out invoking Hartree–Fock theory with the 6-31G** split-valence basis set.[178] The resulting structures were then refined with hybrid density functional theory (DFT) employing Becke's 3-parameter Lee-Yang-Parr exchange-correlation (B3LYP)[154, 158, 176] and the same basis set. Final optimizations were then performed at the B3LYP/6-311G** level of theory.[180] Subsequent to the 'dry' optimizations (i.e., without the addition of H_2O molecules), water molecules were individually added to the optimized systems at a variety of initial positions and full optimizations were performed using the protocol described above. Vibrational frequencies and zero point energies (ZPEs) were determined for all global minimum energy structures at the B3LYP/6-311G** level. The counterpoise (CP) method of Boys and Bernardi[162] was also employed to explore the effects of basis set superposition error (BSSE) on the water binding energies calculated from the CP-corrected minimum energy geometries and vibrational frequencies. As counterpoise optimizations are known possibly to change the resulting minimum energy structure in some molecular systems,[184] these calculations were repeated on different conformations and geometries for each system at all levels of hydration. Additionally, partial charges and electrostatic potentials were obtained according to the CHelpG scheme at the highest level of theory.[173] Potential energy surface (PES) scans of proton transfer were performed at the B3LYP/6-31G** level to obtain relative energy profiles for these events. The scans were carried out by incrementally increasing a specified O–H or N–H bond length across a hydrogen bond in steps of 0.02 Å. The O–H or N–H bond length was the only fixed parameter with an optimization performed over all other degrees of freedom at each step. The relative energies are plotted as a function of the asymmetric stretch coordinate, $q_{asym} = \frac{1}{\sqrt{2}}\left(r_{X1\cdots H} - r_{H\cdots X2}\right)$, where X1 represents the oxygen or nitrogen atom the proton is initially covalently bonded to and X2 represents the oxygen or nitrogen atom receiving the proton.

2.4.2 AIMD Simulations

Ab initio molecular dynamics simulations were performed using the Vienna *Ab Initio* Simulation Package (VASP).[165-167, 185] Core electrons were treated using the projector-augmented-wave (PAW) method.[186, 187] The Perdew–Burke–Ernzerhof (PBE) generalized gradient approximation for the exchange-correlation functional was used,[150, 152] and the electronic subsystem was sampled at the Γ-point of the first Brillouin zone with a plane wave cutoff of 400 eV. CNTs with chirality (14,0) and (17,0), with length of ~12.8 Å and diameters ranging between 11.0 and 14.0 Å, respectively, were chosen as encapsulation vessels for: (1) water molecules, (2) water molecules and an excess proton, and (3) aqueous triflic acid. The inner walls of the CNTs were either left bare or fluorinated to model different hydrophobic environments. The fluorine atoms were added to every next nearest neighbor carbon atom as uniformly as possible. The carbon atoms of the CNT wall and the attached fluorine atoms (when applicable) were held fixed, and periodic boundary conditions were imposed with 4 Å of vacuum added in the perpendicular directions to avoid interactions with other images in the supercell. The systems were initially relaxed to their minimum energy configuration and then annealed to 600 K via repeated velocity rescaling and then returned back to 300 K. This was followed by 3 ps simulations in the canonical ensemble and 3 ps of microcanonical MD for equilibration which were discarded. Born–Oppenheimer AIMD trajectories of 25-30 ps were generated with a time step of 0.5 fs in the microcanonical ensemble for data analysis.

Chapter 3 Results and Discussion

3.1 Electronic Structure Calculations on Local Hydration and Proton Transfer

3.1.1 Side chain flexibility in PFSA ionomers

We performed *ab initio* electronic structure calculations to explore side chain flexibility in three different PFSA ionomers. The fragments each consisted of a CF_3CFCF_3 backbone representation with a single pendant side chain: Nafion ($-OCF_2CF(CF_3)O(CF_2)_2SO_3H$), Aquivion or the short side chain ($-O(CF_2)_2SO_3H$), and the 3M PFSA ($-O(CF_2)_4SO_3H$). Rotational potential energy surfaces for each bond along the length of the side chain were obtained using both dispersion-corrected and non-dispersion-corrected DFT functionals with and without inclusion of a solvation model. Reproduced with permission from.[188] Copyright 2013 American Chemical Society.

Optimized structures and rotational profiles. Figure 3.1 shows the optimized (PCM/B3LYP/6-31G**) structures of each side chain fragment including the atom labels to be used in further discussion. Both the SSC and 3M side chains contain a single ether linkage between the side chain and backbone while Nafion contains both the side chain and backbone linkage and an additional one farther down the side chain. The ether linkage connecting the side chain and backbone in Nafion will be referred to as inner and the additional linkage in the side chain will be referred to as terminal. The results obtained for the upper portion of each side chain fragment revealed only minor differences between the potential energy profiles between the gas phase calculations and those obtained with the solvation model. Unless otherwise stated, the following discussion and figures represent the results obtained including the solvent.

Potential energy profiles for rotation about the $O–CF_2$ bond for each side chain are shown in Figure 3.2. Rotation about each of these bonds results in potential energy profiles with similar shape but different energetic barriers. The maximum value obtained in each case

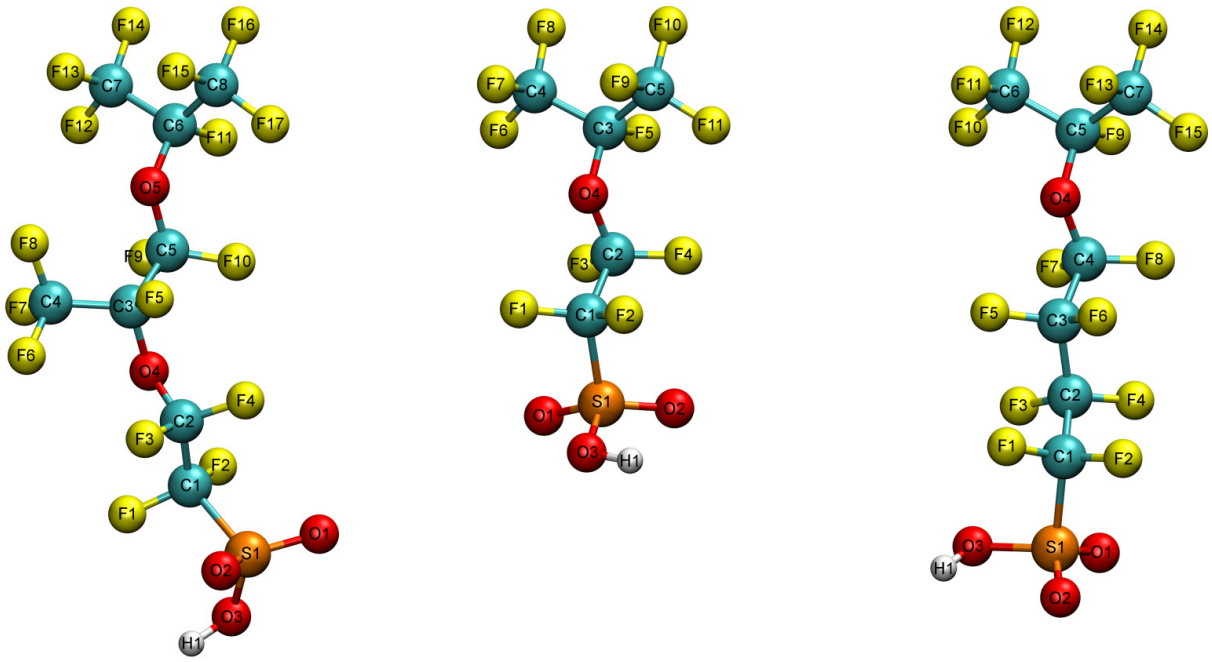

(a) (b) (c)

Figure 3.1. Optimized (PCM/B3LYP/6-31G**) structures with atoms labeled for the all trans side chain fragments: (a) Nafion, (b) SSC, and (c) 3M PFSA. The colored spheres represent different atom types with: gray–carbon, yellow–fluorine, red–oxygen, orange–sulfur, and white–hydrogen.

occurs when the C–O–C–C dihedral angle is at 0° resulting in a *cis* conformation. In the case of the SSC and 3M side chains, this also corresponds to eclipsing the first side chain F_2C–CF_2 bond with the F–C bond located at the point where the side chain attaches to the backbone. For Nafion, the inner maximum results from eclipsing the C5–C3 bond in the side chain with the C6–F11 bond of the backbone with the ether oxygen atoms adopting a *gauche* conformation. The terminal PES scan maximum corresponds to eclipsing the C2–C1 bond with the C3–F5 bond in a nearly identical conformation to that observed for the SSC and is 1.7 kcal/mol lower in energy than the inner maximum. However, the B97D results, shown in Figure 3.3, exhibit much more similar barriers between the two Nafion PES scans along with the other two side chains. This is most pronounced for the inner Nafion barrier which may be due to a favorable gauche conformation of the ether oxygen atoms using B97D, which will become more apparent in the following section. It is important to note that

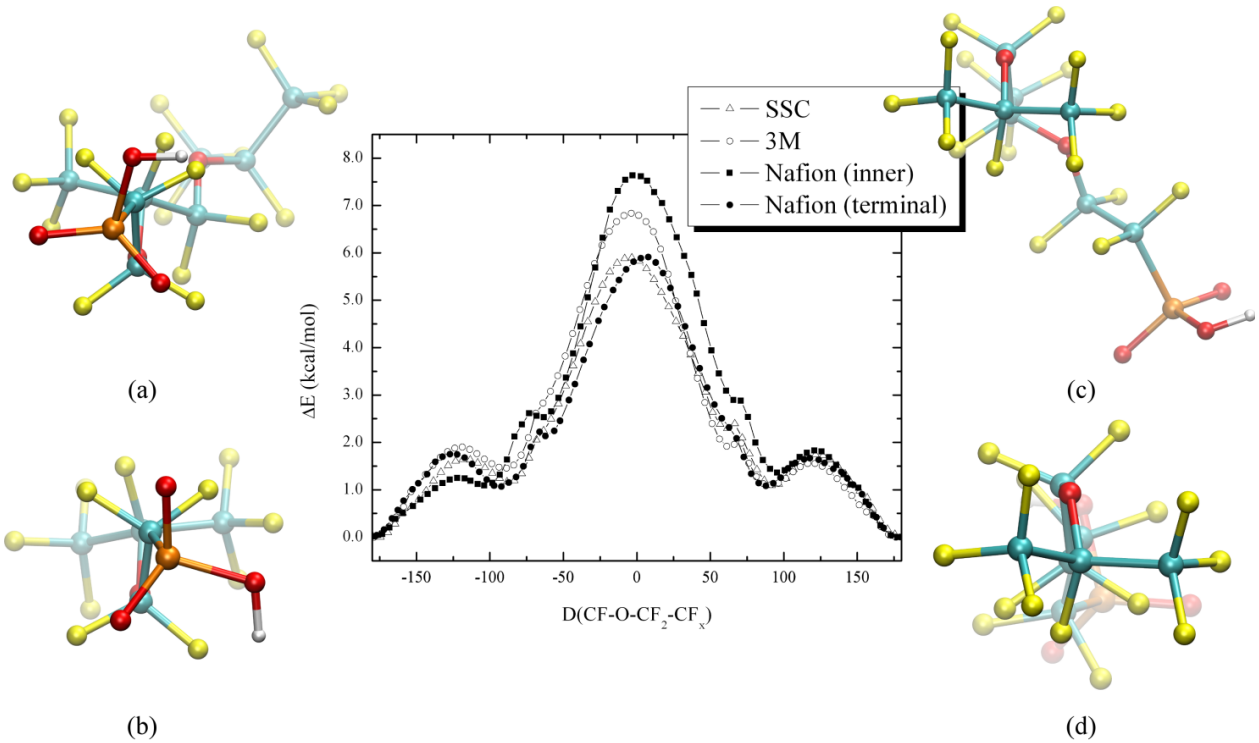

Figure 3.2. Potential energy profile for rotation about the O–CF_2 bonds at the PCM/B3LYP/6-31G** level of theory. The views along the dihedral angle are shown for: (a) 3M, (b) SSC, (c) Nafion (inner), and (d) Nafion (terminal).

obtaining smooth potential energy surfaces for these rotations was considerably more difficult to obtain than those for the other bonds even with the small increments for this rotation. This is likely due to the side chain being caught in high energy conformations that failed to relax properly. When this occurred, the constraint on the dihedral angle was relaxed and a full optimization was performed followed by a partial optimization with the dihedral angle fixed.

The PES scans for rotation about the CF_2–CF_y (y = 1 for Nafion and 2 for 3M) bond for the Nafion and 3M side chains are shown in Figure 3.4 with the maxima shown in the outer panels with top to bottom corresponding to left to right maxima. Distinctly different relative energy profiles were found for the two side chains, as well as with the different functionals. The positions of the maxima and minima correspond to similar dihedral angle conformations regardless of the functional used, but the energetic barriers are

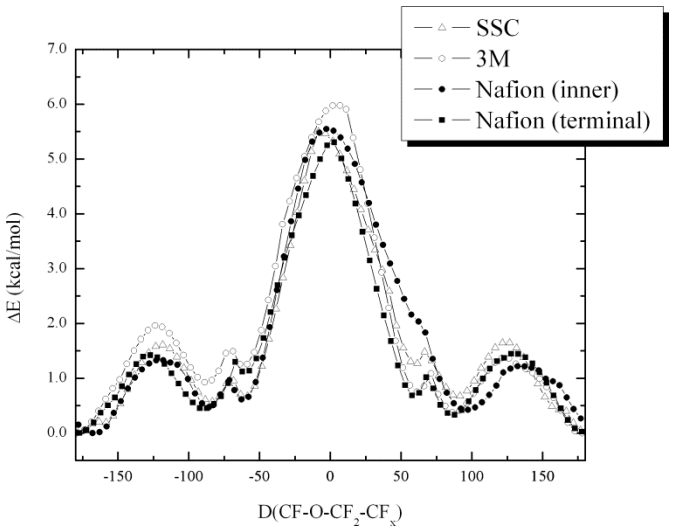

Figure 3.3. Potential energy profiles for rotation about the O–CF_2 bonds at the PCM/B97D/6-31G** level of theory.

considerably different. For Nafion, the first peak at -135° corresponds to eclipsing atoms O5/F5, O4/F10, and F9/C4 with values of 2.4 kcal/mol (B3LYP) and 4.2 kcal/mol (B97D). However, this is only 2.7 kcal/mol (B97D) higher in energy than the initial geometry with the ether oxygen atoms in a *trans* conformation. The side chain is considerably folded at the following minimum with the two ether oxygen atoms in a *gauche* minus (*g*-) conformation. This changes the distance between the central backbone carbon atom and the sulfur atom of the fully elongated conformation from 8.44 to 6.19 Å for B3LYP and 8.48 to 6.12 Å for B97D, and the minimum was found to be 0.18 kcal/mol lower in energy than the fully elongated side chain using B3LYP but 1.5 kcal/mol lower in energy using B97D. The maximum at approximately -20° of 2.1 kcal/mol (B3LYP) and 2.3 kcal/mol (B97D) is due to eclipsing atoms O4/O5, F10/C4, and F5/F9. This is followed by a minimum with ether oxygen atoms *gauche* plus (*g*+) that maintains a folded conformation where the lower portion of the side chain is perpendicular to the backbone (i.e., a C6/C3/S1 angle of ~90°) with a carbon-sulfur distance of 7.45 Å (6.78 Å B97D) that is 0.16 kcal/mol (B3LYP) and 1.2 kcal/mol (B97D) lower in energy than the fully elongated state. This perpendicular conformation in Nafion and reduction in side chain end-to-end distance is consistent with several computational studies.[189-192] The side chain begins to unfold towards the last

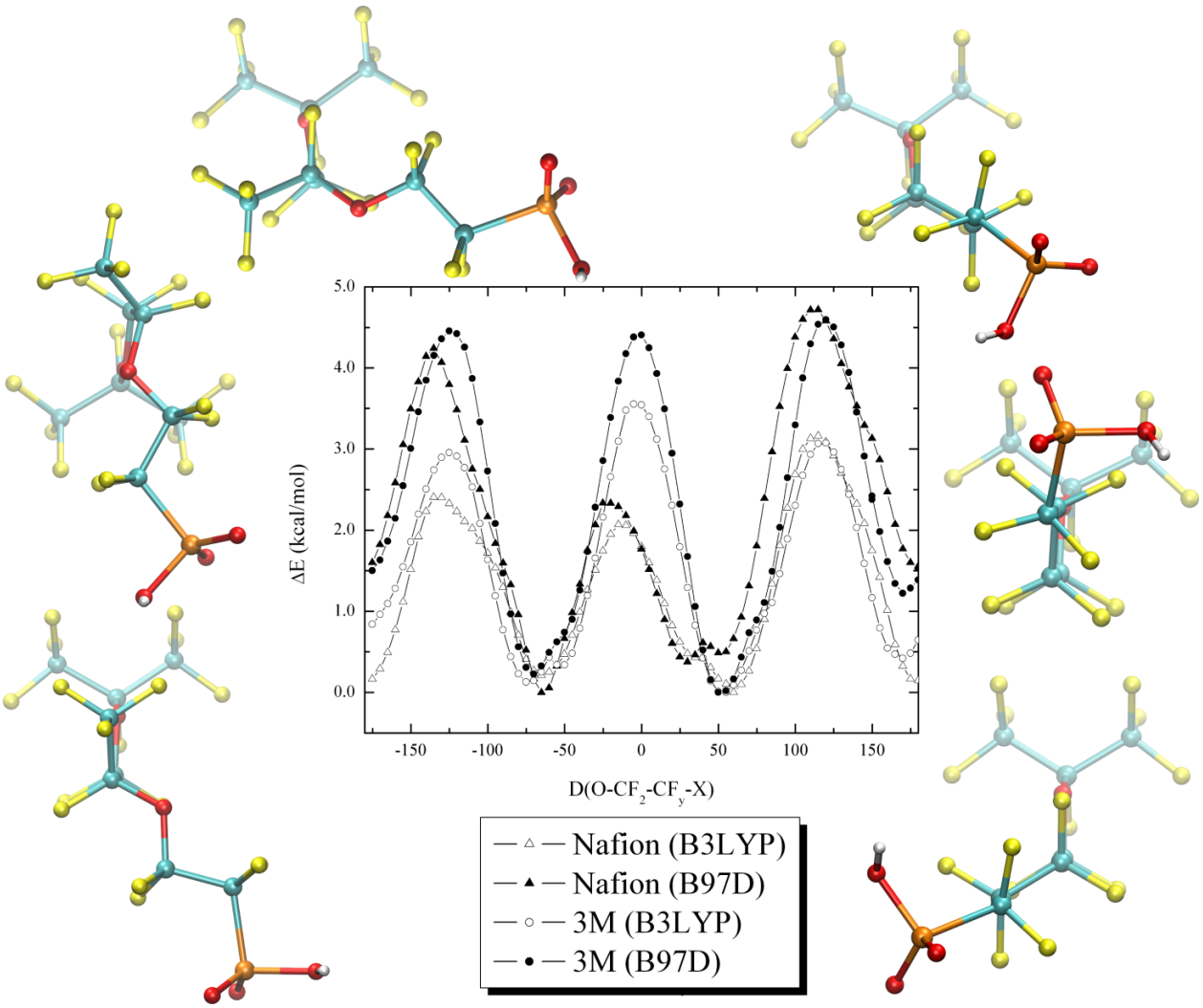

Figure 3.4. Potential energy profiles for rotation about the CF_2–CF_y bond (y = 1, X = $(CF_3)O$ for Nafion; y = 2, X = CF_2 for 3M) using the PCM at B3LYP/6-31G** and B97D/6-31G** levels of theory. The surrounding structures show views along the dihedral angle for the maxima obtained for Nafion (left panel) and 3M (right panel) with the top, middle, and bottom structures representing the left, central, and right maxima, respectively.

barrier at 115° with eclipsing O5/C4, O4/F9, and F5/F10 atoms. Interestingly, the difference between the values obtained using the B3LYP and B97D functionals are most pronounced for the barriers from the folded conformations to the fully elongated conformation while little change was found for the barrier between folded conformations. As mentioned previously, this may be due to increased stabilization of the compact, folded side chain with ether oxygen atoms *gauche* when dispersion corrections are included. The

barrier between *gauche* conformations was also less impacted for the 3M side chain where the maxima at ±120° are 50% higher using B97D and that at 0° is 23% higher. The maxima at ±120° have eclipsed O/F, F/C, and F/F atoms, and the dihedral angle at the central barrier is in a *cis* conformation with eclipsing O/C, F/F, and F/F atoms. As with Nafion, the B97D barriers going from *trans* to *gauche* minima are lower than the reverse, but the barrier between *gauche* conformations is notably higher than that for Nafion and is the highest using B3LYP. The all *trans* minimum at ~170° has a carbon-sulfur distance of 7.90 Å (7.99 Å B97D) while a somewhat bent *g*+ conformation at 50° has a corresponding distance of 6.80 Å (6.72 B97D) and is 0.42 kcal/mol lower in energy than the elongated conformation using B3LYP and 1.2 kcal/mol lower with B97D. The side chain also appears to be more rigid than Nafion showing less change in the end-to-end distance, only varying between 6.65 to 8.00 Å throughout the scan as opposed to 5.65 to 8.56 Å in Nafion. This is likely due to the greater flexibility of the C3–O4 bond of Nafion below the C5–C3 bond than the C3–C2 bond in 3M. The complete rotation of these bonds leads to energetic barriers exceeding 5 kcal/mol for Nafion and 7 kcal/mol for 3M. However, a significant portion of the Nafion C3–O4 rotational profile has less than a 1 kcal/mol energetic penalty which is not the case for the 3M C3–C2 bond, suggesting greater rotational freedom in Nafion.

Relative energy profiles for rotating the C2–C1 bond adjacent to the sulfonic acid group in each side chain are shown in Figure 3.5. The atoms associated with this dihedral angle for the Nafion and SSC side chains are O4–C2–C1–S1, while those for 3M are C3–C2–C1–S1. This leads to a distinctly different energetic profile for the 3M side chain than the other two, which are equivalent. The B3LYP profiles for Nafion and SSC exhibit approximately three-fold degeneracy in both minima and maxima corresponding to staggered and eclipsed F, O, and S atoms, respectively. However, when the B97D functional was used two equivalent minima corresponding to the sulfur atom and the ether oxygen atom in *gauche* conformations were found with the fully elongated *trans* conformation approximately 1 kcal/mol higher in energy. The central rotational barrier using the B97D functional of 3.2 kcal/mol occurs when going between these *gauche* conformations and, again, higher rotational barriers occur when going from *gauche* to *trans* than *trans* to *gauche*

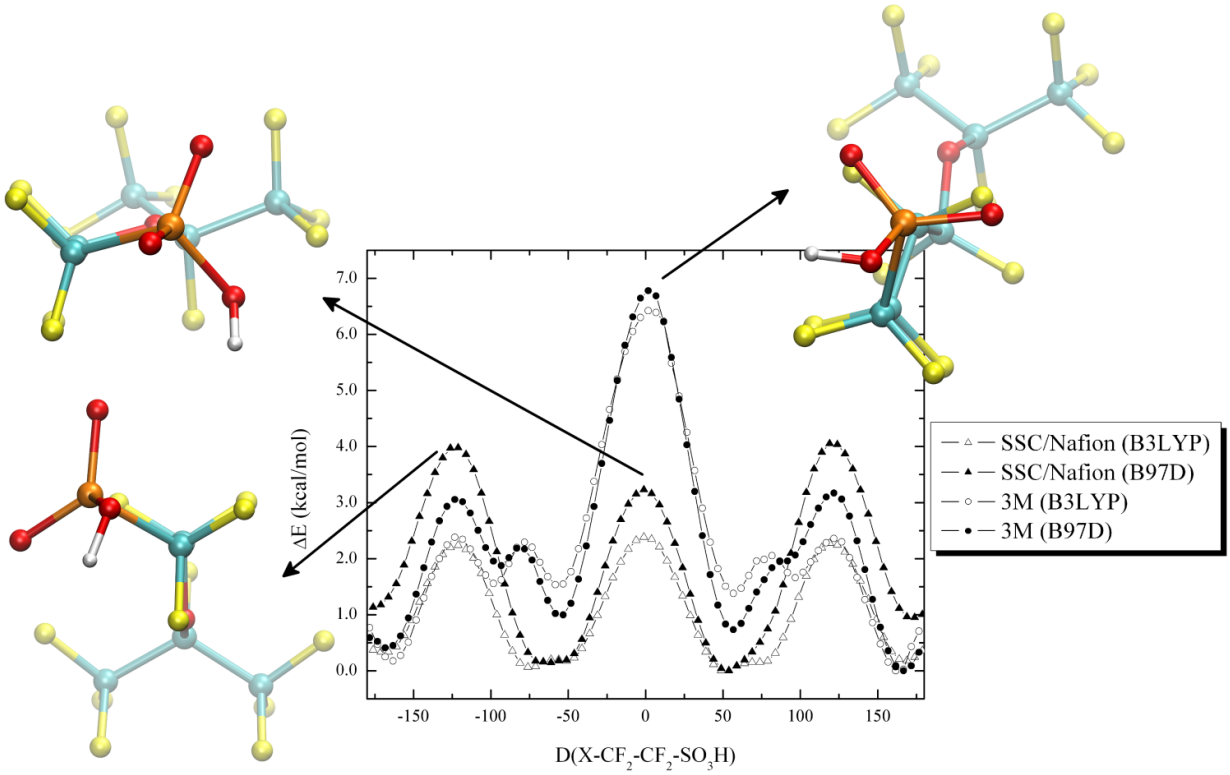

Figure 3.5. Potential energy profiles for rotation about the C1–C2 bond (X = O for SSC/Nafion; X = CF_2 for 3M) using the PCM at B3LYP/6-31G** and B97D/6-31G** levels of theory. The results for the SSC and Nafion side chain were identical. The representations shown in the left panel correspond to the SSC.

conformations. The opposite is true for the 3M PES scan which is also highly symmetric but with multiple distinct maxima and minima. The maxima at approximately ±120° are due to eclipsing of F/F, F/C, and F/S atoms. The two following maxima in the B3LYP profile at ±80° result from a rotation that brings a sulfonic acid group oxygen atom in closer proximity to a fluorine atom of C3. These are less pronounced in the B97D profile. In contrast to the SSC and Nafion results, the *gauche* minima at ±55° are ~1 kcal/mol (1.5 kcal/mol B3LYP) higher in energy than the *trans* conformation likely due to the additional crowding of the of oxygen atoms of the sulfonic acid group and the C3 fluorine atoms. The largest maximum at 0° exhibits less influence on the choice of functional with S1 and C3 in

a cis conformation and eclipsed C1 and C2 fluorine atoms with a great deal of steric hindrance associated with the sulfonic acid oxygen atoms and the C3 fluorine atoms. At 0° both Nafion and SSC do not contain the additional CF_2 group that causes the steric hindrance considerably lowering the rotational energy barrier between *gauche* conformations. The inclusion of the solvation model for the Nafion and SSC side chains for the barriers at ±120° rotation decreased the energetic barriers by approximately 5% with B97D and 9% with B3LYP with no change for the one at 0°. It was observed to have no effect on the energetic profile for the 3M side chain.

Notable differences between the profiles and barriers obtained between the gas phase calculations and those including solvation effects were obtained when rotating about the C1–S1 bond. This is of little surprise as it more directly involves the hydrophilic portion of the side chain that interacts with water. The results for each side chain fragment were identical, and the representative configurations shown in Figure 3.6 correspond to the SSC. The results show three maxima and minima for each level of theory corresponding to configurations with eclipsed and staggered F1, F2, and C2 with the sulfonic acid oxygen atoms, respectively, as shown in the associated structures. These are essentially degenerate for the gas phase B3LYP PES scan. Similar barriers at ±120° were found for the B97D gas phase results. These correspond to the cases where one of the sulfonic acid oxygen atoms without the proton eclipses atom C2 while the protonated oxygen eclipses a fluorine atom. Inclusion of the solvation model reduced these barriers by roughly 30% in each case. However, greater differences between the levels tested were observed for the maximum at ~0° and the minimum at ~70°. This maximum has the protonated sulfonic acid oxygen atom eclipsing C2 and the proton eclipsed with F4 and is the lowest barrier determined using the B97D functional without the solvent indicating there may be a weak interaction due to the eclipsed O–H and C–F bonds. Inclusion of the solvent decreases this barrier by 10% using B3LYP and by 18% using B97D, but it then becomes the highest of the energetic barriers for each functional. This effect is also observed for the minimum at 70°, which was the lowest gas phase B97D result, where the proton is ~0.3 Å closer to the nearest fluorine atom than that associated with the other minima. When the solvation model was employed,

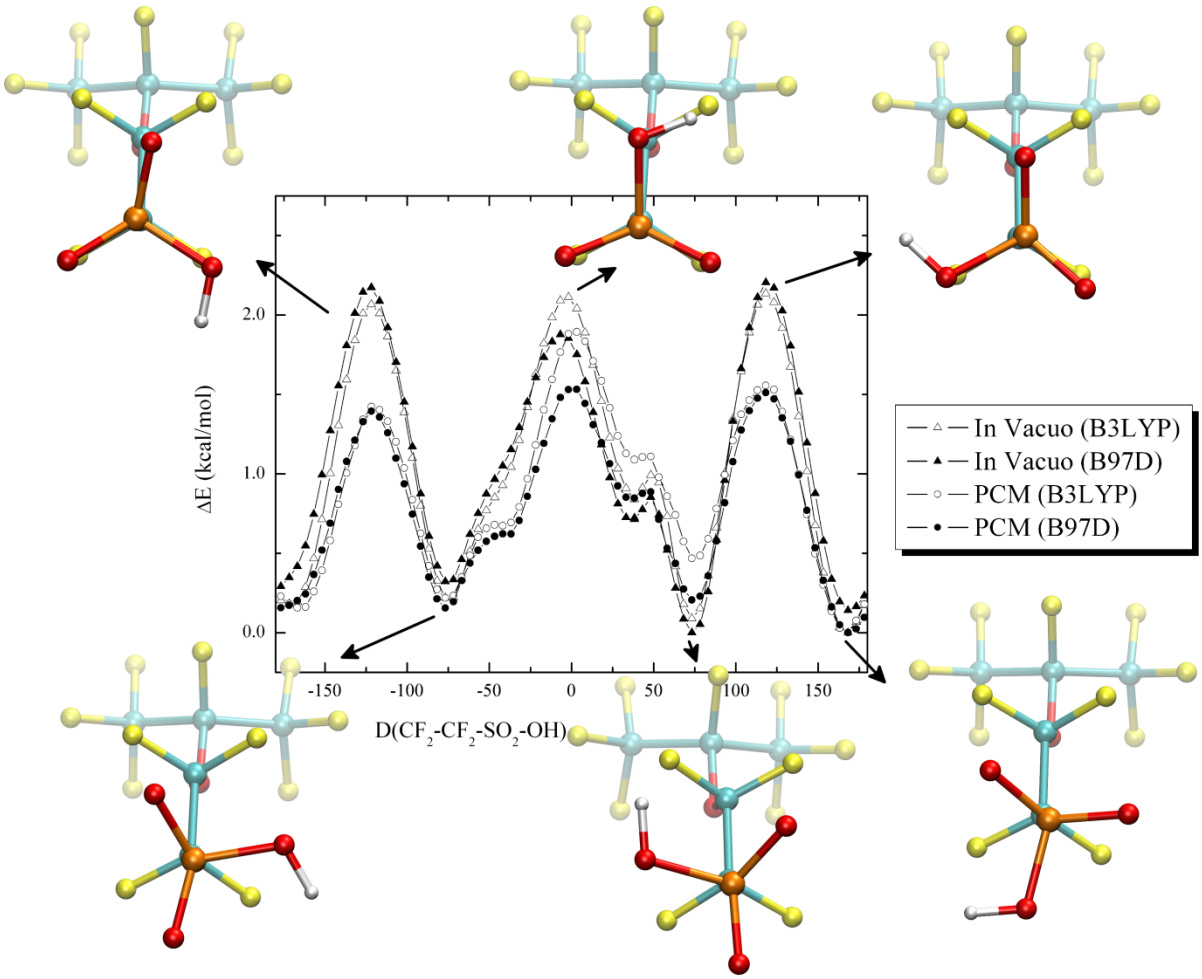

Figure 3.6. Potential energy profiles for rotation about the C1–S1 bond at the B3LYP/6-31G** and B97D/6-31G** levels of theory both in vacuum and with the inclusion of the solvation model. The representations shown in the left panel correspond to the SSC.

this minimum became less favored while the other minima became more favorable.

Lastly, Figure 3.7 shows the relative energy profile for rotation of the S1–O3 bond. Similar to what was found in previous studies,[57, 71] the profile has two similar minima and two different maxima. The higher maximum corresponds to the proton directed inwards with the O–H bond eclipsing the C–S bond, and the lower maximum corresponds to the proton directed outward away from the side chain. The minimum at 85° is 0.32 kcal/mol lower than the minimum at 85° for the gas phase B97D results. As with the previously mentioned results, the proton at this minimum is again located ~0.3 Å closer to the nearest

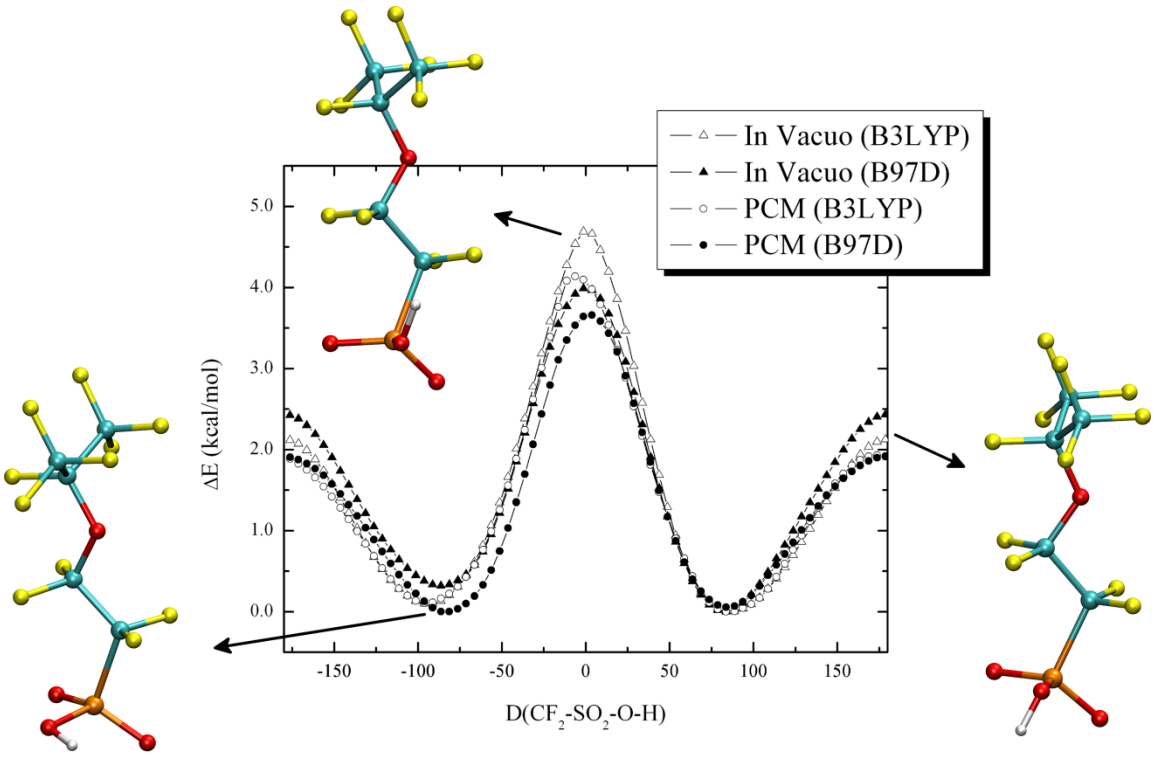

Figure 3.7. Potential energy profiles for rotation about the S–OH bond at the B3LYP/6-31G** and B97D/6-31G** levels of theory both in vacuum and with the inclusion of the solvation model. The representations shown in the left panel correspond to the SSC.

fluorine atom and when the solvation model was included it no longer was the preferred conformation resulting in two isoenergetic minima. The maxima using the B3LYP functional reduce by approximately 10% with the PCM, but the B97D results indicate only an 8% reduction in the central barrier and a 21% reduction in the barrier at ±180°. The latter barrier is equivalent between the PCM results for each functional but is higher for the gas phase calculations. This may be due to the increased stabilization in the gas phase results from the fluorine-hydrogen interaction as the B97D gas phase barrier at ±180° is 0.31 kcal/mol higher in energy than the gas phase B3LYP barrier.

Summary. We have examined the energetic profiles for rotation about side chain bonds of three PFSA side chain fragments: SSC ($-O(CF_2)_2SO_3H$), 3M ($-O(CF_2)_4SO_3H$), and Nafion ($-OCF_2CF(CF_3)O(CF_2)_2SO_3H$) through *ab initio* electronic structure calculations. PES scans

were obtained using the B3LYP functional and the dispersion-corrected B97D functional with and without the inclusion of the PCM solvation model for bond rotations in 5° increments. Solvent effects were found to have little impact on the relative energy profiles for internal rotations near the side chain attachment to the backbone. Closer to the sulfonic acid terminus, the impact of the solvation model becomes much more pronounced. Consistent with previous findings,[71] the lowest barriers were found for rotation about the carbon-sulfur bond for each level tested, and these barriers were significantly reduced when the solvation model was implemented.

The highest barriers for Nafion involved complete rotations about the C–O and O–C bonds of the ether linkages. However, significant portions of the rotational potential energy surfaces had energetic penalties less than 1.5 kcal/mol suggesting a fair amount of conformational freedom in the associated dihedral angles. The results obtained using B97D suggest energetically favored *g*+ or *g*- ether oxygen atom conformations with the side chain folded essentially perpendicular to the backbone, while use of the B3LYP functional led to nearly isoenergetic folded and unfolded conformers. The energetic penalty (B97D) in going from the elongated *trans* structure to the folded *gauche* conformations was lower than that for unfolding the side chain, which may be due to the increased stabilization of the folded conformation when dispersion corrections are included and indicates that the side chain may likely remain folded. Below the second ether linkage of Nafion, the rotational profiles match that of the SSC side chain with energetically preferred *gauche* conformations of the ether oxygen atom to the sulfur atom. This is consistent with several studies which indicate that the Nafion side chain is preferentially in a folded conformation and acts similarly to the SSC PFSA.[58, 189-192] The 3M side chain also exhibited preferential *gauche* conformations for rotations about the upper carbon-carbon bond (i.e., C3–C4). However, the energetic barrier in going between *gauche* conformers was essentially equal to that of going from *gauche* to *trans* with a significantly higher barrier than Nafion. Furthermore, high barriers for complete rotation about the carbon-carbon bonds near the middle of the side chain were found with each functional with less contraction in side chain length suggesting more rigidity in the 3M side chain. These results indicate that minor differences in side chain

length and chemistry can have a pronounced effect on the rotational potential energy surfaces, particularly those involving rotation about different carbon-carbon bonds which had distinctly different character.

It is important to note that in this study we are not attempting to describe characteristics of a full ionomer membrane (or even a representative portion of the hydrated morphology) but to compare relative tendencies in the energetics associated with bond rotations of the three PFSA ionomers with the use of different DFT functionals. The presence of multiple interacting acid groups and the nature of the structural organization of the hydrated extended membrane system will likely change the determined rotational barriers in a non-trivial way. Hence, the calculated energetic barriers for rotation should not be taken as absolute values, but rather as relative comparison as to how side chain length and chemistry affect conformational freedom.

3.1.2 Equivalent weight and side chain connectivity

Electronic structure calculations were performed to explore the roles of side chain separation and the connectivity of adjacent acid groups on proton dissociation and transfer in the 3M PFSA membrane through consideration of oligomeric fragments with a different number of difluoromethylene (CF_2) backbone units separating the side chains. The fragments consist of a poly(tetrafluoroethylene) (PTFE) backbone with two pendant side chains each functionalized by a terminal sulfonic acid group. Two different side chain separations along the PTFE backbone were used to model different equivalent weight (EW) ionomers with chemical formula $CF_3CF(-O(CF_2)_4SO_3H)(CF_2)_nCF(-O(CF_2)_4SO_3H)CF_3$, where n = 5 and 7, corresponding to membrane equivalent weights (EWs) of 590 and 690 grams ionomer per mole acid, respectively. Global minimum energy structures of the fragments with and without the addition of water molecules were obtained from a variety of initial configurations to ascertain the factors that contribute to proton dissociation at low hydration levels. The energetics associated with proton transfer were also determined for several proton transfer events. .[73, 74] Reproduced by permission of the PCCP Owner Societies and Elsevier.

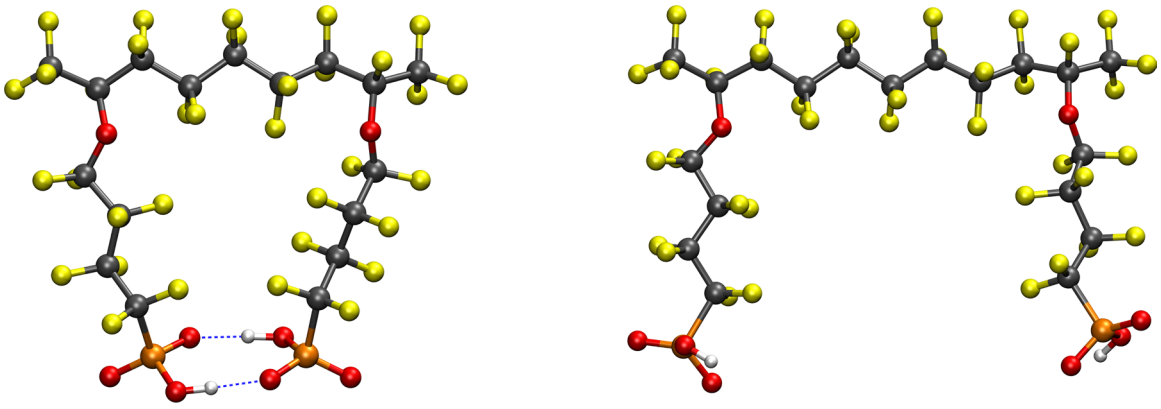

(a) (b)

Figure 3.8. Optimized (B3LYP/6-311G**) 'dry' minimum energy structures of 3M PFSA fragments showing: (a) EW 590 with side chains separated by five CF_2 units exhibiting doubly hydrogen bonded sulfonic acid groups and (b) EW 690 with side chains separated by seven CF_2 units where the side chains remain well separated. The different colored spheres represent different atom types: grey–carbon, red–oxygen, light blue–fluorine, yellow–sulfur, and white–hydrogen. Hydrogen bonds are denoted by dashed lines.

Optimized structures. Fully optimized (B3LYP/6-311G**) minimum energy structures of the EW 590 and 690 fragments are shown in Figure 3.8. The EW 590 (Figure 3.8a) exhibits double hydrogen bonded sulfonic acid groups with a fully extended (i.e., showing no kinking or distortion) PTFE backbone and side chains with a S···S distance of only 4.35 Å. The doubly hydrogen bonded configuration was found to be ~11.1 kcal/mol lower in energy than the optimized geometry containing no hydrogen bonds between sulfonic acid groups, suggesting that the side chains will preferentially interact without the presence of water. However, the EW 690 (Figure 3.8b) with a fully extended backbone conformation does not contain hydrogen bonding between sulfonic acid groups due to the additional CF_2 units separating the side chains resulting in a S···S distance of 12.67 Å.

In order to explore hydrogen bonding and proton dissociation at low hydration, water molecules were sequentially added to the optimized geometries at a variety of initial positions. The addition of a single water molecule to EW 590 resulted in a 'ring-like' hydrogen bond network maintaining one of the direct sulfonic acid group hydrogen bonds

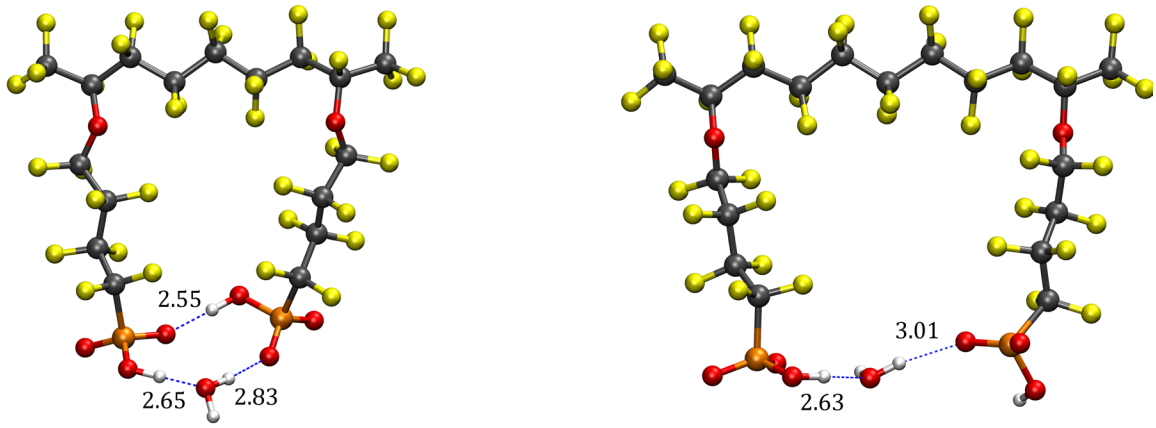

Figure 3.9. Optimized (B3LYP/6-311G**) minimum energy structures of two side chain 3M PFSA fragments with the addition of 1 H_2O molecule with the hydrogen bonds distances (Å) for (a) EW 590 and (b) EW 690.

and a hydrogen bond connectivity of the sulfonic acid groups through the water molecule acting as a hydrogen bond donor and acceptor, as shown in Figure 3.9a. No direct hydrogen bonding between side chain sulfonic acid groups was observed in EW 690 at this hydration level; however, the water molecule did bring about some aggregation of the side chains as the water molecule acts as a hydrogen bond donor and acceptor bridging the sulfonic acid groups reducing the S···S distance to 7.10 Å (Figure 3.9b). These hydrogen bonds are considerably weaker than those of EW 590 (as indicated by the O···O distances), and one acidic proton is not involved in any hydrogen bonding. While no proton dissociation occurred in either oligomeric fragment at this hydration level, the differences observed in the hydrogen bonding between the EW 590 and 690 systems under 'dry' and primarily hydrated conditions affect proton dissociation upon increasing hydration.

The lowest energy structures at all hydration levels maintained similar configurations where hydrogen bonding involved both of the sulfonic acid groups and the water molecules forming a connectivity bridge between the side chains. Hydrogen bonding is fundamental in stabilizing excess charge once proton dissociation occurs. Hence, the extent of this connectivity was found to influence the number of water molecules required to facilitate proton dissociation of the side chain sulfonic acid groups. First proton dissociation was

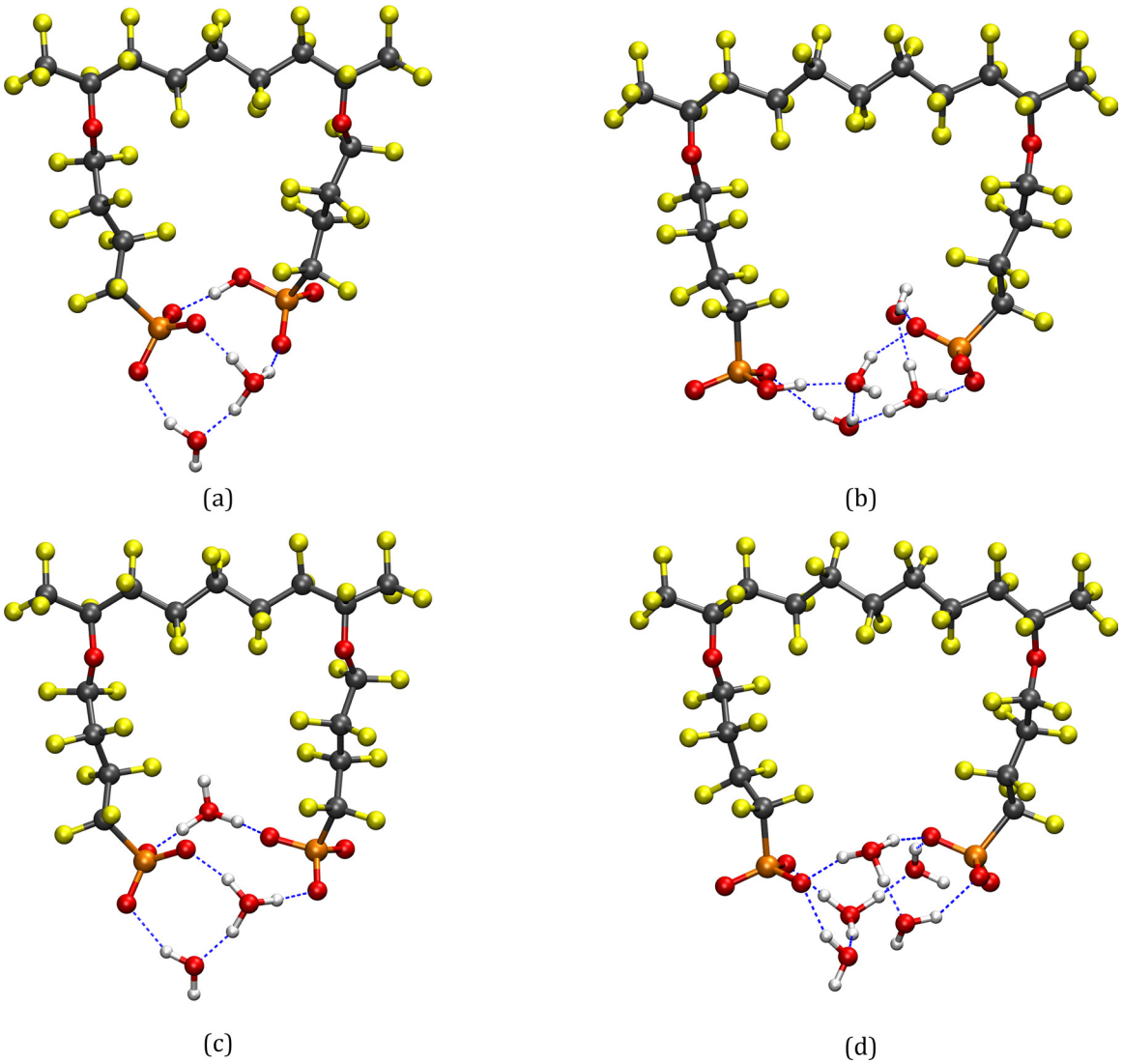

Figure 3.10. Optimized (B3LYP/6-311G**) geometries of the hydrated 3M PFSA fragments showing: 1st proton dissociation requiring the addition of (a) 2 H_2O molecules for EW 590 and (b) 4 H_2O molecules for EW 690, and 2nd proton dissociation requiring the addition of (c) 3 H_2O molecules for EW 590 and (d) 5 H_2O molecules for EW 690.

observed in EW 590 upon addition of only two water molecules (Figure 3.10a). The configuration contains a single direct hydrogen bond between the sulfonic acid group and the, now, sulfonate group which stabilizes the resulting excess negative charge on the sulfonate oxygen atoms. The dissociated proton exists as a hydronium ion which donates hydrogen bonds to the sulfonic acid and sulfonate groups bridging the side chains. The

system with greater separation of the side chains (EW 690) did not exhibit proton dissociation until four water molecules were added (Figure 3.10b) as the greater side chain separation precluded the cooperative interaction through hydrogen bonding that promotes proton dissociation at low hydration in membranes of this type. Furthermore, dissociation of the second acidic proton occurred upon addition of only three water molecules in EW 590 (Figure 3.10c) while this was not observed in the EW 690 system until addition of five water molecules (Figure 3.10d). The closer proximity of side chains in EW 590 effectively promotes stronger hydrogen bonds configured in a more continuous, all-encompassing hydrogen bond network which profoundly affects proton dissociation at low hydration levels.

Proton transfer. The previous discussion showed that the separation of side chains significantly influences the nature of hydrogen bonding and proton dissociation. To more completely understand the energetics of proton transfer in these systems at different EWs, PES scans for proton transfer were performed using the optimized structures previously obtained. Several PES scans were performed for a variety of proton transfer events and only a representative sample are discussed here.

Figures 3.11 and 3.12 show PES scans from an associated sulfonic acid proton to a neighboring water molecule at a hydration of 4 H_2O molecules for EW 590 and EW 690, respectively. The structure in Figure 3.11 containing one proton not dissociated was not the minimum energy structure found for EW 590 at this hydration level, but this optimized geometry provides a means for comparison to the EW 690 minimum energy structure. The energetic barrier for proton transfer was found to be significantly lower in EW 590 than that of EW 690 as it forms a hydrogen bond network that more readily reorients to compensate for the transfer of charge. In EW 590, the water molecule accepting the proton also donates a hydrogen bond to the right sulfonate group. As the proton is transferred, this hydrogen bond distance decreases as a result of the propensity for protonated species to delocalize excess positive charge through strong hydrogen bonds. The additional positive charge delocalized over the sulfonate oxygen atom repels away a different water molecule

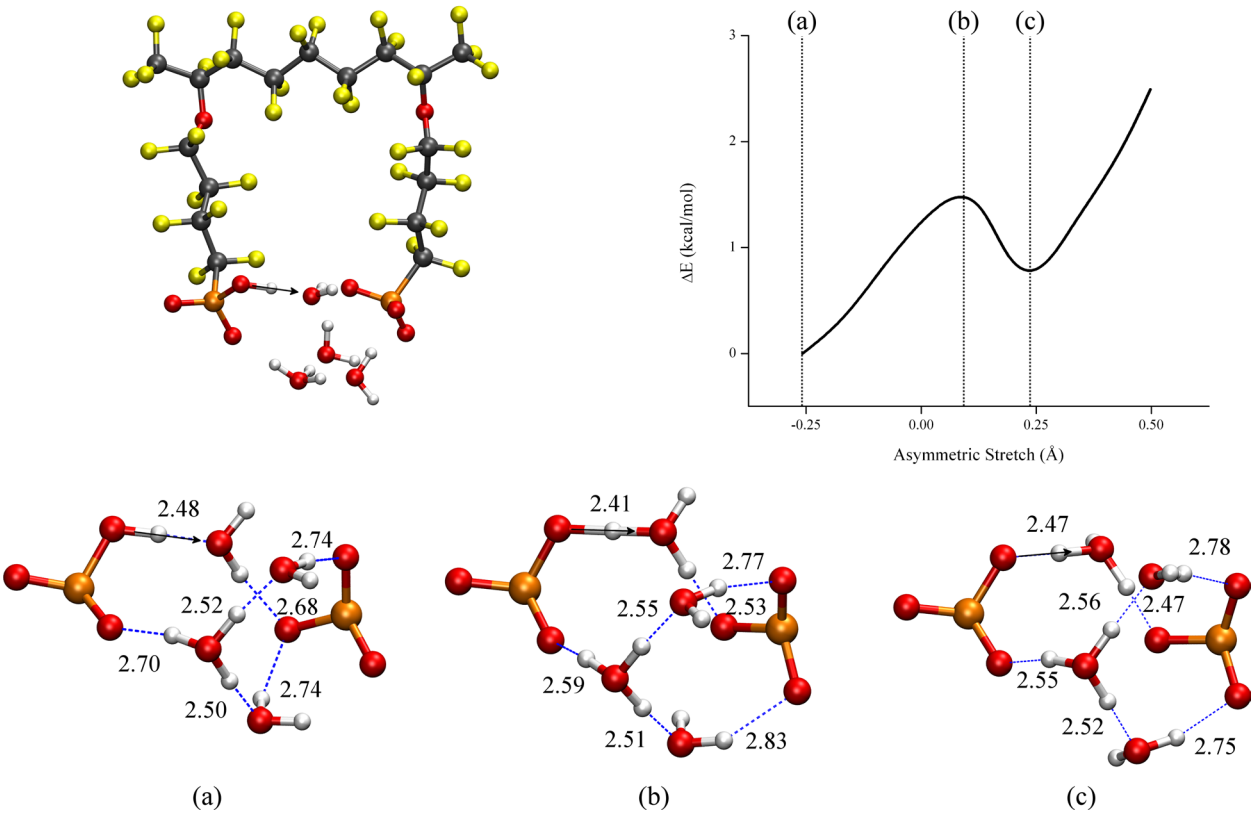

Figure 3.11. Top left panel: Optimized (B3LYP/6-31G**) structure of the EW 590 3M PFSA ionomer at a hydration of 4 H2O molecules used in the PES scan of the proton transfer indicated by the black arrow. Top right panel: Relative energy profile with respect to the original configuration as a function of the asymmetric stretch coordinate. Bottom panel: rotated bottom view of the sulfonic acid/sulfonate and water molecules with hydrogen bonds denoted by dashed lines and hydrogen bond distances (Å): (a) initial configuration; (b) transition state; and (c) the local minimum points of the scan.

initially donating a hydrogen bond to it. This results in a hydrogen bond shift of the water molecule to an oxygen atom on the same sulfonate group which was not originally involved in any hydrogen bonding at the transition state with a barrier of only 1.5 kcal/mol. Both acidic protons are dissociated at the local minimum in the PES scan, which was only 0.7 kcal/mol higher in energy than the original configuration. The analogous proton transfer profile for EW 690 (Figure 3.12) required the breaking of multiple hydrogen bonds. The increased side chain separation in EW 690 promoted greater interactions between water molecules. The water molecule accepting the proton also received a

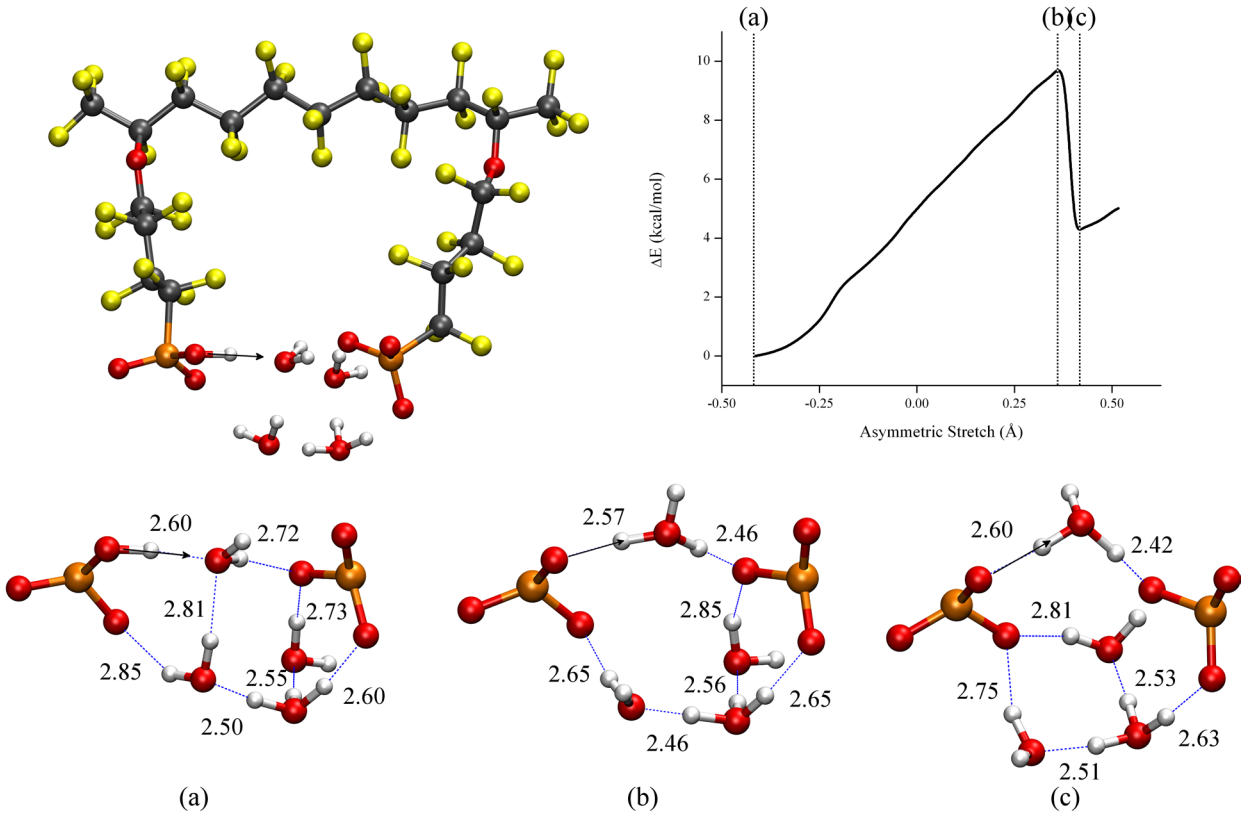

Figure 3.12. Top left panel: Optimized (B3LYP/6-31G**) structure of the EW 690 3M PFSA ionomer at a hydration of 4 H2O molecules used in the PES scan of the proton transfer indicated by the black arrow. Top right panel: Relative energy profile with respect to the original configuration as a function of the asymmetric stretch coordinate. Bottom panel: rotated bottom view of the sulfonic acid/sulfonate and water molecules with hydrogen bonds denoted by dashed lines and hydrogen bond distances (Å): (a) initial configuration; (b) transition state; and (c) local minimum of the scan.

hydrogen bond from a neighboring water molecule, which was quickly broken as a result of the additional positive charge received by the proton accepting water molecule. Other than this, only contractions and expansions in hydrogen bond lengths associated with the transfer of charge were observed up to the transition state with an energetic barrier of 9.8 kcal/mol. This was followed by an abrupt jump to a local minimum 4.1 kcal/mol higher in energy than the initial configuration, requiring a considerable rearrangement in hydrogen bonding and partial transfer of a proton from the newly formed hydronium ion to the right sulfonate group. The considerably high energetic barrier for the doubly

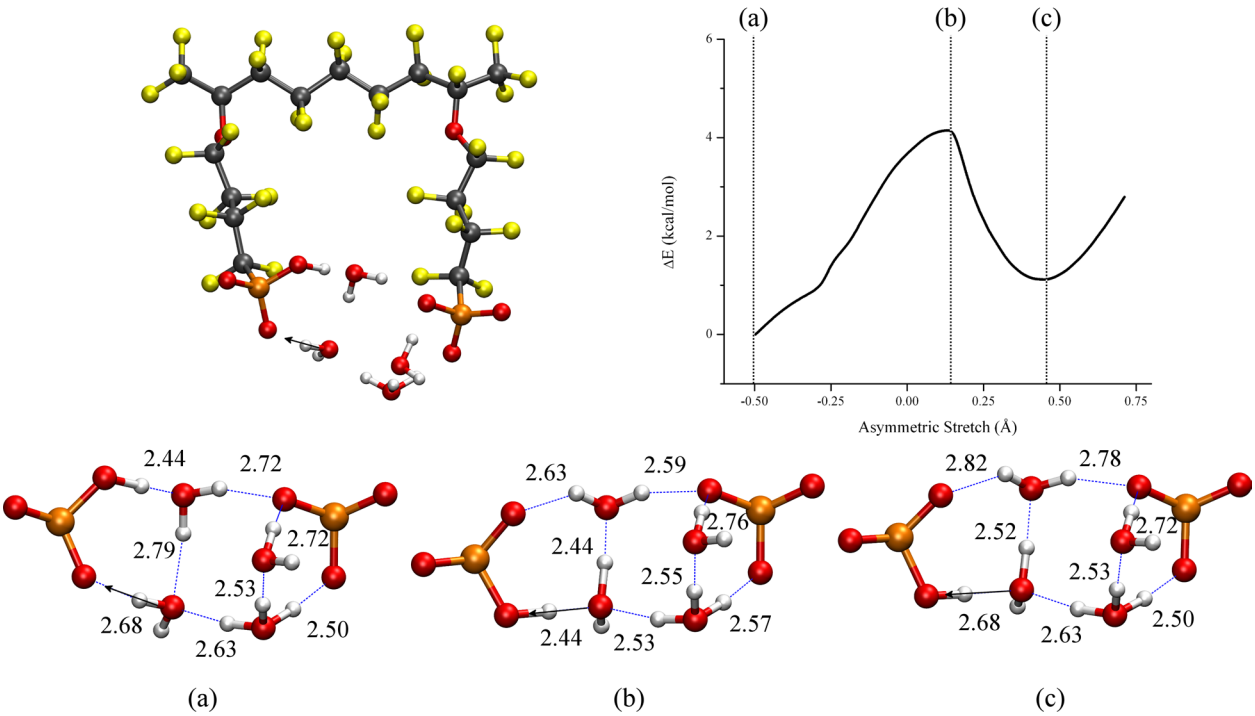

Figure 3.13. Top left panel: Optimized (B3LYP/6-31G**) structure of the EW 590 3M PFSA ionomer at a hydration of 4 H2O molecules used in the PES scan of the proton transfer indicated by the black arrow. Top right panel: Relative energy profile with respect to the original configuration as a function of the asymmetric stretch coordinate. Bottom panel: rotated bottom view of the sulfonic acid/sulfonate and water molecules with hydrogen bonds denoted by dashed lines and hydrogen bond distances (Å): (a) initial configuration; (b) transition state; and (c) local minimum of the scan.

dissociated configuration at the transition state and the subsequent partial charge transfer to the sulfonate group is of little surprise as no geometry for EW 690 with two dissociated protons at this hydration level was found in the previous electronic structure calculations.

Figure 3.13 shows an optimized geometry of EW 590 with the addition of 4 H_2O molecules with one proton dissociated and the other proton partially dissociated with an O–H bond length of 1.11 Å. This, again, is not the global minimum energy EW 590 structure, but it provides a means of comparison to the EW 690 optimized geometry for the following PES scan of proton transfer. A proton was transferred from a water molecule to an oxygen atom of the partially dissociated sulfonic acid group which quickly led to full dissociation of the partially dissociated proton forming a hydronium ion. This hydronium ion then

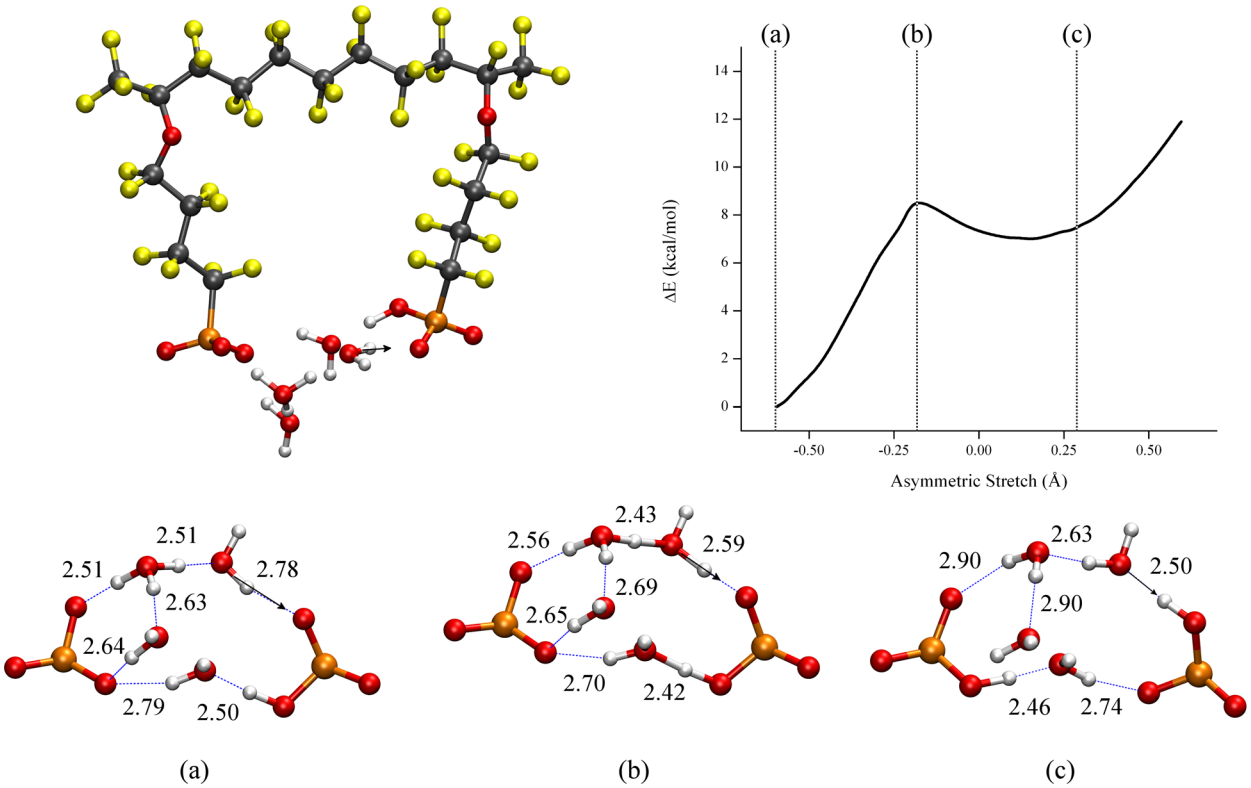

Figure 3.14. Top left panel: Optimized (B3LYP/6-31G**) structure of the EW 690 3M PFSA ionomer at a hydration of 4 H2O molecules used in the PES scan of the proton transfer indicated by the black arrow. Top right panel: Relative energy profile with respect to the original configuration as a function of the asymmetric stretch coordinate. Bottom panel: rotated bottom view of the sulfonic acid/sulfonate and water molecules with hydrogen bonds denoted by dashed lines and hydrogen bond distances (Å): (a) initial configuration; (b) transition state; and (c) point of the scan when the proton is fully transferred to the sulfonic acid group.

transfers a proton to the water molecule losing a proton to compensate for the loss of positive charge, which has little effect on the rest of the hydrogen bond network. The energetic barrier for this was only 4.2 kcal/mol which is followed by a local minimum with a configuration very similar to the initial structure only 1.1 kcal/mol higher in energy. A similar proton transfer event for EW 690 is shown in Figure 3.14. Transferring the proton led to a transition state with an energetic barrier of 9.0 kcal/mol. At this point, the initially associated proton is partially shared between the sulfonic acid intermediate oxygen atom and the neighboring water molecule. The hydronium ion at the top fully transfers a proton

to the water molecule, losing a proton to compensate for the loss of charge at the local minimum 7.0 kcal/mol higher in energy than the original configuration. The loss of the proton by the hydronium ion significantly weakens its charge delocalization capacity resulting in considerably weaker hydrogen bonds to the left sulfonate group oxygen atom and the other neighboring water molecule, which results in an increase in excess negative charge on the sulfonate group. The water molecule receiving the originally associated sulfonic acid proton then compensates for this by transferring a proton to an oxygen atom on the left sulfonate group, which also forces the breaking of a hydrogen bond from the central water molecule to the same oxygen atom. Full reprotonation of the right sulfonic acid group does not occur until farther along the scan (Figure 3.14c), resulting in a configuration where each proton is associated with a sulfonic acid group in a state 7.3 kcal/mol higher in energy than the initial configuration.

***Summary*.** The difference in sulfonic acid group separation in the EW 590 and EW 690 ionomers led to noticeably different hydrogen bonding configurations between the fragments. The fewer water molecules required for proton dissociation in EW 590 than EW 690 was attributed to the interactions between side chains and stronger hydrogen bond capabilities in the fragment with less separation between side chains. The largest energetic penalties for proton transfer were observed when no reorganization of the hydrogen bond network occurred as a result of proton transfer. It was found that, at low water content, the nature of the hydrogen bond network and the degree of dissociation were critical factors in the resulting energetic barrier for proton transfer. Namely, systems in which the hydrogen bond network could easily reorient to accommodate charge transfer, and did not require the breaking of hydrogen bonds, exhibited significantly lower proton transfer energetic barriers than in systems that did not have these qualities. This trait was prominently observed in the EW 590, with less separation between side chains, as continuous, cyclical hydrogen bond networks were more readily formed between the water molecules and the sulfonic acid/sulfonate terminal side chain groups. The hydrogen bond network in the EW 690, with greater side chain separation, contained less order making the reorientation process less feasible at low hydration.

3.1.3 Protogenic group separation and side chain chemistry

Similar electronic structure calculations were performed to explore the roles of protogenic group separation and specific side chain chemistry on proton dissociation and the energetics of proton transfer on single side chain fragments of 3M MASC ionomers, containing two acid groups per side chain. Three ionomers were considered, each containing a bis(sulfonyl imide) group and a sulfonic acid group, with structural and chemical differences mediating protogenic group separation: two structural isomers with protogenic group separation determined by the location of the sulfonic acid group on an aromatic ring (side chains: $-O(CF_2)_4SO_2(NH)\text{-}SO_2C_6H_4SO_3H$) with the sulfonic acid group located in either the *meta* or the *ortho* position) and a perfluorinated ionomer (PFIA) with protogenic groups separated by $-CF_2-$ groups (side chain: $-O(CF_2)_4SO_2(NH)SO_2(CF_2)_3SO_3H$). Global minimum energy structures of the fragments with and without the addition of water molecules were obtained from a variety of initial configurations to ascertain the factors that contribute to proton dissociation at low hydration levels. The energetics associated with proton transfer was also determined for several proton transfer events.[193] Adapted by permission of Elsevier.

***Optimized Structures*.** Fully optimized (B3LYP/6-311G**) 'dry' minimum energy structures of each ionomer fragment along with the electrostatic potential mapped on the total electron density are shown in Figure 3.15. The close proximity of protogenic groups in the *ortho* bis acid (Figure 3.15b) results in the formation of double hydrogen bonds, which delocalizes charge over the sulfonyl imide and the sulfonic acid groups. This interaction was not sterically possible in the *meta* bis acid (Figure 3.15a) as the fixed location of the sulfonic acid group on the phenyl ring led to greater separation of the protogenic groups with no sharing of charge. This effect can be seen in the electrostatic isosurfaces, where the *meta* exhibits more electron rich (darker red) regions surrounding the sulfonyl and sulfonic acid oxygen atoms and more electron deficient (darker blue) regions surrounding the acidic protons than the *ortho*. No direct interaction between protogenic groups was observed in the PFIA fragment (Figure 3.15c); however, the $-CF_2-$ groups separating the

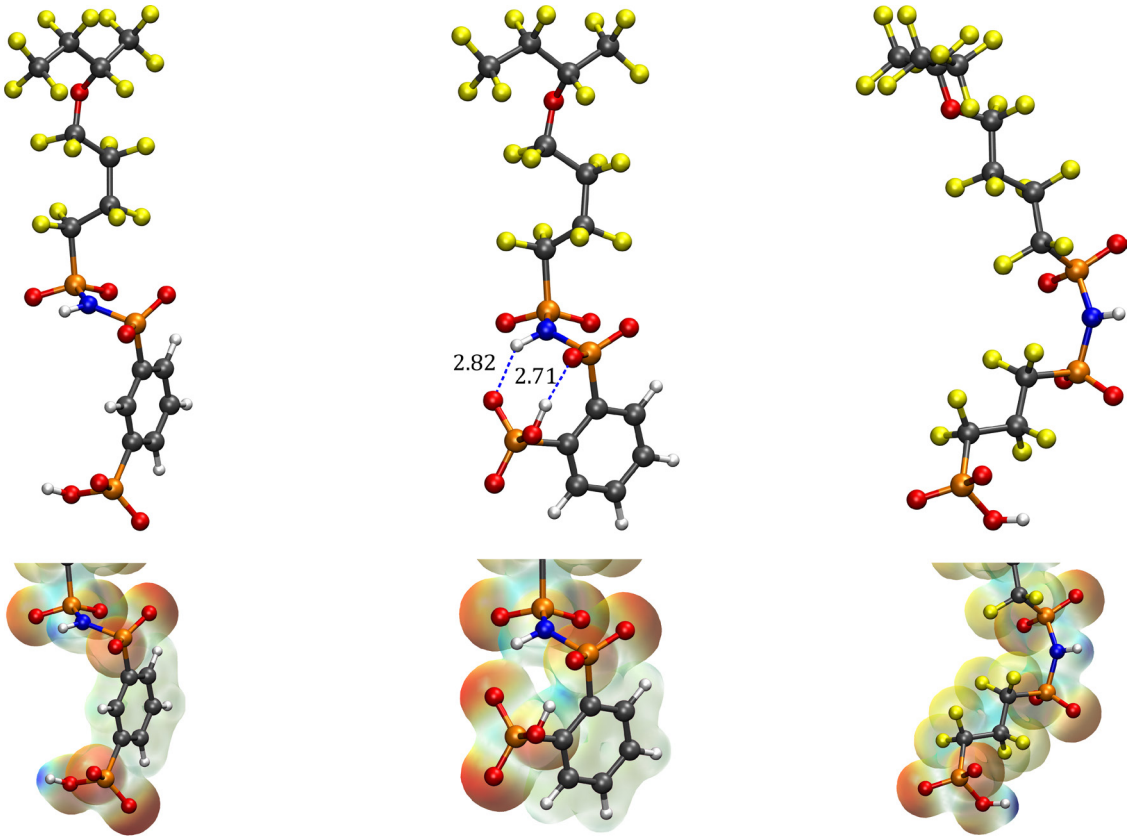

(a) (b) (c)

Figure 3.15. Optimized (B3LYP/6-311G**) minimum energy structures of isolated 3M MASC fragments with the mapped electrostatic isosurfaces (blue regions are electron deficient and red regions are electron rich) for: (a) the *meta* bis acid, (b) the *ortho* bis acid, and (c) the PFIA ionomer. The different colored spheres represent different atom types where: grey–carbon, light blue–fluorine, red–oxygen, yellow–sulfur, blue–nitrogen, and white–hydrogen.

sulfonyl imide and sulfonic acid groups have a significantly greater electron withdrawing capacity than that of a phenyl ring, which effectively decreases the negative charge on the sulfonic acid and lower sulfonyl oxygen atoms as indicated by the lighter red tone surrounding them. The charge delocalizing effects were found to play critical roles in promoting energetically favorable dissociation of a single acidic proton at low levels of hydration, shown in Figure 3.16. Specifically, favorable first proton dissociation in the *ortho* and the PFIA required only three water molecules due to the sufficient charge delocalization stabilizing the excess negative charge after proton dissociation, while the

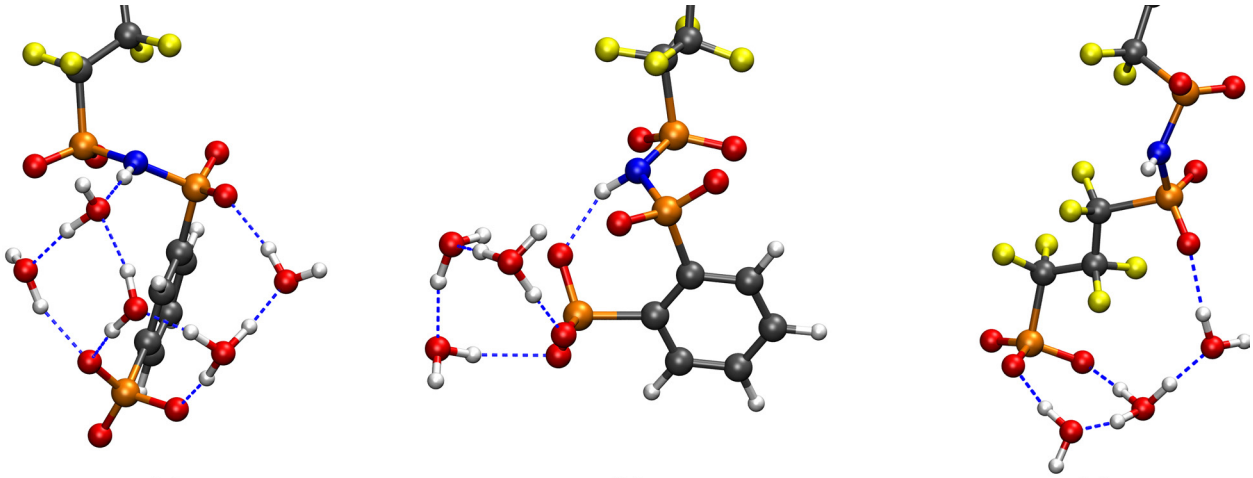

(a) (b) (c)

Figure 3.16. Optimized (B3LYP/6-311G**) minimum energy structures of 3M MASC ionomers with energetically favored first proton dissociation requiring: (a) 5 H_2O molecules in meta, (b) 3 H_2O molecules in ortho, and (c) 3 H_2O molecules in PFIA.

meta required the addition of five. In each case, the proton from the sulfonic acid is the first to dissociate which is counterintuitive as the sulfonyl imide has stronger gas phase acidity. However, hydrogen bond stabilization and orientation appears to be key to proton dissociation in these small isolated systems. A different trend was found for second proton dissociation where the *ortho* fragment required the most water molecules. The close proximity of protogenic groups in the *ortho* bis acid hindered dissociation. First proton dissociation was promoted by the direct hydrogen bonding between protogenic groups; thus, dissociation of the second proton requires the breaking of another strong stabilizing intramolecular hydrogen bond which was found to be considerably energetically unfavorable. Furthermore, the available hydrogen bond acceptor sites along the side chain were more clustered than in the ionomers with well separated protogenic groups leading to more interactions between water molecules precluding strong hydrogen bonds with the ionomer. The clustered group of water molecules resisted accepting the positive charge associated with dissociation of the second acidic proton as localized excess positive charge already exists in the surrounding water cluster resulting from first proton dissociation. Larger separation in the *meta* and PFIA allowed for more widely spread hydrogen bonding and distribution of charge requiring fewer water molecules for second proton dissociation.

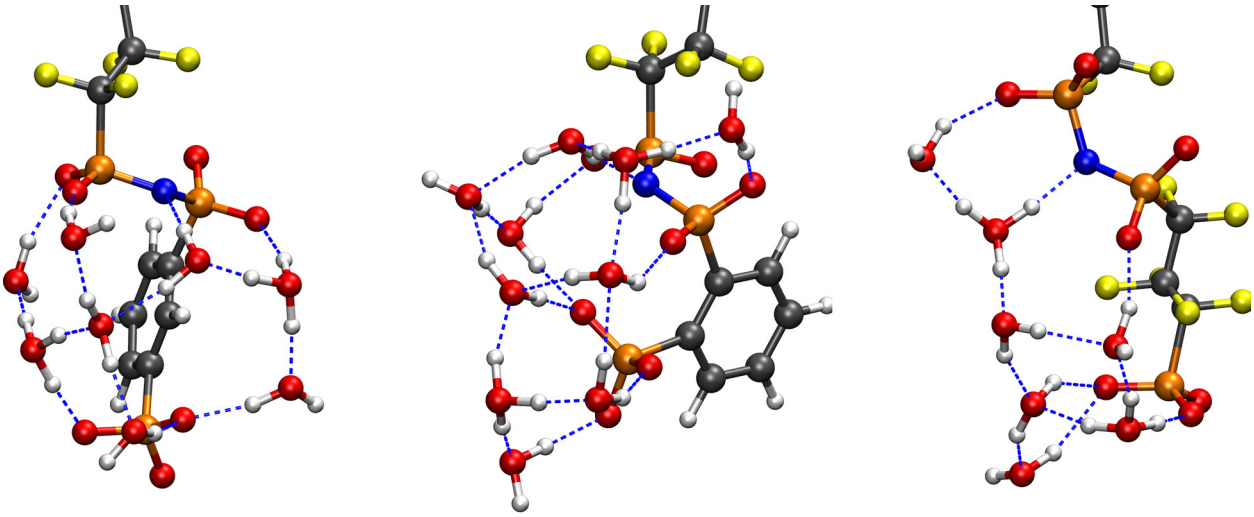

(a) (b) (c)

Figure 3.17. Optimized (B3LYP/6-311G**) minimum energy structures of 3M MASC ionomers with energetically favored second proton dissociation requiring: (a) 8 H_2O molecules in meta, (b) 10 H_2O molecules in ortho, and (c) 7 H_2O molecules in PFIA.

Figure 3.17 shows the optimized structures exhibiting second proton dissociation for each ionomer fragment where full proton dissociation was first found to be energetically preferred over the singly dissociated case.

***Proton transfer*.** The previous section described how protogenic group interactions, side chain chemistry, and hydrogen bonding affect proton dissociation at low hydration levels in these single side chain fragments. To understand better how these factors affect the energetics of proton transfer in these materials, PES scans of proton transfer were performed. At a hydration level of five water molecules, each ionomer had a single dissociated proton from the sulfonic acid group. Figures 3.18, 3.19, and 3.20 show PES scans of proton transfer from the imide group to a neighboring water molecule for the optimized geometries of the *meta*, *ortho*, and PFIA with the addition of five water molecules, respectively. Only expansions and contractions in hydrogen bond lengths to accommodate for the transfer of charge were observed up to the transition state in the *meta* fragment with an associated energetic barrier of 6.8 kcal/mol. Most notably is the repulsion of the neighboring water molecule donating a hydrogen bond to the proton

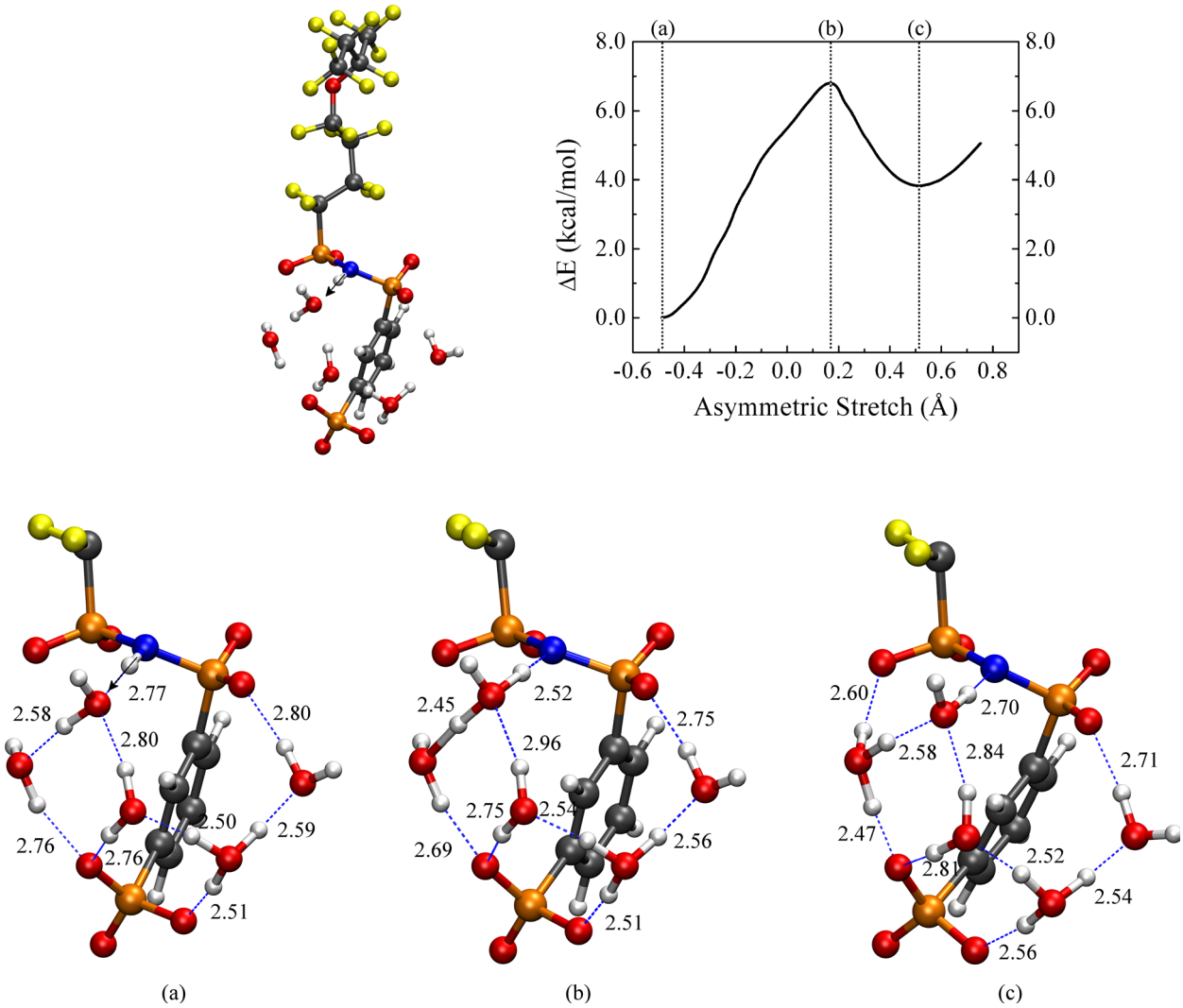

Figure 3.18. Top left panel: Optimized (B3LYP/6-31G**) structure of the *meta* bis acid at a hydration of 5 H_2O molecules used in the PES scan of proton transfer from the associated imide to a neighboring water molecule. Top right panel: Relative energy profile with respect to the original configuration as a function of the asymmetric stretch coordinate. Bottom panel: Water molecules and the bottom portion of the ionomer with hydrogen bonds denoted by dashed lines and hydrogen bond distances (Å): (a) initial configuration; (b) transition state; and (c) the fully transferred points of the scan.

accepting water molecule. However, following the transition state, this repulsion is alleviated as the water molecule receiving the transferred proton transfers a different proton to the left water molecule it originally donated a hydrogen bond to forming a hydronium ion. The additional positive charge on the newly formed hydronium ion results

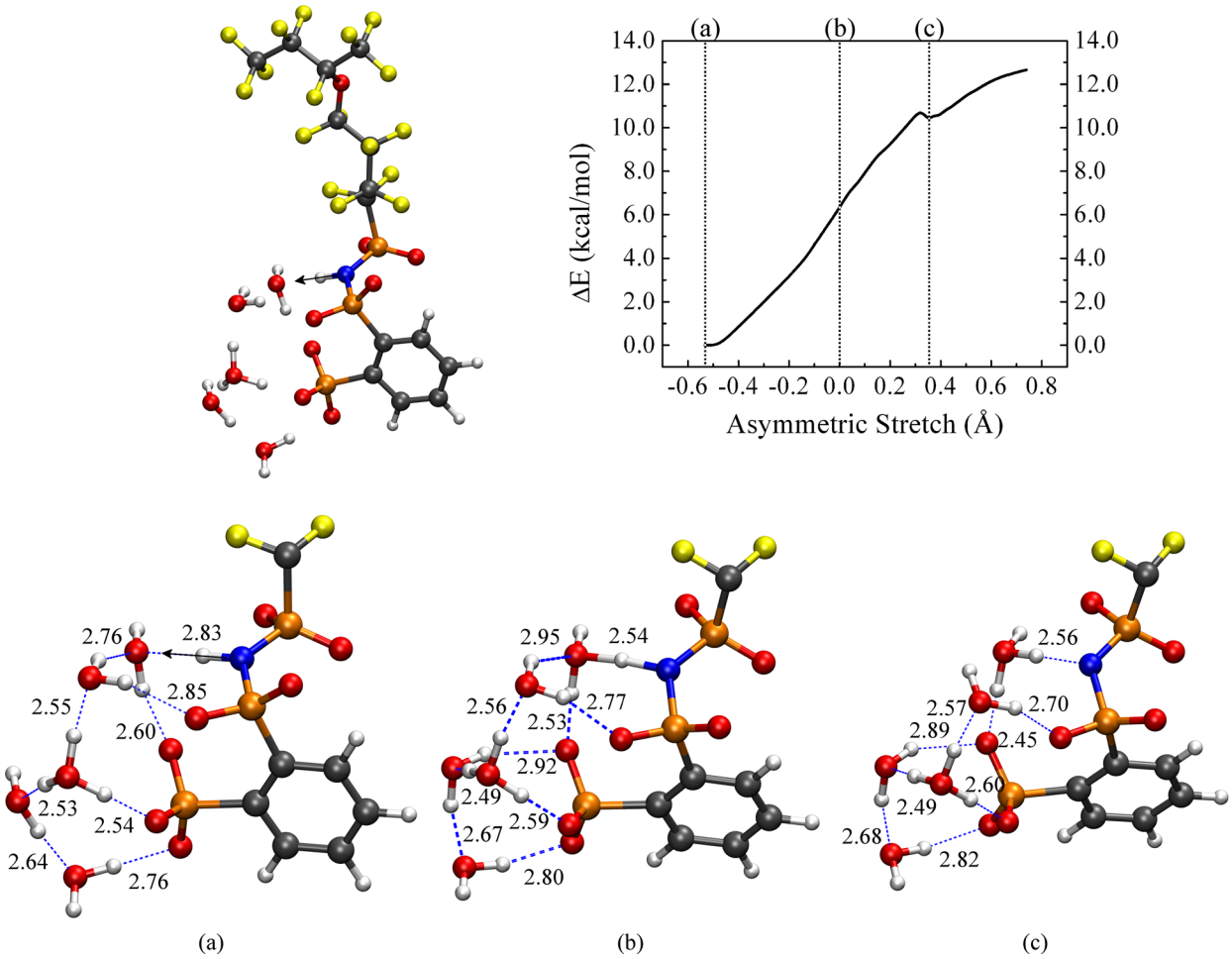

Figure 3.19. Top left panel: Optimized (B3LYP/6-31G**) structure of the *ortho* bis acid at a hydration of 5 H_2O molecules used in the PES scan of proton transfer from the associated imide to a neighboring water molecule. Top right panel: Relative energy profile with respect to the original configuration as a function of the asymmetric stretch coordinate. Bottom panel: Water molecules and the bottom portion of the ionomer with hydrogen bonds denoted by dashed lines and hydrogen bond distances (Å): (a) initial configuration; (b) transition state; and (c) the local minimum points of the scan.

in greater hydrogen bond capacity promoting the formation of a new hydrogen bond with the top left sulfonyl oxygen atom, shown in the fully transferred, local minimum configuration of Figure 3.18. This interaction provides a stabilization effect with a local minimum structure containing two dissociated protons only 3.8 kcal/mol higher in energy than the original configuration with only minor changes to the rest of the hydrogen bond network and hydrogen bond distances. No clear transition state or local minimum were

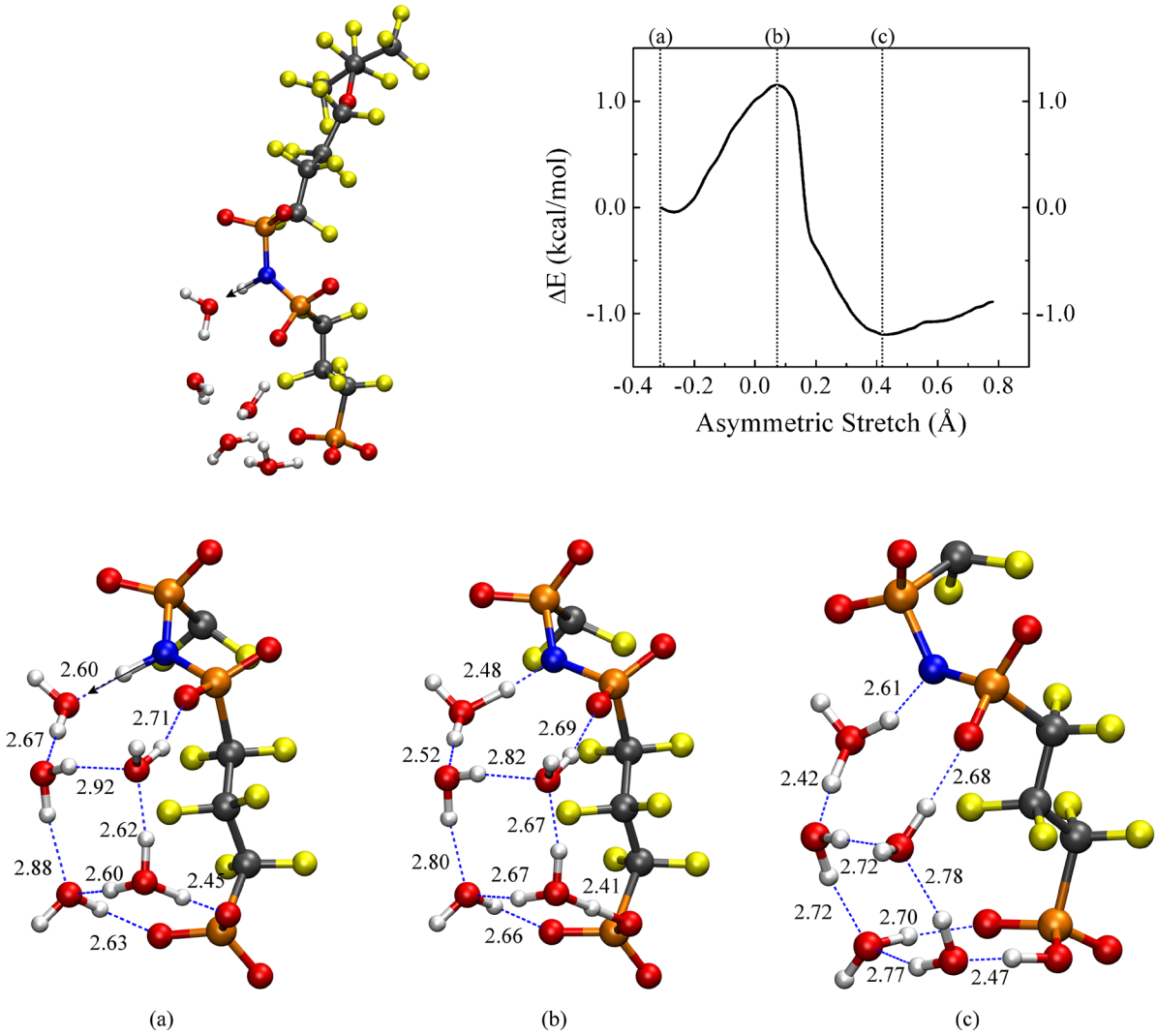

Figure 3.20. Top left panel: Optimized (B3LYP/6-31G**) structure of the PFIA at a hydration of 5 H_2O molecules used in the PES scan of proton transfer from the associated imide to a neighboring water molecule. Top right panel: Relative energy profile with respect to the original configuration as a function of the asymmetric stretch coordinate. Bottom panel: Water molecules and the bottom portion of the ionomer with hydrogen bonds denoted by dashed lines and hydrogen bond distances (Å): (a) initial configuration; (b) transition state; and (c) the local minimum points of the scan.

found for the similar proton transfer in the *ortho* fragment (Figure 3.19). The close proximity of protogenic groups in the *ortho* resulted in a congested configuration with one water molecule accepting a hydrogen bond from the imide and donating a hydrogen bond to the sulfonate acid group connecting the two groups. This water molecule also accepted a

hydrogen bond from a neighboring water molecule which was quickly broken as the scan took place due to the repulsion caused by the additional positive charge received by the proton accepting water molecule which significantly altered the hydrogen bond topography. No open hydrogen bond acceptor sites were available for the newly formed hydronium ion to either transfer a proton (as in the *meta* case) or form a new hydrogen bond that would not further disrupt the hydrogen bond network in doing so. The geometry containing two dissociated proton after the proton is transferred was 10.6 kcal/mol higher in energy than the original state as the close proximity of protogenic groups led to a more clustered network of hydrogen bonds lacking the ability to easily accommodate for the transfer of charge. Results similar to those obtained for the *meta* bis acid were also observed in the PFIA fragment as the well-connected spread out hydrogen bond network undergoes expansions and contractions easily adjusting for the transfer of charge with a barrier of only 1.1 kcal/mol (Figure 3.20). Furthermore, the PFIA side chain does not contain the hindrances associated with fixed side chain separation on an aryl ring which allowed for increased freedom to adjust resulting in a minimum 1.2 kcal/mol lower in energy than the initial structure.

***Summary*.** The explicit water electronic structure calculations on the 3M MASC ionomers revealed that electron withdrawing CF_2 groups in the PFIA and protogenic group hydrogen bonding in the *ortho* provided charge delocalization effects absent in the *meta* that promoted first proton dissociation at low hydration levels. The close proximity of protogenic groups in the *ortho*, however, hindered second proton dissociation as it required the breaking of a strong stabilizing intramolecular hydrogen bond and interactions between water molecules were preferred. Larger separation in the *meta* and PFIA resulted in a less congested hydrogen bond network with more interactions between the water molecules and the side chain requiring fewer water molecules for second proton dissociation. The energetics of proton transfer were also found to be dependent on the nature of hydrogen bonding. Proton transfer in the ortho was strongly resisted and resulted in a considerable disruption in the configuration of the surrounding water molecules as well as the breaking of a hydrogen bond. Similar proton transfer in the *meta*

had a considerably smaller energetic penalty and had less effect on the hydrogen bond network due to the more dispersed hydrogen bonding more readily accommodating for the transfer of charge through the subsequent transfer to a different water molecule which is further stabilized by the formation of an additional hydrogen bond. The well-connected hydrogen bond network in the PFIA also readily accommodated for the transfer of charge via concerted contractions and expansions in hydrogen bond lengths throughout the system leading to an extremely small barrier for proton transfer. These results suggest that the energetic penalty associated with proton transfer is dependent on the connectivity of hydrogen bonding and the extent of disruption in hydrogen bonding where bond breaking is resisted and bond forming has a stabilizing effect.

3.2 *Ab initio* Molecular Dynamics Simulations of Confined Fluids

3.2.1 Water and an excess proton in water confined in carbon nanotubes

AIMD simulations were performed to investigate the effects of nanoscale confinement on structural and dynamical properties of water and slightly acidic water. Two different diameter CNTs (11.0 and 13.3 Å) were used as confinement vessels (corresponding to chirality of (14,0) and (17,0)) with length of ~12.8 Å. The inner walls of the CNT were either left bare or fluorinated to explore the influence of the confined environment on the determined properties. The nomenclature N-14 and N-17 will be used for the nonfluorinated CNTs and F-14 and F-17 for the fluorinated CNTs. The smaller tubes contained 12 water molecules while the larger tubes contained 24 water molecules. When an excess proton was introduced, a neutralizing background charge was applied by VASP. Representative images of the systems are shown in Figure 3.21. As the PBE functional has been shown to over-structure water at 300 K,[194-196] test simulations were performed at 400 K but no significant differences were observed.

***Confined water*.** The distributions of oxygen and hydrogen atoms throughout the trajectory for each system are shown in Figure 3.22. The left and right panels show contour plots of the oxygen and hydrogen atom positions projected onto the xy-plane, respectively, and the middle panel shows the distribution function of the distance of the atoms from the

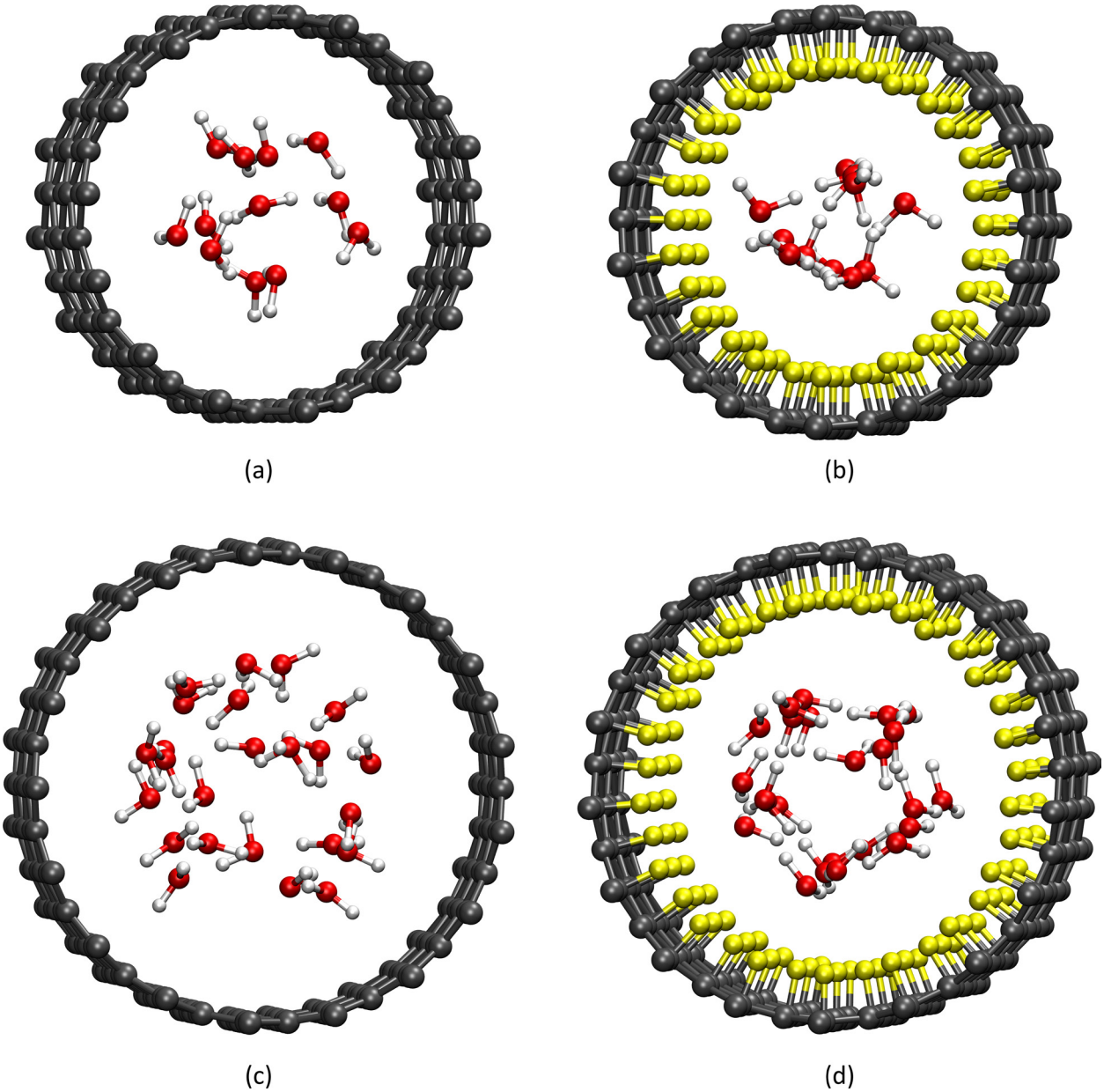

Figure 3.21. CNT+H_2O systems: (a) N-14, (b) F-14, (c) N-17, and (d) F-17. The different colored spheres represent different atom types where: gray–carbon, red–oxygen, white–hydrogen, and yellow–fluorine.

CNT wall. Darker colors in the contour plots indicate a greater tendency for the atoms to be located in the region. In the fluorinated CNTs, the oxygen atoms are highly localized near the fluorinated walls as indicated by the sharp peaks at 2.63 and 2.78 Å in the F-14 and F-17 distribution functions, respectively. The water molecules in F-14 exhibit ordering along

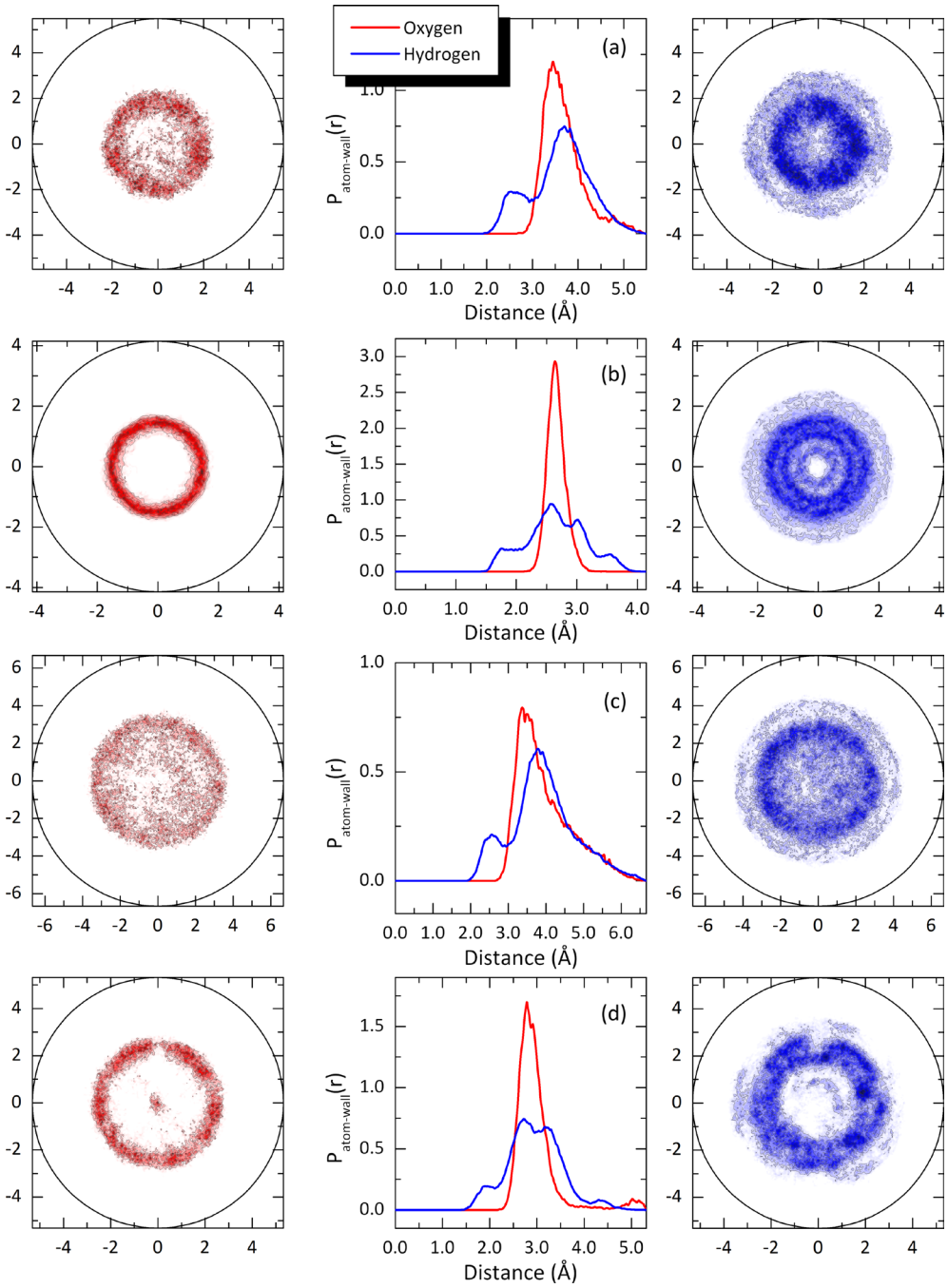

Figure 3.22. (Outer) Contour plots of the distribution of (left) oxygen and (right) hydrogen atoms projected onto the xy-plane throughout the trajectory for: (a) N-14, (b) F-14, (c) N-17, and (d) F-17 shown on the same scale where darker colors indicate more populated regions. (Inner) Corresponding distribution functions of the axial distance of the atoms from the inner wall of the CNT.

the CNT axis with evenly spaced clusters of two or three water molecules (see Figure 3.24c) while those in the larger F-17 form an essentially stacked pentagonal structure (Figure 3.25c and d) which has been observed in other simulations of water confined in single-walled CNTs.[111-114] The oxygen atoms in the bare CNTs, on the other hand, do not exhibit the same degree of preferential arrangement and are more widely dispersed with broad distribution peaks at 3.42 and 3.40 Å for the smaller and larger tubes, respectively. The oxygen atoms in N-14 do, however, show more preference to arrange near the wall than those in N-17 but the configurations do not show any well-defined structure. The distribution of the hydrogen atoms is obviously related to that of the oxygen atoms. Again, in the fluorinated tubes, distributions with atoms located near the fluorinated walls were observed while those of the bare CNTs are more spread out. The distribution functions all contain a first peak at a shorter distance than that for the corresponding oxygen atoms. In the fluorinated tubes these occur at 1.75 and 1.89 Å for the smaller and larger tubes, respectively, and the corresponding distances for the bare CNTs are 2.52 and 2.56 Å.

Radial distribution functions (RDFs) between atoms also provide information on the structural arrangement of water molecules within the CNTs. Figure 3.23 shows the oxygen–oxygen and oxygen–hydrogen radial distribution functions for the (14,0) and (17,0) CNT systems. The first peak in the O–O RDF for the smaller fluorinated tube occurs at 2.67 Å, while in the bare tube it is found at 2.72 Å. The F-14 peak is sharper than N-14 and is followed by a second smaller peak only a short distance away. This results from non-hydrogen bonded water molecules in the neighboring clusters suggesting a fairly regular structure. The structural arrangement of the N-14 water molecules, on the other hand, exhibits less order with a broad second maximum in the RDF. A similar effect was found for the larger fluorinated tube having a relatively narrow first peak in the O–O RDF at 2.68 Å and a highly ordered structure, whereas, in the larger bare tube the water molecules again exhibit a more randomly organized arrangement with greater separation between oxygen atoms (first peak at 2.73 Å) with a similar broad second maximum in the RDF to N-14. The second peak observed in F-14 is absent in F-17 which is likely due to the pentagonal stacking of the water molecules resulting in a greater likelihood of oxygen–oxygen

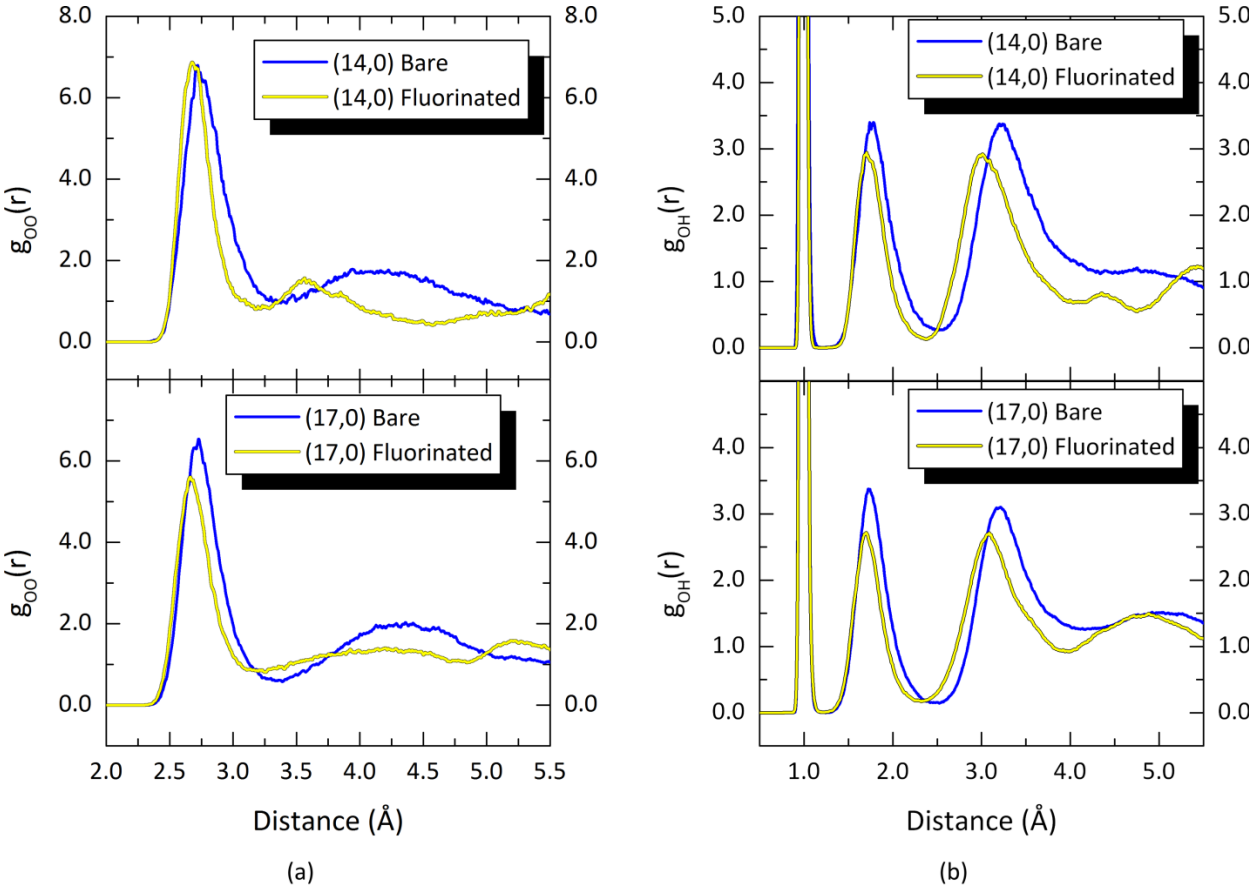

Figure 3.23. Radial distribution functions for the systems of water confined in the different CNTs: (a) oxygen–oxygen and (b) oxygen–hydrogen.

separations over a wide range of distances. Shorter separations in the fluorinated CNTs were also found between the oxygen and hydrogen atoms (Figure 3.23b). The first sharp peak in all of the RDFs corresponds to the covalently bound oxygen and hydrogen atoms of the water molecules. The peak following arises from hydrogen bonding between water molecules which occurs at ~1.68 Å in both fluorinated CNTs but at 1.75 and 1.73 Å in the smaller and larger bare CNTs, respectively, with broader distributions. The third peak in the RDFs further illustrates the tightly packed, highly organized nature of the water molecules in the fluorinated CNTs which occur at 3.01 and 3.07 Å in F-14 and F-17, respectively, versus 3.21 and 3.23 Å in their bare counterparts.

As mentioned earlier, the RDFs are closely related to the hydrogen bond structure

between the water molecules in the CNTs. Hydrogen bonding of water in confined environments is known to exhibit distinctly different behavior than that observed in bulk water. As such, these interactions are a primary focus of this investigation. Similar to the electronic structure calculations in the last section, a hydrogen bond was defined between water molecules having and oxygen–oxygen separation of less than 3.25 Å and an H–O···O of less than 30°.[197, 198] Representative snapshots of the hydrogen bonding in the smaller and larger CNTs are shown in Figures 3.24 and 3.25, respectively. The average O···O hydrogen bond distances vary between the different CNTs. As shown in the RDFs, the water molecules in the fluorinated CNTs are more closely packed and the average O···O hydrogen bond distance is 2.72 Å in both the smaller and larger tubes while the corresponding distances in the bare CNTs are 2.82 and 2.79 Å. Hydrogen bonding in the bare CNTs occurs with nearly random orientation. In the fluorinated systems, on the other hand, there are preferential orientations due to the aforementioned structuring of the water. The organization of the oxygen atoms in F-14 brings about a majority of hydrogen bonds that are either directed inward across the channel axis or essentially parallel to the CNT axis. These correspond to the dark blue inner and outer rings in the hydrogen distribution contours Figure 3.22b). In the larger F-17 system the water molecules localized near the surface are farther apart from other water molecules across the channel axis than in F-14 and, instead, preferentially hydrogen bond to their nearest “inter-pentagon” water molecules around the CNT circumference and the neighboring “intra-pentagon” water molecules along the channel of the CNT.

The distribution of the water molecules in the fluorinated CNTs suggests potential interactions between the water molecules and the fluorinated walls. Previous AIMD investigations on triflic acid and water confined in fluorinated CNTs[86, 87, 137] and hydrates of triflic acid[84, 85] have reported evidence of weak water–fluorine interactions to some extent similar to hydrogen bonds, although longer. Furthermore, results of IR spectroscopy studies on Nafion, a perfluorinated ionomer, have shown evidence that water is exposed to and potentially interacts with the hydrophobic fluorocarbon backbone.[199-201] Although the nature of the interactions are not entirely clear, we examine them here as weak hydrogen

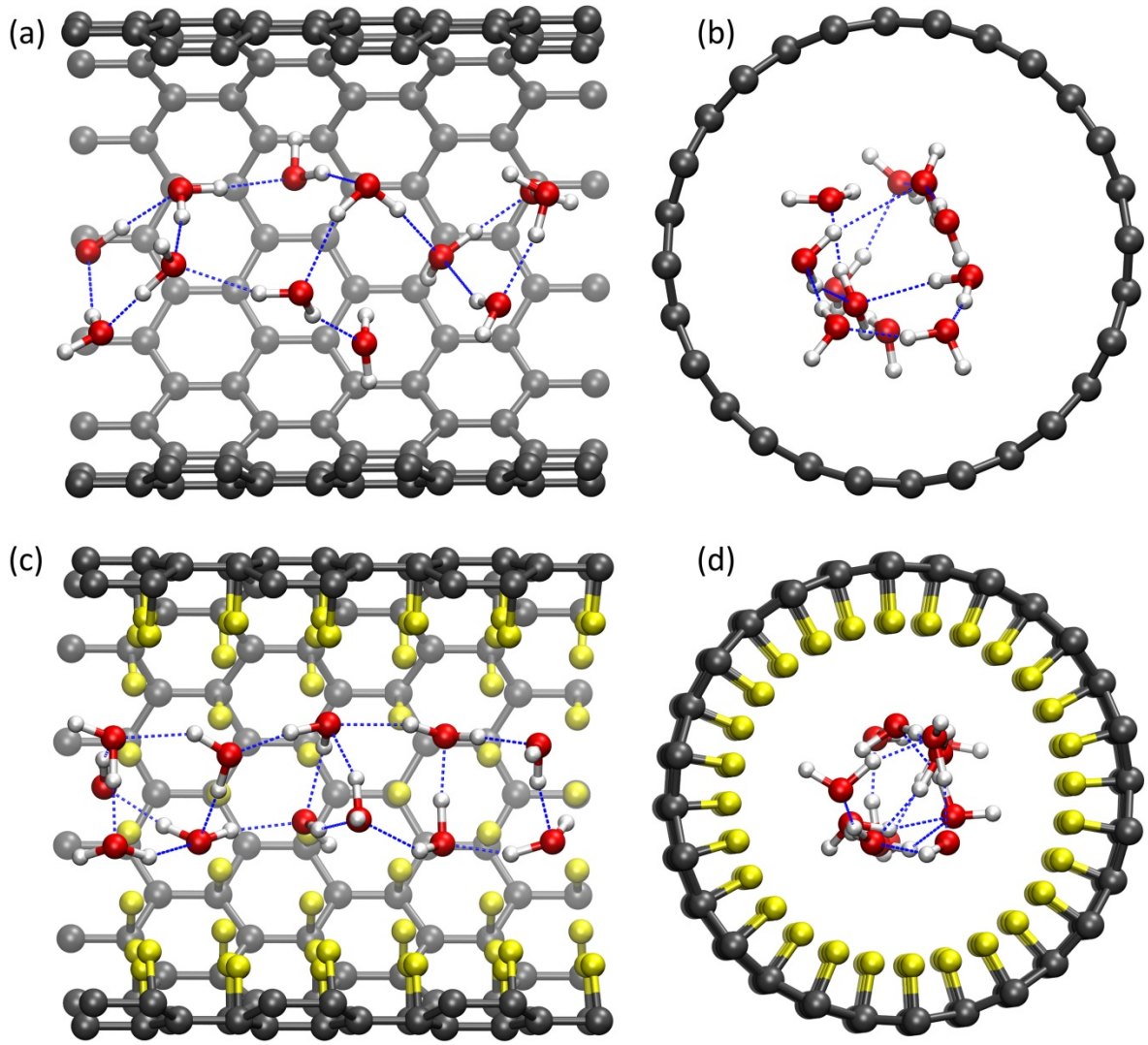

Figure 3.24. Representative snapshots of the hydrogen bond network in the smaller nanotubes showing (left) along the CNT axis and (right) down the CNT axis for the bare (a/b) and fluorinated (c/d) systems. Hydrogen bonds are denoted by dashed lines.

bonds. While the geometric criteria for weak hydrogen bonds typically allows for a wide range of hydrogen bond angles,[202] the angular cutoff in the analysis was not relaxed from that of water–water hydrogen bonds (i.e., the H–O···F angle must be less than 30°) to avoid inclusion of spurious interactions arising from the aforementioned structuring of the confined water. The hydrogen bond distance cutoff, however, was taken as an H···F length less than 2.5 Å which is slightly longer than the first minimum of the O···H RDF in bulk

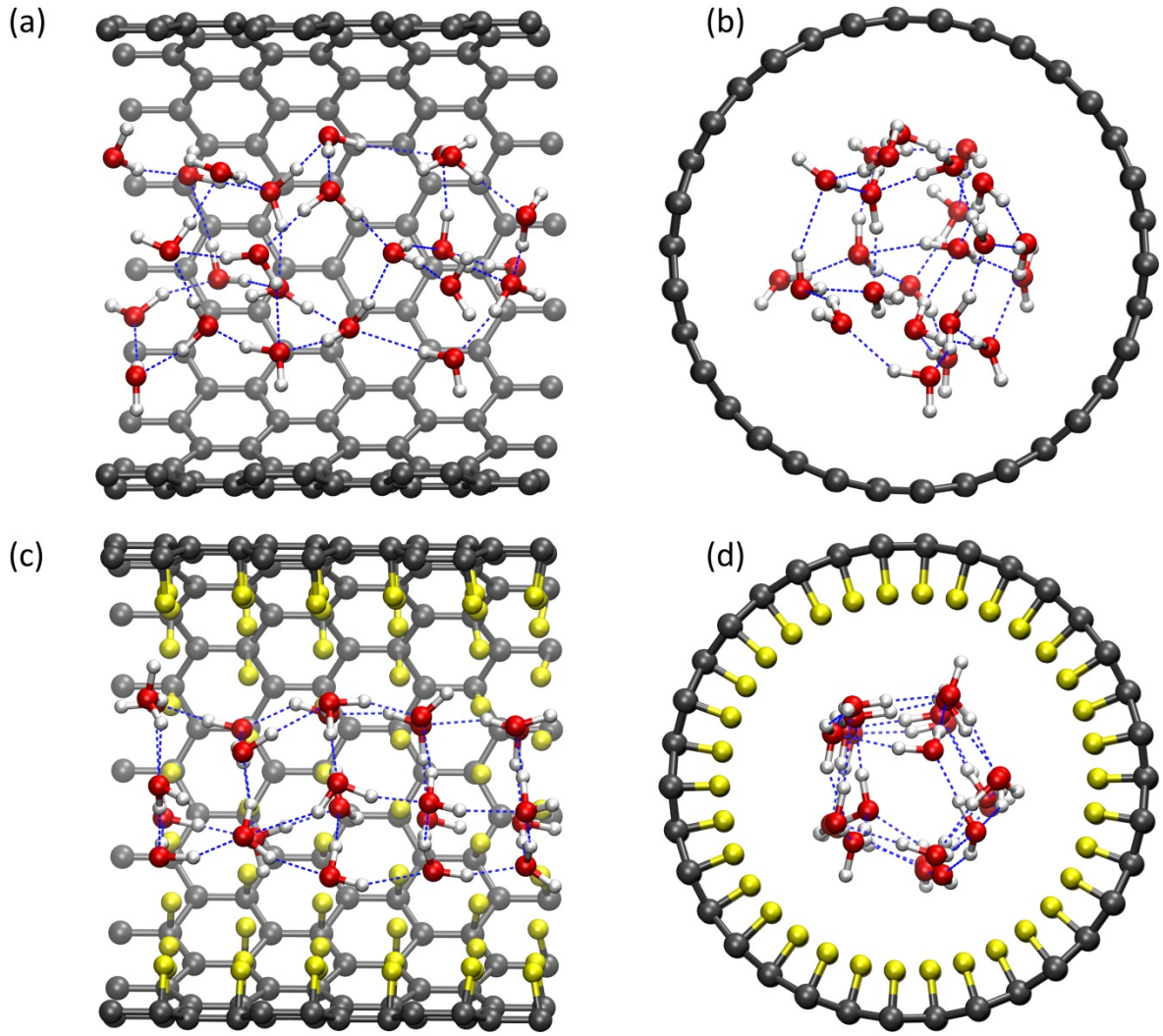

Figure 3.25. Representative snapshots of the hydrogen bond network in the larger nanotubes showing (left) along the CNT axis and (right) down the CNT axis for the bare (a/b) and fluorinated (c/d) systems. Hydrogen bonds are denoted by dashed lines.

water not corresponding to covalently bound hydrogen of ~2.46 Å.[203] The hydrogen bond was required to exist for longer than 5 fs to be considered in the analysis to prevent transient motions of the water molecules from affecting the results. However, if the hydrogen bond hopped between neighboring fluorine atoms while maintaining the geometric criteria, it was still included in the determined number of O–H···F hydrogen bonds. Figure 3.26 shows the percent of time throughout the trajectory O–H···F hydrogen

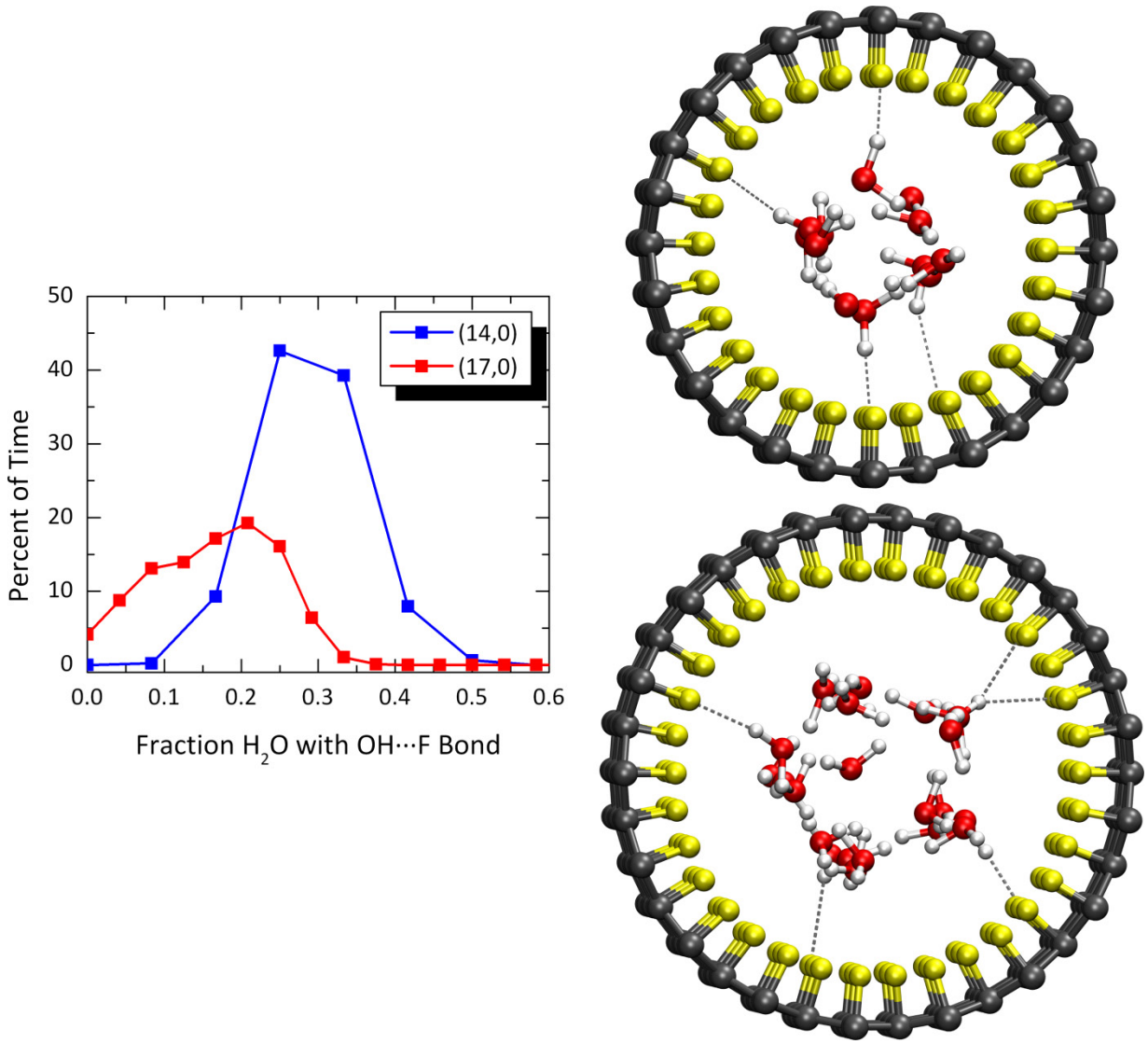

Figure 3.26. Percent of time throughout the trajectory OH···F hydrogen bonds exist versus the fraction of H_2O molecules with an OH···F bond. The right panel shows representative snapshots of F-14 (top) and F-17 (bottom) with OH···F bonds shown as dashed lines.

bonds exist versus the fraction of water molecules containing such a bond along with snapshots displaying hydrogen bonds for the two fluorinated systems. In the smaller CNT, at least one water molecule is involved in an O–H···F bond in each simulation step and there is an average of 29% of the water molecules (~3.5 H_2O) involved in these interactions throughout the trajectory with average H···F and O···F distances of 2.15 and 3.02 Å, respectively. These distances are longer than the H···O and O···O hydrogen bond

distances found here for water as well as for those in bulk water (~1.88 and 2.82 Å)[204] but are still within a reasonable range to be considered as hydrogen bond-like interactions. Hydrogen bonding to the fluorine atoms was also observed in the larger CNT with an average of 16% of the water molecules (~3.8 H_2O) involved in O–H···F interactions throughout the trajectory with average H···F and O···F distances of 2.19 and 3.08 Å, respectively. The continuous lifetime of these interactions in each case is approximately 32 fs. However, there are many instances of bifurcated hydrogen bonds and hydrogen bond jumps between different fluorine atoms. When these are considered as continuous hydrogen bonds, the average lifetime in the smaller tube becomes 107 fs and 82 fs in the larger tube. These results indicate that although fluorine atoms in fluorocarbons are poor hydrogen bond acceptors,[205-207] their nature inside these single-walled CNTs is non-trivial and appears to be influenced by the confinement dimensions.

***Confined water with an excess proton*.** An excess proton was added to each of the CNT systems to explore its effect on the studied properties. The distributions of hydrogen and oxygen atoms for the systems containing an excess proton are shown in Figure 3.27. Similar to what was found in the systems containing only water molecules, the fluorinated and nonfluorinated systems exhibit noticeably different arrangements. The oxygen atoms within the fluorinated tubes again are highly localized near the CNT wall while those in the bare CNTs show less preferential positioning. The distribution functions for the distance of the oxygen atoms to the CNT wall are all nearly identical to those for the systems without the excess proton. There are, however, differences in each of the corresponding hydrogen atom distribution functions and the projections onto the xy-plane. The first peak for each case occurs at marginally shorter distances than those in Figure 3.22 with, again, shorter distances found for the fluorinated systems. However, the amplitudes are higher in all of the distribution functions with the excess proton indicating a greater propensity for the hydrogen atoms to be located near the interface. This is also shown in the contour plots for the hydrogen distribution where darker shades of blue are observed in the outer portions of the ring than in those in Figure 3.22.

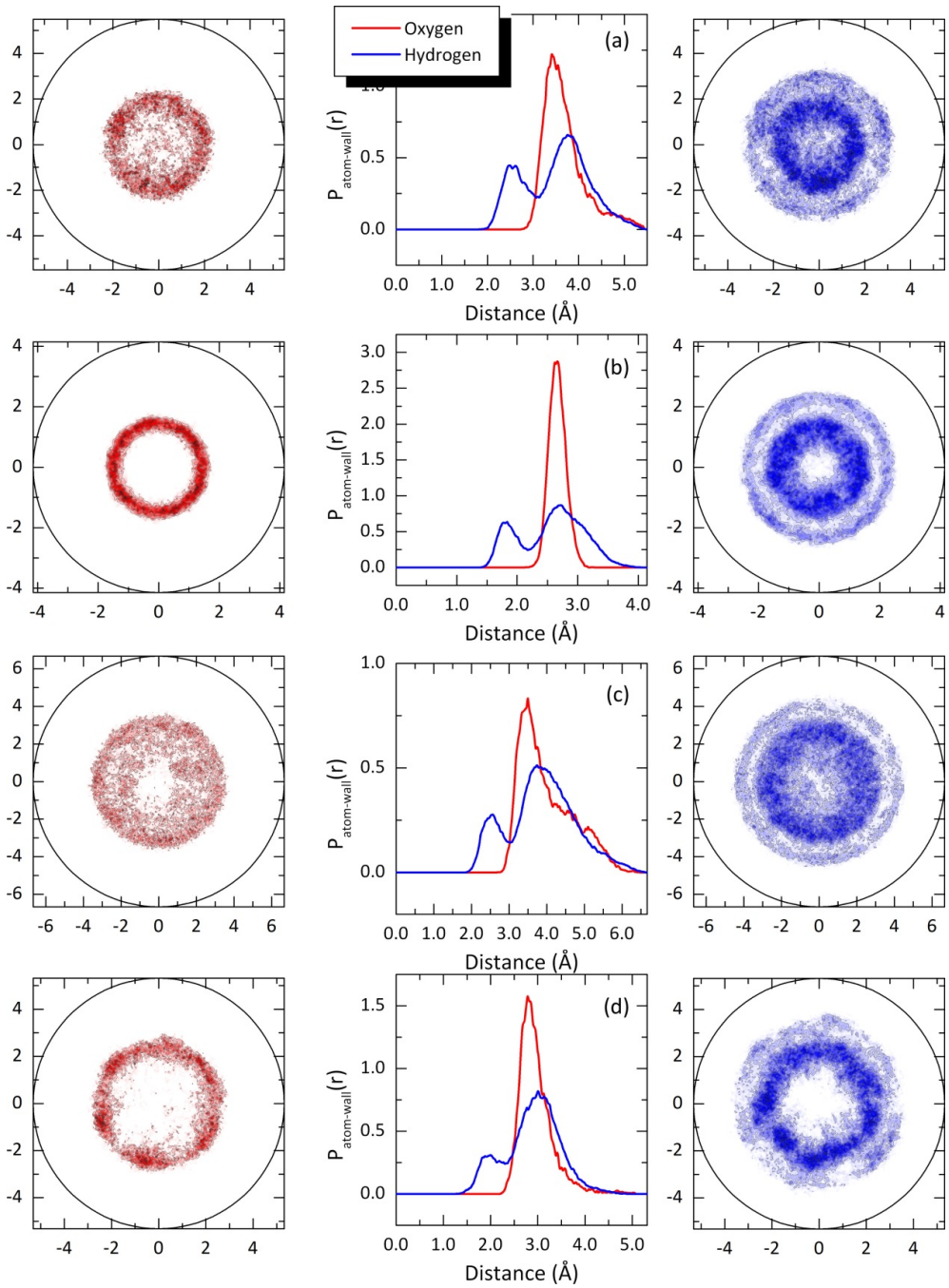

Figure 3.27. (Outer) Contour plots of the distribution of (left) oxygen and (right) hydrogen atoms projected onto the xy-plane throughout the trajectory for the systems containing an excess proton: (a) N-14, (b) F-14, (c) N-17, and (d) F-17 shown on the same scale where darker colors indicate more populated regions. (Inner) Corresponding distribution functions of the axial distance of the atoms from the inner wall of the CNT.

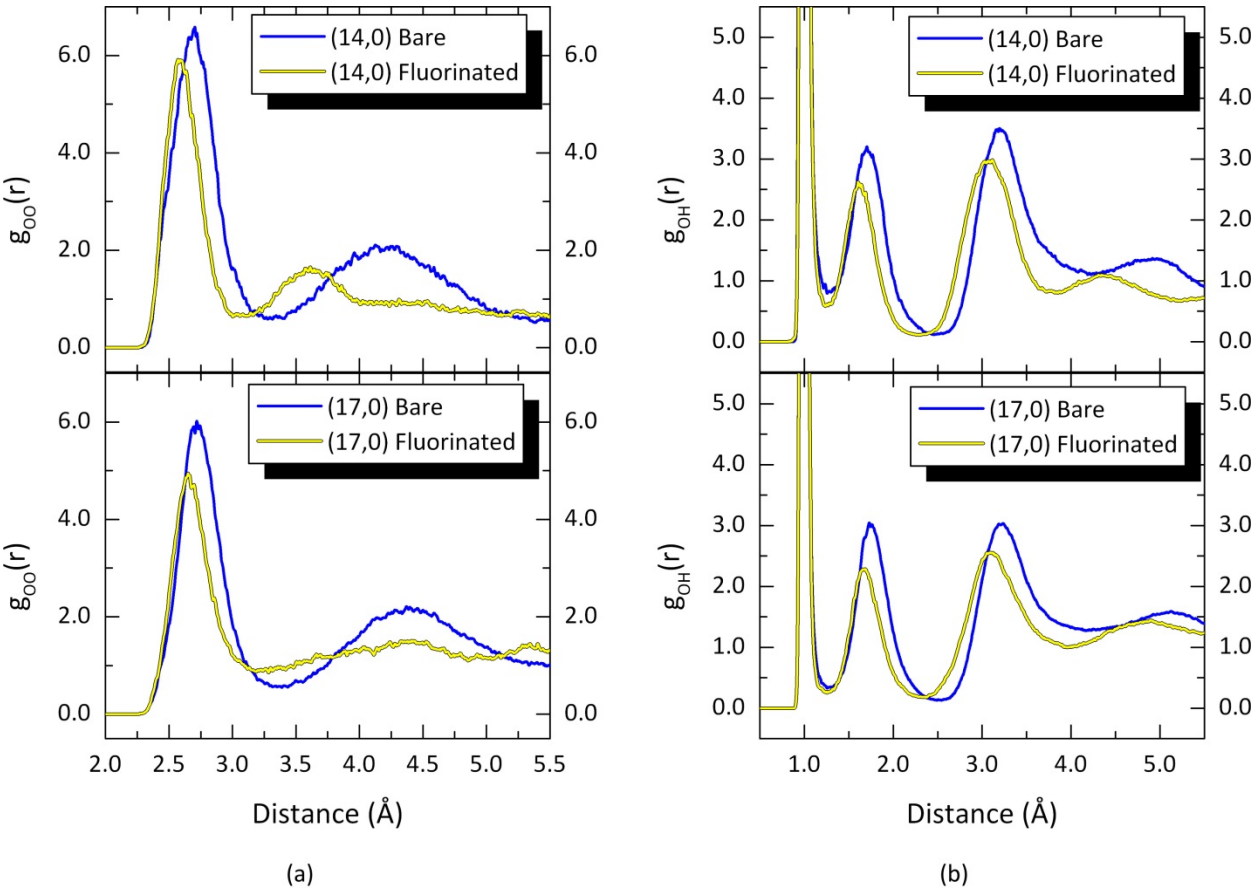

Figure 3.28. Radial distribution functions for the systems of water and an excess proton confined in the different CNTs: (a) oxygen–oxygen and (b) oxygen–hydrogen.

Figure 3.28 shows the oxygen–oxygen and oxygen–hydrogen RDFs for the systems containing an excess proton. These are very similar to those obtained for those systems containing only water molecules where the first peak in the O···O RDFs occur at a shorter distance in the fluorinated CNT than in the bare tubes. However, the distances at which these peaks begin and reach their maximum were found to be shorter than the corresponding distances in the systems without the excess proton. This is most pronounced in both of the smaller CNTs where the peak shifted ~0.08 Å closer while only marginal decreases of 0.02 Å were found for the larger tubes. All of the RDFs exhibit similar character following the first peak as the systems containing only water molecules indicative of their relative order/disorder. The same effects in each case were found for the

peaks following the covalently bound peak in the O···H RDFs. Another primary difference between the O···H RDFs for the systems with and without the excess proton is that the former contains a non-zero probability between the covalently bound peak and the second maximum due to the excess proton sharing and transferring between water molecules. The greater decrease in the distances observed in the smaller CNTs is also reflected in their hydrogen bonding. Snapshots of the hydrogen bond topography for the smaller and larger CNTs are shown in Figures 3.29 and 3.30, respectively. The average hydrogen bond O···O distances in the (14,0) nanotubes decreased from 2.72 to 2.63 Å in F-14 and from 2.82 to 2.73 Å in N-14 but only ~0.02 Å shorter hydrogen bonds were found in the (17,0) systems. The greater propensity for the hydrogen atoms to be closer to the surface when the excess proton is introduced results in fewer hydrogen bonds in the center region of the bare CNT but does not have a pronounced effect on the overall hydrogen bond arrangement or level of disorder. In F-14 the typical structure is a more ordered arrangement than in the system without an excess proton resembling a 'zig-zag ladder-like' structure (Figure 3.29c and d) similar to the so called book isomer form of the water hexamer.[117, 208] In this arrangement, every neighboring pair of water molecules, on average, is located across the channel axis with hydrogen bonds rarely spanning across the center of the CNT. The ordering in F-17, on the other hand, no longer has the well-defined stacked pentagonal structure that was seen earlier. When viewed down the channel axis (Figure 3.30d), the hydrogen bonding somewhat resembles a polygonal shape due to the packing of water molecules near the CNT wall but is clearly distorted, and the view along the CNT axis (Figure 3.30c) clearly shows a loss of the highly aligned structure in this system with an excess proton

Additional insight into these structures and comparison between the acidic systems and those without the excess proton can be obtained by examining the O–H···F interactions in the fluorinated CNTs. Figure 3.31 shows the percent of time throughout the trajectory O–H···F hydrogen bonds exist versus the fraction of water molecules with such a bond along with snapshots displaying such interactions for the fluorinated systems containing an excess proton. In both the larger and smaller CNTs, at least one water molecule is involved in an O–H···F interaction throughout the entire trajectory which was not the case for the

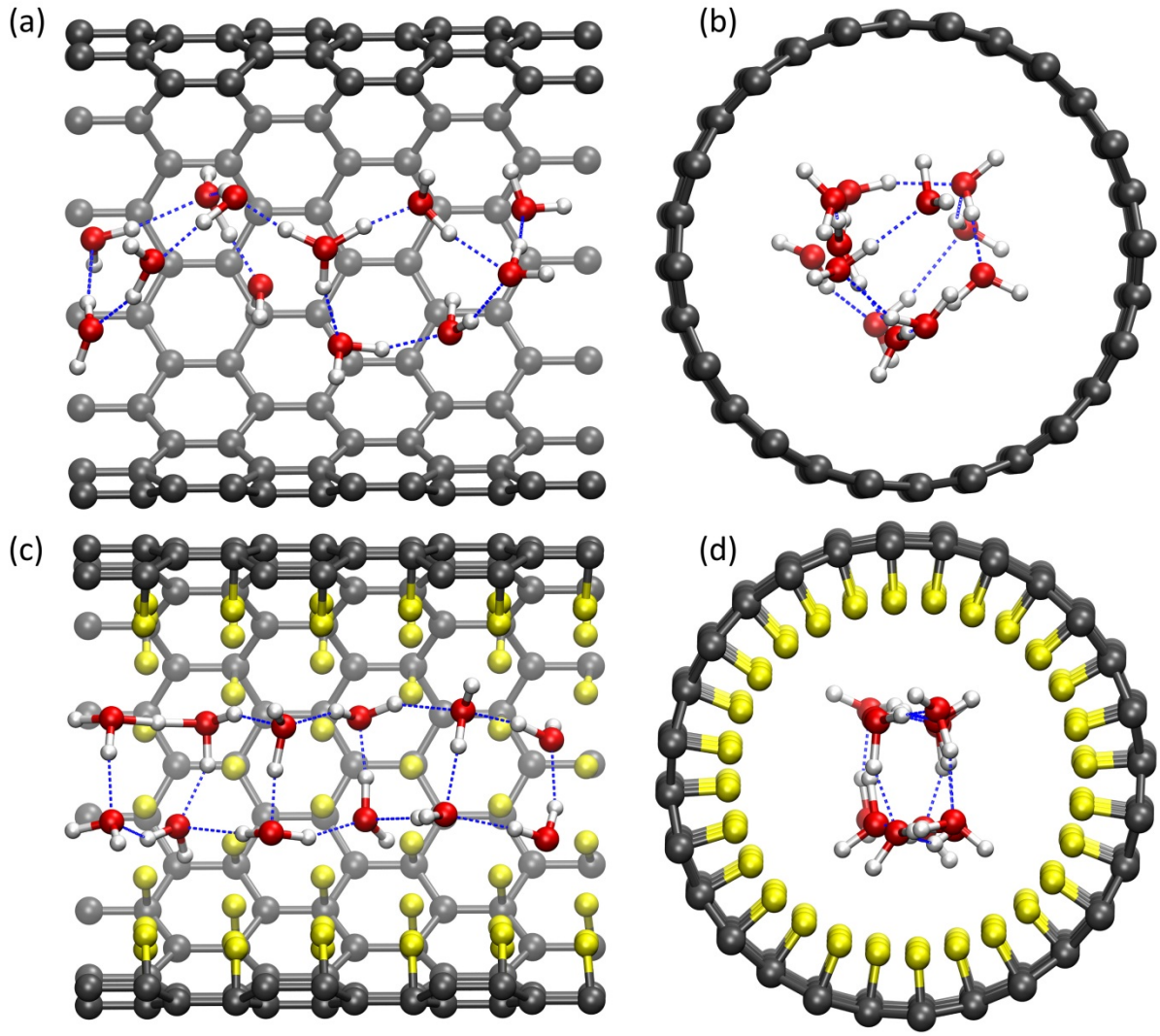

Figure 3.29. Representative snapshots of the hydrogen bond network in the smaller nanotubes containing an excess proton showing (left) along the CNT axis and (right) down the CNT axis for the bare (a/b) and fluorinated (c/d) systems.

larger tube without the excess proton. An average 55% (6.6 H_2O) in F-14 and 29% (~7 H_2O) in F-17 of the water molecules were determined to hydrogen bond to the fluorinated wall throughout the simulation. These are each higher than the previously mentioned results in the neutral systems. The corresponding average H···F and O···F hydrogen bond distances, however, were found to be essentially the same. The continuous lifetimes of these interactions were also the same but a marginal increase to 91 fs in the larger tube

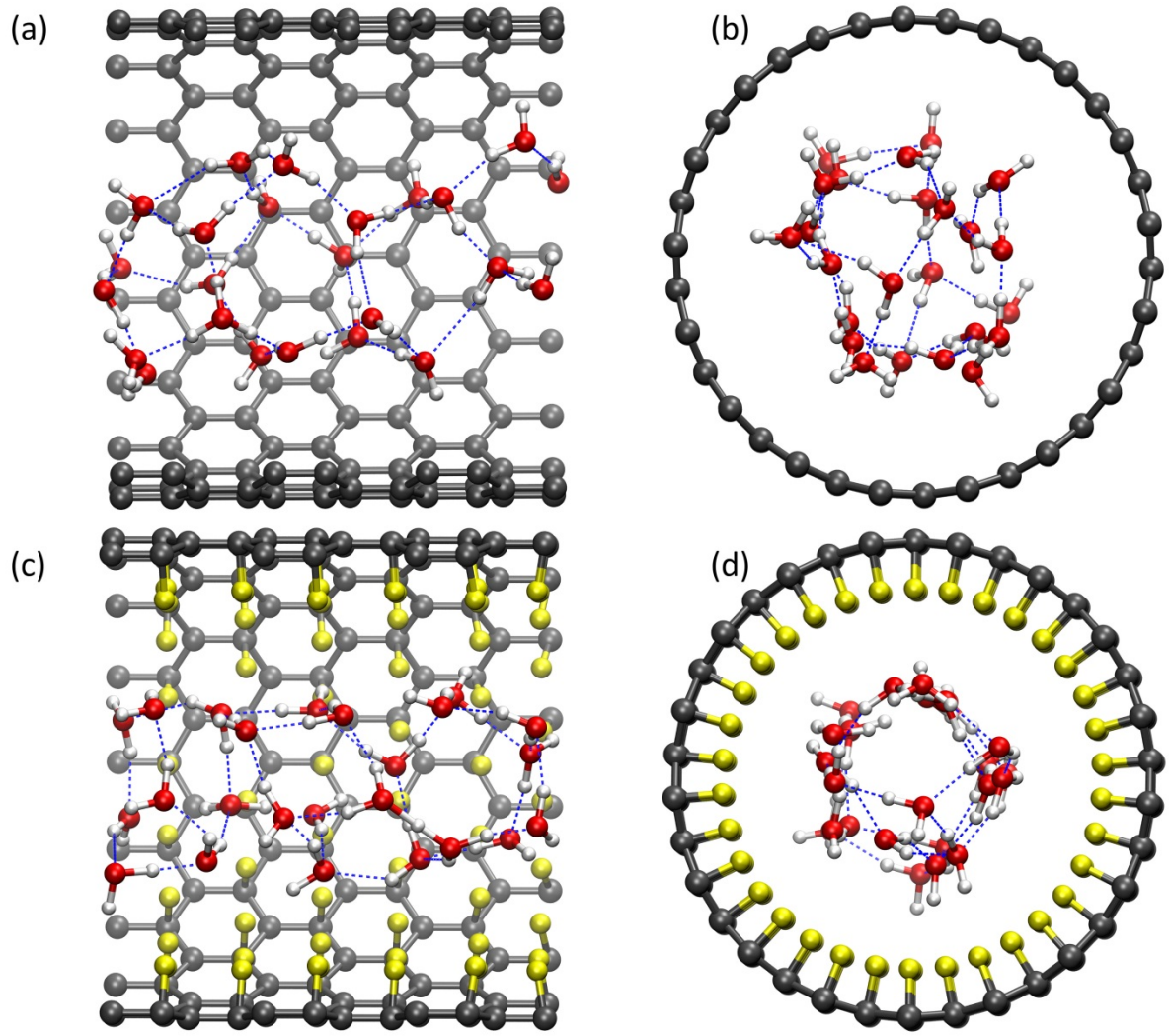

Figure 3.30. Representative snapshots of the hydrogen bond network in the larger nanotubes containing an excess proton showing (left) along the CNT axis and (right) down the CNT axis for the bare (a/b) and fluorinated (c/d) systems.

and a near two-fold increase to 196 fs were determined when bifurcated hydrogen bonds and hydrogen bond jumps were included. The F-14 plot shows a very sharp peak indicating that during 60% of the trajectory 7 H_2O are involved in these interactions while the F-17 plot is broader indicating an influence of the confinement dimensions on the results. It is possible that the increased number of these interactions, in combination with the confinement dimensions, plays a role in the overly ordered structure in F-14. Although an

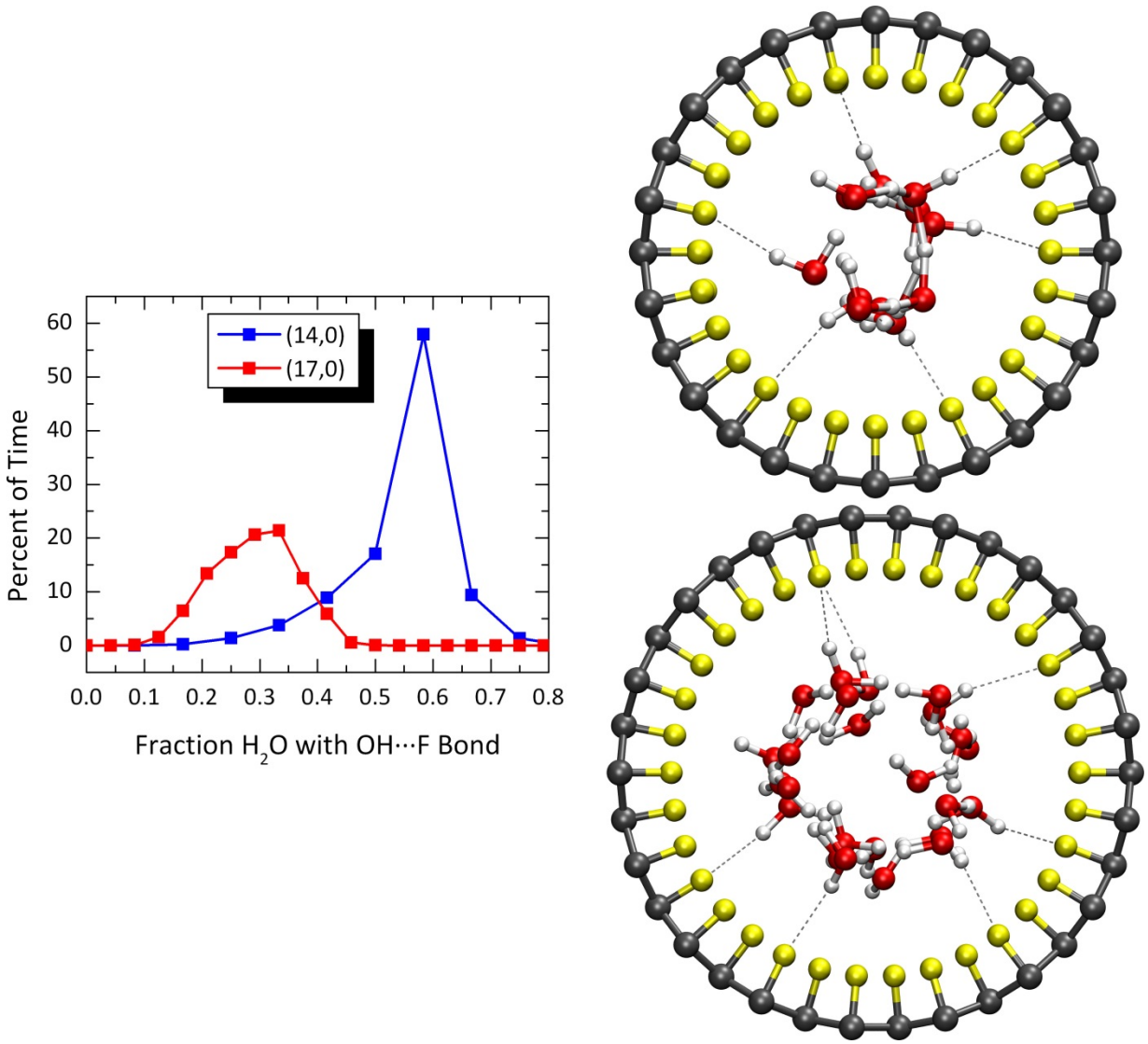

Figure 3.31. Percent of time throughout the trajectory OH···F hydrogen bonds exist versus the fraction of H_2O molecules with an OH···F bond for the fluorine CNT+H_2O+H^+ systems. The right panel shows representative snapshots of F-14(top) and F-17 (bottom) with OH···F bonds shown as dashed lines.

increase in the number of O–H···F bonds was found when the excess proton was included, such an interaction was an exceedingly rare event involving the H_3O^+ defect site.

We adopted the method of Marx *et. al.*[40] to determine the 'most active proton' (H*) involved in the protonated complex. In this procedure, each proton is assigned to its nearest oxygen atom. The oxygen atom in the protonated complex (O*) is then designated

as the one with three nearest neighbor hydrogen atoms. The values of the asymmetric stretch coordinate ($\delta = R_{O^*H^*} - R_{OH^*}$) for the oxygen atoms neighboring O* are determined, and the proton involved in the hydrogen bond with the smallest value of δ is considered the most active proton. Insight into the state of the excess proton can be obtained by examining the two-dimensional distribution function, $P(\delta, R_{O^*O})$, for the most active proton throughout the simulation shown in Figure 3.32, where R_{O^*O} is the distance between the oxygen atoms involved in the most active hydrogen bond. As indicated in the figures, the most active proton exists over a wide range of structures in each of the simulated systems. All of the profiles share a double-peaked structure with a non-zero probability around δ = 0. This corresponds to a symmetric sharing of the proton between two water molecules in a Zundel complex. While the definitions of Zundel and Eigen-like cations are somewhat ambiguous, the idealized forms are generally taken as $|\delta| \leq 0.1$ Å for a Zundel cation and $|\delta| > 0.3$ Å for Eigen-like structures.[40] Adopting this definition, 53% (F-14) and 55% (F-17) of the configurations in the fluorinated CNTs and ~51% in the bare CNTs are unclassified having δ in between these values. Of the remaining configurations, the Zundel structure in F-14 was favored (54.6% versus 45.4% Eigen) while that of N-14 showed the opposite (43.5% versus 56.5%). In the larger bare CNT, these numbers were split 47% to 53% while those in F-17 more closely resembled N-14 with values of 43.8% and 56.2%. It should be noted that these AIMD simulations treat the nuclei as classical particles. Simulations including quantum nuclear effects (QNEs) via *ab initio* path integral techniques have shown that treating the nuclei classically leads to an increased likelihood the proton exists in Eigen-like configurations which leads to the pronounced outer peaks.[40, 48, 84, 85, 209] Inclusion of QNEs enhances the Zundel character, and the $P(\delta, R_{O^*O})$ distribution function in water contains a broad, float ridge spanning over a range of δ encompassing Zundel, Eigen, and intermediate forms indicating that proton defects should be regarded as 'fluxional complexes' rather than the idealized states.[40] This has also been shown for proton transfer in CNTs which showed that QNEs can lead to delocalization of the most active proton

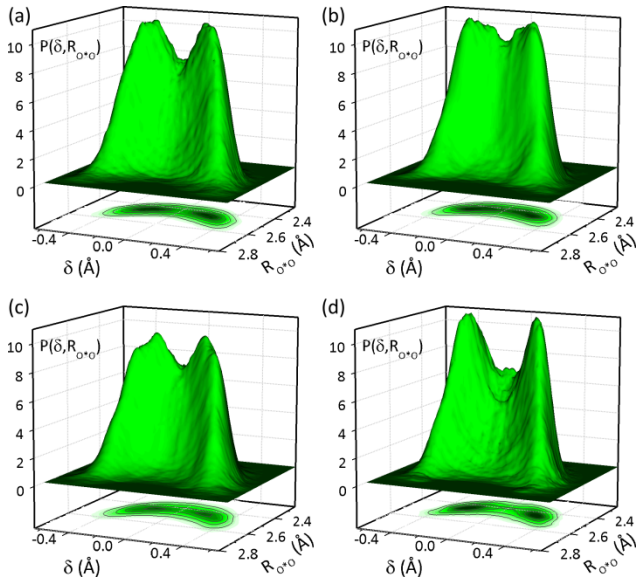

Figure 3.32. Distribution functions $P(\delta, R_{0*0})$ of the proton transfer coordinate $\delta \equiv R_{0*\mathrm{H}} - R_{0\mathrm{H}*}$ and the distance between the corresponding oxygen atoms R_{0*0} where H* is the most active proton (see text) for: (a) N-14, (b) F-14, (c) N-17, and (d) F-17. The distributions have been smoothed and symmetrized about $\delta = 0$ and normalized to unity.

overmultiple hydrogen bonds along a water chain.[209] Thus, the results presented here should not be taken as absolute values but as a relative comparison between the confined systems.

Finally we examine the location of the most active proton throughout the trajectory in the different CNTs. Figure 3.33 shows the two-dimensional projection of the position of H* onto the xy-plane and the three-dimensional trajectories of H* in the smaller and larger CNTs, respectively. The overwhelming majority of proton transfer events rattle back and forth between two water molecules and do not contribute to net or long range transport. In F-14 (Figure 3.33b), the active proton is localized near the CNT walls where it shuttles between the highly ordered 'zigzag ladder' water molecules with little net motion of the water molecules themselves. As mentioned previously, this structure may in part be caused by the several interactions with the fluorinated walls. This leads to a hydrogen bonding topography that contains several water molecules donating two hydrogen bonds to neighboring water molecules along the channel and accepting one perpendicular to it (see

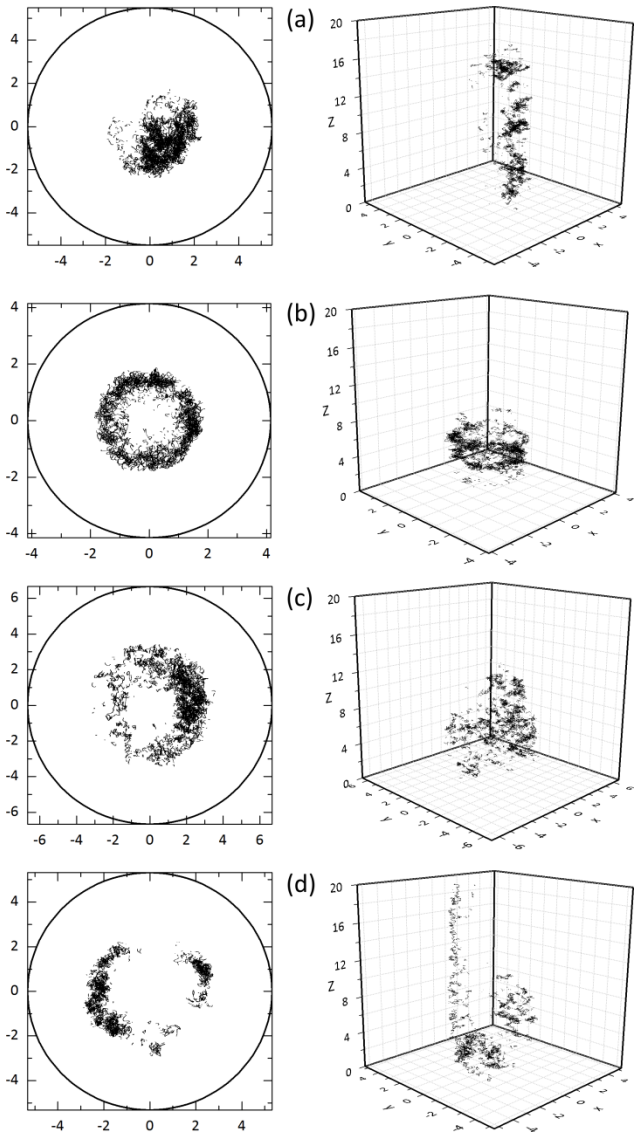

Figure 3.33. Location of H* throughout the trajectory projected onto the xy-plane (left) and the three-dimensional perspective (right) for: (a) N-14, (b) F-14, (c) N-17, and (d) F-17.

the middle four water molecules of Figure 3.29c) which appear to hinder proton transfer along the channel axis. The xy projection of the active proton in N-14 is also localized to a particular region of the nanotube but migrates down the nanotube axis as opposed to around the walls. In the larger N-17, H* was preferentially located in regions near the CNT surface and had less unidirectional motion down the channel than in N-14 which is likely due to the larger confinement dimensions. As in F-14, the active proton in F-17 was also

found to be highly localized near the fluorinated walls due to the hydrogen bond structure. However, the arrangement is considerably more disordered and does not contain the trap states found in F-14 and has a larger number of neighboring proton transfer sites allowing for more overall motion down the channel.

Summary. The degree of confinement and the hydrophobicity led to significant differences in the structure of hydrogen bonding of the water. In the bare CNTs, the systems with and without the excess proton exhibited similar hydrogen bond arrangements without any well-defined structure. There was, however, a somewhat greater tendency for the water molecules to arrange near the nanotube walls in N-14 while those in N-17 were more randomly distributed likely due to the level of confinement. The confinement also appears to influence proton transfer where the proton in N-14 has a more uniform directionality down the CNT axis. The water molecules confined within the fluorinated CNTs were found to localize near the channel surface and formed ordered hydrogen bond networks with well-defined regular structures. When an excess proton was introduced, the stacked pentagonal arrangement in F-17 was considerably disrupted resulting in a distorted hydrogen bond network while in F-14 a highly aligned zigzag ladder structure was formed. In each of these cases, hydrogen bonding to the fluorine atoms of the CNT wall was observed with a higher occurrence in the systems containing an excess proton. This was most pronounced in the smaller F-14 system where roughly half of the water molecules were involved in such an interaction in every simulation step which may contribute to the structural ordering. This arrangement led to several hydrogen bond sites that hinder proton transfer directly along the channel axis and, instead, the proton tends to shuttle between water molecules around the fluorinated surface with more Zundel-like character than the other systems. These sites were not observed in the larger fluorinated nanotube where proton transfer through the CNT occurred more readily indicating an influence of the increased confinement in F-14 on the interaction between the water molecules and the fluorine atoms, the hydrogen bond network, and the nature of the excess proton. It should be noted that there are many factors not probed in this study that may impact the findings including quantum nuclear effects, density of water, and distribution

and density of fluorine atoms. Thus, these results should be regarded as a relative comparison of how the confined environment and the addition of an excess proton affect the structural and dynamical properties in the simulated systems.

3.2.2 Triflic acid and water confined in carbon nanotubes

AIMD simulations were also performed to explore the effects of nanoscale confinement on the properties of aqueous triflic acid molecules. Single-walled carbon nanotubes (CNTs) again with chirality of (14,0) and (17,0) with diameters ranging from ~11 to 14 Å were used as confinement vessels. Systems were simulated at hydration levels of n = 1 – 3 $H2O/CF_3SO_3H$. The total density of triflic acid and water within the CNTs was, as close as possible, the same for all systems. This was maintained by either using nanotubes of different lengths or slightly varying the CNT carbon–carbon bond length. Some relevant system parameters are given in Table 3.1**.** The nomenclature used to distinguish between the different CNT systems is as followed: 14 and 17 are used for the different CNT chirality followed by 'F' or 'N' for fluorinated and nonfluorinated, and 1, 2, or 3 to designate the hydration level. For example, the (14,0) CNT system with fluorinated walls at a hydration of n = 2 would read 14F2. Representative images of the systems are shown in Figure 3.34.

Several of the analyses that follow regard hydrogen bonding between the water molecules and triflic acid groups. As with the other studies, a hydrogen bond was said to exist if the oxygen–oxygen separation was less than 3.25 Å with an H–O···O angle less than 30°.[197, 198] The coordination number (CN) for the water molecules are defined as the average number of donated and accepted hydrogen bonds per water molecule. Figure 3.35 shows the average water CN based on H_2O/H_2O hydrogen bonds, H_2O/CF_3SO_3H hydrogen bonds, and the total CN for each of the systems. It should be noted that at this stage, we refer to the CNs regarding water molecules and the triflic acid sulfonic acid groups for ease of discussion, but these also, respectively, encompass hydrogen bonds involving Zundel and hydronium ions and triflate ($CF_3SO_3^-$) anions and will not be distinguished unless necessary. Representative snapshots of the hydrogen bonding in each system for n = 1, 2, and 3 are shown in Figures 3.36, 3.37, and 3.38 respectively. At a hydration of n = 1, the

Table 3.1. System parameters.

System	Diameter (Å)†	Length (Å)	# H_2O	# CF_3SO_3H
14N1	11.3	13.1	3	3
14N2	11.6	13.5	6	3
14N3	11.0	17.1	9	3
14F1	11.6 (8.9)	13.5	2	2
14F2	11.1 (8.4)	17.3	4	2
14F3	11.4 (8.7)	17.8	6	2
17N1	13.3	12.8	4	4
17N2	13.9	13.3	8	4
17N3	13.3	12.8	9	3
17F1	13.9 (11.2)	13.3	3	3
17F2	13.2 (10.5)	12.7	4	2
17F3	13.3 (10.6)	12.8	6	2

†Based on the CNT carbon atoms, numbers in parentheses subtract C–F bond lengths.

average total H_2O CN is approximately 2 in all cases. In the bare nanotubes, which have a slightly higher total CN, hydrogen bonding between water molecules occurs while in the fluorinated CNTs the water molecules are isolated from each other. Typical configurations in the fluorinated systems involve a water molecule donating a hydrogen bond to a CF_3SO_3H and accepting a hydrogen bond from an adjacent one with no direct interactions between acid molecules. In the smaller CNT, this is in the form of a highly aligned hydrogen bond wire (Figure 3.36b) while in the larger system the pattern is less uniform. Hydrogen bonding between triflic acid molecules in the bare systems occurs regularly which promotes interactions between the water molecules at this low hydration level. An increase in the number of hydrogen bonds between water molecules was observed in all systems upon increasing the hydration to $n = 2$. The total coordination number also increases in all cases except 14F2 which is approximately the same as that of the lower hydration level. The typical structure in this case exhibits somewhat selective solvation of a single CF_3SO_3H by three water molecules with the other CF_3SO_3H oriented parallel to the CNT axis only involved in one hydrogen bond with a single water molecule (Figure 3.37b). The average total H_2O CNs in the bare systems are each ~2.5. In the smaller CNT, the contributions are

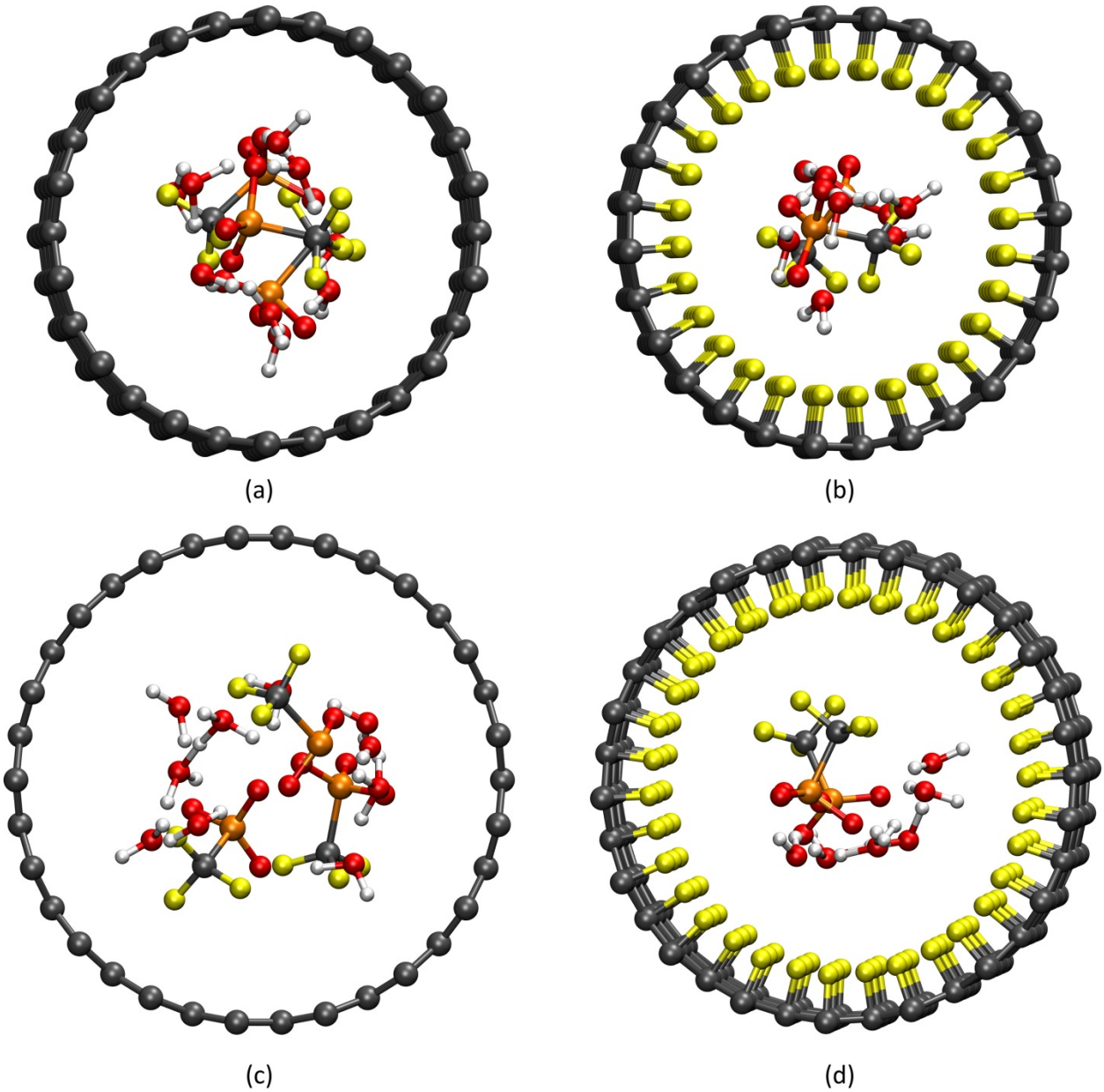

Figure 3.34. Systems shown for n = 3: (a) 14N3, (b) 14F3, (c) 17N3, and (d) 17F3. The different colored spheres represent different atom types where: gray–carbon, red–oxygen, white–hydrogen, yellow–fluorine, and orange–sulfur.

essentially split between hydrogen bonds to and from water and triflic acid molecules. A greater proportion of hydrogen bonds in the larger tube occur between water molecules with slightly less than 1 hydrogen bond per water molecule to or from a CF_3SO_3H, on average, and generally one direct hydrogen bond between triflic acid molecules. The total

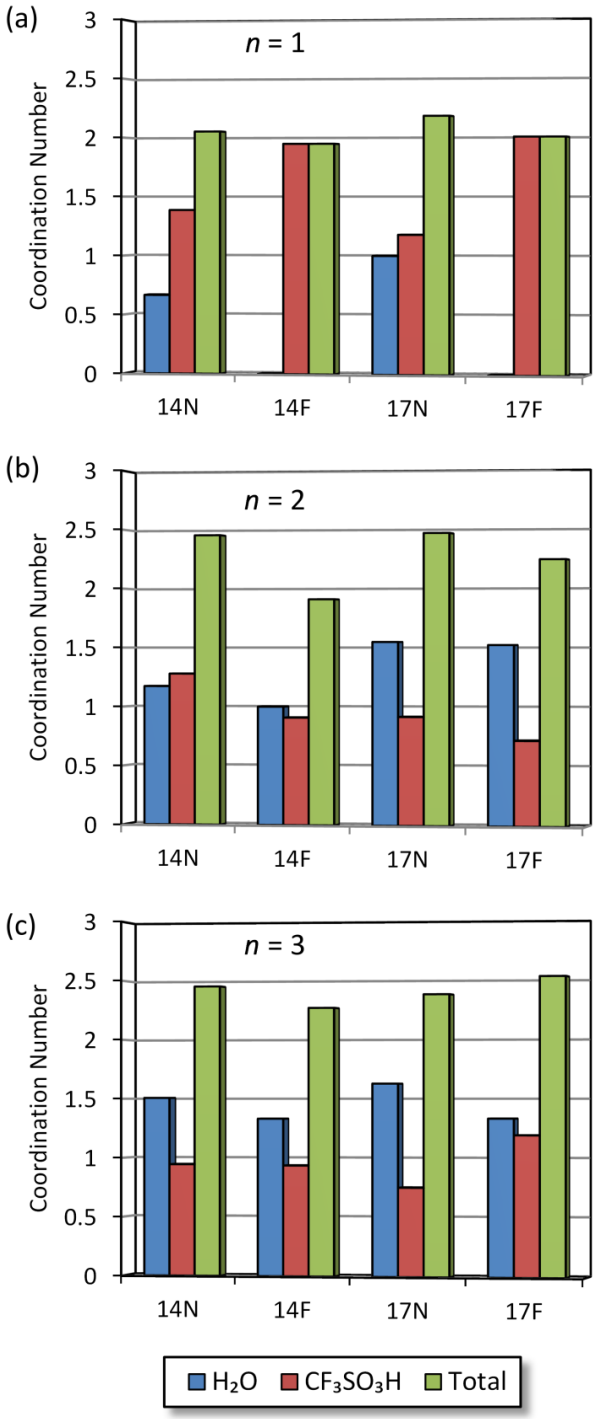

Figure 3.35. Coordination numbers of the water molecules defined by the average number of donated and accepted hydrogen bonds for each system at: (a) n = 1, (b) n = 2, and (c) n = 3.

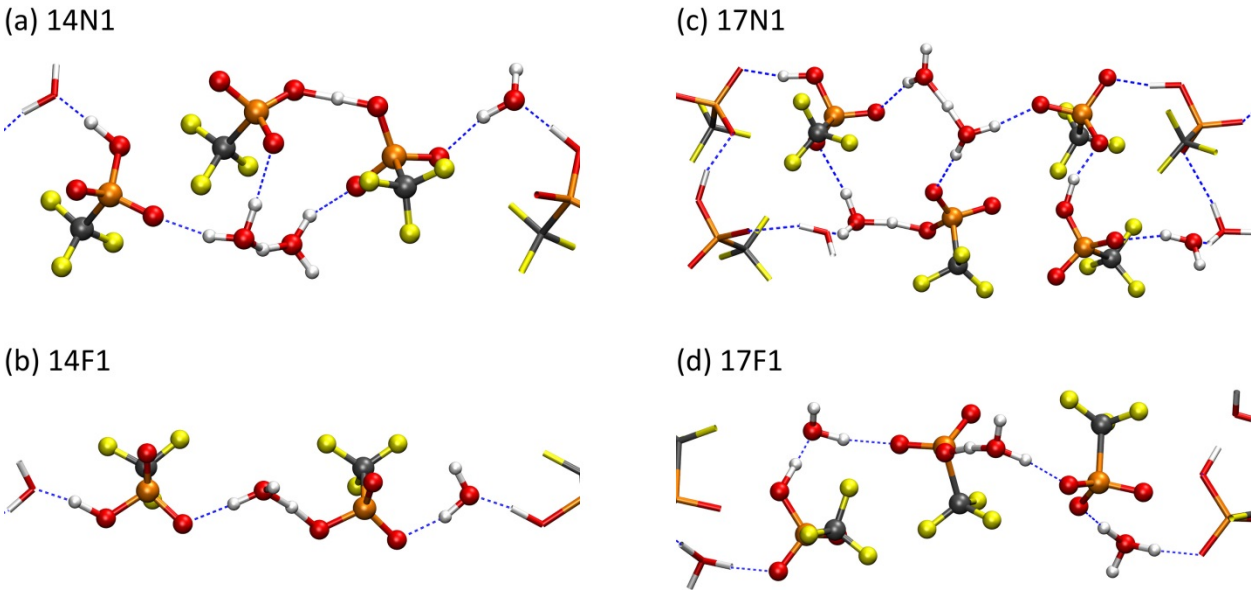

Figure 3.36. Representative snapshots of the hydrogen bond network at n = 1 for: (a) 14N1, (b) 14F1, (c) 17N1, and (d) 17F1. Hydrogen bonds are denoted by dashed lines. A portion of periodic images have been included represented by colored rods to show the local environment. The CNT walls have been omitted for clarity.

CN in 17F2 of ~2.25 is slightly less than 17N2, but with nearly the same CN between water molecules. The typical hydrogen bond structure contains one direct hydrogen bond between triflic acid molecules with the water molecules hydrogen bonding among themselves as well as bridging the other triflic acid oxygen atoms through two or more water molecules. At n = 3, the average H_2O–CF_3SO_3H CNs for the smaller CNTs is ~1. In 14F3, this is a result of configurations where each water molecule donates one hydrogen bond to a triflic acid molecule. In 14N3, on the other hand, this arises due to typical configurations containing two or three water molecules not hydrogen bonded to any triflic acid SO_3H groups but multiple different water molecules involved in direct hydrogen bonds to two different CF_3SO_3H effectively bridging the acid molecules. In 17F3, bridging of two triflic acid molecules through one H_2O occurred frequently as well as one triflate oxygen atom accepting hydrogen bonds from two different water molecules. It was not common to find water molecules isolated from the triflic acid molecules which results in the highest H_2O–CF_3SO_3H CN of all systems at this hydration level. The highest H_2O–H_2O CN and lowest

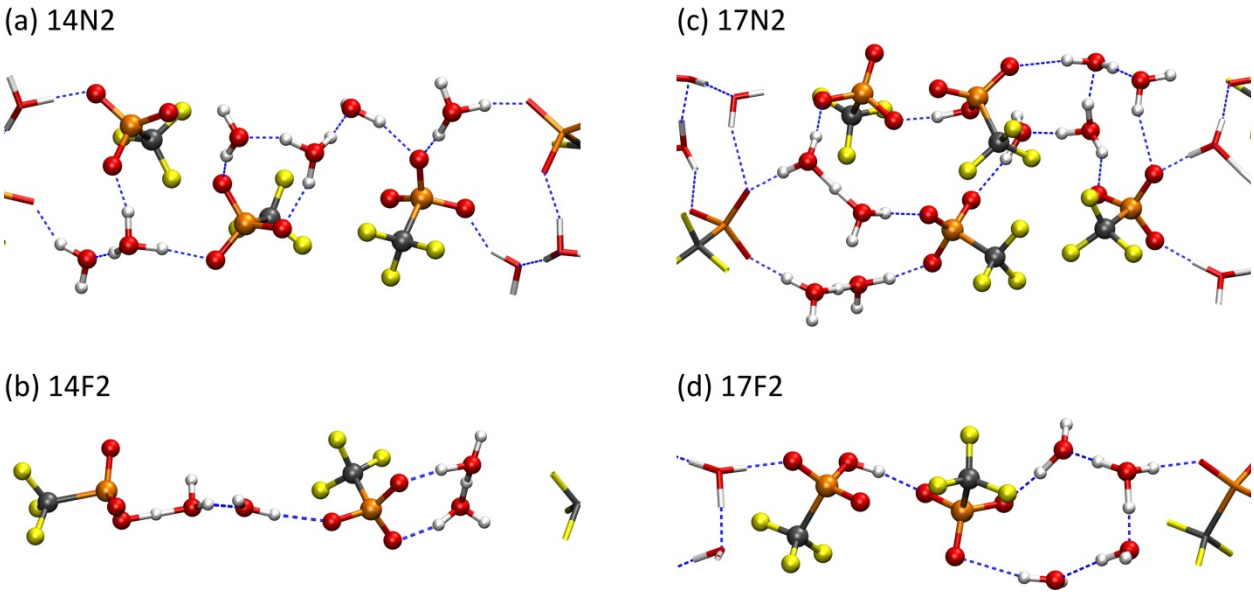

Figure 3.37. Representative snapshots of the hydrogen bond network at n = 2 for: (a) 14N2, (b) 14F2, (c) 17N2, and (d) 17F2. Hydrogen bonds are denoted by dashed lines. A portion of periodic images have been included represented by colored rods to show the local environment. The CNT walls have been omitted for clarity.

H_2O–CF_3SO_3H CN at n = 3 were found in 17N3. This indicates that the water molecules are more clustered together with rare occurrence of a water molecule involved in hydrogen bonds with multiple triflic acid SO_3H groups. At all hydration levels, the larger bare CNT contained strong direct hydrogen bonds between triflic acid molecules with short O···O separations that hindered accessibility of water molecules to these sites.

Along with local hydrogen bonding between neighboring water and triflic acid molecules, the hydrogen bond network connectivity throughout the entire system is important to proton dissociation and transfer in PEMs.[52] To analyze the connectivity, a similar, but not identical, procedure of previous studies was employed.[84-86, 137, 210, 211] An undirected graph with oxygen atoms as nodes and hydrogen bonds involving two oxygen atoms as edges was used to generate an N x N adjacency matrix, A, at each time step (where N is the total number of oxygen atoms). If a hydrogen bond existed between oxygen atoms i and j, the corresponding matrix elements A_{ij} and A_{ji} were set to 1, otherwise the matrix elements were set to 0. This differs from some of the previous studies where a directed graph was

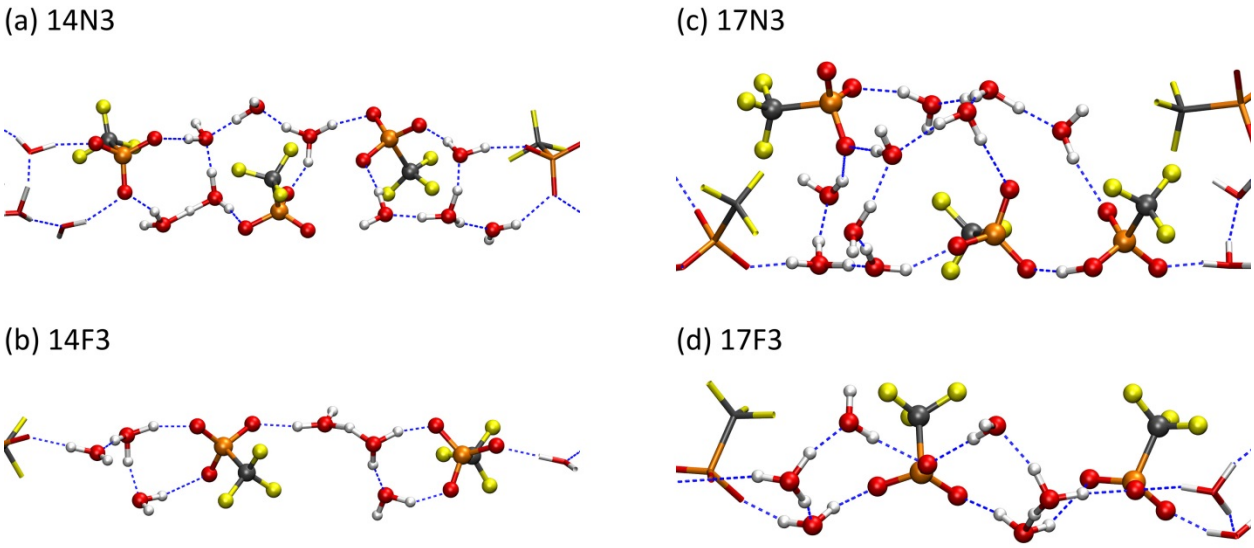

Figure 3.38. Representative snapshots of the hydrogen bond network at n = 3 for: (a) 14N3, (b) 14F3, (c) 17N3, and (d) 17F3. Hydrogen bonds are denoted by dashed lines. A portion of periodic images have been included represented by colored rods to show the local environment. The CNT walls have been omitted for clarity.

used to obtain the adjacency matrix with elements equal to 1 for hydrogen bonds donated from i and accepted by j (i.e., $A_{ij} \neq A_{ji}$). In these studies the property of adjacency matrices that element $A_{ij}^{(n)}$ of A^n gives the number of unique walks with n edges from node i to node j. Although the directionality of hydrogen bonds plays an important role in long range proton transport,[212] the aim here is to gain additional insight into the overall hydrogen bond network structure. If a directed graph was used to map the adjacency matrix in the present study, hydronium ions, which rarely accept hydrogen bonds in these simulations, can terminate a path and defining the donor and acceptor in perfectly symmetric sharing of a proton between oxygen atoms is ambiguous. Additionally, the powers of the adjacency matrix using an undirected graph result in unwanted revisiting of edges leading to fictitiously long chains. Hence, a slightly different approach is used here. A simple depth-first search algorithm was used to determine the connectivity matrix, C, whose elements C_{ij} and C_{ji} are 1 if a path of any length connected atoms i and j and 0 otherwise. This allowed for the decomposition of the entire hydrogen bond network into isolated subnetworks. Within each subnetwork a recursive branching algorithm was used to calculate the length

Table 3.2. Averaged connectivity data.†

System	# Chains	# Chains per CF_3SO_3H	# H_2O Oxygen Atoms	# CF_3SO_3H Oxygen Atoms	# Rings
14N1	1.98 (1.98)	0.66 (0.66)	1.36 (1.36)	1.82 (1.82)	0.0012
14N2	1.73 (1.73)	0.58 (0.58)	3.38 (3.38)	2.37 (1.82)	0.0039
14N3	1.72 (1.63)	0.57 (0.54)	4.51 (3.41)	2.63 (2.33)	0.53
14F1	1.89 (1.89)	0.94 (0.94)	1.00 (1.00)	2.00 (2.00)	-
14F2	2.00 (2.00)	1.00 (1.00)	2.00 (2.00)	1.80 (1.80)	-
14F3	2.00 (2.00)	1.00 (1.00)	2.90 (2.90)	1.95 (1.95)	0.0030
17N1	1.94 (1.94)	0.48 (0.48)	1.80 (1.80)	1.96 (1.96)	0.0026
17N2	1.32 (1.27)	0.33 (0.32)	5.53 (4.98)	2.63 (2.41)	0.29
17N3	1.23 (1.08)	0.41 (0.36)	6.45 (5.80)	2.42 (2.20)	0.33
17F1	2.91 (2.91)	0.97 (0.97)	1.00 (1.00)	2.02 (2.02)	-
17F2	1.00 (0.74)	0.50 (0.37)	3.89 (3.86)	1.85 (1.80)	0.26
17F3	1.08 (1.03)	0.54 (0.51)	5.15 (4.59)	3.06 (2.75)	0.26

†Numbers in parentheses represent values when ring connections are removed.

(determined by the number of oxygen atoms) of all the chains longer than 2 that did not include a complete ring, though individual oxygen atoms that were part of a ring were initially allowed. The longest chain from each subnetwork was extracted for analysis (i.e., no chains that were branches off of the longest chain were included). All rings that did not include smaller rings were included. Further analysis was performed when rings were present by setting all elements of A_{ij} that were part of a ring to 0 and repeating the process to separate networks of rings and chains. The connectivity results are presented in Table 3.2 and Figures 3.39, 3.40, and 3.41.

Figure 3.39 shows the average number of chains in each system with and without the inclusion of ring connections normalized by the number of triflic acid molecules. The rationale behind the normalization becomes evident when comparing the data at n = 1. As previously mentioned, the water molecules in the fluorinated systems at this hydration level are isolated from each other and generally form a hydrogen bond bridge between two CF_3SO_3H. The average number of chains is then dependent on and approximately

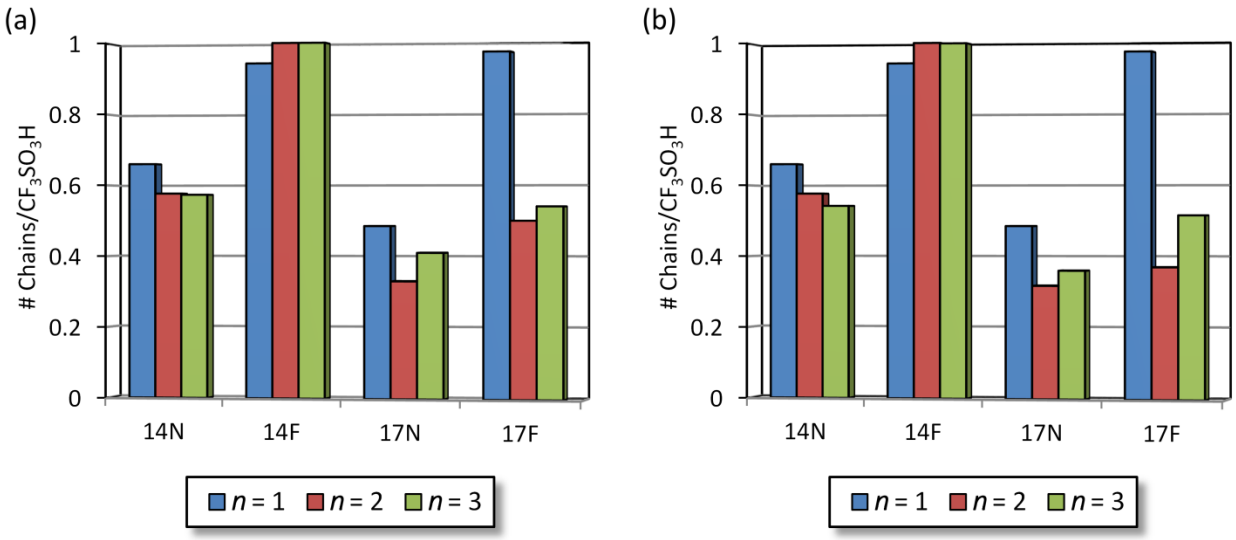

Figure 3.39. The average number of chains per CF_3SO_3H for all CNT/triflic acid+H_2O systems: (a) including oxygen atoms that are part of rings and (b) omitting oxygen atoms involved in ring connections.

determined by the number of triflic acid molecules (2 for 14F1 and 3 for 17F1). Thus, the normalization allows for a more direct comparison between systems showing approximately one chain per CF_3SO_3H in each fluorinated CNT which indicates isolated hydrogen bond networks (note that small values here indicate increased connectivity throughout the system). In the bare CNTs, the water molecules are not isolated and multiple triflic acid molecules can be bridged through multiple H_2O. This is also reflected in the average chain lengths shown in Figure 3.40 where the average number of water molecules in the chains is greater in the bare CNTs than in the fluorinated tubes. While the maximum length of a chain that can be formed is limited by the number of sulfonic acid groups and water molecules, the data shown for the chain length have not been normalized by the number of CF_3SO_3H for convenience of discussion and is partitioned into the type of oxygen atoms involved in the chain. The fraction of total oxygen atoms in the system per chain is also shown as a frame of reference. When the longest chain within a subnetwork terminated in a branch to both a triflic acid and water oxygen atom (i.e., two chains with the same length but different terminating oxygen atoms) the contribution from these particular oxygen atoms to the length of the chain was divided evenly to avoid bias in the

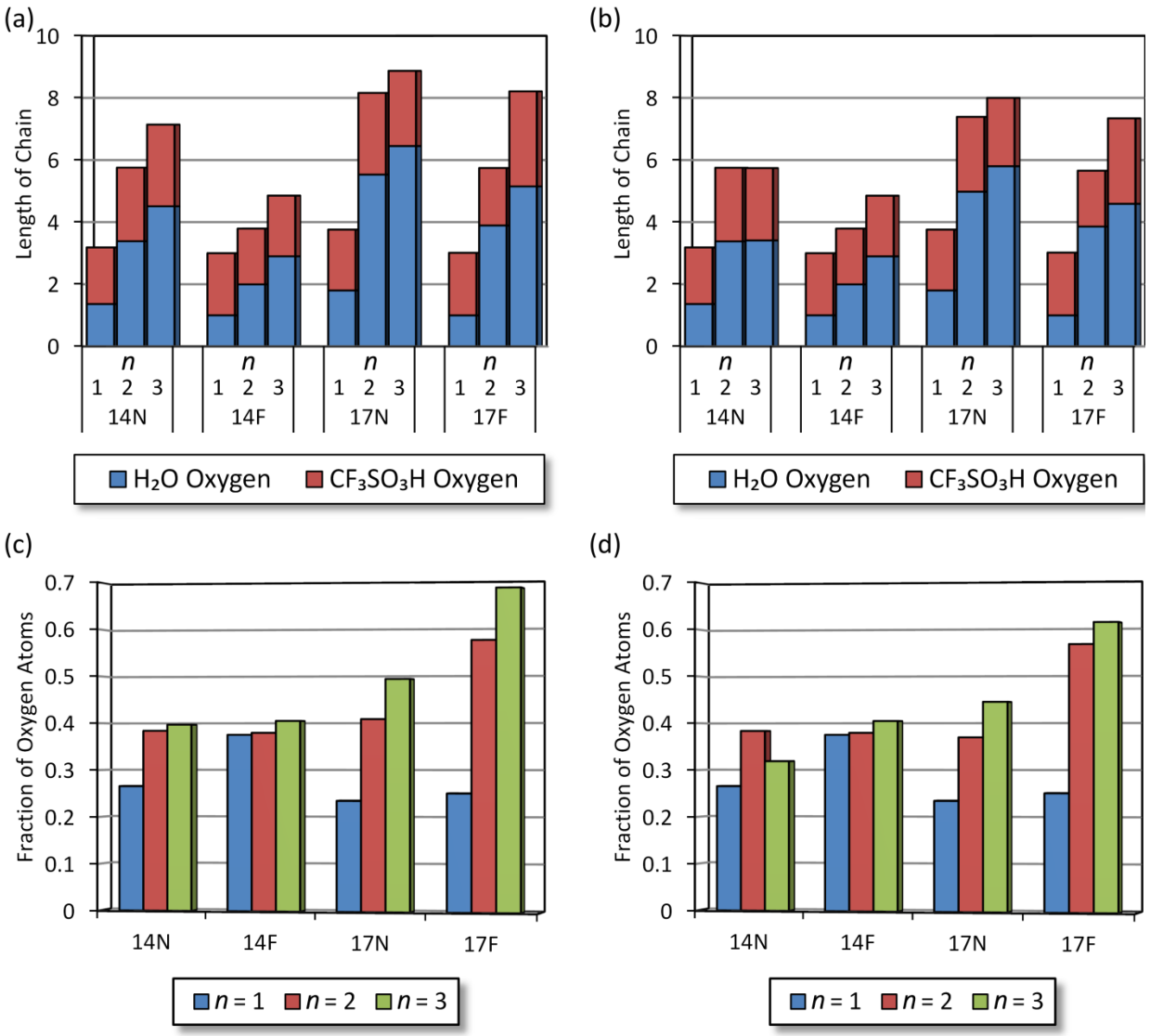

Figure 3.40. Average chain lengths defined by the number of oxygen atoms involved in all systems partitioned into oxygen atoms of H_2O and CF_3SO_3H: (a) with and (b) without oxygen atoms involved in ring connections. (c) and (d) show the average fraction of total oxygen atoms in the system involved per chain.

results. As no rings were observed in the fluorinated systems and were exceedingly rare in the bare tubes at this level of hydration, the results are not affected by omitting ring connections

The average length of the chains in each system, as well as the contribution from oxygen atoms from water molecules, generally increases with increasing hydration as expected.

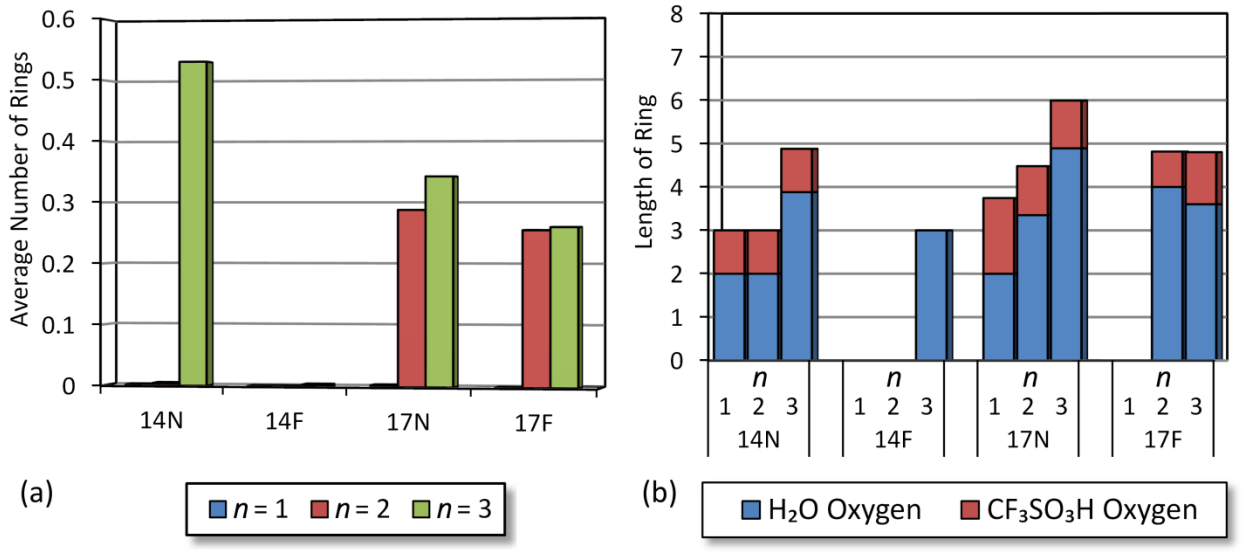

Figure 3.41. The data for rings showing (a) the average number of rings and (b) the average length of rings partitioned into H_2O and CF_3SO_3H oxygen atoms.

The number of chains, however, shows less of an obvious trend. At n = 2 and 3, the number of chains per CF_3SO_3H in the smaller fluorinated tube remains equal to one indicating that the water molecules are still in separated clusters (Figures 3.37b and 3.38b) while a slight decrease in value was observed in the smaller bare tube due to increased connectivity throughout the system. Negligible ring formation was found in either of the smaller CNTs at n = 2. However, at n = 3, rings were frequently found in 14N3 with an average of 0.53 rings in the system, as shown in Figure 3.41a. Note that the average number of rings is not normalized because typically only one ring was present at a time in each system, with a few exceptions, so this number also gives a very close approximation to the fraction of time ring formation was observed. Snapshots of rings in systems where ring formation occurred at least 10% of the time are shown for n = 2 and 3 are shown in Figures 3.42 and 3.43. Omitting ring connections in 14N3 resulted in a slight drop in the number of chains and a considerable drop in the average chain length to approximately the value found at n = 2. which contains the same number of triflic acid molecules but fewer H_2O. The ring generally had the same form when present in the simulation which contained one triflate oxygen atom accepting two hydrogen bonds: one from a hydronium ion that also hydrogen bonded

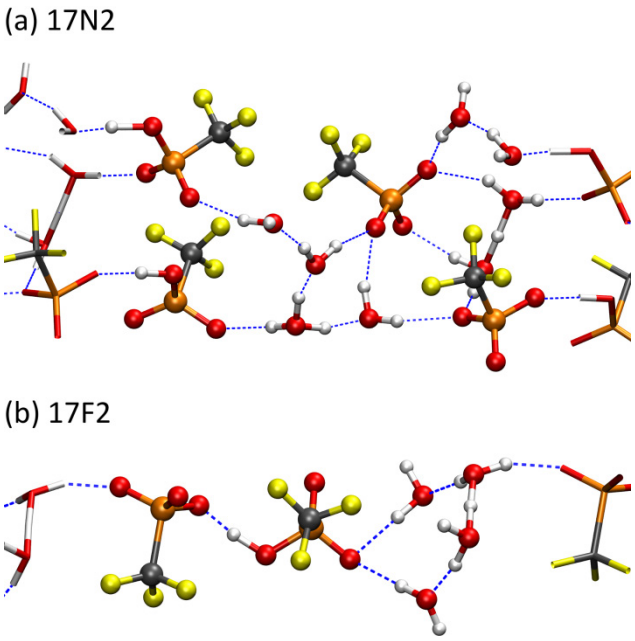

Figure 3.42. Snapshots at *n* = 2 showing ring formation in (a) 17N2 and (b) 17F2.

to a different CF_3SO_3H and the other from a neighboring species that regularly transitioned between H_2O, H_3O^+, and $H_5O_2^+$ states (Figure 3.43b). Ring formation was found in each of the larger CNT systems at both *n* = 2 and 3 which also involved a single triflate oxygen atom receiving two hydrogen bonds from different water molecules. As previously mentioned, each of the larger systems at *n* = 2 contains a direct hydrogen bond between triflic acid molecules, which appears to promote ring formation at this hydration level. The hydrogen bonding in 17F2 has the water molecules clustered between the triflic acid molecules bridging the two together (Figure 3.37d) resulting in only one chain (0.5 per CF_3SO_3H in every step) when ring connections are allowed. However, the cluster forms a ring throughout approximately 26% of the trajectory, and with this hydrogen bond topography and minimal water, chains and rings do not independently exist simultaneously. As such, when the oxygen atoms involved in rings are removed from the analysis, the average number of chains decreases accordingly to ~0.74 (0.34 per CF_3SO_3H) but the average chain length is negligibly impacted. The opposite was found for 17N2, which had the fewest chains per CF_3SO_3H of all systems at all hydration levels with a highly connected hydrogen bond network containing several triflate oxygen atoms accepting multiple hydrogen bonds

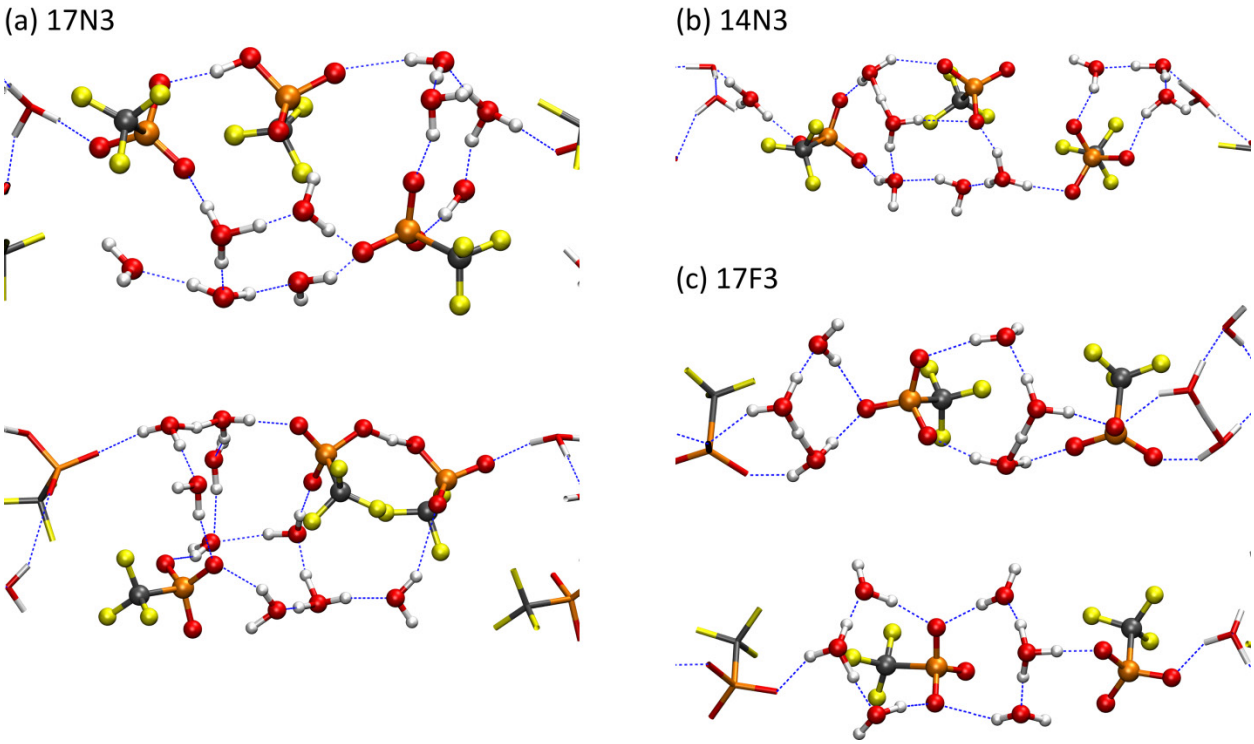

Figure 3.43. Snapshots at *n* = 3 showing ring formation in (a) 17N3 showing a 5-membered ring (top) and a 9-membered ring (bottom), (b) 14N3, and (c) 17F3 showing a 4-membered ring (top) and an 8-membered ring (bottom).

when rings were present. Similar to 14N3, the removal of ring connections disrupts overall connectivity of the longest chain throughout the system, but the high degree of branching in the hydrogen bond network leads to only a slight decrease in the average number of chains but with shorter lengths (Figure 3.42a).

The hydrogen bond networks in the larger tubes at *n* = 3 are well connected with fairly long chains encompassing approximately 50 and 69% of all the oxygen atoms per chain in 17F3 and 17N3, respectively, when ring connections were included. However, rings are, again, fairly common and distinctly different ring structures were commonly found in both systems. The majority of the rings in 17N3 contained one triflate oxygen atom and three or four H_2O/H_3O^+ (Figure 3.43a top) with two such rings occurring at the same time in ~3% of the simulation. However, in roughly 10% of the simulation rings with lengths of 9 or 10 oxygen atoms were observed that that encompassed nearly all of the water molecules

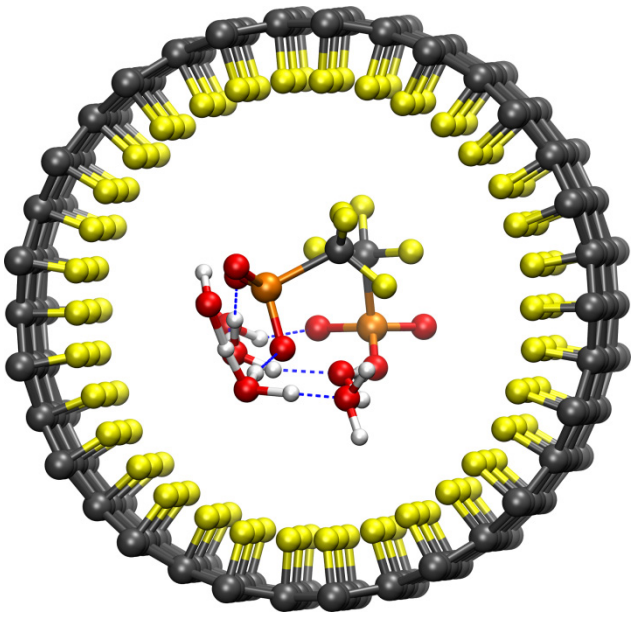

Figure 3.44. Snapshot down the CNT axis in 17F3 showing the water molecules in a structured domain away from the triflic acid CF_3 head groups.

(Figure 3.43a bottom). This led to the increase in average ring length and decrease in average number of chains when ring connections were removed while the smaller five-membered rings were responsible for the decrease in the average length of chains as with 17N2. There was less variability in the size of rings formed in 17F3 where 80% of the rings contained one triflate oxygen atom and three water molecules while the other 20% had two oxygen atoms of the same $CF_3SO_3^-$ accepting two hydrogen bonds surrounded by three H_2O/H_3O^+ on each side (Figure 3.43c) giving an average ring size of 4.8 oxygen atoms. The same reasoning for decreases in the number of chains and the length of chains as 17N3 when ring connections are removed can be applied to 17F3. Interestingly, the high hydrogen bond connectivity in the larger fluorinated tube occurred even though the water molecules were found in separate clusters between triflic acid/triflate molecules. Throughout the trajectory the water molecules and triflic acid molecules were ordered in a regular fashion in what appears to be a domain mostly separated from the CF_3 groups of the triflic acid, shown in Figure 3.44, which was not observed in any other system at this hydration level. Unlike 14F3, which contained isolated water clusters that mostly formed

hydrogen bonds with the triflic acid sulfonate groups from the side, water molecules in the larger fluorinated CNT were able to form hydrogen bonds from both the sides and below the triflic acid sulfonate groups due to the increased space which leads to a more uniform solvation structure. Although the overall connectivity is high, the water molecules in the clusters separated by the triflate anions in 17F3 do not interact while those in 17N3 form a well-connected channel which may impact long-range proton transfer at this hydration level.

Proton dissociation in hydrated PEMs is also known to depend on the level of hydration. In our analysis we define five different states for the acidic protons based on the 'most active hydrogen bond' associated with each site. All protons were first assigned to their nearest neighbor oxygen atom, and the oxygen sites with either one or three nearest neighbor hydrogen atoms were located. The values of the asymmetric stretch coordinate, $\delta = R_{O_dH} - R_{O_aH}$, were then determined for each hydrogen bond associated with the oxygen atom, where R_{O_dH} and R_{O_aH} are the distances from a given hydrogen atom to the donor and acceptor oxygen atoms in the hydrogen bond, respectively. If the nearest neighbor oxygen atom was from a triflic acid molecule, it was considered in the analysis; otherwise, the hydrogen bond with the smallest $|\delta|$ was used to determine the state of the proton. A proton was said to be bound if its nearest neighbor was an oxygen atom of a triflic acid molecule with $|\delta| \geq 0.2$ Å. If any pair had $|\delta| < 0.2$ Å, it was assigned one of three shared states according to the types of the oxygen atoms involved: CF_3SO_3H/CF_3SO_3H shared, CF_3SO_3H/H_2O shared, or H_2O/H_2O shared (i.e., a Zundel cation). It should be noted that the shared states between triflic acid molecules also includes sharing between triflic acid and triflate molecules, which is more commonly observed. Lastly, a hydronium (H_3O^+) state was assigned when a non-triflic acid oxygen atom had three proton neighbors with the smallest $|\delta| \geq 0.2$ Å. The results of the analysis for each system at all hydration levels are shown in Figure 3.45.

As expected, proton dissociation increases as the hydration level increases. At *n* = 1,

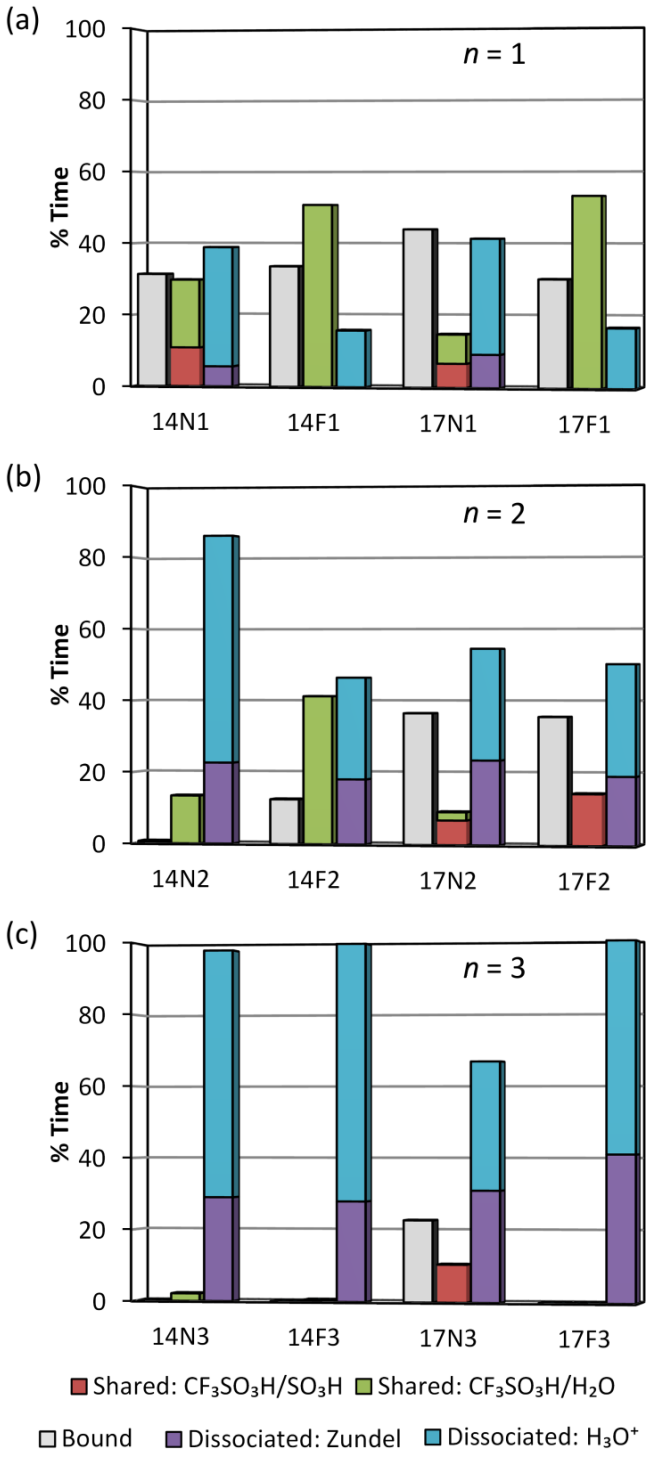

Figure 3.45. State of the protons in each system by hydration level: (a) n = 1, (b) n = 2, and (c) n = 3. See text for definition of different states.

approximately 40% dissociation was observed in the bare CNTs while in the fluorinated systems the percent dissociation was less than 20%. As mentioned earlier, each of the bare CNTs contain instances of sharing a proton between triflic acid/triflate molecules as well as interactions between water molecules, which was not observed in the fluorinated CNTs, which likely leads to the increased dissociation and the presence of Zundel cations. In 17N1, two different triflic acid molecules form direct hydrogen bonds with one triflate anion, each of which are typically in the bound state. This leads to dissociation of the proton originally associated with the $CF_3SO_3^-$ forming a contact ion pair (CIP). These observations are also supported by the radial distribution function (RDF) between the triflic acid/triflate oxygen atoms and the protons shown in Figure 3.46. The 17N1 RDF has the narrowest first peak of all the systems arising from the two bound protons but is followed by a clear minimum indicating less sharing of protons between triflic acid and water molecules. The first peak in the 14N1 RDF, on the other hand, is broader and occurs at a farther distance which is followed by a ridge revealing a greater tendency for sharing of protons both between triflic acid molecules and triflic acid and water molecules. In the fluorinated tubes, the first peak is shifted even farther but the distances between ~1.35-1.55 Å are less pronounced than in the bare systems suggesting that the protons are loosely bound but not fully dissociated with a much larger portion of the observed states as sharing between a water molecule and a CF_3SO_3H.

Increasing the hydration level to n = 2 expectedly increased the degree of dissociation in all systems as well as the Zundel character of the dissociated protons. Surprisingly, ~86% dissociation was observed in 14N2 with less than 1% bound states observed, while between 45 and 55% dissociation was observed in the other systems. At this hydration level the H_2O/CF_3SO_3H CN was the highest in 14N2 and was the only system in which this CN was higher than that between water molecules (Figure 3.35b) indicating that the water molecules and solvated protons have a greater propensity to hydrogen bond with multiple triflic acid molecules. Although electronic structure calculations on isolated PFSA fragments have revealed that proton dissociation requires greater water content,[59, 63, 213] calculations incorporating multiple PFSA side chains have shown that cooperative

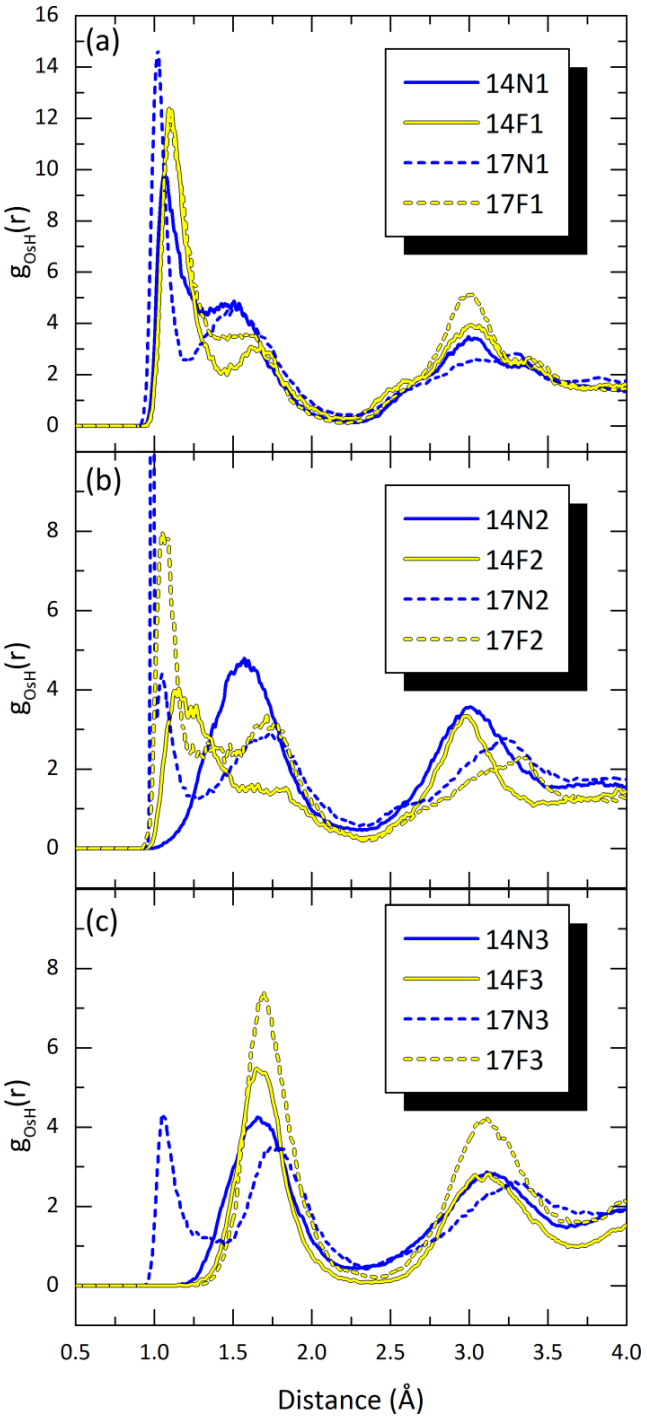

Figure 3.46. Radial distribution functions between oxygen atoms of $CF_3SO_3H/CF_3SO_3^-$ sulfonic acid/sulfonate groups, O_S, and hydrogen atoms by hydration level: (a) n = 1, (b) n = 2, and, (c) n = 3.

interactions between sulfonic acid groups and connectivity through a single water molecule can enhance proton dissociation at relatively low levels of hydration.[69-71, 73, 74, 214] In each of the larger tubes, direct hydrogen bonding between triflic acid molecules lead to larger amounts of bound and shared CF_3SO_3H/CF_3SO_3H states. The dissociated proton(s), however, had greater separation from the triflic acid/triflate groups than in 14N2 as shown in the RDF (Figure 3.46b) with very little instances of shared CF_3SO_3H/H_2O states. These states were quite frequent in 14F2, on the other hand, which exhibited the lowest dissociation but fewer bound states than in the larger tube. As mentioned earlier, the hydrogen bonding in this system exhibited somewhat selective solvation of one of the triflic acid molecules whose proton was generally in a dissociated state while the other acidic proton mostly rattled between the triflic acid and a water molecule oxygen atoms leading to a broader first peak in the RDF than in the larger systems again indicating that the protons are loosely bound but do not fully separate from the triflic acid molecules.

Further increasing the hydration to n = 3 leads to near complete dissociation in all systems except the larger bare nanotube. Again, a hydrogen bond between triflic acid and triflate molecules led to a greater amount of bound and shared CF_3SO_3H/CF_3SO_3H states and decreased the overall proportion of dissociated protons. The average CN between water molecules and triflic acid oxygen atoms was the lowest and that between water molecules was the highest in 17N3 indicating a preference for interactions between water molecules. Indeed, hydrogen bonding from the water molecules to the directly hydrogen bonded triflic acid/triflate molecules occurred but with average O···O and O···H distances of 2.81 and 1.87 Å, respectively, indicating weak hydrogen bonds as compared to that between water molecules which had respective distances of 2.61 and 1.58 Å. In fact, all hydrogen bonds between triflic acid/triflate and water molecules here were relatively weak when compared to the other systems as indicated in the probability distribution of δ for all $O–H\cdots O_s$ hydrogen bonds between the triflic acid and water molecules shown in Figure 3.47 which contains no values of $\delta \geq$ -0.3 Å with a peak at approximately -0.8 Å. Note that since all protons are dissociated aside from the one involved in the direct hydrogen bond in 17N3 and the very few instances of CF_3SO_3H/H_2O sharing in the other systems, the

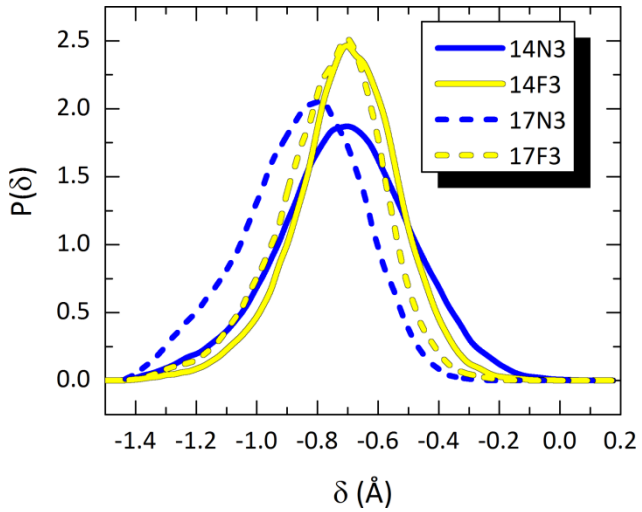

Figure 3.47. Probability distribution of the asymmetric stretch coordinate, $\delta = R_{O_dH} - R_{O_aH}$, for all hydrogen bonds between water and triflic acid molecules for each system at n = 3. In all cases at this hydration level, water molecules/solvated protons act as the hydrogen bond donor.

distribution shown always has water molecules/solvated protons as the hydrogen bond donor in the definition of δ. The dissociated protons in 17N3 were, thus, found to have the greatest separation from the triflic acid oxygen atoms (which is also reflected in the RDF of Figure 3.46c) and over 80% of the time at least one proton was in the solvent-separated ion pair position donating hydrogen bonds to three water molecules resembling an Eigen cation. This was also found for one proton ~60% of the time in 14N3 but the system contained several single water molecules connecting two triflic acid molecules and the other dissociated protons remained more tightly bound as contact ion pairs. No complete separation of the protons from the triflate oxygen atoms was observed in either of the fluorinated CNTs.

Finally, we examine potential interactions between the water molecules and solvated protons with the fluorine atoms. As with the study on confined water and water with an

Table 3.3. O–H···F hydrogen bond data for the fluorinated systems.

System	% Time O–H···F (CNT) Exists	Avg. O–H···F (CNT) Life (fs)	% Time O–H···F (Triflic) Exists	Avg. O–H···F (Triflic) Life (fs)
14F1	64.1	127.2	2.9	21.2
14F2	91.5	54.0	9.2	35.4
14F3	99.2	137.1	3.9	27.0
17F1	63.4	58.2	0.73	20.3
17F2	68.8	70.4	4.1	22.4
17F3	83.3	116.9	6.3	36.7

Table 3.4. O–H···F hydrogen bond data for the bare systems.

System	% Time O–H···F (Triflic) Exists	Avg. O–H···F (Triflic) Life (fs)
14N1	29.3	53.1
14N2	7.2	26.7
14N3	14.7	31.0
17N1	16.9	41.5
17N2	18.2	40.6
17N3	25.5	36.8

excess proton, these interactions are examined as weak hydrogen bonds with the same criteria (i.e., an H–O···F angle less than 30° and a H···F length less than 2.5 Å lasting at least 5 fs). It should be noted though that changing the hydrogen bond criteria did not significantly impact the results. In the bare CNTs, the only potential hydrogen bond accepting fluorine atoms come from the mobile CF_3SO_3H while in the fluorinated systems there are also the sites bound to the inner walls of the nanotube. No hydrogen bonding between a CF_3SO_3H sulfonic acid group and a fluorine atom was observed in any system, so the discussion is restricted to water molecules and solvated protons. The results for the fluorinated and bare systems are summarized in Tables 3.3 and 3.4, respectively, and Figure 3.48 shows the type of species involved in O–H···F hydrogen bonds.

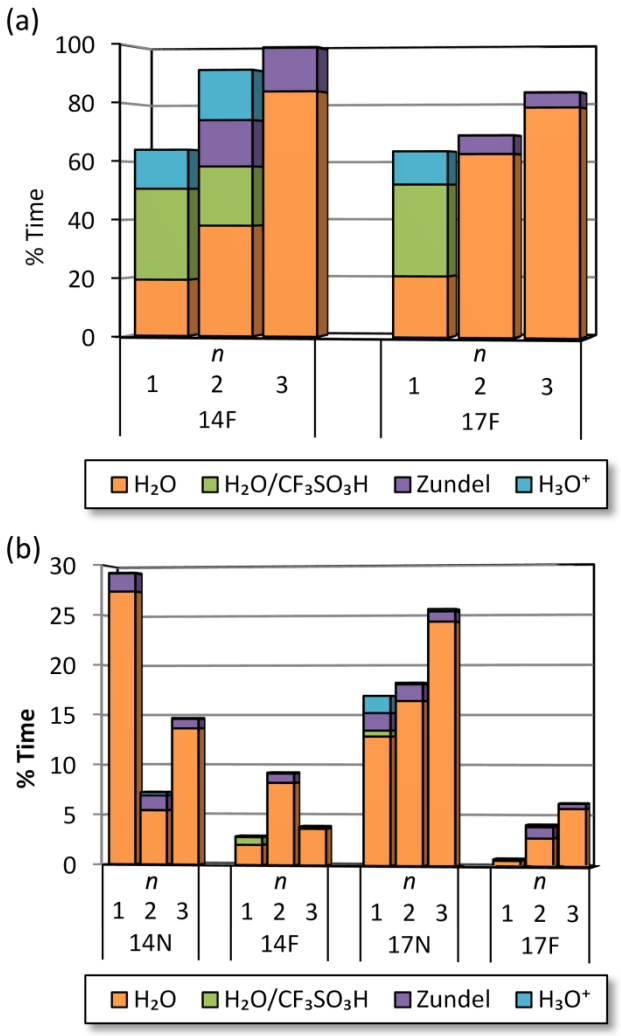

Figure 3.48. Percent time at least one OH···F hydrogen bond exists between the water molecules and/or solvated protons and (a) the fluorinated CNT walls and (b) the fluorine atoms of the mobile triflic acid molecules partitioned into the types of species involved.

The O–H···F hydrogen bonding between water molecules and the triflic acid CF_3 groups had short lifetimes and were typically not found for multiple water molecules at any given time. In the fluorinated CNTs, these interactions were relatively rare with the most observed in 14F2 which occurred 9.2% of the time. This is likely due to the isolated water molecules and the orientation of one of the triflic acid groups (Figure 3.37b) leading to a lack of other available hydrogen bond acceptor sites. There was generally a greater

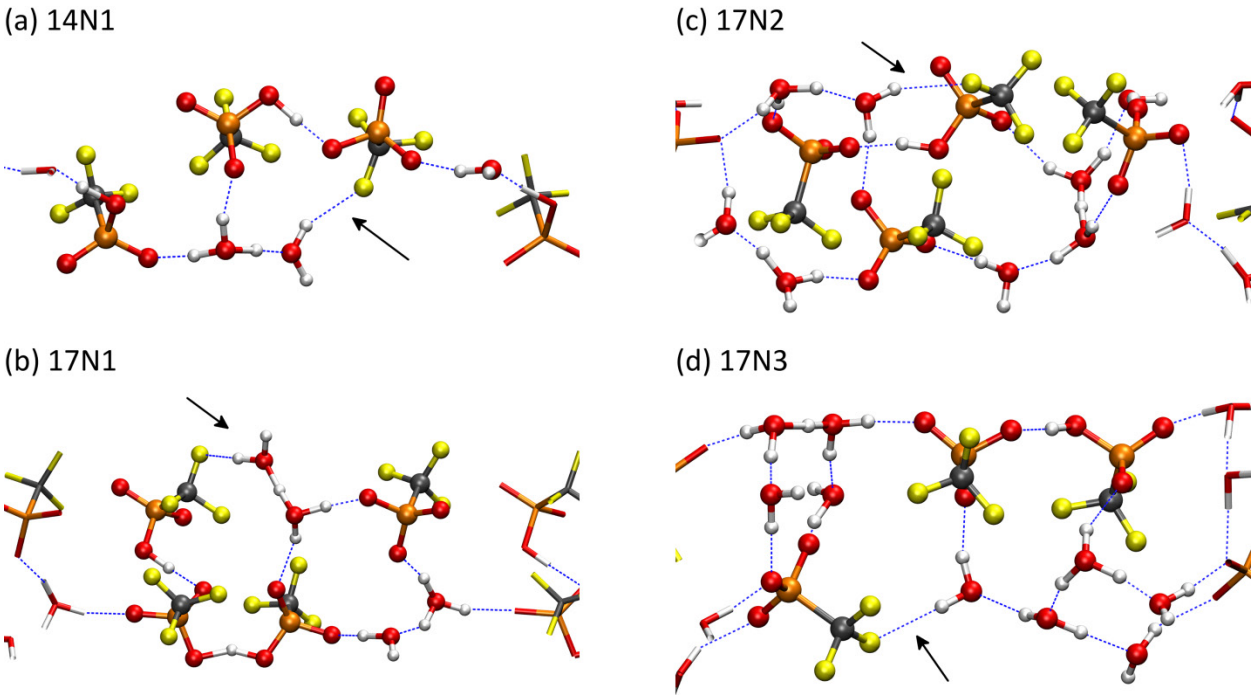

Figure 3.49. Snapshots of the bare CNT systems that contained OH···F hydrogen bond between water molecules and a fluorine atom of triflic acid over 15% of the time: (a) 14N1, (b) 17N1, (c) 17N2, and (d) 17N3.

propensity for O–H···F hydrogen bonding to the CF_3 groups in the bare CNT systems. No clear trend between the frequency of these interactions and the hydration level was found in the smaller bare tube, while in the larger system the amount of time they existed increased with hydration. One common feature observed is that all bare CNT systems that exhibited these interactions more than 15% of the time contained a direct hydrogen bond between sulfonic acid groups which blocked available oxygen atoms to accept hydrogen bonds (Figure 3.49). The percentage of time these O–H···F hydrogen bonds were observed in all systems is considerably higher than what was observed in our previous studies involving the CF_2 groups of CNTs functionalized with $–CF_2SO_3H$ groups[86, 87, 137] suggesting that the additional mobility of the triflic acid groups in the present study has an influence on these interactions.

Interactions between water and the fluorine atoms of the CNT wall were much more common than the fluorine atoms of triflic acid in all of the fluorinated systems, and the

percent of the time at least one such O–H···F hydrogen bond existed increased as the hydration level increased with greater frequency in the smaller CNT. Representative snapshots at all hydration levels of these interactions are shown in Figure 3.50. At n = 1, these were observed slightly over 60% of the time in each system with the majority of the interactions expectedly coming from water molecules in the H_2O/CF_3SO_3H shared state as this state was the most prevalent at this hydration level. The previously discussed hydrogen bond topography and isolation between water molecules at this low level of hydration generally leaves multiple OH bonds not involved in a hydrogen bond with a triflic acid $–SO_3H$ group (or other water molecules) leaving them open to interact with the fluorinated walls. The average H···F and O···F distances were approximately 2.24 and 3.13 Å in each case (which was approximately the same at all hydration levels) but the average lifetimes were found to be over twice as long in the smaller CNT. Nearly all occurrences of proton dissociation as a hydronium ion in 14F1 and the majority of those in 17F1 were accompanied by an O–H···F hydrogen bond indicating the fluorine atoms might provide a means to stabilize the excess charge. As the hydration level increases, the impact of the confinement dimensions on these interactions becomes more pronounced with at least one O–H···F bond occurring 91.5 and 99.1% of the time in the smaller CNT at n = 2 and 3, respectively, compared to 68.8 and 83.3% in the larger diameter tube. The majority of the observed Zundel states and over 60% of the H_3O^+ states in 14F2 were involved in hydrogen bond interactions with the fluorinated walls which is again likely due to the absence of neighboring stabilizing hydrogen bond acceptor sites from other water molecules or triflic acid molecules. In 17F2, however, most of these interactions involved water molecules as the protonated cations, particularly H_3O^+, were typically found to hydrogen bond with other surrounding water molecules or triflic acid molecules as indicated by the higher average total CN than 14F2 (Figure 3.35b). This was observed in both systems at n = 3 where more available hydrogen bond acceptor sites from water molecules promoted interactions that delocalized the excess charge over strong hydrogen bonds with neighboring water molecules or triflate anions.

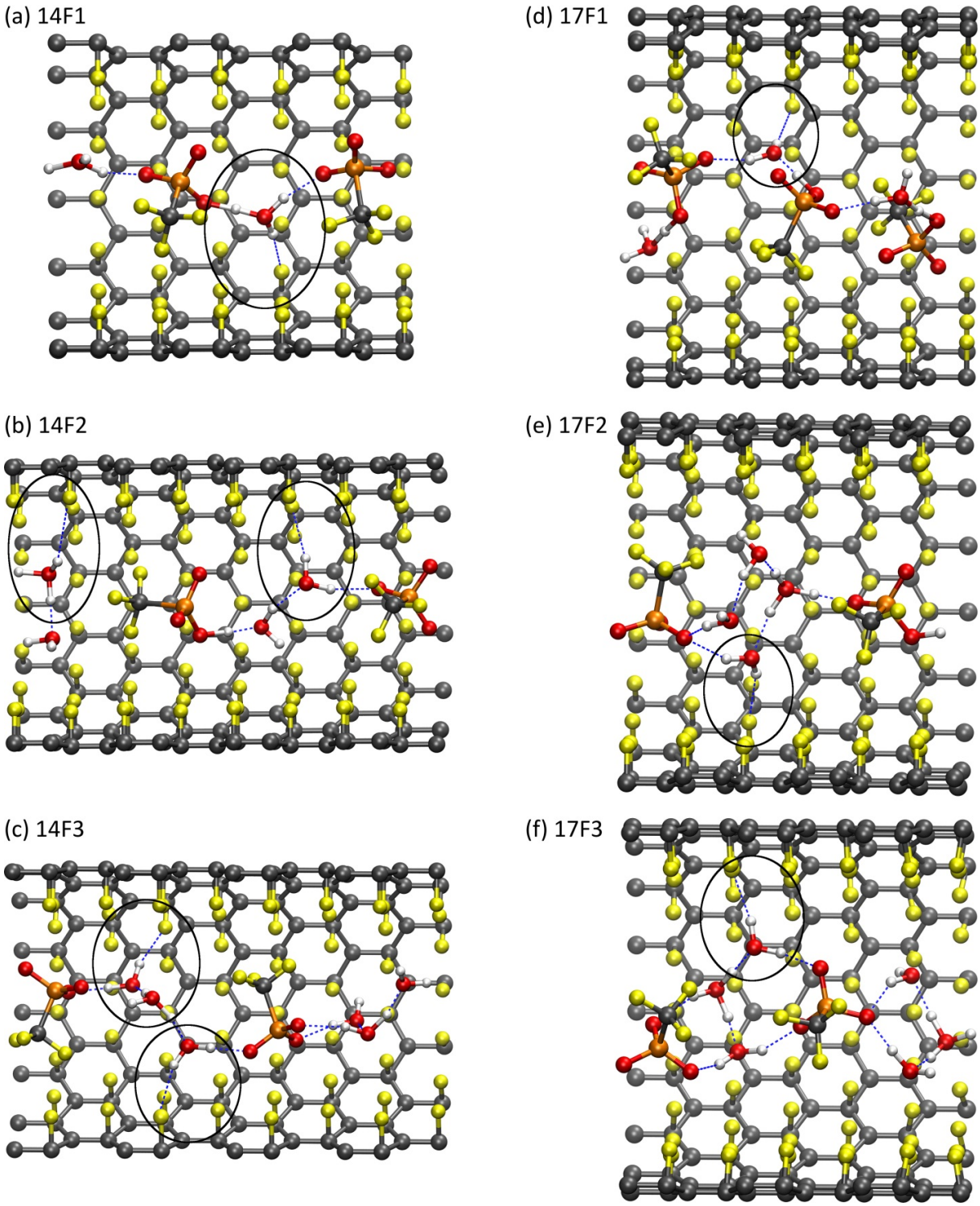

Figure 3.50. Snapshots of hydrogen bonding to the fluorinated wall: (a) 14F1, (b) 14F2, and (c) 14F3, (d) 17F1, (e) 17F2, and (f) 17F3.

***Summary*.** Single-walled CNTs of various diameter with different surface hydrophobicity were used as encapsulation vessels for mobile triflic acid molecules at hydration levels of n = 1 – 3 H_2O/CF_3SO_3H to investigate proton dissociation and transfer at low water content in a confined environment. Each of the different systems exhibited distinctly different hydrogen bonding between water and triflic acid molecules. At the lowest hydration level, the water molecules in the fluorinated CNTs were completely isolated from one another typically forming two hydrogen bonds with neighboring CF_3SO_3H. This led to a propensity for the acidic protons to be shared between water and triflic acid molecules with dissociation occurring less than 20% of the time as a hydronium ion where, in each case, interactions with the fluorinated CNT walls appear to stabilize the hydrogen bond network. Direct hydrogen bonding between triflic acid molecules in the bare CNTs at n = 1 promoted interactions between water molecules and enhanced proton dissociation. Triflic acid hydrogen bond connectivity, both directly and through a single water molecule, had a continued effect on proton dissociation at higher hydration levels. This was most pronounced in 14N2 which had several single water molecules/solvated protons bridging two CF_3SO_3H through hydrogen bonds and exhibited the highest proton dissociation at this hydration level. However, this also led to multiple protons being trapped between triflate anions with less interaction between water molecules that promotes separation of the dissociated protons from the acid necessary for long-range proton transport. The greatest separation of dissociated protons was found in 17N3 but at the cost of a lower overall degree of dissociation due to direct hydrogen bonding between triflic acid/triflate molecules. This also led to strong interactions between water molecules which were able to form long chains that encompassed nearly all the water molecules in the system. These direct hydrogen bonds between CF_3SO_3H were observed at all hydration levels in the larger bare CNT, which led to the highest observed CNs between water molecules at each hydration level, and may be due to the additional free volume allowing for more orientational freedom for the mobile triflic acid to form strong hydrogen bonds with a sulfonate groups upon dissociation to stabilize the charge. Weak hydrogen bonding between the water molecules and CF_3 groups was observed in all systems when open

oxygen sites were not in the vicinity. This was particularly observed in the bare CNT systems that contained direct hydrogen bonds between CF_3SO_3H which reduced the number of available hydrogen bond acceptor sites, and the short-lived OH···F interactions appeared to provide some stabilization to the hydrogen bond network. Hydrogen bonding to the fluorinated walls (when present) occurred much more frequently than to the triflic acid fluorine atoms. In both systems, the frequency of these interactions were found to increase with increasing hydration and to a greater extent in the smaller fluorinated CNT indicating an influence of the confinement dimensions. Unlike our previous work,[86, 87, 137] the fluorine atoms did not appear to promote any particular state of the dissociated protons over those observed in the bare CNTs, aside from those at $n = 1$ where the isolated water molecules could not form Zundel cations. However, at $n = 3$, each of the bare CNT systems contained protons in the solvent-separated ion pair position surrounded by three water molecules as an Eigen cation. This was not observed in the fluorinated tubes due to the clustering of water molecules and the lack of mobility induced by the confinement dimensions and potential stabilization from the large number of OH···F interactions resulting in a fairly regular structure. It should be noted that the studies on hydrates of triflic acid[84, 85] revealed that inclusion of quantum nuclear effects through *ab initio* path integral techniques enhances the Zundel character. As these effects are absent in the present simulations, and the systems used are highly simplified models, the results presented here should not be taken as absolute values but as a relative comparison of how the confinement dimensions and surface hydrophobicity affect hydrogen bonding and proton dissociation.

Chapter 4 Conclusions

Proton exchange membrane fuel cells (PEMFCs) are clean, efficient energy conversion devices that offer potential use for stationary, portable, and automotive power. At the heart of PEMFCs is the proton-conducting polymer electrolyte, or proton exchange, membrane (PEM). A molecular-level understanding of the features and mechanisms of proton dissociation and transfer in proton exchange membranes will aid in the development of superior membrane materials. As with all solid state proton conductors, the transport of protons in PEMs relies heavily on the structural and dynamical properties of the hydrogen bond network. An understanding of this requires insight into the formation and breaking of both covalent and hydrogen bonds within highly complex systems. These features are currently unable to be probed experimentally at the resolution required to ascertain fully the fundamental details governing the process. Thus, molecular modeling and simulation techniques are widely used to investigate the characteristic features of transport properties in PEMs. The body of work encompassed in this dissertation focused on probing several potential contributing factors to proton dissociation and transfer in PEMs at low hydration levels via *ab initio* molecular modeling techniques.

Electronic structure calculations were used to investigate the impact the chemical nature of the membrane material has on several properties. Calculations on ionomer fragments of available membrane materials demonstrated that the dissociation and transfer of protons depends not only on the degree of hydration but also the nature of the inter- and intra-side chain acid group interactions. Results for the 3M PFSA membrane containing two pendant sulfonic acid side chains separated by different numbers of CF_2 backbone units (thus modeling different equivalent weight ionomers) indicated that hydrogen bond connectivity of the acidic groups both directly and through a single water molecule enhanced proton dissociation at very low levels of hydration. These interactions were pronounced when less separation between side chains allowed for facile aggregation of the SO_3H groups. Increasing the number of CF_2 backbone units between side chains precluded these cooperative interactions which hindered proton dissociation at low hydration. The

observed differences in proton dissociation between the different EW fragments were mitigated upon increasing hydration. Proton transfer was found to be highly dependent on the underlying hydrogen bond structure. Reprotonation of the sulfonate groups after (partial or complete) dissociation at sufficient hydration levels ($\lambda \geq 2$) was strongly resisted. This was more pronounced in the model system with less side chain separation as the preferential optimized geometry exhibited complete dissociation. However, irrespective of the separation between side chains, adopted configurations that readily allowed for structural reorganization of the hydrogen bond network led to considerably lower energetic penalties for proton transfer between both neighboring water molecules and sulfonic acid groups.

This was also observed in the calculations of the multi-acid side chain ionomers. Of the two structural isomers differing only by the location of a sulfonic acid group on an aromatic ring, the *ortho* positioned sulfonic acid group (relative to the sulfonyl imide group) exhibited proton dissociation at lower hydration than the *meta* positioned group. This was a result of direct hydrogen bonding between protogenic groups in the *ortho* fragment providing additional charge stabilization that facilitated proton dissociation. In a similar manner, the perfluorinated MASC (PFIA) also allowed for first proton dissociation at low hydration due to delocalization of charge by the electron withdrawing $-CF_2-$ groups in the side chain. However, the strong intramolecular hydrogen bond in the *ortho* bis acid blocked hydrogen bond acceptor sites and promoted interactions between water molecules which hindered dissociation of the second proton. The hydrogen bond network in the other MASC fragments led to a more uniform distribution of charge that more readily allowed for complete dissociation. The uniform charge distribution also impacted the energetics of proton transfer where the hydrogen bonding between acid groups and water molecules in *meta* and PFIA ionomers allowed for facile charge transfer. This was more pronounced in the PFIA fragment which is likely due to the absence of the aromatic ring in the side chain that reduced the conformational freedom in the other ionomers.

In hydrated PEMs, the water molecules, protons, and acidic groups are confined within

domains only a few nanometers in diameter. Probing the impact of this confinement is difficult due to an incomplete molecular-level understanding of the hydrated morphology and simplified models are frequently used. We carried out a series of AIMD simulations using fluorinated and nonfluorinated single-walled CNTs of various diameters as encapsulation vessels for water molecules, slightly acidic water, and triflic acid molecules. The first study focused on the structural and dynamical properties of water and an excess proton in water under confinement. The relative degree of order/disorder of the water structure was found to depend on the confinement dimensions and the hydrophobicity of the confining surface. Specifically, the water molecules in the fluorinated CNTs were found to localize preferentially near the CNT surface and exhibit well-defined regular ordering while those in the bare CNTs were more randomly distributed. The fluorine atoms of the nanotube wall provided sites to which the water molecules could interact via hydrogen bond-like interactions which occurred at a greater frequency in smaller diameter CNTs suggesting an influence of the confinement dimensions. Addition of an excess proton nearly doubled the number of water molecules involved in these interactions throughout the simulation. The hydrogen bond structure in the smaller fluorinated system with an excess proton was highly ordered and contained regular orientational defects that hindered proton transfer. In the larger fluorinated CNT, on the other hand, addition of a proton disrupted the regular structure which allowed for proton transfer down the nanotube channel near the surface. Proton transfer through the channel was also observed in the smaller nonfluorinated system, however, the proton was located closer to the center of the CNT, while in the larger nonfluorinated CNT proton transfer exhibited less directional preference indicating an impact of the scale of confinement and nature of the surface on proton transfer.

The study that followed this explored proton dissociation and transfer of aqueous triflic acid confined within the same nanotube systems at water contents of 1 – 3 H_2O/CF_3SO_3H. Again, fluorine atoms participated in weak hydrogen bond-like interactions with water molecules. Here, however, these could involve covalently bound fluorine atoms to the interior nanotube walls or fluorine atoms of the CF_3 group of the triflic acid molecules. In

all cases, the interactions appeared to provide a means to stabilize the hydrogen bond network when no other available hydrogen bond acceptor sites were in the near vicinity. In the fluorinated systems, the overwhelming majority of these involved the fluorinated CNT wall which were found more frequently as the water content was increased. As with the systems containing only water molecules, this was more pronounced in the smaller diameter CNT further suggesting an impact of the confinement dimensions. Proton dissociation expectedly increased with increasing water content. Cooperative interactions through direct hydrogen bonds between adjacent triflic acid molecules or connectivity via a hydrogen bond bridge through a single water molecule also played a role on proton dissociation. At the lowest water content, direct hydrogen bonds between triflic acid molecules were observed in the bare systems which promoted interactions between water molecules enhancing proton dissociation. These were found in the larger bare CNT at all water contents which allowed for greater separation of the protons from the triflate group upon dissociation than was found for the other systems. However, this also effectively reduced the overall proportion of dissociated protons as at least one proton was always bound or shared between the acid molecules even at the highest water content while complete dissociation occurred in the other systems at 3 H_2O/CF_3SO_3H.

In summary, the results obtained here from both static calculations and dynamic simulations provide additional insight into the fundamental role hydrogen bonding plays on proton transfer properties in water and PEMs. The structure and dynamics of hydrogen bond networks were influenced by several factors in these studies including both inter- and intra- side chain protogenic group separation, the specific side chain chemistry, nanoscale confinement dimensions, and the nature of the confining surface. This information adds to the overall understanding of proton dissociation and transfer in PEMs and confined fluids and provides a framework for potential future directions.

References

1. B. Smitha, S. Sridhar and A. A. Khan, Solid polymer electrolyte membranes for fuel cell applications - a review, *Journal of Membrane Science*, 2005, **259**, 10-26.
2. A. B. Stambouli and E. Traversa, Fuel cells, an alternative to standard sources of energy, *Renewable & Sustainable Energy Reviews*, 2002, **6**, 295-304.
3. M. Granovskii, I. Dincer and M. A. Rosen, Life cycle assessment of hydrogen fuel cell and gasoline vehicles, *International Journal of Hydrogen Energy*, 2006, **31**, 337-352.
4. K. D. Kreuer, S. J. Paddison, E. Spohr and M. Schuster, Transport in proton conductors for fuel-cell applications: Simulations, elementary reactions, and phenomenology, *Chemical Reviews*, 2004, **104**, 4637-4678.
5. IEA, *Hydrogen and Fuel Cells: Review of National R&D Programs*, OECD Publishing, Paris, 2004.
6. O. Savadogo, Emerging membranes for electrochemical systems - Part II. High temperature composite membranes for polymer electrolyte fuel cell (PEFC) applications, *Journal of Power Sources*, 2004, **127**, 135-161.
7. M. A. Hickner, H. Ghassemi, Y. S. Kim, B. R. Einsla and J. E. McGrath, Alternative polymer systems for proton exchange membranes (PEMs), *Chemical Reviews*, 2004, **104**, 4587-4611.
8. Y. Y. Shao, G. P. Yin, Z. B. Wang and Y. Z. Gao, Proton exchange membrane fuel cell from low temperature to high temperature: Material challenges, *Journal of Power Sources*, 2007, **167**, 235-242.
9. S. M. Haile, Fuel cell materials and components, *Acta Materialia*, 2003, **51**, 5981-6000.
10. K. D. Kreuer, On solids with liquidlike properties and the challenge to develop new proton-conducting separator materials for intermediate-temperature fuel cells, *ChemPhysChem*, 2002, **3**, 771-775.
11. J. A. Kerres, Development of ionomer membranes for fuel cells, *Journal of Membrane Science*, 2001, **185**, 3-27.
12. F. Wang, M. Hickner, Y. S. Kim, T. A. Zawodzinski and J. E. McGrath, Direct polymerization of sulfonated poly(arylene ether sulfone) random (statistical)

copolymers: candidates for new proton exchange membranes, *Journal of Membrane Science*, 2002, **197**, 231-242.

13. J. L. Zhang, Z. Xie, J. J. Zhang, Y. H. Tanga, C. J. Song, T. Navessin, Z. Q. Shi, D. T. Song, H. J. Wang, D. P. Wilkinson, et al., High temperature PEM fuel cells, *Journal of Power Sources*, 2006, **160**, 872-891.
14. S. J. Hamrock and M. A. Yandrasits, Proton exchange membranes for fuel cell applications, *Polymer Reviews*, 2006, **46**, 219-244.
15. S. Matsumura, A. R. Hlil, C. Lepiller, J. Gaudet, D. Guay, Z. Q. Shi, S. Holdcroft and A. S. Hay, Ionomers for proton exchange membrane fuel cells with sulfonic acid groups on the end groups: Novel branched poly(ether-ketone)s, *Macromolecules*, 2008, **41**, 281-284.
16. *U.S. Pat.,* U.S. Patent 4,358,412, 1982.
17. M. Schaberg, J. Abulu, G. Haugen, M. Emery, S. O'Conner, P. Xiong and S. Hamrock, New multi acid side-chain ionomers for proton exchange membrane fuel cells, *ECS Transactions*, 2010, **33**, 627-633.
18. K. D. Kreuer, M. Schuster, B. Obliers, O. Diat, U. Traub, A. Fuchs, U. Klock, S. J. Paddison and J. Maier, Short-side-chain proton conducting perfluorosulfonic acid ionomers: Why they perform better in PEM fuel cells, *Journal of Power Sources*, 2008, **178**, 499-509.
19. T. A. Zawodzinski, T. E. Springer, J. Davey, R. Jestel, C. Lopez, J. Valerio and S. Gottesfeld, A comparative study of water uptake by and transport through ionomeric fuel cell membranes, *Journal of the Electrochemical Society*, 1993, **140**, 1981-1985.
20. C. A. Edmondson, P. E. Stallworth, M. E. Chapman, J. J. Fontanella, M. C. Wintersgill, S. H. Chung and S. G. Greenbaum, Complex impedance studies of proton-conducting membranes, *Solid State Ionics*, 2000, **135**, 419-423.
21. C. A. Edmondson and J. J. Fontanella, Free volume and percolation in S-SEBS and fluorocarbon proton conducting membranes, *Solid State Ionics*, 2002, **152**, 355-361.

22. L. M. Rivard, D. Pierpont, H. T. Freemeyer, A. Thaler and S. Hamrock, presented in part at the Fuel Cell seminar, Miami Beach, FL., 2003.
23. M. Emery, M. Frey, M. Guerra, G. Haugen, K. Hintzer, K. H. Lochhaas, P. Pham, D. Pierpont, M. Schaberg, A. Thaler, et al., The development of new membranes for proton exchange membrane fuel cells, *ECS Transactions*, 2007, **11**, 3-14.
24. J. J. Sumner, S. E. Creager, J. J. Ma and D. D. DesMarteau, Proton conductivity in Nafion® 117 and in a novel bis[(perfluoroalkyl)sulfonyl]imide ionomer membrane, *Journal of the Electrochemical Society*, 1998, **145**, 107-110.
25. I. A. Koppel, R. W. Taft, F. Anvia, S. Z. Zhu, L. Q. Hu, K. S. Sung, D. D. Desmarteau, L. M. Yagupolskii, Y. L. Yagupolskii, N. V. Ignatev, et al., The gas-phase acidities of very strong neutral Brønsted acids, *Journal of the American Chemical Society*, 1994, **116**, 3047-3057.
26. S. E. Creager, J. J. Sumner, R. D. Bailey, J. J. Ma, W. T. Pennington and D. D. DesMarteau, Equivalent weight and crystallinity effects on water content and proton conductivity in bis[(perfluoroalkyl)sulfonyl]imide-based ionomers, *Electrochemical and Solid-State Letters*, 1999, **2**, 434-436.
27. S. J. Peighambardoust, S. Rowshanzamir and M. Amjadi, Review of the proton exchange membranes for fuel cell applications, *International Journal of Hydrogen Energy*, 2010, **35**, 9349-9384.
28. P. Costamagna and S. Srinivasan, Quantum jumps in the PEMFC science and technology from the 1960s to the year 2000 Part I. Fundamental scientific aspects, *Journal of Power Sources*, 2001, **102**, 242-252.
29. K. D. Kreuer, On the development of proton conducting materials for technological applications, *Solid State Ionics*, 1997, **97**, 1-15.
30. K. D. Kreuer, On the development of proton conducting polymer membranes for hydrogen and methanol fuel cells, *Journal of Membrane Science*, 2001, **185**, 29-39.
31. Q. W. Tang, G. Q. Qian and K. Huang, Hydrophobic hydrogel caged H3PO4 as a new class of high-temperature proton exchange membranes with enhanced acid retention, *RSC Advances*, 2013, **3**, 3520-3525.

32. J. A. Asensio, E. M. Sanchez and P. Gomez-Romero, Proton-conducting membranes based on benzimidazole polymers for high-temperature PEM fuel cells. A chemical quest, *Chemical Society Reviews*, 2010, **39**, 3210-3239.
33. K. D. Kreuer, A. Fuchs, M. Ise, M. Spaeth and J. Maier, Imidazole and pyrazole-based proton conducting polymers and liquids, *Electrochimica Acta*, 1998, **43**, 1281-1288.
34. K. D. Kreuer, Proton conductivity: Materials and applications, *Chemistry of Materials*, 1996, **8**, 610-641.
35. D. Marx, Proton transfer 200 years after von Grotthuss: Insights from ab initio simulations, *ChemPhysChem*, 2006, **7**, 1848-1870.
36. T. E. DeCoursey, Voltage-gated proton channels and other proton transfer pathways, *Physiological Reviews*, 2003, **83**, 475-579.
37. N. Agmon, The Grotthuss Mechanism, *Chemical Physics Letters*, 1995, **244**, 456-462.
38. M. E. Tuckerman, K. Laasonen, M. Sprik and M. Parrinello, *Ab initio* molecular dynamics simulation of the solvation and transport of hydronium and hydroxyl ions in water, *Journal of Chemical Physics*, 1995, **103**, 150-161.
39. M. E. Tuckerman, D. Marx, M. L. Klein and M. Parrinello, On the quantum nature of the shared proton in hydrogen bonds, *Science*, 1997, **275**, 817-820.
40. D. Marx, M. E. Tuckerman, J. Hutter and M. Parrinello, The nature of the hydrated excess proton in water, *Nature*, 1999, **397**, 601-604.
41. H. Lapid, N. Agmon, M. K. Petersen and G. A. Voth, A bond-order analysis of the mechanism for hydrated proton mobility in liquid water, *Journal of Chemical Physics*, 2005, **122**, 014506.
42. T. C. Berkelbach, H. S. Lee and M. E. Tuckerman, Concerted hydrogen-bond dynamics in the transport mechanism of the hydrated proton: A first-principles molecular dynamics study, *Physical Review Letters*, 2009, **103**, 238302.
43. C. J. D. von Grotthuss, Sur la décomposition de l'eau et des corps qu'elle tient en dissolution à l'aide de l'électricité galvanique, *Annali di Chimica*, 1806, **58**, 54-74.
44. M. Eigen and L. Demaeyer, Self-dissociation and protonic charge transport in water and ice, *Proceedings of the Royal Society of London Series A*, 1958, **247**, 505-533.

45. M. Eigen, Protonenubertragung, saure-base-katalyse und enzymatische hydrolyse .1. Elementarvorgange, *Angewandte Chemie-International Edition*, 1963, **75**, 489-508.
46. G. Zundel, Hydrogen bonds with large proton polarizability and proton transfer processes in electrochemistry and biology, *Advances in Chemical Physics*, 2000, **111**, 1-217.
47. M. E. Tuckerman, D. Marx and M. Parrinello, The nature and transport mechanism of hydrated hydroxide ions in aqueous solution, *Nature*, 2002, **417**, 925-929.
48. D. Marx, A. Chandra and M. E. Tuckerman, Aqueous basic solutions: hydroxide solvation, structural diffusion, and comparison to the hydrated proton, *Chemical Reviews*, 2010, **110**, 2174-2216.
49. M. E. Tuckerman, K. Laasonen, M. Sprik and M. Parrinello, *Ab initio* molecular dynamics simulation of the solvation and transport of H_3O^+ and OH^- ions in water, *Journal of Physical Chemistry*, 1995, **99**, 5749-5752.
50. A. Chandra, M. E. Tuckerman and D. Marx, Connecting solvation shell structure to proton transport kinetics in hydrogen-bonded networks via population correlation functions, *Physical Review Letters*, 2007, **99**.
51. L. Rubatat, A. L. Rollet, G. Gebel and O. Diat, Evidence of elongated polymeric aggregates in Nafion, *Macromolecules*, 2002, **35**, 4050-4055.
52. S. J. Paddison, Proton conduction mechanisms at low degrees of hydration in sulfonic acid-based polymer electrolyte membranes, *Annual Review of Materials Research*, 2003, **33**, 289-319.
53. M. Eikerling, A. A. Kornyshev, A. M. Kuznetsov, J. Ulstrup and S. Walbran, Mechanisms of proton conductance in polymer electrolyte membranes, *Journal of Physical Chemistry B*, 2001, **105**, 3646-3662.
54. S. J. Paddison and R. Paul, The nature of proton transport in fully hydrated Nafion®, *Physical Chemistry Chemical Physics*, 2002, **4**, 1158-1163.
55. S. J. Paddison, R. Paul and K. D. Kreuer, Theoretically computed proton diffusion coefficients in hydrated PEEKK membranes, *Physical Chemistry Chemical Physics*, 2002, **4**, 1151-1157.

56. E. Spohr, P. Commer and A. A. Kornyshev, Enhancing proton mobility in polymer electrolyte membranes: Lessons from molecular dynamics simulations, *Journal of Physical Chemistry B*, 2002, **106**, 10560-10569.

57. S. J. Paddison, L. R. Pratt, T. Zawodzinski and D. W. Reagor, Molecular modeling of trifluoromethanesulfonic acid for solvation theory, *Fluid Phase Equilibrium*, 1998, **151**, 235-243.

58. S. J. Paddison and T. A. Zawodzinski Jr, Molecular modeling of the pendant chain in Nafion®, *Solid State Ionics*, 1998, **113-115**, 333-340.

59. S. J. Paddison, The modeling of molecular structure and ion transport in sulfonic acid based ionomer membranes, *Journal of New Materials for Electrochemical Systems*, 2001, **4**, 197-207.

60. V. A. Glezakou, M. Dupuis and C. J. Mundy, Acid/base equilibria in clusters and their role in proton exchange membranes: computational insight, *Physical Chemistry Chemical Physics*, 2007, **9**, 5752-5760.

61. K. Sagarik, M. Phonyiem, C. Lao-Ngam and S. Chaiwongwattana, Mechanisms of proton transfer in Nafion®: elementary reactions at the sulfonic acid groups, *Physical Chemistry Chemical Physics*, 2008, **10**, 2098-2112.

62. M. Phonyiem, S. Chaiwongwattana, C. Lao-ngam and K. Sagarik, Proton transfer reactions and dynamics of sulfonic acid group in Nafion®, *Physical Chemistry Chemical Physics*, 2011, **13**, 10923-10939.

63. C. Wang, J. K. Clark, M. Kumar and S. J. Paddison, An *ab initio* study of the primary hydration and proton transfer of CF_3SO_3H and $CF_3O(CF_2)_2SO_3H$: Effects of the hybrid functional and inclusion of diffuse functions, *Solid State Ionics*, 2011, **199**, 6-13.

64. M. Eikerling, S. J. Paddison and T. A. Zawodzinski, Molecular orbital calculations of proton dissociation and hydration of various acidic moieties for fuel cell polymers, *Journal of New Materials for Electrochemical Systems*, 2002, **5**, 15-23.

65. S. J. Paddison, K. D. Kreuer and J. Maier, About the choice of the protogenic group in polymer electrolyte membranes: *Ab initio* modelling of sulfonic acid, phosphonic

acid, and imidazole functionalized alkanes, *Physical Chemistry Chemical Physics*, 2006, **8**, 4530-4542.

66. C. Wang and S. J. Paddison, Proton transfer in functionalized phosphonic acid molecules, *Physical Chemistry Chemical Physics*, 2010, **12**, 970-981.
67. L. Vilciauskas, S. J. Paddison and K. D. Kreuer, Ab initio modeling of proton transfer in phosphoric acid clusters, *Journal of Physical Chemistry A*, 2009, **113**, 9193-9201.
68. S. Urata, J. Irisawa, A. Takada, S. Tsuzuki, W. Shinoda and M. Mikami, Intermolecular interaction between the pendant chain of perfluorinated ionomer and water, *Physical Chemistry Chemical Physics*, 2004, **6**, 3325-3332.
69. S. J. Paddison and J. A. Elliott, Molecular modeling of the short-side-chain perfluorosulfonic acid membrane, *Journal of Physical Chemistry A*, 2005, **109**, 7583-7593.
70. S. J. Paddison and J. A. Elliott, The effects of backbone conformation on hydration and proton transfer in the 'short-side-chain' perfluorosulfonic acid membrane, *Solid State Ionics*, 2006, **177**, 2385-2390.
71. S. J. Paddison and J. A. Elliott, On the consequences of side chain flexibility and backbone conformation on hydration and proton dissociation in perfluorosulfonic acid membranes, *Physical Chemistry Chemical Physics*, 2006, **8**, 2193-2203.
72. S. J. Paddison and J. A. Elliott, Selective hydration of the 'short-side-chain' perfluorosulfonic acid membrane. An ONIOM study, *Solid State Ionics*, 2007, **178**, 561-567.
73. J. K. Clark and S. J. Paddison, The effect of side chain connectivity and local hydration on proton transfer in 3M perfluorosulfonic acid membranes, *Solid State Ionics*, 2012, **213**, 83-91.
74. J. K. Clark II, S. J. Paddison and S. J. Hamrock, The effect of hydrogen bond reorganization and equivalent weight on proton transfer in 3M perfluorosulfonic acid ionomers, *Physical Chemistry Chemical Physics*, 2012, **14**, 16349-16359.

75. T. J. F. Day, A. V. Soudackov, M. Cuma, U. W. Schmitt and G. A. Voth, A second generation multistate empirical valence bond model for proton transport in aqueous systems, *Journal of Chemical Physics*, 2002, **117**, 5839-5849.

76. F. Wang and G. A. Voth, A linear-scaling self-consistent generalization of the multistate empirical valence bond method for multiple excess protons in aqueous systems, *Journal of Chemical Physics*, 2005, **122**, 144105.

77. Y. J. Wu, H. N. Chen, F. Wang, F. Paesani and G. A. Voth, An improved multistate empirical valence bond model for aqueous proton solvation and transport, *Journal of Physical Chemistry B*, 2008, **112**, 467-482.

78. M. K. Petersen, F. Wang, N. P. Blake, H. Metiu and G. A. Voth, Excess proton solvation and delocalization in a hydrophilic pocket of the proton conducting polymer membrane Nafion, *Journal of Physical Chemistry B*, 2005, **109**, 3727-3730.

79. M. K. Petersen and G. A. Voth, Characterization of the solvation and transport of the hydrated proton in the perfluorosulfonic acid membrane Nafion, *Journal of Physical Chemistry B*, 2006, **110**, 18594-18600.

80. M. K. Petersen, A. J. Hatt and G. A. Voth, Orientational dynamics of water in the Nafion polymer electrolyte membrane and its relationship to proton transport, *Journal of Physical Chemistry B*, 2008, **112**, 7754-7761.

81. S. Feng and G. A. Voth, Proton solvation and transport in hydrated Nafion, *Journal of Physical Chemistry B*, 2011, **115**, 5903-5912.

82. M. Eikerling, S. J. Paddison, L. R. Pratt and T. A. Zawodzinski, Defect structure for proton transport in a triflic acid monohydrate solid, *Chemical Physics Letters*, 2003, **368**, 108-114.

83. Y. K. Choe, E. Tsuchida, T. Ikeshoji, S. Yamakawa and S. Hyodo, Nature of proton dynamics in a polymer electrolyte membrane, Nafion: a first-principles molecular dynamics study, *Physical Chemistry Chemical Physics*, 2009, **11**, 3892-3899.

84. R. L. Hayes, S. J. Paddison and M. E. Tuckerman, Proton transport in triflic acid hydrates studied via path integral Car-Parrinello molecular dynamics, *Journal of Physical Chemistry B*, 2009, **113**, 16574-16589.

85. R. L. Hayes, S. J. Paddison and M. E. Tuckerman, Proton transport in triflic acid pentahydrate studied via ab initio path integral molecular dynamics, *Journal of Physical Chemistry A*, 2011, **115**, 6112-6124.

86. B. F. Habenicht, S. J. Paddison and M. E. Tuckerman, The effects of the hydrophobic environment on proton mobility in perfluorosulfonic acid systems: An *ab initio* molecular dynamics study, *Journal of Materials Chemistry*, 2010, **20**, 6342-6351.

87. B. F. Habenicht, S. J. Paddison and M. E. Tuckerman, *Ab initio* molecular dynamics simulations investigating proton transfer in perfluorosulfonic acid functionalized carbon nanotubes, *Physical Chemistry Chemical Physics*, 2010, **12**, 8728-8732.

88. Y. K. Choe, E. Tsuchida, T. Ikeshoji, S. Yamakawa and S. Hyodo, Nature of water transport and electro-osmosis in Nafion: Insights from first-principles molecular dynamics simulations under an electric field, *Journal of Physical Chemistry B*, 2008, **112**, 11586-11594.

89. W. Munch, K. D. Kreuer, W. Silvestri, J. Maier and G. Seifert, The diffusion mechanism of an excess proton in imidazole molecule chains: first results of an ab initio molecular dynamics study, *Solid State Ionics*, 2001, **145**, 437-443.

90. Y. K. Choe, E. Tsuchida, T. Ikeshoji, A. Ohira and K. Kidena, An *ab initio* modeling study on a modeled hydrated polymer electrolyte membrane, sulfonated polyethersulfone (SPES), *Journal of Physical Chemistry B*, 2010, **114**, 2411-2421.

91. R. Zangi, Water confined to a slab geometry: a review of recent computer simulation studies, *Journal of Physics-Condensed Matter*, 2004, **16**, S5371-S5388.

92. M. F. Chaplin, in *Adsorption and Phase Behaviour in Nanochannels and Nanotubes*, eds. L. J. Dunne and G. Manos, Springer Science, New York, 2010, pp. 241-255.

93. J. C. Rasaiah, S. Garde and G. Hummer, Water in nonpolar confinement: From nanotubes to proteins and beyond, *Annual Review of Physical Chemistry*, 2008, **59**, 713-740.

94. S. Vaitheeswaran, H. Yin, J. C. Rasaiah and G. Hummer, Water clusters in nonpolar cavities, *Proceedings of the National Academy of Sciences of the United States of America*, 2004, **101**, 17002-17005.

95. G. Cicero, J. C. Grossman, E. Schwegler, F. Gygi and G. Galli, Water confined in nanotubes and between graphene sheets: A first principle study, *Journal of the American Chemical Society*, 2008, **130**, 1871-1878.

96. D. Munoz-Santiburcio, C. Wittekindt and D. Marx, Nanoconfinement effects on hydrated excess protons in layered materials, *Nature Communications*, 2013, **4**, 2349.

97. A. L. Ferguson, N. Giovambattista, P. J. Rossky, A. Z. Panagiotopoulos and P. G. Debenedetti, A computational investigation of the phase behavior and capillary sublimation of water confined between nanoscale hydrophobic plates, *Journal of Chemical Physics*, 2012, **137**, 144501.

98. N. Giovambattista, P. J. Rossky and P. G. Debenedetti, Effect of temperature on the structure and phase behavior of water confined by hydrophobic, hydrophilic, and heterogeneous surfaces, *Journal of Physical Chemistry B*, 2009, **113**, 13723-13734.

99. S. R. V. Castrillon, N. Giovambattista, I. A. Aksay and P. G. Debenedetti, Evolution from surface-influenced to bulk-like dynamics in nanoscopically confined water, *Journal of Physical Chemistry B*, 2009, **113**, 7973-7976.

100. S. R. V. Castrillon, N. Giovambattista, I. A. Aksay and P. G. Debenedetti, Effect of surface polarity on the structure and dynamics of water in nanoscale confinement, *Journal of Physical Chemistry B*, 2009, **113**, 1438-1446.

101. J. Kofinger, G. Hummer and C. Dellago, Single-file water in nanopores, *Physical Chemistry Chemical Physics*, 2011, **13**, 15403-15417.

102. J. A. Thomas and A. J. H. McGaughey, Water flow in carbon nanotubes: Transition to subcontinuum transport, *Physical Review Letters*, 2009, **102**, 184502.

103. T. Nanok, N. Artrith, P. Pantu, P. A. Bopp and J. Limtrakul, Structure and dynamics of water confined in single-wall nanotubes, *Journal of Physical Chemistry A*, 2009, **113**, 2103-2108.

104. Y. C. Liu and Q. Wang, Transport behavior of water confined in carbon nanotubes, *Physical Review B*, 2005, **72**, 085420.

105. Y. C. Liu, Q. Wang, T. Wu and L. Zhang, Fluid structure and transport properties of water inside carbon nanotubes, *Journal of Chemical Physics*, 2005, **123**, 234701.
106. D. J. Mann and M. D. Halls, Water alignment and proton conduction inside carbon nanotubes, *Physical Review Letters*, 2003, **90**, 195503.
107. O. Byl, J. C. Liu, Y. Wang, W. L. Yim, J. K. Johnson and J. T. Yates, Unusual hydrogen bonding in water-filled carbon nanotubes, *Journal of the American Chemical Society*, 2006, **128**, 12090-12097.
108. G. Hummer, J. C. Rasaiah and J. P. Noworyta, Water conduction through the hydrophobic channel of a carbon nanotube, *Nature*, 2001, **414**, 188-190.
109. M. Whitby and N. Quirke, Fluid flow in carbon nanotubes and nanopipes, *Nature Nanotechnology*, 2007, **2**, 87-94.
110. Z. Cao, Y. X. Peng, T. Y. Yan, S. Li, A. L. Li and G. A. Voth, Mechanism of fast proton transport along one-dimensional water chains confined in carbon nanotubes, *Journal of the American Chemical Society*, 2010, **132**, 11395-11397.
111. G. Perez-Hernandez and B. Schmidt, Anisotropy of the water-carbon interaction: molecular simulations of water in low-diameter carbon nanotubes, *Physical Chemistry Chemical Physics*, 2013, **15**, 4995-5006.
112. D. Takaiwa, I. Hatano, K. Koga and H. Tanaka, Phase diagram of water in carbon nanotubes, *Proceedings of the National Academy of Sciences of the United States of America*, 2008, **105**, 39-43.
113. J. Shiomi, T. Kimura and S. Maruyama, Molecular dynamics of ice-nanotube formation inside carbon nanotubes, *Journal of Physical Chemistry C*, 2007, **111**, 12188-12193.
114. H. Kyakuno, K. Matsuda, H. Yahiro, Y. Inami, T. Fukuoka, Y. Miyata, K. Yanagi, Y. Maniwa, H. Kataura, T. Saito, et al., Confined water inside single-walled carbon nanotubes: Global phase diagram and effect of finite length, *Journal of Chemical Physics*, 2011, **134**, 244501.

115. A. Alexiadis and S. Kassinos, Self-diffusivity, hydrogen bonding and density of different water models in carbon nanotubes, *Molecular Simulation*, 2008, **34**, 671-678.
116. M. C. Gordillo and J. Marti, Hydrogen bond structure of liquid water confined in nanotubes, *Chemical Physics Letters*, 2000, **329**, 341-345.
117. J. Hernandez-Rojas, F. Calvo, J. Breton and J. M. G. Llorente, Confinement effects on water clusters inside carbon nanotubes, *Journal of Physical Chemistry C*, 2012, **116**, 17019-17028.
118. M. J. O'Connell, P. Boul, L. M. Ericson, C. Huffman, Y. H. Wang, E. Haroz, C. Kuper, J. Tour, K. D. Ausman and R. E. Smalley, Reversible water-solubilization of single-walled carbon nanotubes by polymer wrapping, *Chemical Physics Letters*, 2001, **342**, 265-271.
119. T. A. Pascal, W. A. Goddard and Y. Jung, Entropy and the driving force for the filling of carbon nanotubes with water, *Proceedings of the National Academy of Sciences of the United States of America*, 2011, **108**, 11794-11798.
120. M. S. P. Sansom and P. C. Biggin, Biophysics - Water at the nanoscale, *Nature*, 2001, **414**, 156-159.
121. Y. S. Tao, H. Muramatsu, M. Endo and K. Kaneko, Evidence of water adsorption in hydrophobic nanospaces of highly pure double-walled carbon nanotubes, *Journal of the American Chemical Society*, 2010, **132**, 1214-1215.
122. Y. Gogotsi, J. A. Libera, A. Guvenc-Yazicioglu and C. M. Megaridis, In situ multiphase fluid experiments in hydrothermal carbon nanotubes, *Applied Physics Letters*, 2001, **79**, 1021-1023.
123. Y. Maniwa, H. Kataura, M. Abe, A. Udaka, S. Suzuki, Y. Achiba, H. Kira, K. Matsuda, H. Kadowaki and Y. Okabe, Ordered water inside carbon nanotubes: formation of pentagonal to octagonal ice-nanotubes, *Chemical Physics Letters*, 2005, **401**, 534-538.

124. A. I. Kolesnikov, J. M. Zanotti, C. K. Loong, P. Thiyagarajan, A. P. Moravsky, R. O. Loutfy and C. J. Burnham, Anomalously soft dynamics of water in a nanotube: A revelation of nanoscale confinement, *Physical Review Letters*, 2004, **93**, 035503.

125. K. Matsuda, T. Hibi, H. Kadowaki, H. Kataura and Y. Maniwa, Water dynamics inside single-wall carbon nanotubes: NMR observations, *Physical Review B*, 2006, **74**, 073415.

126. G. Reiter, C. Burnham, D. Homouz, P. M. Platzman, J. Mayers, T. Abdul-Redah, A. P. Moravsky, J. C. Li, C. K. Loong and A. I. Kolesnikov, Anomalous behavior of proton zero point motion in water confined in carbon nanotubes, *Physical Review Letters*, 2006, **97**, 247801.

127. G. F. Reiter, A. I. Kolesnikov, S. J. Paddison, P. M. Platzman, A. P. Moravsky, M. A. Adams and J. Mayers, Evidence for an anomalous quantum state of protons in nanoconfined water, *Physical Review B*, 2012, **85**, 045403.

128. A. Alexiadis and S. Kassinos, Molecular simulation of water in carbon nanotubes, *Chemical Reviews*, 2008, **108**, 5014-5034.

129. C. Dellago, M. M. Naor and G. Hummer, Proton transport through water-filled carbon nanotubes, *Physical Review Letters*, 2003, **90**, 105902.

130. M. L. Brewer, U. W. Schmitt and G. A. Voth, The formation and dynamics of proton wires in channel environments, *Biophysical Journal*, 2001, **80**, 1691-1702.

131. G. Gebel and O. Diat, Neutron and x-ray scattering: Suitable tools for studying ionomer membranes, *Fuel Cells*, 2005, **5**, 261-276.

132. K. A. Mauritz and R. B. Moore, State of understanding of Nafion, *Chemical Reviews*, 2004, **104**, 4535-4585.

133. H. G. Haubold, T. Vad, H. Jungbluth and P. Hiller, Nano structure of NAFION: a SAXS study, *Electrochimica Acta*, 2001, **46**, 1559-1563.

134. L. Rubatat, G. Gebel and O. Diat, Fibrillar structure of Nafion: Matching Fourier and real space studies of corresponding films and solutions, *Macromolecules*, 2004, **37**, 7772-7783.

135. K. Schmidt-Rohr and Q. Chen, Parallel cylindrical water nanochannels in Nafion fuel-cell membranes, *Nature Materials*, 2008, **7**, 75-83.
136. W. Y. Hsu and T. D. Gierke, Ion transport and clustering in Nafion perfluorinated membranes, *Journal of Membrane Science*, 1983, **13**, 307-326.
137. B. F. Habenicht and S. J. Paddison, *Ab initio* simulations of the effects of nanoscale confinement on proton transfer in hydrophobic environments, *Journal of Physical Chemistry B*, 2011, **115**, 10826-10835.
138. M. A. Ilhan and E. Spohr, *Ab initio* molecular dynamics of proton networks in narrow polymer electrolyte pores, *J. Phys.: Condens. Matter*, 2011, **23**, 234104.
139. C. J. Cramer, *Essentials of Computational Chemistry Theories and Models*, John Wiley & Sons Ltd., Chichester, West Sussex, UK, 2004.
140. I. N. Levine, *Quantum Chemistry*, Prentice Hall, Upper Saddle River, NJ, 2000.
141. M. Born and R. Oppenheimer, Quantum theory of molecules, *Annalen Der Physik*, 1927, **84**, 0457-0484.
142. D. R. Hartree, The wave mechanics of an atom with a non-Coulomb central field Part I theory and methods, *Proceedings of the Cambridge Philosophical Society*, 1928, **24**, 89-110.
143. V. Fock, Approximation method for the solution of the quantum mechanical multibody problems, *Zeitschrift Fur Physik*, 1930, **61**, 126-148.
144. C. Moller and M. S. Plesset, Note on an approximation treatment for many-electron systems, *Physical Review*, 1934, **46**, 0618-0622.
145. I. Shavitt, in *Modern Theoretical Chemistry*, ed. H. F. Schaefer, Plenum Press, New York, 1977.
146. R. G. Parr and W. Yang, *Density Functional Theory of Atoms and Molecules*, Oxford, New York, 1989.
147. P. Hohenberg and W. Kohn, Inhomogeneous electron gas, *Physical Review B*, 1964, **136**, B864-&.
148. W. Kohn and L. J. Sham, Self-consistent equations including exchange and correlation effects, *Physical Review*, 1965, **140**, 1133-&.

149. D. M. Ceperley and B. J. Alder, Ground-state of the electron-gas by a stochastic method, *Physical Review Letters*, 1980, **45**, 566-569.
150. J. P. Perdew, K. Burke and M. Ernzerhof, Generalized gradient approximation made simple, *Physical Review Letters*, 1996, **77**, 3865-3868.
151. J. P. Perdew, in *Electronic Structure of Solids*, eds. P. Ziesche and H. Eschrig, Akademie Verlag, Berlin, 1991.
152. J. P. Perdew, K. Burke and M. Ernzerhof, Generalized gradient approximation made simple (vol 77, pg 3865, 1996), *Physical Review Letters*, 1997, **78**, 1396-1396.
153. A. D. Becke, Density-functional exchange-energy approximation with correct asymptotic-behavior, *Physical Review A*, 1988, **38**, 3098-3100.
154. C. T. Lee, W. T. Yang and R. G. Parr, Development of the colle-salvetti correlation-energy formula into a functional of the electron-density, *Physical Review B*, 1988, **37**, 785-789.
155. J. P. Perdew, Density-functional approximation for the correlation-energy of the inhomogeneous electron-gas, *Physical Review B*, 1986, **33**, 8822-8824.
156. J. P. Perdew, Correction, *Physical Review B*, 1986, **34**, 7406-7406.
157. S. H. Vosko, L. Wilk and M. Nusair, Accurate spin-dependent electron liquid correlation energies for local spin-density calculations - A critical analysis, *Canadian Journal of Physics*, 1980, **58**, 1200-1211.
158. A. D. Becke, A new mixing of Hartree-Fock and local density-functional theories, *Journal of Chemical Physics*, 1993, **98**, 1372-1377.
159. S. F. Boys, Electronic wave functions .1. A general method of calculation for the stationary states of any molecular system, *Proceedings of the Royal Society of London Series a-Mathematical and Physical Sciences*, 1950, **200**, 542-554.
160. R. Ditchfield, W. J. Hehre and J. A. Pople, Self-consistent molecular-orbital methods .9. Extended gaussian-type basis for molecular-orbital studies of organic molecules, *Journal of Chemical Physics*, 1971, **54**, 724-728.

161. W. J. Hehre, Ditchfie.R and J. A. Pople, Self-consistent molecular-orbital methods .12. Further extensions of gaussian-type basis sets for use in molecular-orbital studies of organic-molecules, *Journal of Chemical Physics*, 1972, **56**, 2257-2261.
162. S. F. Boys and F. Bernardi, Calculation of small molecular interactions by differences of separate total energies - some procedures with reduced errors, *Molecular Physics*, 1970, **19**, 553-566.
163. R. Car and M. Parrinello, Unified approach for molecular-dynamics and density-functional theory, *Physical Review Letters*, 1985, **55**, 2471-2474.
164. D. Marx and J. Hutter, *Ab Initio Molecular Dynamics: Basic Theory and Advanced Methods*, Cambridge University Press, New York, 2009.
165. G. Kresse and J. Hafner, Ab-initio molecular-dynamics for liquid-metals, *Physical Review B*, 1993, **47**, 558-561.
166. G. Kresse and J. Hafner, Ab-initio molecular-dynamics simulation of the liquid-metal amorphous-semiconductor transition in germanium, *Physical Review B*, 1994, **49**, 14251-14269.
167. G. Kresse and J. Furthmuller, Efficient iterative schemes for ab initio total-energy calculations using a plane-wave basis set, *Physical Review B*, 1996, **54**, 11169-11186.
168. R. P. Feynman, Forces in molecules, *Physical Review*, 1939, **56**, 340-343.
169. H. Hellmann, *Einführung in die Quantenchemie*, Franz Deuticke, Leipzig, 1937.
170. M. E. Tuckerman, Ab initio molecular dynamics: basic concepts, current trends and novel applications, *Journal of Physics-Condensed Matter*, 2002, **14**, R1297-R1355.
171. U. C. Singh and P. A. Kollman, An approach to computing electrostatic charges for molecules, *Journal of Computational Chemistry*, 1984, **5**, 129-145.
172. B. H. Besler, K. M. Merz and P. A. Kollman, Atomic charges derived from semiempirical methods, *Journal of Computational Chemistry*, 1990, **11**, 431-439.
173. C. M. Breneman and K. B. Wiberg, Determining atom-centered monopoles from molecular electrostatic potentials. The need for high sampling density in formamide conformational analysis, *Journal of Computational Chemistry*, 1990, **11**, 361-373.

174. M. J. Frisch, G. W. Trucks, H. B. Schlegel, G. E. Scuseria, M. A. Robb, J. R. Cheeseman, J. A. Montgomery, T. Vreven, K. N. Kudin, J. C. Burant, et al., Gaussian Inc., Wallingford, CT, Revision C.02 edn., 2004.

175. M. J. Frisch, G. W. Trucks, H. B. Schlegel, G. E. Scuseria, M. A. Robb, J. R. Cheeseman, G. Scalmani, V. Barone, B. Mennucci, G. A. Petersson, et al., Gaussian Inc., Wallingford CT, Revision A.1 edn., 2009.

176. A. D. Becke, Density-functional thermochemistry. III. The role of exact exchange, *Journal of Chemical Physics*, 1993, **98**, 5648-5652.

177. S. Grimme, Semiempirical GGA-type density functional constructed with a long-range dispersion correction, *Journal of Computational Chemistry*, 2006, **27**, 1787-1799.

178. P. C. Harihara and J. A. Pople, Influence of polarization functions on molecular-orbital hydrogenation energies, *Theoretica Chimica Acta*, 1973, **28**, 213-222.

179. G. Scalmani and M. J. Frisch, Continuous surface charge polarizable continuum models of solvation. I. General formalism, *Journal of Chemical Physics*, 2010, **132**, 114110.

180. A. D. McLean and G. S. Chandler, Contracted Gaussian basis sets for molecular calculations. I. Second row atoms, Z=11-18, *Journal of Chemical Physics*, 1980, **72**, 5639-5648.

181. R. Krishnan, J. S. Binkley, R. Seeger and J. A. Pople, Self-consistent molecular-orbital methods .20. Basis set for correlated wave-functions, *Journal of Chemical Physics*, 1980, **72**, 650-654.

182. T. Clark, J. Chandrasekhar, G. W. Spitznagel and P. V. Schleyer, Efficient diffuse function-augmented basis-sets for anion calculations .3. The 3-21+g basis set for 1st-row elements, Li-F, *Journal of Computational Chemistry*, 1983, **4**, 294-301.

183. M. J. Frisch, J. A. Pople and J. S. Binkley, Self-consistent molecular-orbital methods .25. Supplementary functions for Gaussian-basis sets, *Journal of Chemical Physics*, 1984, **80**, 3265-3269.

184. N. Kobko and J. J. Dannenberg, Effect of basis set superposition error (BSSE) upon ab initio calculations of organic transition states, *Journal of Physical Chemistry A*, 2001, **105**, 1944-1950.

185. G. Kresse and J. Furthmuller, Efficiency of ab-initio total energy calculations for metals and semiconductors using a plane-wave basis set, *Computational Materials Science*, 1996, **6**, 15-50.

186. P. E. Blochl, Projector augmented-wave method, *Physical Review B*, 1994, **50**, 17953-17979.

187. G. Kresse and D. Joubert, From ultrasoft pseudopotentials to the projector augmented-wave method, *Physical Review B*, 1999, **59**, 1758-1775.

188. J. K. Clark and S. J. Paddison, Side Chain Flexibility in Perfluorosulfonic Acid Ionomers: An ab Initio Study, *Journal of Physical Chemistry A*, 2013, **117**, 10534-10543.

189. S. J. Paddison, L. R. Pratt and T. A. Zawodzinski, Conformations of perfluoroether sulfonic acid side chains for the modeling of Nafion (R), *J. New Mater. Electrochem. Sys.*, 1999, **2**, 183-188.

190. D. Brandell, J. Karo, A. Liivat and J. O. Thomas, Molecular dynamics studies of the Nafion (R), Dow (R) and Aciplex (R) fuel-cell polymer membrane systems, *Journal of Molecular Modeling*, 2007, **13**, 1039-1046.

191. S. Urata, J. Irisawa, A. Takada, W. Shinoda, S. Tsuzuki and M. Mikami, Molecular dynamics simulation of swollen membrane of perfluorinated ionomer, *Journal of Physical Chemistry B*, 2005, **109**, 4269-4278.

192. R. Devanathan and M. Dupuis, Insight from molecular modelling: Does the polymer side chain length matter for transport properties of perfluorosulfonic acid membranes?, *Physical Chemistry Chemical Physics*, 2012, **14**, 11281-11295.

193. J. K. Clark II and S. J. Paddison, Proton dissociation and transfer in proton exchange membrane ionomers with multiple and distinct pendant acid groups: An ab initio study, *Electrochimica Acta*, 2013, **101**, 279-292.

194. J. C. Grossman, E. Schwegler, E. W. Draeger, F. Gygi and G. Galli, Towards an assessment of the accuracy of density functional theory for first principles simulations of water, *Journal of Chemical Physics*, 2004, **120**, 300-311.
195. J. VandeVondele, F. Mohamed, M. Krack, J. Hutter, M. Sprik and M. Parrinello, The influence of temperature and density functional models in ab initio molecular dynamics simulation of liquid water, *Journal of Chemical Physics*, 2005, **122**, 014515.
196. B. Santra, A. Michaelides and M. Scheffler, Coupled cluster benchmarks of water monomers and dimers extracted from density-functional theory liquid water: The importance of monomer deformations, *Journal of Chemical Physics*, 2009, **131**, 124509.
197. D. Laage and J. T. Hynes, A molecular jump mechanism of water reorientation, *Science*, 2006, **311**, 832-835.
198. R. Kumar, J. R. Schmidt and J. L. Skinner, Hydrogen bonding definitions and dynamics in liquid water, *Journal of Chemical Physics*, 2007, **126**, 204107.
199. M. Falk, An infrared study of water in perfluorosulfonate (Nafion) membranes, *Canad. J. Chem.*, 1980, **58**, 1495.
200. R. Basnayake, G. R. Peterson, D. J. Casadonte and C. Korzeniewski, Hydration and interfacial water in nafion membrane probed by transmission infrared spectroscopy, *Journal of Physical Chemistry B*, 2006, **110**, 23938-23943.
201. D. E. Moilanen, I. R. Piletic and M. D. Fayer, Tracking water's response to structural changes in Nafion membranes, *Journal of Physical Chemistry A*, 2006, **110**, 9084-9088.
202. T. Steiner, The hydrogen bond in the solid state, *Angewandte Chemie-International Edition*, 2002, **41**, 48-76.
203. A. K. Soper, The radial distribution functions of water as derived from radiation total scattering experiments: Is there anything we can say for sure?, *ISRN Physical Chemistry*, 2013, **2013**, 67.
204. K. Modig, B. G. Pfrommer and B. Halle, Temperature-dependent hydrogen-bond geometry in liquid water, *Physical Review Letters*, 2003, **90**.

205. J. D. Dunitz and R. Taylor, Organic fluorine hardly ever accepts hydrogen bonds, *Chemistry A European Journal*, 1997, **3**, 89-98.
206. J. A. K. Howard, V. J. Hoy, D. Ohagan and G. T. Smith, How good is fluorine as a hydrogen bond acceptor?, *Tetrahedron*, 1996, **52**, 12613-12622.
207. J. D. Dunitz, Organic fluorine: Odd man out, *Chembiochem*, 2004, **5**, 614-621.
208. B. Santra, A. Michaelides, M. Fuchs, A. Tkatchenko, C. Filippi and M. Scheffler, On the accuracy of density-functional theory exchange-correlation functionals for H bonds in small water clusters. II. The water hexamer and van der Waals interactions, *Journal of Chemical Physics*, 2008, **129**.
209. J. Chen, X. Z. Li, Q. F. Zhang, A. Michaelides and E. G. Wang, Nature of proton transport in a water-filled carbon nanotube and in liquid water, *Physical Chemistry Chemical Physics*, 2013, **15**, 6344-6349.
210. B. C. Wood and N. Marzari, Proton dynamics in superprotonic CsHSO4, *Physical Review B*, 2007, **76**.
211. L. Vilciauskas, M. E. Tuckerman, G. Bester, S. J. Paddison and K. D. Kreuer, The mechanism of proton conduction in phosphoric acid, *Nature Chemistry*, 2012, **4**, 461-466.
212. A. Hassanali, F. Giberti, J. Cuny, T. D. Kuhne and M. Parrinello, Proton transfer through the water gossamer, *Proceedings of the National Academy of Sciences of the United States of America*, 2013, **110**, 13723-13728.
213. J. K. Clark, S. J. Paddison, M. Eikerling, M. Dupuis and T. A. Zawodzinski, A comparative ab initio study of the primary hydration and proton dissociation of various imide and sulfonic acid ionomers, *Journal of Physical Chemistry A*, 2012, **116**, 1801-1813.
214. J. A. Elliott and S. J. Paddison, Modelling of morphology and proton transport in PFSA membranes, *Physical Chemistry Chemical Physics*, 2007, **9**, 2602-2618.

Appendices

Appendix A. Data Analysis Routines/Programs

```
PROGRAM all_analysis

USE data_type
USE common_data
USE Format_atoms
USE calc_pbc
USE calc_MIC
USE H3O_water
IMPLICIT NONE

INTEGER :: i,j,k,m,dim,a(3),b(3),c,d(5)
REAL(dp) :: dummy, mat2(3,3),prod_M(3,3)
CHARACTER (len=10) :: dum, char
WRITE(*,*) 'What is the system?'
WRITE(*,*) '1 - Water'
WRITE(*,*) '2 - Water + Proton'
WRITE(*,*) '3 - Triflic Acid'
READ(*,*) sim_type   ! globally declared variable
! user created file within working directory
OPEN(1,file='data.dat')
READ(1,*) radius
READ(1,*) stps
READ(1,*) num_SO3
READ(1,*) lambda
CLOSE(1)
! VASP POSCAR file to get unit cell dimensions and number of atoms
OPEN(2,file='POSCAR')
READ(2,*) dum
READ(2,*) dummy
READ(2,*) x_len
READ(2,*) dummy, y_len
READ(2,*) dummy, dummy, z_len
READ(2,*) nC, nF, nH, nO, nS
CLOSE(2)
dim = 3
allocate(O_type(nO))  ! contains 1 for SO3 oxygen and 2 for H2O
IF (sim_type.EQ.1.OR.sim_type.EQ.2) THEN
        num_H2O = nO
        num_SO3 = 0
        F_trif = 0
        C_trif = 0
        allocate(atoms_H(dim,nH,stps))
        allocate(atoms_O(dim,nO,stps))
        allocate(atoms_F(dim,nF))
        allocate(atoms_C(dim,nC))
```

```
        atoms_O=0.0d0
        atoms_H=0.0d0
        atoms_F=0.0d0
        atoms_C=0.0d0
        O_type = 2
ELSEIF (sim_type.EQ.3) THEN
        num_H2O = lambda*num_SO3
        F_trif = num_SO3*3
        C_trif = num_SO3
        nF = nF - F_trif
        nC = nC - C_trif
        allocate(atoms_H(dim,nH,stps))
        allocate(atoms_O(dim,nO,stps))
        allocate(atoms_S(dim,nS,stps))
        allocate(F_mobile(dim,F_trif,stps))
        allocate(C_mobile(dim,C_trif,stps))
        allocate(atoms_F(dim,nF))
        allocate(atoms_C(dim,nC))
        allocate(so3_O(num_SO3*3))
        allocate(h2o_O(num_H2O))
        atoms_O=0.0d0
        atoms_H=0.0d0
        atoms_S=0.0d0
        atoms_F=0.0d0
        atoms_C=0.0d0
        F_mobile=0.0d0
        C_mobile=0.0d0
        so3_O = 0
        h2o_O = 0
        O_type = 0
ENDIF
CALL read_atoms
CALL center_atoms

CALL calc_msd
ALLOCATE(Oxy_state(nO,stps))  ! global variable to be used later
Oxy_state=0
CALL calc_hbond
CALL rdf_data
CALL xy_contour
CALL connectivity
IF (sim_type.EQ.2) THEN
        CALL Excess_H
        CALL delta_data
ENDIF
IF (sim_type.EQ.1.OR.sim_type.EQ.2.AND.nF.NE.0) THEN
        CALL HF_bonds
ELSEIF (sim_type.EQ.3) THEN
```

```
        CALL HF_bonds
        CALL HF_bonds_mobile
ENDIF

END PROGRAM all_analysis
!-----End Main Program--------
!
!***** S/R Read_Atoms ********
SUBROUTINE read_atoms
USE data_type
USE common_data
implicit none
INTEGER :: i,j,k,count
CHARACTER (len=10) :: dum
REAL, ALLOCATABLE :: C_tmp(:,:,:),F_tmp(:,:,:)
REAL :: C_chk, F_chk,cntF,cntC
INTEGER :: C_ind(C_trif),F_ind(F_trif),Fct,Cct,F_ncnt(nF),wtf
INTEGER :: C_ncnt(nC)
wtf=0
C_chk = 0.0d0
F_chk = 0.0d0
C_ind = 0
F_ind = 0
F_ncnt = 0
Fct = 0
Cct = 0
cntF = 0
! file containing the xyz coordinates from trajectory
OPEN(3,file='x_traj.xyz')
IF (nS.NE.0) THEN
ALLOCATE(C_tmp(3,nC+C_trif,stps))
ALLOCATE(F_tmp(3,nF+F_trif,stps))
DO i=1,stps
        READ(3,*) num_atoms
        READ(3,*) dum
        DO j=1,nC+C_trif
                READ(3,*) dum, (C_tmp(k,j,i),k=1,3)
        ENDDO
        DO j=1,nF+F_trif
                READ(3,*) dum, (F_tmp(k,j,i),k=1,3)
        ENDDO
        DO j=1,nH
                READ(3,*) dum, (atoms_H(k,j,i),k=1,3)
        ENDDO
        DO j=1,nO
                READ(3,*) dum, (atoms_O(k,j,i),k=1,3)
        ENDDO
        DO j=1,nS
```

```
                READ(3,*) dum, (atoms_S(k,j,i),k=1,3)
        ENDDO
ENDDO
ELSEIF (nS.EQ.0) THEN
DO i=1,stps
        READ(3,*) num_atoms
        READ(3,*) dum
        DO j=1,nC
                READ(3,*) dum, (atoms_C(k,j),k=1,3)
        ENDDO
        DO j=1,nF
                READ(3,*) dum, (atoms_F(k,j),k=1,3)

        ENDDO
        DO j=1,nH
                READ(3,*) dum, (atoms_H(k,j,i),k=1,3)
        ENDDO
        DO j=1,nO
                READ(3,*) dum, (atoms_O(k,j,i),k=1,3)
        ENDDO
ENDDO
ENDIF
IF (nS.NE.0.AND.nF.EQ.0) THEN
        F_mobile = F_tmp
ELSEIF (nS.NE.0.AND.nF.NE.0) THEN
        DO i=1,nF+F_trif
                F_chk = SUM(F_tmp(:,i,1)-F_tmp(:,i,2))
                IF (F_chk.NE.0.0d0) THEN
                        Fct = Fct+1
                        F_ind(Fct) = i
                ELSE
                        cntF = cntF+1
                        F_ncnt(cntF) = i
                ENDIF
        ENDDO
        atoms_F = F_tmp(:,F_ncnt,1)
        F_mobile = F_tmp(:,F_ind,:)
ENDIF
ENDIF
IF (stps.GT.1) THEN
IF (nS.NE.0) THEN
        DO i=1,nC+C_trif
                C_chk = SUM(C_tmp(:,i,1)-C_tmp(:,i,2))
                IF (C_chk.NE.0.0d0) THEN
                        Cct = Cct+1
                        C_ind(Cct) = i
                ELSE
                        cntC = cntC+1
```

```
                        C_ncnt(cntC) = i
                    ENDIF
            ENDDO
            C_mobile = C_tmp(:,C_ind,:)
            atoms_C = C_tmp(:,C_ncnt,1)
ELSE
            C_mobile = 0.0d0
ENDIF
ENDIF

END SUBROUTINE read_atoms
```

```
  MODULE Format_atoms
  USE data_type
  USE common_data
  IMPLICIT none

  CONTAINS

  !**** S/R center_atoms *******
  SUBROUTINE center_atoms
  IMPLICIT none
  INTEGER :: i,j,k,m
REAL(dp) :: x_half, y_half, z_half
  REAL(dp) :: crd_shift(3), cell_shift(3)
  x_half = x_len/2.0d0
  y_half = y_len/2.0d0
  z_half = z_len/2.0d0
  ! Center atoms at origin
  DO i=1,stps
        DO j=1,nH
              atoms_H(:,j,i)=atoms_H(:,j,i) - crd_shift
        ENDDO
        DO j=1,nO
              atoms_O(:,j,i)=atoms_O(:,j,i) - crd_shift
        ENDDO
        DO j=1,nS
              atoms_S(:,j,i)=atoms_S(:,j,i) - crd_shift
        ENDDO
        DO j=1,F_trif
              F_mobile(:,j,i)=F_mobile(:,j,i) - crd_shift
        ENDDO
        DO j=1,C_trif
              C_mobile(:,j,i)=C_mobile(:,j,i) - crd_shift
        ENDDO
  ENDDO
  DO i=1,nF
        atoms_F(:,i)=atoms_F(:,i) - crd_shift
  ENDDO
  DO i=1,nC
        atoms_C(:,i)=atoms_C(:,i) - crd_shift
  ENDDO
  IF (nS.NE.0) THEN
        CALL oxy_type
  ENDIF
```

```
END SUBROUTINE center_atoms

!*** S/R oxy_type ***
SUBROUTINE oxy_type
! type 1 is SO3 type 2 is H2O stored in global variable O_type
IMPLICIT none
INTEGER :: i,j,k,min_SO(1)
REAL(dp) :: so3_cut, oo(3), Scrd_tmp(3,nS), SO(nS)
INTEGER :: w_ct, s_ct
ALLOCATE(so_ind(nO))
so_ind = 0
so3_cut = 4.0d0
w_ct = 1
s_ct = 1
DO i=1,nO
	oo = atoms_O(:,i,1)
	FORALL (j=1:nS) Scrd_tmp(:,j)=atoms_S(:,j,1)-oo
	FORALL (j=1:nS) Scrd_tmp(3,j)=Scrd_tmp(3,j)-z_len*&
	ANINT(Scrd_tmp(3,j)/(z_len))
	FORALL (j=1:nS) SO(j)=SUM(Scrd_tmp(:,j)**2,dim=1)
	min_SO = MINLOC(SO)
	IF (SO(min_SO(1)).LE.so3_cut) THEN
		O_type(i) = 1
		so_ind(i) = min_SO(1)
	ELSE
		O_type(i) = 2
	ENDIF
ENDDO
DO i=1,nO
	IF (O_type(i) .eq. 1) THEN
		so3_O(s_ct) = i
		s_ct = s_ct + 1
	ELSE
		h2o_O(w_ct) = i
		w_ct = w_ct + 1
	ENDIF
ENDDO

END SUBROUTINE oxy_type

!*** S/R format_pbc
SUBROUTINE format_pbc(O_pbc,H_pbc)
IMPLICIT none
REAL(dp), ALLOCATABLE :: O_tmp(:,:,:), H_tmp(:,:,:)
```

```
REAL(dp) :: oz_chk, hz_chk
INTEGER :: i,j,k
REAL(dp), INTENT(OUT) :: O_pbc(stps,nO,3), H_pbc(stps,nH,3)
ALLOCATE(O_tmp(3,nO,stps))
ALLOCATE(H_tmp(3,nH,stps))
O_tmp = atoms_O
H_tmp = atoms_H
O_pbc = RESHAPE(O_tmp,(/stps,nO,3/),ORDER=(/3,2,1/))
H_pbc = RESHAPE(H_tmp,(/stps,nH,3/),ORDER=(/3,2,1/))
DEALLOCATE(O_tmp)
DEALLOCATE(H_tmp)
oz_chk = 0.0d0
hz_chk = 0.0d0
DO i=1,nO
	DO j=1,stps-1
		oz_chk = O_pbc(j+1,i,3)-O_pbc(j,i,3)
		O_pbc(j+1,i,3)=O_pbc(j+1,i,3)-ANINT(oz_chk/z_len)*z_len
	ENDDO
ENDDO
DO i=1,nH
	DO j=1,stps-1
		hz_chk = H_pbc(j+1,i,3)-H_pbc(j,i,3)
		H_pbc(j+1,i,3)=H_pbc(j+1,i,3)-ANINT(hz_chk/z_len)*z_len
	ENDDO
ENDDO

END SUBROUTINE format_pbc

END MODULE Format_atoms
```

```
MODULE calc_pbc
USE data_type
USE common_data
USE Format_atoms
implicit none

CONTAINS

!*** S/R calc_msd ***
SUBROUTINE calc_msd
implicit none
INTEGER :: n_origin,i,j,k
REAL, ALLOCATABLE :: time_vec(:)
REAL(dp) :: dt
REAL(dp), ALLOCATABLE :: msd_so3(:,:), msd_h2o(:,:), SOmsd_avg(:)
REAL(dp), ALLOCATABLE :: SOmsd_tot(:), H2Omsd_tot(:), H2Omsd_avg(:)
REAL(dp) :: O_pbc(stps,nO,3), H_pbc(stps,nH,3)
REAL(dp) :: SO3_pbc(stps,num_SO3*3,3), H2O_pbc(stps,lambda*num_SO3,3)

CALL format_pbc(O_pbc,H_pbc)
IF (nS.NE.0) THEN
      SO3_pbc = O_pbc(:,so3_O,:)
      H2O_pbc = O_pbc(:,h2o_O,:)
ELSE
      SO3_pbc = 0
      H2O_pbc = O_pbc(:,:,:)
ENDIF
n_origin = stps/2
dt = 0.5d0
ALLOCATE(time_vec(n_origin+1))
DO i=1,n_origin+1
      time_vec(i)=DBLE(i)*dt - dt
ENDDO
ALLOCATE(msd_so3(n_origin+1,num_SO3*3))
ALLOCATE(SOmsd_tot(n_origin+1))
ALLOCATE(msd_h2o(n_origin+1,num_H2O))
ALLOCATE(H2Omsd_tot(n_origin+1))
msd_so3 = 0.0d0
msd_h2o = 0.0d0
DO i=1,n_origin
      FORALL (j=1:num_SO3*3) msd_so3(:,j)=msd_so3(:,j)+&
      (SO3_pbc(i:i+n_origin,j,3)-SO3_pbc(i,j,3))**2
      FORALL (k=1:num_H2O) msd_h2o(:,k)=msd_h2o(:,k)&
      + (H2O_pbc(i:i+n_origin,k,3)-H2O_pbc(i,k,3))**2
```

```
ENDDO
SOmsd_tot = SUM(msd_so3,dim=2)
H2Omsd_tot = SUM(msd_h2o,dim=2)
DEALLOCATE(msd_so3)
DEALLOCATE(msd_h2o)
ALLOCATE(SOmsd_avg(n_origin+1))
ALLOCATE(H2Omsd_avg(n_origin+1))
SOmsd_avg = SOmsd_tot/DBLE(n_origin*num_SO3*3)
H2Omsd_avg = H2Omsd_tot/DBLE(n_origin*num_H2O)
DEALLOCATE(SOmsd_tot)
DEALLOCATE(H2Omsd_tot)
OPEN(32,file='MSD_SO3.dat')
OPEN(33,file='MSD_H2O.dat')
DO i=1,n_origin+1
      WRITE(32,'(2f15.6)') time_vec(i),SOmsd_avg(i)
      WRITE(33,'(2f15.6)') time_vec(i),H2Omsd_avg(i)
ENDDO
CLOSE(32)
CLOSE(33)
END SUBROUTINE calc_msd

END MODULE calc_pbc
```

```
MODULE calc_MIC

USE data_type
USE common_data
USE Format_atoms
USE calc_pbc

implicit none

CONTAINS

!*** S/R calc_hbond ****

SUBROUTINE calc_hbond

implicit none

INTEGER :: i,j,k,m,n,w,o_n,state_del(5)
REAL(dp) :: hy_tmp(3),Ocrd_tmp(3,nO), HO(nO)
INTEGER :: n_ho1(1),n_ho2(1),hb_count(4),CN_count(4),sql(5)
REAL(dp) :: ang_thresh, oh_thresh, d_ho1(1),d_ho2(1),d_oo,oo_thresh
REAL(dp) :: sqr_h1,sqr_h2,sqr_oo,hoo
REAL(dp) :: oo_dist(4),ho_dist(4),avg_hoo(4),hb_ct_avg(4),CN_avg(4)
REAL(dp) :: delta,state_frac_2(5), disso_2, drD
INTEGER :: H3O_chk_2(nO),H3O_cnt_2,H3O_chk_3(nO),max_bin_D
REAL(dp),ALLOCATABLE :: d_bin_rng(:),del_bin(:)

ang_thresh = DCOS(30.0d0*(pi/180.0d0))
oh_thresh = 2.4d0**2
oo_thresh = 3.25d0**2

state_frac_2 = 0.0d0
disso_2=0.0d0
sqr_h1 = 0.0d0 ; sqr_h2 = 0.0d0; sqr_oo = 0.0d0; hoo = 0.0d0
oo_dist = 0.0d0 ; ho_dist = 0.0d0 ; d_oo = 0.0d0 ; HO = 0.0d0
hy_tmp = 0.0d0 ; Ocrd_tmp = 0.0d0
n_ho1 = 0; n_ho2 = 0
d_ho1 = 0.0d0; d_ho2 = 0.0d0
avg_hoo = 0.0d0
CN_count = 0
hb_count = 0
CN_avg = 0.0d0

max_bin_D=121
drD=0.025d0
ALLOCATE(d_bin_rng(max_bin_d))
ALLOCATE(del_bin(max_bin_d+1))
del_bin=0.0d0
```

```
d_bin_rng=0.0d0
DO i=1,max_bin_D
        d_bin_rng(i)=DBLE(i-61)*drD
ENDDO

delta = 0.0d0

! o_n holds the type of hydrogen bond (1)SO3/SO3,(2)SO3/H2O,(3)H2O/SO3,(4)H2O/H2O
o_n = 0

! state_del: (1)bound,(2)SO3/SO3 shared,(3)SO3/H2O shared,(4)zundel,(5)H3O+
state_del = 0

ALLOCATE(HB_track(stps,nH,5))
ALLOCATE(num_HB(stps))
ALLOCATE(Oxy_state_2(nO,stps))
Oxy_state_2=0
num_HB=0
HB_track = 0

DO i=1,stps
        H3O_chk_2 = 0
        H3O_cnt_2 = 0
        H3O_chk_3 = 0

        Oxy_state(:,i)=O_type

        DO j=1,nH
                hy_tmp = atoms_H(:,j,i)
                ! center coordinates around this hydrogen atom
                FORALL (k=1:nO) Ocrd_tmp(:,k)=atoms_O(:,k,i)-hy_tmp
                FORALL (k=1:nO) Ocrd_tmp(3,k)=Ocrd_tmp(3,k)-z_len*&
                ANINT(Ocrd_tmp(3,k)/z_len)

                FORALL (k=1:nO) HO(k) = SUM(Ocrd_tmp(:,k)**2,dim=1)

                n_ho1 = MINLOC(HO)
                n_ho2 = MINLOC(HO,MASK=HO.GT.HO(n_ho1(1)))

                d_ho1 = MINVAL(HO)
                d_ho2 = MINVAL(HO,MASK=HO.GT.HO(n_ho1(1)))

                sqr_h1 = DSQRT(d_ho1(1))
                sqr_h2 = DSQRT(d_ho2(1))
                delta = sqr_h2-sqr_h1

                o_n = 2*O_type(n_ho1(1))+O_type(n_ho2(1))-2
```

```
! determine state
IF (nS.GT.0) THEN

        IF (delta.LT.0.2d0) THEN
                IF (o_n.EQ.1) THEN
                        state_del(2)=state_del(2)+1
                ELSEIF (o_n.EQ.2) THEN
                        state_del(3)=state_del(3)+1
                        Oxy_state(n_ho2(1),i)=3
                ELSEIF (o_n.EQ.3) THEN
                        state_del(3)=state_del(3)+1
                        Oxy_state(n_ho1(1),i)=3
                ELSEIF (o_n.EQ.4) THEN
                        state_del(4)=state_del(4)+1
                        H3O_chk_3(n_ho1(1))=H3O_chk_3(n_ho1(1))+1
                        Oxy_state(n_ho1(1),i)=4
                        Oxy_state(n_ho2(1),i)=4
                ENDIF
        ELSEIF (delta.GT.0.2d0) THEN
                IF (o_n.EQ.1.OR.o_n.EQ.2) THEN
                        state_del(1)=state_del(1)+1
                ELSE
                        H3O_chk_2(n_ho1(1))=H3O_chk_2(n_ho1(1))+1
                        H3O_chk_3(n_ho1(1))=H3O_chk_3(n_ho1(1))+1
                ENDIF
        ENDIF

        IF (j.EQ.nH) THEN
                H3O_cnt_2 = COUNT(H3O_chk_2.GT.2)
                state_del(5)=state_del(5)+H3O_cnt_2
                WHERE (H3O_chk_3.GT.2) Oxy_state_2(:,i)=1
                WHERE (H3O_chk_2.GT.2) Oxy_state(:,i)=5
        ENDIF

ENDIF

! find hydrogen bonds
IF (d_ho1(1).LT.oh_thresh.AND.d_ho2(1).LT.oh_thresh) THEN
        d_oo = SUM((Ocrd_tmp(:,n_ho1(1))-&
                Ocrd_tmp(:,n_ho2(1)))**2,dim=1)
        IF (d_oo.LE.oo_thresh) THEN
                sqr_oo = DSQRT(d_oo)
                hoo = (d_ho1(1)+d_oo-d_ho2(1))/(2.0d0*sqr_h1*sqr_oo)
                IF (hoo.GE.ang_thresh) THEN
                        hb_count(o_n)=hb_count(o_n)+1

                        IF (o_n.EQ.2.OR.o_n.EQ.3) THEN
```

```
                                        CN_count(o_n)=CN_count(o_n)+1
                                    ELSE
                                        CN_count(o_n)=CN_count(o_n)+2
                                    ENDIF

                                    oo_dist(o_n) = oo_dist(o_n)+sqr_oo
                                    ho_dist(o_n) = ho_dist(o_n)+sqr_h2
                                    avg_hoo(o_n) = avg_hoo(o_n)+DACOS(hoo)*(180.0d0/pi)

                                    sql(:) = (/i,o_n,j,n_ho1(1),n_ho2(1)/)
                                    HB_track(i,j,:) = sql

                                    num_HB(i)=num_HB(i)+1

                                    IF (o_n.EQ.2) THEN
                                        DO w=1,max_bin_D-1
                                            IF (delta.GT.d_bin_rng(w).AND.delta.LT.&
                                            d_bin_rng(w+1)) THEN
                                            del_bin(w+1)=del_bin(w+1)+1.0d0
                                            ENDIF
                                        ENDDO
                                    ELSEIF (o_n.EQ.3) THEN
                                        delta=delta*-1.0d0
                                        DO w=1,max_bin_D-1
                                            IF (delta.GT.d_bin_rng(w).AND.delta.LT.&
                                            d_bin_rng(w+1)) THEN
                                            del_bin(w+1)=del_bin(w+1)+1.0d0
                                            ENDIF
                                        ENDDO
                                    ENDIF
                                ENDIF
                            ENDIF
                        ENDIF

                ENDDO

        ENDDO

IF (sim_type.NE.1) THEN
        state_frac_2 = state_del/DBLE(SUM(state_del))
        disso_2 = DBLE(state_del(4)+state_del(5))/DBLE(SUM(state_del))
        OPEN(20,file='Dissociation.dat')
        WRITE(20,*) '  Bound   SO3/SO3   SO3/H2O  Zundel   H3O+  &
  Disso'
        WRITE(20,'(6f10.5)') state_frac_2(:),disso_2
        CLOSE(20)
ENDIF
```

```
del_bin=del_bin/drD/DBLE(SUM(del_bin))
OPEN(24,file='delta_bin.dat')
DO i=1,max_bin_D
        WRITE(24,*) d_bin_rng(i),del_bin(i)
ENDDO
CLOSE(24)
oo_dist = oo_dist/DBLE(hb_count)
ho_dist = ho_dist/DBLE(hb_count)
avg_hoo = avg_hoo/DBLE(hb_count)
hb_ct_avg = DBLE(hb_count)/DBLE(stps)

CN_avg(1) = CN_count(1)/DBLE(num_SO3*3)
CN_avg(2) = (CN_count(2)+CN_count(3))/DBLE(num_SO3*3)
CN_avg(3) = (CN_count(2)+CN_count(3))/DBLE(num_H2O)
CN_avg(4) = CN_count(4)/DBLE(num_H2O)

CN_avg = CN_avg/DBLE(stps)

14 FORMAT(4a10)
OPEN(21,file='Coordination.dat')
WRITE(21,14) 'SO3/SO3', 'SO3/H2O', 'H2O/SO3', 'H2O/H2O'
WRITE(21,'(4f10.5)') CN_avg(:)
CLOSE(21)

15 FORMAT(a8,4f15.5)
16 FORMAT(a8,4a15)
OPEN(22,file='Hbond_data.dat')
WRITE(22,16) ' ','SO3/SO3','SO3/H2O','H2O/SO3','H2O/H2O'
WRITE(22,15) 'OO  ',oo_dist(:)
WRITE(22,15) 'OH  ',ho_dist(:)
WRITE(22,15) 'HOO ',avg_hoo(:)
CLOSE(22)

END SUBROUTINE calc_hbond


!******* S/R rdf_data **********

SUBROUTINE rdf_data

IMPLICIT NONE

INTEGER :: i,j,k,m,n,t,w
REAL(dp) :: dr,r_val,dr_C,r_val_C
INTEGER :: max_bins,bin_nO(nO),type_o1,type_o2,oo_type
INTEGER :: max_bins_C,bin_nC(nO),r_cnt(1000)
REAL(dp) :: Ocrd_tmp(3,nO),OO(nO),o1_tmp(3),rho(2)
```

```
REAL(dp) :: d_Ocnt(nO),dxy_O(nO),rdf_norm(4),rdf_denom,rsq,frac
REAL(dp) :: rand_1(1000),rand_2(1000),phi_1(1000),theta_1(1000)
REAL(dp) :: y_1(1000),x_1(1000),x(1000),y(1000),r_dist(1000),points
INTEGER :: bin_HO(nO),type_O,bin_HC(nH),rH_cnt(1000)
INTEGER :: bin_Ocyl(nO),bin_Hcyl(nH)
REAL(dp) :: HO(nO),Ocrd_Htmp(3,nO),frac_H,rH_dist(1000)
REAL(dp):: OO_bins(4,1001),HO_bins(2,1001)
REAL(dp) :: rdf_Hnorm(2),dxy_H(nH),d_Hcnt(nH),h1_tmp(3)
REAL(dp) :: OC_bins(2,251),HC_bins(251),OC_cyl(251),HC_cyl(251)
REAL(dp) :: H3O_bins(1001),H3O_denom,H3O_norm,H3O_OH(1001)
REAL(dp) :: SS_bins(1001),CC_bins(1001),FC_bins(251)
REAL(dp) :: norm_FC, norm_SS, norm_CC,dxy_F(F_trif),d_Fcnt(F_trif)
INTEGER :: bin_FC(F_trif),bin_CC(C_trif),bin_SS(nS)
REAL(dp) :: Scrd_tmp(3,nS),Ccrd_tmp(3,C_trif),s1_tmp(3),c1_tmp(3)
REAL(dp) :: CC(C_trif),SS(nS),dxy_C(C_trif),dxy_S(nS)
REAL(dp) :: d_Scnt(nS),d_Ccnt(C_trif)

max_bins = 1000
max_bins_C = 250
OC_cyl = 0
HO_bins = 0.0d0
HC_bins = 0.0d0
FC_bins = 0.0d0
OO_bins = 0.0d0
OC_bins = 0.0d0
SS_bins = 0.0d0
CC_bins = 0.0d0
bin_FC = 0
H3O_denom = 0.0d0
H3O_bins = 0.0d0
H3O_OH = 0.0d0
H3O_norm = 0.0d0

rsq = radius**2
dr = z_len/(2.0d0*DBLE(max_bins))
!dr = 0.025d0

dr_C = radius/(DBLE(max_bins_C))

! rho: (1) is for SO3 (2) is for H2O
rho(1) = DBLE(num_SO3*3)/(pi*rsq*z_len)
rho(2) = DBLE(num_H2O)/(pi*rsq*z_len)

rdf_norm(1) = rho(1)*DBLE(num_SO3*3)*dr*DBLE(stps)*4.0d0*pi
rdf_norm(2) = rho(2)*DBLE(num_SO3*3)*dr*DBLE(stps)*4.0d0*pi
rdf_norm(3) = rho(1)*DBLE(num_H2O)*dr*DBLE(stps)*4.0d0*pi
rdf_norm(4) = rho(2)*DBLE(num_H2O)*dr*DBLE(stps)*4.0d0*pi
```

```
rdf_Hnorm(1) = DBLE(num_SO3*3)*dr*DBLE(stps)*4.0d0*pi*&
DBLE(nH)/(pi*rsq*z_len)

rdf_Hnorm(2) = DBLE(num_H2O)*dr*DBLE(stps)*4.0d0*pi*&
DBLE(nH)/(pi*rsq*z_len)

points = 1000.0d0

CALL RANDOM_SEED()

DO m=1,stps
        ! Get distances to the CNT wall
        FORALL (n=1:nO) dxy_O(n)=DSQRT(atoms_O(1,n,m)**2+atoms_O(2,n,m)**2)
        FORALL (n=1:nO) d_Ocnt(n)=radius - dxy_O(n)
        FORALL (n=1:nO) bin_nC(n)=INT(d_Ocnt(n)/dr_C)+1
        FORALL (n=1:nO) bin_Ocyl(n)=INT(dxy_O(n)/dr_C)+1

        FORALL (n=1:nH) dxy_H(n)=DSQRT(atoms_H(1,n,m)**2+atoms_H(2,n,m)**2)
        FORALL (n=1:nH) d_Hcnt(n)=radius - dxy_H(n)
        FORALL (n=1:nH) bin_HC(n)=INT(d_Hcnt(n)/dr_C)+1
        FORALL (n=1:nH) bin_Hcyl(n)=INT(dxy_H(n)/dr_C)+1

        H3O_denom = rdf_norm(4)*DBLE(SUM(Oxy_state_2(:,m)))/(DBLE(num_H2O))

        ! Generate points to be used for excluded volume normalization
        CALL RANDOM_NUMBER (rand_1)
        CALL RANDOM_NUMBER (rand_2)

        phi_1 = 2.0d0*pi*rand_1
        theta_1 = 2.0d0*(rand_2 - 0.5d0)
        theta_1 = DACOS(theta_1)

        x_1 = DSIN(theta_1)*DCOS(phi_1)
        y_1 = DSIN(theta_1)*DSIN(phi_1)


DO i=1,nO
        type_o1 = O_type(i)

        OC_bins(type_o1,bin_nC(i))=OC_bins(type_o1,bin_nC(i))+1.0d0
        OC_cyl(bin_Ocyl(i))=OC_cyl(bin_Ocyl(i))+1.0d0

        o1_tmp = atoms_O(:,i,m)

        FORALL (k=1:nO) Ocrd_tmp(:,k)=atoms_O(:,k,m)-o1_tmp
        FORALL (k=1:nO) Ocrd_tmp(3,k)=Ocrd_tmp(3,k)-z_len*&
        ANINT(Ocrd_tmp(3,k)/(z_len))
```

```
        FORALL (k=1:nO) OO(k)=SUM(Ocrd_tmp(:,k)**2,dim=1)
        OO = DSQRT(OO)
        FORALL (k=1:nO) bin_nO(k)=INT(OO(k)/dr)+1

        DO j=1,nO

                r_cnt = 0
                type_o2 = O_type(j)
                oo_type = 2*type_o1 + type_o2 - 2

                IF (bin_nO(j).LE.max_bins+1.AND.bin_nO(j).NE.1) THEN

                !!! Now test for excluded volume in normalization

                        IF (OO(j).LT.d_Ocnt(i)) THEN
                                rdf_denom=rdf_norm(oo_type)*(OO(j)**2)
                                OO_bins(oo_type,bin_nO(j))=OO_bins(oo_type,bin_nO(j))+&
                                1.0d0/(rdf_denom)

                                IF (Oxy_state_2(i,m).EQ.1.AND.type_o2.EQ.2) THEN
                                        H3O_norm = H3O_denom*(OO(j)**2)

                                        H3O_bins(bin_nO(j))=H3O_bins(bin_nO(j))+&
                                        1.0d0/(H3O_norm)


                                ENDIF

                        ELSEIF (OO(j).GT.d_Ocnt(i))THEN
                                x = x_1*OO(j) + dxy_O(i)
                                y = y_1*OO(j)
                                r_dist = x*x + y*y

                                WHERE (r_dist.LT.rsq)
                                        r_cnt=1
                                ENDWHERE

                                frac = DBLE(SUM(r_cnt))/points

                                rdf_denom=rdf_norm(oo_type)*(OO(j)**2)*frac
                                OO_bins(oo_type,bin_nO(j))=OO_bins(oo_type,bin_nO(j))+&
                                1.0d0/(rdf_denom)

                        ENDIF

                ENDIF
        ENDDO   ! END LOOP OVER OXYGEN (2)
ENDDO   ! END LOOP OVER OXYGEN (1)
```

```
DO t=1,nH   ! LOOP OVER HYDROGEN
        HC_bins(bin_HC(t))=HC_bins(bin_HC(t))+1.0d0
        HC_cyl(bin_Hcyl(t))=HC_cyl(bin_Hcyl(t))+1.0d0


        h1_tmp = atoms_H(:,t,m)
        FORALL (k=1:nO) Ocrd_Htmp(:,k)=atoms_O(:,k,m)-h1_tmp
        FORALL (k=1:nO) Ocrd_Htmp(3,k)=Ocrd_Htmp(3,k)-z_len*&
        ANINT(Ocrd_Htmp(3,k)/(z_len))

        FORALL (k=1:nO) HO(k)=SUM(Ocrd_Htmp(:,k)**2,dim=1)
        HO = DSQRT(HO)
        FORALL (k=1:nO) bin_HO(k)=INT(HO(k)/dr)+1

        DO w=1,nO   ! LOOP OVER OXYGEN (3)
                rH_cnt = 0
                type_O = O_type(w)



                IF (bin_HO(w).LE.max_bins+1.AND.bin_HO(w).NE.1) THEN

                        IF (HO(w).LT.d_Hcnt(t)) THEN
                                rdf_denom = rdf_Hnorm(type_O)*(HO(w)**2)
                                HO_bins(type_O,bin_HO(w))=HO_bins(type_O,bin_HO(w))+&
                                1.0d0/(rdf_denom)

                                !IF (t.EQ.actH(m)) THEN
                                IF (Oxy_state_2(w,m).EQ.1) THEN
                                        H3O_OH(bin_HO(w))=H3O_OH(bin_HO(w))+&
                                        1.0d0/(rdf_denom)
                                ENDIF

                        ELSEIF (HO(w).GT.d_Hcnt(t)) THEN
                                x = x_1*HO(w) + dxy_H(t)
                                y = y_1*HO(w)
                                rH_dist = x*x + y*y
                                WHERE (rH_dist.LT.rsq) rH_cnt=1
                                frac_H = DBLE(SUM(rH_cnt))/points

                                rdf_denom=rdf_Hnorm(type_O)*(HO(w)**2)*frac_H
                                HO_bins(type_O,bin_HO(w))=HO_bins(type_O,bin_HO(w))+&
                                1.0d0/(rdf_denom)


                        ENDIF
```

```
                ENDIF
        ENDDO    ! END LOOP OVER OXYGEN (3)
ENDDO ! END LOOP OVER HYDROGEN

ENDDO  ! END LOOP OVER TIME



IF (nS.NE.0) THEN
        norm_FC=2.0d0*pi*z_len*dr_C*DBLE(stps)*DBLE(F_trif)/(pi*rsq*z_len)
        norm_SS=4.0d0*pi*dr*DBLE(stps)*DBLE(nS*2)/(pi*rsq*z_len)
        norm_CC=4.0d0*pi*dr*DBLE(stps)*DBLE(C_trif*2)/(pi*rsq*z_len)
        Scrd_tmp=0.0d0; Ccrd_tmp=0.0d0
        s1_tmp=0.0d0; c1_tmp=0.0d0
        CC = 0.0d0; SS = 0.0d0
        bin_CC = 0; bin_SS = 0

DO m=1,stps
        FORALL (n=1:F_trif) dxy_F(n)=DSQRT(F_mobile(1,n,m)**2&
        +F_mobile(2,n,m)**2)

        FORALL (n=1:F_trif) d_Fcnt(n)=radius - dxy_F(n)

        FORALL (n=1:F_trif) bin_FC(n)=INT(d_Fcnt(n)/dr_C)+1


        CALL RANDOM_NUMBER (rand_1)
        CALL RANDOM_NUMBER (rand_2)

        phi_1 = 2.0d0*pi*rand_1
        theta_1 = 2.0d0*(rand_2 - 0.5d0)
        theta_1 = DACOS(theta_1)

        x_1 = DSIN(theta_1)*DCOS(phi_1)
        y_1 = DSIN(theta_1)*DSIN(phi_1)

        DO i=1,F_trif
                FC_bins(bin_FC(i))=FC_bins(bin_FC(i))+1.0d0
        ENDDO


        FORALL (n=1:C_trif) dxy_C(n)=DSQRT(C_mobile(1,n,m)**2&
        +C_mobile(2,n,m)**2)

        FORALL (n=1:C_trif) d_Ccnt(n)=radius - dxy_C(n)

        FORALL (n=1:nS) dxy_S(n)=DSQRT(atoms_S(1,n,m)**2&
```

```
+atoms_S(2,n,m)**2)

FORALL (n=1:nS) d_Scnt(n)=radius - dxy_S(n)

DO j=1,C_trif



        c1_tmp = C_mobile(:,j,m)

        FORALL (k=1:C_trif) Ccrd_tmp(:,k)=C_mobile(:,k,m)-c1_tmp
        FORALL (k=1:C_trif) Ccrd_tmp(3,k)=Ccrd_tmp(3,k)-z_len*&
        ANINT(Ccrd_tmp(3,k)/z_len)

        FORALL (k=1:C_trif) CC(k)=SUM(Ccrd_tmp(:,k)**2,dim=1)
        CC = DSQRT(CC)
        FORALL (k=1:C_trif) bin_CC(k)=INT(CC(k)/dr)+1


        DO t=1,C_trif
                IF (bin_CC(t).LE.max_bins+1.AND.bin_CC(t).NE.1) THEN

        !!! Now test for excluded volume in normalization

                IF (CC(t).LT.d_Ccnt(j)) THEN
                        rdf_denom=norm_CC*(CC(t)**2)
                        CC_bins(bin_CC(t))=CC_bins(bin_CC(t))+&
                        1.0d0/(rdf_denom)


                ELSEIF (CC(t).GT.d_Ccnt(j))THEN
                        x = x_1*CC(t) + dxy_C(j)
                        y = y_1*CC(t)
                        r_dist = x*x + y*y

                        WHERE (r_dist.LT.rsq) r_cnt=1

                        !WHERE (r_dist.LT.(radius-2.7)**2) r_cnt=1

                        frac = DBLE(SUM(r_cnt))/points


                        rdf_denom=norm_CC*(CC(t)**2)*frac
                        CC_bins(bin_CC(t))=CC_bins(bin_CC(t))+&
                        1.0d0/(rdf_denom)

                ENDIF
```

```
                ENDIF

        ENDDO
ENDDO


DO n=1,nS



        s1_tmp = atoms_S(:,n,m)

        FORALL (k=1:nS) Scrd_tmp(:,k)=atoms_S(:,k,m)-s1_tmp
        FORALL (k=1:nS) Scrd_tmp(3,k)=Scrd_tmp(3,k)-z_len*&
        ANINT(Scrd_tmp(3,k)/z_len)

        FORALL (k=1:nS) SS(k)=SUM(Scrd_tmp(:,k)**2,dim=1)
        SS = DSQRT(SS)
        FORALL (k=1:nS) bin_SS(k)=INT(SS(k)/dr)+1


        DO w=1,nS
                IF (bin_SS(w).LE.max_bins+1.AND.bin_SS(w).NE.1) THEN

        !!! Now test for excluded volume in normalization

                IF (SS(w).LT.d_Scnt(n)) THEN
                        rdf_denom=norm_SS*(SS(w)**2)
                        SS_bins(bin_SS(w))=SS_bins(bin_SS(w))+&
                        1.0d0/(rdf_denom)


                ELSEIF (SS(w).GT.d_Scnt(n))THEN
                        x = x_1*SS(w) + dxy_S(n)
                        y = y_1*SS(w)
                        r_dist = x*x + y*y

                        WHERE (r_dist.LT.rsq) r_cnt=1


                        frac = DBLE(SUM(r_cnt))/points


                        rdf_denom=norm_SS*(SS(w)**2)*frac
                        SS_bins(bin_SS(w))=SS_bins(bin_SS(w))+&
                        1.0d0/(rdf_denom)

                ENDIF
```

```
                        ENDIF

                ENDDO
        ENDDO
ENDDO
ENDIF



IF (nS.NE.0) THEN
        FC_bins = FC_bins/(SUM(FC_bins)*dr_C)
        OPEN(32,file='RDF_SS.dat')
        OPEN(33,file='RDF_CC.dat')
        OPEN(34,file='RDF_CNT_F.dat')
        DO i=1,max_bins+1
                r_val=DBLE(i-1)*dr
                WRITE(32,*) r_val,SS_bins(i)
                WRITE(33,*) r_val,CC_bins(i)
        ENDDO
        CLOSE(32)
        CLOSE(33)

        DO j=1,max_bins_C+1
                r_val_C = DBLE(j-1)*dr_C
                WRITE(34,*) r_val_C,FC_bins(j)
        ENDDO
        CLOSE(34)

ENDIF

OPEN(25,file='RDF_Oxy.dat')
OPEN(26,file='RDF_Hyd.dat')
OPEN(27,file='RDF_H3O.dat')
DO i=1,max_bins+1
        r_val = DBLE(i-1)*dr
        IF (nS.NE.0) THEN
                WRITE(25,'(5f15.6)') r_val,OO_bins(:,i)
                WRITE(26,'(3f15.6)') r_val,HO_bins(:,i)
                WRITE(27,'(3f15.6)') r_val,H3O_bins(i), H3O_OH(i)
        ELSE
                WRITE(25,'(5f15.6)') r_val,OO_bins(4,i)
                WRITE(26,'(3f15.6)') r_val,HO_bins(2,i)

        ENDIF
ENDDO
```

```
CLOSE(25)
CLOSE(26)
CLOSE(27)

OPEN(28,file='RDF_CNT_O.dat')
OPEN(29,file='RDF_CNT_H.dat')
!OPEN(30,file='RDF_O_Cyl.dat')
!OPEN(31,file='RDF_H_Cyl.dat')

HC_bins = HC_bins/(SUM(HC_bins)*dr_C)
OC_bins(1,:) = OC_bins(1,:)/(SUM(OC_bins(1,:))*dr_C)
OC_bins(2,:) = OC_bins(2,:)/(SUM(OC_bins(2,:))*dr_C)

DO i=1,max_bins_C+1
        r_val_C = DBLE(i-1)*dr_C


        WRITE(28,'(3f15.6)') r_val_C, OC_bins(:,i)
        WRITE(29,'(2f15.6)') r_val_C,HC_bins(i)
        !WRITE(30,'(2f15.6)') r_val_C,OC_cyl(i)
        !WRITE(31,'(2f15.6)') r_val_C,HC_cyl(i)
ENDDO

CLOSE(28)
CLOSE(29)
!CLOSE(30)
!CLOSE(31)



END SUBROUTINE rdf_data

!******* S/R HF_bonds
! An identical S/R titled HF_bonds_mobile is used to calculate
! HF bonds using the fluorine atoms of mobile triflic acid molecules
SUBROUTINE HF_bonds

implicit none

INTEGER :: i,j,k,m
INTEGER :: life_ct, life_sum, n_bond, HF_ndist,HF_nlife(stps)
REAL(dp) :: Hcrd_tmp(3), Fcrd_tmp(3,nF), HF(nF), Ocrd_tmp(3,nO)
REAL(dp) :: hf_cut, OF_tmp, HOF,ang_thresh,HF_life,of_cut
INTEGER :: HF_track(stps,nH)
REAL(dp) :: HF_dist, avg_HF_dist, avg_life_bi, OF_dist, H3O_HF(stps)
INTEGER :: life_bi, num_bi(stps), nchk, n_sum,Ox_HF(nH,stps)
INTEGER :: ox_ind(1), state_HF(5)
REAL(dp) :: HO(nO),OFsqr,HOsqr
```

```
state_HF=0; ox_ind = 0
Ox_HF = 0 ;H3O_HF = 0.0d0;OFsqr=0.0d0;HOsqr=0.0d0
hf_cut = 2.5d0**2; ang_thresh = DCOS(30.0*(pi/180.0));of_cut = 3.50d0
HOF = 0.0d0; num_bi = 0; HF_track = 0
life_ct = 0; life_sum = 0; n_bond = 0; HF_dist = 0.0d0
HF_ndist = 0; avg_HF_dist = 0.0d0
HF_nlife = 0; life_bi = 0
avg_life_bi = 0.0d0
nchk = 0
n_sum = 0
OF_dist = 0.0d0

DO i=1,stps
        DO j=1,nH
        IF (HB_track(i,j,1).EQ.0) THEN

                Hcrd_tmp=atoms_H(:,j,i)
                FORALL (m=1:nF) Fcrd_tmp(:,m)=atoms_F(:,m)-Hcrd_tmp
                FORALL (m=1:nF) Fcrd_tmp(3,m)=Fcrd_tmp(3,m) - z_len*&
                ANINT(Fcrd_tmp(3,m)/(z_len))

                FORALL (m=1:nO) Ocrd_tmp(:,m) = atoms_O(:,m,i)-Hcrd_tmp
                FORALL (m=1:nO) Ocrd_tmp(3,m) = Ocrd_tmp(3,m) - z_len*&
                ANINT(Ocrd_tmp(3,m)/(z_len))

                FORALL (m=1:nF) HF(m) = SUM(Fcrd_tmp(:,m)**2,dim=1)
                FORALL (m=1:nO) HO(m) = SUM(Ocrd_tmp(:,m)**2,dim=1)
                ox_ind = MINLOC(HO)
                DO k=1,nF
                        IF (HF(k).LE.hf_cut) THEN

                        OF_tmp = SUM((Ocrd_tmp(:,ox_ind(1))&
                        -Fcrd_tmp(:,k))**2)

                        OFsqr = DSQRT(OF_tmp)
                        HOsqr = DSQRT(HO(ox_ind(1)))

                        HOF = (HO(ox_ind(1))+OF_tmp-HF(k))/(2.0*&
                                OFsqr*HOsqr)

                        IF (HOF.GE.ang_thresh) THEN

                                HF_track(i,j) = k
                                HF_dist = HF_dist + DSQRT(HF(k))
                                HF_ndist = HF_ndist + 1
                                OF_dist = OF_dist + OFsqr
                                Ox_HF(j,i)=ox_ind(1)
```

```
                        IF (sim_type.EQ.2.AND.ox_ind(1).EQ.ex_loc(i)) THEN
                                H3O_HF(i) = H3O_HF(i)+1.0d0
                        ENDIF
                ENDIF


                ENDIF

        ENDDO
        ENDIF
    ENDDO
ENDDO



DO i=1,nH
    life_ct = 0
    life_bi = 0
    DO j=1,stps-1
        IF (HF_track(j,i).NE.0.AND.HF_track(j+1,i).NE.0) THEN
            life_bi = life_bi + 1

            IF (life_bi.GE.10) THEN
                num_bi(j+1)=num_bi(j+1) + 1

                state_HF(Oxy_state(Ox_HF(i,j+1),j+1))=&
                    state_HF(Oxy_state(Ox_HF(i,j+1),j+1))+1

            ENDIF

            IF (HF_track(j,i).EQ.HF_track(j+1,i)) THEN
                life_ct = life_ct + 1
                IF (life_ct.GE.10) THEN
                    HF_nlife(j)=HF_nlife(j)+1
                ENDIF
            ELSEIF (life_ct.GE.10) THEN
                life_sum = life_sum + life_ct
                life_ct = 0
                n_bond = n_bond+1
            ENDIF


            IF (j.EQ.stps-1.AND.life_ct.GE.10) THEN
                life_sum=life_sum+life_ct
                n_bond=n_bond+1
                !n_sum = n_sum + life_bi
                !nchk = nchk+1
```

```
                ENDIF

                IF (j.EQ.stps-1.AND.life_bi.GE.10) THEN
                        n_sum = n_sum + life_bi
                        nchk = nchk+1
                ENDIF

        ELSE
                IF (life_ct.GE.10) THEN
                life_sum = life_sum + life_ct
                life_ct = 0
                n_bond = n_bond + 1
                ENDIF

                IF (life_bi.GE.10) THEN
                        nchk = nchk + 1
                        n_sum = n_sum + life_bi
                        life_bi = 0
                ENDIF
                life_ct = 0
                life_bi = 0

        ENDIF
    ENDDO

ENDDO


HF_life = DBLE(life_sum)/DBLE(n_bond)/2.0d0

avg_life_bi = DBLE(n_sum)/DBLE(nchk)/2.0d0

avg_HF_dist = HF_dist/DBLE(HF_ndist)
OF_dist = OF_dist/DBLE(HF_ndist)


OPEN(50,file='HF_bond_stps.dat')
DO i=1,stps
    WRITE(50,*) num_bi(i)
ENDDO
CLOSE(50)

OPEN(51,file='HF_info.dat')
WRITE(51,*) 'HF Life     HF_bi_life       HF dist    OF dist'
WRITE(51,'(4f10.3)') HF_life,avg_life_bi,avg_HF_dist,OF_dist
CLOSE(51)

IF (sim_type.EQ.2) THEN
```

```
        OPEN(52,file='H3O_HF_stps.dat')
        WRITE(52,*) SUM(H3O_HF)
        DO i=1,stps
                WRITE(52,*) H3O_HF(i)
        ENDDO
ENDIF
CLOSE(52)

21 FORMAT(A20,I)
22 FORMAT(A20,f10.4)
OPEN(53,file='HF_CNT_Otype.dat')
WRITE(53,22) '% Time HF bond = ',100.0d0*DBLE(COUNT(num_bi.GT.0))&
/DBLE(stps)
WRITE(53,21) 'n SO3H bound = ',state_HF(1)
WRITE(53,21) 'n H2O = ',state_HF(2)
WRITE(53,21) 'n H2O/SO3H = ',state_HF(3)
WRITE(53,21) 'n Zundel = ',state_HF(4)
WRITE(53,21) 'n Eigen = ',state_HF(5)
CLOSE(53)

END SUBROUTINE HF_bonds

!**** S/R xy_contour ****

SUBROUTINE xy_contour

implicit none

INTEGER :: i,j,k,m
REAL(DP) :: dr_xy
INTEGER :: max_xy,x_tmp,y_tmp
REAL(DP) :: n_densO_h2o,n_densH,n_densO_so3,n_densF
REAL(DP), ALLOCATABLE :: xvec(:), yvec(:), Hxy_loc(:,:)
REAL(DP), ALLOCATABLE :: Fxy_loc(:,:), SO3_Oloc(:,:), H2O_Oloc(:,:)

dr_xy = 0.05d0
max_xy = INT((2.0d0*radius)/dr_xy)+1

ALLOCATE(xvec(max_xy+1))
ALLOCATE(yvec(max_xy+1))
ALLOCATE(H2O_Oloc(max_xy+1,max_xy+1))
ALLOCATE(SO3_Oloc(max_xy+1,max_xy+1))
ALLOCATE(Hxy_loc(max_xy+1,max_xy+1))
ALLOCATE(Fxy_loc(max_xy+1,max_xy+1))

n_densH = DBLE(nH)*DBLE(stps)*dr_xy*dr_xy/(pi*radius**2*z_len)
n_densO_h2o=DBLE(num_H2O)*DBLE(stps)*dr_xy*dr_xy/(pi*radius**2*z_len)
n_densO_so3=DBLE(num_so3*3)*DBLE(stps)*dr_xy*dr_xy/(pi*radius**2*z_len)
```

```
n_densF=DBLE(F_trif)*DBLE(stps)*dr_xy*dr_xy/(pi*radius**2*z_len)

xvec = 0.0d0
yvec = 0.0d0
H2O_Oloc = 0.0d0
SO3_Oloc = 0.0d0
Hxy_loc = 0.0d0
Fxy_loc = 0.0d0
x_tmp = 0
y_tmp = 0


DO i=1,max_xy+1
        xvec(i) = -radius + DBLE(i-1)*dr_xy
        yvec(i) = -radius + DBLE(i-1)*dr_xy
ENDDO


DO i=1,stps

DO j=1,nO
        DO k=1,max_xy
                IF (atoms_O(1,j,i).LE.xvec(k+1).AND.atoms_O(1,j,i).GE.&
                xvec(k)) THEN
                        x_tmp = k

                        DO m=1,max_xy
                                IF (atoms_O(2,j,i).LE.yvec(m+1).AND.&
                                atoms_O(2,j,i).GE.yvec(m)) THEN
                                y_tmp = m

                                IF (O_type(j).EQ.1) THEN
                                SO3_Oloc(k,m) = SO3_Oloc(k,m) + 1.0d0
                                ELSEIF (O_type(j).EQ.2) THEN
                                H2O_Oloc(k,m) = H2O_Oloc(k,m) + 1.0d0
                                ENDIF


                                ENDIF
                        ENDDO
                ENDIF
        ENDDO
ENDDO

DO j=1,nH
        DO k=1,max_xy
                IF (atoms_H(1,j,i).LE.xvec(k+1).AND.atoms_H(1,j,i).GE.&
                xvec(k)) THEN
```

```
                        x_tmp = k

                        DO m=1,max_xy
                                IF (atoms_H(2,j,i).LE.yvec(m+1).AND.&
                                atoms_H(2,j,i).GE.yvec(m)) THEN
                                y_tmp = m

                                Hxy_loc(k,m) = Hxy_loc(k,m) + 1.0d0

                                ENDIF
                        ENDDO
                ENDIF
        ENDDO
ENDDO
ENDDO

H2O_Oloc = H2O_Oloc/n_densO_h2o
SO3_Oloc = SO3_Oloc/n_densO_so3
Hxy_loc = Hxy_loc/n_densH


OPEN(60,file='H2O_loc.dat')
OPEN(61,file='Hxy_loc.dat')
OPEN(62,file='SO3_loc.dat')


DO i=1,max_xy+1

        DO j=1,max_xy+1

                WRITE(60,*) xvec(i), yvec(j), H2O_Oloc(i,j)
                WRITE(61,*) xvec(i), yvec(j), Hxy_loc(i,j)
                WRITE(62,*) xvec(i), yvec(j), SO3_Oloc(i,j)

        ENDDO
ENDDO

CLOSE(60)
CLOSE(61)
CLOSE(62)

END SUBROUTINE xy_contour

!****** S/R connectivity *******

SUBROUTINE connectivity

IMPLICIT NONE
```

```
INTEGER :: i,j,k,m,n,w,t,r
INTEGER :: chn_ct,nHB(nO),new_O
INTEGER :: first_O,adj_ij(nO,nO)
INTEGER :: adj_3(4,nO),adj_cnt
INTEGER :: chain_node(nO,20,30),chn_nde,nde_num
INTEGER :: ring_node(nO,20,30),nRing,nChain,maxC_stp(1)
INTEGER :: chn_Ind(nO,30),maxC_loc(2)
REAL(dp) :: chn_avg,ring_avg
INTEGER :: new_chain(nO), chain_ones(nO,nO,30),ring_ones(nO,nO,30)
INTEGER :: chn_ones2(nO,nO,30),rng_ones2(nO,nO,30)
INTEGER :: H2O_chn,H2O_rng,SO3_chn,SO3_rng
REAL(dp) :: num_chn_avg,num_rng_avg
REAL(dp) :: H2O_chn_avg,H2O_rng_avg,SO3_chn_avg,SO3_rng_avg
INTEGER :: stp_n,o_start,color_v(nO), ring_used,bchk2,chn_branch(nO,20)
REAL(dp) :: Otmp(3,nO), z_adj,oxy_Z(nO,nO)
REAL(dp) :: oxy_Ztmp(nO),z_check(30),z_chk2
INTEGER :: chn_noRng(nO,nO,30),rng_noRng(nO,nO,30)
INTEGER :: H2O_Nchn,H2O_Nrng,SO3_Nchn,SO3_Nrng,nRingN,nChainN
REAL(dp) :: chn_Navg,ring_Navg, newN_rng(nO)
REAL(dp) :: so3_frac, h2o_frac,chn_stdev,Nchn_stdev

SO3_chn_2 = 0
H2O_chn_2 = 0
SO3_Nchn_2=0
H2O_Nchn_2=0
so3_frac = 0.0d0
h2o_frac = 0.0d0
color_v = 0chn_Navg=0.0d0;ring_Navg=0.0d0
H2O_Nchn=0;H2O_Nrng=0;SO3_Nchn=0;SO3_Nrng=0;nRingN=0;nChainN=0
rng_noRng=0
chn_noRng=0
stp_n=0; n_zcheck=0
H2O_chn_avg=0.0d0;H2O_rng_avg=0.0d0;SO3_chn_avg=0.0d0;SO3_rng_avg=0.0d0
num_chn_avg=0.0d0
num_rng_avg=0.0d0
H2O_chn=0
H2O_rng=0
SO3_chn=0
SO3_rng=0
z_chk2=0.0d0
nRing=0
nChain=0
chn_avg=0.0d0
ring_avg=0.0d0
! below are globally defined
ALLOCATE(disco(nO))
dir_path=0; parent=0; dir_ones=0; dir_chk=0
```

```
dir_rng_ones=0;dir_num=0;disco=0
DO i=1,stps
	oxy_Z = 0.0d0
	oxy_Ztmp = 0.0d0
	maxC_stp = 0
	chain_ones=0
	ring_ones=0
	ring_used=0
	new_chain = 0
	chn_ct = 1
	chn_num = 1
	nHB=0
	new_O = 0
	first_O = 0
	adj_ij=0
	adj_3=0
	chain_node=0
	ring_node=0
	chn_nde=1
	nde_num=0
	DO j=1,nH
		IF (HB_track(i,j,1).NE.0) THEN
			nHB(HB_track(i,j,5))=nHB(HB_track(i,j,5))+1
			nHB(HB_track(i,j,4))=nHB(HB_track(i,j,4))+1
			adj_ij(HB_track(i,j,4),HB_track(i,j,5))=HB_track(i,j,5)
			adj_ij(HB_track(i,j,5),HB_track(i,j,4))=HB_track(i,j,4)
		ENDIF
	ENDDO
	DO w=1,nO
		adj_cnt=0
		DO n=1,nH
			IF (HB_track(i,n,4).EQ.w) THEN
				adj_cnt=adj_cnt+1
				adj_3(adj_cnt,w)=HB_track(i,n,5)
			ELSEIF (HB_track(i,n,5).EQ.w) THEN
				adj_cnt=adj_cnt+1

				adj_3(adj_cnt,w)=HB_track(i,n,4)
			ENDIF
		ENDDO
	ENDDO
	! set up matrix with oxygen separations in the z direction
	! so chains spanning entire cell are not considered rings
	DO w=1,nO

		FORALL (t=1:nO) oxy_Ztmp(t)=atoms_O(3,t,i)-atoms_O(3,w,i)
		FORALL (t=1:nO) oxy_Ztmp(t)=oxy_Ztmp(t)-z_len*&
		ANINT(oxy_Ztmp(t)/z_len)
```

```
        DO j=1,nO
            oxy_Z(w,j)=oxy_Ztmp(j)
        ENDDO
ENDDO
stp_n = i
DO k=1,nO
        ring_used=0
        chn_branch=0
        z_adj = 0
        z_check=0
        chn_nde=1
        o_start=k
        chain_node(k,1,:)=k
        chain_ones(k,k,:)=1
        CALL DFS2(adj_3,k,color_v,stp_n)
        IF (nHB(k).EQ.1) THEN
            chn_ct=1
            chn_nde = 1
            nde_num=k
            chain_node(nde_num,chn_ct,chn_nde)=k
            chain_ones(nde_num,k,:)=1
            first_O = k
            IF (nHB(adj_3(1,k)).EQ.1) THEN
                chn_ct=chn_ct+1
                chain_node(nde_num,chn_ct,chn_nde)=adj_3(1,k)
                chain_ones(nde_num,adj_3(1,k),chn_nde)=1
                chn_num=chn_num+1
                chn_ct=1
            ELSEIF (nHB(adj_3(1,k)).GT.1) THEN
                z_check = 0.0d0
                chn_ct=chn_ct+1
                new_O=adj_3(1,k)
                chain_node(nde_num,chn_ct,chn_nde)=new_O
                chain_ones(nde_num,new_O,chn_nde)=1
                z_check(chn_nde)=z_check(chn_nde) + oxy_Z(k,new_O)
                bchk2 = 0
                chn_branch=0
                CALL find_nbr3(new_O,chn_ct,nHB,first_O,&
                adj_3,chn_nde,nde_num,chain_node,ring_node,&
                chain_ones,ring_ones,ring_used,stp_n,z_check,o_start,&
                z_adj,Otmp,oxy_Z,chn_branch,bchk2)
            ENDIF
        ELSEIF (nHB(k).EQ.2) THEN
            DO r=1,2
                z_check = 0.0d0
                z_adj = 0.0d0
                nde_num=k
                chn_ct=2
```

```
                first_O=k
                new_O = adj_3(r,k)
                chain_node(nde_num,chn_ct,chn_nde)=new_O
                chain_ones(nde_num,new_O,chn_nde)=1
                z_check(chn_nde)=z_check(chn_nde) + oxy_Z(k,new_O)
                chn_branch=0
                bchk2 = 0
                CALL find_nbr3(new_O,chn_ct,nHB,first_O,&
                adj_3,chn_nde,nde_num,chain_node,ring_node,&
                chain_ones,ring_ones,ring_used,stp_n,z_check,o_start,&
                z_adj,Otmp,oxy_Z,chn_branch,bchk2)
                chn_nde = chn_nde + 1
        ENDDO
    ELSEIF (nHB(k).EQ.3) THEN
        DO r=1,3
            z_check=0.0d0
            z_adj = 0.0d0
            nde_num=k
            chn_ct=2
            first_O=k
            new_O=adj_3(r,k)
            chain_node(nde_num,chn_ct,chn_nde)=new_O
            chain_ones(nde_num,new_O,chn_nde)=1
            z_check(chn_nde)=z_check(chn_nde) + oxy_Z(k,new_O)
            chn_branch=0
            bchk2 = 0
            CALL find_nbr3(new_O,chn_ct,nHB,first_O,&
            adj_3,chn_nde,nde_num,chain_node,ring_node,&
            chain_ones,ring_ones,ring_used,stp_n,z_check,o_start,&
            z_adj,Otmp,oxy_Z,chn_branch,bchk2)
            chn_nde = chn_nde + 1
        ENDDO

    ENDIF
ENDDO
DO k=1,nO
DO m=1,30
    IF (chain_node(k,2,m).EQ.0) THEN
        chain_node(k,:,m)=0
        chain_ones(k,:,m)=0
    ENDIF
    IF (ring_node(k,2,m).EQ.0) THEN
        ring_node(k,:,m)=0
        ring_ones(k,:,m)=0
    ENDIF
    z_chk2=0.0d0
    IF (ring_node(k,1,m).NE.0) THEN
    DO w=2,20
```

```
                IF (ring_node(k,w,m).NE.0) THEN
                        z_chk2=z_chk2+oxy_Z(ring_node(k,w-1,m),&
                        ring_node(k,w,m))
                ENDIF
        ENDDO
        ENDIF
        IF (DABS(z_chk2).GE.z_len-1.0d0) THEN
                n_zcheck_stp(i)=n_zcheck_stp(i)+1
                ring_node(k,:,m)=0.0d0
                ring_ones(k,:,m)=0
        ENDIF
ENDDO
ENDDO
DO m=1,nO
        chn_Ind(m,:) = SUM(chain_ones(m,:,:),dim=1)
ENDDO
maxC_loc = MAXLOC(chn_Ind)
new_chain = chain_ones(maxC_loc(1),:,maxC_loc(2))
! create a backup copy to use for analysis in both
! including ring connections and omitting
chn_ones2 = chain_ones
rng_ones2 = ring_ones
chn_noRng = chain_ones
rng_noRng = ring_ones
DO m=1,nO
        newN_rng=0
        DO w=1,30
                IF (ring_node(m,1,w).NE.0) THEN
                        newN_rng = rng_noRng(m,:,w)
                        DO r=1,nO
                                DO k=1,30
                                IF (ANY(chn_noRng(r,:,k).EQ.newN_rng.AND.&
                                rng_noRng(m,:,w).GT.0)) THEN
                                        chn_noRng(r,:,k)=0
                                ENDIF
                                ENDDO
                        ENDDO
                ENDIF
        ENDDO
ENDDO
CALL sub_chain(chain_ones,ring_ones,chn_avg,nChain,chn_ones2,&
rng_ones2,nRing,ring_avg,H2O_chn,H2O_rng,SO3_chn,SO3_rng,stp_n,&
adj_3)
chn_Ind=0
new_chain=0
DO m=1,nO
chn_Ind(m,:) = SUM(chn_noRng(m,:,:),dim=1)
ENDDO
```

```
        maxC_loc = MAXLOC(chn_Ind)
        new_chain = chn_noRng(maxC_loc(1),:,maxC_loc(2))
        CALL sub_chain2(chain_ones,ring_ones,chn_Navg,nChainN,&
        chn_noRng,rng_noRng,nRingN,ring_Navg,H2O_Nchn,H2O_Nrng,&
        SO3_Nchn,SO3_Nrng,stp_n,adj_3)
ENDDO

chn_avg = chn_avg/DBLE(nChain)
num_chn_avg = DBLE(nChain)/DBLE(stps)
ring_avg = ring_avg/DBLE(nRing)
num_rng_avg = DBLE(nRing)/DBLE(stps)
H2O_chn_avg = DBLE(H2O_chn)/DBLE(nChain)
H2O_rng_avg = DBLE(H2O_rng)/DBLE(nRing)
SO3_chn_avg = DBLE(SO3_chn)/DBLE(nChain)
SO3_rng_avg = DBLE(SO3_rng)/DBLE(nRing)
h2o_frac = DBLE(H2O_chn_2)/DBLE(H2O_chn_2+SO3_chn_2)
so3_frac = DBLE(SO3_chn_2)/DBLE(H2O_chn_2+SO3_chn_2)

17 FORMAT(A40,f12.4)
18 FORMAT(A40,I0)
OPEN(71,file='connectivity.dat')
WRITE(71,17) 'Average Number of Chains = ',num_chn_avg
WRITE(71,17) 'Average Length of Chains = ',chn_avg
WRITE(71,*) ' '
WRITE(71,17) 'H2O Oxygen in Chains = ',chn_avg*h2o_frac
WRITE(71,17) 'SO3 Oxygen in Chains = ',chn_avg*so3_frac
WRITE(71,*) ' '
WRITE(71,17) 'Average Number of Rings = ',num_rng_avg
WRITE(71,17) 'Average Length of Rings = ',ring_avg
WRITE(71,*) ' '
WRITE(71,17) 'Average H2O Oxygen in Rings = ',H2O_rng_avg
WRITE(71,17) 'Average SO3 Oxygen in Rings = ',SO3_rng_avg
WRITE(71,*) ' '
WRITE(71,17) 'Total Number of Chains = ',DBLE(nChain)
WRITE(71,17) 'Total Number of Rings = ',DBLE(nRing)
CLOSE(71)

IF (nRing.NE.0) THEN
chn_Navg = chn_Navg/DBLE(nChainN)
num_chn_avg = DBLE(nChainN)/DBLE(stps)
ring_Navg = ring_Navg/DBLE(nRingN)
num_rng_avg = DBLE(nRingN)/DBLE(stps)
H2O_chn_avg = DBLE(H2O_Nchn)/DBLE(nChainN)
H2O_rng_avg = DBLE(H2O_Nrng)/DBLE(nRingN)
SO3_chn_avg = DBLE(SO3_Nchn)/DBLE(nChainN)
SO3_rng_avg = DBLE(SO3_Nrng)/DBLE(nRingN)
h2o_frac = DBLE(H2O_Nchn_2)/DBLE(H2O_Nchn_2+SO3_Nchn_2)
so3_frac = DBLE(SO3_Nchn_2)/DBLE(H2O_Nchn_2+SO3_Nchn_2)
```

```
OPEN(72,file='no_ring_connectivity.dat')
WRITE(72,17) 'Average Number of Chains = ',num_chn_avg
WRITE(72,17) 'Average Length of Chains = ',chn_Navg
WRITE(72,*) ' '
WRITE(72,17) 'H2O Oxygen in Chains = ',chn_Navg*h2o_frac
WRITE(72,17) 'SO3 Oxygen in Chains = ',chn_Navg*so3_frac
WRITE(72,*) ' '
WRITE(72,17) 'Average Number of Rings = ',num_rng_avg
WRITE(72,17) 'Average Length of Rings = ',ring_avg
WRITE(72,*) ' '
WRITE(72,17) 'Average H2O Oxygen in Rings = ',H2O_rng_avg
WRITE(72,17) 'Average SO3 Oxygen in Rings = ',SO3_rng_avg
WRITE(72,*) ' '
WRITE(72,17) 'Total Number of Chains = ',DBLE(nChainN)
WRITE(72,17) 'Total Number of Rings = ',DBLE(nRingN)
CLOSE(72)
ENDIF
END SUBROUTINE connectivity

! **** S/R DFS depth-first search ****

SUBROUTINE DFS2(adj_3,v_start,color_v,stp_n)

IMPLICIT NONE
INTEGER i,j,k
INTEGER, INTENT(INOUT) :: adj_3(4,nO)
INTEGER, INTENT(IN) :: v_start
INTEGER,INTENT(INOUT) :: color_v(nO),stp_n
parent = v_start
dir_cnt=1
! color_v=1 if unused, 2 if used but not finished, 3 if finished
! parent is a global
color_v = 1
color_v(v_start)=2
dir_path(parent,1,:)=v_start
dir_ones(parent,v_start,:)=1
dir_chk=1
disco=0
DO i=1,4
        IF (adj_3(i,v_start).NE.0.AND.color_v(adj_3(i,v_start)).EQ.1) THEN
                disco(adj_3(i,v_start))=2
                CALL DFS_visit(color_v,adj_3,adj_3(i,v_start),stp_n)
        ENDIF
ENDDO

END SUBROUTINE DFS2

!**** S/R DFS_visit ******
```

```
RECURSIVE SUBROUTINE DFS_visit2(color_v,adj_3,next_0,stp_n)

IMPLICIT NONE
INTEGER i,j,k
INTEGER, INTENT(INOUT) :: adj_3(4,n0)
INTEGER, INTENT(IN) :: next_0
INTEGER, INTENT(INOUT) :: color_v(n0),stp_n
color_v(next_0) = 2
dir_chk=disco(next_0)
dir_path(parent,dir_chk,dir_cnt)=next_0
dir_ones(parent,next_0,dir_cnt)=1
DO i=1,3
        IF (adj_3(i,next_0).NE.0.AND.color_v(adj_3(i,next_0)).EQ.1) THEN
                dir_chk=disco(next_0)
                dir_path(parent,dir_chk,dir_cnt)=next_0
                dir_ones(parent,next_0,dir_cnt)=1
                disco(adj_3(i,next_0))=dir_chk+1
                CALL DFS_visit(color_v,adj_3,adj_3(i,next_0),stp_n)
        ELSEIF (adj_3(i,next_0).NE.0.AND.adj_3(i,next_0).EQ.parent) THEN
                dir_rng_ones(parent,:,dir_cnt)=dir_ones(parent,:,dir_cnt)
        ENDIF
ENDDO
color_v(next_0)=3
dir_chk=0
dir_cnt=dir_cnt+1

ENDSUBROUTINE DFS_visit2

!**** S/R find_nbr3 ***** determines chains

RECURSIVE SUBROUTINE find_nbr3(new_0,chn_ct,nHB,&
first_0,adj_3,chn_nde,nde_num,chain_node,ring_node,&
chain_ones,ring_ones,ring_used,stp_n,z_check,o_start,z_adj,0tmp,&
oxy_Z,chn_branch,bchk2)
INTEGER :: i,j,k,m,n,w,t,p,rng_size
INTEGER, INTENT(INOUT) :: new_0, ring_used
INTEGER, INTENT(INOUT) :: chn_ct,nHB(n0),first_0,stp_n
INTEGER :: 0brnch(3),o_init,bchk(3),chn_ct_now
INTEGER, INTENT(INOUT) :: adj_3(3,n0),ring_ones(n0,n0,30)
INTEGER, INTENT(INOUT) :: chn_nde,nde_num,chain_node(n0,20,30)
INTEGER, INTENT(INOUT) :: ring_node(n0,20,30),chain_ones(n0,n0,30)
INTEGER :: mino(1),oNo,o_ct,ones_now(n0),ones_ring(n0)
INTEGER :: chn_now(n0), ring_0(20),ring_02(20),in_chk
INTEGER :: chn_now2(20),0_now,bchk3
REAL(dp),INTENT(INOUT) :: z_check(30),z_adj,0tmp(3,n0),oxy_Z(n0,n0)
INTEGER, INTENT(INOUT) :: o_start,chn_branch(n0,20),bchk2
REAL(dp) :: z_chk_now(30)
```

```
in_chk=0
rng_size=0
mino=0
IF (nHB(new_O).EQ.1) THEN
        chn_nde = chn_nde + 1
        z_check(chn_nde) = 0.0d0
        z_adj = 0.0d0
        ring_used=ring_used+1
ELSEIF (nHB(new_O).EQ.2) THEN
        chn_ct = COUNT(chain_node(nde_num,:,chn_nde).GT.0)+1
        DO j=1,2
                in_chk = COUNT(chain_node(nde_num,:,chn_nde).EQ.adj_3(j,new_O))
                IF (in_chk.EQ.0) THEN
                        chain_node(nde_num,chn_ct,chn_nde)=adj_3(j,new_O)
                        chain_ones(nde_num,:,chn_nde)=0
                        WHERE (chain_node(nde_num,:,chn_nde).NE.0) chain_ones(nde_num,&
                chain_node(nde_num,:,chn_nde),chn_nde)=1
                        first_O=new_O
                        new_O=adj_3(j,new_O)
                        z_check(chn_nde)=z_check(chn_nde) + oxy_Z(first_O,new_O)
                        ring_used=ring_used+1
                        CALL find_nbr3(new_O,chn_ct,nHB,&
first_O,adj_3,chn_nde,nde_num,chain_node,ring_node,&
chain_ones,ring_ones,ring_used,stp_n,z_check,o_start,z_adj,Otmp,&
oxy_Z,chn_branch,bchk2)
                ELSEIF (in_chk.EQ.1.AND.adj_3(j,new_O).NE.first_O.AND.&
                adj_3(j,new_O).EQ.nde_num) THEN
                        z_check(chn_nde)=z_check(chn_nde)+&
                        oxy_Z(new_O,adj_3(j,new_O))
                        IF (DABS(z_check(chn_nde)).GE.z_len-0.5d0) THEN
                                chn_nde=chn_nde+1
                                n_zcheck_stp(stp_n)=n_zcheck_stp(stp_n)+1
                                IF (bchk2.GT.0) THEN
                                chain_node(nde_num,:,chn_nde)=&
                                        chain_node(nde_num,:,chn_nde-1)
                                ENDIF
                        ELSEIF (DABS(z_check(chn_nde)).LT.z_len-0.5d0) THEN
                                ring_used = ring_used+1
                                ring_O = 0
                                ring_O2 = 0
                                ring_O = chain_node(nde_num,:,chn_nde)
                                mino=0
                                oNo=0
                                oNo=adj_3(j,new_O)
                                ring_O(chn_ct)=adj_3(j,new_O)
                                mino=MINLOC(ring_O,MASK=ring_O.EQ.oNo)
                                oNo = mino(1)
                                o_ct = 0
```

```
                DO w=oNo,chn_ct
                        o_ct=o_ct+1
                        ring_O2(o_ct)=ring_O(w)
                ENDDO
                ones_ring=0
                WHERE (ring_O2.NE.0) ones_ring(ring_O2)=1
                ring_ones(nde_num,:,chn_nde)=ones_ring
                ring_node(nde_num,:,chn_nde) = ring_O2
                IF (bchk2.GT.0) THEN
                        chn_nde=chn_nde+1
                        chain_node(nde_num,:,chn_nde)=&
                                chain_node(nde_num,:,chn_nde-1)

                ENDIF
        ENDIF
ELSEIF (in_chk.EQ.1.AND.adj_3(j,new_O).NE.first_O.AND.&
adj_3(j,new_O).NE.0..AND.adj_3(j,new_O).NE.nde_num.&
AND.bchk2.GT.0) THEN
        z_check(chn_nde)=z_check(chn_nde)+oxy_Z(new_O,adj_3(j,new_O))
        IF (DABS(z_check(chn_nde)).GE.z_len-0.5d0) THEN
                n_zcheck_stp(stp_n)=n_zcheck_stp(stp_n)+1
                chn_nde=chn_nde+1
                bchk2=bchk2-1
                IF (bchk2.GT.0) THEN
                chain_node(nde_num,:,chn_nde)=&
                        chain_node(nde_num,:,chn_nde-1)
                ENDIF
        ELSEIF (DABS(z_check(chn_nde)).LT.z_len-0.5) THEN
                ring_used = ring_used+1
                ring_O = 0
                ring_O2 = 0
                ring_O = chain_node(nde_num,:,chn_nde)
                mino=0
                oNo=0
                oNo=adj_3(j,new_O)
                ring_O(chn_ct)=adj_3(j,new_O)
                mino=MINLOC(ring_O,MASK=ring_O.EQ.oNo)
                oNo = mino(1)
                o_ct = 0
                DO w=oNo,chn_ct
                        o_ct=o_ct+1
                        ring_O2(o_ct)=ring_O(w)
                ENDDO
                ones_ring=0
                WHERE (ring_O2.NE.0) ones_ring(ring_O2)=1
                ring_ones(nde_num,:,chn_nde)=ones_ring
                ring_node(nde_num,:,chn_nde) = ring_O2
                IF (bchk2.GT.0) THEN
```

```
                                        chn_nde=chn_nde+1
                                        chain_node(nde_num,:,chn_nde)=&
                                                chain_node(nde_num,:,chn_nde-1)
                                ENDIF
                        ENDIF
                ENDIF
        ENDDO
ELSEIF (nHB(new_O).EQ.3) THEN
        bchk=0
        o_init = first_O
        O_now=new_O
        chn_now2 = chain_node(nde_num,:,chn_nde)
        chn_branch(O_now,:)=0
        chn_branch(O_now,:)=chain_node(nde_num,:,chn_nde)
        chn_now = chain_ones(nde_num,:,chn_nde)
        ones_now=chain_ones(nde_num,:,chn_nde)
        ones_now = chn_now
        z_chk_now(chn_nde) = z_check(chn_nde)
        chn_ct_now = COUNT(chn_branch(O_now,:).GT.0)
        Obrnch=0
        bchk2 = 0
        bchk3=0
        DO k=1,3
                Obrnch(k)=adj_3(k,new_O)
                bchk(k)=COUNT(chn_branch(O_now,:).EQ.Obrnch(k))
        ENDDO
        bchk3 = COUNT(bchk(:).EQ.0)
        DO n=1,3
                bchk2 = bchk3
                in_chk = COUNT(chn_branch(O_now,:).EQ.Obrnch(n))
                IF (in_chk.EQ.0) THEN
                        bchk3 = bchk3-1
                chain_node(nde_num,:,chn_nde)=chn_branch(O_now,:)
                chain_ones(nde_num,:,chn_nde)=0
                WHERE (chain_node(nde_num,:,chn_nde).NE.0) chain_ones(nde_num,&
                chain_node(nde_num,:,chn_nde),chn_nde)=1
                chn_ct=chn_ct_now+1
                chain_node(nde_num,chn_ct,chn_nde)=Obrnch(n)
                chain_ones(nde_num,Obrnch(n),chn_nde)=1
                first_O = O_now
                new_O = Obrnch(n)
                z_check(chn_nde)=z_chk_now(chn_nde)+oxy_Z(first_O,new_O)
                ring_used=ring_used+1
                CALL find_nbr3(new_O,chn_ct,nHB,&
first_O,adj_3,chn_nde,nde_num,chain_node,ring_node,&
chain_ones,ring_ones,ring_used,stp_n,z_check,o_start,z_adj,Otmp,&
oxy_Z,chn_branch,bchk2)
```

```
ELSEIF (in_chk.EQ.1.AND.Obrnch(n).NE.o_init&
.AND.Obrnch(n).NE.0.AND.bchk3.GT.0) THEN
z_check(chn_nde)=z_check(chn_nde)+oxy_Z(O_now,Obrnch(n))
        IF (DABS(z_check(chn_nde)).GE.z_len-0.5d0) THEN
                chn_nde=chn_nde+1
                bchk2=bchk2-1
                n_zcheck_stp(stp_n)=n_zcheck_stp(stp_n)+1
                IF (bchk2.GT.0) THEN
                chain_node(nde_num,:,chn_nde)=chn_branch(O_now,:)
                ENDIF
        ELSEIF (DABS(z_check(chn_nde)).LT.z_len-0.5) THEN
                ring_used=ring_used+1
                ring_O = 0
                ring_O2 = 0
                ring_O = chain_node(nde_num,:,chn_nde)
                mino=0
                oNo=0
                oNo=Obrnch(n)
                chn_ct = COUNT(ring_O.GT.0)+1
                ring_O(chn_ct)=Obrnch(n)
                mino=MINLOC(ring_O,MASK=ring_O.EQ.oNo)
                oNo=mino(1)
                o_ct=0
                DO w=oNo,chn_ct
                        o_ct = o_ct+1
                        ring_O2(o_ct)=ring_O(w)
                ENDDO
                ones_ring=0
                WHERE (ring_O2.NE.0) ones_ring(ring_O2)=1
                ring_ones(nde_num,:,chn_nde)=ones_ring
                ring_node(nde_num,:,chn_nde)=ring_O2
                IF (bchk2.GT.0) THEN
                        chn_nde=chn_nde+1
                        chain_node(nde_num,:,chn_nde)=chn_branch(O_now,:)
                        bchk3=bchk3-1
                        !bchk2=bchk2-1
                ENDIF
        ENDIF
ELSEIF (in_chk.EQ.1.AND.Obrnch(n).NE.o_init&
.AND.Obrnch(n).NE.0.AND.bchk3.EQ.0) THEN
        IF (Obrnch(n).EQ.nde_num.AND.nHB(O_now).EQ.3) THEN
                chn_nde=chn_nde+1
                chain_node(nde_num,:,chn_nde)=chn_now2
                ring_used=ring_used+1
                ring_O = 0
                ring_O2 = 0
                ring_O = chain_node(nde_num,:,chn_nde)
                mino=0
```

```
                                oNo=0
                                oNo=Obrnch(n)
                                chn_ct = COUNT(ring_O.GT.0)+1
                                ring_O(chn_ct)=Obrnch(n)
                                mino=MINLOC(ring_O,MASK=ring_O.EQ.oNo)
                                oNo=mino(1)
                                o_ct=0
                                DO w=oNo,chn_ct
                                        o_ct = o_ct+1
                                        ring_O2(o_ct)=ring_O(w)
                                ENDDO
                                ones_ring=0
                                WHERE (ring_O2.NE.0) ones_ring(ring_O2)=1
                                ring_ones(nde_num,:,chn_nde)=ones_ring
                                ring_node(nde_num,:,chn_nde)=ring_O2

                        ENDIF
                ENDIF
        ENDDO

ENDIF
END SUBROUTINE find_nbr3


!****** S/R sub_chain *********
! there is a similar routine sub_chain2 for when ring connections
! are omitted that only does not contain the ring calculation portion

RECURSIVE SUBROUTINE sub_chain(chain_ones,ring_ones,chn_avg,nChain,&
chn_ones2,rng_ones2,nRing,ring_avg,H2O_chn,H2O_rng,SO3_chn,SO3_rng&
,stp_n,adj_3)
IMPLICIT NONE
INTEGER :: i,j,k
INTEGER, INTENT(INOUT) :: chain_ones(nO,nO,30),ring_ones(nO,nO,30)
REAL(dp),INTENT(INOUT) :: chn_avg,ring_avg
INTEGER, INTENT(INOUT) :: H2O_chn,H2O_rng,SO3_chn,SO3_rng
INTEGER, INTENT(INOUT) :: nChain,chn_ones2(nO,nO,30)
INTEGER, INTENT(INOUT) :: rng_ones2(nO,nO,30),nRing,stp_n
INTEGER :: chn_loc(2), chn_sum(nO,30),chn_max,new_rng(nO)
INTEGER :: new_chn(nO),rng_loc(2),rng_sum(nO,30),rng_max,new_chn2(nO)
INTEGER :: chn_oxy(nO),rng_oxy(nO),chn_br(nO),adj_list(nO)
INTEGER, INTENT(INOUT) :: adj_3(3,nO)
INTEGER :: chn_oxy_br(nO),max_2(30),rng_dif,rng_comp(nO)
adj_list=0
rng_dif=0
max_2=0
chn_br=0
chn_loc=0
```

```
chn_max=0
new_chn=0
new_chn2=0
rng_loc=0
rng_max=0
new_rng=0
rng_oxy=0
chn_oxy=0
chn_oxy_br=0
rng_comp=0
DO i=1,nO
        chn_sum(i,:) = SUM(chn_ones2(i,:,:),dim=1)
        rng_sum(i,:) = SUM(rng_ones2(i,:,:),dim=1)

ENDDO

chn_loc = MAXLOC(chn_sum)
chn_max = chn_sum(chn_loc(1),chn_loc(2))
new_chn = chn_ones2(chn_loc(1),:,chn_loc(2))
adj_list = new_chn
DO i=1,nO
        IF (new_chn(i).EQ.1) THEN
        DO j=1,3
                IF (adj_3(j,i).NE.0) THEN
                        adj_list(adj_3(j,i))=1
                ENDIF
        ENDDO
        ENDIF
ENDDO



WHERE(chn_sum(chn_loc(1),:).EQ.chn_max) max_2=1
rng_loc = MAXLOC(rng_sum)
rng_max = rng_sum(rng_loc(1),rng_loc(2))
new_rng = rng_ones2(rng_loc(1),:,rng_loc(2))
IF (chn_max.GT.2) THEN
        nChain=nChain+1
        chn_avg = chn_avg + DBLE(chn_max)
        chn_oxy=0
        WHERE (new_chn.GT.0) chn_oxy=O_type

        H2O_chn = H2O_chn + COUNT(chn_oxy.EQ.2)
        SO3_chn = SO3_chn + COUNT(chn_oxy.EQ.1)

        SO3_chn_2 = SO3_chn_2 + COUNT(chn_oxy.EQ.1)
        H2O_chn_2 = H2O_chn_2 + COUNT(chn_oxy.EQ.2)
        new_chn2=new_chn
```

```
DO i=1,nO
        DO j=1,30
                chn_br = 0
                chn_oxy_br=0
                IF (ANY(chn_ones2(i,:,j).EQ.adj_list.AND.adj_list.GT.0)) THEN
                WHERE (chn_ones2(i,:,j).NE.new_chn2.AND.new_chn2.EQ.0)
                        chn_br = 1
                        new_chn2 = 1
                ENDWHERE

                WHERE (chn_br.GT.0) chn_oxy_br = O_type
                        chn_ones2(i,:,j)=0
                        IF (i.EQ.chn_loc(1).AND.max_2(j).EQ.1.AND.j.&
                        NE.chn_loc(2)) THEN
                                H2O_chn_2=H2O_chn_2+COUNT(chn_oxy_br.EQ.2)
                                SO3_chn_2=SO3_chn_2+COUNT(chn_oxy_br.EQ.1)
                        ENDIF
                ENDIF
        ENDDO
ENDDO
CALL sub_chain(chain_ones,ring_ones,chn_avg,nChain,&
chn_ones2,rng_ones2,nRing,ring_avg,H2O_chn,H2O_rng,SO3_chn,SO3_rng,&
stp_n,SO3_brchn,H2O_brchn,adj_3)
ELSEIF (chn_max.LE.2.AND.rng_max.GT.2) THEN
        nRing=nRing+1
        ring_avg = ring_avg + DBLE(rng_max)
        WHERE (new_rng.GT.0) rng_oxy=O_type
        H2O_rng = H2O_rng + COUNT(rng_oxy.EQ.2)
        SO3_rng = SO3_rng + COUNT(rng_oxy.EQ.1)

DO i=1,nO
        DO j=1,30
        IF (ALL(rng_ones2(i,:,j).EQ.new_rng)) THEN
                rng_ones2(i,:,j)=0
        ENDIF
        ENDDO
ENDDO
DO i=1,nO
        DO j=1,30
                rng_dif = 0
                rng_comp = 0
                IF (ANY(rng_ones2(i,:,j).EQ.new_rng.AND.new_rng.GT.0)) THEN
                        WHERE (rng_ones2(i,:,j).EQ.1.AND.new_rng.EQ.1) rng_comp=1
                        rng_dif = SUM(rng_comp)-rng_sum(i,j)
                IF (rng_dif.EQ.0) THEN
                        nRing=nRing-1
                        ring_avg = ring_avg - DBLE(rng_max)
```

```
                    H2O_rng = H2O_rng - COUNT(rng_oxy.EQ.2)
                    SO3_rng = SO3_rng - COUNT(rng_oxy.EQ.1)
                    GOTO 10
                ENDIF
                ENDIF
            ENDDO
ENDDO
10 CALL sub_chain(chain_ones,ring_ones,chn_avg,nChain,&
chn_ones2,rng_ones2,nRing,ring_avg,H2O_chn,H2O_rng,SO3_chn,SO3_rng&
,stp_n,SO3_brchn,H2O_brchn,adj_3)
ENDIF

END SUBROUTINE sub_chain


END MODULE calc_MIC
```

```
MODULE H3O_water

USE data_type
USE common_data
USE Format_atoms
USE calc_MIC
IMPLICIT NONE

CONTAINS

!****** S/R Excess_H ********
SUBROUTINE Excess_H
IMPLICIT NONE
INTEGER :: i,j,k,m,n,p,b,q
INTEGER :: new_loc(stps),ox_ind(1)
REAL(dp) :: Oxyz(3),Hxyz(3,nH),HOd(nH), h3_chk(nO)
REAL(dp) :: h1(1),h2(1),h3(1),hyd_dist(3,nO)
INTEGER :: ind1(1),ind2(1),ind3(1), ox_hy(nH),pchk(stps)
ALLOCATE(ex_loc(stps))
ALLOCATE(hyd_ind(3,nO,stps))
ox_ind = 0
ex_loc = 0
hyd_ind = 0
pchk=0
OPEN(10,file='H3O_oxy.dat')
DO i=1,stps
        h3_chk = 0.0d0
        ox_hy = 0
        DO j=1,nO
                Oxyz = 0.0d0
                Hxyz = 0.0d0
                HOd = 0.0d0
                h1 = 0.0d0
                h2 = 0.0d0
                h3 = 0.0d0
                ind1 = 0
                ind2 = 0
                ind3 = 0
                Oxyz = atoms_O(:,j,i)
                FORALL (k=1:nH) Hxyz(:,k)=atoms_H(:,k,i)-Oxyz
                FORALL (k=1:nH) Hxyz(3,k)=Hxyz(3,k)-z_len*&
                ANINT(Hxyz(3,k)/(z_len))

                FORALL (k=1:nH) HOd(k)=SUM(Hxyz(:,k)**2,dim=1)
                HOd = DSQRT(HOd)
                h1 = MINVAL(HOd)
                ind1 = MINLOC(HOd)
                h2 = MINVAL(HOd,MASK=HOd.GT.h1(1))
```

```
                ind2 = MINLOC(HOd,MASK=HOd.GT.h1(1))
                h3 = MINVAL(HOd,MASK=HOd.GT.h2(1))
                ind3 = MINLOC(HOd,MASK=HOd.GT.h2(1))
                hyd_ind(1,j,i) = ind1(1)
                hyd_ind(2,j,i) = ind2(1)
                hyd_ind(3,j,i) = ind3(1)
                hyd_dist(1,j) = h1(1)
                hyd_dist(2,j) = h2(1)
                hyd_dist(3,j) = h3(1)
                ox_hy(ind1(1)) = 1
                ox_hy(ind2(1)) = 1

        ENDDO

        DO m=1,nO
                DO n=1,nO
                IF (m.NE.n) THEN
                        IF (hyd_ind(2,n,i).EQ.hyd_ind(2,m,i)) THEN
                                ox_hy(hyd_ind(2,m,i)) = 1
                                IF (hyd_dist(3,n).LT.hyd_dist(3,m)) THEN
                                        ox_hy(hyd_ind(3,n,i)) = 1
                                ENDIF
                        ENDIF
                ENDIF
                ENDDO
        ENDDO
        DO q=1,nH
                IF (ox_hy(q).EQ.0) THEN
                        pchk(i) = pchk(i)+1
                        WHERE (hyd_ind(3,:,i).EQ.q)
                                h3_chk = hyd_dist(3,:)
                        ELSEWHERE
                                h3_chk = 10.0d0
                        ENDWHERE
                        ox_ind = MINLOC(hyd_dist(3,:))
                ENDIF
        ENDDO
        ox_ind = MINLOC(h3_chk)
        new_loc(i) = ox_ind(1)
        ex_loc(i) = ox_ind(1)
        WRITE(10,*) ex_loc(i)
ENDDO
CLOSE(10)
END SUBROUTINE Excess_H

!***** S/R delta data ****

SUBROUTINE delta_data
```

```
IMPLICIT NONE
INTEGER :: i,j,k,n_origin
REAL(dp) :: delta_all(101),d_OO_bin(101,201),delta_bin(101),dAB(3)
INTEGER :: max_bin_d,max_bin_O,bin_d,bin_O,d_stop,O_start,O_stop
REAL(dp) :: sm_avg,lg_avg,dr_d,dr_O,p_cord(3,stps),del_1,sum_h3o
INTEGER :: Hact(stps),bin_Dall, p_count,h_ind(3),tmpH(1)
REAL(dp) :: d_small, d_large, d_tot, pct_sm, pct_lg,rval_d,rval_O
REAL(dp) :: hz_chk,t_val,dt,minz(1)
REAL(dp), ALLOCATABLE :: msd_H(:)
REAL(dp) :: H_bin(251),dr_H,H_xy,H_wall,Hd_val
INTEGER :: max_bin_H,bin_H
H_bin=0.0d0
Hd_val=0.0d0
bin_H = 0
max_bin_H = 250
dr_H = radius/DBLE(max_bin_H)
H_xy=0.0d0
H_wall=0.0d0
hz_chk=0.0d0;minz=0.0d0
delta_all=0.0d0; d_OO_bin=0.0d0; delta_bin=0.0d0;dAB=0.0d0
sm_avg=0.0d0; lg_avg=0.0d0; del_1=0.0d0;pct_sm=0.0d0;pct_lg=0.0d0
max_bin_d=100; max_bin_O=200; p_count=0
bin_d=0; bin_O=0; bin_Dall=0;h_ind=0
d_stop=65; O_start=161; O_stop=196; Hact=0
p_cord = 0.0d0; d_small=0.0d0; d_large=0.0d0; d_tot=0.0d0
dr_d=1.0d0/DBLE(max_bin_d); dr_O=2.8d0/DBLE(max_bin_O)
rval_d = 0.0d0; rval_O = 0.0d0; sum_h3o=0.0d0
n_origin = stps/2
t_val = 0.0d0; dt = 0.5d0
ALLOCATE(msd_H(n_origin+1))
msd_h=0.0d0
DO i=1,stps
        p_count = 0
        dAB = 10.0d0
        h_ind = 0
        tmpH = 0
        DO j=1,nH
                IF (HB_track(i,j,1).NE.0) THEN
                        del_1 = -1.0d0*(HB_d(1,j,i)-HB_d(2,j,i))
                        bin_Dall = INT(del_1/dr_d)+1
                        IF (bin_Dall.LT.max_bin_d) THEN
                                delta_all(bin_Dall)=delta_all(bin_Dall)+1.0d0
                        ENDIF
                        IF (HB_track(i,j,4).EQ.ex_loc(i)) THEN
                                p_count = p_count+1
                                h_ind(p_count) = j
                                dAB(p_count)= del_1
```

```
                        ENDIF
                ENDIF
        ENDDO
        tmpH = MINLOC(dAB)
        Hact(i) = h_ind(tmpH(1))
        p_cord(:,i) = atoms_H(:,Hact(i),i)

        bin_d = INT(dAB(tmpH(1))/dr_d)+1
        bin_O = INT(HB_d(3,Hact(i),i)/dr_O)+1
        d_OO_bin(bin_d,bin_O)=d_OO_bin(bin_d,bin_O)+1.0d0
        delta_bin(bin_d) = delta_bin(bin_d)+1.0d0
        IF (dAB(tmpH(1)).LE.0.1d0) THEN
                d_small = d_small + 1.0d0
                d_tot = d_tot + 1.0d0
        ELSEIF (dAB(tmpH(1)).GT.0.3d0) THEN
                d_large = d_large + 1.0d0
                d_tot = d_tot + 1.0d0
        ENDIF
ENDDO
DO i=1,stps-1
        hz_chk = p_cord(3,i+1)-p_cord(3,i)
        p_cord(3,i+1)=p_cord(3,i+1)-ANINT(hz_chk/z_len)*z_len
ENDDO
minz = MINVAL(p_cord(3,:))
IF (minz(1).LT.0.0d0) THEN
        DO i=1,stps
                p_cord(3,i) = p_cord(3,i) + minz(1)
        ENDDO
ELSEIF (minz(1).GE.0.0d0) THEN
        DO i=1,stps
                p_cord(3,i) = p_cord(3,i) - minz(1)
        ENDDO
ENDIF


DO i=1,n_origin
        msd_H(:)=msd_H(:)+(p_cord(3,i:i+n_origin)-p_cord(3,i))**2
ENDDO
msd_H = msd_H/DBLE(n_origin)
OPEN(40,file='Proton_coord.dat')
DO i=1,stps
        WRITE(40,*) p_cord(:,i)
ENDDO
CLOSE(40)
OPEN(44,file='MSD_Proton.dat')
DO i=1,n_origin+1
        t_val = DBLE(i-1)*dt
```

```
        WRITE(44,*) t_val,msd_H(i)
ENDDO
CLOSE(44)
DO i=1,stps
        H_xy = DSQRT(p_cord(1,i)**2+p_cord(2,i)**2)
        H_wall = radius - H_xy
        bin_H = INT(H_wall/dr_H)+1
        H_bin(bin_H)=H_bin(bin_H)+1.0d0
ENDDO
OPEN(45,file='Proton_wall_RDF.dat')
DO i=1,max_bin_H+1
        Hd_val = DBLE(i-1)*dr_H
        WRITE(45,*) Hd_val,H_bin(i)
ENDDO
CLOSE(45)
sm_avg = d_small/stps
lg_avg = d_large/stps
pct_sm = d_small/d_tot
pct_lg = d_large/d_tot
OPEN(46,file='excess_state.dat')
WRITE(46,*) 'Zundel total   ',sm_avg
WRITE(46,*) 'Eigen total    ',lg_avg
WRITE(46,*) 'Class. Zundel  ',pct_sm
WRITE(46,*) 'Class. Eigen   ',pct_lg
CLOSE(46)
sum_h3o=SUM(d_OO_bin)
DO i=2,max_bin_d+1
        DO j=1,max_bin_O+1
                IF (d_OO_bin(i,j).NE.0.0d0) THEN
                        sum_h3o=sum_h3o+d_OO_bin(i,j)
                ENDIF
        ENDDO
ENDDO
d_OO_bin = d_OO_bin/(dr_d*dr_O*sum_h3o)
delta_bin = delta_bin/(dr_d*SUM(delta_bin))
delta_all = delta_all/(dr_d*SUM(delta_all))
OPEN(41,file='delta_bin.dat')
OPEN(42,file='3d_distr.dat')
OPEN(43,file='all_delta.dat')
DO i=1,d_stop+1
        rval_d = DBLE(i-1)*dr_d
        WRITE(41,*) rval_d,delta_bin(i)

        DO j=O_start,O_stop+1
                rval_O = DBLE(j-1)*dr_O
                WRITE(42,*) rval_d,rval_O,d_OO_bin(i,j)
                IF (rval_d.NE.0.0d0) THEN
                        WRITE(42,*) -1.0d0*rval_d,rval_O,d_OO_bin(i,j)
```

```
                ENDIF
        ENDDO
ENDDO
DO i=1,max_bin_d+1
        rval_d = DBLE(i-1)*dr_d
        WRITE(43,*) rval_d,delta_all(i)
ENDDO
END SUBROUTINE delta_data

END MODULE H3O_water
```

Appendix B. Publications and Presentations

Presentations:

1. "*First Principles Based Simulations of Confinement of Water and Triflic Acid*" Oral presentation at the 223rd ECS Meeting, *Toronto, Ontario, Canada May 15, 2013*.
2. "*Proton Dissociation and Transfer in PEM Ionomers with Multiple and Distinct Pendant Acid Groups: An Ab Initio Study*" Poster presentation at SSPC 16 Conference. *Grenoble, France, September 13, 2012*.
3. "*Hydration and Proton Transfer in 3M™ PEM Ionomers: An Ab Initio Study*" Poster presentation at 221st ECS Meeting, *Seattle, WA May 9, 2012*.
4. "*Proton Dissociation and Transfer in PEM Ionomers with Multiple and Distinct Pendant Acid Groups: An Ab Initio Study*" Poster presentation at NSF IGERT 2012 Annual PI Meeting, *Washington, D.C. May 31, 2012*.
5. "*Proton Dissociation and Transfer in PEM Ionomers with Multiple and Distinct Pendant Acid Groups: An Ab Initio Study*" Poster presentation at the 2012 Electrochemical Energy Storage and Conversion Forum, *Knoxville, TN April 19-20, 2012*.
6. "*Local Hydration and Proton Transport in PEM Ionomers with Various Protogenic Groups*" Poster presentation at Fall Creek Falls 2011 Conference – Virtualizing Energy, *Gatlinburg, TN September 15, 2011*.
7. "*Hydration and Proton Transfer in 3M™ PEM Ionomers: An Ab Initio Study*" Poster presentation at the 2011 Materials Research Society Fall Meeting and Exhibit, *Boston, MA November 2, 2011*.
8. "*3M PFSA and Imide-Based Ionomer Fragments*" Oral presentation at PacifiChem 2010 in *Honolulu, HI December 19, 2010.*
9. "*Hydration and Proton Transfer in Oligomeric Fragments of 3M Ionomers with various Protogenic Groups*" Poster at Solid State Proton Conductors 15 (SSPC-15),*Santa Barbara, CA August 16-17, 2010*.

Publications:

1. Clark II, J. K.; Paddison, S. J., *Ab Initio* Modeling of Transport and Structure of Solid State Proton Conductors. In *Solid State Proton Conductors: Properties and Applications in Fuel Cells*, Knauth, P.; Di Vona, M. L., Eds. Wiley: Chichester, UK, 2012; pp. 241-290.
2. Clark II, J. K.; Habenicht, B. F.; Paddison, S. J., *Ab initio Molecular Dynamics Simulations of Aqueous Triflic Acid Confined in Carbon Nanotubes*. Physical Chemistry Chemical Physics, **2014**, submitted, manuscript ID: CP-ART-03-2014-001066.
3. Clark II, J. K.; Paddison, S. J., *Ab initio Molecular Dynamics Simulations of Water and an Excess Proton in Water Confined in Carbon Nanotubes*. Physical Chemistry Chemical Physics, **2014**, submitted, manuscript ID: CP-ART-01-2014-000415.

4. Clark II, J. K.; Paddison, S. J., *Proton Dissociation and Transfer in Proton Exchange Membrane Ionomers with Multiple and Distinct Pendant Acid Groups*: *An Ab Initio Study*. Electrochimica Acta, **2013**, *101*, 279-292.

5. Clark II, J. K.; Paddison, S. J., *Side Chain Flexibility in Perfluorosulfonic Acid Ionomers: An Ab Initio Study*. Journal of Physcial Chemistry A, **2013**, *117*, 10534-10543.

6. Clark II, J. K.; Paddison, S. J.; Hamrock, S. J., *The Effect of Hydrogen Bond Reorganization and Equivalent Weight on Proton Transfer in 3M Perfluorosulfonic Acid Ionomers*. Physical Chemistry Chemical Physics, **2012**, *14*, 16349-16359.

7. Clark II, J. K.; Paddison, S. J.; Eikerling, M.; Dupuis, M.; Zawodzinski, T. A., *A Comparative Ab Initio Study of the Primary Hydration and Proton Dissociation of Various Imide and Sulfonic Acid Ionomers*. Journal of Physical Chemistry A, **2012**, *7*, 1801-1813.

8. Clark II, J. K.; Paddison, S. J., *Hydration and Proton Transfer in 3M™ PEM Ionomers: An Ab Initio Study*. MRS Proceedings, **2012**, *1384*, doi:10.1557/opl.2012.187.

9. Clark II, J. K.; Paddison, S. J., *The Effect of Side Chain Connectivity and Local Hydration on Proton Transfer in 3M Perfluorosulfonic Acid Membranes*. Solid State Ionics, **2012**, *213*, 83-91.

10. Wang, C.; Clark II, J. K.; Kumar, M.; Paddison, S. J., *An Ab Initio Study of the Primary Hydration and Proton Transfer of CF_3SO_3H and $CF_3O(CF_2)_2SO_3H$: Effects of the Hybrid Functional and Inclusion of Diffuse Functions*. Solid State Ionics, **2011**, *199*, 6-13.

THE JOURNAL OF PHYSICAL CHEMISTRY A

Article

pubs.acs.org/JPCA

A Comparative Ab Initio Study of the Primary Hydration and Proton Dissociation of Various Imide and Sulfonic Acid Ionomers

Jeffrey K. Clark, II,[†] Stephen J. Paddison,*[,†] Michael Eikerling,[‡] Michel Dupuis,[§] and Thomas A. Zawodzinski, Jr.[†]

[†]Department of Chemical and Biomolecular Engineering, University of Tennessee, Knoxville, Tennessee 37996, United States

[‡]Department of Chemistry, Simon Fraser University, Burnaby, BC V5A 1S6, Canada

[§]Chemical and Materials Science Division, Pacific Northwest National Laboratory, Richland, Washington 99352, United States

Supporting Information

ABSTRACT: We compare the role of neighboring group substitutions on proton dissociation of hydrated acidic moieties suitable for proton exchange membranes through electronic structure calculations. Three pairs of ionomers containing similar electron withdrawing groups within the pair were chosen for the study: two fully fluorinated sulfonyl imides ($CF_3SO_2NHSO_2CF_3$ and $CF_3CF_2SO_2NHSO_2CF_3$), two partially fluorinated sulfonyl imides ($CH_3SO_2NHSO_2CF_3$ and $C_6H_5SO_2NHSO_2CF_2CF_3$), and two aromatic sulfonic acid based materials ($CH_3C_6H_4SO_3H$ and $CH_3OC_6H_3OCH_3C_6H_4SO_3H$). Fully optimized counterpoise (CP) corrected geometries were obtained for each ionomer fragment with the inclusion of water molecules at the B3LYP/6-311G** level of density functional theory. Spontaneous proton dissociation was observed upon addition of three water molecules in each system, and the transition to a solvent-separated ion pair occurred when four water molecules were introduced. No considerable quantitative or qualitative differences in proton dissociation, hydrogen bond networks formed, or water binding energies were found between systems containing similar electron withdrawing groups. Each of the sulfonyl imide ionomers exhibited qualitatively similar results regarding proton dissociation and separation. The fully fluorinated sulfonyl imides, however, showed a greater propensity to exist in dissociated and ion-pair separated states at low degrees of hydration than the partially fluorinated sulfonyl imides. This effect is due to the additional electron withdrawing groups providing charge stabilization as the dissociated proton migrates away from the imide anion.

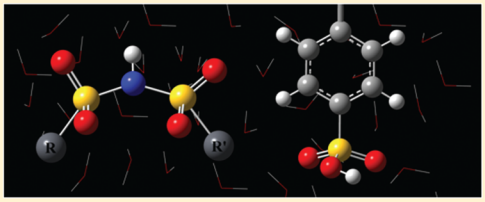

INTRODUCTION

The ever increasing demand for energy and simultaneously rising concerns about global climate change associated with the burning of fossil fuels have led to intense efforts in the development of renewable sources of energy. Among the promising candidates is hydrogen to be converted electrochemically in proton exchange membrane (PEM) fuel cells. Currently, these are the frontrunners in fuel cell technology due to their high energy conversion efficiency, wide range of applicability, and minimal environmental impact.[1,2] The PEM fulfills key functions as both the separator of the electrodes and reactant gases and the proton-conducting electrolyte in these devices.[3] The potential utilization of PEM fuel cells for vehicular, stationary, and portable applications places specific demands on the membrane material, including high proton selectivity, long-time chemical and thermal stability in an oxidative environment at temperatures as high as 120 °C, and high proton conductivity ($\geq$0.1 S cm^{-1}) under low humidity conditions (25−50% relative humidity).[4] While considerable efforts have been made in the development of materials that meet all of these requirements, the most widely used PEM materials are perfluorosulfonic acid (PFSA) ionomers with Nafion manufactured by DuPont serving as the benchmark.

A PFSA ionomer consists of a hydrophobic poly(tetrafluoroethylene) (PTFE) backbone functionalized with pendant perfluorinated side chains each terminated by a single hydrophilic sulfonic acid group ($-SO_3H$). Hydrophilic domains are formed upon hydration of these materials through solvation and aggregation of the sulfonic acid groups.[3,5,6] The hydration of these protogenic groups leads to proton dissociation into the aqueous domain where the protons become mobile, facilitating long-range proton transport through the membrane[3,7] via vehicular or structural diffusion.[8−12] Mechanisms and rates bear features similar to those observed in bulk water.[13−17] The presence of water plays a critical role in the formation of free protonic charge carriers and, thus, proton mobility in PFSA ionomers. The high proton conductivity in Nafion, however, is only observed under high degrees of hydration (relative humidity).[18] The necessity of

Received: October 12, 2011
Revised: January 19, 2012
Published: January 25, 2012

high hydration for sufficient operation restricts the working temperature to below the boiling point of water which, in turn, adversely affects the carbon monoxide tolerance of the electrocatalyst. Moreover, significant water "crossover" due to electro-osmotic drag and permeation in highly hydrated systems severely affects the efficiency of the fuel cell.[19]

These challenges have led efforts toward finding alternative PEM materials which exhibit high proton conductivity under lower humidity conditions. Ongoing research on how the chemical structure determines proton conductivity in PEM ionomers has been reviewed by several authors and continues to expand the fundamental understanding needed for the further development of alternative materials.[2,3,7,20−23] Many approaches have focused on modification of currently available PFSA ionomers, such as replacing the sulfonic acid groups with other protogenic groups and alteration to the backbone and/or side chain chemistry, while other methods concentrate on the synthesis of entirely novel proton conducting polymeric materials.[24−26] Among the materials receiving interest are sulfonyl imide analogues of Nafion and sulfonated aryl main-chain polymers. With regard to the former, bis-[(perfluoroalkyl)sulfonyl] imide analogues of Nafion exhibit greater thermal stability,[27] stronger gas phase acidity,[28] and higher proton conductivity at low hydration levels when compared to typical PFSA ionomers.[27,29] Furthermore, these materials contain two independent sites for structural modification adjacent to the sulfonyl imide, while the sulfonic acid based membranes only contain one site, thus giving them greater potential for optimizing ionomer properties. Aryl main-chain polymers, such as sulfonated poly(ether ether ketone) (sPEEK), have also been an area of interest, as they are relatively inexpensive, widely available in various chemical compositions, and have been shown to exhibit good chemical, mechanical, and thermal stability.[5,20,30−32] A recent experimental study reported on the synthesis of several sPEEK ionomers via post sulfonation reactions of PEEKs with various side substituents and evaluated the properties related to PEM ionomers for fuel cell application.[32] One promising material uncovered in this investigation was phenylated sulfonated poly(ether ether ketone ketone) (Ph-sPEEKK) which exhibited lower methanol permeability than Nafion with a higher proton conductivity (0.15 S cm^{-1}) at 100 °C.

The PEMs mentioned above exhibit proton conductivities that are strongly dependent on the level of hydration.[4] Furthermore, hydrogen bonding is known to be an essential component to proton mobility in materials of this type. However, exactly how the specific ionomer chemistry governs proton conductivity remains to be completely elucidated. A full understanding of how protons transfer through the membrane will undoubtedly aid in the progression of PEM materials. This, however, requires a molecular-level understanding of the formation and breaking of hydrogen bonds within these highly complex systems. In particular, the structural diffusion of protons in aqueous media requires shuttling of the proton through the hydrogen bonding by means of a series of transformations between an Eigen cation ($H_9O_4^+$) and a Zundel cation ($H_5O_2^+$).[33−36] As few experimental techniques are capable of resolving this information, molecular modeling techniques have been utilized in attempts to reveal the underlying characteristics of proton transport in these materials. Empirical valence bond (EVB) schemes[37−39] designed to allow for dynamic proton shuttling have been utilized to study proton mobility and solvation in PFSA systems.[40−43] These simulations revealed the significant influence sulfonate ions have on the proton solvation structure. Structural diffusion was found to be the dominant mechanism for contact ion pair/solvent-separated ion pair transitions important in proton diffusion. Evidence of structural diffusion has also been observed in *ab initio* molecular dynamics (AIMD) simulations employed to study proton transport in model PFSA systems,[44−49] as well as other PEMs,[50,51] at various levels of hydration and protogenic group density. Further insight into the specific molecular features that contribute to proton dissociation and separation in PEM ionomers has also been gained through extensive utilization of *ab initio* electronic structure calculations.

The significant computational cost of electronic structure calculations limited early investigations on PEM membranes to small, representative fragments of these materials, such as triflic acid (CF_3SO_3H) and the Nafion side chain, with only a single added water molecule.[52,53] Later studies explored the local hydration and proton dissociation of larger fragments of PFSA ionomers.[54−58] In addition to PFSA ionomers, electronic structure calculations have been used to explore local hydration and proton dissociation in other fragments of various PEM ionomers and acidic moieties including aryl main-chain sulfonic acids,[54,59] sulfonyl imides,[59,60] imidazole,[61] phosphonic acid,[61,62] phosphoric acid,[63] and carboxylic acid.[64] The effects multiple pendant perfluorinated sulfonic acid side chains located on the same PTFE backbone have on local hydration and proton dissociation have also been investigated on the short side chain (SSC) PFSA membrane[65−68] and the 3 M PFSA membrane.[69] These studies revealed the importance protogenic group separation and side chain connectivity through hydrogen bonding have on proton dissociation and the state of the dissociated proton(s) in these materials under conditions of low hydration. Many of the studies also went beyond solely the choice of protogenic group by exploring how the side chain chemistry governs proton dissociation in a variety of ionomer fragments with different substituent groups.[54,58−60,62]

The present study revisits previous calculations on various sulfonyl imide moieties[59,60] and aryl main-chain sulfonic acid ionomers[54,59] to provide a direct comparison between systems having similar protogenic groups but different chemical groups bonded β to the acid group. Specifically, we compare (1) the fully fluorinated sulfonyl imide $CF_3SO_2NHSO_2CF_3$ with $CF_3CF_2SO_2NHSO_2CF_3$, (2) the partially fluorinated sulfonyl imide $CH_3SO_2NHSO_2CF_3$ with $C_6H_5SO_2NHSO_2CF_2CF_3$, and (3) the *para*-toluene sulfonic acid ($CH_3C_6H_4SO_3H$) with a representative sPEEK fragment ($CH_3OC_6H_3OCH_3C_6H_4SO_3H$). In each pair, the local hydration of the acidic groups along with the binding energies of the water molecules to the fragments are compared.

This paper is organized as follows. The first section contains a brief description of the computational methods used to determine the energetic and structural information for each acid moiety. The results are then presented and discussed in the following section for each pair of systems comparing proton dissociation, energetically preferred optimized geometries, hydrogen bonding, binding energies, and partial atomic charges.

■ COMPUTATIONAL METHODS

All electronic structure calculations of the ionomeric fragments were performed using the Gaussian 09 suite of programs.[70] Geometry optimizations over all degrees of freedom were

Table 1. Energies of Optimized $CF_3SO_2NHSO_2CF_3$ Fragments[a]

n H_2O	E_{elec}[b]	E_{ZPE}[c]	ΔE[d] (kcal/mol)	ΔE_{ZPE}[e] (kcal/mol)	ΔE_{BSSE}[f] (kcal/mol)
0	−1828.05495	0.064973			
1	−1904.52580	0.089502	−14.7 (−14.7)[g]	−12.7 (−12.7)[g]	−9.1 (−9.1)[g]
2	−1980.99732	0.114664	−29.8 (−14.9)	−25.4 (−12.7)	−18.0 (−9.0)
3	−2057.47673	0.141299	−49.8 (−16.6)	−42.1 (−14.0)	−29.9 (−10.0)
4	−2133.95013	0.165860	−66.1 (−16.5)	−56.3 (−14.1)	−40.7 (−10.2)
5	−2210.42720	0.192585	−84.7 (−16.9)	−71.5 (−14.3)	−50.3 (−10.1)

[a]Energetics for structures optimized at the B3LYP/6-311G** level. [b]Total electronic energy in hartrees. [c]Zero point energy (ZPE) in hartrees. [d]Binding energy based on uncorrected total electronic energy. [e]Binding energy based on ZPE corrected electronic energy. [f]Binding energy based on CP correction to the BSSE of reoptimized structure. [g]Value in parentheses is binding energy per water molecule.

carried out on each of the acid moieties via conjugate gradient methods[71] without symmetry constraints. Initial optimizations invoked Hartree−Fock theory with the 6-31G** split valence basis set.[72] The resulting structures were then refined with hybrid density functional theory (DFT) employing Becke's three-parameter functional (B3LYP)[73,74] and the same basis set followed by optimizations performed using a larger basis set at the B3LYP/6-311G** level of theory.[75] Water molecules were subsequently added to the fully optimized systems at a variety of different initial positions, and full optimizations were performed using the protocol described above. Additional searches for minimum energy conformations were carried out by performing optimizations on initially dissociated and/or solvent-separated ion pair configurations. Vibrational frequencies and zero point energies (ZPEs) were determined for all minimum energy structures at the B3LYP/6-311G** level. The counterpoise (CP) method of Boys and Bernardi[76] was employed to explore the effects of basis set superposition error (BSSE) on the water binding energies calculated from the CP-corrected optimized geometries and vibrational frequencies at the B3LYP/6-311G** level. As counterpoise optimizations are known to potentially change the resulting minimum energy structure in some molecular systems,[77] these calculations were repeated on different conformations and geometries for each system at all levels of hydration. All reported data and optimized geometries presented are based on the CP-corrected optimized geometries. The binding energies of water molecules to the ionomer fragments were calculated using uncorrected, ZPE-corrected, and BSSE-corrected minimum electronic energies. Partial atomic charges were also computed with the Merz−Singh−Kollman (MK) scheme on the fully optimized CP-corrected geometries (B3LYP/6-311G**) for all systems at each hydration level.[78,79]

The B3LYP functional was selected for these DFT calculations for comparison of this work to previous studies on these ionomer fragments which used B3LYP.[53,54,58,60,65−68,80,81] Although these calculations were meant to provide only relative information about the different ionomer fragments, not to test the validity of the use of DFT over other methods or the choice of DFT functional, calculations were also performed using the M06 density functional[82] and second-order Møller−Plesset theory (MP2) using the 6-311G** basis set to compare the results to those obtained with B3LYP. Complete information concerning the results obtained with the M06 functional and MP2 theory is reported in the Supporting Information, and only a summary is given here.

The M06 and MP2 calculations were not corrected for BSSE due to the overwhelming computational cost of counterpoise-corrected optimizations. Thus, the results were compared to those obtained from the non-CP-corrected optimizations and vibrational frequencies at the B3LYP/6-311G** level. The optimized geometries obtained using the M06 functional and MP2 calculations were qualitatively similar to those obtained using B3LYP for each ionomer fragment. Namely, the average hydrogen bond lengths at all hydration levels agreed very well among each level tested and root-mean-square (rms) deviations from the B3LYP hydrogen bond topography (as determined by changes in the O···O distances of hydrogen bonds) were minimal as nearly identical optimized geometries were obtained at each level. In each of the fragments hydrated with 1−3 water molecules, the rms deviation in hydrogen bond lengths from the B3LYP calculations did not exceed 0.03 Å. After the addition of four water molecules, the deviation was found to increase in each ionomer but was still less than 0.07 Å. Furthermore, the uncorrected and ZPE-corrected B3LYP binding energies of the water molecule(s) to the ionomer fragments agreed to within less than 1 kcal/mol, in general, with the values determined for the higher level MP2 calculations. The values obtained using the M06 density functional resulted in binding energy magnitudes consistently higher than those of the MP2 calculations with greater deviation than the B3LYP binding energies but still to within a reasonable degree. Hence, the choice of density functional does not appear to greatly affect the results of these calculations at low hydration levels. The relative energy differences related to different adopted configurations of individual ionomers at the same hydration level contained variability between the B3LYP and MP2 calculations, but these values were within a reasonable range and the same overall trends were observed. The computational cost of geometry optimizations and frequency calculations starting from the same HF optimized geometries was immensely more computationally expensive for the MP2 calculations than the B3LYP calculations which each yielded nearly identical optimized geometries and comparable relative energies and binding energies. Thus, while DFT is known to have limitation in the description of weak interactions, the difference in the obtained information using MP2 over DFT does not merit the overwhelmingly greater computational expense, especially without experimental measures to test the validity of the results. Nonetheless, the insight into the relative energies and the strength of the interaction of these molecules from the computed binding energies is only a relative comparison among the different ionomers, not absolute values.

■ RESULTS AND DISCUSSION

Fully Fluorinated Sulfonyl Imides. Uncorrected, ZPE-corrected, and BSSE-corrected binding energies of the water molecules to the $CF_3SO_2NHSO_2CF_3$ and CF_3CF_2-

Table 2. Energies of Optimized $CF_3CF_2SO2NHSO_2CF_3$ Fragments[a]

n H_2O	E_{elec}[b]	E_{ZPE}[c]	ΔE[d] (kcal/mol)	ΔE_{ZPE}[e] (kcal/mol)	ΔE_{BSSE}[f] (kcal/mol)
0	−2065.90522	0.07697			
1	−2142.37599	0.10150	−14.6 (−14.6)[g]	−12.6 (−12.6)[g]	−9.0 (−9.0)[g]
2	−2218.84730	0.12665	−29.6 (−14.8)	−25.2 (−12.6)	−17.9 (−9.0)
3	−2295.32518	0.15300	−48.7 (−16.2)	−41.1 (−13.7)	−29.6 (−9.9)
4	−2371.80091	0.17794	−66.5 (−16.6)	−56.6 (−14.2)	−40.8 (−10.2)
5	−2448.27792	0.20461	−85.0 (−17.0)	−71.8 (−14.4)	−50.4 (−10.1)

[a]Energetics for structures optimized at the B3LYP/6-311G** level. [b]Total electronic energy in hartrees. [c]Zero point energy (ZPE) in hartrees. [d]Binding energy based on uncorrected total electronic energy. [e]Binding energy based on ZPE corrected electronic energy. [f]Binding energy based on CP correction to the BSSE of reoptimized structure. [g]Value in parentheses is binding energy per water molecule.

$SO_2NHSO_2CF_3$ sulfonyl imide minimum energy conformations are given in Tables 1 and 2, respectively. As hydrogen bonding is a crucial feature of proton transport in PEM materials, these interactions were a key focus in this study. The requirements for a hydrogen bond were an O···O or O···N distance between 2.45 and 3.25 Å and an O−H···O, N−H···O, or O−H···N bond angle greater than 145°. In the presented structures that follow, hydrogen bonds are denoted by dashed lines with the corresponding hydrogen bond lengths (as measured by the O···O or O···N distance) given in angstroms. Initial isolated optimizations of the two ionomer fragments for each system exhibited nearly identical structures with end group fluorine atoms and, in the case of $CF_3CF_2SO_2NHSO_2CF_3$, the terminal carbon atom in a staggered conformation with respect to the neighboring sulfonyl oxygen atoms and the nitrogen atom (not shown). The similarity between the two systems was also observed after the addition of a single water molecule to each system (also not shown) where no proton dissociation occurred irrespective of the initial position of the water molecule but a slight increase in the N−H distance from 1.02 to 1.04 Å occurred in each case. No spontaneous proton dissociation (i.e., a dissociated state which results from an initially nondissociated geometry) was found upon addition of two water molecules to either system; however, dissociated states were obtained by starting from an initially dissociated configuration. Parts a and c of Figure 1 show the BSSE-corrected optimized nondissociated structures of $CF_3SO_2NHSO_2CF_3$ and $CF_3CF_2SO_2NHSO_2CF_3$, respectively; the corresponding structures exhibiting proton dissociation are shown in Figure 1b and d. The dissociated state was found to be 1.5 kcal/mol higher in energy for each case. It should be noted that this is in contrast to an earlier study on the $CF_3SO_2NHSO_2CF_3$ sulfonyl imide in which the dissociated state was found to be the energetically preferred state.[60] However, these results were obtained at the B3LYP/6-31G** level of theory without CP-corrected geometries; we reconfirmed this result in the current study by repeating the calculation at the lower level of theory. When comparing the similar structures between the two molecules (Figure 1a and c and Figure 1b and d), it is clear that the additional $-CF_2-$ in $CF_3CF_2SO_2NHSO_2CF_3$ has a negligible effect on the hydrogen bond network formed as each system adopts a similar conformation and essentially identical hydrogen bond distances.

Spontaneous dissociation was observed in each of the fully fluorinated sulfonyl imide fragments only upon addition of three or more water molecules. However, different dissociated conformations were obtained which either included or did not include the nitrogen atom in the hydrogen bond network. Parts a and c of Figure 2 show BSSE-corrected optimized geometries

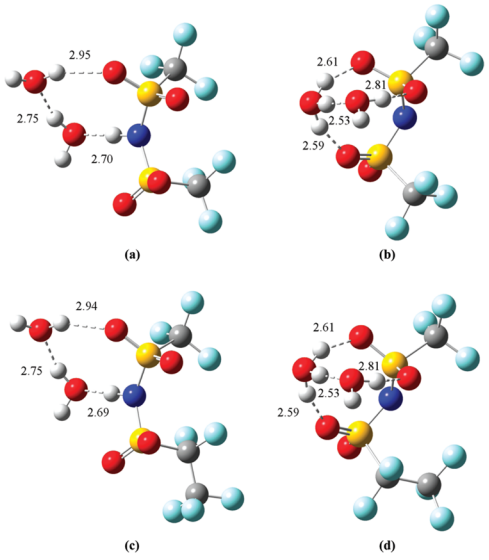

Figure 1. Optimized (B3LYP/6-311G**) structures of the fully fluorinated sulfonyl imides with the addition of two water molecules with hydrogen bonds (dashed lines) and hydrogen bond distances (in angstroms) shown: (a) the minimum energy $CF_3SO_2NHSO_2CF_3$ structure where the proton remains associated; (b) the dissociated $CF_3SO_2NHSO_2CF_3$ configuration obtained from optimization of an initially dissociated geometry with a hydronium ion hydrogen bonded to two sulfonyl oxygen atoms and a water molecule; (c) the minimum energy $CF_3CF_2SO_2NHSO_2CF_3$ structure where the proton remains associated; (d) the dissociated $CF_3CF_2SO_2NHSO_2CF_3$ configuration with a hydronium ion hydrogen bonded to two sulfonyl oxygen atoms and a water molecule obtained from optimization of an initially dissociated geometry. In each system, the nondissociated state is energetically preferred by 1.5 kcal/mol. The different colored spheres represent different atom types in the structures, where gray, carbon; red, oxygen; light blue, fluorine; yellow, sulfur; blue, nitrogen; white, hydrogen.

of $CF_3SO_2NHSO_2CF_3$ and $CF_3CF_2SO_2NHSO_2CF_3$ with three water molecules added which exclude the nitrogen atom in the hydrogen bond network; the corresponding structures which include the nitrogen atom in the hydrogen bond network are shown in Figure 2b and d. In each case, the former structures were found to be energetically preferred by ~2 kcal/mol with the dissociated proton stabilized as a hydronium ion in a contact ion pair with the imide anion but hydrogen bonded to a

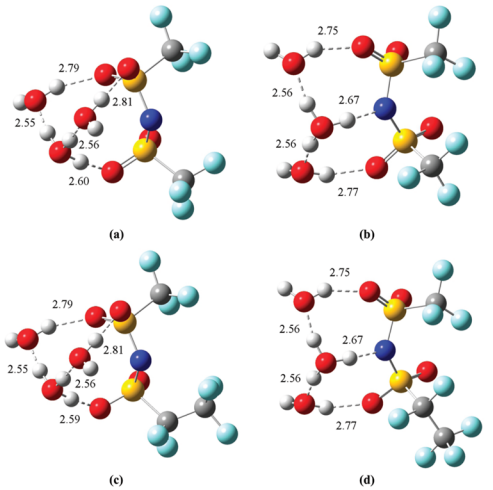

Figure 2. Optimized (B3LYP/6-311G**) structures of the fully fluorinated sulfonyl imides with the addition of three water molecules with hydrogen bonds (dashed lines) and hydrogen bond distances (in angstroms) shown: (a) the minimum energy $CF_3SO_2NHSO_2CF_3$ structure where the proton has dissociated and the nitrogen atom is not included in the hydrogen bond network with the hydronium ion forming hydrogen bonds with two water molecules and a sulfonyl oxygen atom; (b) the dissociated configuration for $CF_3SO_2NHSO_2CF_3$ with the nitrogen atom incorporated in the hydrogen bond network; (c) the minimum energy $CF_3CF_2SO_2NHSO_2CF_3$ structure where the proton has dissociated with the hydronium ion forming hydrogen bonds with two water molecules and a sulfonyl oxygen atom excluding the nitrogen atom in the hydrogen bond network; (d) the dissociated configuration of $CF_3CF_2SO_2NHSO_2CF_3$ with the nitrogen atom incorporated in the hydrogen bond network. In each system, the configuration without the nitrogen atom involved in hydrogen bonding is energetically preferred by ~2 kcal/mol.

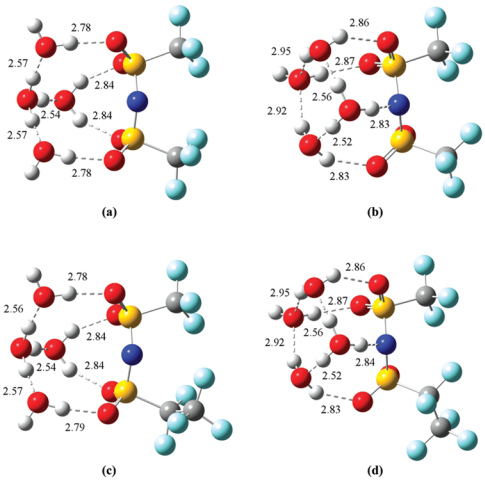

Figure 3. Optimized (B3LYP/6-311G**) structures of the fully fluorinated sulfonyl imides with the addition of four water molecules with hydrogen bonds (dashed lines) and hydrogen bond distances (in angstroms) shown: (a) the minimum energy $CF_3SO_2NHSO_2CF_3$ structure where the proton is in the solvent-separated ion pair configuration existing as an Eigen cation; (b) $CF_3SO_2NHSO_2CF_3$ where the dissociated proton exists as a hydronium ion maintaining a contact ion pair with the imide anion; (c) the minimum energy $CF_3CF_2SO_2NHSO_2CF_3$ structure where the dissociated proton exists as a solvent-separated hydronium ion hydrogen bonded to three water molecules in an Eigen ion configuration; (d) $CF_3CF_2SO_2NHSO_2CF_3$ where the dissociated proton exists as a hydronium ion maintaining a contact ion pair with the imide anion. In each system, the solvent-separated ion pair configuration is energetically preferred by ~3.8 kcal/mol.

sulfonyl oxygen atom. The hydrogen bond distances and the hydrogen bond networks formed are, again, essentially identical between the two systems, revealing the negligible effect of the additional $-CF_2-$ group in $CF_3CF_2SO_2NHSO_2CF_3$ on these parameters. This observation continues upon addition of a fourth water molecule where hydrogen bond networks that either include or do not include the nitrogen atom were, again, found, as shown in Figure 3a and c and Figure 3b and d, respectively. The systems that exclude the nitrogen atom in the hydrogen bond network resulted in the removal of the contact ion pair as the dissociated proton is fully separated, leading to the formation of an Eigen cation. One of the hydrogen bond distances of the hydronium ion to the water molecules is somewhat shorter in length than the others. This is consistent with the earlier study on $CF_3SO_2NHSO_2CF_3$ in which the authors suggest this result is an indicator of the importance of Eigen and Zundel cation transitions in a dynamic system.[60] The solvent-separated ion pair configurations in the present study were ~3.8 kcal/mol lower in energy than those that maintain the contact ion pair between the hydronium ion and the sulfonyl imide anion, reflecting the propensity of the hydronium ion to delocalize positive excess charge over the maximum number of water molecules.[60] The structures in Figure 3a and c contain one water molecule which forms two hydrogen bonds with two opposite sulfonyl oxygen atoms. This configuration is lost after the addition of five water molecules where each water molecule hydrogen bonds to one sulfonyl oxygen atom and the dissociated proton remains as a solvent-separated Eigen cation, as shown in Figure 4.

The similarity between the two fully fluorinated sulfonyl imides is further illustrated in comparing the BSSE-corrected binding energies of the water molecules to the ionomer fragments. As with the hydrogen bond distances, the binding energies are essentially identical in the two systems at all levels of hydration. At a hydration of three water molecules, where the dissociated state was first found to be energetically preferred, an increase in the magnitude of the binding energy was observed. This value further increased slightly after four water molecules were added where the solvent-separated state is preferred. Of additional interest is the total atomic charge residing on the nitrogen atom and the sulfonyl oxygen atoms as a function of the number of water molecules added, shown in Figure 9 for all of the sulfonyl imide fragments. For the fully fluorinated ionomers, a slight decrease in the total negative charge on the nitrogen atoms and the sulfonyl oxygen atoms is observed up to the addition of two water molecules as a result of the strong electron withdrawing groups paired with the hydrogen bonding with the water molecule(s). As expected, this charge becomes significantly more negative upon proton

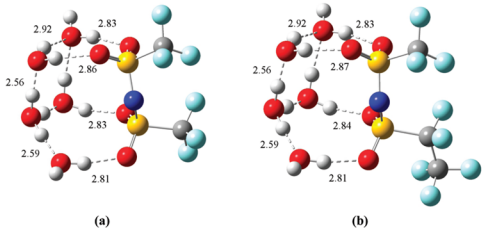

Figure 4. Optimized (B3LYP/6-311G**) structures of the fully fluorinated sulfonyl imides with the addition of five water molecules with hydrogen bonds (dashed lines) and hydrogen bond distances (in angstroms) shown: (a) the minimum energy $CF_3SO_2NHSO_2CF_3$ structure with the proton is in the solvent-separated ion pair configuration; (b) the minimum energy $CF_3CF_2SO_2NHSO_2CF_3$ structure with the proton is in the solvent-separated ion pair configuration. Some of the hydrogen bond distances have been intentionally omitted for clarity.

dissociation and gradually increases upon further hydration. Aside from the charges observed at the hydration level of three water molecules, where the two fully fluorinated values are essentially identical, there is less negative charge residing on the $CF_3CF_2SO_2NHSO_2CF_3$ nitrogen and sulfonyl oxygen atoms as a result of the additional electron withdrawing $-CF_2-$ group. Although these values are not significantly different between the two fragments, this was the only notable quantitative difference found between the two fully fluorinated ionomers.

Partially Fluorinated Sulfonyl Imides. Uncorrected, ZPE-corrected, and BSSE-corrected binding energies of the water molecules to the $CH_3SO_2NHSO_2CF_3$ and $C_6H_5SO_2NHSO_2CF_2CF_3$ minimum energy conformations are presented in Tables 3 and 4, respectively. As was the case for the fully fluorinated sulfonyl imides, the isolated optimizations resulted in similar configurations between the two partially fluorinated sulfonyl imides. Consistent with the previous studies on $CH_3SO_2NHSO_2CF_3$ and $C_6H_5SO_2NHSO_2CF_2CF_3$,[59,60] no spontaneous proton dissociation was observed in either fragment upon addition of one or two water molecules regardless of the initial position(s) of the water molecule(s). A dissociated state, however, was obtained in each system with two water molecules by starting from an initially dissociated geometry. Parts a and b of Figure 5 show the BSSE-corrected optimized geometries for $CH_3SO_2NHSO_2CF_3$ with the addition of two water molecules in the nondissociated state and the dissociated state, respectively; the corresponding structures for $C_6H_5SO_2NHSO_2CF_2CF_3$ are shown in Figure 5c and d. Similar to what was found in the fully fluorinated fragments, the hydrogen bond networks formed between the partially fluorinated sulfonyl imides and the water molecules are essentially identical between the two fragments. At this level of hydration, the nondissociated state is energetically preferred by 2.5 kcal/mol for $CH_3SO_2NHSO_2CF_3$ and 3.3 kcal/mol for $C_6H_5SO_2NHSO_2CF_2CF_3$. These values are greater than those observed in the fully fluorinated systems which may be attributed to the additional electron withdrawing groups in the fully fluorinated fragments, providing a means for charge stabilization after proton dissociation.

After three water molecules were introduced, nondissociated and spontaneously dissociated states were found, as well as multiple dissociated configurations obtained from initially dissociated states for each partially fluorinated sulfonyl imide. The optimized dissociated structures, shown in Figure 6a and c for $CH_3SO_2NHSO_2CF_3$ and $C_6H_5SO_2NHSO_2CF_2CF_3$, respectively, were more than 3.5 kcal/mol lower in energy (at the non-BSSE corrected B3LYP/6-311G** level) than the corresponding nondissociated states. This result conflicts with earlier results on the $C_6H_5SO_2NHSO_2CF_2CF_3$ sulfonyl imide[59] where no spontaneous dissociation was observed until five water molecules were added and the dissociated state was not energetically preferred until the addition of four water molecules. The dissociated state was, indeed, found to be energetically preferred at this hydration level in the earlier study on $CH_3SO_2NHSO_2CF_3$, but no spontaneous dissociation was observed.[60] As with the fully fluorinated systems, dissociated states were found that both included (Figure 6b and d) and excluded (Figure 6a and c) the nitrogen atom in the hydrogen bond network. The states in which the nitrogen atom was not involved in hydrogen bonding with the surrounding water molecules were found to be ~1.2 kcal/mol lower in energy than those that included the nitrogen atom. In each case, the hydrogen bond networks in the two partially fluorinated systems were nearly identical, as shown in the optimized conformations and corresponding hydrogen bond distances in Figure 6. The minimum energy structures resemble those found in the fully fluorinated fragments where a hydronium ion forms a hydrogen bond with one of the sulfonyl oxygen atoms and two water molecules which form hydrogen bonds with the opposite sulfonyl group oxygen atoms.

A solvent-separated ion pair configuration with a hydronium ion hydrogen bonded to three water molecules as an Eigen cation was found to be the minimum energy structure upon addition of four water molecules in each partially fluorinated sulfonyl imide fragment where, as with the fully fluorinated case, one of the hydrogen bond lengths is somewhat contracted. These are shown in Figure 7a and c for $CH_3SO_2NHSO_2CF_3$ and $C_6H_5SO_2NHSO_2CF_2CF_3$, respec-

Table 3. Energies of Optimized $CH_3SO_2NHSO_2CF_3$ Fragments[a]

n H_2O	E_{elec}[b]	E_{ZPE}[c]	ΔE[d] (kcal/mol)	ΔE_{ZPE}[e] (kcal/mol)	ΔE_{BSSE}[f] (kcal/mol)
0	−1530.27735	0.08839			
1	−1606.74778	0.11332	−14.4 (−14.4)[g]	−12.2 (−12.2)[g]	−8.3 (−8.3)[g]
2	−1683.21900	0.13842	−29.3 (−14.7)	−24.7 (−12.4)	−17.1 (−8.5)
3	−1759.69408	0.16487	−46.7 (−15.6)	−38.8 (−12.9)	−26.5 (−8.8)
4	−1836.16973	0.19054	−64.4 (−16.1)	−53.8 (−13.4)	−36.6 (−9.2)
5	−1912.64835	0.21746	−83.9 (−16.8)	−69.8 (−14.0)	−46.1 (−9.2)

[a]Energetics for structures optimized at the B3LYP/6-311G** level. [b]Total electronic energy in hartrees. [c]Zero point energy (ZPE) in hartrees. [d]Binding energy based on uncorrected total electronic energy. [e]Binding energy based on ZPE corrected electronic energy. [f]Binding energy based on CP correction to the BSSE of reoptimized structure. [g]Value in parentheses is binding energy per water molecule.

Table 4. Energies of Optimized $C_6H_5SO_2NHSO_2CF_3CF_2$ Fragments[a]

n H_2O	E_{elec}[b]	E_{ZPE}[c]	ΔE[d] (kcal/mol)	ΔE_{ZPE}[e] (kcal/mol)	ΔE_{BSSE}[f] (kcal/mol)
0	−1959.90372	0.15307			
1	−2036.37320	0.17800	−13.8 (−13.8)[g]	−11.6 (−11.6)[g]	−7.8 (−7.8)[g]
2	−2112.84391	0.20307	−28.4 (−14.2)	−23.8 (−11.9)	−16.3 (−8.2)
3	−2189.31855	0.22939	−45.5 (−15.2)	−37.7 (−12.6)	−25.3 (−8.4)
4	−2265.79276	0.25427	−62.3 (−15.6)	−52.3 (−13.1)	−35.8 (−9.0)
5	−2342.27032	0.28119	−81.2 (−16.2)	−67.7 (−13.5)	−44.8 (−9.0)

[a]Energetics for structures optimized at the B3LYP/6-311G** level. [b]Total electronic energy in hartrees. [c]Zero point energy (ZPE) in hartrees. [d]Binding energy based on uncorrected total electronic energy. [e]Binding energy based on ZPE corrected electronic energy. [f]Binding energy based on CP correction to the BSSE of reoptimized structure. [g]Value in parentheses is binding energy per water molecule.

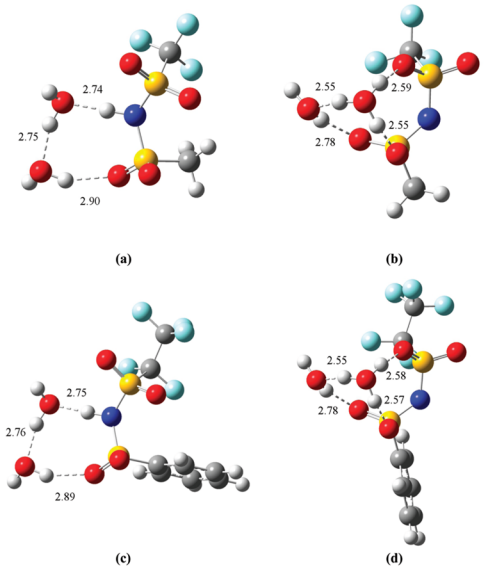

Figure 5. Optimized (B3LYP/6-311G**) structures of the partially fluorinated sulfonyl imides with the addition of two water molecules with hydrogen bonds (dashed lines) and hydrogen bond distances (in angstroms) shown: (a) the minimum energy $CH_3SO_2NHSO_2CF_3$ structure where the proton remains associated; (b) the dissociated $CH_3SO_2NHSO_2CF_3$ configuration obtained from optimization of an initially dissociated geometry with a hydronium ion hydrogen bonded to two sulfonyl oxygen atoms and a water molecule; (c) the minimum energy $C_6H_5SO_2NHSO_2CF_3CF_2$ structure where the proton remains associated; (d) the dissociated $C_6H_5SO_2NHSO_2CF_3CF_2$ configuration with a hydronium ion hydrogen bonded to two sulfonyl oxygen atoms and a water molecule obtained from optimization of an initially dissociated geometry. The nondissociated state is energetically preferred by 2.5 kcal/mol in the $CH_3SO_2NHSO_2CF_3$ fragment and 3.3 kcal/mol in the $C_6H_5SO_2NHSO_2CF_3CF_2$ fragment.

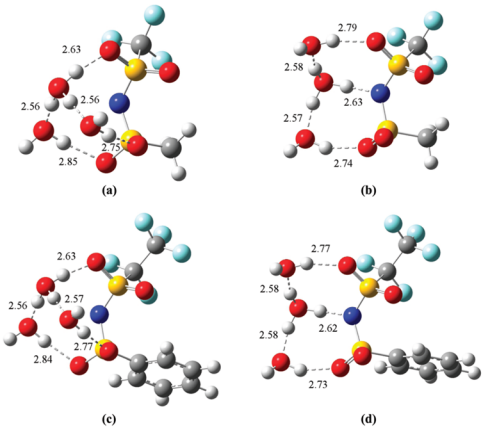

Figure 6. Optimized (B3LYP/6-311G**) structures of the partially fluorinated sulfonyl imides with the addition of three water molecules with hydrogen bonds (dashed lines) and hydrogen bond distances (in angstroms) shown: (a) the minimum energy $CH_3SO_2NHSO_2CF_3$ structure where the proton has dissociated and is stabilized as a hydronium ion hydrogen bonded to two water molecules and a sulfonyl oxygen atom excluding the nitrogen in the hydrogen bond network; (b) the dissociated configuration for $CH_3SO_2NHSO_2CF_3$ with the nitrogen atom incorporated in the hydrogen bond network; (c) the minimum energy $C_6H_5SO_2NHSO_2CF_3CF_2$ structure where the proton has dissociated and the nitrogen atom is not included in the hydrogen bond network with the hydronium ion forming hydrogen bonds with two water molecules and a sulfonyl oxygen atom; (d) the dissociated configuration of $C_6H_5SO_2NHSO_2CF_3CF_2$ with the nitrogen atom incorporated in the hydrogen bond network. In each system, the configuration without the nitrogen atom involved in hydrogen bonding is energetically preferred by 1.3 kcal/mol.

tively. The hydrogen bond networks and molecular configurations adopted by each system at this hydration level remain to be, in essence, identical, and the nitrogen atom is not included in the hydrogen bond network for the minimum energy structures. Identical structures were also found for dissociated states in which the nitrogen atom is hydrogen bonded to a hydronium ion shown in Figure 7b and d. The solvent-separated configuration for $CH_3SO_2NHSO_2CF_3$ was found to be 0.5 kcal/mol lower in energy than the contact ion pair configuration and 1.2 kcal/mol lower in energy for $C_6H_5SO_2NHSO_2CF_2CF_3$. It should be noted that the energetic differences between the solvent-separated and contact ion pair configurations were, again, considerably lower than those found in the fully fluorinated systems at this hydration level which is likely due to the strong electron withdrawing groups in the fully fluorinated sulfonyl imides, providing a stabilizing effect as the dissociated proton migrates farther away from the conjugate base.

The optimized configurations of $CH_3SO_2NHSO_2CF_3$ and $C_6H_5SO_2NHSO_2CF_2CF_3$ upon addition of five water molecules are shown in Figure 8a and b, respectively. A solvent-separated ion pair configuration remains as the minimum energy state in the partially fluorinated systems; however, these structures are

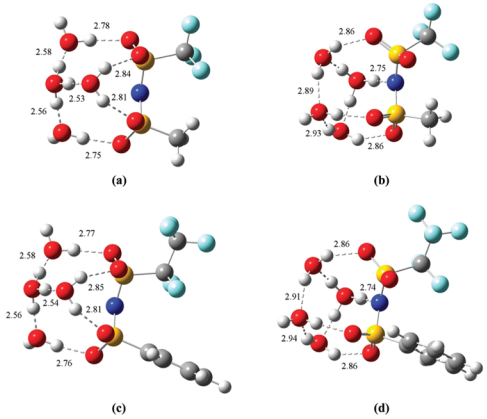

Figure 7. Optimized (B3LYP/6-311G**) structures of the partially fluorinated sulfonyl imides with the addition of four water molecules with hydrogen bonds (dashed lines) and hydrogen bond distances (in angstroms) shown: the minimum energy $CH_3SO_2NHSO_2CF_3$ structure where the proton is in the solvent-separated ion pair configuration existing as an Eigen cation; (b) $CH_3SO_2NHSO_2CF_3$ where the dissociated proton exists as a hydronium ion maintaining a contact ion pair with the imide anion; (c) the minimum energy $C_6H_5SO_2NHSO_2CF_3CF_2$ structure where the dissociated proton is in the solvent-separated ion pair position forming an Eigen ion; (d) $C_6H_5SO_2NHSO_2CF_3CF_2$ where the dissociated proton exists as a hydronium ion maintaining a contact ion pair with the imide anion. The solvent-separated ion pair configuration is energetically preferred by 0.5 kcal/mol for the $CH_3SO_2NHSO_2CF_3$ system and 1.2 kcal/mol for the $C_6H_5SO_2NHSO_2CF_3CF_2$ system.

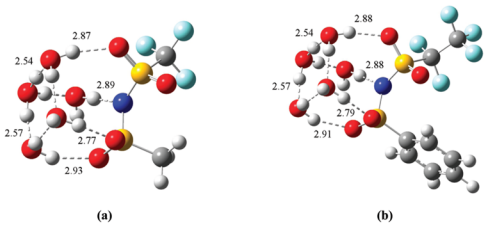

Figure 8. Optimized (B3LYP/6-311G**) structures of the partially fluorinated sulfonyl imides with the addition of five water molecules with hydrogen bonds (dashed lines) and hydrogen bond distances (in angstroms) shown: (a) the minimum energy $CH_3SO_2NHSO_2CF_3$ structure with the proton is in the solvent-separated ion pair configuration and the nitrogen atom is hydrogen bonded to a single water molecule; (b) the minimum energy $C_6H_5SO_2NHSO_2CF_3CF_2$ structure with the proton is in the solvent-separated ion pair configuration and the nitrogen atom is hydrogen bonded to a single water molecule. Some of the hydrogen bond distances have been intentionally omitted for clarity.

noticeably different from those obtained for the fully fluorinated case. The optimized partially fluorinated geometries include the nitrogen atom in the hydrogen bond network, whereas it was not in the fully fluorinated fragments. This conformation was only energetically preferred by 0.1 kcal/mol for $C_6H_5SO_2NHSO_2CF_2CF_3$ and only slightly greater for $CH_3SO_2NHSO_2CF_3$ (0.3 kcal/mol). The hydrogen bond networks formed in the partially fluorinated systems remain to be essentially identical.

The calculated binding energies of the water molecules to the ionomeric fragments also exemplify the similarity between the two partially fluorinated sulfonyl imides. While there are slightly greater differences in the binding energies between the partially fluorinated fragments than were found between the two fully fluorinated fragments, the values are, nonetheless, almost identical. The increase in the magnitude of the binding energy after proton dissociation and separation observed in the fully fluorinated sulfonyl imides also occurred in the partially fluorinated systems but to a lesser degree. Furthermore, the magnitudes of the binding energies in the partially fluorinated sulfonyl imides are roughly 1 kcal/mol lower in energy than those of the fully fluorinated imides at all levels of hydration; this may be attributed to the additional electron withdrawing capacity of the fully fluorinated ionomers leading to more tightly bound hydrogen bonds. This can be further realized through examination of the total atomic charge residing on the nitrogen atom and the sulfonyl oxygen atoms as a function of water content shown in Figure 9. As shown, there is a

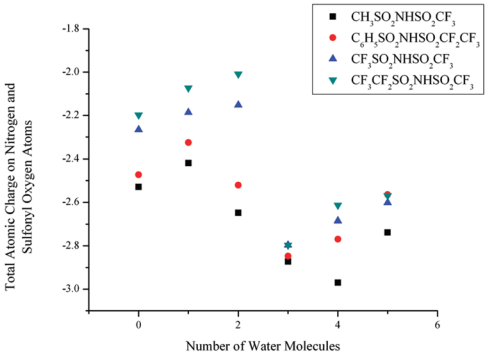

Figure 9. Total atomic charge as computed with the MK routine residing on the sulfonyl oxygen atoms and nitrogen atom as a function of the number of added water molecules for each sulfonyl imide ionomer.

noticeable difference between the obtained charges in the partially fluorinated fragments than those of the fully fluorinated fragments. As expected, there is more negative charge residing on the nitrogen atoms and sulfonyl oxygen atoms in the partially fluorinated ionomers up to the addition of four water molecules due to the lack of additional strong electron withdrawing groups. After the addition of five water molecules, the energetically preferred configurations between the fully fluorinated and the partially fluorinated sulfonyl imides have noticeably different hydrogen bond networks, making the direct comparison less relevant. When comparing the two partially fluorinated fragments, less negative charge resides on the $C_6H_5SO_2NHSO_2CF_2CF_3$ nitrogen and sulfonyl oxygen atoms at all levels of hydration due to the greater electron withdrawing capacity of the $-CF_2CF_3$ group, as well as the somewhat greater electron withdrawing capacity of the $-C_6H_5$ group than the $-CH_3$ group.

Aromatic Sulfonic Acid Ionomers. The uncorrected, ZPE-corrected, and BSSE-corrected binding energies of the

Table 5. Energies of Optimized *para*-Toluene Fragments[a]

n H_2O	E_{elec}[b]	E_{ZPE}[c]	ΔE[d] (kcal/mol)	ΔE_{ZPE}[e] (kcal/mol)	ΔE_{BSSE}[f] (kcal/mol)
0	−895.51998	0.14118			
1	−971.99219	0.16702	−15.5 (−15.5)[g]	−12.8 (−12.8)[g]	−8.9 (−8.9)[g]
2	−1048.46583	0.19228	−32.0 (−16.0)	−26.8 (−13.4)	−18.7 (−9.3)
3	−1124.93904	0.21802	−48.1 (−16.0)	−40.2 (−13.4)	−28.3 (−9.4)
4	−1201.41242	0.24315	−64.4 (−16.1)	−54.1 (−13.5)	−38.0 (−9.5)
5	−1277.89329	0.27172	−85.4 (−17.1)	−70.5 (−14.1)	−45.3 (−9.1)
6	−1354.36708	0.29740	−101.9 (−17.0)	−84.3 (−14.1)	−55.7 (−9.3)

[a]Energetics for structures optimized at the B3LYP/6-311G** level. [b]Total electronic energy in hartrees. [c]Zero point energy (ZPE) in hartrees. [d]Binding energy based on uncorrected total electronic energy. [e]Binding energy based on ZPE corrected electronic energy. [f]Binding energy based on CP correction to the BSSE of reoptimized structure. [g]Value in parentheses is binding energy per water molecule.

Table 6. Energies of Optimized sPEEK Fragments[a]

n H_2O	E_{elec}[b]	E_{ZPE}[c]	ΔE[d] (kcal/mol)	ΔE_{ZPE}[e] (kcal/mol)	ΔE_{BSSE}[f] (kcal/mol)
0	−1316.40354	0.25920			
1	−1392.87565	0.28484	−15.5 (−15.5)[g]	−12.8 (−12.8)[g]	−8.7 (−8.7)[g]
2	−1469.34927	0.31021	−31.9 (−15.9)	−26.6 (−13.3)	−18.5 (−9.2)
3	−1545.82229	0.33573	−47.9 (−16.0)	−40.1 (−13.4)	−28.2 (−9.4)
4	−1622.29569	0.36126	−64.2 (−16.1)	−53.7 (−13.4)	−37.8 (−9.5)
5	−1698.77658	0.38974	−85.2 (−17.0)	−70.2 (−14)	−46.0 (−9.2)
6	−1775.24985	0.41519	−101.4 (−16.9)	−83.8 (−14)	−55.5 (−9.3)

[a]Energetics for structures optimized at the B3LYP/6-311G** level. [b]Total electronic energy in hartrees. [c]Zero point energy (ZPE) in hartrees. [d]Binding energy based on uncorrected total electronic energy. [e]Binding energy based on ZPE corrected electronic energy. [f]Binding energy based on CP correction to the BSSE of reoptimized structure. [g]Value in parentheses is binding energy per water molecule.

water molecules to the ionomeric fragment for the *para*-toluene and sPEEK systems are given in Tables 5 and 6, respectively. Local hydration and proton dissociation in the *para*-toluene sulfonic acid were investigated in an early explicit water electronic structure study[54] and a more recent study on sPEEK.[59] These calculations have been revisited here, using BSSE-corrected optimized geometries and a larger basis set, to directly compare the effect of the extended main chain in the model sPEEK system. Consistent with the previous findings on *para*-toluene sulfonic acid[54] and sPEEK,[59] no dissociated state was found for either system until the addition of three water molecules. However, spontaneous proton dissociation was observed in the present study in both of the aryl sulfonic acid ionomers at this level of hydration which was found previously for *para*-toluene sulfonic acid but not in the more recent study on sPEEK. The dissociated and nondissociated states were essentially isoenergetic for each system with the dissociated state energetically preferred by only ∼0.1 kcal/mol. The hydrogen bond configuration and bond distances adopted by the *para*-toluene and sPEEK fragments at this hydration level are essentially identical, as can be seen in Figure 10a and b, respectively. In each case, two oxygen atoms from the, now, sulfonate group are involved in hydrogen bonds with two individual water molecules, and the dissociated proton exists as a hydronium ion in a contact ion pair with the $R-SO_3^-$ anion. The hydronium ion also forms hydrogen bonds with the two water molecules, effectively creating a "ring-like" hydrogen bond network.

The minimum energy conformations for *para*-toluene and sPEEK upon addition of four water molecules are shown in Figures 11a and b, respectively. As shown, the contact ion pair has been broken as the excess proton moves to the solvent-separated position with the hydronium ion forming a highly symmetric Eigen cation with the surrounding water molecules. These structures were obtained by starting from an initially

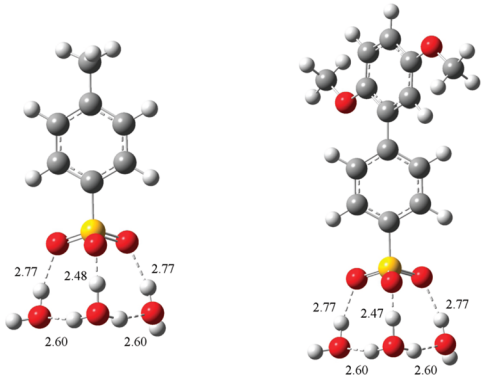

Figure 10. Optimized (B3LYP/6-311G**) minimum energy structures of the sulfonic acid moieties with the addition of three water molecules with hydrogen bonds (dashed lines) and hydrogen bond distances (in angstroms) shown: (a) *para*-toluene resulting in proton dissociation with the hydronium ion in a contact ion pair with the $R-SO_3^-$ anion ($R = CH_3C_6H_4$); (b) sPEEK resulting in proton dissociation with the hydronium ion in a contact ion pair with the $R-SO_3^-$ anion ($R = CH_3OC_6H_3OCH_3C_6H_4$). The different colored spheres represent different atom types in the structures where gray, carbon; red, oxygen; yellow, sulfur; white, hydrogen.

solvent-separated geometry and are ∼2.7 kcal/mol lower in energy than the systems which maintain the contact ion pair at this hydration level. The solvent-separated ion pair configuration found previously for *para*-toluene was not observed until the addition of six water molecules;[54] it should be noted, however, that this study only focused on the systematic

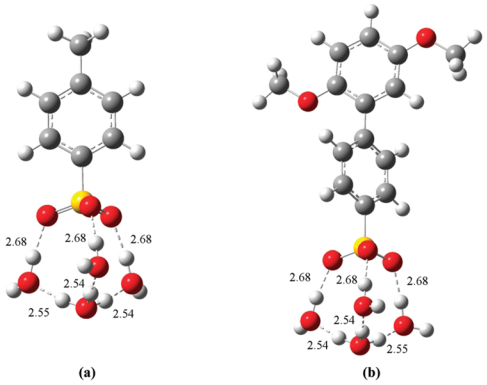

Figure 11. Optimized (B3LYP/6-311G**) minimum energy structures of the sulfonic acid moieties with the addition of four water molecules with hydrogen bonds (dashed lines) and hydrogen bond distances (in angstroms) shown: (a) *para*-toluene with the proton in the solvent-separated ion pair configuration with the hydronium ion hydrogen bonding to three water molecules forming an Eigen cation; (b) sPEEK with the proton in the solvent-separated ion pair configuration with the hydronium ion hydrogen bonding to three water molecules forming an Eigen cation.

addition of water molecules to the system as opposed to starting from initially solvent-separated states. The resulting geometries and hydrogen bond networks formed remain essentially identical between the two aryl sulfonic acids, revealing the negligible effects the main chain extension in the sPEEK fragment has on proton dissociation and local hydration. This is further reinforced upon increasing hydration as the systems maintain identical structural properties, as can be seen in Figure 12 after the addition of six water molecules, where, like the sulfonyl imides, each system contains an Eigen cation with asymmetric hydrogen bond lengths.

At each hydration level considered, the binding energies of the water molecules to the ionomeric fragments were essentially identical between the sulfonic acid moieties, again revealing the negligible difference associated with the extended fragment in the sPEEK model. The total atomic charge residing on the sulfonic/ate oxygen atoms as a function of water content is shown in Figure 13. These values are, in essence, identical between the two fragments at all levels of hydration. The charges obtained after the addition of four water molecules are shown for both the solvent-separated configurations and the contact ion pair configurations obtained. As expected, there is more negative charge residing on the sulfonate oxygen atoms in the solvent-separated configuration as the proton has moved farther away from the corresponding conjugate base.

■ CONCLUSIONS

Our revisited study of various sulfonyl imide and sulfonic acid moieties reveals that the exchange of substituents having similar electron withdrawing groups has negligible effects on proton dissociation, hydrogen bond configurations, or the binding energies of water molecules to the ionomer. No spontaneous proton dissociation was observed in any system until the addition of three water molecules where spontaneous dissociation was observed in each case. A dissociated state,

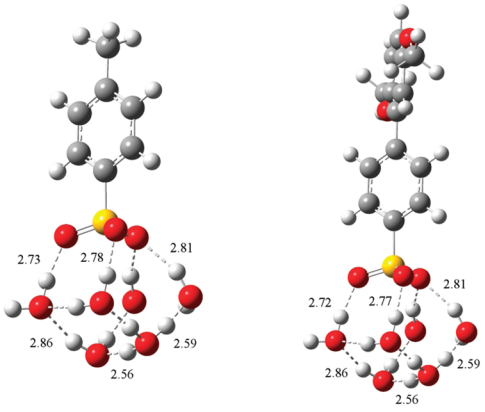

Figure 12. Optimized (B3LYP/6-311G**) minimum energy structures of the sulfonic acid moieties with the addition of six water molecules with hydrogen bonds (dashed lines) and hydrogen bond distances (in angstroms) shown: (a) *para*-toluene; (b) sPEEK. Some of the hydrogen bond distances have been intentionally omitted for clarity.

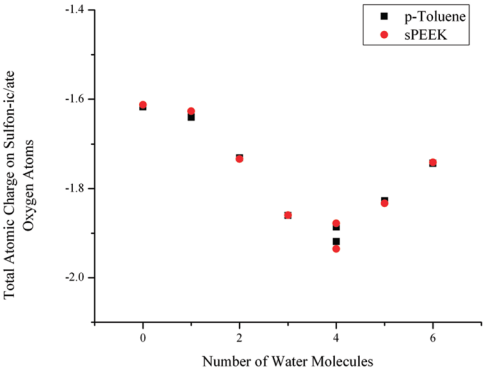

Figure 13. Total atomic charge as computed with the MK routine residing on the sulfonic/ate oxygen atoms as a function of the number of added water molecules for *para*-toluene and sPEEK.

however, was found for the sulfonyl imide ionomers with two water molecules by starting from an initially dissociated configuration; this was not observed in the sulfonic acid moieties. At this hydration level, the dissociated state was 1.5 kcal/mol higher in energy for the fully fluorinated sulfonyl imides and 2.5 and 3.3 kcal/mol for $CH_3SO_2NHSO_2CF_3$ and $C_6H_5SO_2NHSO_2CF_2CF_3$, respectively.

The minimum energy conformations of all of the sulfonyl imide ionomers were qualitatively similar up to and including a water content of four water molecules. The dissociated state was found to be energetically preferred after the addition of three water molecules for all sulfonyl imides. A solvent-separated ion pair configuration containing an Eigen cation was energetically preferred after the addition of four water molecules in each of the sulfonyl imides. This state was 3.8

kcal/mol lower in energy than the configuration that maintained a contact ion pair in the fully fluorinated ionomers, while it was only 0.5 and 1.2 kcal/mol higher in the partially fluorinated $CH_3SO_2NHSO_2CF_3$ and $C_6H_5SO_2NHSO_2CF_2CF_3$ molecules, respectively. The greater energetic difference between these states in the fully fluorinated fragments at this level of hydration was attributed to the greater electron withdrawing capacity of the fully fluorinated substituents, providing a means for charge stabilization as the dissociated proton moves farther away from the conjugate base. It should be noted that there was more quantitative variability in the energetic data obtained between the partially fluorinated fragments than the fully fluorinated fragments. This may be due to the replacement of a substituent methyl group with an aromatic ring being less trivial than the extension of an additional $-CF_2-$ group.

Negligible differences in all of the collected data between the *para*-toluene and sPEEK aryl sulfonic acids were found, revealing the inconsequential contribution the extended chain in the sPEEK model has on the determined properties. In each case, the dissociated state was found to be energetically preferred at a hydration level of three water molecules but by only 0.1 kcal/mol. This is noticeably different than what was found for the sulfonyl imides at this hydration level where the nondissociated state was significantly higher in energy for the partially fluorinated cases and no nondissociated state was found in the fully fluorinated fragments. This is likely due to the greater acidity of the sulfonyl imide protogenic group. A solvent-separated ion pair configuration was found to be energetically preferred in the sulfonic acid moieties upon the addition of four water molecules with the formation of a highly symmetric Eigen cation which, upon further hydration, becomes less symmetric, resulting in contracted and extended hydrogen bond lengths. The asymmetric hydrogen bond lengths within Eigen cations were found in all of the sulfonyl imide and the sulfonic acid fragments, illustrating the importance of structural diffusion through Eigen–Zundel transitions in proton transfer at low levels of hydration in materials of this type.[60]

The results of this study underscore the overwhelming contribution to the factors that affect proton dissociation and separation from the substituent group(s) at the α-carbon site(s) relative to sites further away from the acidic functional group. This is in agreement with an earlier study on triflic acid (CF_3SO_3H) and an extended fluorinated ionomer ($CF_3O(CF_2)_2SO_3H$) where the effects of the additional electron withdrawing groups in the extended fragment on proton dissociation, structural parameters, and binding energies were found to be relatively minor.[58] The only noteworthy difference found was the total atomic charge residing on the SO_3H oxygen atoms which was less negative in $CF_3O(CF_2)_2SO_3H$, indicative of the increased acidity due to the electron withdrawing groups. As expected, no discernible difference in the total atomic charge on the sulfonic/ate oxygen atoms was observed between the sulfonic acid-based ionomers in the present study, as the alteration of the substituent group was introduced well beyond the α-carbon. However, a noticeable dissimilarity was observed in the total atomic charge on the nitrogen atom and sulfonyl oxygen atoms between the sulfonyl imides as substituent group modifications were much closer to the acidic functional group. Namely, based on the observed charge distribution, the rank of acid strength, in order of decreasing acidity, is (1) $CF_3CF_2SO_2NHSO_2CF_3$, (2) $CF_3SO_2NHSO_2CF_3$, (3) $C_6H_5SO_2NHSO_2CF_2CF_3$, and (4) $CH_3SO_2NHSO_2CF_3$. Thus, while the results of this study reveal that substituents having similar electron withdrawing groups result in negligible changes to structural parameters, proton dissociation, and binding energies in these acidic moieties, variations in chemical structure close to the protogenic group, as has been shown experimentally,[28] affect the ionomer acidity.

It is important to note that results from *ab initio* molecular dynamics simulations[44,46−49,83−85] show that the presence of multiple interacting acidic groups and dynamic configurational changes and bond length fluctuations strongly influence proton mobility and the nature and state of the acidic protons. Thus, obtaining a full understanding of the chemical and structural properties that affect dynamic proton transport in a fuel cell membrane requires additional complex ingredients not present in the static electronic structure calculations on these isolated acid/water molecule complexes. Hence, in this comparative study of various imide and sulfonic acid ionomers, we are not attempting to describe the characteristics of a full ionomer membrane (or even a representative portion of the hydrated morphology of the ionomer) but to explore how specific ionomer chemistry affects proton dissociation within the primary hydration of the acidic group. This information provides some insight into the choice of the acidic moiety for use in PEMs and the connection to transport properties in PEMs under minimally hydrated conditions.

■ ASSOCIATED CONTENT

Supporting Information

Tables comparing the determined binding energies, hydrogen bond information, and the computational cost of calculations using the M06 density functional and MP2 theory with the results obtained using B3LYP are provided. This material is available free of charge via the Internet at http://pubs.acs.org.

■ AUTHOR INFORMATION

Corresponding Author

*E-mail: spaddison@utk.edu.

Notes

The authors declare no competing financial interest.

■ ACKNOWLEDGMENTS

This work was supported by the National Science Foundation under Grant No. DGE0801470, "Sustainable Technology through Advanced Interdisciplinary Research" (STAIR), awarded to the University of Tennessee, Knoxville.

■ REFERENCES

(1) Granovskii, M.; Dincer, I.; Rosen, M. A. *Int. J. Hydrogen Energy* **2006**, *31*, 337.
(2) Shao, Y. Y.; Yin, G. P.; Wang, Z. B.; Gao, Y. Z. *J. Power Sources* **2007**, *167*, 235.
(3) Kreuer, K. D.; Paddison, S. J.; Spohr, E.; Schuster, M. *Chem. Rev.* **2004**, *104*, 4637.
(4) Savadogo, O. *J. Power Sources* **2004**, *127*, 135.
(5) Kreuer, K. D. *J. Membr. Sci.* **2001**, *185*, 29.
(6) Rubatat, L.; Rollet, A. L.; Gebel, G.; Diat, O. *Macromolecules* **2002**, *35*, 4050.
(7) Paddison, S. J. *Ann. Rev. Mater. Res.* **2003**, *33*, 289.
(8) von Grotthuss, C. J. D. *Ann. Chim.* **1806**, *LVIII*, 54.
(9) Eikerling, M.; Kornyshev, A. A.; Kuznetsov, A. M.; Ulstrup, J.; Walbran, S. *J. Phys. Chem. B* **2001**, *105*, 3646.
(10) Paddison, S. J.; Paul, R. *Phys. Chem. Chem. Phys.* **2002**, *4*, 1158.

(11) Paddison, S. J.; Paul, R.; Kreuer, K. D. *Phys. Chem. Chem. Phys.* **2002**, *4*, 1151.
(12) Spohr, E.; Commer, P.; Kornyshev, A. A. *J. Phys. Chem. B* **2002**, *106*, 10560.
(13) Agmon, N. *Chem. Phys. Lett.* **1995**, *244*, 456.
(14) Tuckerman, M.; Laasonen, K.; Sprik, M.; Parrinello, M. *J. Chem. Phys.* **1995**, *103*, 150.
(15) Tuckerman, M. E.; Marx, D.; Klein, M. L.; Parrinello, M. *Science* **1997**, *275*, 817.
(16) Marx, D.; Tuckerman, M. E.; Hutter, J.; Parrinello, M. *Nature* **1999**, *397*, 601.
(17) Lapid, H.; Agmon, N.; Petersen, M. K.; Voth, G. A. *J. Chem. Phys.* **2005**, *122*, 014506.
(18) Kreuer, K. D. *ChemPhysChem* **2002**, *3*, 771.
(19) Ise, M.; Kreuer, K. D.; Maier, J. *Solid State Ionics* **1999**, *125*, 213.
(20) Hickner, M. A.; Ghassemi, H.; Kim, Y. S.; Einsla, B. R.; McGrath, J. E. *Chem. Rev.* **2004**, *104*, 4587.
(21) Biyikoglu, A. *Int. J. Hydrogen Energy* **2005**, *30*, 1181.
(22) Cheddie, D.; Munroe, N. *J. Power Sources* **2005**, *147*, 72.
(23) Haile, S. M. *Acta Mater.* **2003**, *51*, 5981.
(24) Ezzell, B. R.; Carl, W. P.; Mod, W. A., The Dow Chemical Company: U.S. Patent 4,358,412, November 9, 1982.
(25) Yang, Z. Y.; Rajendran, R. G. *Angew. Chem., Int. Ed.* **2005**, *44*, 564.
(26) Hamrock, S. J.; Yandrasits, M. A. *Polym. Rev.* **2006**, *46*, 219.
(27) Sumner, J. J.; Creager, S. E.; Ma, J. J.; DesMarteau, D. D. *J. Electrochem. Soc.* **1998**, *145*, 107.
(28) Koppel, I. A.; Taft, R. W.; Anvia, F.; Zhu, S. Z.; Hu, L. Q.; Sung, K. S.; Desmarteau, D. D.; Yagupolskii, L. M.; Yagupolskii, Y. L.; Ignatev, N. V.; Kondratenko, N. V.; Volkonskii, A. Y.; Vlasov, V. M.; Notario, R.; Maria, P. C. *J. Am. Chem. Soc.* **1994**, *116*, 3047.
(29) Creager, S. E.; Sumner, J. J.; Bailey, R. D.; Ma, J. J.; Pennington, W. T.; DesMarteau, D. D. *Electrochem. Solid-State Lett.* **1999**, *2*, 434.
(30) Kreuer, K. D. *Solid State Ionics* **1997**, *97*, 1.
(31) Li, Q. F.; He, R. H.; Jensen, J. O.; Bjerrum, N. J. *Chem. Mater.* **2003**, *15*, 4896.
(32) Liu, B. J.; Robertson, G. P.; Kim, D. S.; Guiver, M. D.; Hu, W.; Jiang, Z. H. *Macromolecules* **2007**, *40*, 1934.
(33) Chandra, A.; Tuckerman, M. E.; Marx, D. *Phys. Rev. Lett.* **2007**, *33*, 145901.
(34) Markovitch, O.; Chen, H.; Izvekov, S.; Paesani, F.; Voth, G. A.; Agmon, N. *J. Phys. Chem. B* **2008**, *112*, 9456.
(35) Tuckerman, M. E.; Chandra, A.; Marx, D. *J. Chem. Phys.* **2010**, *133*, 124108.
(36) Chen, H. N.; Voth, G. A.; Agmon, N. *J. Phys. Chem. B* **2010**, *114*, 333.
(37) Day, T. J. F.; Soudackov, A. V.; Cuma, M.; Schmitt, U. W.; Voth, G. A. *J. Chem. Phys.* **2002**, *117*, 5839.
(38) Wang, F.; Voth, G. A. *J. Chem. Phys.* **2005**, *122*, 144105.
(39) Wu, Y. J.; Chen, H. N.; Wang, F.; Paesani, F.; Voth, G. A. *J. Phys. Chem. B* **2008**, *112*, 467.
(40) Petersen, M. K.; Wang, F.; Blake, N. P.; Metiu, H.; Voth, G. A. *J. Phys. Chem. B* **2005**, *109*, 3727.
(41) Petersen, M. K.; Voth, G. A. *J. Phys. Chem. B* **2006**, *110*, 18594.
(42) Petersen, M. K.; Hatt, A. J.; Voth, G. A. *J. Phys. Chem. B* **2008**, *112*, 7754.
(43) Feng, S.; Voth, G. A. *J. Phys. Chem. B* **2011**, *115*, 5903.
(44) Eikerling, M.; Paddison, S. J.; Pratt, L. R.; Zawodzinski, T. A. *Chem. Phys. Lett.* **2003**, *368*, 108.
(45) Choe, Y. K.; Tsuchida, E.; Ikeshoji, T.; Yamakawa, S.; Hyodo, S. *Phys. Chem. Chem. Phys.* **2009**, *11*, 3892.
(46) Hayes, R. L.; Paddison, S. J.; Tuckerman, M. E. *J. Phys. Chem. B* **2009**, *113*, 16574.
(47) Hayes, R. L.; Paddison, S. J.; Tuckerman, M. E. *J. Phys. Chem. A* **2011**, *115*, 6112.
(48) Habenicht, B. F.; Paddison, S. J.; Tuckerman, M. E. *J. Mater. Chem.* **2010**, *20*, 6342.
(49) Habenicht, B. F.; Paddison, S. J.; Tuckerman, M. E. *Phys. Chem. Chem. Phys.* **2010**, *12*, 8728.
(50) Munch, W.; Kreuer, K. D.; Silvestri, W.; Maier, J.; Seifert, G. *Solid State Ionics* **2001**, *145*, 437.
(51) Choe, Y. K.; Tsuchida, E.; Ikeshoji, T.; Ohira, A.; Kidena, K. *J. Phys. Chem. B* **2010**, *114*, 2411.
(52) Paddison, S. J.; Pratt, L. R.; Zawodzinski, T.; Reagor, D. W. *Fluid Phase Equilib.* **1998**, *151*, 235.
(53) Paddison, S. J.; Zawodzinski, T. A. Jr. *Solid State Ionics* **1998**, *113−115*, 333.
(54) Paddison, S. J. *J. New Mater. Electrochem. Syst.* **2001**, *4*, 197.
(55) Glezakou, V. A.; Dupuis, M.; Mundy, C. J. *Phys. Chem. Chem. Phys.* **2007**, *9*, 5752.
(56) Sagarik, K.; Phonyiem, M.; Lao-Ngam, C.; Chaiwongwattana, S. *Phys. Chem. Chem. Phys.* **2008**, *10*, 2098.
(57) Phonyiem, M.; Chaiwongwattana, S.; Lao-ngam, C.; Sagarik, K. *Phys. Chem. Chem. Phys.* **2011**, *13*, 10923.
(58) Wang, C.; Clark, J. K.; Kumar, M.; Paddison, S. J. *Solid State Ionics* **2011**, *199*, 6.
(59) Idupulapati, N.; Devanathan, R.; Dupuis, M. *J. Phys. Chem. A* **2010**, *114*, 6904.
(60) Eikerling, M.; Paddison, S. J.; Zawodzinski, T. A. *J. New Mater. Electrochem. Syst.* **2002**, *5*, 15.
(61) Paddison, S. J.; Kreuer, K. D.; Maier, J. *Phys. Chem. Chem. Phys.* **2006**, *8*, 4530.
(62) Wang, C.; Paddison, S. J. *Phys. Chem. Chem. Phys.* **2009**, *12*, 970.
(63) Vilciauskas, L.; Paddison, S. J.; Kreuer, K. D. *J. Phys. Chem. A* **2009**, *113*, 9193.
(64) Urata, S.; Irisawa, J.; Takada, A.; Tsuzuki, S.; Shinoda, W.; Mikami, M. *Phys. Chem. Chem. Phys.* **2004**, *6*, 3325.
(65) Paddison, S. J.; Elliott, J. A. *J. Phys. Chem. A* **2005**, *109*, 7583.
(66) Paddison, S. J.; Elliott, J. A. *Solid State Ionics* **2006**, *177*, 2385.
(67) Paddison, S. J.; Elliott, J. A. *Phys. Chem. Chem. Phys.* **2006**, *8*, 2193.
(68) Paddison, S. J.; Elliott, J. A. *Solid State Ionics* **2007**, *178*, 561.
(69) Clark, J. K.; Paddison, S. J. *Solid State Ionics* **2011**, DOI: 10.1016/j.ssi.2011.07.011.
(70) Frisch, M. J.; Trucks, G. W.; Schlegel, H. B.; Scuseria, G. E.; Robb, M. A.; Cheeseman, J. R.; Scalmani, G.; Barone, V.; Mennucci, B.; Petersson, G. A.; Nakatsuji, H.; Caricato, M.; Li, X.; Hratchian, H. P.; Izmaylov, A. F.; Bloino, J.; Zheng, G.; Sonnenberg, J. L.; Hada, M.; Ehara, M.; Toyota, K.; Fukuda, R.; Hasegawa, J.; Ishida, M.; Nakajima, T.; Honda, Y.; Kitao, O.; Nakai, H.; Vreven, T.; J. A. Montgomery, J.; Peralta, J. E.; Ogliaro, F.; Bearpark, M.; Heyd, J. J.; Brothers, E.; Kudin, K. N.; Staroverov, V. N.; Kobayashi, R.; Normand, J.; Raghavachari, K.; Rendell, A.; Burant, J. C.; Iyengar, S. S.; Tomasi, J.; Cossi, M.; Rega, N.; Millam, J. M.; Klene, M.; Knox, J. E.; Cross, J. B.; Bakken, V.; Adamo, C.; Jaramillo, J.; Gomperts, R.; Stratmann, R. E.; Yazyev, O.; Austin, A. J.; Cammi, R.; Pomelli, C.; Ochterski, J. W.; Martin, R. L.; Morokuma, K.; Zakrzewski, V. G.; Voth, G. A.; Salvador, P.; Dannenberg, J. J.; Dapprich, S.; Daniels, A. D.; Farkas, O.; Foresman, J. B.; Ortiz, J. V.; Cioslowski, J.; Fox, D. J. *Gaussian 09*, revision A.1 ed.; Gaussian Inc.: Wallingford, CT, 2009.
(71) Schlegel, H. B. *J. Comput. Chem.* **1982**, *3*, 214.
(72) Harihara, P. C.; Pople, J. A. *Theor. Chim. Acta* **1973**, *28*, 213.
(73) Becke, A. D. *J. Chem. Phys.* **1993**, *98*, 5648.
(74) Becke, A. D. *J. Chem. Phys.* **1993**, *98*, 1372.
(75) McLean, A. D.; Chandler, G. S. *J. Chem. Phys.* **1980**, *72*, 5639.
(76) Boys, S. F.; Bernardi, F. *Mol. Phys.* **1970**, *19*, 553.
(77) Kobko, N.; Dannenberg, J. J. *J. Phys. Chem. A* **2001**, *105*, 1944.
(78) Singh, U. C.; Kollman, P. A. *J. Comput. Chem.* **1984**, *5*, 129.
(79) Besler, B. H.; Merz, K. M.; Kollman, P. A. *J. Comput. Chem.* **1990**, *11*, 431.
(80) Paddison, S. J.; Pratt, L. R.; Zawodzinski, T. A. *J. New Mater. Electrochem. Syst.* **1999**, *2*, 183.
(81) Elliott, J. A.; Paddison, S. J. *Phys. Chem. Chem. Phys.* **2007**, *9*, 2602.
(82) Zhao, Y.; Truhlar, D. G. *Theor. Chem. Acc.* **2008**, *120*, 215.
(83) Habenicht, B. F.; Paddison, S. J. *J. Phys. Chem. B* **2011**, *115*, 10826.
(84) Ilhan, M. A.; Spohr, E. *J. Phys.: Condens. Matter* **2011**, 23.

(85) Roudgar, A.; Narasimachary, S. P.; Eikerling, M. *J. Phys. Chem. B* **2006**, *110*, 20469.

Electrochimica Acta 101 (2013) 279–292

Contents lists available at SciVerse ScienceDirect

Electrochimica Acta

journal homepage: www.elsevier.com/locate/electacta

Proton dissociation and transfer in proton exchange membrane ionomers with multiple and distinct pendant acid groups: An *ab initio* study

Jeffrey K. Clark II, Stephen J. Paddison*

Department of Chemical and Biomolecular Engineering, University of Tennessee, Knoxville, TN 37996, USA

ARTICLE INFO

Article history:
Received 2 September 2012
Received in revised form
27 November 2012
Accepted 27 November 2012
Available online 14 December 2012

Keywords:
Proton exchange membrane
Sulfonyl imide
Proton transfer and dissociation

ABSTRACT

The role of the separation of the protogenic groups and side chain chemistry on proton dissociation and the energetics of proton transfer is compared on single side chain fragments of 3M multi acid side chain (MASC) ionomers. Three ionomers were considered each containing a bis(sulfonyl imide) group and a sulfonic acid group with structural and chemical differences mediating protogenic group separation: two structural isomers with protogenic group separation determined by the location of the sulfonic acid group on an aromatic ring (side chains: $-O(CF_2)_4SO_2(NH)-SO_2C_6H_4SO_3H$) with the sulfonic acid group located in either the *meta* or the *ortho* position) and a perfluorinated ionomer (PFIA) with protogenic groups separated by $-CF_2-$ groups (side chain: $-O(CF_2)_4SO_2(NH)SO_2(CF_2)_3SO_3H$). Optimized (B3LYP/6-311G**) geometries on isolated fragments revealed that differences in side chain chemistry and proximity of the protogenic groups resulted in charge delocalization effects that facilitated proton dissociation at low hydration levels. Specifically, direct hydrogen bonding between the acid groups in the *ortho* bis acid and electron withdrawing $-CF_2-$ groups in PFIA allowed for first proton dissociation at a lower hydration than the *meta* bis acid which lacked these effects. However, the tightly held intramolecular hydrogen bond in the *ortho* bis acid promoted interactions between water molecules and precluded dissociation of the second proton which required more water molecules to occur than the other MASC ionomers with more widely spread distribution of charge and hydrogen bonding. This was also realized through potential energy surface scans of proton transfer for second proton dissociation where the energetic penalty associated with proton transfer was found to be considerably higher in the *ortho* bis acid than the other MASC ionomers. The calculations reveal that the electron withdrawing $-CF_2-$ units between protogenic groups in the PFIA not only promote proton dissociation but also do not sterically fix the protogenic group separation, as with the aromatic-based MASC ionomers, allowing for the development of a hydrogen bond network that readily adjusts for the transfer of charge at low hydration levels.

1. Introduction

Fuel cells offer immense potential to replace conventional energy systems based on the combustion of fossil fuels due to their wide range of applicability and minimal environmental impact [1,2]. These devices provide energy through electrochemical conversion of a fuel, typically hydrogen, into electricity. There are a wide variety of fuel cells that differ primarily in the type of electrolyte they employ. Among the most commonly used electrolytes are proton exchange membranes (PEMs) utilizing hydrogen as the fuel. In a PEM fuel cell, the solid polymer membrane not only acts as the electrolyte, but also as the internal ion-conducting medium and the separator of the electrodes and reactant gases [3]. PEM fuel cells offer high power density, fast startup time, and are light weight which makes them promising candidates for stationary, portable, and automotive use [4]. An ideal PEM material must be highly proton conducting with low electrical conductivity, have good mechanical integrity, and high chemical and thermal stability in an oxidative environment at temperatures as high as 120 °C [5]. Presently, the most widely used PEM materials are perfluorosulfonic acid (PFSA) ionomers with Nafion® serving as the benchmark.

PFSA ionomers consist of a hydrophobic poly(tetrafluoroethylene) (PTFE) backbone functionalized with pendant perfluorinated side chains each terminated by a single hydrophilic sulfonic acid group ($-SO_3H$). Currently available PFSA materials must be sufficiently hydrated to conduct protons at high rates as the presence of water plays a critical role in the formation of free protonic charge carriers and overall proton mobility in these materials. For example, Nafion® only exhibits high proton conductivity ($\sim 10^{-1}$ Scm^{-1}) under conditions of near full hydration (i.e., 95% relative humidity) [6]. When hydrated, these ionomers phase separate into hydrophilic and hydrophobic

* Corresponding author. Tel.: +1 865 974 2026; fax: +1 865 974 7076.
E-mail address: spaddison@utk.edu (S.J. Paddison).

0013-4686/$ – see front matter © 2012 Elsevier Ltd. All rights reserved.
http://dx.doi.org/10.1016/j.electacta.2012.11.138

domains through aggregation of the ionomer backbones, resulting from their hydrophobicity, and solvation and subsequent aggregation of the sulfonic acid groups [3,7,8]. This leads to proton dissociation from the sulfonic acid groups into the aqueous domain allowing for long-range proton transport through the membrane [3,9] by means of both vehicular and structural diffusion [10–14] with some characteristics resembling those observed in bulk water [15–19]. There are several complications that arise due to the necessity for these materials to be highly hydrated. One primary obstacle is that this restricts the operating temperature to below 100 °C (i.e., the boiling point of water) to prevent the membrane from drying out. This limitation necessitates the use of expensive platinum or platinum alloy catalysts due to poor electrode reaction kinetics at low temperatures. Furthermore, at temperatures below 120 °C the platinum-based catalysts are more susceptible to carbon monoxide poisoning through preferential adsorption of CO onto the platinum surface blocking the reaction sites [2]. Highly hydrated conditions also adversely affect the efficiency of the fuel cell due to water 'cross-over' resulting from electroosmotic drag and permeation [20]. This has led to immense efforts to develop membrane materials that exhibit high proton conductivity at lower hydration levels allowing for higher temperature operation and removing the issues associated with water management [21–26].

A variety of PFSA chemical homologs of Nafion® comprised of different perfluorinated side chains exist, such as Aciplex® from Asahi Kasei [27,28], Flemion® from Asahi Glass [29], the 3M PFSA membrane [25], and the short side chain (SSC) PFSA membrane originally synthesized by Dow Chemical Company [30] but now as Aquivion® (formerly Hyflon®) by Solvay-Solexis [31–33]. These modifications provide a means for lowering the ionomer equivalent weight (EW≡grams ionomer per mole of acid) which is known to increase proton conductivity [25]. While many of these materials have been shown to exhibit higher proton conductivity than Nafion® [25,34–36], they remain limited by high cost and their proton conductivities still rely heavily on the level of hydration. Sulfonated aromatic main-chain polymers, such as sulfonated poly(ether ether ketone) (sPEEK), have also received interest, as they are easily synthesized and relatively low cost, but have lower proton conductivity than the PFSA ionomers at low hydration [7,23,27,37,38]. Other approaches include replacing the sulfonic acid group in currently available membranes with another protogenic group, such as bis(sulfonyl imides). Bis[(perfluoroalkyl)sulfonyl] imide analogs of Nafion® have been shown to exhibit greater thermal stability [39], stronger gas phase acidity [40], and higher proton conductivity at low hydration levels when compared to typical PFSA ionomers [39,41]. Current developments at 3M go even further by introducing novel perfluorinated and partially perfluorinated ionomers with multiple protogenic groups per side chain based on the 3M PFSA ionomer (3M PFSA: PTFE backbone with $-O(CF_2)_4SO_3H$ side chains) [42,43]. These materials are synthesized by converting the sulfonyl fluoride precursor of the 3M PFSA ionomer ($-O(CF_2)_4SO_2F$) to perfluoro bis(sulfonyl imides) which serve as a protogenic group and provide a site for further modification to link a sulfonic acid containing aromatic or perfluorinated functional group [43]. This allows for the generation of ionomers with lower EW than the PFSA counterparts without loss of backbone tetrafluoroethylene units important to the mechanical integrity of the membrane. These ionomers exhibit higher proton conductivities than the 3M PFSA membranes made from the same ionomer precursors at high hydration levels, but at low hydration levels the proton conductivity in the aromatic-based ionomers with multiple acidic groups per side chain drops below that of the 3M PFSA. However, the fully fluorinated ionomer maintains higher proton conductivity than the 3M PFSA made from the same EW precursor at all hydration levels [43]. While several of the above membrane materials offer promising characteristics, none of them currently meet all of the requirements for widespread use in hydrogen fuel cells. A more complete understanding of the specific molecular features of PEMs that contribute to proton mobility at low hydration levels will undoubtedly aide in the development of superior membranes.

Despite the wide variety of available PEM materials, it is well known that hydrogen bonding is an essential component to proton mobility in them all [3,44]. While the mechanisms for proton transfer in these materials have been studied extensively, discussion continues regarding the fundamental nature of the atomistic process. Structural diffusion of protons requires shuttling of protons through the hydrogen bond network by means of a series of transformations between Eigen ($H_9O_4^+$) and Zundel ($H_5O_2^+$) cations [10–19,45]. Investigation into how specific ionomer chemistry governs this requires a molecular-level understanding of the formation and breaking of hydrogen bonds within highly complex systems which is difficult to deduce from experimental measurements alone. As such, multiscale modeling techniques capable of probing specific structural and dynamical features of PEM materials have provided insight into how the chemical functionalities and molecular-level structural properties affect proton transport in materials of this type. Empirical valence bond (EVB) schemes [46–48] capable of predicting dynamic proton shuttling have been utilized to study proton mobility and solvation in PFSA systems revealing evidence of structural diffusion [49–52]. Evidence of structural diffusion has also been observed in *ab initio* molecular dynamics (AIMD) simulations employed to study proton transport in model PFSA systems [53–59], as well as other PEMs [60,61], at various levels of hydration and protogenic group density. *Ab initio* electronic structure calculations have also been utilized to investigate local hydration and proton dissociation and separation in single side chain fragments of PFSA ionomers [62–68]. In addition to PFSA ionomers, electronic structure calculations have been used to explore local hydration and proton dissociation in other fragments of various PEM ionomers and acidic moieties including: aryl main-chain sulfonic acids [64,69], imidazole [70], phosphonic acid [70,71], phosphoric acid [72], carboxylic acid [73], and sulfonyl imides [69,74]. Calculations on trifluoromethane sulfonic acid (triflic acid) and *para*-toluene sulfonic acid revealed that more negative charge resided on the sulfonic acid/sulfonate oxygen atoms of *para*-toluene sulfonic acid than those of triflic acid indicating the enhanced electron-withdrawing capacity of a trifluoromethyl group over an aromatic ring [64]. The effects of electron withdrawing groups were also found in studies on bis(sulfonyl imides) with different neighboring group substitutions [69,74]. Namely, the results indicated that fully fluorinated bis(sulfonyl imides) exhibited more favorable proton dissociation at low hydration than partially fluorinated bis(sulfonyl imides) containing an aromatic ring or methyl substituent group. Additional studies incorporating multiple PFSA side chains along the same PTFE backbone have demonstrated the importance of backbone flexibility, EW, and cooperative interactions between adjacent side chains have on hydrogen bonding, proton dissociation, and the state of the dissociated proton(s) [75–79]. Specifically, calculations on the SSC [75–78] and 3M PFSA [79,80] ionomers revealed that side chain separation had a profound effect on the nature of the hydrogen bond network and the hydrogen bond connectivity of sulfonic acid groups both directly and through water molecules. These effects were found to influence proton dissociation and the state of the dissociated proton where proton dissociation more readily occurred in systems with less separation between sulfonic acid groups. These studies investigated features relating to protogenic group separation in neighboring side chains each containing a single acid group. However, calculations exploring the effect of protogenic group separation and side chain chemistry on hydrogen bonding and

proton dissociation and transfer in PEM ionomers with multiple acid groups per side chain have yet to be reported.

The present study explores the effects specific side chain chemistry and protogenic group separation have in facilitating proton dissociation and transfer in three novel multi acid side chain (MASC) ionomers containing two acidic groups per side chain through *ab initio* electronic structure calculations. The ionomers consist of a PTFE backbone functionalized with side chains each containing a sulfonic acid group and a bis(sulfonyl imide) group with separation mediated by distinct structural differences. Two of the ionomers are structural isomers with protogenic group separation determined by the location of the sulfonic acid group on an aromatic ring with side chain chemical formula $-O(CF_2)_4SO_2(NH)-SO_2C_6H_4SO_3H$ where the sulfonic acid group is located in either the *meta* or the *ortho* position. The third ionomer, termed the PFIA, has protogenic groups separated by difluoromethylene (CF_2) units with side chain formula $-O(CF_2)_4SO_2(NH)SO_2(CF_2)_3SO_3H$. The calculations were performed on single side chain fragments of the ionomers with and without the addition of water molecules to assess the factors that contribute to proton dissociation and the energetics associated with proton transfer.

This paper is organized as follows. The first section contains a brief description of the computational methods used in geometry optimizations and potential energy surface (PES) scans for proton transfer. The results are then presented and discussed first comparing optimized structures and proton dissociation for the three ionomers followed by a relative comparison of the energetics of proton transfer in these materials. Finally, the main results are summarized in the conclusion section.

2. Computational methods

Electronic structure calculations were performed using the Gaussian 09 suite of programs [81]. Full optimizations (i.e. over all degrees of freedom) were then carried out by conjugate gradient methods [82] without symmetry constraints initially invoking Hartree–Fock theory with the 6-31G** split-valence basis set [83]. The resulting structures were then refined with density functional theory (DFT) employing Becke's 3-parameter hybrid functional (B3LYP) [84,85] and the same basis set. Final optimizations were then performed at the B3LYP/6-311G** level of theory [86]. Subsequent to the 'dry' optimizations (i.e., without explicit H_2O molecules), water molecules were individually added to the optimized systems at a variety of initial positions and full optimizations were performed using the protocol described above. Vibrational frequencies and zero point energies (ZPEs) were determined for all global minimum energy structures at the B3LYP/6-311G** level. The counterpoise (CP) method of Boys and Bernardi [87] was also employed to explore the effects of basis set superposition error (BSSE) on the water binding energies calculated from the CP-corrected optimized geometries and vibrational frequencies. Additionally, partial charges and electrostatic potentials were obtained according to the CHelpG scheme at the highest level of theory [88]. Potential energy surface (PES) scans of proton transfer were performed at the B3LYP/6-31G** level to obtain relative energy profiles for these events. A variety of optimized structures were chosen as starting points for the PES scans, and the scans were carried out by incrementally increasing a specified O—H or N—H bond length across a hydrogen bond in steps of 0.002 nm. The O—H/N—H bond length was the only fixed parameter with an optimization performed over all other degrees of freedom at each step. Vibrational frequencies were obtained for transition state geometries (when applicable) to ensure the existence of a single imaginary frequency corresponding to the reaction coordinate. As these scans are based on optimized static structures, they only reveal the relative tendencies in the energetics of proton transfer, not absolute values. Furthermore, collective effects of the extended environment have been neglected.

3. Results and discussion

3.1. Local hydration and proton dissociation

Uncorrected, ZPE-corrected, and BSSE-corrected binding energies of the water molecules to the *meta*, *ortho*, and PFIA minimum energy conformations are given in Tables 1–3, respectively (empty cells in the BSSE-corrected binding energies represent cases where full convergence did not occur). As it is well known that hydrogen bonding is a critical feature of proton transport in materials of this type, these interactions were a primary focus in this study. The requirements for a hydrogen bond in the structures that follow were an O···O or O···N distance between 0.24 and 0.32 nm and an O—H···O, O—H···N or N—H···O bond angle greater than 140° [55,89–92]. The figures that follow are the optimized BSSE-corrected geometries with hydrogen bonds denoted by dashed lines with the corresponding hydrogen bond lengths (measured by the O···O or N···O distance) given in nm; in most cases, the top portion of the hydrated fragments have been omitted for clarity. The top panel of Fig. 1 shows the initial 'dry' (i.e., without the addition of any water molecules) optimized structure of each ionomer fragment. The bottom panel of Fig. 1 depicts the electrostatic potential mapped on the total electron density for each fragment where blue regions are electron deficient and red regions are electron rich. These figures illustrate key differences in how protogenic group separation and specific side chain chemistry affect the atomic charges of the protogenic groups in the three systems under 'dry' conditions. Namely, the proximity of protogenic groups in the *ortho* (Fig. 1b) allows for hydrogen bonding between them resulting in delocalization of charge. This interaction, however, is not sterically possible in the *meta* bis acid (Fig. 1a) where no sharing of charge between protogenic groups is observed. This effect can be seen in the electrostatic isosurfaces where the *meta* exhibits more electron rich (darker red) regions surrounding the sulfonyl and sulfonic acid oxygen atoms and more electron deficient (darker blue) regions surrounding the acidic protons than the *ortho*. Charge delocalization is brought about in the PFIA system (Fig. 1c) through the electron withdrawing —CF_2— groups effectively decreasing the negative charge on the sulfonic acid and lower sulfonyl oxygen atoms as indicated by the lighter red tone surrounding them. These charge delocalizing effects were found to play critical roles in first proton dissociation at low levels of hydration.

First proton dissociation in PFIA was observed at a hydration of three water molecules with a variety of optimized configurations. Fig. 2a shows the minimum energy structure where the proton from the sulfonic acid group has dissociated resulting in the formation of a hydronium ion hydrogen bonded to the, now, sulfonate group. The hydronium ion also donates hydrogen bonds to the two other water molecules, one of which donates a single hydrogen bond to a different sulfonate oxygen atom and the other donates a hydrogen bond to a sulfonyl oxygen atom forming a hydrogen bond connectivity bridge between the protogenic groups. The sulfonic acid proton has also dissociated to form a hydronium ion in the optimized structure shown in Fig. 2b. In this case, however, each of the water molecules form hydrogen bonds with the oxygen atoms of the sulfonate group without any connectivity to the bis(sulfonyl imide) group resulting in a configuration 5.0 kJ/mol higher in energy than the previous structure. In the third configuration (Fig. 2c), the proton from the imide group has dissociated forming a hydronium ion that donates hydrogen bonds to the two other water molecules which each

Table 1
Energetics of optimized *meta* bis acid fragments.[a]

n H_2O	E_{elec}[b]	E_{ZPE}[c]	ΔE (kJ/mol)[d]	ΔE_{ZPE} (kJ/mol)[e]	ΔE_{BSSE} (kJ/mol)[f]
0	−4086.12424	0.24361	–	–	–
1	−4162.60082	0.26956	−76.6	−64.4	−46.0
2	−4239.07881	0.29580	−78.2	−65.7	−43.1
3	−4315.55291	0.32101	−75.7	−63.6	−41.4
4	−4392.02796	0.34644	−74.9	−63.2	−42.7
5	−4468.50121	0.37267	−73.2	−61.5	−41.4
6	−4544.97769	0.39933	−73.6	−61.5	−41.8
7	−4621.44703	0.42422	−71.5	−59.8	−40.6
8	−4697.91939	0.44828	−70.7	−59.4	−41.0
9	−4774.39007	0.47309	−69.5	−58.6	–

[a] Energetics for structures optimized at the B3LYP/6-311G** level.
[b] Total electronic energy in Hartrees.
[c] Zero point energy (ZPE) in Hartrees.
[d] Binding energy per water molecule based on uncorrected total electronic energy.
[e] Binding energy per water molecule based on ZPE corrected electronic energy.
[f] Binding energy per water molecule based on BSSE corrected CP optimized structures.

Table 2
Energetics of optimized *ortho* bis acid fragments.[a]

n H_2O	E_{elec}[b]	E_{ZPE}[c]	ΔE (kJ/mol)[d]	ΔE_{ZPE} (kJ/mol)[e]	ΔE_{BSSE} (kJ/mol)[f]
0	−4086.13064	0.24559	–	–	–
1	−4162.60033	0.27005	−58.6	−50.2	−30.1
2	−4239.06724	0.29486	−54.8	−46.0	−28.4
3	−4315.54620	0.32076	−64.0	−54.4	−36.4
4	−4392.02209	0.34712	−66.5	−56.1	−39.7
5	−4468.49394	0.37255	−66.1	−55.6	−40.2
6	−4544.97053	0.39880	−67.8	−56.9	−38.9
7	−4621.44163	0.42518	−66.9	−55.4	−40.6
8	−4697.91687	0.45040	−67.8	−56.5	−36.4
9	−4774.39056	0.47657	−67.8	−56.5	−38.1
10	−4850.86736	0.50298	−69.0	−57.3	−37.7

[a] Energetics for structures optimized at the B3LYP/6-311G** level.
[b] Total electronic energy in Hartrees.
[c] Zero point energy (ZPE) in Hartrees.
[d] Binding energy per water molecule based on uncorrected total electronic energy.
[e] Binding energy per water molecule based on ZPE corrected electronic energy.
[f] Binding energy per water molecule based on BSSE corrected CP optimized structures.

donate a single hydrogen bond to different sulfonyl oxygen atoms. As was the case in Fig. 2b, no hydrogen bond connectivity between protogenic groups was observed, and the resulting structure was found to be 31.0 kJ/mol higher in energy than the minimum energy configuration. These results suggest that connectivity of protogenic groups through hydrogen bonding is favorable in promoting proton dissociation at low levels of hydration. Furthermore, proton dissociation from the sulfonic acid group seems to occur more readily than in the imide group at low levels of hydration. This is counter-intuitive since the bis(sulfonyl imide) group has a higher gas phase acidity than that of sulfonic acid; however, the hydrogen bonding appears to play an important role in proton dissociation under minimally hydrated conditions.

The *ortho* fragment also exhibited preferential first proton dissociation at a hydration of three water molecules with multiple optimized configurations (Fig. 3). Again, the energetically preferred state contains the proton dissociated from the sulfonic acid group, shown in Fig. 3a. A direct hydrogen bond between the imide and a sulfonate oxygen atom remains, and the dissociated proton exists as a hydronium ion which forms a hydrogen bond with a

Table 3
Energetics of optimized PFIA fragments.[a]

n H_2O	E_{elec}[b]	E_{ZPE}[c]	ΔE (kJ/mol)[d]	ΔE_{ZPE} (kJ/mol)[e]	ΔE_{BSSE} (kJ/mol)[f]
0	−4568.54071	0.19963	–	–	–
1	−4645.01586	0.22456	−72.8	−63.2	−45.6
2	−4721.49022	0.24923	−71.5	−62.8	−44.3
3	−4797.96945	0.27577	−75.7	−64.8	−48.9
4	−4874.43981	0.30124	−71.5	−61.1	−47.7
5	−4950.92138	0.32692	−75.3	−64.4	−44.3
6	−5027.39773	0.35287	−75.3	−64.4	−43.9
7	−5103.86686	0.37912	−72.8	−61.5	−43.1
8	−5180.34076	0.40453	−72.4	−61.1	−41.8
9	−5256.81516	0.43052	−72.0	−60.7	–

[a] Energetics for structures optimized at the B3LYP/6-311G** level.
[b] Total electronic energy in Hartrees.
[c] Zero point energy (ZPE) in Hartrees.
[d] Binding energy per water molecule based on uncorrected total electronic energy.
[e] Binding energy per water molecule based on ZPE corrected electronic energy.
[f] Binding energy per water molecule based on BSSE corrected CP optimized structures.

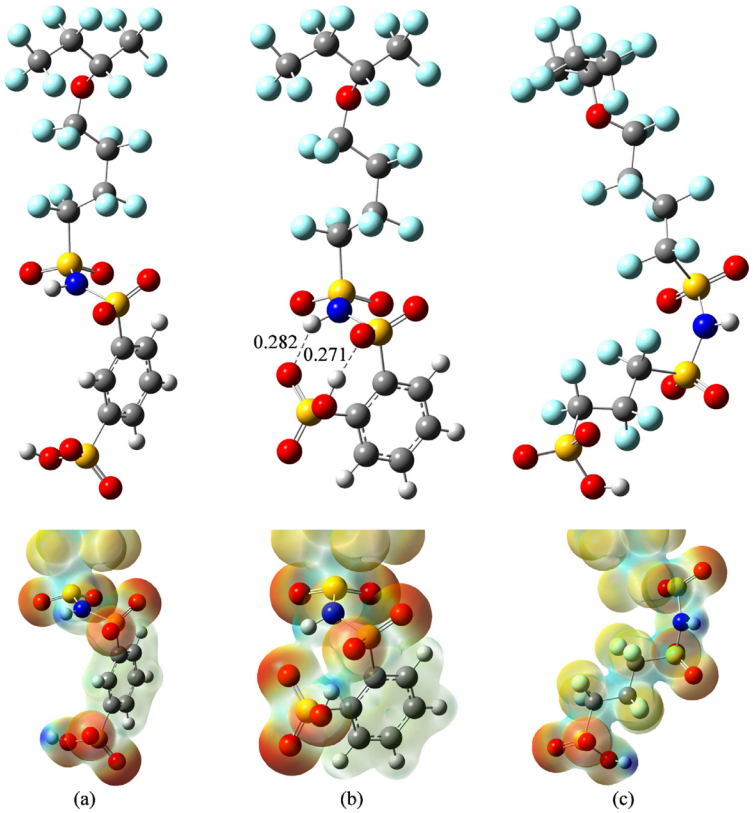

Fig. 1. Optimized (B3LYP/6-311G**) minimum energy structures of isolated 3M MASC ionomer fragments with the mapped electrostatic isosurfaces (blue regions are electron deficient and red regions are electron rich) for: (a) the *meta* bis acid, (b) the *ortho* bis acid, and (c) the PFIA ionomer. The different colored spheres represent different atom types where: gray – carbon, light blue – fluorine, red – oxygen, yellow – sulfur, blue – nitrogen, and white – hydrogen. (For interpretation of the references to color in this figure legend, the reader is referred to the web version of the article.)

neighboring water molecule. One hydronium ion proton does not form a hydrogen bond based strictly on our definitions. However, the O—H···O angle between the hydronium ion and the nearby sulfonyl oxygen atom was 135° with an O···O distance of 0.277 nm revealing an interaction which could be considered a hydrogen bond under looser criteria. This configuration was found to be only 3.8 kJ/mol lower in energy than the optimized structure with the imide proton dissociated (Fig. 3b). The structure contains the sulfonic acid group hydrogen bonded to a sulfonyl oxygen atom directly connecting the two groups, and the dissociated proton is well separated from the imide. Unlike the PFIA fragment, the *ortho* inherently has connectivity between protogenic groups through direct hydrogen bonds. One of these direct hydrogen bonds is maintained in each of these configurations for first proton dissociation. This results in a sharing of charge that facilitates proton dissociation from either protogenic group at this low level of hydration. Each configuration contains a somewhat 'congested' hydrogen bond network due to the fixed protogenic group distance resulting in less separation between available hydrogen bonding sites of the ionomer.

In the *meta* fragment, first proton dissociation was only found to be energetically favorable upon the addition of five water molecules due to the lack of charge delocalization at low hydration levels (Fig. 4). The proton from the sulfonic acid group was again found to preferentially dissociate first over the imide. The dissociated proton is in the form of a hydronium ion which delocalizes its excess positive charge over two water molecules through hydrogen bonds. The greater fixed protogenic group separation than the *ortho* promotes hydrogen bonding that is much more spread out in a 'cage-like' fashion due to the lack of spatial hindrances.

As mentioned, first proton dissociation was promoted in the *ortho* through hydrogen bonding between protogenic groups. These hydrogen bonds must be broken before dissociation of the second acidic proton can occur. Although these static electronic structure calculations neglect collective effects of extended ionomer interactions and dynamic configurational changes, examination of various *ortho* configurations upon addition of four water molecules provides some relative insight into the energetics associated with these protogenic group hydrogen bonds. Fig. 5 shows three optimized structures containing different hydrogen bond patterns. The configurations in Fig. 5a and b contain a single dissociated proton where one of the hydrogen bonds is maintained between the associated imide and an oxygen atom of the sulfonate group and the sulfonic acid and a sulfonyl oxygen atom, respectively. These structures were found to be isoenergetic. The structure in Fig. 5c also contains one dissociated proton, but does not contain a direct hydrogen

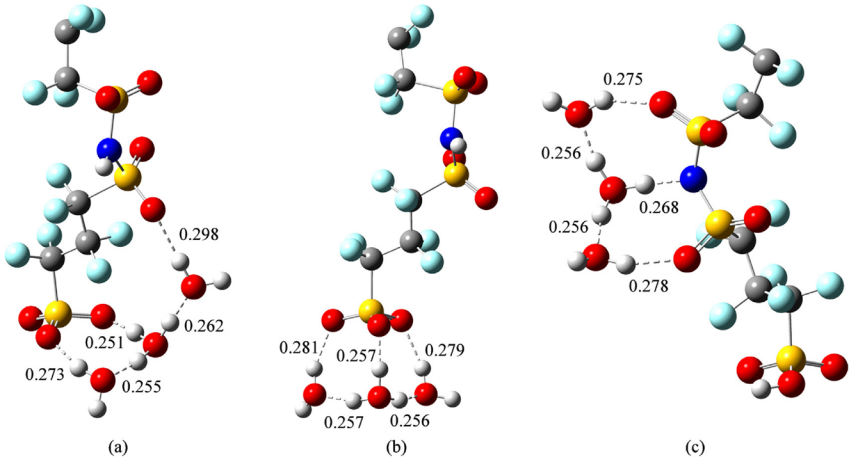

Fig. 2. Optimized (B3LYP/6-311G**) structures of the 3M PFIA showing first proton dissociation upon addition of three water molecules with different configurations and hydrogen bonds (dashed lines) and hydrogen bond distances (nm) showing: (a) the minimum energy structure where the sulfonic acid is dissociated and the hydrogen bonding connects the sulfonate group to the bis(sulfonyl imide) group; (b) a configuration 5.0 kJ/mol higher in energy with the sulfonic acid group dissociated with selective solvation to the sulfonate group containing no hydrogen bond connectivity between acid groups; and (c) a configuration 31.0 kJ/mol higher in energy with the imide dissociated with selective solvation to the bis(sulfonyl imide) group containing no hydrogen bond connectivity to the sulfonic acid.

bond between the protogenic groups. This configuration was found to be 37.2 kJ/mol higher in energy than the others which maintain a direct hydrogen bond which suggests that this interaction may be preferential at low hydration levels.

This point is further supported in the examination of second proton dissociation, shown in Fig. 6. The favorable single direct hydrogen bond connectivity between protogenic groups in the *ortho* was maintained until the addition of eight water molecules and second proton dissociation required ten water molecules (Fig. 6b). While first proton dissociation was promoted through intramolecular hydrogen bonding, the second acidic proton is held tightly through this stabilization effect resisting dissociation. The close proximity of protogenic groups and competition between available hydrogen bond sites on the ionomer also promote greater interactions between water molecules in this isolated system. This precludes the charge delocalization effects associated with strong donated hydrogen bonds from the water molecules to the hydrogen bond acceptor sites on the ionomer important for stabilization after proton dissociation. Furthermore, the additional positive charge in the surrounding water cluster after first proton dissociation is localized around the acid groups which resists further acceptance of positive charge at low hydration. The PFIA (Fig. 6c) and *meta* (Fig. 6a), on the other hand, only required seven and eight water molecules, respectively, for preferential second proton dissociation as the greater protogenic group separation led to a more widely spread charge distribution and less competition between hydrogen

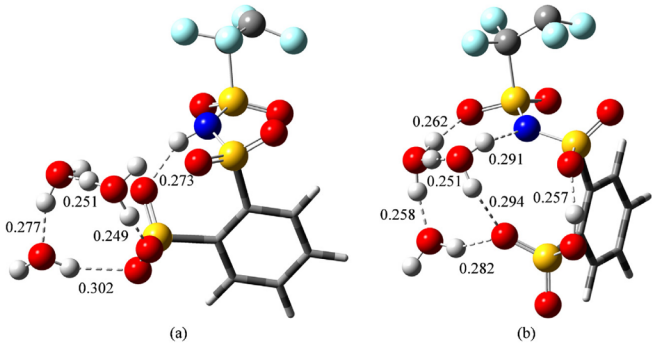

Fig. 3. Optimized (B3LYP/6-311G**) structures of the 3M *ortho* bis acid showing first proton dissociation upon addition of three water molecules with different configurations and hydrogen bonds (dashed lines) and hydrogen bond distances (nm) showing: (a) the minimum energy structure where the sulfonic acid is dissociated and the imide forms a direct hydrogen bond with a sulfonate oxygen atom; and (b) a configuration 3.8 kJ/mol higher in energy with the imide dissociated and the sulfonic acid forms a direct hydrogen bond to a sulfonyl oxygen atom.

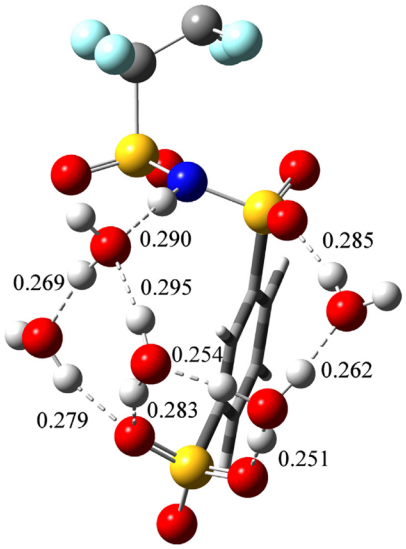

Fig. 4. Optimized (B3LYP/6-311G**) minimum energy structure of the 3M *meta* bis acid and hydrogen bonds (dashed lines) and hydrogen bond distances (nm) showing energetically preferred first proton dissociation requiring five water molecules.

bond acceptor sites on the ionomer promoting stronger hydrogen bonds. This is supported by the trends in the magnitude of the binding energies of the water molecules to the ionomers where, at low hydration, the binding energies to the *ortho* fragment were found to be lower than those of the *meta* and PFIA. It is important to note that a doubly dissociated PFIA geometry at a hydration of six water molecules was found that was only 0.54 kJ/mol higher in energy than the minimum energy state with one dissociated proton which may provide some insight into the higher experimental proton conductivity in the PFIA than the other MASC ionomers at low hydration levels [43].

3.2. Energetics of proton transfer

In the following figures, the top left panel shows the optimized structures used in the PES scans for proton transfer. The relative energy profiles obtained from the scans are shown in the top right panel and are plotted as a function of the asymmetric stretch coordinate, $q_{asym} = 1/\sqrt{2}\,(r_{X1\cdots H} - r_{H\cdots X2})$, where X1 represents the oxygen or nitrogen atom the proton is initially covalently bonded to and X2 represents the oxygen or nitrogen atom receiving the proton. The bottom panels of the figures show the bottom portion of the ionomer fragment with the surrounding water molecules; hydrogen bonds are denoted by dashed lines with the corresponding O···O and N···O distances reported in nm for relevant steps throughout the PES scans, all other atoms were removed for clarity. Figs 7 and 8 compare two different proton transfer profiles for the *meta* bis acid starting from the same minimum energy geometry found at a hydration of 3 H_2O molecules. The energy profile shown in Fig. 7 and the corresponding points of the PES scan result from transferring the associated proton of the imide group to a neighboring water molecule. The water molecule receiving the proton only accepts a hydrogen bond from the imide group while donating hydrogen bonds to the other two water molecules. Expansions and contractions in hydrogen bond lengths are observed up to the transition state (Fig. 7b) to accommodate for the transfer of charge without significant change in the hydrogen bond topography. The energetic barrier to this point was found to be only ~7.5kJ/mol higher in energy than the initial geometry. Once the proton has transferred to the water molecule, the newly formed hydronium ion is capable of donating stronger hydrogen bonds to the other two water molecules which is indicated by the decrease in the respective hydrogen bond lengths. Furthermore, the rightmost water molecule undergoes a slight orientational shift to form a new hydrogen bond with a sulfonyl oxygen atom not originally involved in hydrogen bonding which has a stabilizing effect leading to the shallow minimum (Fig. 7c) only ~7.3 kJ/mol higher in energy than the original configuration. As mentioned previously, the preferential dissociated state in the *meta* was not observed until the addition of 5 H_2O molecules. Thus, even with the formation of a new stabilizing hydrogen bond, the higher energy of the final structure is not surprising. Proton transfer from the sulfonic acid to a neighboring water molecule, however, reveals considerably different results, as shown in Fig. 8, where a monotonically increasing relative energy profile was observed. In this case, the water

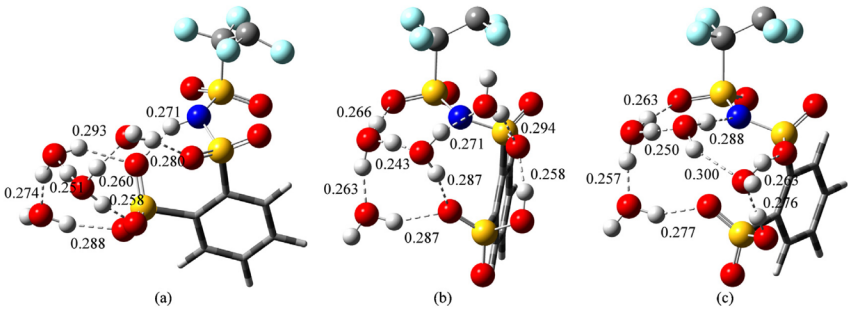

Fig. 5. Optimized (B3LYP/6-311G**) structures of the 3M *ortho* bis acid with the addition of four water molecules with singly dissociated geometries and hydrogen bonds (dashed lines) and hydrogen bond distances (nm) showing configurations where: (a) the sulfonic acid is dissociated and the imide maintains a direct hydrogen bond with a sulfonate oxygen atom; (b) the imide is dissociated and the sulfonic acid maintains a direct hydrogen bond to a sulfonyl oxygen atom; and (c) the imide is dissociated and no direct hydrogen bonding between protogenic groups occurs. Minimum energy structures (a) and (b) are isoenergetic while structure (c) without the direct hydrogen bond is 37.2 kJ/mol higher in energy.

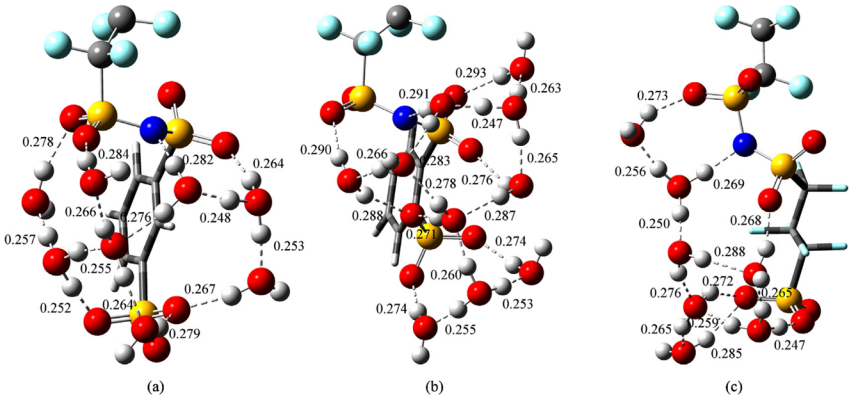

Fig. 6. Optimized (B3LYP/6-311G**) minimum energy structures of 3M MASC ionomers with energetically favored second proton dissociation and hydrogen bonds (dashed lines) and hydrogen bond distances (nm) requiring: (a) eight water molecules in *meta* bis acid, (b) ten water molecule in *ortho* bis acid, and (c) seven water molecules in PFIA.

molecule receiving the proton not only initially accepts a hydrogen bond from the sulfonic acid group but also from the central water molecule. Again, expansions and contractions in the hydrogen bond lengths were observed as a result of charge transfer in the early stages of the scan up to $q_{assym} = 0$ (Fig. 8b) where the most notable change is the increase in the hydrogen bond length between the aforementioned proton receiving water molecule and the central water molecule from 0.290 to 0.311 nm. The sulfonyl oxygen atom

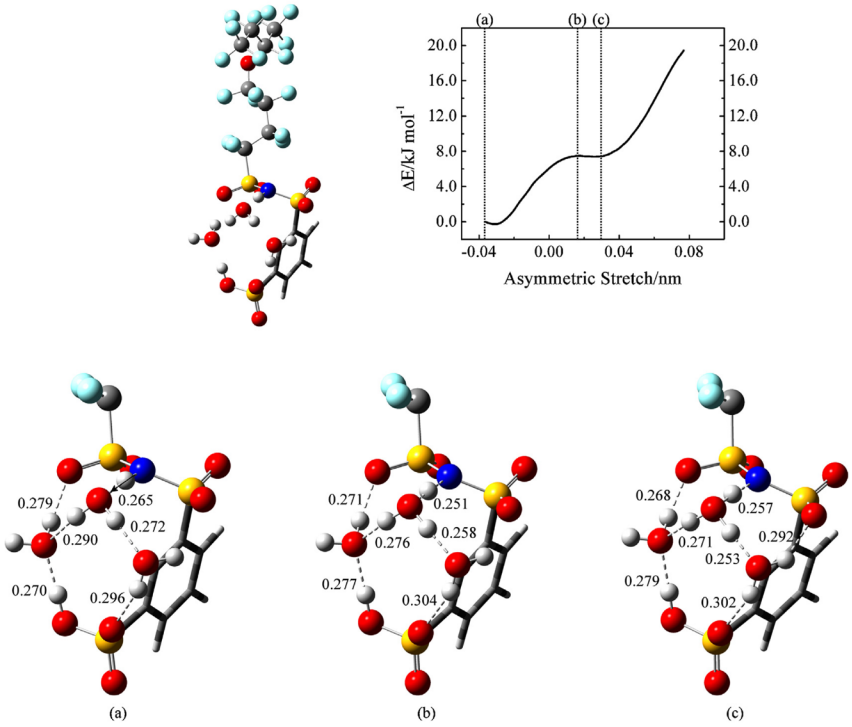

Fig. 7. Top left panel: Optimized (B3LYP/6-31G**) structure of the *meta* bis acid at a hydration of three water molecules used in the PES scan of proton transfer from the associated imide to a neighboring water molecule. Top right panel: Relative energy profile with respect to the original configuration as a function of the asymmetric stretch coordinate. Bottom panel: Water molecules and the bottom portion of the ionomer with hydrogen bonds denoted by dashed lines and hydrogen bond distances (nm): (a) initial configuration; (b) transition state; and (c) the local minimum points of the scan.

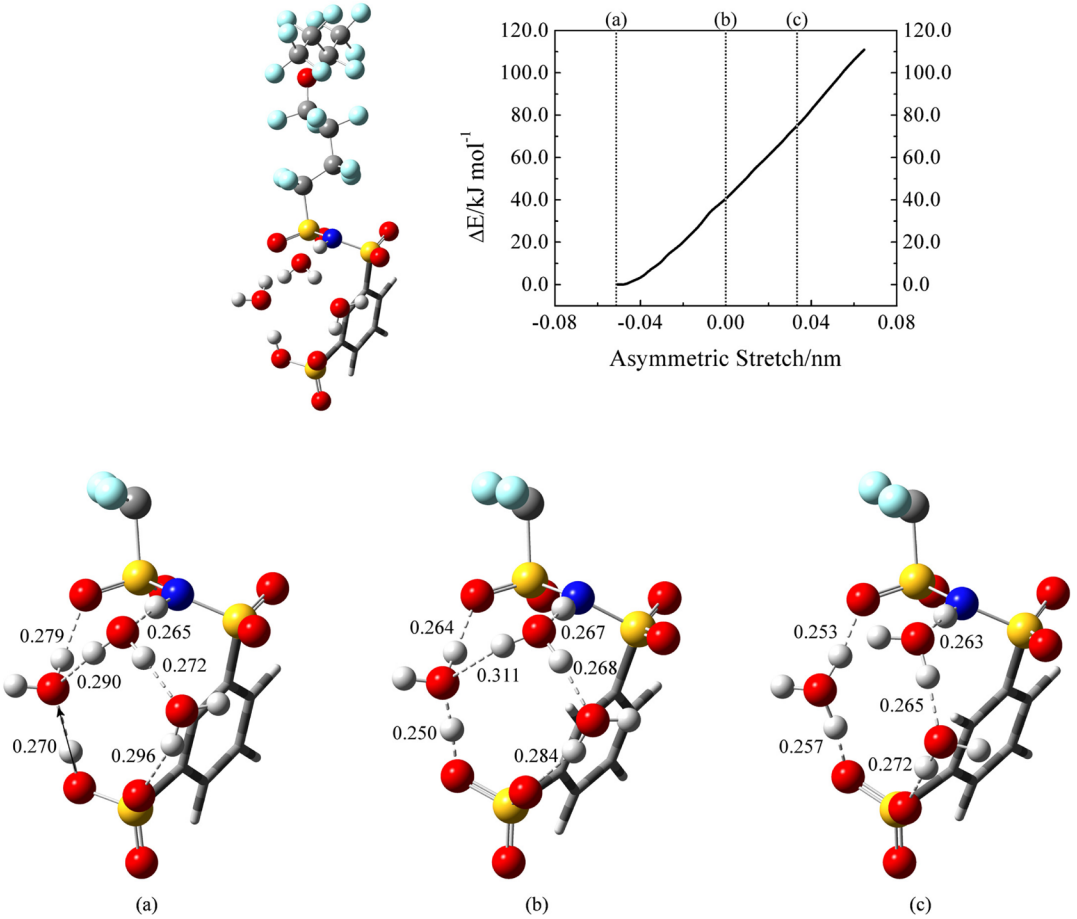

Fig. 8. Top left panel: Optimized (B3LYP/6-31G**) structure of the *meta* bis acid at a hydration of three water molecules used in the PES scan of proton transfer from the associated sulfonic acid to a neighboring water molecule. Top right panel: Relative energy profile with respect to the original configuration as a function of the asymmetric stretch coordinate. Bottom panel: Water molecules and the bottom portion of the ionomer with hydrogen bonds denoted by dashed lines and hydrogen bond distances (nm): (a) initial configuration; (b) an intermediate point in the scan where $q_{assym} = 0$; and (c) the point in the scan where the proton is fully transferred from the sulfonic acid to the water molecule.

the water molecule donates a hydrogen bond to strongly resist protonation precluding subsequent proton transfer which forces the hydrogen bond between the central water molecule and the proton accepting water molecule to break further along the scan as a result of the repulsion from the additional positive charge on the newly formed hydronium ion. Hydronium ions have been shown to preferentially delocalize excess positive charge over the maximum number of hydrogen bonds [74]. Since there are no open hydrogen bond sites in the near vicinity, the hydronium ion contains one proton not involved in any hydrogen bonds (Fig. 8c). This along with the breaking of a hydrogen bond without formation of a new one leads to the considerably higher energetic penalty for this proton transfer event of ~75.3kJ/mol. Since proton dissociation in the *meta* was not observed until higher hydration, these results do not imply that the imide should dissociate first.

Fig. 9 shows the results of a PES scan for proton transfer from the associated imide to a neighboring water molecule in the *meta* fragment at a hydration of 5 H_2O molecules. The minimum energy structure found at the B3LYP/6-31G** level was used as the starting configuration which contains a single dissociated proton but with different hydrogen bond lengths than those for first proton dissociation at the higher level of theory (Fig. 4). The water molecules and the ionomer are involved in a widespread hydrogen bond network with the water molecule receiving the proton accepting two hydrogen bonds, one from the imide and one from another water molecule, as well as donating a hydrogen bond to the left water molecule. As the proton is transferred, the length of the hydrogen bond between the two central water molecules increases from 0.280 to 0.296 nm at the transition state (Fig. 9b) as a result of the additional positive charge on the proton accepting oxygen

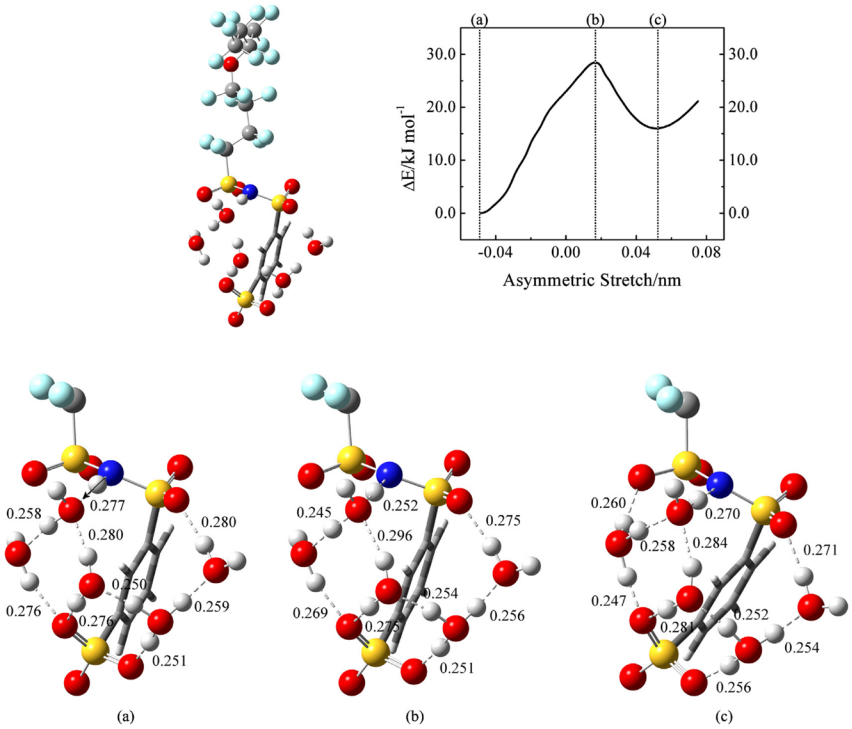

Fig. 9. Top left panel: Optimized (B3LYP/6-31G**) structure of the *meta* bis acid at a hydration of five water molecules used in the PES scan of proton transfer from the associated imide to a neighboring water molecule. Top right panel: Relative energy profile with respect to the original configuration as a function of the asymmetric stretch coordinate. Bottom panel: Water molecules and the bottom portion of the ionomer with hydrogen bonds denoted by dashed lines and hydrogen bond distances (nm): (a) initial configuration; (b) transition state; and (c) the local minimum points of the scan.

atom repelling away the water molecule donating a hydrogen bond to it. This repulsion was also observed in the aforementioned proton transfer from the sulfonic acid group to a neighboring water molecule in the *meta* at a hydration of 3 H_2O molecules (Fig. 8) which led to the breaking of a hydrogen bond as there was no additional proton transfer pathway available to accommodate for the transfer of charge. The situation in Fig. 9, on the other hand, contains an additional proton transfer path to the neighboring water molecule on the left which accepts a hydrogen bond from the proton receiving water molecule which contracts in length from 0.258 to 0.245 nm. This leads to a transition state where a different proton is shared between the left water molecule and the proton accepting water molecule which alleviates the repulsion between the central water molecules. The energetic barrier to this event was found to be ~28.4 kJ/mol. The shared proton is then fully transferred to the left water molecule following the transition state to the local minimum forming a hydronium ion, and the hydrogen bond between the central water molecules that was repelled in the early stages of the scan relaxes back to a distance of 0.284 nm. The newly formed hydronium ion has additional positive charge to delocalize over hydrogen bonds leading to a slight shift toward the top left sulfonyl oxygen atom forming a new stabilizing hydrogen bond. Its donated hydrogen bond to the sulfonate group oxygen atom considerably contracts in length which may be a due to the propensity for the system to be singly dissociated at this hydration level. This results in a local minimum 15.9 kJ/mol higher in energy than the starting geometry and containing two dissociated protons (Fig. 9c).

The results of proton transfer from the associated imide to a neighboring water molecule in the *ortho* at the same hydration level are shown in Fig. 10. The minimum energy *ortho* fragment at this hydration maintained the favorable hydrogen bond between the associated imide and the sulfonate group with no water molecule available for proton transfer. Hence, a different optimized geometry was used for comparison to the *meta* fragment. As mentioned previously, the close proximity of protogenic groups results in 'congested' hydrogen bonding that favors interactions between water molecules. The initial geometry contains a dissociated sulfonic acid group and one water molecule accepting a hydrogen bond from the imide and donating a hydrogen bond to a sulfonate group oxygen atom connecting the protogenic groups. The connecting water molecule also accepts a hydrogen bond from a neighboring water molecule. The length of this accepted hydrogen bond increases from 0.276 to 0.295 nm at the point where $q_{assym} = 0$ (Fig. 10b) due to the repulsion from the additional received positive charge as the proton is transferred. This bond fully breaks upon full transfer of the proton as the newly formed hydronium ion further repels away the water molecule (Fig. 10c). The hydronium ion contains one proton

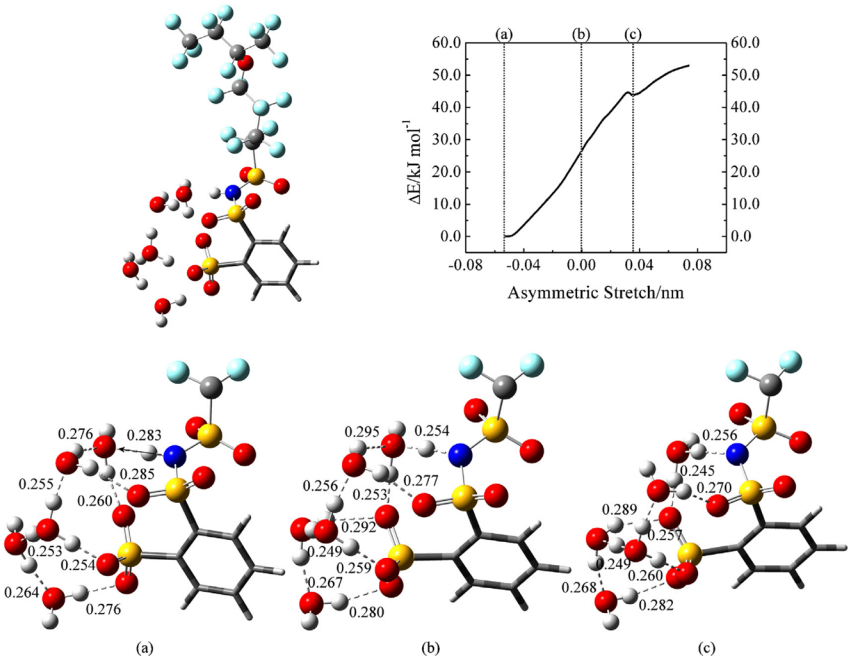

Fig. 10. Top left panel: Optimized (B3LYP/6-31G**) structure of the *ortho* bis acid at a hydration of five water molecules used in the PES scan of proton transfer from the associated imide acid to a neighboring water molecule. Top right panel: Relative energy profile with respect to the original configuration as a function of the asymmetric stretch coordinate. Bottom panel: Water molecules and the bottom portion of the ionomer with hydrogen bonds denoted by dashed lines and hydrogen bond distances (nm): (a) initial configuration; (b) an intermediate point in the scan where $q_{assym} = 0$; and (c) the point in the scan where the proton is fully transferred from the imide to the water molecule.

not involved in hydrogen bonding and does not donate a hydrogen bond to any water molecule. This causes delocalization of the excess positive charge over the sulfonate group and the hydrogen bond length between the hydronium ion and the sulfonate oxygen atom decreases from initially 0.260 nm to a final distance of 0.245 nm. In turn, the other hydrogen bonds initially donated to the sulfonate group from the other hydronium ion and water molecule lengthen to accommodate for the change in charge and further conformational changes are observed. Initially, one water molecule accepted a hydrogen bond of 0.253 nm from the central hydronium ion and was not involved in hydrogen bonding with the ionomer. The lengthening of the hydrogen bond between the central hydronium ion and the sulfonate group after proton transfer yields greater charge the hydronium ion delocalizes over the water molecule contracting the hydrogen bond length to 0.249 nm. The water molecule then has additional charge and shifts to form a new hydrogen bond with a sulfonate oxygen atom. This hydrogen bond, however, is very weak, as indicated by the O···O distance of 0.289 nm, and does not result in the strong stabilizing effect observed in the *meta* especially after the breaking of a hydrogen bond. This results in a considerably higher energetic penalty for proton transfer of 44.3 kJ/mol.

The PES scan and relevant geometries for proton transfer in the PFIA from the imide to a neighboring water molecule at the same hydration level are shown in Fig. 11. The initial configuration again contains a dissociated sulfonic acid group proton with well-connected hydrogen bonding. The proton receiving water molecule initially donates a hydrogen bond to a neighboring water molecule which contracts in length from 0.267 to 0.252 nm at the transition state (Fig. 11b). The nature of the hydrogen bonding readily allows for several expansions and contractions in hydrogen bond lengths throughout the system to accommodate for the transfer of charge resulting in an energetic barrier of only 4.6 kJ/mol. A local minimum is reached upon full transfer of the proton to the water molecule forming a hydronium ion (Fig. 11c). The hydronium ion, however, does not delocalize hydrogen bonds over the maximum number of oxygen atoms, based on our hydrogen bond definition, but there is an apparent interaction to the sulfonate oxygen atom with a O···O distance of 0.272 nm and an O—H···O angle of 135°. Nevertheless, this causes a further contraction in the hydrogen bond length between the hydronium ion and the left water molecule to 0.242 nm where the proton is actually shared between the two species. This increases the positive charge the water molecule can delocalize over the neighboring water molecules strengthening the hydrogen bonds it forms with them, as indicated by the decrease in O···O distance from 0.292 to 0.272 nm and 0.288 to 0.272 nm. As was the case up to the transition state, proton transfer continues to propagate charge throughout the well-connected hydrogen bond network (Fig. 11c). The initially dissociated sulfonic acid proton partially transfers back to the sulfonate group due to the propensity for the system to be singly dissociated at this hydration level. This reduces the charge

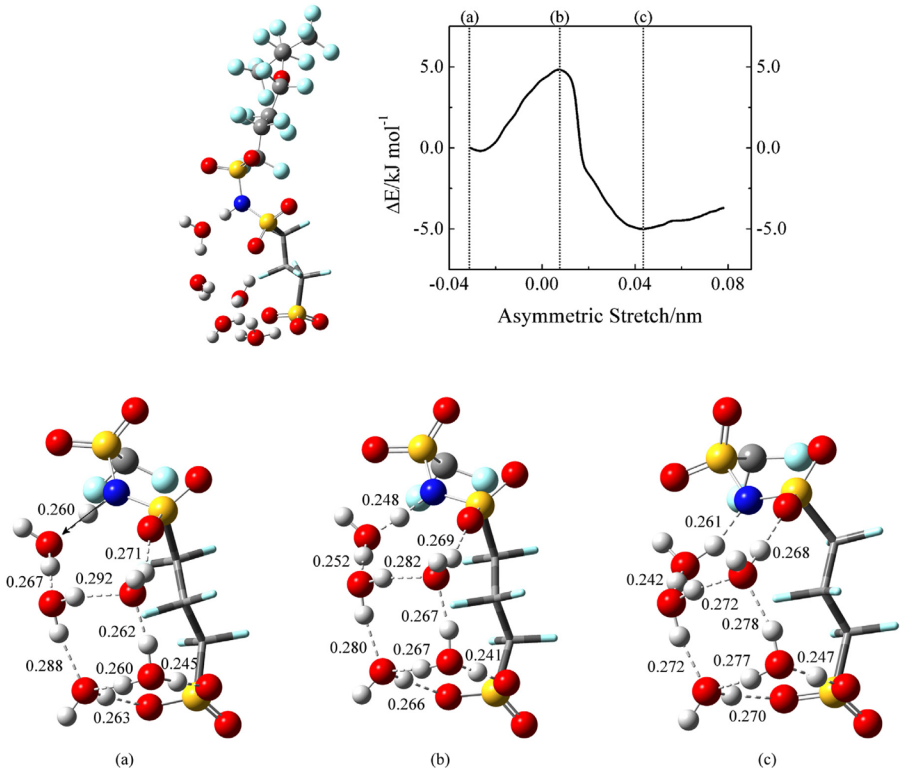

Fig. 11. Top left panel: Optimized (B3LYP/6-31G**) structure of the PFIA at a hydration of five water molecules used in the PES scan of proton transfer from the associated imide to a neighboring water molecule. Top right panel: Relative energy profile with respect to the original configuration as a function of the asymmetric stretch coordinate. Bottom panel: Water molecules and the bottom portion of the ionomer with hydrogen bonds denoted by dashed lines and hydrogen bond distances (nm): (a) initial configuration; (b) transition state; and (c) the local minimum points of the scan.

delocalization capacity of the hydronium ion resulting in weaker donated hydrogen bonds to its neighboring water molecules. The ability of the interconnected hydrogen bonds to easily adjust to charge transfer in this system results in a final geometry 5.0 kJ/mol lower in energy than the initial structure.

4. Conclusions

The effects of protogenic group separation and side chain chemistry on proton dissociation and transfer were examined through electronic structure calculations on three MASC ionomers containing two acidic groups per side chain. Electron withdrawing $-CF_2-$ groups in the PFIA and cooperative interaction between protogenic groups through hydrogen bonding in the *ortho* gave rise to charge delocalization effects absent in the *meta* bis acid. These charge delocalization effects played a crucial role in first proton dissociation where the *ortho* and PFIA required the addition of three water molecules for energetically preferred dissociation while the *meta* required five. The lowest energy dissociated state in the PFIA was found to have hydrogen bond connectivity between the protogenic groups through water molecules.

The direct hydrogen bond connectivity in the *ortho*, on the other hand, hindered second proton dissociation as it required the breaking of this strong stabilizing intramolecular hydrogen bond which was found to be considerably energetically unfavorable. Furthermore, the available hydrogen bond acceptor sites along the side chain were more clustered than in the ionomers with well separated protogenic groups leading to more interactions between water molecules precluding strong hydrogen bonds with the ionomer. The clustered group of water molecules resisted accepting the positive charge associated with dissociation of the second acidic proton as localized excess positive charge already exists in the surrounding water cluster resulting from first proton dissociation. Larger separation in the *meta* and PFIA allowed for more widely spread hydrogen bonding and distribution of charge requiring fewer water molecules for second proton dissociation.

The energetics of proton transfer were also found to be dependent on the nature of hydrogen bonding. When transferring the proton from the imide group to a neighboring water molecule in the *meta* at a hydration of three water molecules, a smooth transfer pathway was observed and resulted in the formation of an additional hydrogen bond with little disruption in hydrogen bonding and a small associated energetic penalty. On the other hand, transferring the proton from the sulfonic acid group to a neighboring water molecule required the breaking of a hydrogen bond which leads to a monotonically increasing relative energy profile with a much higher energetic penalty for proton transfer. The effects of hydrogen bonding were further realized in the energetics of proton transfer from the imide to a neighboring water molecule at a hydration of five water molecules in each fragment. Proton transfer

in the *ortho* was strongly resisted and resulted in a considerable disruption in the configuration of the surrounding water molecules as well as the breaking of a hydrogen bond. Similar proton transfer in the *meta* had a considerably smaller energetic penalty and had less effect on the hydrogen bond network due to the more dispersed hydrogen bonding more readily accommodating for the transfer of charge through the subsequent transfer of a proton to a different water molecule which is further stabilized by the formation of an additional hydrogen bond. The well-connected hydrogen bond network in the PFIA also readily accommodated for the transfer of charge via concerted contractions and expansions in hydrogen bond lengths throughout the system leading to an extremely small barrier for proton transfer. These results suggest that the energetic penalty associated with proton transfer is dependent on the connectivity of hydrogen bonding and the extent of disruption in hydrogen bonding where bond breaking is resisted and bond forming has a stabilizing effect.

It is important to note that results from *ab initio* molecular dynamics simulations [53,55–59,93,94] show that the presence of multiple interacting acidic groups and dynamic configurational changes and bond length fluctuations strongly influence proton mobility and the nature and state of the acidic protons. Furthermore, the nature of the structural organization of the ionomer into the hydrophobic and hydrophilic domains along with the nano-confinement of the water molecules and protons further complicates the system and could change the molecular level features observed here in a non-trivial way. Thus, obtaining a full understanding of the chemical and structural properties that affect dynamic proton transport in a fuel cell membrane requires additional ingredients not present in the static electronic structure calculations on these isolated acid/water molecule complexes. Hence, in this study we are not attempting to describe characteristics of a full ionomer membrane (or even a representative portion of the hydrated morphology) but to relatively compare how specific ionomer chemistry and protogenic group separation affect proton dissociation and the energetics of proton transfer. The results expand upon a line of electronic structure calculations performed on a variety of different ionomers providing a means for comparison of molecular level information of different materials.

Acknowledgments

JKC acknowledges support by the National Science Foundation under grant no. DGE0801470, “Sustainable Technology through Advanced Interdisciplinary Research” (STAIR), awarded to the University of Tennessee, Knoxville. SJP acknowledges support by the DOE under contract number DE-FG36-07G017006. DOE support does not constitute an endorsement by DOE of the views expressed in this work.

References

[1] M. Granovskii, I. Dincer, M.A. Rosen, Life cycle assessment of hydrogen fuel cell and gasoline vehicles, International Journal of Hydrogen Energy 31 (2006) 337.
[2] Y.Y. Shao, G.P. Yin, Z.B. Wang, Y.Z. Gao, Proton exchange membrane fuel cell from low temperature to high temperature: Material challenges, Journal of Power Sources 167 (2007) 235.
[3] K.D. Kreuer, S.J. Paddison, E. Spohr, M. Schuster, Transport in proton conductors for fuel-cell applications: Simulations, elementary reactions, and phenomenology, Chemical Reviews 104 (2004) 4637.
[4] IEA, Hydrogen and Fuel Cells: Review of National R&D Programs, OECD Publishing, Paris, 2004.
[5] O. Savadogo, Emerging membranes for electrochemical systems - Part II. High temperature composite membranes for polymer electrolyte fuel cell (PEFC) applications, Journal of Power Sources 127 (2004) 135.
[6] K.D. Kreuer, On solids with liquidlike properties and the challenge to develop new proton-conducting separator materials for intermediate-temperature fuel cells, ChemPhysChem 3 (2002) 771.
[7] K.D. Kreuer, On the development of proton conducting polymer membranes for hydrogen and methanol fuel cells, Journal of Membrane Science 185 (2001) 29.
[8] L. Rubatat, A.L. Rollet, G. Gebel, O. Diat, Evidence of elongated polymeric aggregates in Nafion, Macromolecules 35 (2002) 4050.
[9] S.J. Paddison, Proton conduction mechanisms at low degrees of hydration in sulfonic acid-based polymer electrolyte membranes, Annual Review of Materials Research 33 (2003) 289.
[10] C.J.D. von Grotthuss, Sur la décomposition de l’eau et des corps qu’elle tient en dissolution à l’aide de l’électricité galvanique, Annali di Chimica 58 (1806) 54.
[11] M. Eikerling, A.A. Kornyshev, A.M. Kuznetsov, J. Ulstrup, S. Walbran, Mechanisms of proton conductance in polymer electrolyte membranes, Journal of Physical Chemistry, Journal of Physical Chemistry B 105 (2001) 3646.
[12] S.J. Paddison, R. Paul, The nature of proton transport in fully hydrated Nafion®, Physical, Physical Chemistry Chemical Physics 4 (2002) 1158.
[13] S.J. Paddison, R. Paul, K.D. Kreuer, Theoretically computed proton diffusion coefficients in hydrated PEEKK membranes, Physical Chemistry Chemical Physics 4 (2002) 1151.
[14] E. Spohr, P. Commer, A.A. Kornyshev, Enhancing proton mobility in polymer electrolyte membranes: Lessons from molecular dynamics simulations, Journal of Physical Chemistry B 106 (2002) 10560.
[15] N. Agmon, The grotthuss mechanism, Chemical Physics Letters 244 (1995) 456.
[16] M.E. Tuckerman, K. Laasonen, M. Sprik, M. Parrinello, *Ab initio* molecular dynamics simulation of the solvation and transport of hydronium and hydroxyl ions in water, Journal of Chemical Physics 103 (1995) 150.
[17] M.E. Tuckerman, D. Marx, M.L. Klein, M. Parrinello, On the quantum nature of the shared proton in hydrogen bonds, Science 275 (1997) 817.
[18] D. Marx, M.E. Tuckerman, J. Hutter, M. Parrinello, The nature of the hydrated excess proton in water, Nature 397 (1999) 601.
[19] H. Lapid, N. Agmon, M.K. Petersen, G.A. Voth, A bond-order analysis of the mechanism for hydrated proton mobility in liquid water, Journal of Chemical Physics 122 (2005) 014506.
[20] M. Ise, K.D. Kreuer, J. Maier, Electroosmotic drag in polymer electrolyte membranes: an electrophoretic NMR study, Solid State Ionics 125 (1999) 213.
[21] J.A. Kerres, Development of ionomer membranes for fuel cells, Journal of Membrane Science 185 (2001) 3.
[22] F. Wang, M. Hickner, Y.S. Kim, T.A. Zawodzinski, J.E. McGrath, Direct polymerization of sulfonated poly(arylene ether sulfone) random (statistical) copolymers: candidates for new proton exchange membranes, Journal of Membrane Science 197 (2002) 231.
[23] M.A. Hickner, H. Ghassemi, Y.S. Kim, B.R. Einsla, J.E. McGrath, Alternative polymer systems for proton exchange membranes (PEMs), Chemical Reviews 104 (2004) 4587.
[24] J.L. Zhang, Z. Xie, J.J. Zhang, Y.H. Tanga, C.J. Song, T. Navessin, Z.Q. Shi, D.T. Song, H.J. Wang, D.P. Wilkinson, et al., High temperature PEM fuel cells, Journal of Power Sources 160 (2006) 872.
[25] S.J. Hamrock, M.A. Yandrasits, Proton exchange membranes for fuel cell applications, Polymer Reviews 46 (2006) 219.
[26] S. Matsumura, A.R. Hlil, C. Lepiller, J. Gaudet, D. Guay, Z.Q. Shi, S. Holdcroft, A.S. Hay, Ionomers for proton exchange membrane fuel cells with sulfonic acid groups on the end groups: Novel branched poly(ether-ketone)s, Macromolecules 41 (2008) 281.
[27] Q.F. Li, R.H. He, J.O. Jensen, N.J. Bjerrum, Approaches and recent development of polymer electrolyte membranes for fuel cells operating above 100 degrees C, Chemistry of Materials 15 (2003) 4896.
[28] M. Saito, N. Arimura, K. Hayamizu, T. Okada, Mechanisms of ion and water transport in perfluorosulfonated ionomer membranes for fuel cells, Journal of Physical Chemistry B 108 (2004) 16064.
[29] N. Yoshida, T. Ishisaki, A. Watakabe, M. Yoshitake, Characterization of Flemion® membranes for PEFC, Electrochimica Acta 43 (1998) 3749.
[30] B.R. Ezzell, W.P. Carl, W.A. Mod, The Dow Chemical Company, U.S. Patent 4,358,412, November 9, 1982.
[31] V. Arcella, A. Ghielmi, G. Tommasi, High performance perfluoropolymer films and membranes, Annals of the New York Academy of Sciences 984 (2003) 226.
[32] V. Arcella, C. Troglia, A. Ghielmi, Hyflon ion membranes for fuel cells, Industrial and Engineering Chemistry Research 44 (2005) 7646.
[33] A. Ghielmi, P. Vaccarono, C. Troglia, V. Arcella, Proton exchange membranes based on the short-side-chain perfluorinated ionomer, Journal of Power Sources 145 (2005) 108.
[34] T.A. Zawodzinski, T.E. Springer, J. Davey, R. Jestel, C. Lopez, J. Valerio, S. Gottesfeld, A comparative study of water uptake by and transport through ionomeric fuel cell membranes, Journal of the Electrochemical Society 140 (1993) 1981.
[35] C.A. Edmondson, P.E. Stallworth, M.E. Chapman, J.J. Fontanella, M.C. Wintersgill, S.H. Chung, S.G. Greenbaum, Complex impedance studies of proton-conducting membranes, Solid State Ionics 135 (2000) 419.
[36] C.A. Edmondson, J.J. Fontanella, Free volume and percolation in S-SEBS and fluorocarbon proton conducting membranes, Solid State Ionics 152 (2002) 355.
[37] K.D. Kreuer, On the development of proton conducting materials for technological applications, Solid State Ionics 97 (1997) 1.
[38] B.J. Liu, G.P. Robertson, D.S. Kim, M.D. Guiver, W. Hu, Z.H. Jiang, Aromatic poly(ether ketone)s with pendant sulfonic acid phenyl groups prepared by a mild sulfonation method for proton exchange membranes, Macromolecules 40 (2007) 1934.
[39] J.J. Sumner, S.E. Creager, J.J. Ma, D.D. DesMarteau, Proton conductivity in Nafion® 117 and in a novel bis[(perfluoroalkyl)sulfonyl]imide ionomer membrane, Journal of the Electrochemical Society 145 (1998) 107.

[40] I.A. Koppel, R.W. Taft, F. Anvia, S.Z. Zhu, L.Q. Hu, K.S. Sung, D.D. Desmarteau, L.M. Yagupolskii, Y.L. Yagupolskii, N.V. Ignatev, et al., The gas-phase acidities of very strong neutral Brønsted acids, Journal of the American Chemical Society 116 (1994) 3047.
[41] S.E. Creager, J.J. Sumner, R.D. Bailey, J.J. Ma, W.T. Pennington, D.D. DesMarteau, Equivalent weight and crystallinity effects on water content and proton conductivity in bis[(perfluoroalkyl)sulfonyl]imide-based ionomers, Electrochemical and Solid-State Letters 2 (1999) 434.
[42] M. Emery, M. Frey, M. Guerra, G. Haugen, K. Hintzer, K.H. Lochhaas, P. Pham, D. Pierpont, M. Schaberg, A. Thaler, et al., The development of new membranes for proton exchange membrane fuel cells, ECS Transactions 11 (2007) 3.
[43] M. Schaberg, J. Abulu, G. Haugen, M. Emery, S. O'Conner, P. Xiong, S. Hamrock, New multi acid side-chain ionomers for proton exchange membrane fuel cells, ECS Transactions 33 (2010) 627.
[44] A. Potier, The hydrogen bond and chemical parameters favouring proton mobility in solids, in: P. Colomban (Ed.), Proton Conductors: Solids, Membranes and Gels- Materials and Devices, Cambridge University Press, Cambridge; New York, 1992, p. 1.
[45] M.E. Tuckerman, K. Laasonen, M. Sprik, M. Parrinello, *Ab initio* molecular dynamics simulation of the solvation and transport of H_3O^+ and OH^- ions in water, Journal of Physical Chemistry 99 (1995) 5749.
[46] T.J.F. Day, A.V. Soudackov, M. Cuma, U.W. Schmitt, G.A. Voth, A second generation multistate empirical valence bond model for proton transport in aqueous systems, Journal of Chemical Physics 117 (2002) 5839.
[47] F. Wang, G.A. Voth, A linear-scaling self-consistent generalization of the multistate empirical valence bond method for multiple excess protons in aqueous systems, Journal of Chemical Physics 122 (2005) 144105.
[48] Y.J. Wu, H.N. Chen, F. Wang, F. Paesani, G.A. Voth, An improved multistate empirical valence bond model for aqueous proton solvation and transport, Journal of Physical Chemistry B 112 (2008) 467.
[49] M.K. Petersen, F. Wang, N.P. Blake, H. Metiu, G.A. Voth, Excess proton solvation and delocalization in a hydrophilic pocket of the proton conducting polymer membrane Nafion, Journal of Physical Chemistry B 109 (2005) 3727.
[50] M.K. Petersen, G.A. Voth, Characterization of the solvation and transport of the hydrated proton in the perfluorosulfonic acid membrane Nafion, Journal of Physical Chemistry B 110 (2006) 18594.
[51] M.K. Petersen, A.J. Hatt, G.A. Voth, Orientational dynamics of water in the Nafion polymer electrolyte membrane and its relationship to proton transport, Journal of Physical Chemistry B 112 (2008) 7754.
[52] S. Feng, G.A. Voth, Proton solvation and transport in hydrated Nafion, Journal of Physical Chemistry B 115 (2011) 5903.
[53] M. Eikerling, S.J. Paddison, L.R. Pratt, T.A. Zawodzinski, Defect structure for proton transport in a triflic acid monohydrate solid, Chemical Physics Letters 368 (2003) 108.
[54] Y.K. Choe, E. Tsuchida, T. Ikeshoji, S. Yamakawa, S. Hyodo, Nature of proton dynamics in a polymer electrolyte membrane, Nafion: a first-principles molecular dynamics study, Physical Chemistry Chemical Physics 11 (2009) 3892.
[55] R.L. Hayes, S.J. Paddison, M.E. Tuckerman, Proton transport in triflic acid hydrates studied via path integral Car-Parrinello molecular dynamics, Journal of Physical Chemistry B 113 (2009) 16574.
[56] R.L. Hayes, S.J. Paddison, M.E. Tuckerman, Proton transport in triflic acid pentahydrate studied via ab initio path integral molecular dynamics, Journal of Physical Chemistry A 115 (2011) 6112.
[57] B.F. Habenicht, S.J. Paddison, M.E. Tuckerman, The effects of the hydrophobic environment on proton mobility in perfluorosulfonic acid systems: An *ab initio* molecular dynamics study, Journal of Materials Chemistry 20 (2010) 6342.
[58] B.F. Habenicht, S.J. Paddison, M.E. Tuckerman, *Ab initio* molecular dynamics simulations investigating proton transfer in perfluorosulfonic acid functionalized carbon nanotubes, Physical Chemistry Chemical Physics 12 (2010) 8728.
[59] B.F. Habenicht, S.J. Paddison, *Ab initio* simulations of the effects of nanoscale confinement on proton transfer in hydrophobic environments, Journal of Physical Chemistry B 115 (2011) 10826.
[60] W. Munch, K.D. Kreuer, W. Silvestri, J. Maier, G. Seifert, The diffusion mechanism of an excess proton in imidazole molecule chains: first results of an *ab initio* molecular dynamics study, Solid State Ionics 145 (2001) 437.
[61] Y.K. Choe, E. Tsuchida, T. Ikeshoji, A. Ohira, K. Kidena, An *ab initio* modeling study on a modeled hydrated polymer electrolyte membrane, sulfonated polyethersulfone (SPES), Journal of Physical Chemistry B 114 (2010) 2411.
[62] S.J. Paddison, T.A. Zawodzinski Jr., Molecular modeling of the pendant chain in Nafion®, Solid State Ionics 113–115 (1998) 333.
[63] S.J. Paddison, L.R. Pratt, T. Zawodzinski, D.W. Reagor, Molecular modeling of trifluoromethanesulfonic acid for solvation theory, Fluid Phase Equilibria 151 (1998) 235.
[64] S.J. Paddison, The modeling of molecular structure and ion transport in sulfonic acid based ionomer membranes, Journal of New Materials for Electrochemical Systems 4 (2001) 197.
[65] V.A. Glezakou, M. Dupuis, C.J. Mundy, Acid/base equilibria in clusters and their role in proton exchange membranes: computational insight, Physical Chemistry Chemical Physics 9 (2007) 5752.
[66] K. Sagarik, M. Phonyiem, C. Lao-Ngam, S. Chaiwongwattana, Mechanisms of proton transfer in Nafion®: elementary reactions at the sulfonic acid groups, Physical Chemistry Chemical Physics 10 (2008) 2098.
[67] M. Phonyiem, S. Chaiwongwattana, C. Lao-ngam, K. Sagarik, Proton transfer reactions and dynamics of sulfonic acid group in Nafion®, Physical Chemistry Chemical Physics 13 (2011) 10923.
[68] C. Wang, J.K. Clark, M. Kumar, S.J. Paddison, An *ab initio* study of the primary hydration and proton transfer of CF_3SO_3H and $CF_3O(CF_2)_2SO_3H$: Effects of the hybrid functional and inclusion of diffuse functions, Solid State Ionics 199 (2011) 6.
[69] J.K. Clark, S.J. Paddison, M. Eikerling, M. Dupuis, T.A. Zawodzinski, A comparative ab initio study of the primary hydration and proton dissociation of various imide and sulfonic acid ionomers, Journal of Physical Chemistry A 116 (2012) 1801.
[70] S.J. Paddison, K.D. Kreuer, J. Maier, About the choice of the protogenic group in polymer electrolyte membranes: *Ab initio* modelling of sulfonic acid, phosphonic acid, and imidazole functionalized alkanes, Physical Chemistry Chemical Physics 8 (2006) 4530.
[71] C. Wang, S.J. Paddison, Proton transfer in functionalized phosphonic acid molecules, Physical Chemistry Chemical Physics 12 (2009) 970.
[72] L. Vilciauskas, S.J. Paddison, K.D. Kreuer, *Ab initio* modeling of proton transfer in phosphoric acid clusters, Journal of Physical Chemistry A 113 (2009) 9193.
[73] S. Urata, J. Irisawa, A. Takada, S. Tsuzuki, W. Shinoda, M. Mikami, Intermolecular interaction between the pendant chain of perfluorinated ionomer and water, Physical Chemistry Chemical Physics 6 (2004) 3325.
[74] M. Eikerling, S.J. Paddison, T.A. Zawodzinski, Molecular orbital calculations of proton dissociation and hydration of various acidic moieties for fuel cell polymers, Journal of New Materials for Electrochemical Systems 5 (2002) 15.
[75] S.J. Paddison, J.A. Elliott, Molecular modeling of the short-side-chain perfluorosulfonic acid membrane, Journal of Physical Chemistry A 109 (2005) 7583.
[76] S.J. Paddison, J.A. Elliott, On the consequences of side chain flexibility and backbone conformation on hydration and proton dissociation in perfluorosulfonic acid membranes, Physical Chemistry Chemical Physics 8 (2006) 2193.
[77] S.J. Paddison, J.A. Elliott, The effects of backbone conformation on hydration and proton transfer in the 'short-side-chain' perfluorosulfonic acid membrane, Solid State Ionics 177 (2006) 2385.
[78] S.J. Paddison, J.A. Elliott, Selective hydration of the 'short-side-chain' perfluorosulfonic acid membrane. An ONIOM study, Solid State Ionics 178 (2007) 561.
[79] J.K. Clark, S.J. Paddison, The effect of side chain connectivity and local hydration on proton transfer in 3 M perfluorosulfonic acid membranes, Solid State Ionics 213 (2012) 83.
[80] J.K.I.I. Clark, S.J. Paddison, S.J. Hamrock, The effect of hydrogen bond reorganization and equivalent weight on proton transfer in 3 M perfluorosulfonic acid ionomers, Physical Chemistry Chemical Physics 14 (2012) 16349.
[81] M.J. Frisch, G.W. Trucks, H.B. Schlegel, G.E. Scuseria, M.A. Robb, J.R. Cheeseman, G. Scalmani, V. Barone, B. Mennucci, G.A. Petersson, et al., Gaussian 09, Gaussian Inc., Wallingford CT, 2009.
[82] H.B. Schlegel, Optimization of equilibrium geometries and transition structures, Journal of Computational Chemistry 3 (1982) 214.
[83] P.C. Harihara, J.A. Pople, Influence of polarization functions on molecular-orbital hydrogenation energies, Theoretica Chimica Acta 28 (1973) 213.
[84] A.D. Becke, Density-functional thermochemistry. III. The role of exact exchange, Journal of Chemical Physics 98 (1993) 5648.
[85] A.D. Becke, A new mixing of Hartree-Fock and local density-functional theories, Journal of Chemical Physics 98 (1993) 1372.
[86] A.D. McLean, G.S. Chandler, Contracted Gaussian basis sets for molecular calculations. I. Second row atoms, Z = 11-18, Journal of Chemical Physics 72 (1980) 5639.
[87] S.F. Boys, F. Bernardi, Calculation of small molecular interactions by differences of separate total energies - some procedures with reduced errors, Molecular Physics 19 (1970) 553.
[88] C.M. Breneman, K.B. Wiberg, Determining atom-centered monopoles from molecular electrostatic potentials. The need for high sampling density in formamide conformational analysis, Journal of Computational Chemistry 11 (1990) 361.
[89] C. Mijoule, Z. Latajka, D. Borgis, Density functional theory applied to proton-transfer systems. A numerical test, Chemical Physics Letters 208 (1993) 364.
[90] Y.M. Xie, R.B. Remington, H.F. Schaefer, The protonated water dimer: Extensive theoretical studies of H_5O_{2+}, Journal of Chemical Physics 101 (1994) 4878.
[91] T. Steiner, The hydrogen bond in the solid state, Angewandte Chemie International Edition 41 (2002) 48.
[92] R. Kumar, J.R. Schmidt, J.L. Skinner, Hydrogen bonding definitions and dynamics in liquid water, Journal of Chemical Physics 126 (2007) 204107.
[93] M.A. Ilhan, E. Spohr, *Ab initio* molecular dynamics of proton networks in narrow polymer electrolyte pores, Journal of Physics: Condensed Matter 23 (2011) 234104.
[94] A. Roudgar, S.P. Narasimachary, M. Eikerling, Hydrated arrays of acidic surface groups as model systems for interfacial structure and mechanisms in PEMs, Journal of Physical Chemistry B 110 (2006) 20469.

Solid State Ionics 213 (2012) 83–91

Contents lists available at ScienceDirect

Solid State Ionics

journal homepage: www.elsevier.com/locate/ssi

The effect of side chain connectivity and local hydration on proton transfer in 3M perfluorosulfonic acid membranes

Jeffrey K. Clark II, Stephen J. Paddison *

Department of Chemical and Biomolecular Engineering, University of Tennessee, Knoxville, TN 37996, USA

ARTICLE INFO

Article history:
Received 7 October 2010
Received in revised form 5 July 2011
Accepted 19 July 2011
Available online 17 August 2011

Keywords:
Perfluorosulfonic acid
Electronic structure
Proton transfer
Molecular modeling
3M ionomers

ABSTRACT

We present a molecular modeling study on the role the connectivity of adjacent acid groups of 3M perfluorosulfonic acid (PFSA) membranes has on proton dissociation and transfer through a consideration of oligomeric fragments with different poly(tetrafluoroethylene) (PTFE) backbone segments separating the side chains. Electronic structure calculations were performed at the B3LYP/6-311G** level of theory on fragments with chemical formula: $CF_3CF(-O(CF_2)_4SO_3H)(CF_2)_nCF(-O(CF_2)_4SO_3H)CF_3$, where n = 5 or 7, corresponding to membrane equivalent weights of 590 and 690 g/mol, respectively. Fully optimized structures of these fragments with and without the addition of water molecules revealed that connectivity of the SO_3H groups through hydrogen bonding is critical for proton dissociation and the state of the dissociated proton. Proton dissociation was first observed in the EW 590 fragment at a water content of only 1 H_2O/SO_3H; the system with greater separation of the side chains (EW 690) did not exhibit proton dissociation until four water molecules (i.e., 2 H_2O/SO_3H) were added as the greater side chain separation precluded the cooperative interaction through hydrogen bonding that promotes proton dissociation at low hydration in membranes of this type. Second proton dissociation in the EW 590 system occurred upon addition of three water molecules; this required five water molecules in the EW 690 fragment. The differences in dissociation and the state of the dissociated proton were mitigated after six water molecules were added to each system where one of the dissociated protons exists as a 'Zundel-like' cation and the other as more of an 'Eigen-like' complex. These calculations further substantiate prior work on the importance of the interaction of sulfonic acid groups through hydrogen bonding in the transfer and state of the dissociated protons.

1. Introduction

Interest in the use of fuel cells as highly efficient, clean energy conversion devices has been rapidly increasing over the past twenty years. Currently, proton exchange membrane (PEM) fuel cells are regarded as the paramount type of fuel cell due to their wide range of applicability [1]. The PEM functions not only as the electrolyte in current hydrogen fuel cells but also as the separator of the electrodes and reactant gases and importantly as the internal ion conductor [2]. Efficient operation of PEM fuel cells in diverse applications (i.e., vehicular, portable, and stationary) places demands on the PEM which include: long-time thermal and chemical stability (including resistance to oxidation and degradation by reactive species) at temperatures as high as 120 °C and high proton conductivity ($\approx 10^{-1}$ S cm^{-1}) under low humidity conditions (25–50% relative humidity) [3]. Although a large number of strategies have been devised in the pursuit to design membrane materials that meet these requirements, current PEM fuel cells still utilize perfluorosulfonic acid (PFSA) ionomers such as Nafion®. PFSA membranes consist of a poly(tetrafluoroethylene) (PTFE) backbone functionalized with pendant side chains each terminated with a single sulfonic acid group. Substantial research on the chemical structure, properties, and functionality in PFSA membranes and other PEMs has been reviewed by several authors and continues to expand the overall understanding crucial for further development of these materials [2,4–13]. However, utilization of current materials is limited due to high production costs and the high levels of hydration necessary for sufficient proton conductivity [14]. Considerable effort is being undertaken toward improving the efficiency and reducing the economic cost of PFSA membranes along with efforts to develop membranes with structural and chemical variations to the acidic side chains and/or protogenic groups [15–17]. The potential PFSA membranes have for wide spread application as the electrolyte in PEMFCs operating under relatively dry conditions will not only be enhanced through extensive testing and characterization but also through obtaining a molecular-level understanding of proton transfer and primary hydration of the protogenic groups in materials of this type.

* Corresponding author. Tel.: +1 865 974 2026; fax: +1 865 974 7076.
E-mail address: spaddison@utk.edu (S.J. Paddison).

0167-2738/$ – see front matter © 2011 Elsevier B.V. All rights reserved.
doi:10.1016/j.ssi.2011.07.011

Molecular modeling can be used in the progression towards one of the primary goals of current PFSA membrane research, the development of materials that exhibit high proton conductivity at elevated temperatures and low hydration levels, by providing insight into the mechanisms of proton transport within these systems [2]. Hydration is essential to proton transfer in PFSA membranes. Theoretical and experimental studies suggest aggregation of the sulfonic acid groups occurs to some extent in nominally dry membranes and to a greater degree in hydrated membranes where the acidic groups are solvated by the water molecules; the solvation of these acidic groups leads to proton dissociation into the aqueous domain. Dissociated protons in these systems are mobile which facilitates long-range proton transport through the aqueous domains of the material [18–21]. The protons may not only move through the aqueous medium through simple vehicular diffusion but also via a Grotthuss or structural diffusion mechanism [22–24] resembling that of bulk-water [25–30]. This structural diffusion involves proton shuttling through the hydrogen bond network through a series of transformations between an Eigen cation ($H_9O_4^+$) and a Zundel cation ($H_5O_2^+$). Hence, an understanding of the formation and the nature of hydrogen bond networks between acidic groups and water molecules is a necessary requirement for the further development of PEM materials. Within PFSA membranes, the connectivity and cooperativity exhibited by the side chains are critical to the formation of complex hydrogen bond networks and, thus, crucial for facilitation of proton transport [31,32]. Full understanding of this requires insight into the formation and breaking of hydrogen bonds within these complex systems. As there are few experimental techniques that can reach this level of resolution, molecular simulations have been utilized to describe these interactions.

We continue our investigations in the present work on understanding the role side chain connectivity [33–35] and local hydration [36–38] have on proton dissociation and separation. Specifically, we report electronic structure calculations of fragments of the 3 M PFSA ionomer consisting of two side chains ($-O(CF_2)_4SO_3H$) with different separation along the PTFE backbone: $CF_3CF(-O(CF_2)_4SO_3H)(CF_2)_n CF(-O(CF_2)_4SO_3H)CF_3$, where $n=5$ and 7 which correspond to equivalent weights (EWs) of 590 and 690 grams of ionomer per mole acid, respectively. The nomenclature EW 590 and EW 690 is henceforth used to distinguish the two different fragments.

2. Computational methods

All electronic structure calculations of the oligomeric fragments were performed using the GAUSSIAN 03 suite of programs [39]. Each of the initial structures were constructed by adding the two acidic side chains with a specified spacing between them to fully optimized perfluorinated alkanes of two different lengths (i.e., C_9F_{20} and $C_{11}F_{24}$). The initial backbone geometry exhibited the expected structure of PTFE (i.e., staggered fluorine atoms along an all *trans* arrangements of the carbon atoms thereby exhibiting an alpha helical pitch when viewed down the length of the backbone). Two side chains ($-O(CF_2)_4SO_3H$) were added to each alkane with a variety of different initial configurations. Full optimizations (i.e. over all degrees of freedom) were then carried out by conjugate gradient methods [40] without symmetry constraints initially invoking Hartree–Fock theory with the 6–31G** split valence basis set [41]. The resulting structures were then refined with hybrid density functional theory (DFT) employing Becke's 3-parameter functional (B3LYP) [42,43] and the same basis set. Final optimizations were then performed at the B3LYP/6–311G** level of theory [44]. Subsequent to the 'dry' optimizations (i.e., without explicit H_2O molecules), water molecules were individually added to the optimized system at a variety of initial positions and full optimization was performed using the protocol described above. Vibrational frequencies and zero point energies (ZPEs) were determined for all global minimum energy structures at the B3LYP/6–311G** level. The binding energies of water molecules to the oligomeric fragments were calculated using both uncorrected and ZPE corrected minimum electronic energies using the equation

$$\Delta E = \frac{\left[E_{elec}^{total} - \left(E_{elec}^{frag} + n_{H_2O} E_{elec}^{H_2O}\right)\right]}{n_{H_2O}}$$

where E_{elec}^{total} is the total electronic energy of the system including the water molecules, E_{elec}^{frag} is the electronic energy of the initial 'dry' fragment, $E_{elec}^{H_2O}$ is the electronic energy of a single water molecule, and $n_{elec}^{H_2O}$ is the number of water molecules in the system. The counterpoise (CP) method of Boys and Bernardi [45] was also employed to explore the effects of basis set superposition error (BSSE) on the water binding energies calculated from the CP-corrected optimized geometries and vibrational frequencies. Lastly, partial atomic electrostatic charges were obtained using the CHelpG scheme for the fully optimized structures (B3LYP/6–311G**) in both systems at all levels of hydration.

3. Results and discussion

3.1. 'Dry' fragments

As it is well known that hydrogen bonding is a critical feature of proton transport in materials of this type, these interactions were a primary focus in this study. The requirements for a hydrogen bond in these electronic structure calculations were an O···O distance between 2.45 and 3.25 Å and an O–H···O bond angle greater than 145°. Throughout this paper, the global minimum energy structures (i.e., lowest of all fully optimized structures determined) at each hydration level are presented in the top panel of the figures discussed throughout the text; the bottom panel of the figures shows a rotated bottom view of the sulfonic acid/sulfonate groups and water molecule(s) (with the exception of the 'dry' case) with hydrogen bonds denoted by dotted lines and the O···O distance reported, all other atoms have been removed for clarity. The global minimum energy structure of the EW 590 fragment exhibits double hydrogen bonded sulfonic acid groups (shown in the bottom panel of Fig. 1a) with a fully extended PTFE backbone and side chains, the latter exhibiting no kinking or distortion, as shown in Fig. 1a (top panel). The doubly hydrogen bonded configuration was significantly lower in energy than systems where there was no hydrogen bonding of the acid moieties; this result is consistent with results obtained using fragments of the short-side chain (SSC) PFSA membrane consisting of a PTFE backbone and two pendant $-O(CF_2)_2SO_3H$ side chains separated by only four $-CF_2-$ backbone units [9]. The EW 690 fragment, on the other hand, does not exhibit the same 'relaxed' interaction (i.e. does not require forced distortion or kinking of bond and dihedral angles of the backbone or side chains) between the side chains under 'dry' conditions due to the additional tetrafluoroethylene unit in the backbone separating them. Instead, to maintain a fully extended backbone and 'relaxed' side chains, the side chains remain well separated without any hydrogen bonding between them, shown in Fig. 1b (as hydrogen bonds are not present in this configuration, no bottom view of this 'dry' system has been included). The 'relaxed' and well separated configuration of the side chains seen in the EW 690 system was also observed in electronic structure calculations on oligomeric fragments of the SSC PFSA membrane having a fully extended backbone with side chains separated by 5, 7, and 9 $-CF_2-$ units [33–35]. The extension of the side chains of the SSC ionomer by an additional tetrafluoroethylene unit (as is the case for the 3M PFSA membranes in this study) evidently allows for favorable hydrogen bonding between the sulfonic acid groups when the side chains are separated by five $-CF_2-$ groups. However, increasing side chain separation to seven $-CF_2-$ groups in the 3M PFSA ionomer does not lead to this type of configuration for fragments with an all *trans* (i.e. fully extended) backbone.

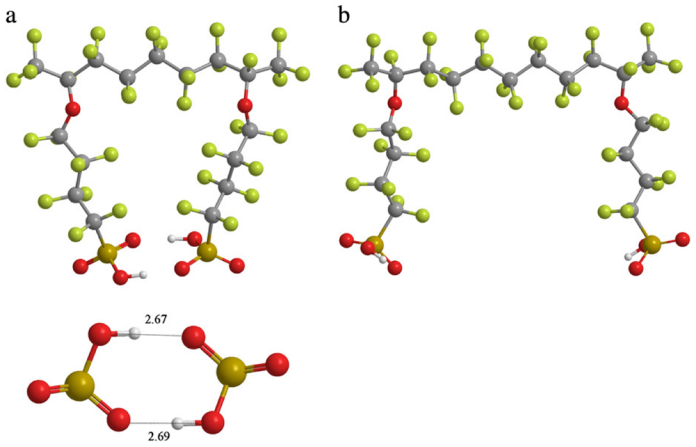

Fig. 1. Optimized (B3LYP/6-311G**) 'dry' global minimum energy structures of isolated two side chain 3 M PFSA fragments with fully extended PTFE backbones showing: (a) the EW 590 system with side chains separated by five CF_2 units exhibiting two hydrogen bonds between the sulfonic acid groups of the side chains. The lower panel shows the rotated bottom view of the sulfonic acid groups with hydrogen bonds indicated by dotted lines and the associated hydrogen bond distances (measured as the O···O separation) given in Å, all other atoms have been omitted for clarity; (b) the EW 690 system with side chains separated by seven CF_2 units where side chains remain well separated. The different colored spheres represent different atom types in the structures where: grey—carbon, red—oxygen, green—fluorine, orange—sulfur, and white—hydrogen.

It should be noted that conformational changes to the backbone or distortion of the side chains in the EW 690 system does bring about closer proximity between the terminal acid groups [34] which allows them to interact and form hydrogen bonds. However, this comes with the loss of either the typical fully extended PTFE backbone or the extended conformation of the side chains. This study focuses on side chain connectivity and local hydration in 'relaxed', fully extended initial geometries for these systems.

3.2. Hydrated fragments

For each level of hydration, it was found that the lowest energy structure resulted in systems where the hydrogen bonding involved both of the -SO_3H groups and H_2O molecules. Specifically, the water molecule(s) form a connectivity 'bridge' between the acid groups via continuous hydrogen bond chains [33]. The calculated electronic energies, zero point energies, and uncorrected, ZPE corrected, and BSSE-corrected binding energies of the water molecules to the oligomers for the EW 590 and 690 systems are reported in Tables 1 and 2, respectively.

Fig. 2a shows the global minimum energy conformation of the EW 590 fragment with the addition of a single water molecule. This structure exhibits hydrogen bonding between the side chains through the water molecule and directly between the two sulfonic acid groups (Fig. 2a bottom panel). This effectively creates a continuous 'ring-like' hydrogen bond network between the water molecule and the acid groups involving three hydrogen bonds. The addition of a single water molecule to the EW 690 system brings about association of the side chains, in contrast to what was observed in the 'dry' structure, as the water acts as both a hydrogen bond acceptor and hydrogen bond donor to the two sulfonic acid groups, as seen in the global minimum energy structure shown in Fig. 2b. However, contrary to what was seen in the EW 590 system, no direct hydrogen bonding between the –SO_3H groups was observed in the larger EW 690 fragment. Furthermore, the hydrogen bond distances (indicated as O···O separation distances) in the EW 690 system are 2.63 and 3.01 Å between the water molecule and the sulfonic acid groups donating and accepting hydrogen bonds, respectively. In the EW 590 system the corresponding hydrogen bond lengths were 2.55 and 2.83 Å, respectively. This suggests that the single water molecule in the EW 590 system forms stronger hydrogen bonds with the sulfonic acid groups at minimal hydration. The BSSE-

Table 1
Energies of optimized $CF_3CF(-O(CF_2)_4SO_3H)-(CF_2)_5-CF(-O(CF_2)_4SO_3H)CF_3$ fragments[a].

n H_2O	E_{elec}[b]	E_{ZPE}[c]	ΔE (kcal/mol)[d]	ΔE_{ZPE} (kcal/mol)[e]	ΔE_{BSSE} (kcal/mol)[f]
0	−5442.891834	0.263263			
1	−5519.367948	0.287332	−18.0 (−18.0)[g]	−16.3 (−16.3)[g]	−11.4 (−11.4)[g]
2	−5595.846357	0.313836	−37.4 (−18.7)	−32.4 (−16.2)	−24.6 (−12.3)
3	−5672.321907	0.338832	−55.0 (−18.3)	−47.8 (−15.9)	−34.9 (−11.6)
4	−5748.796235	0.364732	−71.9 (−18.0)	−61.8 (−15.4)	−45.7 (−11.4)
5	−5825.274125	0.390604	−91.0 (−18.2)	−78.0 (−15.6)	−57.5 (−11.5)
6	−5901.750124	0.416287	−108.9 (−18.2)	−93.2 (−15.5)	−66.2 (−11.0)

[a] Energetics for structures optimized at the B3LYP/6-311G** level.
[b] Total electronic energy in Hartrees.
[c] Zero point energy (ZPE) in Hartrees.
[d] Binding energy based on uncorrected total electronic energy.
[e] Binding energy based on ZPE corrected electronic energy.
[f] Binding energy based on CP correction to BSSE of reoptimized structure.
[g] Value in parenthesis is binding energy per water molecule.

Table 2
Energies of optimized $CF_3CF(-O(CF_2)_4SO_3H)-(CF_2)_7-CF(-O(CF_2)_4SO_3H)CF_3$ fragments[a].

n H_2O	E_{elec}[b]	E_{ZPE}[c]	ΔE (kcal/mol)[d]	ΔE_{ZPE} (kcal/mol)[e]	ΔE_{BSSE} (kcal/mol)[f]
0	−5918.575028	0.286022			
1	−5995.051613	0.311681	−18.3 (−18.3)[g]	−15.5 (−15.5)[g]	−10.8 (−10.8)[g]
2	−6071.536307	0.337958	−41.7 (−20.8)	−35.8 (−17.9)	−25.0 (−12.5)
3	−6148.007368	0.362489	−56.5 (−18.8)	−48.6 (−16.2)	−34.1 (−11.4)
4	−6224.492165	0.389996	−79.9 (−20.0)	−68.1 (−17.0)	−47.8 (−12.0)
5	−6300.972269	0.415785	−100.4 (−20.1)	−85.8 (−17.2)	−60.7 (−12.1)
6	−6377.448377	0.441058	−118.4 (−19.7)	−101.3 (−16.9)	−74.6 (−12.4)

[a] Energetics for structures optimized at the B3LYP/6-311G** level.
[b] Total electronic energy in Hartrees.
[c] Zero point energy (ZPE) in Hartrees.
[d] Binding energy based on uncorrected total electronic energy.
[e] Binding energy based on ZPE corrected electronic energy.
[f] Binding energy based on CP correction to BSSE of reoptimized structure.
[g] Value in parenthesis is binding energy per water molecule.

corrected binding energy of the water molecule to the sulfonic acid groups in the EW 590 system (Table 1) is approximately 0.6 kcal/mol higher than that for the EW 690 system (Table 2) at this hydration level which is an indicator of the strength of the hydrogen bonds. Clearly, the hydrogen bonding is fundamental in stabilizing excess charge once proton dissociation has occurred. Although no proton dissociation is yet observed at a hydration of $\lambda = 0.5$ (where λ is defined as the number of water molecules per sulfonic acid group), the differences in the nature of the hydrogen bond network formed in the two systems at this low level of hydration appear to qualitatively affect proton dissociation upon increasing hydration.

The role the 'dry' connectivity observed in the EW 590 system has on proton dissociation at low hydration levels becomes increasingly apparent as the hydration shells of the groups are completed. Figs. 3 and 4 show the minimum energy structures for both systems with the addition of two and three explicit water molecules, respectively, with the hydrogen bond network between water molecules and the sulfonic acid/sulfonate groups, as seen from the bottom of the structure, shown in the bottom panels. The addition of two water molecules brings about dissociation of one of the protons in the EW 590 ionomeric fragment, as shown in Fig. 3a. No other systems found in our investigation on fragments of the 3M membranes exhibited proton dissociation after the addition of only two water molecules. However, a similar result was observed regarding side chain separation and proton dissociation in calculations performed on the SSC PFSA ionomer with two side chain fragments ($-O(CF_2)_2SO_3H$) separated by five, seven, and nine $-CF_2-$ backbone units where it was determined that the number of water molecules required for proton dissociation increases as the number of $-CF_2-$ groups separating side chains increases [33]. The resultant hydronium ion connecting the side chains after the addition of only two water molecules in the EW 590 system has been observed to be important in proton transport in other systems at low hydration including the hydrates of trifluoromethanesulfonic acid [46,47]. This configuration having direct hydrogen bonding between the protogenic groups (one which is a sulfonic acid and the other a sulfonate), stabilizes the excess negative charge in the first hydration shell for both side chain terminal groups and enables proton dissociation. The importance of the connectivity is further illustrated in Fig. 4a for the EW 590 system with three water molecules. In this system both acidic protons have dissociated. The

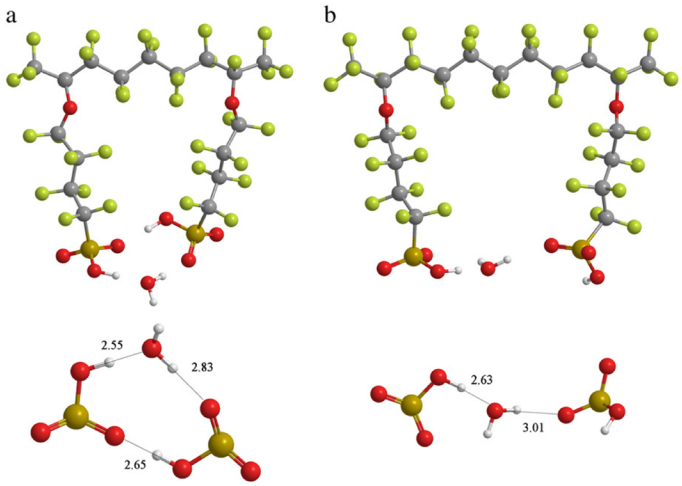

Fig. 2. Optimized (B3LYP/6-311G**) global minimum energy structures of two side chain oligomeric fragments of 3M PFSA polymer with fully extended PTFE backbones upon addition of one water molecule with the hydrogen bonding between hydrophilic groups and water molecules illustrated in the bottom panels: (a) the EW 590 system which maintains a single direct hydrogen bond between the sulfonic acid groups as well as a hydrogen bond 'bridge' between sulfonic acid groups via the additional water molecule; (b) the EW 690 system where the water molecule draws the side chain hydrophilic groups closer together via hydrogen bond connectivity but no direct hydrogen bonding between sulfonic acid groups occurs.

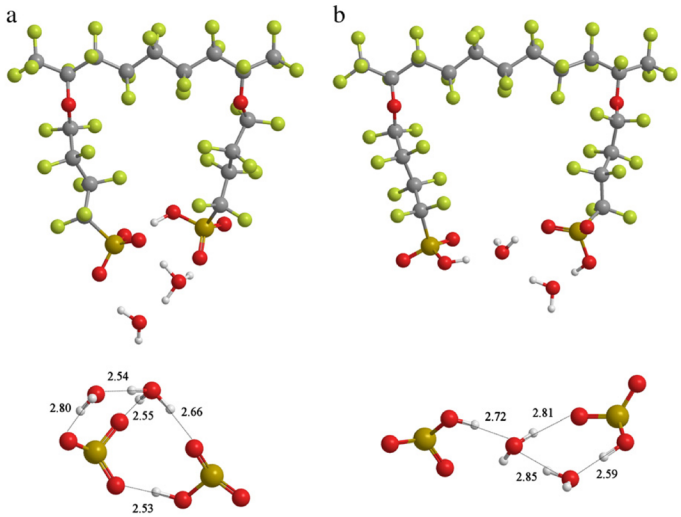

Fig. 3. Optimized (B3LYP/6-311G**) global minimum energy structures of two side chain oligomeric fragments of 3M PFSA polymer with fully extended PTFE backbones upon addition of two explicit water molecules with the hydrogen bonding between hydrophilic groups and water molecules illustrated in the bottom panels: (a) the EW 590 system revealing the first instance of dissociation of a single acidic proton; the system exhibits direct hydrogen bonding between side chain sulfonic/ate groups and a connectivity 'bridge' through a hydronium ion; (b) no dissociation of either acidic proton in the EW 690 system at this level of hydration; however, the resulting hydrogen bond connectivity between hydrophilic groups now includes both acidic protons.

positive charge is delocalized as two hydronium ions which connect the two sulfonate groups via strong hydrogen bonds as indicated by the O···O distances. The charge delocalization can be realized through the partial atomic charge analysis of the side chains. Figs. 8 and 9 show the plots of the summed partial atomic charges of the sulfonate/sulfonic acid oxygen atoms and the electron withdrawing $-CF_2-$ groups located at the α- and β-carbon sites of each side chain as a function of water content for the EW 590 and EW 690 systems,

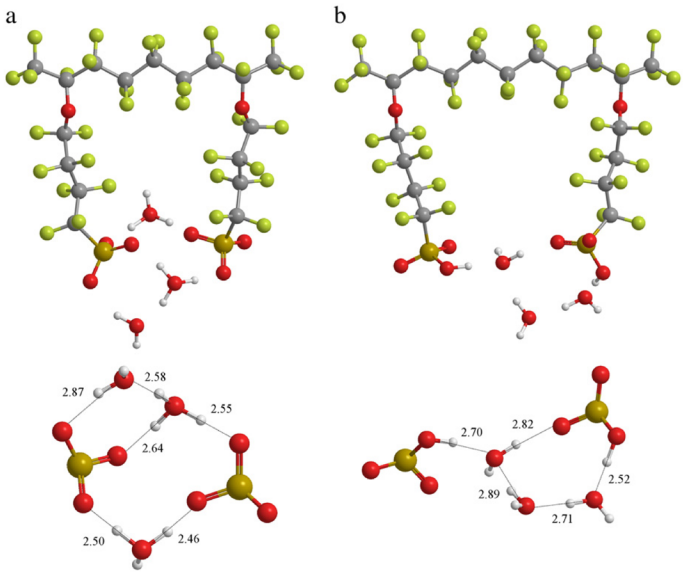

Fig. 4. Optimized (B3LYP/6-311G**) global minimum energy structures of two side chain oligomeric fragments of 3M PFSA polymer with fully extended PTFE backbones upon addition of three explicit water molecules with the hydrogen bonding between hydrophilic groups and water molecules illustrated in the bottom panels: (a) the EW 590 system shows dissociation of both acidic protons with side chain hydrophilic groups no longer directly hydrogen bonded but instead are doubly 'bridged' through two hydronium ions; (b) the EW 690 system again does not exhibit dissociation of either acidic proton; however, the O–H bond length in the sulfonic acid group on the right has increased to 1.04 Å.

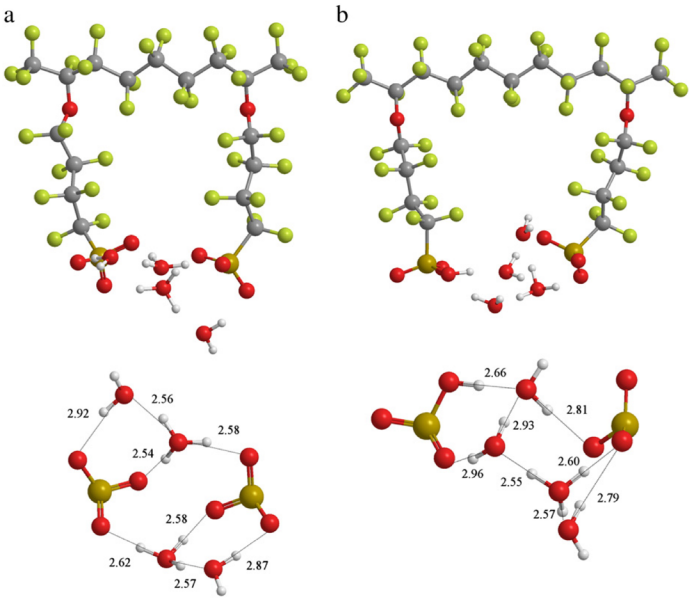

Fig. 5. Optimized (B3LYP/6-311G**) global minimum energy structures of two side chain oligomeric fragments of 3M PFSA polymer with fully extended PTFE backbones with the addition of four explicit water molecules with the hydrogen bonding between hydrophilic groups and water molecules illustrated in the bottom panels: (a) double hydrogen bond connectivity between side chains is maintained through hydronium ions in the EW 590 system with the additional water molecules further filling the first hydration shell; (b) dissociation of a single acidic proton is first observed in the EW 690 system at this hydration; the side chain sulfonic/ate groups are 'bridged' via hydrogen bonding through a single water molecule as well as a 'bridge' consisting of one water molecule and a hydronium ion.

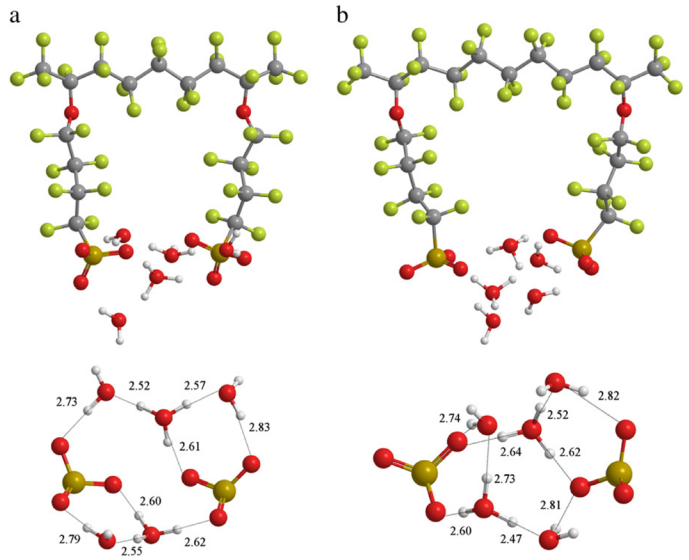

Fig. 6. Optimized (B3LYP/6-311G**) global minimum energy structures of two side chain oligomeric fragments of 3M PFSA polymer with fully extended PTFE backbones upon addition of five explicit water molecules with the hydrogen bonding between hydrophilic groups and water molecules illustrated in the bottom panels: (a) one of hydronium ions connecting the side chains in the EW 590 system has been broken to form an 'Eigen-like' connection (see text) where the hydronium ion is now hydrogen bonded to one of the sulfonate groups and two water molecules that form a hydrogen bond 'bridge' between the side chains; (b) dissociation of both acidic protons is finally observed in the EW 690 system with the side chains 'bridged' through one hydronium ion as well as a chain consisting of a hydronium ion and one water molecule with hydrogen bond lengths resembling that of a Zundel cation hydrogen bonded to each of the sulfonate groups and a water molecule.

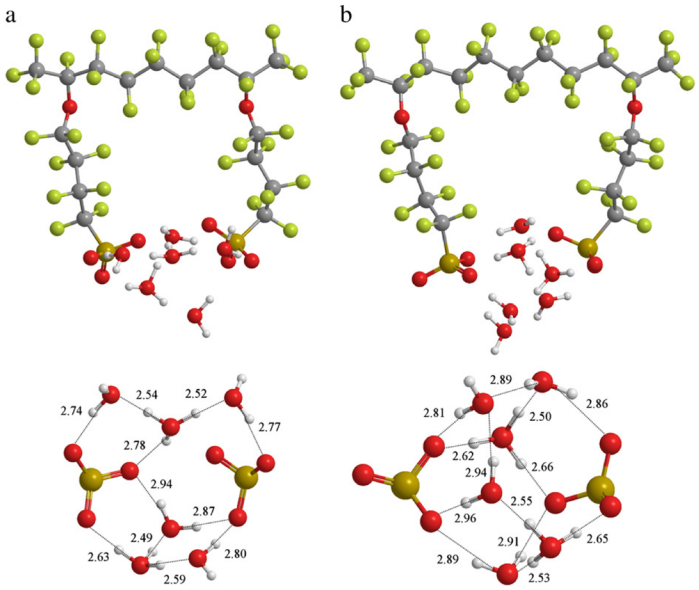

Fig. 7. Optimized (B3LYP/6-311G**) global minimum energy structures of two side chain oligomeric fragments of 3M PFSA polymer with fully extended PTFE backbones upon addition of six explicit water molecules with the hydrogen bonding between hydrophilic groups and water molecules illustrated in the bottom panels: (a) one of the dissociated acidic protons in the EW 590 system now exists as a 'Zundel-like' ion which connects the terminal sulfonate groups and an 'Eigen-like' connection also maintains connectivity between the side chains; (b) one of the dissociated acidic protons in the EW 690 system also forms a 'Zundel-like' ion between the top hydronium ion and the uppermost water molecule connecting the side chains through hydrogen bonds, while a more 'Eigen-like' connectivity is observed in the bottom hydronium ion complex.

respectively. The total charge on the two $-(CF_2)_2SO_3$ terminal portions of the side chains in the EW 590 system is, as expected, the least negative under 'dry' conditions as no proton dissociation has occurred. This charge becomes significantly more negative after first proton dissociation at $\lambda = 1$ and has the most negative value at $\lambda = 1.5$ upon which dissociation of the second acidic proton occurs. The side chain connectivity through strong hydrogen bonding between side chain sulfonic acid groups and hydronium ions/water molecules in the EW 590 system was not observed in the EW 690 system and no proton dissociation has occurred after the addition of two or three water molecules as shown in the minimum energy structures displayed in Figs. 3b and 4b, respectively. The minimum energy structure of the EW

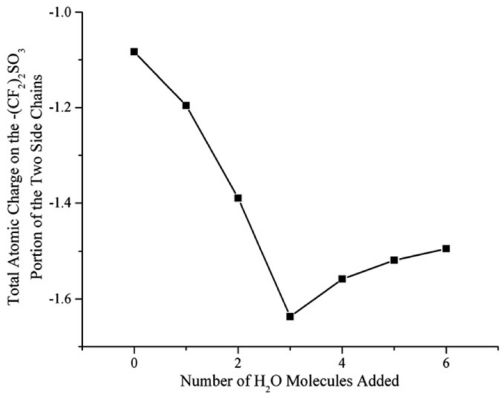

Fig. 8. Total atomic charge as computed with the CHelpG routine residing on the $-(CF_2)_2SO_3$ terminal portions of the side chains in the EW 590 system as a function of the number of added water molecules. The charge becomes significantly more negative after the addition of two water molecules where first proton dissociation was observed and undergoes an additional considerable decrease after second proton dissociation occurs upon addition of three water molecules.

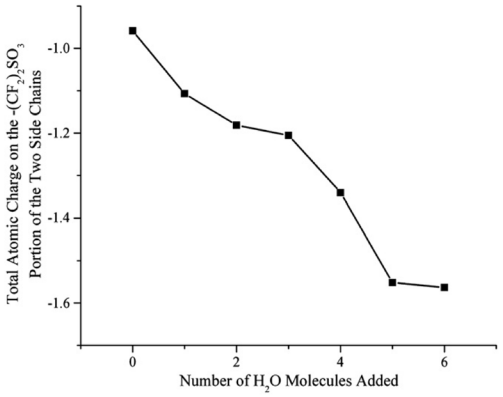

Fig. 9. Total atomic charge as computed with the CHelpG routine residing on the $-(CF_2)_2SO_3$ terminal portions of the side chains in the EW 690 system as a function of the number of added water molecules. The charge is considerably more negative after the addition of four water molecules where first proton dissociation was observed and undergoes an even greater decrease after second proton dissociation occurs upon addition of five water molecules.

690 system with the addition of two water molecules (Fig. 3b) does exhibit hydrogen bonding that 'bridges' the side chains through a central water molecule as well as interaction between the other water molecule, the acidic proton on the left sulfonic acid group, and the central water molecule, but the hydrogen bond distances between the 'bridging' water molecule and the sulfonic acid groups are significantly greater than those observed in the EW 590 system. The BSSE-corrected binding energy per water molecule in the EW 690 system at this hydration, however, has the greatest incremental increase in strength observed in either system at all hydration levels. This may be attributed to the resulting configuration in which each sulfonic acid group donates a hydrogen bond to individual water molecules. Although the hydrogen bond length between the left sulfonic acid group and the hydrogen bond accepting central 'bridging' water molecule has increased ~0.9 Å from that observed at $\lambda = 0.5$, the hydrogen bond length from the central water molecule to the hydrogen bond accepting sulfonic acid group on the right has decreased ~0.2 Å and a strong hydrogen bond has formed between the additional water molecule and the donating right sulfonic acid group. A similar configuration was also found upon addition of three water molecules in the EW 690 system (Fig. 4b) where the minimum energy structure maintains favorable linkage between side chains, but without the continuous connectivity through strong hydrogen bonding seen in the EW 590 system. This appears to preclude proton dissociation in this system despite conformational changes in the side chains that bring the side chains somewhat closer to one another.

Upon addition of a fourth water molecule, the connectivity between the sulfonic acid groups is further increased with global minimum energy structures of the two systems shown in Fig. 5. The EW 590 system with four added water molecules preserves dissociation of both protons, and the connectivity between sulfonate groups through strong hydrogen bonds from the two hydronium ions is maintained with additional hydrogen bonding between hydronium ions, water molecules, and the sulfonate groups, as shown in Fig. 5a. Furthermore, the total charge on the $-(CF_2)_2SO_3$ terminal portions of the side chains (Fig. 8) has become less negative as the additional water molecule acts as a hydrogen bond donor to its neighboring sulfonate group. In the EW 690 system, a hydration level of $\lambda = 2$ results in dissociation of one of the acidic protons. The side chain shown on the right in Fig. 5b exhibits the same (as in Fig. 4b) twisted conformation of the sulfonate group which appears to be important in stabilizing the protonic charge through interaction with the other sulfonic acid group. Similar to what was observed after first proton dissociation in the EW 590 system, the total charge on the $-(CF_2)_2SO_3$ terminal portions of the side chains in the EW 690 system (Fig. 9) undergoes a significant decrease after proton dissociation has occurred.

Once sufficient water molecules have been added to the system to establish hydration and connectivity of the groups, the two systems become intrinsically more similar. Fig. 6 displays the global minimum energy structures of both the EW 590 and EW 690 systems with the addition of five water molecules. The addition of a fifth water molecule in the EW 590 system brings about reorganization of the side chain connectivity through one of the hydronium ions in favor of connectivity in the form of an 'Eigen-like' complex. The term 'Eigen-like' is used here to refer to a complex that contains a hydronium ion which forms hydrogen bonds with lengths similar to the true Eigen cation bulk-water [25–30] but between two water molecules and an oxygen atom from a sulfonate group as opposed to three water molecules. This complex forms a hydrogen bond 'bridge' between the side chains through the hydronium ion and a single water molecule and the other hydronium ion maintains the connectivity of the side chains observed at $\lambda = 2$, as shown in Fig. 6a. The addition of the fifth water molecule in the EW 690 system (Fig. 6b) brings about proton dissociation in both sulfonic acid groups with similar side chain connectivity through a single hydronium ion as well as a hydronium ion and water 'bridge' connection as observed in the EW 590 system. The hydronium ion/water molecule bridge in the EW 690 system, however, has a $H_3O^+ \cdots H_2O$ hydrogen bond length resembling that of a Zundel cation bulk-water [25–30] hydrogen bonded to each of the sulfonate groups and a water molecule.

The connectivity between side chains through hydrogen bond 'bridges' continues after a sixth water molecule is added to each fragment; the global minimum energy structures and bottom views of the water molecules and sulfonate groups are shown in Fig. 7. However, a notable configurational change was observed with regard to the state of the dissociated protons in both oligomeric fragments. In the EW 590 fragment, the dissociated proton existing as a single hydronium ion connecting the side chains reorients to form a 'Zundel-like' cation which hydrogen bonds to each of the sulfonate groups and a single water molecule. The 'Zundel-like' ion formed in the this system, shown in Fig. 7a, has an O···O distance of 2.49 Å (O···H bond distances of 1.43 and 1.06 Å). This system also maintains connectivity through a more 'Eigen-like' structure but has migrated away from the sulfonate group as indicated by the longer hydrogen bond length. The Zundel cation connecting the side chains through a hydronium ion and a water molecule at a hydration of $\lambda = 2.5$ now resembles more of an 'Eigen-like' complex while the single hydronium ion connectivity is maintained but with more 'Zundel-like' character (O···O = 2.5 Å) (Fig. 7b). Prior electronic structure calculations of oligomeric fragments of the SSC PFSA ionomer at a hydration of $\lambda = 3$ also revealed the formation of a Zundel cation state for one of the dissociated protons [33] and ab initio molecular dynamics simulations of the mono- and di-hydrates of triflic acid [47] also attest to the importance of this moiety in proton transfer in these solids. Clearly, structural diffusion is important in the transport of protons in PFSA systems even under conditions of very little water.

4. Conclusions

The separation of side chains was determined to have an effect on the connectivity of the sulfonic acid groups in both 'dry' and minimally hydrated fragments of the 3M PFSA ionomer. Specifically, when the side chains are separated by five difluoromethylene units, connectivity via double hydrogen bonds between the sulfonic acid groups was observed in the global minimum energy structure without any added water molecules through hydrogen bonding of the groups. When the side chains are separated by seven difluoromethylene units, this connectivity cannot be achieved for systems with fully extended backbones. Dissociation of a single acidic proton was observed in the EW 590 system after only two water molecules where added, but this was not observed in the larger EW 690 system until the addition of four water molecules. The EW 590 global minimum energy structures resulted in a more continuous, all-encompassing hydrogen bond network between the sulfonic acid groups and water molecules than the EW 690 system at low hydration. This effectively provides means for stabilization of excess charge on the oligomer once proton dissociation occurs, an effect not seen in the EW 690 system at minimal hydration. The close proximity of terminal sulfonic acid groups in the EW 590 system also promotes dissociation of the second acidic proton with the addition of as few as three water molecules. This is a result of its ability to connect side chain terminal sulfonic acid groups, both directly and with as few as one water molecule, to form a hydrogen bonding network at low hydration. The larger EW 690 system lacks a means of stabilizing the excess negative charge on the sulfonate groups hindering proton dissociation at very low hydration levels. The ability to form a hydrogen bond network 'bridge' via 'Eigen-like' connections facilitates proton dissociation by providing means for stabilization of the protonic charge from one or more SO_3H groups. The differences in the hydration and proton dissociation were mitigated at a water content of 3 H_2O/SO_3H where in both systems one of the dissociated protons was found to exist as a 'Zundel-like' complex and the other as more of an 'Eigen-like' complex. These

calculations underscore the importance of the interaction of sulfonic acid groups through hydrogen bonding in the transfer and state of the dissociated protons at low levels of hydration.

References

[1] Y.Y. Shao, G.P. Yin, Z.B. Wang, Y.Z. Gao, J. Power Sources 167 (2007) 235.
[2] K.D. Kreuer, S.J. Paddison, E. Spohr, M. Schuster, Chem. Rev. 104 (2004) 4637.
[3] O. Savadogo, J. Power Sources 127 (2004) 135.
[4] K.D. Kreuer, Handbook of Fuel Cells-Fundamentals, Technology and Applications, Volume 3-Fuel Cell Technology and Applications, J. Wiley and Sons, Chichester, UK, 2003.
[5] M. Doyle, G. Rajendran, Handbook of Fuel Cells-Fundamentals Technology and Applications, Volume 3-Fuel Cell Technology and Applications, Wiley and Sons, Chichester, UK, 2003.
[6] G. Alberti, M. Casciola, Ann. Rev. Mater. Res. 33 (2003) 129.
[7] M.E. Schuster, W.H. Meyer, Ann. Rev. Mater. Res. 33 (2003) 233.
[8] J. Roziere, D.J. Jones, Ann. Rev. Mater. Res. 33 (2003) 503.
[9] S.J. Paddison, Ann. Rev. Mater. Res. 33 (2003) 289.
[10] K.A. Mauritz, R.B. Moore, Chem. Rev. 104 (2004) 4535.
[11] M.A. Hickner, H. Ghassemi, Y.S. Kim, B.R. Einsla, J.E. McGrath, Chem. Rev. 104 (2004) 4587.
[12] A. Biyikoglu, Int. J. Hydrogen Energy 30 (2005) 1181.
[13] D. Cheddie, N. Munroe, J. Power Sources 147 (2005) 72.
[14] K.D. Kreuer, ChemPhysChem 3 (2002) 771.
[15] B.R. Ezzell, W.P. Carl, W.A. Mod, The Dow Chemical Company, U.S, 1982.
[16] Z.Y. Yang, R.G. Rajendran, Angew. Chem. Int. Ed. 44 (2005) 564.
[17] S.J. Hamrock, M.A. Yandrasits, Polym. Rev. 46 (2006) 219.
[18] A. Vishnyakov, A.V. Neimark, J. Phys. Chem. B 104 (2000) 4471.
[19] J.A. Elliott, S. Hanna, A.M.S. Elliott, G.E. Cooley, Polymer 42 (2001) 2251.
[20] E. Spohr, P. Commer, A.A. Kornyshev, J. Phys. Chem. B 106 (2002) 10560.
[21] S.S. Jang, V. Molinero, T. Cagin, W.A. Goddard, J. Phys. Chem. B 108 (2004) 3149.
[22] M. Eikerling, A.A. Kornyshev, A.M. Kuznetsov, J. Ulstrup, S. Walbran, J. Phys. Chem. B 105 (2001) 3646.
[23] S.J. Paddison, R. Paul, Phys. Chem. Chem. Phys. 4 (2002) 1158.
[24] S.J. Paddison, R. Paul, K.D. Kreuer, Phys. Chem. Chem. Phys. 4 (2002) 1151.
[25] N. Agmon, Chem. Phys. Lett. 244 (1995) 456.
[26] M. Tuckerman, K. Laasonen, M. Sprik, M. Parrinello, J. Chem. Phys. 103 (1995) 150.
[27] M.E. Tuckerman, D. Marx, M.L. Klein, M. Parrinello, Science 275 (1997) 817.
[28] D. Marx, M.E. Tuckerman, J. Hutter, M. Parrinello, Nature 397 (1999) 601.
[29] C.J.D. von Grotthuss, Ann. Chim. LVIII (1806) 54.
[30] H. Lapid, N. Agmon, M.K. Petersen, G.A. Voth, J. Chem. Phys. 122 (2005) 014506.
[31] S.J. Paddison, K.D. Kreuer, J. Maier, Phys. Chem. Chem. Phys. 8 (2006) 4530.
[32] S.J. Paddison, Device and Materials Modeling in PEM Fuel Cells, Springer-Verlag Berlin, Berlin, 2009, pp. 385–412.
[33] S.J. Paddison, J.A. Elliott, J. Phys. Chem. A 109 (2005) 7583.
[34] S.J. Paddison, J.A. Elliott, Phys. Chem. Chem. Phys. 8 (2006) 2193.
[35] S.J. Paddison, J.A. Elliott, Solid State Ionics 177 (2006) 2385.
[36] S.J. Paddison, L.R. Pratt, T.A. Zawodzinski, J. Phys. Chem. A 105 (2001) 6266.
[37] S.J. Paddison, J. New Mater. Electrochem. Syst. 4 (2001) 197.
[38] M. Eikerling, S.J. Paddison, T.A. Zawodzinski, J. New Mater. Electrochem. Syst. 5 (2002) 15.
[39] M.J. Frisch, G.W. Trucks, H.B. Schlegel, G.E. Scuseria, M.A. Robb, J.R. Cheeseman, J.A. Montgomery, T. Vreven, K.N. Kudin, J.C. Burant, J.M. Millam, S.S. Iyengar, J. Tomasi, V. Barone, B. Mennucci, M. Cossi, G. Scalmani, N. Rega, G.A. Petersson, H. Nakatsuji, M. Hada, M. Ehara, K. Toyota, R. Fukuda, J. Hasegawa, M. Ishida, T. Nakajima, Y. Honda, O. Kitao, H. Nakai, M. Klene, X. Li, J.E. Knox, H.P. Hratchian, J.B. Cross, C. Adamo, J. Jaramillo, R. Gomperts, R.E. Stratmann, O. Yazyev, A.J. Austin, R. Cammi, C. Pomelli, J.W. Ochterski, P.Y. Ayala, K. Morokuma, G.A. Voth, P. Salvador, J.J. Dannenberg, V.G. Zakrzewski, S. Dapprich, A.D. Daniels, M.C. Strain, O. Farkas, D.K. Malick, A.D. Rabuck, K. Raghavachari, J.B. Foresman, J.V. Ortiz, Q. Cui, A.G. Baboul, S. Clifford, J. Cioslowski, B.B. Stefanov, G. Liu, A. Liashenko, P. Piskorz, I. Komaromi, R.L. Martin, D.J. Fox, T. Keith, M.A. Al-Laham, C.Y. Peng, A. Nanayakkara, M. Challacombe, P.M.W. Gill, B. Johnson, W. Chen, M.W. Wong, C. Gonzalez, J.A. Pople, Gaussian 03, Gaussian Inc., Wallingford, CT, 2004.
[40] H.B. Schlegel, J. Comput. Chem. 3 (1982) 214.
[41] Pc Harihara, J.A. Pople, Theor. Chim. Acta 28 (1973) 213.
[42] A.D. Becke, J. Chem. Phys. 98 (1993) 5648.
[43] A.D. Becke, J. Chem. Phys. 98 (1993) 1372.
[44] A.D. McLean, G.S. Chandler, J. Chem. Phys. 72 (1980) 5639.
[45] S.F. Boys, F. Bernardi, Mol. Phys. 19 (1970) 553.
[46] M. Eikerling, S.J. Paddison, L.R. Pratt, T.A. Zawodzinski, Chem. Phys. Lett. 368 (2003) 108.
[47] R.L. Hayes, S.J. Paddison, M.E. Tuckerman, J. Phys. Chem. B 113 (2009) 16574.

PCCP

Cite this: *Phys. Chem. Chem. Phys.*, 2012, **14**, 16349–16359

www.rsc.org/pccp

PAPER

The effect of hydrogen bond reorganization and equivalent weight on proton transfer in 3M perfluorosulfonic acid ionomers†

Jeffrey K. Clark II,[a] Stephen J. Paddison*[a] and Steven J. Hamrock[b]

Received 1st August 2012, Accepted 19th October 2012
DOI: 10.1039/c2cp42678a

We present an investigation into the energetics associated with proton transfer in ionomeric fragments of the 3M™ perfluorosulfonic acid (PFSA) membrane at different equivalent weights (EW). Electronic structure calculations were performed on two fragments each with two pendant side chains separated along a poly(tetrafluoroethylene) (PTFE) backbone with chemical formula $CF_3CF(–O(CF_2)_4SO_3H)(CF_2)_nCF(–O(CF_2)_4SO_3H)CF_3$, where $n = 5$ or 7, corresponding to membrane equivalent weights of 590 and 690 g mol^{-1}. Potential energy surface (PES) scans were performed for the transfer of a proton in various hydrogen bonds between water molecules, sulfonic acid groups, and charged species. The scans involved incrementally increasing an O–H bond length in steps of 0.02 Å with geometry optimizations performed at each step at the B3LYP/6-31G** level over all other degrees of freedom. The nature of the hydrogen bond network and the degree of dissociation were found to be critical factors in determining the resulting energetic barrier for proton transfer. The smaller fragment was found to more readily reorient to compensate for the transfer of charge resulting in a lower energetic barrier to proton transfer through stabilization of the new hydrogen bonds. However, when each ionomer had the same degree of dissociation, reprotonation of the sulfonate groups was the most energetically unfavorable in EW 590 when no structural reorganization was observed to occur due to its greater propensity to exist in a dissociated state.

Introduction

The use of hydrogen fuel cells as highly efficient, clean energy conversion devices is a growing area of interest as the global demand for energy continues to rise along with the pressure towards reducing emissions of carbon dioxide and other gases emitted from conventional energy systems based on fossil fuels.[1] Critical to the efficient operation of hydrogen fuel cells is a proton-conducting electrolyte which separates the electrodes and reactant gases. This material must be highly proton conducting and exhibit long-time chemical, thermal, and mechanical stability.[2] A number of solid state proton-conducting materials are available that operate across a large range of temperature. Proton-conducting ceramic oxides, typically perovskites, exhibit good thermal stability and high proton conductivities ($\sim 10^{-2}$ S cm^{-1}) at high temperature, *i.e.*, ~800–1200 K.[3] In the intermediate temperature range (~370–800 K), superprotonic phase solid acids[4–6] and heterocycle-based (*e.g.*, imidazole) materials show proton conductivities also on the order of 10^{-2} S cm^{-1}.[7] For operating temperatures below 370 K, proton exchange membrane (PEM) ionomers are widely utilized as the electrolyte due to their high proton conductivity ($\sim 10^{-1}$ S cm^{-1}) when fully hydrated and good chemical stability.[8] Furthermore, the favorable power-to-weight ratio of PEM fuel cells make them an attractive candidate for vehicular and portable applications.[9] The most commonly employed PEMs are perfluorosulfonic acid (PFSA) ionomers with Nafion® currently representing the industry standard.

PFSA ionomers are comprised of a hydrophobic poly(tetrafluoroethylene) (PTFE) backbone functionalized with pendant side chains each terminated with a single hydrophilic sulfonic acid group. These materials must be sufficiently hydrated to conduct protons at high rates.[10] Hydration results in the formation of hydrophilic domains through the aggregation of the side chain sulfonic acid groups.[2,11,12] Solvation of the acid groups by the water molecules leads to dissociation of the acidic protons into the aqueous domain; the dissociated protons are then mobile facilitating long-range proton transport.[2,13] The transport of protons in the membrane occurs *via* vehicular diffusion (as $H_3O^+_{aq}$) and structural diffusion[14–18] with mechanisms and rates bearing features comparable to that of bulk water.[19–25] Proton conductivity

[a] *Department of Chemical and Biomolecular Engineering, University of Tennessee, Knoxville, TN 37996, USA. E-mail: spaddison@utk.edu*
[b] *3M Fuel Cell Components Program, 3M Center, St. Paul, Minnesota 55144, USA*
† Electronic supplementary information (ESI) available: See DOI: 10.1039/c2cp42678a

in PFSA ionomers is dependent on the level of hydration as the high proton conductivity of Nafion® is only observed under conditions of high hydration (*i.e.*, 95% relative humidity).[26] Highly hydrated conditions are known to increase the occurrence of water 'cross-over' due to electro-osmotic drag and permeation which has negative consequences on the efficiency of the fuel cell.[27] Due to the strong dependence of proton conductivity on absorbed water, use of PFSA ionomers in fuel cells is restricted to operating temperatures below 100 °C (to prevent evaporation and drying out) which adversely affects the carbon monoxide tolerance of the electrocatalyst.[2]

Considerable effort is being undertaken to develop membranes which exhibit high proton conductivity at lower hydration levels.[28–33] Some approaches have focused on the design of entirely novel proton-conducting PEM materials while many others correspond to chemical and structural modification of currently available PFSA ionomers, such as changing the protogenic group (*e.g.*, phosphonic acid and imidazole) and altering the specific side chain chemistry. Regarding the latter, materials which maintain the PTFE backbone but replace the Nafion® side chain with shorter perfluorinated sulfonic acid side chains, which may lower the equivalent weight (EW), have been developed including the short side chain (SSC) PFSA membrane[34] ($-O(CF_2)_2SO_3H$) and the 3M™ PFSA membrane[32] ($-O(CF_2)_4SO_3H$) each of which exhibit higher proton conductivity than Nafion®.[32,35–37] The lower EW of these ionomers, however, does not entirely dictate the improved performance over Nafion®, and the underlying reasons for the improved proton conductivities are not entirely understood. Elucidating the molecular-level features that contribute to proton mobility in PEMs is, thus, necessary for the further development of superior membranes. It is widely known that hydrogen bonding is a fundamental characteristic of proton transport shared amongst all classes of solid state proton conductors.[38,39] The structural diffusion of protons involves the shuttling of protons through the hydrogen bond network through a succession of transformations between Eigen ($H_9O_4^+$) and Zundel ($H_5O_2^+$) cations.[14–23] Thus, an understanding of how the specific chemistry of the materials affects proton mobility requires a molecular-level insight into the formation and breaking of hydrogen bonds in highly complex systems. There are few experimental techniques capable of resolving this information leading to the widespread utilization of molecular modeling techniques in attempts to understand the principle characteristics of proton transport in PEMs.

Multiscale modeling techniques have contributed to the understanding of proton conduction in these systems.[40] Classical molecular dynamics (MD) simulations, capable of treating systems of tens of thousands of atoms, have been used to study the transport properties of PEMs.[41–48] Also included in these are empirical valence bond (EVB) schemes[49–51] capable of predicting dynamic proton shuttling events which have revealed the importance of structural diffusion in the diffusion of protons.[52–55] *Ab initio* molecular dynamics (AIMD) simulations on model systems with a high perfluorosulfonic acid density have also provided insight into the contribution of structural diffusion on the nature of proton transfer in PFSA systems under minimally hydrated conditions.[56–61] On a smaller scale, extensive *ab initio* electronic structure calculations have revealed molecular features that govern proton dissociation and separation in fragments of PFSA membranes and other PEMs. Early electronic structure calculations on PFSA ionomers were restricted to the primary hydration of single PFSA side chains, such as triflic acid (CF_3SO_3H).[62,63] An increase in computational capability allowed for later studies to explore larger PFSA ionomer fragments at higher levels of hydration.[64–68] Studies on other PEMs and acidic moieties have also been conducted to explore how the protogenic groups and specific side chain chemistry govern proton dissociation and separation.[64,69–74] The inclusion of more than one side chain on a single PTFE backbone to investigate the effects of neighboring side chain interactions and ionomer EW on proton dissociation and local hydration has been explored on the SSC[75–78] and 3M™ PFSA[79] ionomers. These studies revealed the importance of side chain connectivity through hydrogen bonding under dry or minimally hydrated conditions on proton dissociation. The present study extends the investigation of the 3M™ PFSA ionomers to understand the factors that contribute to the energetics of proton transfer.

Previously reported electronic structure calculations on the 3M™ PFSA ionomer at different EWs revealed the importance of side chain separation and the extent and nature of the hydrogen bonding on proton dissociation at low levels of hydration.[79] Fragments with two different side chain separations were used to model different EW ionomers with the chemical formula $CF_3CF(-O(CF_2)_4SO_3H)(CF_2)_nCF(-O(CF_2)_4SO_3H)CF_3$, where $n = 5$ and 7 corresponding to EWs of 590 and 690 grams ionomer per mole acid, respectively, and water molecules were systematically added. The nomenclature EW 590 and EW 690 is hereafter used to distinguish the two different fragments. The optimized geometries showed that increasing the separation between side chains also increased the number of water molecules required to facilitate proton dissociation of the side chain sulfonic acid groups. Specifically, dissociation of a single acidic proton was observed in EW 590 at a water content of only 1 H_2O/SO_3H, but the ionomer with greater separation of the side chains (EW 690) did not exhibit first proton dissociation until 2 H_2O/SO_3H. The greater side chain separation seemed to preclude a cooperative interaction through hydrogen bonding that promotes proton dissociation at low hydration in membranes of this type. Dissociation of the second acidic proton occurred at a hydration of 1.5 H_2O/SO_3H for EW 590, while this was not observed in the EW 690 system until 2.5 H_2O/SO_3H. The differences in the hydration required for proton dissociation for the different EW ionomers was attributed to the interactions between side chains and the capability to form continuous, all-encompassing hydrogen bonding in systems with less separation between the acidic groups.[79] The present work focuses on the roles hydrogen bond reorganization and separation of sulfonic acid groups have on the energetics of proton transfer in 3M™ PFSA ionomers. Specifically, we report potential energy surface scans for the transfer of a proton oxygen atoms of sulfonic acid/sulfonate groups, water molecules, or hydronium ions in optimized geometries of the 3M™ EW 590 and EW 690 PFSA ionomers obtained from the study mentioned above to investigate how the hydrogen bond network configuration affects the energetics of proton transfer.

This paper is organized as follows. The first section contains a brief description of the computational methods used in

the potential energy surface (PES) scans for proton transfer across various hydrogen bonds. The results are then presented and discussed according to the type of proton transfer event. This is followed by a comparison of the energetics for proton transfer reactions and the resulting hydrogen bond networks formed. Lastly, the main results are summarized in the conclusion section.

Computational methods

Electronic structure calculations were performed using the Gaussian 09 suite of programs.[80] Potential energy surface (PES) scans for the transfer of a proton in fully optimized EW 590 and EW 690 fragments with four or five added water molecules obtained from an earlier study[79] were performed to obtain relative energy profiles for these events. It is important to note that a hydration of four water molecules resulted in a global minimum energy structure with both acidic protons dissociated in EW 590; however, some fully optimized structures were found where the proton of a sulfonic acid group was not dissociated. The PES scans of proton transfer were obtained for structures with and without complete dissociation for comparative purposes with the EW 690 fragment with only one dissociated proton at this hydration level. The final fully optimized structures reported in this study were obtained using hybrid density functional theory (DFT) employing Becke's 3-parameter functional (B3LYP)[81,82] and the 6-311G** split valence basis set[83,84] (*i.e.*, the B3LYP/6-311G** level of theory). However, the geometries obtained at the B3LYP/6-31G** level of theory were used due to the computational expense of performing PES scans on these relatively large electronic systems. The PES scans involved increasing a specified O–H bond length of either a water molecule, a hydronium ion, or a sulfonic acid group across a hydrogen bond in incremental steps of 0.02 Å. The O–H bond length was the only fixed parameter with an optimization performed over all other degrees of freedom using conjugate gradient methods[85] without symmetry constraints. It is well known that the B3LYP functional does not account for dispersion interactions. Although these calculations were meant to provide only relative information about the two ionomers at different side chain separation, sample calculations were also performed using Grimme's B97-D functional[86] which includes an empirical correction for dispersion interactions. These calculations were performed on each fragment from the previous study[79] without the addition of water molecules using the 6-311G** basis set to ensure that dispersion corrections would not affect the side chains, particularly the well-separated nature of the side chains in the EW 690 fragment. The structures exhibited only slightly different hydrogen bond distances between the sulfonic acid groups in the 'dry' EW 590 which maintained double hydrogen bonds between sulfonic acid groups, and the side chains in the EW 690 remained well separated. Furthermore, the PES scan shown in Fig. 3 of this manuscript for the EW 590 ionomer was repeated using the B97-D/6-31G** level of theory, and is reported in Fig. S1 (ESI†). The relative energy profiles obtained exhibit similar features, but lower transition state and local minimum energies were obtained using the B97-D functional. However, the structures obtained throughout the scan contained nearly identical hydrogen bond lengths as those using B3LYP/6-31G** and did not change the qualitative information regarding the PES scan. As these scans are based on optimized static structures, they only reveal the relative tendencies in the energetics of proton transfer, not absolute values. Furthermore, collective effects of the extended environment have been neglected.

Results and discussion

SO_3H to H_2O

Fig. 1 shows an optimized EW 590 geometry at a hydration of $\lambda = 2$ (where $\lambda \equiv$ the number of water molecules per sulfonic acid group) which contains one dissociated proton and one proton associated the sulfonic acid group on the left. As it is well known that hydrogen bonding is a critical feature of proton transport in materials of this type, these interactions were a primary focus in this study. The requirements for a hydrogen bond in the structures that follow are an O···O distance between 2.4 and 3.2 Å and an O–H···O bond angle greater than 140°.[58,87–90] Throughout this paper, the proton being transferred is indicated by a black arrow in the optimized structures used in the PES scans and is displayed in the top left panel of the figures. The relative energy profiles obtained from the scans are plotted as a function of the asymmetric stretch coordinate, $q_{asym} = \frac{1}{\sqrt{2}}(r_{O1\cdots H} - r_{H\cdots O2})$, in the top right panel of the figures, and the bottom panels of the figures show expanded views of the sulfonic acid/sulfonate groups and water molecules with hydrogen bonds denoted by dashed lines and the corresponding O···O distances reported for relevant steps throughout the PES scans with all other atoms removed for clarity. In the results shown in Fig. 1, the associated proton was chosen for the PES scan for transfer across the hydrogen bond between the associated sulfonic acid oxygen atom and the neighboring water molecule. The dissociated proton exists as a hydronium ion donating hydrogen bonds to two water molecules and an oxygen atom on the left sulfonic acid group, the latter having an initial O···O distance of 2.70 Å (Fig. 1a). The hydronium ion shifts towards the sulfonic acid–sulfonate intermediate state as the proton is transferred away from the sulfonic acid group which increases the strength of the hydrogen bond by decreasing the O···O separation to accommodate the excess negative charge resulting from dissociation. At the transition state (Fig. 1b), the O···O distance of the hydronium ion to the sulfonic acid–sulfonate intermediate oxygen atom has decreased to 2.59 Å. The hydrogen bond distance between the water molecule receiving the transferred proton and the oxygen atom from the right sulfonate group also decreased as a result of the propensity for protonated species to delocalize excess positive charge through strong hydrogen bonds. The additional positive charge received by the sulfonate oxygen atom repels away the bottom right water molecule initially donating a hydrogen bond to the oxygen atom. This results in a hydrogen bond shift of the water molecule to an oxygen atom on the same sulfonate group which was not originally involved in any hydrogen bonding. Both acidic protons are in a dissociated state at the local minimum in the PES, displayed in Fig. 1c. The originally associated proton now exists as a hydronium ion connecting the two side chains through hydrogen bonds. The energetic

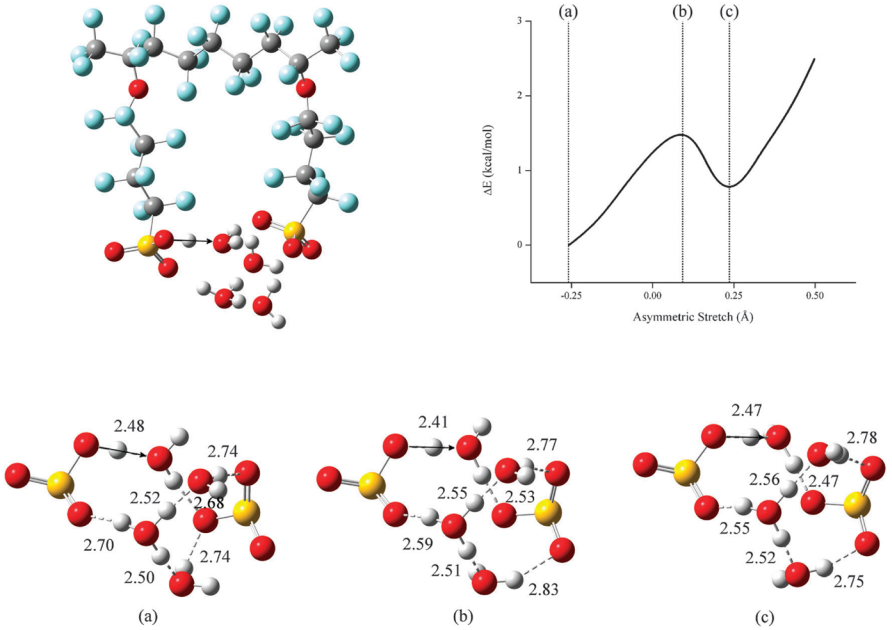

Fig. 1 Top left panel: Optimized (B3LYP/6-31G**) structure of the EW 590 3M™ PFSA ionomer at a hydration of $\lambda = 2$ used in the PES scan of the proton transfer indicated by the arrow. Top right panel: Relative energy profile with respect to the original configuration as a function of the asymmetric stretch coordinate. Bottom panel: rotated bottom view of the sulfonic acid/sulfonate and water molecules with hydrogen bonds denoted by dashed lines and hydrogen bond distances (Å): (a) initial configuration; (b) transition state; and (c) the local minimum points of the scan.

barrier for transferring the proton from the sulfonic acid to the neighboring water molecule is only 1.51 kcal mol^{-1} with the local minimum 0.73 kcal mol^{-1} higher in energy than the original configuration. As mentioned earlier, the global minimum energy configuration found for EW 590 in the earlier study[79] had both protons dissociated. The slightly higher energy of the doubly dissociated state resulting from the PES may be attributed to the newly formed hydronium ion containing one proton not in the hydrogen bond network since hydronium ions have been shown to preferentially delocalize excess positive charge over the maximum number of hydrogen bonds.[69]

The optimized geometry and results of the PES scan of the transfer of an associated proton to a neighboring water molecule for EW 690 at $\lambda = 2$ are shown in Fig. 2. This was found to be the minimum energy EW 690 configuration in the previous study at this level of hydration.[79] As with the EW 590 configuration mentioned above, this system contains one dissociated proton existing as a hydronium ion donating hydrogen bonds to two water molecules, shown in Fig. 2a. However, it donates one hydrogen bond to the sulfonate group oxygen atom in which the dissociated proton originated, as opposed to being well separated from it. A slight reorganization in the hydrogen bonding occurred at the point in the scan where the transferred proton lies directly in between the two oxygen atoms (*i.e.*, $q_{asym} = 0$), as shown in Fig. 2b. Prior to this point, the water molecule receiving the proton accepted a hydrogen bond from a neighboring water molecule. This hydrogen bond breaks as a result of both the repulsion from the additional positive charge on the proton accepting oxygen atom and the reorientation of the neighboring water molecule towards the sulfonic acid–sulfonate intermediate to accommodate the decrease in positive charge. Contractions and expansions in hydrogen bond lengths associated with the transfer of charge were observed up to the transition state (Fig. 2c), but no major reorganization of the hydrogen bonding occurred. At this point, both protons are in a dissociated state with an energetic barrier of ~9.8 kcal mol^{-1}, and the newly formed hydronium ion connects the sulfonate groups *via* hydrogen bonds. A significant structural reorganization took place upon reaching the local minimum, shown in Fig. 2d, which was found to be 4.14 kcal mol^{-1} higher in energy than the original configuration. The proton accepting hydronium ion bridging the two sulfonate groups at the transition state has partially transferred a proton to the sulfonate group on the right as the O–H bond length in the hydronium ion has increased to 1.11 Å and the O···H bond length associated with the sulfonate oxygen atom decreased to 1.31 Å. The corresponding bond lengths for EW 590 were 1.06 and 1.42 Å. The significantly high energetic penalty for achieving a fully dissociated conformation at the transition state and the subsequent partial charge transfer is of little surprise as

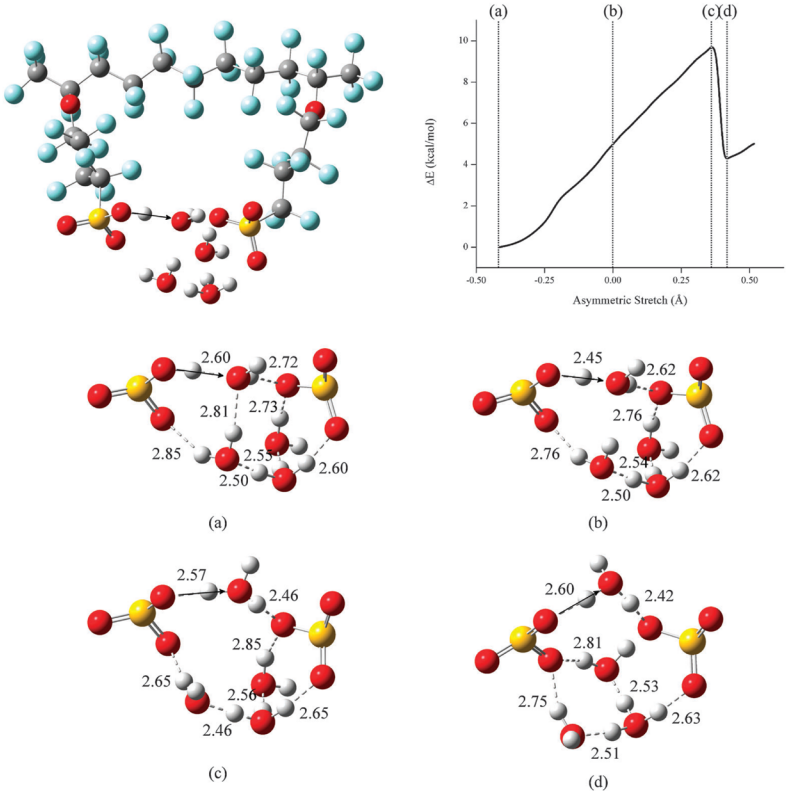

Fig. 2 Top left panel: Optimized (B3LYP/6-31G**) structure of the EW 690 3M™ PFSA ionomer at a hydration of $\lambda = 2$ used in the PES scan of the proton transfer indicated by the arrow. Top right panel: Relative energy profile with respect to the original configuration as a function of the asymmetric stretch coordinate. Bottom panel: rotated bottom view of the sulfonic acid/sulfonate and water molecules with hydrogen bonds denoted by dashed lines and hydrogen bond distances (Å): (a) initial configuration; (b) an intermediate point in the scan at $q_{asym} = 0$; (c) transition state; and (d) local minimum of the scan.

no stable geometry for EW 690 with both protons dissociated at this hydration level was found in the previous study.[79]

H_2O to SO_3H

Fig. 3 shows an optimized geometry of EW 590 at a hydration of $\lambda = 2$ with one proton fully dissociated and the other proton partially dissociated with an O–H bond length of 1.11 Å. While this, again, is not the global minimum energy EW 590 structure found in the previous study,[79] it provides a means of comparison to the similar EW 690 optimized geometry for the following PES scan of proton transfer. A proton was transferred from a water molecule to an oxygen atom of the partially dissociated sulfonic acid group, as indicated by the arrow. Transferring the proton quickly results in dissociation of the originally associated proton to the neighboring water molecule forming a hydronium ion. This hydronium ion then transfers a proton to the water molecule losing a proton to compensate for the loss of positive charge which has little effect on the hydrogen bond topography of the other hydronium ion, water molecule, and right sulfonate group. At the transition state in Fig. 3b, an intermediate configuration is formed where the water molecule shares a proton with both the hydronium ion and the oxygen atom of the sulfonic acid intermediate having O···H distances of 1.11 Å for the sulfonic acid intermediate and the hydronium ion and 1.33 Å from the water molecule oxygen atom to both protons. The energetic barrier for proton transfer to this configuration was found to be only 4.2 kcal mol^{-1}. The transferred proton is fully associated to the receiving oxygen atom at the local minimum, reforming the sulfonic acid, and the hydronium ion completely transfers the shared proton to the water molecule resulting in a configuration very similar to the initial structure only 1.1 kcal mol^{-1} higher in energy (Fig. 3c).

The optimized structure for proton transfer from a water molecule to a sulfonic acid group for EW 690 is shown in Fig. 4. The hydrogen bond network resembles that of the EW 590 structure (Fig. 3) with the exception that there is no hydrogen bond between the water molecule transferring the

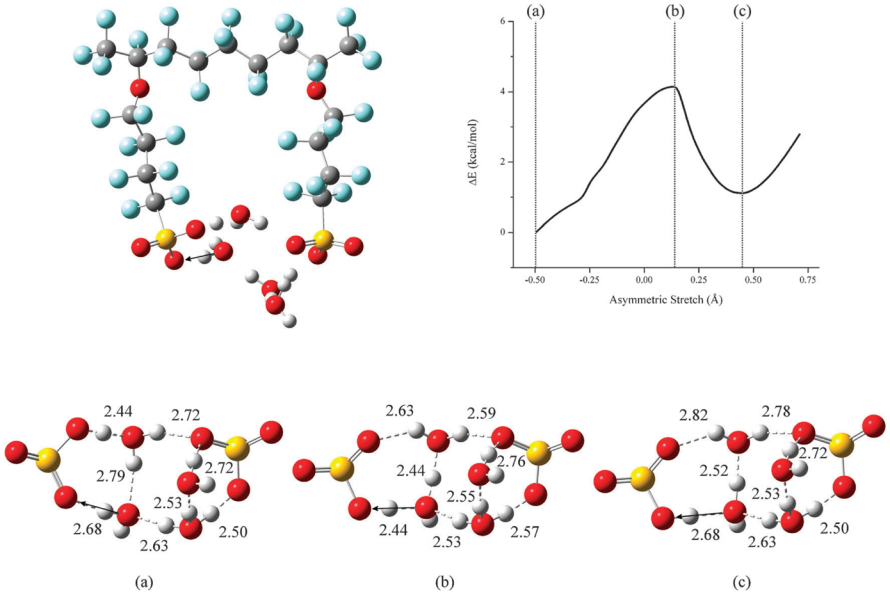

Fig. 3 Top left panel: Optimized (B3LYP/6-31G**) structure of the EW 590 3M™ PFSA ionomer at a hydration of $\lambda = 2$ used in the PES scan of the proton transfer indicated by the arrow. Top right panel: Relative energy profile with respect to the original configuration as a function of the asymmetric stretch coordinate. Bottom panel: rotated bottom view of the sulfonic acid/sulfonate and water molecules with hydrogen bonds denoted by dashed lines and the hydrogen bond distances (Å): (a) initial configuration; (b) transition state; and (c) local minimum points of the scan.

proton and the water molecule accepting a hydrogen bond from the sulfonic acid group. The lack of this additional hydrogen bond proved to be a major contributing factor in determining the energetics associated with this proton transfer event. Transferring the proton led to a transition state with an energetic barrier of 9.0 kcal mol^{-1}. At this point, the proton being transferred is shared between the water molecule and the receiving oxygen atom, and the initially associated proton of the sulfonic acid group is shared between the sulfonic acid intermediate oxygen atom and the neighboring water molecule (Fig. 4b). The local minimum structure (Fig. 4c) was found to be 7.0 kcal mol^{-1} higher in energy than the original state. Without the aforementioned hydrogen bond between the two water molecules, the neighboring hydronium ion hydrogen bonded to the left sulfonate group must donate a proton to the water molecule losing a proton to compensate for the loss of charge. This significantly weakens the hydrogen bond to the left sulfonate group resulting in an increase in excess negative charge on the sulfonate group. The water molecule receiving the originally associated proton then compensates for this effect by partially transferring a proton to an oxygen atom of the left sulfonate group which pushes away the other water molecule that initially donated a hydrogen bond to it. At this point, the proton being transferred is still shared between the water molecule and sulfonic acid–sulfonate intermediate oxygen atom. Full reprotonation of the sulfonic acid group results in a configuration where each proton is associated with a sulfonic acid group in a state 7.3 kcal mol^{-1} higher in energy than the initial structure (Fig. 4d).

H_3O^+ to SO_3^-

Fig. 5 shows the optimized EW 590 at a hydration of $\lambda = 2$ with both protons dissociated each existing as hydronium ions connecting the sulfonate groups through hydrogen bonds; this was the minimum energy EW 590 structure found in the previous study.[79] The proton from the hydronium ion indicated by the arrow was transferred to an oxygen atom of the left sulfonate group. This results in a contraction in the O···O distance between the oxygen atoms involved in proton transfer with an associated transfer of positive charge to the sulfonate group. The O···O contraction and transfer of the proton from the hydronium ion results in less excess positive charge the hydronium ion can delocalize over its additional hydrogen bonds causing an increase in these hydrogen bond lengths. The transfer of positive charge to the sulfonate group repels away its other accepted hydrogen bonds without any major hydrogen bonding reorganization up to the transition state (Fig. 5b). However, the hydronium ion transferring the proton has shifted towards the lower part of the fragment (with respect to the view depicted in the top left panel). This effectively brings the hydronium ion closer to the bottom right water molecule (from 4.61 Å initially to 4.07 Å as measured by the O···O distance) which contains a proton not involved in a

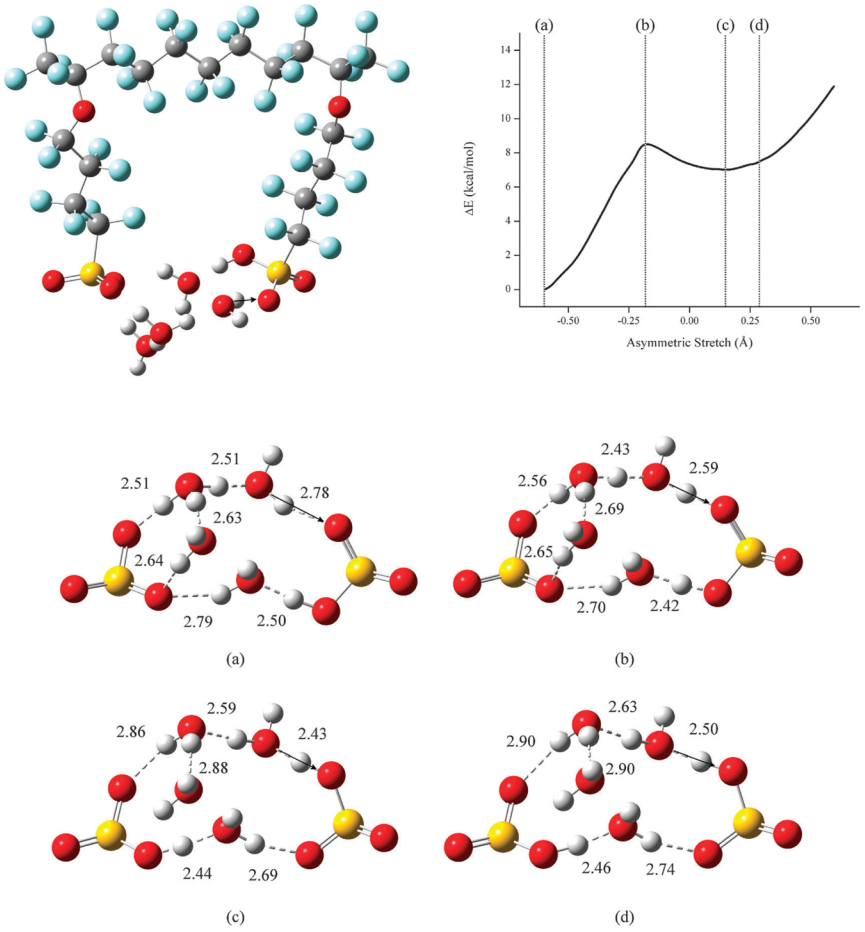

Fig. 4 Top left panel: Optimized (B3LYP/6-31G**) structure of the EW 690 3M™ PFSA ionomer at a hydration of $\lambda = 2$ used in the PES scan of the proton transfer indicated by the arrow. Top right panel: Relative energy profile with respect to the original configuration as a function of the asymmetric stretch coordinate. Bottom panel: rotated bottom view of the sulfonic acid/sulfonate and water molecules with hydrogen bonds denoted by dashed lines and the hydrogen bond distances (Å): (a) initial configuration; (b) transition state; (c) local minimum; and (d) the point in the scan when the proton is fully transferred to the sulfonic acid group.

hydrogen bond. The closer proximity promotes the first truly significant change in the hydrogen bonding at the local minimum. Namely, the water molecule donating only one hydrogen bond to the right sulfonate group reorients to form an additional hydrogen bond with the oxygen atom transferring the proton to stabilize the loss of excess positive charge resulting from proton transfer (Fig. 5c). The barrier of proton transfer was found to be 4.5 kcal mol^{-1} with a local minimum 3.0 kcal mol^{-1} higher in energy than the original geometry. However, the transferred proton is shared between the water molecule and the sulfonic acid–sulfonate intermediate oxygen atom at the local minimum with O–H bond lengths of 1.38 and 1.09 Å, respectively. Reprotonation of the sulfonate group occurs further along the scan (Fig. 5d) with an energetic difference of only ~4.0 kcal mol^{-1} which is likely due to the stabilization of the newly formed hydrogen bond. However, when a proton was transferred across the hydrogen bond between the bottom hydronium ion and the oxygen atom of the left sulfonate group (not shown) no hydrogen bond network reorganization was observed resulting in a monotonically increasing relative energy profile with a singly dissociated state 7.6 kcal mol^{-1} higher in energy than the initial configuration. There was, again, a water molecule with a free proton to potentially donate an additional hydrogen bond to the hydronium ion. However, the water molecule was located 5.90 Å away from the hydronium ion which precluded the reorganization of hydrogen bonds resulting in the higher energetic penalty.

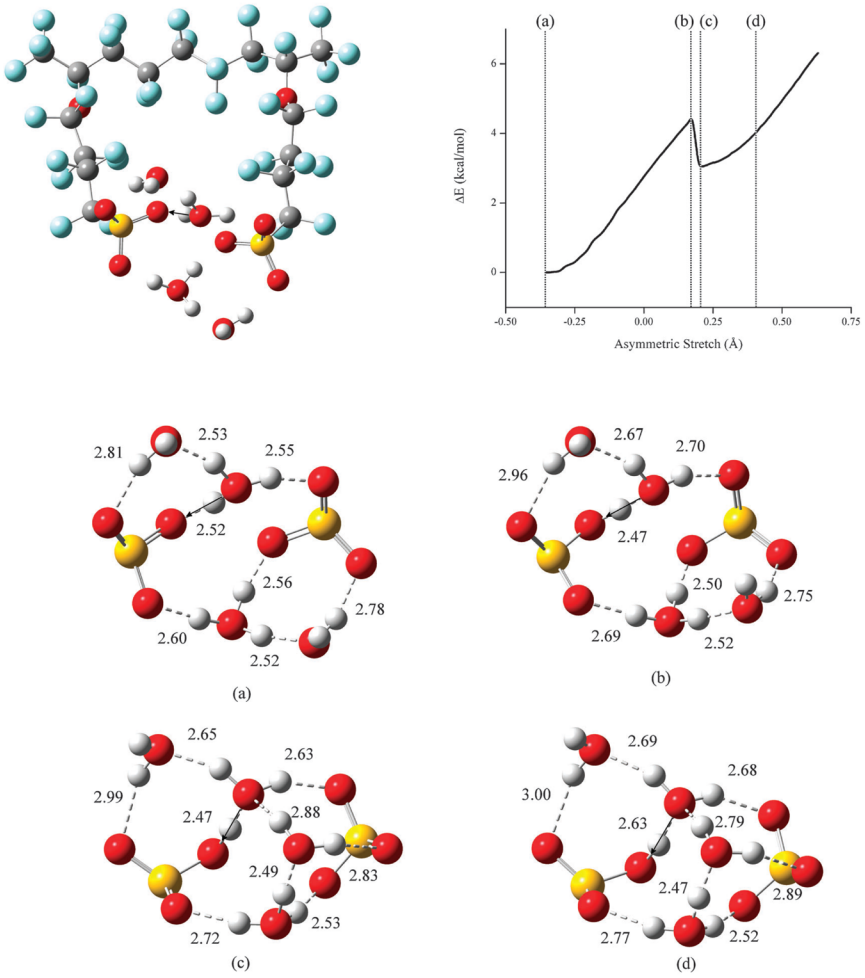

Fig. 5 Top left panel: Optimized (B3LYP/6-31G**) structure of the EW 590 3M™ PFSA ionomer at a hydration of $\lambda = 2$ used in the PES scan of the proton transfer indicated by the arrow. Top right panel: Relative energy profile with respect to the original configuration as a function of the asymmetric stretch coordinate. Bottom panel: rotated bottom view of the sulfonic acid/sulfonate and water molecules with hydrogen bonds denoted by dashed lines and the hydrogen bond distances (Å): (a) initial configuration; (b) transition state; (c) local minimum; and (d) the point in the scan when the proton is fully transferred to the sulfonic acid group.

The optimized minimum energy EW 690 geometry at $\lambda = 2$ used for the PES scan in Fig. 2 was also used for the transfer of a proton from a hydronium ion to a sulfonate group, indicated in Fig. 6. Critical differences between this minimum energy conformation and that of EW 590 (Fig. 5) can be easily noticed. As mentioned in the introduction, only one proton has dissociated in EW 690 while both protons are dissociated for EW 590 in the minimum energy conformations at this hydration level.[79] Additionally, all of the sulfonate oxygen atoms in EW 590 are included in the rather symmetric hydrogen bond network, while two of the sulfonic acid/sulfonate oxygen atoms in EW 690 are not involved in any hydrogen bonds. This configuration contains somewhat selective solvation of the right sulfonate group as only one oxygen atom of the left sulfonate group accepts a hydrogen bond from a water molecule which, furthermore, is relatively weak, as indicated by an O···O distance of 2.85 Å. The other water molecules and the hydronium ion each donate a hydrogen bond to the right sulfonate group. The results of the PES scan reveal a monotonically increasing proton transfer energy profile. The scan steps up to $q_{asym} = 0$ (Fig. 6b) led to increases in all of the hydrogen bond distances (except for the one over which the proton is transferred) with little change in the S···S distance. This effect is most pronounced in the vicinity of the hydronium

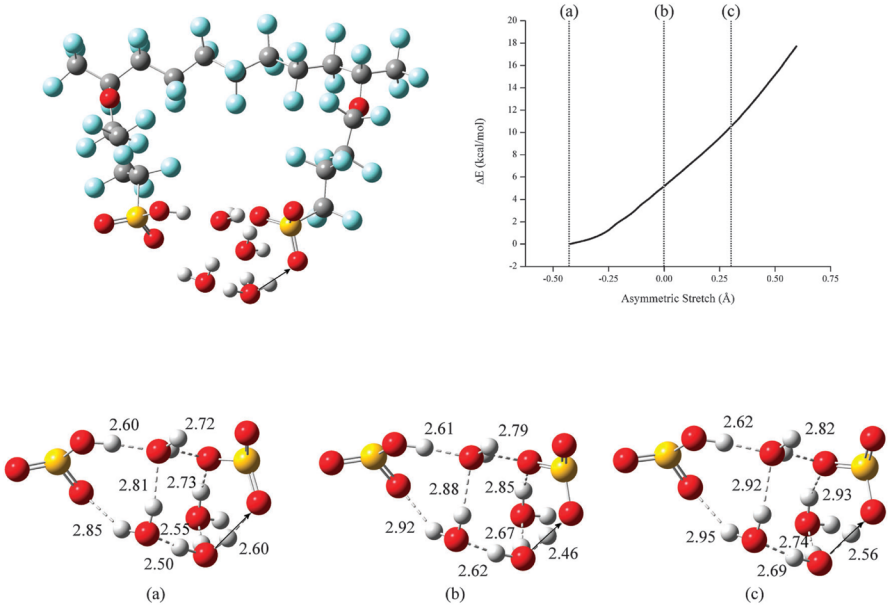

Fig. 6 Top left panel: Optimized (B3LYP/6-31G**) structure of the EW 690 3M™ PFSA ionomer at a hydration of $\lambda = 2$ used in the PES scan of the proton transfer indicated by the arrow. Top right panel: Relative energy profile with respect to the original configuration as a function of the asymmetric stretch coordinate. Bottom panel: rotated bottom view of the sulfonic acid/sulfonate and water molecules with hydrogen bonds denoted by dashed lines and the hydrogen bond distances (Å): (a) initial configuration; (b) an intermediate point in the scan at $q_{asym} = 0$; and (c) the point in the scan when the proton is fully transferred to the sulfonic acid group.

ion transferring the proton, particularly on the right most water molecule accepting a hydrogen bond from the hydronium ion. This water molecule donates a hydrogen bond to a neighboring sulfonate oxygen atom which also accepts a hydrogen bond from the top central water molecule. The O···O contraction across the hydrogen bond over which the proton is transferred and the corresponding positive charge accepted by the sulfonate group weaken all of the hydrogen bonds formed by the water molecule. As there are no surrounding open hydrogen bonding sites within a reasonable range, the water molecule is merely pushed away from the sulfonate group and the rest of the hydrogen bond network. This effect continues as the scan progresses, and the reprotonation of the sulfonate group results in a state with both protons associated (Fig. 6c) that is $\sim$10.5 kcal mol^{-1} higher in energy than the initial configuration.

At a hydration of $\lambda = 2.5$ the minimum energy geometries for EW 590 and EW 690 each contained two dissociated protons.[79] PES scans were performed on each ionomer for transferring a proton from a hydronium ion back to a sulfonate group. Complete detailed information concerning these results are reported in the ESI,† and only a summary is given here. Monotonically increasing relative energy profiles were found for the transfer from a hydronium ion to a sulfonate group in each case due to the resistance of reprotonation. In one case for EW 590 (Fig. S2, ESI†) no hydrogen bond network rearrangement occurred, and only contractions and expansions in the hydrogen bond lengths were observed as a result of charge transfer. This led to a configuration with one associated proton 11.4 kcal mol^{-1} higher in energy than the initial configuration. However, in a situation involving a hydrogen bond network rearrangement (Fig. S3, ESI†), the monotonically increasing relative energy profile was considerably less steep. The shift in the hydrogen bond network evidently provides some degree of stabilization resulting in a singly dissociated state only 6.0 kcal mol^{-1} higher in energy than the initial structure. In the EW 690, multiple cases led to the breaking of a hydrogen bond without further reorganization of the hydrogen bond network. Thus, only expansions and contractions in the hydrogen bonds lengths were observed resulting in a configuration 8.5 kcal mol^{-1} higher in energy upon reprotonation (Fig. S4, ESI†).

H_2O to SO_3^-

Complete detailed information concerning these results are also reported in the ESI,† and only a summary is given here. A PES scan for proton transfer from a water molecule to a sulfonate group was performed using the initial structures of Fig. 5 (for EW 590) and Fig. 2 and 6 (for EW 690) at $\lambda = 2$, shown in Fig. S4 and S5 (ESI†). The early steps in each scan resulted in relatively steep energy profiles likely due to the water molecules not containing an 'excess' proton like a hydronium ion. Once a neighboring hydronium ion transfers an 'excess' proton to the water molecule, the relative energy

profiles broaden. Upon reprotonation, a hydrogen bond between a water molecule and the sulfonate group receiving the proton breaks in each system as excess charge is transferred. In EW 590, the broken hydrogen bond slightly shifts between two oxygen atoms forming 'quasi' hydrogen bonds resulting in an energetic penalty of 7.4 kcal mol^{-1}. As for EW 690, the sulfonate oxygen atom receiving the proton also accepted a hydrogen bond from another water molecule which breaks upon reprotonation leading to a configuration with both protons associated 10.1 kcal mol^{-1} higher in energy than the initial configuration. It is important to note that, although this energetic penalty for reprotonation is higher than that of EW 590, this does not suggest that EW 690 has a greater propensity for proton dissociation at this level of hydration as each system started and ended with a different number of dissociated protons and hydrogen bonds.

Similar changes in the hydrogen bond network to the transfer of a proton from a hydronium ion to a sulfonate group oxygen atom at $\lambda = 2.5$ were observed for the transfer of a proton from a water molecule to a sulfonate oxygen atom at the same hydration level. The PES scan for EW 590 resembled the monotonically increasing case where no change in the hydrogen bond topography was observed. As with the other results containing no reorientation events, only fluctuations in the hydrogen bond distances to adjust for charge transfer were observed leading to an energetic penalty of 11.7 kcal mol^{-1} for reprotonation. This transfer in the EW 690 led to the breaking of a hydrogen bond and only contractions and expansions of hydrogen bond lengths were observed resulting in a configuration with only one dissociated proton 8.6 kcal mol^{-1} higher in energy than the initial doubly dissociated geometry.

Conclusions

The energetics of proton transfer in hydrated 3M™ PFSA ionomers at different equivalent weights were investigated by performing PES scans for the transfer of a proton across hydrogen bonds between water molecules, sulfonic acid groups, and charged species using optimized geometries obtained from previously reported electronic structure calculations.[79] The difference in sulfonic acid group separation in the EW 590 and EW 690 ionomers led to noticeably different hydrogen bond network configurations between the two fragments. This was determined to have a profound effect on the energetic barriers and the determined local minima resulting from proton transfer. Namely, systems with only one dissociated proton where a proton was transferred either to or from the sulfonic acid group that could easily reorient to accommodate charge transfer and, generally, return to a similar state (*i.e.* equivalent number of hydrogen bonds and dissociated protons) exhibited significantly lower energetic barriers for proton transfer than systems that did not have these qualities. These traits were more dominantly found in EW 590 having less side chain separation as continuous, cyclical hydrogen bond networks were more readily formed between the water molecules and the sulfonic acid/sulfonate terminal side chain groups. Hydrogen bonding in EW 690 contained less order making the reorientation process less viable at low hydration. After dissociation, reprotonation of a sulfonate group was strongly resisted in each ionomer fragment. The largest energetic penalties were observed when no reorganization of the hydrogen bonding occurred as a result of proton transfer. If, however, structural reorganization of the hydrogen bond network did occur, which was predominantly found for EW 590, the resistance to reprotonation was considerably reduced through stabilization of newly formed hydrogen bonds. The direct comparison of the energetic penalties associated with reprotonation between the two ionomers is not trivial at a hydration of $\lambda = 2$ as the PES scans for EW 590 contained two dissociated protons while EW 690 only contained one. When each ionomer fragment began and ended with the same number of dissociated protons, without a reorganization event, EW 590 was found to always exhibit a higher energetic penalty for reprotonation than EW 690 due to its greater propensity to exist in a dissociated state.

It is important to note that quantum nuclear effects play an important role in a variety of hydrogen bonded systems due to the small mass of protons. Inclusion of these effects requires sophisticated *ab initio* path integral techniques which have shown to affect certain characteristics in water and PFSA systems, such as the delocalization of protons. While these effects are absent in these electronic structure calculations, it must be pointed out that their influence may change the results of the PES scans in a non-trivial way, potentially softening the response. Furthermore, dynamic bond length fluctuations and the effects of the extended ionomer environment absent in these static electronic structure calculations containing only two pendant side chains would strongly influence the nature and state of the acidic protons. As such, the results of this study should not be taken as absolute values, but rather as a relative comparison as to how side chain separation and hydrogen bonding affect the energetics of proton transfer.

Acknowledgements

JKC acknowledges support by the National Science Foundation under Grant No. DGE0801470, "Sustainable Technology through Advanced Interdisciplinary Research" (STAIR), awarded to the University of Tennessee, Knoxville. SJP and SJH acknowledge support by the DOE under contract number DE-FG36-07G017006. DOE support does not constitute an endorsement by DOE of the views expressed in this work.

References

1 A. B. Stambouli and E. Traversa, *Renewable Sustainable Energy Rev.*, 2002, **6**, 295–304.
2 K. D. Kreuer, S. J. Paddison, E. Spohr and M. Schuster, *Chem. Rev.*, 2004, **104**, 4637–4678.
3 K. D. Kreuer, *Solid State Ionics*, 1999, **125**, 285–302.
4 A. I. Baranov, L. A. Shuvalov and N. M. Shchagina, *JETP Lett.*, 1982, **36**, 459–462.
5 S. M. Haile, G. Lentz, K. D. Kreuer and J. Maier, *Solid State Ionics*, 1995, **77**, 128–134.
6 S. M. Haile, D. A. Boysen, C. R. I. Chisholm and R. B. Merle, *Nature*, 2001, **410**, 910–913.
7 K. D. Kreuer, A. Fuchs, M. Ise, M. Spaeth and J. Maier, *Electrochim. Acta*, 1998, **43**, 1281–1288.
8 S. M. Haile, *Acta Mater.*, 2003, **51**, 5981–6000.

9 IEA, *Hydrogen and Fuel Cells: Review of National R&D Programs*, OECD Publishing, 2004.
10 K. D. Kreuer, *Solid State Ionics*, 1997, **97**, 1–15.
11 K. D. Kreuer, *J. Membr. Sci.*, 2001, **185**, 29–39.
12 L. Rubatat, A. L. Rollet, G. Gebel and O. Diat, *Macromolecules*, 2002, **35**, 4050–4055.
13 S. J. Paddison, *Annu. Rev. Mater. Res.*, 2003, **33**, 289–319.
14 C. J. D. von Grotthuss, *Ann. Chim.*, 1806, **58**, 54–74.
15 M. Eikerling, A. A. Kornyshev, A. M. Kuznetsov, J. Ulstrup and S. Walbran, *J. Phys. Chem. B*, 2001, **105**, 3646–3662.
16 S. J. Paddison and R. Paul, *Phys. Chem. Chem. Phys.*, 2002, **4**, 1158–1163.
17 S. J. Paddison, R. Paul and K. D. Kreuer, *Phys. Chem. Chem. Phys.*, 2002, **4**, 1151–1157.
18 E. Spohr, P. Commer and A. A. Kornyshev, *J. Phys. Chem. B*, 2002, **106**, 10560–10569.
19 N. Agmon, *Chem. Phys. Lett.*, 1995, **244**, 456–462.
20 M. Tuckerman, K. Laasonen, M. Sprik and M. Parrinello, *J. Chem. Phys.*, 1995, **103**, 150–161.
21 M. E. Tuckerman, D. Marx, M. L. Klein and M. Parrinello, *Science*, 1997, **275**, 817–820.
22 D. Marx, M. E. Tuckerman, J. Hutter and M. Parrinello, *Nature*, 1999, **397**, 601–604.
23 H. Lapid, N. Agmon, M. K. Petersen and G. A. Voth, *J. Chem. Phys.*, 2005, **122**, 014506.
24 D. Marx, *ChemPhysChem*, 2006, **7**, 1848–1870.
25 T. C. Berkelbach, H. S. Lee and M. E. Tuckerman, *Phys. Rev. Lett.*, 2009, **103**, 238302.
26 K. D. Kreuer, *ChemPhysChem*, 2002, **3**, 771–775.
27 M. Ise, K. D. Kreuer and J. Maier, *Solid State Ionics*, 1999, **125**, 213–223.
28 J. A. Kerres, *J. Membr. Sci.*, 2001, **185**, 3–27.
29 F. Wang, M. Hickner, Y. S. Kim, T. A. Zawodzinski and J. E. McGrath, *J. Membr. Sci.*, 2002, **197**, 231–242.
30 M. A. Hickner, H. Ghassemi, Y. S. Kim, B. R. Einsla and J. E. McGrath, *Chem. Rev.*, 2004, **104**, 4587–4611.
31 J. L. Zhang, Z. Xie, J. J. Zhang, Y. H. Tanga, C. J. Song, T. Navessin, Z. Q. Shi, D. T. Song, H. J. Wang and D. P. Wilkinson, *et al.*, *J. Power Sources*, 2006, **160**, 872–891.
32 S. J. Hamrock and M. A. Yandrasits, *Polym. Rev.*, 2006, **46**, 219–244.
33 S. Matsumura, A. R. Hlil, C. Lepiller, J. Gaudet, D. Guay, Z. Q. Shi, S. Holdcroft and A. S. Hay, *Macromolecules*, 2008, **41**, 281–284.
34 B. R. Ezzell, W. P. Carl and W. A. Mod, *The Dow Chemical Company, U.S. Patent*, 4,358,412, 1982.
35 T. A. Zawodzinski, T. E. Springer, J. Davey, R. Jestel, C. Lopez, J. Valerio and S. Gottesfeld, *J. Electrochem. Soc.*, 1993, **140**, 1981–1985.
36 C. A. Edmondson, P. E. Stallworth, M. E. Chapman, J. J. Fontanella, M. C. Wintersgill, S. H. Chung and S. G. Greenbaum, *Solid State Ionics*, 2000, **135**, 419–423.
37 C. A. Edmondson and J. J. Fontanella, *Solid State Ionics*, 2002, **152**, 355–361.
38 A. Potier, in *Proton Conductors: Solids, Membranes and Gels-Materials and Devices*, ed. P. Colomban, Cambridge University Press, 1992, pp. 1–17.
39 K. D. Kreuer, *Chem. Mater.*, 1996, **8**, 610–641.
40 J. A. Elliott and S. J. Paddison, *Phys. Chem. Chem. Phys.*, 2007, **9**, 2602–2618.
41 A. Vishnyakov and A. V. Neimark, *J. Phys. Chem. B*, 2000, **104**, 4471–4478.
42 S. S. Jang, V. Molinero, T. Cagin and W. A. Goddard, *J. Phys. Chem. B*, 2004, **108**, 3149–3157.
43 S. Urata, J. Irisawa, A. Takada, W. Shinoda, S. Tsuzuki and M. Mikami, *J. Phys. Chem. B*, 2005, **109**, 4269–4278.
44 S. Urata, J. Irisawa, A. Takada, W. Shinoda, S. Tsuzuki and M. Mikami, *J. Phys. Chem. B*, 2005, **109**, 17274–17280.
45 N. P. Blake, G. Mills and H. Metiu, *J. Phys. Chem. B*, 2007, **111**, 2490–2494.
46 A. Venkatnathan, R. Devanathan and M. Dupuis, *J. Phys. Chem. B*, 2007, **111**, 7234–7244.
47 I. H. Hristov, S. J. Paddison and R. Paul, *J. Phys. Chem. B*, 2008, **112**, 2937–2949.
48 N. P. Blake, M. K. Petersen, G. A. Voth and H. Metiu, *J. Phys. Chem. B*, 2005, **109**, 24244–24253.
49 T. J. F. Day, A. V. Soudackov, M. Cuma, U. W. Schmitt and G. A. Voth, *J. Chem. Phys.*, 2002, **117**, 5839–5849.
50 F. Wang and G. A. Voth, *J. Chem. Phys.*, 2005, **122**, 144105.
51 Y. J. Wu, H. N. Chen, F. Wang, F. Paesani and G. A. Voth, *J. Phys. Chem. B*, 2008, **112**, 467–482.
52 M. K. Petersen, F. Wang, N. P. Blake, H. Metiu and G. A. Voth, *J. Phys. Chem. B*, 2005, **109**, 3727–3730.
53 M. K. Petersen and G. A. Voth, *J. Phys. Chem. B*, 2006, **110**, 18594–18600.
54 M. K. Petersen, A. J. Hatt and G. A. Voth, *J. Phys. Chem. B*, 2008, **112**, 7754–7761.
55 S. Feng and G. A. Voth, *J. Phys. Chem. B*, 2011, **115**, 5903–5912.
56 M. Eikerling, S. J. Paddison, L. R. Pratt and T. A. Zawodzinski, *Chem. Phys. Lett.*, 2003, **368**, 108–114.
57 Y. K. Choe, E. Tsuchida, T. Ikeshoji, S. Yamakawa and S. Hyodo, *Phys. Chem. Chem. Phys.*, 2009, **11**, 3892–3899.
58 R. L. Hayes, S. J. Paddison and M. E. Tuckerman, *J. Phys. Chem. B*, 2009, **113**, 16574–16589.
59 R. L. Hayes, S. J. Paddison and M. E. Tuckerman, *J. Phys. Chem. A*, 2011, **115**, 6112–6124.
60 B. F. Habenicht, S. J. Paddison and M. E. Tuckerman, *J. Mater. Chem.*, 2010, **20**, 6342–6351.
61 B. F. Habenicht, S. J. Paddison and M. E. Tuckerman, *Phys. Chem. Chem. Phys.*, 2010, **12**, 8728–8732.
62 S. J. Paddison, L. R. Pratt, T. Zawodzinski and D. W. Reagor, *Fluid Phase Equilib.*, 1998, **151**, 235–243.
63 S. J. Paddison and T. A. Zawodzinski Jr, *Solid State Ionics*, 1998, **113–115**, 333–340.
64 S. J. Paddison, *J. New Mater. Electrochem. Syst.*, 2001, **4**, 197–207.
65 V. A. Glezakou, M. Dupuis and C. J. Mundy, *Phys. Chem. Chem. Phys.*, 2007, **9**, 5752–5760.
66 K. Sagarik, M. Phonyiem, C. Lao-Ngam and S. Chaiwongwattana, *Phys. Chem. Chem. Phys.*, 2008, **10**, 2098–2112.
67 M. Phonyiem, S. Chaiwongwattana, C. Lao-ngam and K. Sagarik, *Phys. Chem. Chem. Phys.*, 2011, **13**, 10923–10939.
68 C. Wang, J. K. Clark, M. Kumar and S. J. Paddison, *Solid State Ionics*, 2011, **199**, 6–13.
69 M. Eikerling, S. J. Paddison and T. A. Zawodzinski, *J. New Mater. Electrochem. Syst.*, 2002, **5**, 15–23.
70 S. J. Paddison, K. D. Kreuer and J. Maier, *Phys. Chem. Chem. Phys.*, 2006, **8**, 4530–4542.
71 C. Wang and S. J. Paddison, *Phys. Chem. Chem. Phys.*, 2009, **12**, 970–981.
72 L. Vilciauskas, S. J. Paddison and K. D. Kreuer, *J. Phys. Chem. A*, 2009, **113**, 9193–9201.
73 S. Urata, J. Irisawa, A. Takada, S. Tsuzuki, W. Shinoda and M. Mikami, *Phys. Chem. Chem. Phys.*, 2004, **6**, 3325–3332.
74 J. K. Clark, S. J. Paddison, M. Eikerling, M. Dupuis and T. A. Zawodzinski, *J. Phys. Chem. A*, 2012, **116**, 1801–1813.
75 S. J. Paddison and J. A. Elliott, *J. Phys. Chem. A*, 2005, **109**, 7583–7593.
76 S. J. Paddison and J. A. Elliott, *Solid State Ionics*, 2006, **177**, 2385–2390.
77 S. J. Paddison and J. A. Elliott, *Phys. Chem. Chem. Phys.*, 2006, **8**, 2193–2203.
78 S. J. Paddison and J. A. Elliott, *Solid State Ionics*, 2007, **178**, 561–567.
79 J. K. Clark and S. J. Paddison, *Solid State Ionics*, 2012, **213**, 83–91.
80 M. J. Frisch, G. W. Trucks, H. B. Schlegel, G. E. Scuseria, M. A. Robb, J. R. Cheeseman, G. Scalmani, V. Barone, B. Mennucci and G. A. Petersson, *et al.*, Gaussian Inc., Wallingford, CT, Revision A.1 edn, 2009.
81 A. D. Becke, *J. Chem. Phys.*, 1993, **98**, 5648–5652.
82 A. D. Becke, *J. Chem. Phys.*, 1993, **98**, 1372–1377.
83 P. C. Harihara and J. A. Pople, *Theor. Chim. Acta*, 1973, **28**, 213–222.
84 A. D. McLean and G. S. Chandler, *J. Chem. Phys.*, 1980, **72**, 5639–5648.
85 H. B. Schlegel, *J. Comput. Chem.*, 1982, **3**, 214–218.
86 S. Grimme, *J. Comput. Chem.*, 2006, **27**, 1787–1799.
87 C. Mijoule, Z. Latajka and D. Borgis, *Chem. Phys. Lett.*, 1993, **208**, 364–368.
88 Y. M. Xie, R. B. Remington and H. F. Schaefer, *J. Chem. Phys.*, 1994, **101**, 4878–4884.
89 T. Steiner, *Angew. Chem., Int. Ed.*, 2002, **41**, 48–76.
90 R. Kumar, J. R. Schmidt and J. L. Skinner, *J. Chem. Phys.*, 2007, **126**, 204107.

THE JOURNAL OF PHYSICAL CHEMISTRY A

Article

pubs.acs.org/JPCA

Side Chain Flexibility in Perfluorosulfonic Acid Ionomers: An ab Initio Study

Jeffrey K. Clark, II and Stephen J. Paddison*

Department of Chemical and Biomolecular Engineering, University of Tennessee, Knoxville, Tennessee 37996, United States

Supporting Information

ABSTRACT: Side chain flexibility in perfluorosulfonic acid (PFSA) ionomers has been explored through ab initio electronic structure calculations. Three different PFSA side chain fragments were considered with a CF_3CFCF_3 backbone representation: Nafion ($-OCF_2CF(CF_3)O-(CF_2)_2SO_3H$), Aquivion or the short side chain (SSC) ($-O(CF_2)_2SO_3H$), and the 3M PFSA ($-O(CF_2)_4SO_3H$). Rotational potential energy surfaces for each bond along the length of the side chains were obtained using density functional theory with the B3LYP and the dispersion-corrected B97D functionals with and without the inclusion of a solvation model. Solvent effects were found to have minimal effect on bond rotations close to the tetrafluoroethylene backbone but had greater impact near the terminal sulfonic acid group. The carbon−sulfur bond was found to be the most flexible portion of the side chain in each of the fragments which was further enhanced with the inclusion of the solvent. Complete rotation about either the $O-CF_2$ or $CF-O$ bond in the Nafion side chain resulted in fairly high energetic barriers, but significant portions of these rotational surfaces had energetic penalties less than 1.5 kcal/mol indicating substantial conformational freedom. Fully extended and folded conformations of the Nafion side chain exhibit considerable contraction in side chain end-to-end distance and were observed to be nearly isoenergetic using B3LYP, but the folded structures with the ether oxygen atoms in gauche conformations were ∼1.5 kcal/mol lower in energy using B97D. Below the second ether linkage of the Nafion side chain, the rotational potential energy profiles were identical to that determined for the SSC side chain. The 3M side chain was generally found to be the most rigid with barriers for complete rotation about the central carbon−carbon bonds of approximately 7 kcal/mol. These results indicate that minor differences in side chain length and chemistry may have a pronounced effect on the rotational potential energy surfaces, particularly those involving rotation about different carbon−carbon bonds with distinctly different character.

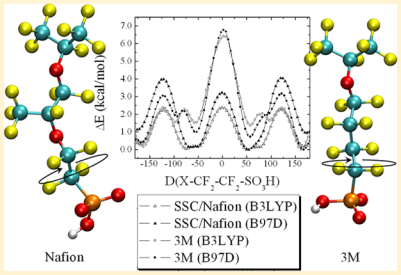

INTRODUCTION

As the global demand for energy continues to rise, proton exchange membrane (PEM) fuel cells have received a great deal of interest as clean, efficient energy conversion devices.[1,2] PEM fuel cells offer high power density and fast startup time and are lightweight which makes them promising candidates for a variety of applications, including stationary, portable, and automotive power.[3,4] The solid PEM acts as the electrolyte in these devices, as well as, the internal ion conductor and separator of the electrodes and reactant gases.[5] This material must exhibit high proton conductivity but low electrical conductivity, sustained mechanical durability over several operating cycles, and high chemical and thermal stability in an oxidative environment at temperatures as high as 120 °C.[6,7] Nearly all currently available PEMs rely heavily on the absorption of water to conduct protons. The most widely utilized PEMs are perfluorosulfonic acid (PFSA) ionomers, such as Nafion, as they exhibit high proton conductivity (∼10^{-1} S cm^{-1}) and good chemical and mechanical stability.[8] PFSA membranes consist of a hydrophobic poly(tetrafluoroethylene) (PTFE) backbone with hydrophilic sulfonic acid-terminated perfluoroether pendant side chains. The high proton conductivity of Nafion, however, is only observed at high levels of hydration (relative humidity) leading to adverse water "cross-over" due to electroosmotic drag and permeation.[9−11] This also limits the operating temperature to below the boiling point of water which demands the use of an expensive platinum-based electrocatalyst due to poor electrode reaction kinetics. At these low temperatures, the electrocatalyst is less tolerant to carbon monoxide poisoning which reduces the catalyst activity.[2,10]

These complications have led to considerable effort in the development of membrane materials exhibiting high proton conductivity at low hydration levels to remove the issues associated with water management.[7,12−16] These include changing the side chain acidic group or incorporation of multiple acid groups per side chain, the use of sulfonated aryl main chain polymers and heterocyclic polymers, and the modification of the backbone and/or side chain chemistry of currently available materials.[2,15,17,18] However, the majority of readily available PEM materials are PFSA derivatives of Nafion.

Received: July 30, 2013
Published: September 16, 2013

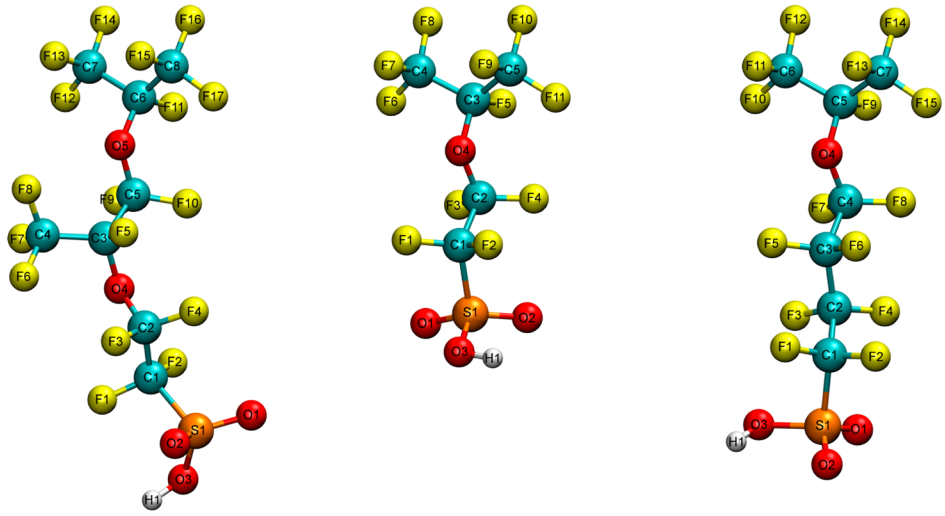

(a) (b) (c)

Figure 1. Optimized (B3LYP/6-31G**) structures with atoms labeled of the all trans side chain fragments: (a) Nafion, (b) SSC, and (c) 3M PFSA ionomers. The colored spheres represent different atom types where: gray, carbon; light blue, fluorine; red, oxygen; yellow, sulfur; blue, nitrogen; and white, hydrogen.

It is known that proton conductivity can be increased by reducing the ionomer equivalent weight (EW) resulting in a higher ion exchange capacity (IEC).[19] This allows for improved performance in both fully hydrated membranes, as well as, under drier conditions at higher temperatures.[15] However, too low of an EW can lead to excess swelling of the membrane with water which compromises the mechanical integrity of the system and the polymer can become water soluble.[7,20] Reduction of the EW is commonly done by shortening the Nafion side chain ($-OCF_2CF(CF_3)O(CF_2)_2SO_3H$) as in the Aquivion or short side chain (SSC) PFSA membrane[17] ($-O(CF_2)_2SO_3H$) from Solvay and the 3M PFSA membrane[15] ($-O(CF_2)_4SO_3H$). These materials have been shown to exhibit higher proton conductivity than Nafion while still maintaining good mechanical properties.[15,21−24]

The improved performance of these lower EW ionomers is primarily due to the increased IEC as the shorter side chain ionomers exhibit similar proton conductivities to Nafion at the same EW.[19] However, it remains unclear how changing the side chain length and/or chemistry affects some other membrane properties. Several molecular modeling studies have provided insight into the effects of side chain or backbone conformational changes (flexibility) on protogenic group separation and proton transfer.[25−42] Early electronic structure calculations on a single Nafion side chain revealed that the side chain likely adopts a folded conformation but that nearly isoenergetic unfolded conformations also exist.[29,30] Several other studies have also suggested that the Nafion side chain exists in a folded conformation nearly perpendicular to the backbone reducing the end-to-end distance to more closely resemble the SSC.[41,42] Stiff dihedral angles at the upper portion of the side chain were found for a SSC side chain fragment where the energetic penalty for rotation of the O−CF_2 bond at the top of the side chain resulted in a considerably higher energetic penalty than that of the F_2C-CF_2 bond further along the chain and was less impacted by the inclusion of an implicit solvation model.[43] Later electronic structure calculations incorporating multiple Aquivion side chain fragments separated by different numbers of backbone units revealed insight into the influence of side chain and backbone flexibility on cooperative interactions between adjacent protogenic groups and proton dissociation and transfer.[33−36] Specifically, when the side chains were separated by very few backbone units, the sulfonic acid groups were able to form double hydrogen bonds without the addition of any water molecules. On the other hand, when the number of CF_2 units separating the side chains was 5 or more this interaction did not occur with a fully extended backbone. However, it was found that through kinking of the backbone, the distance between sulfonic acid groups could be significantly reduced leading to more prominent interactions between them. This facilitated proton dissociation at lower levels of hydration than when the side chains remained well-separated. Similar studies on the 3M membrane revealed that the slightly longer side chain allowed for direct hydrogen bonding between sulfonic acid groups when separated by 5 CF_2 units but not when the side chains were separated by 7 CF_2 units. The system with less separation between side chains was found to exhibit proton dissociation at lower hydration levels and have smaller energetic barriers for proton transfer than in the more separated case.[39,40]

The present study explores the effects of side chain length and chemistry on the energetic barriers for bond rotation in PFSA side chains with ab initio electronic structure calculations. Three different ionomer fragments have been considered each with a CF_3CFCF_3 backbone representation: the Aquivion side chain ($-O(CF_2)_2SO_3H$), the 3M side chain (−O-

$(CF_2)_4SO_3H$), and the Nafion side chain ($-OCF_2CF(CF_3)O-(CF_2)_2SO_3H$). The effect of the presence of a solvent on the energetics is also assessed.

This paper is organized as follows. The first section contains a brief description of the computational methods used to determine the rotational potential energy surfaces of the side chain dihedral angles. This is followed by the results and discussion regarding the flexibility of the side chains. Finally, the main results are summarized in the conclusion.

■ COMPUTATIONAL METHODS

All electronic structure calculations were performed using the *Gaussian 09* suite of programs.[44] Optimizations over all degrees of freedom of the all trans conformation for each side chain fragment were initially carried out by conjugate gradient methods[45] without symmetry constraints using density functional theory (DFT) invoking Becke's 3-parameter functional (B3LYP)[46−48] and Grimme's B97D[49] functional, which includes empirical dispersion corrections, both using the 6-31G** split-valence basis set.[50−52] Potential energy surface (PES) scans for rotation about the bonds along the side chains were then performed on the optimized structures to obtain relative energy profiles. The scans were carried out by systematically rotating the chosen bond in 5° increments. The dihedral angle of the bond was the only fixed parameter with geometry optimizations performed over all other degrees of freedom. Scans were also performed with each functional using the integral equation formalism (IEF) polarizable continuum model (PCM)[53] with water as the solvent to assess the solvation effect on the relative energy profiles. Test calculations were also performed for one of the SSC profiles using B97D with the 6-311++G(2d,2p) basis set and second-order Møller−Plesset theory (MP2) with the 6-31G** basis set to compare the results. Due to the computational cost, the calculations were performed without inclusion of the solvation model. The results are given in the Supporting Information Figure S1, with a brief summary provided here. The profiles using MP2/6-31G** and B97D/6-311++G(2d,2p)[54−57] follow a similar trend as the B97D results with the smaller basis set but differ considerably from the B3LYP results. The energy maxima for the B97D scan with the larger basis set were only marginally higher than those obtained with the smaller basis set, and the MP2 maxima were found to be only slightly lower. The differences obtained did not merit the significantly greater computational cost of these calculations. Nevertheless, the insight into the different rotational barriers is only a relative comparison between side chain fragments and different functionals, not absolute values. Furthermore, collective effects of the extended environment have not been included.

■ RESULTS AND DISCUSSION

Figure 1 shows the optimized (PCM/B3LYP/6-31G**) structures of each side chain fragment including atom labels used in the following discussion. Selected geometric parameters for the Nafion, SSC, and 3M side chains are given in Tables 1−3, respectively. Both the SSC and 3M side chains contain a single ether linkage between the side chain and backbone, while the Nafion side chain has one connecting the side chain and backbone and an additional one in the side chain. The ether linkage connecting the side chain and backbone in Nafion will be referred to as "inner" and the additional linkage in the side chain will be referred to as "terminal". The results obtained for the upper portion of each side chain fragment showed only minor differences in the potential energy profiles computed in the gas phase and those obtained with the PCM solvation model. Unless otherwise indicated, the following discussion and figures concern the results obtained with the inclusion of the aqueous solvent.

Table 1. Geometric Parameters for Nafion[a]

parameter	B3LYP	B97D
r(S1−C1)[b]	1.88	1.92
r(C1−C2)	1.55	1.57
r(C2−O4)	1.37	1.38
r(O4−C3)	1.41	1.42
r(C3−C4)	1.55	1.57
r(C3−C5)	1.56	1.57
r(C5−O5)	1.37	1.38
r(O5−C6)	1.41	1.42
r(S1···C6)	8.44	8.54
d(S1−C1−C2−O4)[c]	169.1	172.8
d(C1−C2−O4−C3)	177.5	179.2
d(C2−O4−C3−C5)	122.0	120.4
d(O4−C3−C5−O5)	178.4	−179.9
d(C3−C4−O5−C6)	176.2	−173.3

[a]Obtained including the solvation model. [b]Distances given in Å. [c]Angles given in degrees.

Table 2. Geometric Parameters for the SSC Ionomer[a]

parameter	B3LYP	B97D
r(S1−C1)[b]	1.89	1.92
r(C1−C2)	1.55	1.57
r(C2−O4)	1.37	1.38
r(O4−C3)	1.41	1.42
r(S1···C3)	5.27	5.33
d(S1−C1−C2−O4)[c]	169.0	172.5
d(C1−C2−O4−C4)	177.2	179.3

[a]Obtained including the solvation model. [b]Distances given in Å. [c]Angles given in degrees.

Table 3. Geometric Parameters for the 3M Ionomer[a]

parameter	B3LYP	B97D
r(S1−C1)[b]	1.89	1.93
r(C1−C2)	1.55	1.57
r(C2−C3)	1.56	1.58
r(C3−C4)	1.56	1.58
r(C4−O4)	1.37	1.38
r(O4−C5)	1.41	1.42
r(S1−C5)	7.90	7.99
d(S1−C1−C2−C3)[c]	166.6	168.9
d(C1−C2−C3−C4)	164.4	168.3
d(C2−C3−C4−O4)	169.2	172.4
d(C3−C4−O4−C5)	174.9	177.6

[a]Obtained including the solvation model. [b]Distances given in Å. [c]Angles given in degrees.

Potential energy profiles for rotation about the O−CF_2 bond for each side chain at the PCM/B3LYP/6-31G** level are shown in Figure 2. Rotation about each of these bonds results in potential energy profiles with similar shape but different energetic barriers. The maxima at 0° occur when the C−O−C−C dihedral angle is in a *cis* conformation. In the case of the SSC and 3M side chains, this corresponds to eclipsing the first side chain F_2C-CF_2 bond with the F−C bond located at the point

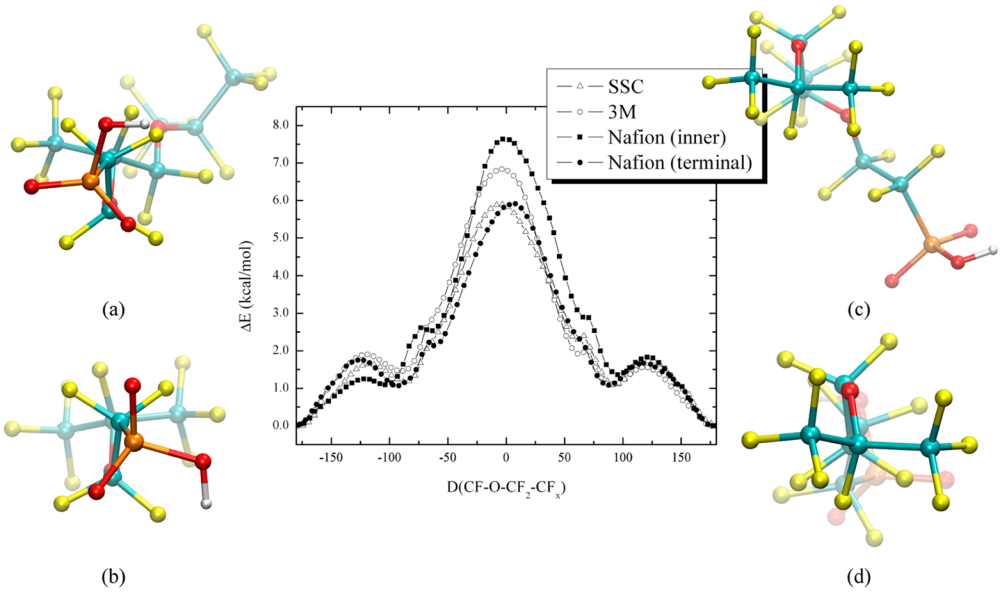

Figure 2. Potential energy profiles for rotation about the O−CF_2 bonds at the PCM/B3LYP/6-31G** level of theory. The views along the dihedral angle are shown for (a) 3M, (b) SSC, (c) Nafion (inner), and (d) Nafion (terminal).

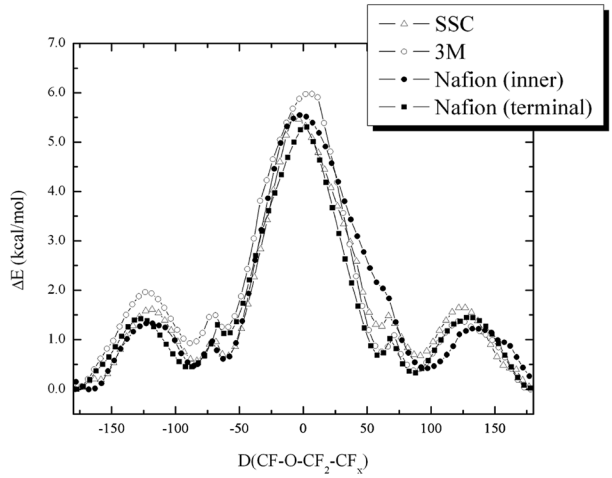

Figure 3. Potential energy profiles for rotation about the O−CF_2 bonds at the PCM/B97D/6-31G** level of theory.

where the side chain attaches to the backbone. For the Nafion side chain, the inner maximum results from eclipsing the C5−C3 bond with the C6−F11 bond of the backbone with the ether oxygen atoms adopting a gauche conformation. The terminal PES scan maximum corresponds to eclipsing the C2−C1 bond with the C3−F5 bond in a nearly identical conformation to that observed for the SSC and is 1.7 kcal/mol lower in energy than the inner maximum. However, the B97D results, shown in Figure 3, exhibit similar barriers between the two Nafion PES scans along with the other two side chains. This is most pronounced for the inner Nafion barrier which may be due to a favorable gauche conformation of the ether oxygen atoms using B97D which will become more apparent in the following section. It is important to note that obtaining smooth potential energy surfaces for these rotations was considerably more difficult to obtain than those for the

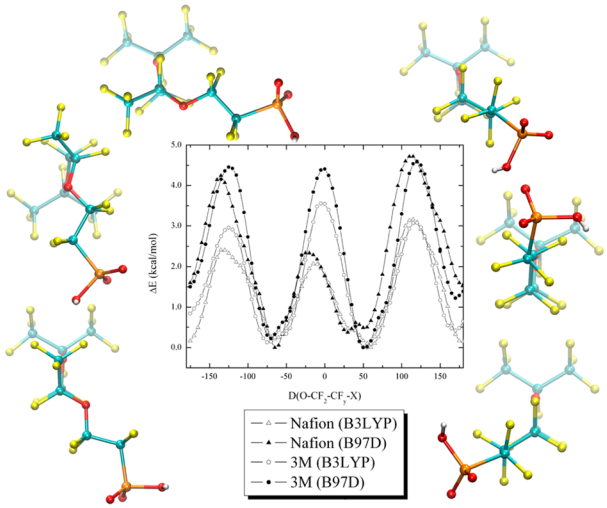

Figure 4. Potential energy profiles for rotation about the CF_2−CF_y bond (y = 1, X = $(CF_3)O$ for Nafion; y = 2, X = CF_2 for 3M) using the PCM at B3LYP/6-31G** and B97D/6-31G** levels of theory. The surrounding structures show views along the dihedral angle for the maxima obtained for Nafion (left panel) and 3M (right panel) with the top, middle, and bottom structures representing the left, central, and right maxima, respectively.

other bonds even with the small increments for this rotation. This is likely due to the side chain existing in high energy conformations that fail to properly relax during the optimization. When this occurred, the constraint on the dihedral angle was relaxed and a full optimization was performed followed by a partial optimization with the dihedral angle fixed.

The PES scans for rotation about the CF_2−CF_y (y = 1 for Nafion and 2 for 3M) bond for the Nafion and 3M side chains are shown in Figure 4 with the maxima shown in the outer panels where the top to bottom figures correspond to the left to right maxima. Distinctly different relative energy profiles were found for the two side chains, as well as, with the different functionals. The position of the maxima and minima correspond to similar dihedral angle conformations regardless of the functional used, but the energetic barriers are considerably different. For the Nafion side chain, the first peak at −135° corresponds to eclipsing atoms O5/F5, O4/F10, and F9/C4 with values of 2.4 kcal/mol (B3LYP) and 4.2 kcal/mol (B97D). However, this is only 2.7 kcal/mol (B97D) higher in energy than the initial geometry with the ether oxygen atoms in a trans conformation. The side chain is considerably folded at the following minimum with the two ether oxygen atoms in a gauche minus (g−) conformation. This reduces the distance between the central backbone carbon atom and the sulfur atom of the fully elongated conformation from 8.44 to 6.19 Å for B3LYP and 8.48 to 6.12 Å for B97D. This minimum was found to be 0.18 kcal/mol lower in energy than the fully elongated side chain using B3LYP but 1.5 kcal/mol lower in energy using B97D. The maximum at approximately −20° of 2.1 kcal/mol (B3LYP) and 2.3 kcal/mol (B97D) is due to eclipsing atoms O4/O5, F10/C4, and F5/F9. This is followed by a minimum with ether oxygen atoms gauche plus (g+) that maintains a folded conformation where the lower portion of the side chain is perpendicular to the backbone (i.e., a C6/C3/S1 angle of ∼90°) with a carbon-sulfur distance of 7.45 Å (6.78 Å B97D) that is 0.16 kcal/mol (B3LYP) and 1.2 kcal/mol (B97D) lower in energy than the fully elongated state. This perpendicular conformation in Nafion and reduction in side chain end-to-end distance is consistent with earlier computational studies.[30,41,42] The side chain begins to unfold toward the last barrier at 115° with eclipsing O5/C4, O4/F9, and F5/F10 atoms. Interestingly, the difference between the values obtained using the B3LYP and B97D functionals are most pronounced for the barriers from the folded conformations to the fully elongated conformation while little change was found for the barrier between the folded conformations. As mentioned previously, this may be due to increased stabilization of the compact, folded side chain with the ether oxygen atoms gauche when dispersion corrections are included.

The barrier between gauche conformations was also less affected for the 3M side chain where the maxima at ±120° are 50% higher using B97D and that at 0° is 23% higher. The maxima at ±120° have eclipsed O/F, F/C, and F/F atoms, and the dihedral angle at the central barrier is in a cis conformation with eclipsing O/C, F/F, and F/F atoms. As with the Nafion side chain, the B97D barriers from trans to gauche minima are lower than the reverse, but the barrier between the gauche conformations is notably higher than that for the Nafion side chain and is the greatest using B3LYP. The all trans minimum at ∼170° has a carbon-sulfur distance of 7.90 Å (7.99 Å B97D), while a somewhat bent g+ conformation at 50° has a corresponding distance of 6.80 Å (6.72 B97D) and is 0.42 kcal/mol lower in energy than the elongated conformation using B3LYP and 1.2 kcal/mol lower with B97D. The 3M side chain appears to be more rigid than the Nafion side chain showing less change in the end-to-end distance only varying between 6.65 to 8.00 Å throughout the scan as opposed to 5.65 to 8.56 Å in the Nafion side chain. This is likely due to the greater flexibility of the C3−O4 bond in the longer side chain

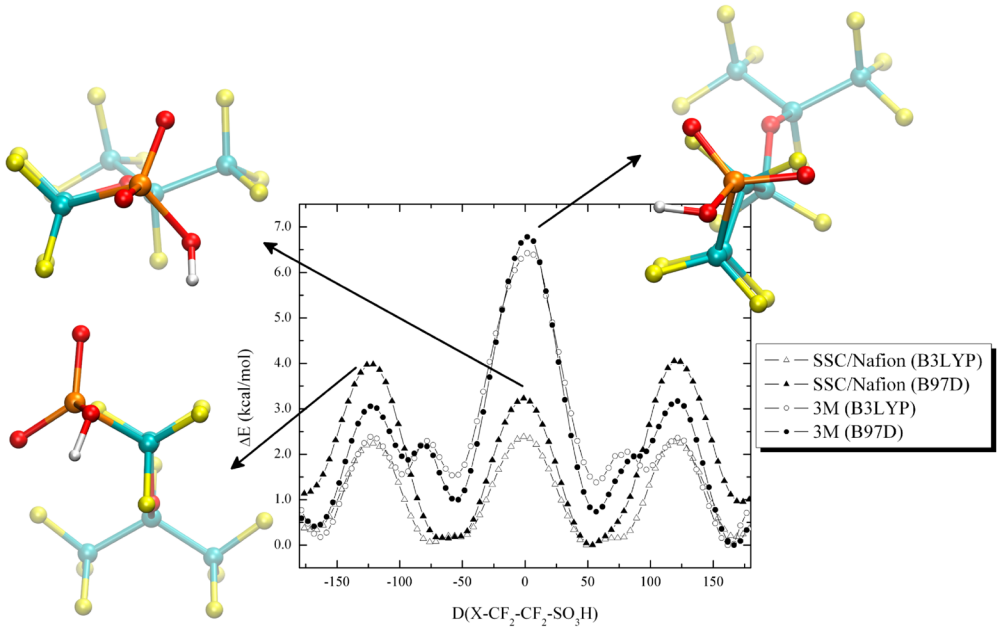

Figure 5. Potential energy profiles for rotation about the C1−C2 bond (X = O for SSC/Nafion; X = CF_2 for 3M) using the PCM at B3LYP/6-31G** and B97D/6-31G** levels of theory. The results for the SSC and Nafion side chain are identical. The representations shown in the left panel correspond to the SSC ionomer.

below the C5−C3 bond than the C3−C2 bond in the 3M side chain. Complete rotation of these bonds leads to energetic barriers exceeding 5 and 7 kcal/mol for the Nafion and 3M side chains, respectively (see Figure S2 in the Supporting Information). However, a significant portion of the C3−O4 rotational profile in the longer side chain has less than a 1 kcal/mol energetic penalty which is not the case for the C3−C2 bond in the 3M side chain suggesting greater rotational freedom in the Nafion side chain.

Relative energy profiles for rotating the C2−C1 bond adjacent to the sulfonic acid group in each side chain are shown in Figure 5. The atoms associated with this dihedral angle for the Nafion and SSC side chains are O4−C2−C1−S1, while those for the 3M side chain are C3−C2−C1−S1. This leads to a distinctly different energetic profile for the 3M side chain than the other side chains, which appear to be essentially equivalent. The B3LYP profiles for the Nafion and Aquivion side chains exhibit approximately 3-fold degeneracy in both minima and maxima corresponding to staggered and eclipsed F, O, and S atoms, respectively. However, when the B97D functional was used two equivalent minima corresponding to the sulfur atom and the ether oxygen atom in gauche conformations were found with the fully elongated trans conformation approximately 1 kcal/mol higher in energy. The central rotational barrier using the B97D functional of 3.2 kcal/mol occurs when going between these gauche conformations, and again, higher rotational barriers occur when going from gauche to trans than trans to gauche conformations. The opposite is true for the 3M PES scan which is also highly symmetric but with multiple distinct maxima and minima. The maxima at approximately ±120° are due to eclipsing of the F/F, F/C, and F/S atoms. The two following maxima in the B3LYP profile at ±80° result from a rotation that brings an oxygen atom of the sulfonic acid group in closer proximity to a fluorine atom bonded to C3. These are less pronounced in the B97D profile. In contrast to the results for the SSC and Nafion, the gauche minima at ±55° are ∼1 kcal/mol (1.5 kcal/mol B3LYP) higher in energy than the trans conformation likely due to the additional crowding of the of oxygen atoms of the sulfonic acid group and the C3 fluorine atoms. The largest maximum at 0° exhibits less influence on the choice of functional with S1 and C3 in a cis conformation and eclipsed C1 and C2 fluorine atoms with a great deal of steric hindrance associated with the sulfonic acid oxygen atoms and the C3 fluorine atoms. At 0° both the Nafion and Aquivion side chains do not contain the additional CF_2 group that causes the steric hindrance, considerably lowering the rotational energy barrier between the gauche conformations. The inclusion of the aqueous solvent with the Nafion and Aquivion side chains for the barriers at ±120° rotation decreased the energetic barriers by approximately 5% with B97D and 9% with B3LYP with no change for the one at 0°. It was observed to have no effect on the energetic profile for the 3M side chain.

Notable differences between the profiles and barriers obtained between the gas phase calculations and those which included solvation effects were obtained when rotating about the C1−S1 bond. This is of little surprise as it more directly involves the hydrophilic portion of the side chain that interacts with water. The results for each side chain fragment were identical, and the representative configurations shown in Figure

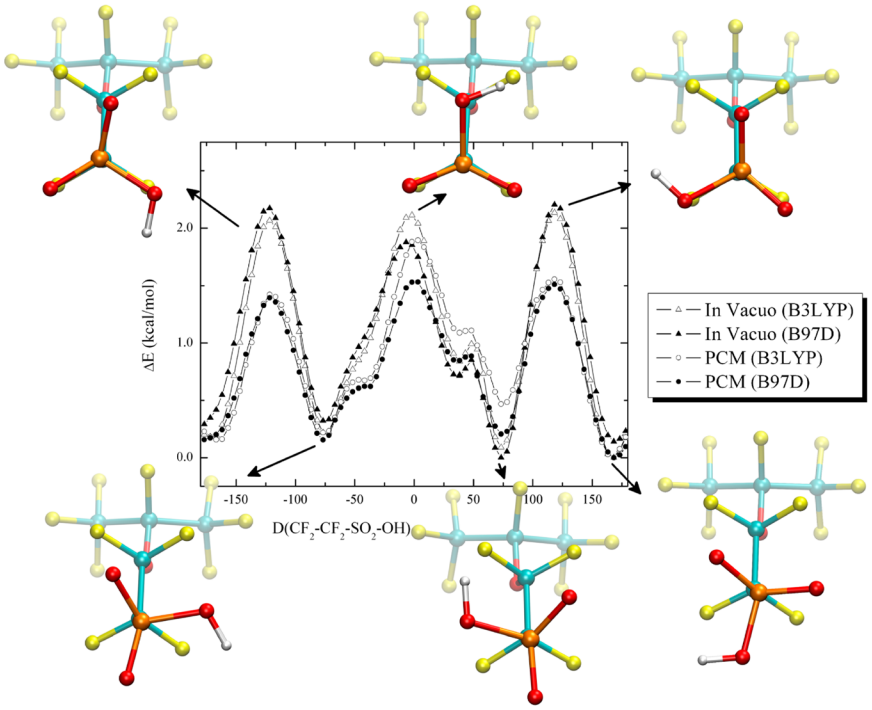

Figure 6. Potential energy profiles for rotation about the C1−S1 bond at the B3LYP/6-31G** and B97D/6-31G** levels of theory both in vacuum and with the inclusion of the solvation model. The representations shown in the left panel correspond to the SSC ionomer.

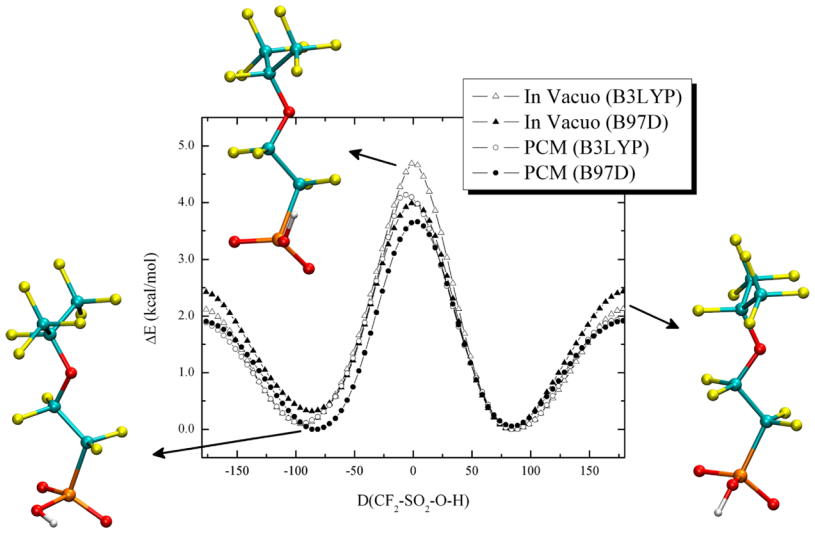

Figure 7. Potential energy profiles for rotation about the S−OH bond at the B3LYP/6-31G** and B97D/6-31G** levels of theory both in vacuum and with the inclusion of the solvation model. The representations shown in the left panel correspond to the SSC ionomer.

6 correspond to the SSC PFSA ionomer. The results show three maxima and minima for each level of theory corresponding to configurations with eclipsed and staggered F1, F2, and C2 with the sulfonic acid oxygen atoms, respectively, as shown in the associated structures. These are essentially degenerate for the gas phase B3LYP PES scan. Similar barriers at ±120° were found for the B97D gas phase results. These correspond to the cases where one of the sulfonic acid oxygen atoms without the proton eclipses atom C2 while the protonated oxygen eclipses a fluorine atom. Inclusion of the solvation model reduced these barriers by roughly 30% in each case. However, greater differences between the levels tested were observed for the maximum at ∼0° and the minimum at ∼70°. This maximum has the protonated sulfonic acid oxygen atom eclipsing C2 and the proton eclipsed with F4 and is the lowest barrier determined using the B97D functional without the solvent indicating there may be a weak interaction due to the eclipsed O−H and C−F bonds. Inclusion of the solvent decreases this barrier by 10% using B3LYP and by 18% using B97D, but it then becomes the highest of the energetic barriers for each functional. This effect is also observed for the minimum at 70°, which was the lowest gas phase B97D result, where the proton is ∼0.3 Å closer to the nearest fluorine atom than that associated with the other minima. When the solvation model was employed, this minimum became less favored while the other minima became more favorable.

Finally, Figure 7 shows the relative energy profile for rotation of the S1−O3 bond. In agreement with what was found in previous studies,[34,58] the profile has two similar minima and two different maxima. The higher maximum corresponds to the proton directed inward with the O−H bond eclipsing the C−S bond, and the lower maximum corresponds to the proton directed outward away from the side chain. The minimum at 85° is 0.32 kcal/mol lower than the minimum at −85° for the gas phase B97D results. As with the results previously mentioned, the proton at this minimum is again located ∼0.3 Å closer to the nearest fluorine atom and when the solvation model was included it no longer was the preferred conformation resulting in two isoenergetic minima. The maxima using the B3LYP functional reduced by approximately 10% with the PCM, but the B97D results indicate only an 8% reduction in the central barrier and a 21% reduction in the barrier at ±180°. The latter barrier is equivalent between the PCM results for each functional but is higher for the gas phase calculations. This may be due to the increased stabilization in the gas phase results from the fluorine-hydrogen interaction as the B97D gas phase barrier at ±180° is 0.31 kcal/mol higher in energy than the gas phase B3LYP barrier.

■ CONCLUSIONS

We have examined the energetic profiles for bond rotations of the side chains in three PFSA side chains: SSC ($-O-(CF_2)_2SO_3H$), 3M ($-O(CF_2)_4SO_3H$), and Nafion ($-OCF_2CF(CF_3)O(CF_2)_2SO_3H$) through ab initio electronic structure calculations. PES scans were obtained using both the B3LYP functional and the dispersion-corrected B97D functional with and without the inclusion of the PCM solvation model. Solvent effects were found to have little impact on the relative energy profiles for internal rotations near the side chain attachment to the backbone. Closer to the sulfonic acid terminus, the impact of the solvation model becomes much more pronounced. Consistent with previous findings,[34] the lowest energetic barriers were observed for rotation about the carbon-sulfur bond for each level tested, and these barriers were significantly reduced when the solvation model was implemented.

The highest barriers for the Nafion side chain involved complete rotations about the C−O and O−C bonds of the ether linkages. However, significant portions of the rotational potential energy surfaces had energetic penalties less than 1.5 kcal/mol suggesting a fair amount of conformational freedom in the associated bonds. The results obtained using B97D suggest energetically favored g+ or g− ether oxygen atom conformations with the side chain folded essentially perpendicular to the backbone, while use of the B3LYP functional led to nearly isoenergetic folded and unfolded conformers. The energetic penalty (B97D) in going from the elongated trans structure to the folded gauche conformations was lower than that for unfolding the side chain which may be due to the increased stabilization of the folded conformation when dispersion corrections are included and indicates that the side chain may remain folded. Below the second ether linkage in the Nafion side chain, the rotational profiles match that of the SSC side chain with energetically preferred gauche conformations of the ether oxygen atom to the sulfur atom. This is consistent with several studies which indicate that the Nafion side chain is preferentially in a folded conformation and acts similarly to the SSC PFSA.[29,30,41,42] The 3M side chain also exhibited preferential gauche conformations for rotations about the upper carbon−carbon bond (i.e., C3−C4). However, the energetic barrier in going between gauche conformers was essentially equal to that of going from gauche to trans with a significantly higher barrier than Nafion. Furthermore, high barriers for complete rotation about the carbon−carbon bonds near the middle of the side chain were found with each functional with less contraction in side chain length suggesting more rigidity in the 3M side chain. These results indicate that minor differences in side chain length and chemistry can have a pronounced effect on the rotational potential energy surfaces, particularly those involving rotation about different carbon−carbon bonds which had distinctly different character.

It is important to note that in this study we are not attempting to describe characteristics of the actual ionomer membrane (or even a representative portion of the hydrated morphology) but to compare relative tendencies in the energetics associated with the flexibility (i.e., rotational degrees of freedom) of the side chains of three PFSA ionomers with the use of different DFT functionals. The presence of multiple interacting acid groups and the nature of the structural organization of the hydrated membrane will likely change the determined rotational barriers in a nontrivial way. Hence, the calculated energetic barriers for rotation should not be taken as absolute values, but rather as a relative comparison as to how side chain length and chemistry affect conformational freedom.

■ ASSOCIATED CONTENT

Ⓢ Supporting Information

C−C bond rotational potential energy profiles for the SSC side chain comparing MP2/6-31G**, B97D/6-311++G(2d,2p), B97D/6-31G**, and B3LYP/6-31G** levels of theory discussed in the Computational Methods section and the additional profiles mentioned within the Results and Discussion for the Nafion and 3M side chains. This material is available free of charge via the Internet at http://pubs.acs.org.

AUTHOR INFORMATION

Corresponding Author

*E-mail: spaddison@utk.edu.

Notes

The authors declare no competing financial interest.

ACKNOWLEDGMENTS

The authors acknowledge support by the National Science Foundation under Grant No. DGE0801470, "Sustainable Technology through Advanced Interdisciplinary Research" (STAIR), awarded to the University of Tennessee, Knoxville.

REFERENCES

(1) Granovskii, M.; Dincer, I.; Rosen, M. A. Life Cycle Assessment of Hydrogen Fuel Cell and Gasoline Vehicles. *Int. J. Hydrog. Energy* **2006**, *31*, 337−352.

(2) Shao, Y. Y.; Yin, G. P.; Wang, Z. B.; Gao, Y. Z. Proton Exchange Membrane Fuel Cell From Low Temperature to High Temperature: Material Challenges. *J. Power Sources* **2007**, *167*, 235−242.

(3) IEA; *Hydrogen and Fuel Cells: Review of National R&D Programs*; OECD Publishing: Paris, 2004.

(4) Smitha, B.; Sridhar, S.; Khan, A. A. Solid Polymer Electrolyte Membranes for Fuel Cell Applications - A Review. *J. Membr. Sci.* **2005**, *259*, 10−26.

(5) Kreuer, K. D.; Paddison, S. J.; Spohr, E.; Schuster, M. Transport in Proton Conductors for Fuel-Cell Applications: Simulations, Elementary Reactions, and Phenomenology. *Chem. Rev.* **2004**, *104*, 4637−4678.

(6) Savadogo, O. Emerging Membranes for Electrochemical Systems - Part II. High Temperature Composite Membranes for Polymer Electrolyte Fuel Cell (PEFC) Applications. *J. Power Sources* **2004**, *127*, 135−161.

(7) Hickner, M. A.; Ghassemi, H.; Kim, Y. S.; Einsla, B. R.; McGrath, J. E. Alternative Polymer Systems for Proton Exchange Membranes (PEMs). *Chem. Rev.* **2004**, *104*, 4587−4611.

(8) Haile, S. M. Fuel Cell Materials and Components. *Acta Mater.* **2003**, *51*, 5981−6000.

(9) Kreuer, K. D. On Solids With Liquidlike Properties and the Challenge to Develop New Proton-conducting Separator Materials for Intermediate-Temperature Fuel Cells. *ChemPhysChem* **2002**, *3*, 771−775.

(10) Kreuer, K. D. On the Development of Proton Conducting Polymer Membranes for Hydrogen and Methanol Fuel Cells. *J. Membr. Sci.* **2001**, *185*, 29−39.

(11) Yang, C.; Costamagna, P.; Srinivasan, S.; Benziger, J.; Bocarsly, A. B. Approaches and Technical Challenges to High Temperature Operation of Proton Exchange Membrane Fuel Cells. *J. Power Sources* **2001**, *103*, 1−9.

(12) Kerres, J. A. Development of Ionomer Membranes for Fuel Cells. *J. Membr. Sci.* **2001**, *185*, 3−27.

(13) Wang, F.; Hickner, M.; Kim, Y. S.; Zawodzinski, T. A.; McGrath, J. E. Direct Polymerization of Sulfonated Poly(arylene ether sulfone) Random (Statistical) Copolymers: Candidates for New Proton Exchange Membranes. *J. Membr. Sci.* **2002**, *197*, 231−242.

(14) Zhang, J. L.; Xie, Z.; Zhang, J. J.; Tanga, Y. H.; Song, C. J.; Navessin, T.; Shi, Z. Q.; Song, D. T.; Wang, H. J.; Wilkinson, D. P.; et al. High Temperature PEM Fuel Cells. *J. Power Sources* **2006**, *160*, 872−891.

(15) Hamrock, S. J.; Yandrasits, M. A. Proton Exchange Membranes for Fuel Cell Applications. *Polym. Rev.* **2006**, *46*, 219−244.

(16) Matsumura, S.; Hlil, A. R.; Lepiller, C.; Gaudet, J.; Guay, D.; Shi, Z. Q.; Holdcroft, S.; Hay, A. S. Ionomers for Proton Exchange Membrane Fuel Cells with Sulfonic Acid Groups on the End Groups: Novel Branched Poly(ether-ketone)s. *Macromolecules* **2008**, *41*, 281−284.

(17) Ezzell, B. R.; Carl, W. P.; Mod, W. A. U.S. Patent 4,358,412, November 9, 1982.

(18) Schaberg, M.; Abulu, J.; Haugen, G.; Emery, M.; O'Conner, S.; Xiong, P.; Hamrock, S. New Multi Acid Side-Chain Ionomers for Proton Exchange Membrane Fuel Cells. *ECS Trans.* **2010**, *33*, 627−633.

(19) Kreuer, K. D.; Schuster, M.; Obliers, B.; Diat, O.; Traub, U.; Fuchs, A.; Klock, U.; Paddison, S. J.; Maier, J. Short-Side-Chain Proton Conducting Perfluorosulfonic Acid Ionomers: Why They Perform Better in PEM Fuel Cells. *J. Power Sources* **2008**, *178*, 499−509.

(20) Yandrasits, M. A.; Hamrock, S. J. Membranes for PEM Fuel Cells. In *Fuel Cell Chemistry and Operation*; Herring, A. M., Zawodzinski, T. A., Hamrock, S. J., Eds.; American Chemical Society: Washington, DC, 2010; pp 15−29.

(21) Edmondson, C. A.; Stallworth, P. E.; Chapman, M. E.; Fontanella, J. J.; Wintersgill, M. C.; Chung, S. H.; Greenbaum, S. G. Complex Impedance Studies of Proton-Conducting Membranes. *Solid State Ionics* **2000**, *135*, 419−423.

(22) Edmondson, C. A.; Fontanella, J. J. Free Volume and Percolation in S-SEBS and Fluorocarbon Proton Conducting Membranes. *Solid State Ionics* **2002**, *152*, 355−361.

(23) Rivard, L. M.; Pierpont, D.; Freemeyer, H. T.; Thaler, A.; Hamrock, S., Development of a New Electrolyte Membrane for PEM Fuel Cells. DOE. Fuel Cell Seminar, Miami Beach, FL. 2003.

(24) Emery, M.; et al. The Development of New Membranes for Proton Exchange Membrane Fuel Cells. *ECS Trans.* **2007**, *11*, 3−14.

(25) Spohr, E.; Commer, P.; Kornyshev, A. A. Enhancing Proton Mobility in Polymer Electrolyte Membranes: Lessons from Molecular Dynamics Simulations. *J. Phys. Chem. B* **2002**, *106*, 10560−10569.

(26) Roudgar, A.; Narasimachary, S. P.; Eikerling, M. Hydrated Arrays of Acidic Surface Groups as Model Systems for Interfacial Structure and Mechanisms in PEMs. *J. Phys. Chem. B* **2006**, *110*, 20469−20477.

(27) Vishnyakov, A.; Neimark, A. V. Molecular Simulation Study of Nafion Membrane Solvation in Water and Methanol. *J. Phys. Chem. B* **2000**, *104*, 4471−4478.

(28) Vishnyakov, A.; Neimark, A. V. Molecular Dynamics Simulation of Nafion Oligomer Solvation in Equimolar Methanol-Water Mixture. *J. Phys. Chem. B* **2001**, *105*, 7830−7834.

(29) Paddison, S. J.; Zawodzinski, T. A., Jr. Molecular Modeling of the Pendant Chain in Nafion. *Solid State Ionics* **1998**, *113*−*115*, 333−340.

(30) Paddison, S. J.; Pratt, L. R.; Zawodzinski, T. A. Conformations of Perfluoroether Sulfonic Acid Side Chains for the Modeling of Nafion. *J. New Mater. Electrochem. Syst.* **1999**, *2*, 183−188.

(31) Paddison, S. J.; Pratt, L. R.; Zawodzinski, T. A. Variation of the Dissociation Constant of Triflic Acid with Hydration. *J. Phys. Chem. A* **2001**, *105*, 6266−6268.

(32) Eikerling, M.; Paddison, S. J.; Zawodzinski, T. A. Molecular Orbital Calculations of Proton Dissociation and Hydration of Various Acidic Moieties for Fuel Cell Polymers. *J. New Mater. Electrochem. Syst.* **2002**, *5*, 15−23.

(33) Paddison, S. J.; Elliott, J. A. Molecular Modeling of the Short-Side-Chain Perfluorosulfonic Acid Membrane. *J. Phys. Chem. A* **2005**, *109*, 7583−7593.

(34) Paddison, S. J.; Elliott, J. A. On the Consequences of Side Chain Flexibility and Backbone Conformation on Hydration and Proton Dissociation in Perfluorosulfonic Acid Membranes. *Phys. Chem. Chem. Phys.* **2006**, *8*, 2193−2203.

(35) Paddison, S. J.; Elliott, J. A. The Effects of Backbone Conformation on Hydration and Proton Transfer in the 'Short-Side-Chain' Perfluorosulfonic Acid Membrane. *Solid State Ionics* **2006**, *177*, 2385−2390.

(36) Paddison, S. J.; Elliott, J. A. Selective Hydration of the 'Short-Side-Chain' Perfluorosulfonic Acid Membrane. An ONIOM Study. *Solid State Ionics* **2007**, *178*, 561−567.

(37) Elliott, J. A.; Paddison, S. J. Modelling of Morphology and Proton Transport in PFSA Membranes. *Phys. Chem. Chem. Phys.* **2007**, *9*, 2602−2618.

(38) Wang, C.; Clark, J. K.; Kumar, M.; Paddison, S. J. An *ab initio* Study of the Primary Hydration and Proton Transfer of CF_3SO_3H and

$CF_3O(CF_2)_2SO_3H$: Effects of the Hybrid Functional and Inclusion of Diffuse Functions. *Solid State Ionics* **2011**, *199*, 6−13.
(39) Clark, J. K., II; Paddison, S. J.; Hamrock, S. J. The Effect of Hydrogen Bond Reorganization and Equivalent Weight on Proton Transfer in 3M Perfluorosulfonic Acid Ionomers. *Phys. Chem. Chem. Phys.* **2012**, *14*, 16349−16359.
(40) Clark, J. K., II; Paddison, S. J. The Effect of Side Chain Connectivity and Local Hydration on Proton Transfer in 3M Perfluorosulfonic Acid Membranes. *Solid State Ionics* **2012**, *213*, 83−91.
(41) Devanathan, R.; Dupuis, M. Insight From Molecular Modelling: Does the Polymer Side Chain Length Matter for Transport Properties of Perfluorosulfonic Acid Membranes? *Phys. Chem. Chem. Phys.* **2012**, *14*, 11281−11295.
(42) Urata, S.; Irisawa, J.; Takada, A.; Shinoda, W.; Tsuzuki, S.; Mikami, M. Molecular Dynamics Simulation of Swollen Membrane of Perfluorinated Ionomer. *J. Phys. Chem. B* **2005**, *109*, 4269−4278.
(43) Johansson, P.; Tegenfeldt, J.; Lindgren, J. Conformational Analysis of a Model of the Sidechains in Perfluorosulfonated Membranes. *Electrochim. Acta* **2000**, *45*, 3055−3061.
(44) Frisch, M. J.; et al. *Gaussian 09*, revision A.1; Gaussian Inc.: Wallingford, CT, 2009.
(45) Schlegel, H. B. Optimization of Equilibrium Geometries and Transition Structures. *J. Comput. Chem.* **1982**, *3*, 214−218.
(46) Becke, A. D. Density-Functional Thermochemistry. III. The Role of Exact Exchange. *J. Chem. Phys.* **1993**, *98*, 5648−5652.
(47) Becke, A. D. A New Mixing of Hartree-Fock and Local Density-Functional Theories. *J. Chem. Phys.* **1993**, *98*, 1372−1377.
(48) Lee, C. T.; Yang, W. T.; Parr, R. G. Development of the Colle-Salvetti Correlation-Energy Formula into a Functional of the Electron-Density. *Phys. Rev. B* **1988**, *37*, 785−789.
(49) Grimme, S. Semiempirical GGA-Type Density Functional Constructed With a Long-Range Dispersion Correction. *J. Comput. Chem.* **2006**, *27*, 1787−1799.
(50) Harihara, P. C.; Pople, J. A. Influence of Polarization Functions on Molecular-Orbital Hydrogenation Energies. *Theor. Chim. Acta* **1973**, *28*, 213−222.
(51) Ditchfield, R.; Hehre, W. J.; Pople, J. A. Self-Consistent Molecular-Orbital Methods. 9. Extended Gaussian-Type Basis for Molecular-Orbital Studies of Organic Molecules. *J. Chem. Phys.* **1971**, *54*, 724−728.
(52) Hehre, W. J.; Ditchfield, R.; Pople, J. A. Self-Consistent Molecular-Orbital Methods. 12. Further Extensions of Gaussian-Type Basis Sets for Use in Molecular-Orbital Studies of Organic-Molecules. *J. Chem. Phys.* **1972**, *56*, 2257−2261.
(53) Scalmani, G.; Frisch, M. J. Continuous Surface Charge Polarizable Continuum Models of Solvation. I. General Formalism. *J. Chem. Phys.* **2010**, *132*, 114110.
(54) McLean, A. D.; Chandler, G. S. Contracted Gaussian Basis Sets for Molecular Calculations. I. Second Row Atoms, Z=11−18. *J. Chem. Phys.* **1980**, *72*, 5639−5648.
(55) Krishnan, R.; Binkley, J. S.; Seeger, R.; Pople, J. A. Self-Consistent Molecular-Orbital Methods. 20. Basis Set for Correlated Wave-Functions. *J. Chem. Phys.* **1980**, *72*, 650−654.
(56) Clark, T.; Chandrasekhar, J.; Spitznagel, G. W.; Schleyer, P. V. Efficient Diffuse Function-Augmented Basis-Sets for Anion Calculations. 3. The 3−21+G Basis Set for 1st-Row Elements, Li-F. *J. Comput. Chem.* **1983**, *4*, 294−301.
(57) Frisch, M. J.; Pople, J. A.; Binkley, J. S. Self-Consistent Molecular-Orbital Methods 0.25. Supplementary Functions for Gaussian-Basis Sets. *J. Chem. Phys.* **1984**, *80*, 3265−3269.
(58) Paddison, S. J.; Pratt, L. R.; Zawodzinski, T.; Reagor, D. W. Molecular Modeling of Trifluoromethanesulfonic Acid for Solvation Theory. *Fluid Phase Equilib.* **1998**, *151*, 235−243.

Ab initio Molecular Dynamics Simulations of Water and an Excess Proton in Water Confined in Carbon Nanotubes

Jeffrey K. Clark II and Stephen J. Paddison*

Department of Chemical and Biomolecular Engineering, University of Tennessee, Knoxville, TN 37996

ABSTRACT

Ab initio molecular dynamics simulations were performed to investigate the effects of nanoscale confinement on the structural and dynamical properties of water and slightly acidic water. Single-walled carbon nanotubes (CNTs) of two different diameters (11.0 and 13.3 Å) were used as confinement vessels, and the inner walls of the CNT were either left bare or fluorinated to explore the influence of the confined environment on the determined properties. The water in the fluorinated nanotubes were found to preferentially localize near the CNT surface and exhibit highly ordered structures while those in the bare CNTs were more randomly distributed. Inclusion of the fluorine atoms seemed to provide sites to which the water molecules would interact which occurred at a greater frequency in the smaller diameter CNT indicating an influence of the confinement dimensions on these interactions. This was further pronounced when an excess proton was added where approximately half of the water molecules in the smaller tube were involved in hydrogen bonds to the surface throughout the simulation. This also led to a structured hydrogen bond network with regular defect sites that hindered proton transfer along the channel axis. Addition of the proton in the larger fluorinated CNT, however, disrupted the structural ordering and proton transfer down the nanotube axis near the surface of the CNT wall readily occurred. Proton transfer through the channel was also observed in the smaller nonfluorinated system, however, the proton was located closer to the center of the CNT, while in the larger nonfluorinated CNT proton transfer exhibited less directional preference indicating an impact of the scale of confinement and nature of the surface on proton transfer.

Keywords: ab initio molecular dynamics, confinement, water, proton transfer

Corresponding Author
*E-mail: spaddison@utk.edu.

Submitted to PCCP. Manuscript ID: CP-ART-01-2014-000415

Introduction

Fluids in confined environments exhibit considerably different structural and dynamic properties than those observed in bulk. Water is among the most widely studied confined fluids.[1, 2] There have been many studies on water confined in a variety of environments including fullerenes,[3] between graphene sheets,[4] and other nanostructures.[2, 5-11] Carbon nanotubes (CNTs) have also been used to study confinement effects on water.[1, 4, 12-27] While these nanostructures are hydrophobic in bulk water,[28, 29] both simulations[2, 18, 29, 30] and experiments[31-35] have shown that water molecules can readily fill open-ended carbon nanotubes. Deep inelastic neutron scattering experiments revealed that the proton momentum distribution in water confined in CNTs is vastly different from that observed in bulk water indicating a significant impact confinement has on the state of water.[36, 37] The structure of the water in CNTs exhibits a great deal of diversity depending on several properties, including channel diameter.[29] In small diameter CNTs (< 10 Å), simulations have shown that the water molecules inside the tube exhibit a one-dimensional, single-file hydrogen bonding pattern.[2, 18] With increasing diameter there is a greater region in which the water molecules can access the interior, and layered, well-structured arrangements of water molecules form.[1] Though a variety of arrangements have been reported dependent on CNT chirality and simulation conditions, they each maintain that there are considerably different characteristics of confined water than those in bulk water revealing a solid-like structure with a liquid-like degree of hydrogen bonding.[38] Several studies have also reported the existence of ice-like ordering of water confined in CNTs even under ambient conditions.[5, 22, 30, 39-43] The nature of the surfaces between which the water is confined may also have an effect on the properties of water, and the exact nature of the surface–water interaction has been shown to be important.[30, 38] Simulations have revealed that even slight changes in the carbon–water interaction parameters considerably impact the results. Furthermore, water molecules near the CNT walls can potentially hydrogen bond to it depending on the surface composition which also affects the structural and dynamical properties.[1]

The transport of protons in confined water plays an important role in biological systems,[44, 45] fuel cell membranes,[46] and other processes. The structure of water formed within confined hydrophobic surfaces offer an effective proton-conducting medium, especially in the one-dimensional water wires.[2] Proton transport, both in bulk and confined water, is highly dependent on the structural dynamics of hydrogen bonding.[1, 2, 38, 47-52] Excess protons in water exist as hydrated cations which can take on various solvation structures, such as Eigen ($H_9O_4^+$)[53, 54] and Zundel cations ($H_5O_2^+$).[55] In bulk water, proton transfer occurs through a series of transformations between these complexes which is known as the Grotthuss mechanism or structural diffusion.[48-50, 52, 56-59] The highly aligned structure of water confined in CNTs allows for rapid proton transport via hopping with a mechanism determined by the confinement dimensions. *Ab initio* molecular dynamics and empirical valence bond simulations have

shown that the proton mobility in the confined environment of a very narrow CNT can exceed that of bulk water by over an order of magnitude.[60] The rationale behind the increased proton transport is the formation of a quasi-one dimensional water wire where proton transfer is essentially a local hopping event that does not require hydrogen bond rearrangements beyond the first solvation shell but does require the wire to be highly ordered and defect-free.[60] This has been shown to resemble a "Zundel–Zundel" mechanism with an intermediate state of $H_7O_3^+$.[20, 61] With increasing diameter, however, the hydrogen bonding becomes more three dimensional in nature allowing for the formation of Eigen cations and the protons no longer are restricted to transfer solely along the CNT axis. This also allows for certain configurations to be formed that impede proton transfer through the CNT, such as proton transfer perpendicular to the tube axis.[62] This suggests that proton transport in CNTs is highly dependent on the influence the geometric confinement has on the hydrogen bonding.

Here, we present results of an *ab initio* molecular dynamics (AIMD) investigation on the behavior of water and water with an excess proton confined in single-walled CNTs of various diameters. The impact of the nature of the confined environment on structural properties is also investigated through functionalizing the nanotube walls with fluorine atoms. This paper is organized as follows. The systems and computational methodology are first described. This is followed by presentation and discussion of the results for the systems containing only water molecules which include the distribution of atoms under confinement, radial distribution functions and hydrogen bonding, and interactions between the water molecules and the wall of the CNT. The same properties are then described for systems containing an excess proton but further discussion is added on the nature and state of the excess proton. Finally, important results are summarized in the conclusions section.

Computational Methods

Ab initio molecular dynamics simulations were performed using the Vienna *Ab Initio* Simulation Package (VASP).[63-66] Core electrons were treated using the projector-augmented-wave (PAW) method.[67, 68] The Perdew–Burke–Ernzerhof (PBE) generalized gradient approximation for the exchange-correlation functional was used,[69, 70] and the electronic subsystem was sampled at the Γ-point of the first Brillouin zone with a plane wave cutoff of 400 eV. CNTs with chirality (14,0) and (17,0), with length of ~12.8 Å and diameters of ~11.0 and 13.3 Å, respectively, were chosen as encapsulation vessels for the water molecules and (when applicable) excess proton. When an excess proton was introduced, a neutralizing background charge was applied by VASP. The inner walls of the CNTs were either left bare or fluorinated to model different hydrophobic environments. The fluorine atoms were added to every next nearest neighbor carbon atom as uniformly as possible. The smaller tubes contained 12 water molecules while the larger tubes contained 24 water molecules. The nomenclature N-14 and N-17 will be used for the nonfluorinated CNTs and F-14 and F-17 for the fluorinated CNTs. Representative images of the systems are shown in Figure 1. As with our previous

studies,[71-73] the carbon atoms of the CNT wall and the attached fluorine atoms (when applicable) were held fixed, and periodic boundary conditions were imposed with 4 Å of vacuum added in the perpendicular directions to avoid interactions with other images in the supercell. The systems were initially relaxed to their minimum energy configuration and then annealed to 600 K via repeated velocity rescaling and then returned back down to 300 K. This was followed by 3 ps simulations in the canonical ensemble and 3 ps of microcanonical MD for equilibration which were discarded. Born–Oppenheimer AIMD trajectories of 25-30 ps were generated with a time step of 0.5 fs in the microcanonical ensemble for data analysis. As the PBE functional has been shown to over-structure water at 300 K,[74-76] test simulations were performed at 400 K but no significant differences were observed.

Results and Discussion

Confined Water

The distributions of oxygen and hydrogen atoms throughout the trajectory for each system are shown in Figure 2. The left and right panels show contour plots of the oxygen and hydrogen atom positions projected onto the xy-plane, respectively, and the middle panel shows the distribution function of the distance of the atoms from the CNT wall. Darker colors in the contour plots indicate a greater tendency for the atoms to be located in the region. In the fluorinated CNTs, the oxygen atoms are highly localized near the fluorinated walls as indicated by the sharp peaks at 2.63 and 2.78 Å in the F-14 and F-17 distribution functions, respectively. The water molecules in F-14 exhibit ordering along the CNT axis with evenly spaced clusters of two or three water molecules (see Figure 4c) while those in the larger F-17 form an essentially stacked pentagonal structure (Figure 5c and d) which has been observed in other simulations of water confined in single-walled CNTs.[21-24] The oxygen atoms in the bare CNTs, on the other hand, do not exhibit the same degree of preferential arrangement and are more widely dispersed with broad distribution peaks at 3.42 and 3.40 Å for the smaller and larger tubes, respectively. The oxygen atoms in N-14 do, however, show more preference to arrange near the wall than those in N-17 but the configurations do not show any well-defined structure. The distribution of the hydrogen atoms is obviously related to that of the oxygen atoms. Again, in the fluorinated tubes, distributions with atoms located near the fluorinated walls were observed while those of the bare CNTs are more spread out. The distribution functions all contain a first peak at a shorter distance than that for the corresponding oxygen atoms. In the fluorinated tubes these occur at 1.75 and 1.89 Å for the smaller and larger tubes, respectively, and the corresponding distances for the bare CNTs are 2.52 and 2.56 Å.

Radial distribution functions (RDFs) between atoms also provide information on the structural arrangement of water molecules within the CNTs. Figure 3 shows the oxygen–oxygen and oxygen–hydrogen radial distribution functions for the (14,0) and (17,0) CNT systems. The first peak in the O–O

RDF for the smaller fluorinated tube occurs at 2.67 Å, while in the bare tube it is found at 2.72 Å. The F-14 peak is sharper than N-14 and is followed by a second smaller peak only a short distance away. This results from non-hydrogen bonded water molecules in the neighboring clusters suggesting a fairly regular structure. The structural arrangement of the N-14 water molecules, on the other hand, exhibits less order with a broad second maximum in the RDF. A similar effect was found for the larger fluorinated tube having a relatively narrow first peak in the O–O RDF at 2.68 Å and a highly ordered structure, whereas, in the larger bare tube the water molecules again exhibit a more randomly organized arrangement with greater separation between oxygen atoms (first peak at 2.73 Å) with a similar broad second maximum in the RDF to N-14. The second peak observed in F-14 is absent in F-17 which is likely due to the pentagonal stacking of the water molecules resulting in a greater likelihood of oxygen–oxygen separations over a wide range of distances. Shorter separations in the fluorinated CNTs were also found between the oxygen and hydrogen atoms (Figure 3b). The first sharp peak in all of the RDFs corresponds to the covalently bound oxygen and hydrogen atoms of the water molecules. The peak following arises from hydrogen bonding between water molecules which occurs at ~1.68 Å in both fluorinated CNTs but at 1.75 and 1.73 Å in the smaller and larger bare CNTs, respectively, with broader distributions. The third peak in the RDFs further illustrates the tightly packed, highly organized nature of the water molecules in the fluorinated CNTs which occur at 3.01 and 3.07 Å in F-14 and F-17, respectively, versus 3.21 and 3.23 Å in their bare counterparts.

As mentioned earlier, the RDFs are closely related to the hydrogen bond structure between the water molecules in the CNTs. Hydrogen bonding of water in confined environments is known to exhibit distinctly different behavior than that observed in bulk water. As such, these interactions are a primary focus of this investigation. A hydrogen bond was defined between water molecules having and oxygen–oxygen separation of less than 3.25 Å and an H–O···O of less than 30°.[77, 78] Representative snapshots of the hydrogen bonding in the smaller and larger CNTs are shown in Figures 4 and 5, respectively. The average O···O hydrogen bond distances vary between the different CNTs. As shown in the RDFs, the water molecules in the fluorinated CNTs are more closely packed and the average O···O hydrogen bond distance is 2.72 Å in both the smaller and larger tubes while the corresponding distances in the bare CNTs are 2.82 and 2.79 Å. Hydrogen bonding in the bare CNTs occurs with nearly random orientation. In the fluorinated systems, on the other hand, there are preferential orientations due to the aforementioned structuring of the water. The organization of the oxygen atoms in F-14 brings about a majority of hydrogen bonds that are either directed inward across the channel axis or essentially parallel to the CNT axis. These correspond to the dark blue inner and outer rings in the hydrogen distribution contours (Figure 2b). In the larger F-17 system the water molecules localized near the surface are farther apart from other water molecules across the channel axis than in F-14 and, instead,

preferentially hydrogen bond to their nearest "inter-pentagon" water molecules around the CNT circumference and the neighboring "intra-pentagon" water molecules along the channel of the CNT.

The distribution of the water molecules in the fluorinated CNTs suggests potential interactions between the water molecules and the fluorinated walls. Previous AIMD investigations on triflic acid and water confined in fluorinated CNTs[71-73] and hydrates of triflic acid[79, 80] have reported evidence of weak water–fluorine interactions to some extent similar to hydrogen bonds, though longer. Furthermore, results of IR spectroscopy studies on Nafion, a perfluorinated ionomer, have shown evidence that water is exposed to and potentially interacts with the hydrophobic fluorocarbon backbone.[81-83] Although the nature of the interactions are not entirely clear, we examine them here as weak hydrogen bonds. While the geometric criteria for weak hydrogen bonds typically allows for a wide range of hydrogen bond angles,[84] the angular cutoff in the analysis was not relaxed from that of water–water hydrogen bonds (i.e., the H–O···F angle must be less than 30°) to avoid inclusion of spurious interactions arising from the aforementioned structuring of the confined water. The hydrogen bond distance cutoff, however, was taken as an H···F length less than 2.5 Å which is slightly longer than the first minimum of the O···H RDF in bulk water not corresponding to covalently bound hydrogen of ~2.46 Å.[85] The hydrogen bond was required to exist for longer than 5 fs to be considered in the analysis to prevent transient motions of the water molecules from affecting the results. However, if the hydrogen bond hopped between neighboring fluorine atoms while maintaining the geometric criteria, it was still included in the determined number of O–H···F hydrogen bonds. Figure 6 shows the percent of time throughout the trajectory O–H···F hydrogen bonds exist versus the fraction of water molecules containing such a bond along with snapshots displaying hydrogen bonds for the two fluorinated systems. In the smaller CNT, at least one water molecule is involved in an O–H···F bond in each simulation step and there is an average of 29% of the water molecules (~3.5 H_2O) involved in these interactions throughout the trajectory with average H···F and O···F distances of 2.15 and 3.02 Å, respectively. These distances are longer than the H···O and O···O hydrogen bond distances found here for water as well as for those in bulk water (~1.88 and 2.82 Å)[86] but are still within a reasonable range to be considered as hydrogen bond-like interactions. Hydrogen bonding to the fluorine atoms was also observed in the larger CNT with an average of 16% of the water molecules (~3.8 H_2O) involved in O–H···F interactions throughout the trajectory with average H···F and O···F distances of 2.19 and 3.08 Å, respectively. The continuous lifetime of these interactions in each case is approximately 32 fs. However, there are many instances of bifurcated hydrogen bonds and hydrogen bond jumps between different fluorine atoms. When these are considered as continuous hydrogen bonds, the average lifetime in the smaller tube becomes 107 fs and 82 fs in the larger tube. These results indicate that although fluorine atoms in fluorocarbons are poor hydrogen bond acceptors,[87-89] their nature inside these single-walled CNTs is non-trivial and appear to be influenced by the confinement dimensions.

Confined Water with an Excess Proton

An excess proton was added to each of the CNT systems to explore its effect on the studied properties. The distributions of hydrogen and oxygen atoms for the systems containing an excess proton are shown in Figure 7. Similar to what was found in the systems containing only water molecules, the fluorinated and nonfluorinated systems exhibit noticeably different arrangements. The oxygen atoms within the fluorinated tubes again are highly localized near the CNT wall while those in the bare CNTs show less preferential positioning. The distribution functions for the distance of the oxygen atoms to the CNT wall are all nearly identical to those for the systems without the excess proton. There are, however, differences in each of the corresponding hydrogen atom distribution functions and the projections onto the xy-plane. The first peak for each case occurs at marginally shorter distances than those in Figure 2 with, again, shorter distances found for the fluorinated systems. However, the amplitudes are higher in all of the distribution functions with the excess proton indicating a greater propensity for the hydrogen atoms to be located near the interface. This is also shown in the contour plots for the hydrogen distribution where darker shades of blue are observed in the outer portions of the ring than in those in Figure 2.

Figure 8 shows the oxygen–oxygen and oxygen–hydrogen RDFs for the systems containing an excess proton. These are very similar to those obtained for those systems containing only water molecules where the first peak in the O···O RDFs occur at a shorter distance in the fluorinated CNT than in the bare tubes. However, the distances at which these peaks begin and reach their maximum were found to be shorter than the corresponding distances in the systems without the excess proton. This is most pronounced in both of the smaller CNTs where the peak shifted ~0.08 Å closer while only marginal decreases of 0.02 Å were found for the larger tubes. All of the RDFs exhibit similar character following the first peak as the systems containing only water molecules indicative of their relative order/disorder. The same effects in each case were found for the peaks following the covalently bound peak in the O···H RDFs. Another primary difference between the O···H RDFs for the systems with and without the excess proton is that the former contains a non-zero probability between the covalently bound peak and the second maximum due to the excess proton sharing and transferring between water molecules. The greater decrease in the distances observed in the smaller CNTs is also reflected in their hydrogen bonding. Snapshots of the hydrogen bond topography for the smaller and larger CNTs are shown in Figures 9 and 10, respectively. The average hydrogen bond O···O distances in the (14,0) nanotubes decreased from 2.72 to 2.63 Å in F-14 and from 2.82 to 2.73 Å in N-14 but only ~0.02 Å shorter hydrogen bonds were found in the (17,0) systems. The greater propensity for the hydrogen atoms to be closer to the surface when the excess proton is introduced results in fewer hydrogen bonds in the center region of the bare CNT but does not have a pronounced effect on the overall hydrogen bond arrangement or level of disorder. In F-14 the typical structure is a more ordered arrangement

than in the system without an excess proton resembling a "zig-zag ladder-like" structure (Figure 9c and d) similar to the so called book isomer form of the water hexamer.[27, 90] In this arrangement, every neighboring pair of water molecules, on average, is located across the channel axis with hydrogen bonds rarely spanning across the center of the CNT. The ordering in F-17, on the other hand, no longer has the well-defined stacked pentagonal structure that was seen earlier. When viewed down the channel axis (Figure 10d), the hydrogen bonding somewhat resembles a polygonal shape due to the packing of water molecules near the CNT wall but is clearly distorted, and the view along the CNT axis (Figure 10c) clearly shows a loss of the highly aligned structure in this system with an excess proton.

Additional insight into these structures and comparison between the acidic systems and those without the excess proton can be obtained by examining the O–H···F interactions in the fluorinated CNTs. Figure 11 shows the percent of time throughout the trajectory O–H···F hydrogen bonds exist versus the fraction of water molecules with such a bond along with snapshots displaying such interactions for the fluorinated systems containing an excess proton. In both the larger and smaller CNTs, at least one water molecule is involved in an O–H···F interaction throughout the entire trajectory which was not the case for the larger tube without the excess proton. An average 55% (6.6 H_2O) in F-14 and 29% (~7 H_2O) in F-17 of the water molecules were determined to hydrogen bond to the fluorinated wall throughout the simulation. These are each higher than the previously mentioned results in the neutral systems. The corresponding average H···F and O···F hydrogen bond distances, however, were found to be essentially the same. The continuous lifetimes of these interactions were also the same but a marginal increase to 91 fs in the larger tube and a near two-fold increase to 196 fs were determined when bifurcated hydrogen bonds and hydrogen bond jumps were included. The F-14 plot shows a very sharp peak indicating that during 60% of the trajectory 7 H_2O are involved in these interactions while the F-17 plot is broader off indicating an influence of the confinement dimensions on the results. It is possible that the increased number of these interactions, in combination with the confinement dimensions, plays a role in the overly ordered structure in F-14. Although an increase in the number of O–H···F bonds was found when the excess proton was included, such an interaction was an exceedingly rare event involving the H_3O^+ defect site.

We adopted the method of Marx *et. al.*[50] to determine the 'most active proton' (H*) involved in the protonated complex. In this procedure, each proton is assigned to its nearest oxygen atom. The oxygen atom in the protonated complex (O*) is then designated as the one with three nearest neighbor hydrogen atoms. The values of the asymmetric stretch coordinate ($\delta = R_{O^*H^*} - R_{OH^*}$) for the oxygen atoms neighboring O* are determined, and the proton involved in the hydrogen bond with the smallest value of δ is considered the most active proton. Insight into the state of the excess proton can be obtained by examining the two-dimensional distribution function, $P\left(\delta, R_{O^*O}\right)$, for the most active

proton throughout the simulation shown in Figure 12, where R_{0^*0} is the distance between the oxygen atoms involved in the most active hydrogen bond. As indicated in the figures, the most active proton exists over a wide range of structures in each of the simulated systems. All of the profiles share a double-peaked structure with a non-zero probability around δ = 0. This corresponds to a symmetric sharing of the proton between two water molecules in a Zundel complex. While the definitions of Zundel and Eigen-like cations are somewhat ambiguous, the idealized forms are generally taken as $|\delta| \leq 0.1$ Å for a Zundel cation and $|\delta| > 0.3$ Å for Eigen-like structures.[50] Adopting this definition, 53% (F-14) and 55% (F-17) of the configurations in the fluorinated CNTs and ~51% in the bare CNTs are unclassified having δ in between these values. Of the remaining configurations, the Zundel structure in F-14 was favored (54.6% versus 45.4% Eigen) while that of N-14 showed the opposite (43.5% versus 56.5%). In the larger bare CNT, these numbers were split 47% to 53% while those in F-17 more closely resembled N-14 with values of 43.8% and 56.2%. It should be noted that these AIMD simulations treat the nuclei as classical particles. Simulations including quantum nuclear effects (QNEs) via *ab initio* path integral techniques have shown that treating the nuclei classically leads to an increased likelihood the proton exists in Eigen-like configurations which leads to the pronounced outer peaks.[50, 52, 61, 79, 80] Inclusion of QNEs enhances the Zundel character, and the $P(\delta, R_{0^*0})$ distribution function in water contains a broad, float ridge spanning over a range of δ encompassing Zundel, Eigen, and intermediate forms indicating that proton defects should be regarded as "fluxional complexes" rather than the idealized states.[50] This has also been shown for proton transfer in CNTs which showed that QNEs can lead to delocalization of the most active proton over multiple hydrogen bonds along a water chain.[61] Thus, the results presented here should not be taken as absolute values but as a relative comparison between the confined systems.

Finally we examine the location of the most active proton throughout the trajectory in the different CNTs. Figure 13 shows the two-dimensional projection of the position of H* onto the xy-plane and the three-dimensional trajectories of H* in the smaller and larger CNTs, respectively. The overwhelming majority of proton transfer events rattle back and forth between two water molecules and do not contribute to net or long range transport. In F-14 (Figure 13b), the active proton is localized near the CNT walls where it shuttles between the highly ordered "zigzag ladder" water molecules with little net motion of the water molecules themselves. As mentioned previously, this structure may in part be caused by the several interactions with the fluorinated walls. This leads to a hydrogen bonding topography that contains several water molecules donating two hydrogen bonds to neighboring water molecules along the channel and accepting one perpendicular to it (see the middle four water molecules of Figure 9c) which appear to hinder proton transfer along the channel axis. The xy

projection of the active proton in N-14 is also localized to a particular region of the nanotube but migrates down the nanotube axis as opposed to around the walls. In the larger N-17, H* was preferentially located in regions near the CNT surface and had less unidirectional motion down the channel than in N-14 which is likely due to the larger confinement dimensions. As in F-14, the active proton in F-17 was also found to be highly localized near the fluorinated walls due to the hydrogen bond structure. However, the arrangement is considerably more disordered and does not contain the trap states found in F-14 and has a larger number of neighboring proton transfer sites allowing for more overall motion down the channel.

Conclusions

The degree of confinement and the hydrophobicity led to significant differences in the structure of hydrogen bonding of the water. In the bare CNTs, the systems with and without the excess proton exhibited similar hydrogen bond arrangements without any well-defined structure. There was, however, a somewhat greater tendency for the water molecules to arrange near the nanotube walls in N-14 while those in N-17 were more randomly distributed likely due to the level of confinement. The confinement also appears to influence proton transfer where the proton in N-14 has a more uniform directionality down the CNT axis. The water molecules confined within the fluorinated CNTs were found to localize near the channel surface and formed ordered hydrogen bond networks with well-defined regular structures. When an excess proton was introduced, the stacked pentagonal arrangement in F-17 was considerably disrupted resulting in a distorted hydrogen bond network while in F-14 a highly aligned zigzag ladder structure was formed. In each of these cases, hydrogen bonding to the fluorine atoms of the CNT wall was observed with a higher occurrence in the systems containing an excess proton. This was most pronounced in the smaller F-14 system where roughly half of the water molecules were involved in such an interaction in every simulation step which may contribute to the structural ordering. This arrangement led to several hydrogen bond sites that hinder proton transfer directly along the channel axis and, instead, the proton tends to shuttle between water molecules around the fluorinated surface with more Zundel-like character than the other systems. These sites were not observed in the larger fluorinated nanotube where proton transfer through the CNT occurred more readily indicating an influence of the increased confinement in F-14 on the interaction between the water molecules and the fluorine atoms, the hydrogen bond network, and the nature of the excess proton. It should be noted that there are many factors not probed in this study that may impact the findings including quantum nuclear effects, density of water, and distribution and density of fluorine atoms. Thus, these results should be regarded as a relative comparison of how the confined environment and the addition of an excess proton affect the structural and dynamical properties in the simulated systems.

Acknowledgement

JKC acknowledges support by the National Science Foundation under Grant No. DGE0801470, “Sustainable Technology through Advanced Interdisciplinary Research” (STAIR), awarded to the University of Tennessee, Knoxville. SJP acknowledges support by the DOE under contract number DE-FG36-07G017006. DOE support does not constitute an endorsement by DOE of the views expressed in this work.

References

1. Chaplin, M. F., Structuring and Behaviour of Water in Nanochannels and Confined Spaces. In *Adsorption and Phase Behaviour in Nanochannels and Nanotubes*, Dunne, L. J.; Manos, G., Eds. Springer Science: New York, 2010; pp 241-255.
2. Rasaiah, J. C.; Garde, S.; Hummer, G., *Annual Review of Physical Chemistry* 2008, **59**, 713-740.
3. Vaitheeswaran, S.; Yin, H.; Rasaiah, J. C.; Hummer, G., *Proc. Nat. Acad. Sci. USA* 2004, **101**, 17002-17005.
4. Cicero, G.; Grossman, J. C.; Schwegler, E.; Gygi, F.; Galli, G., *J. Am. Chem. Soc.* 2008, **130**, 1871-1878.
5. Munoz-Santiburcio, D.; Wittekindt, C.; Marx, D., *Nat. Commun.* 2013, **4**, 2349.
6. Ferguson, A. L.; Giovambattista, N.; Rossky, P. J.; Panagiotopoulos, A. Z.; Debenedetti, P. G., *J. Chem. Phys.* 2012, **137**, 144501.
7. Giovambattista, N.; Rossky, P. J.; Debenedetti, P. G., *J. Phys. Chem. B* 2009, **113**, 13723-13734.
8. Castrillon, S. R. V.; Giovambattista, N.; Aksay, I. A.; Debenedetti, P. G., *J. Phys. Chem. B* 2009, **113**, 7973-7976.
9. Castrillon, S. R. V.; Giovambattista, N.; Aksay, I. A.; Debenedetti, P. G., *J. Phys. Chem. B* 2009, **113**, 1438-1446.
10. Kofinger, J.; Hummer, G.; Dellago, C., *Phys. Chem. Chem. Phys.* 2011, **13**, 15403-15417.
11. Zangi, R., *J. Phys. Condens. Matter.* 2004, **16**, S5371-S5388.
12. Thomas, J. A.; McGaughey, A. J. H., *Phys. Rev. Lett.* 2009, **102**, 184502.
13. Nanok, T.; Artrith, N.; Pantu, P.; Bopp, P. A.; Limtrakul, J., *J. Phys. Chem. A* 2009, **113**, 2103-2108.
14. Liu, Y. C.; Wang, Q., *Phys. Rev. B* 2005, **72**, 085420.
15. Liu, Y. C.; Wang, Q.; Wu, T.; Zhang, L., *J. Chem. Phys.* 2005, **123**, 234701.
16. Mann, D. J.; Halls, M. D., *Phys. Rev. Lett.* 2003, **90**, 195503.
17. Byl, O.; Liu, J. C.; Wang, Y.; Yim, W. L.; Johnson, J. K.; Yates, J. T., *J. Am. Chem. Soc.* 2006, **128**, 12090-12097.
18. Hummer, G.; Rasaiah, J. C.; Noworyta, J. P., *Nature* 2001, **414**, 188-190.
19. Whitby, M.; Quirke, N., *Nat. Nanotechnol.* 2007, **2**, 87-94.
20. Cao, Z.; Peng, Y. X.; Yan, T. Y.; Li, S.; Li, A. L.; Voth, G. A., *J. Am. Chem. Soc.* 2010, **132**, 11395-11397.
21. Perez-Hernandez, G.; Schmidt, B., *Phys. Chem. Chem. Phys.* 2013, **15**, 4995-5006.
22. Takaiwa, D.; Hatano, I.; Koga, K.; Tanaka, H., *Proc. Nat. Acad. Sci. USA* 2008, **105**, 39-43.
23. Shiomi, J.; Kimura, T.; Maruyama, S., *J. Phys. Chem. C* 2007, **111**, 12188-12193.
24. Kyakuno, H.; Matsuda, K.; Yahiro, H.; Inami, Y.; Fukuoka, T.; Miyata, Y.; Yanagi, K.; Maniwa, Y.; Kataura, H.; Saito, T.; Yumura, M.; Iijima, S., *J. Chem. Phys.* 2011, **134**, 244501.
25. Alexiadis, A.; Kassinos, S., *Molecular Simulation* 2008, **34**, 671-678.
26. Gordillo, M. C.; Marti, J., *Chem. Phys. Lett.* 2000, **329**, 341-345.
27. Hernandez-Rojas, J.; Calvo, F.; Breton, J.; Llorente, J. M. G., *J. Phys. Chem. C* 2012, **116**, 17019-17028.
28. O'Connell, M. J.; Boul, P.; Ericson, L. M.; Huffman, C.; Wang, Y. H.; Haroz, E.; Kuper, C.; Tour, J.; Ausman, K. D.; Smalley, R. E., *Chem. Phys. Lett.* 2001, **342**, 265-271.
29. Pascal, T. A.; Goddard, W. A.; Jung, Y., *Proc. Nat. Acad. Sci. USA* 2011, **108**, 11794-11798.
30. Sansom, M. S. P.; Biggin, P. C., *Nature* 2001, **414**, 156-159.
31. Tao, Y. S.; Muramatsu, H.; Endo, M.; Kaneko, K., *J. Am. Chem. Soc.* 2010, **132**, 1214-1215.
32. Gogotsi, Y.; Libera, J. A.; Guvenc-Yazicioglu, A.; Megaridis, C. M., *Appl. Phys. Lett.* 2001, **79**, 1021-1023.
33. Maniwa, Y.; Kataura, H.; Abe, M.; Udaka, A.; Suzuki, S.; Achiba, Y.; Kira, H.; Matsuda, K.; Kadowaki, H.; Okabe, Y., *Chem. Phys. Lett.* 2005, **401**, 534-538.
34. Kolesnikov, A. I.; Zanotti, J. M.; Loong, C. K.; Thiyagarajan, P.; Moravsky, A. P.; Loutfy, R. O.; Burnham, C. J., *Phys. Rev. Lett.* 2004, **93**, 035503.

35. Matsuda, K.; Hibi, T.; Kadowaki, H.; Kataura, H.; Maniwa, Y., *Phys. Rev. B* 2006, **74**, 073415.
36. Reiter, G.; Burnham, C.; Homouz, D.; Platzman, P. M.; Mayers, J.; Abdul-Redah, T.; Moravsky, A. P.; Li, J. C.; Loong, C. K.; Kolesnikov, A. I., *Phys. Rev. Lett.* 2006, **97**, 247801.
37. Reiter, G. F.; Kolesnikov, A. I.; Paddison, S. J.; Platzman, P. M.; Moravsky, A. P.; Adams, M. A.; Mayers, J., *Phys. Rev. B* 2012, **85**, 045403.
38. Alexiadis, A.; Kassinos, S., *Chem. Rev.* 2008, **108**, 5014-5034.
39. Koga, K.; Gao, G. T.; Tanaka, H.; Zeng, X. C., *Nature* 2001, **412**, 802-805.
40. Noon, W. H.; Ausman, K. D.; Smalley, R. E.; Ma, J. P., *Chem. Phys. Lett.* 2002, **355**, 445-448.
41. Granick, S., *Science* 1991, **253**, 1374-1379.
42. Thompson, W. H., Solvation Dynamics and Proton Transfer in Nanoconfined Liquids. In *Annual Review of Physical Chemistry, Vol 62*, Leone, S. R.; Cremer, P. S.; Groves, J. T.; Johnson, M. A., Eds. 2011; Vol. 62, pp 599-619.
43. Bocquet, L.; Charlaix, E., *Chem. Soc. Rev.* 2010, **39**, 1073-1095.
44. DeCoursey, T. E., *Physiol. Rev.* 2003, **83**, 475-579.
45. Mulkidjanian, A. Y.; Heberle, J.; Cherepanov, D. A., *Biochim. Biophys. Acta* 2006, **1757**, 913-930.
46. Kreuer, K. D.; Paddison, S. J.; Spohr, E.; Schuster, M., *Chem. Rev.* 2004, **104**, 4637-4678.
47. Tuckerman, M. E.; Laasonen, K.; Sprik, M.; Parrinello, M., *J. Phys. Chem.* 1995, **99**, 5749-5752.
48. Tuckerman, M. E.; Laasonen, K.; Sprik, M.; Parrinello, M., *J. Chem. Phys.* 1995, **103**, 150-161.
49. Tuckerman, M. E.; Marx, D.; Klein, M. L.; Parrinello, M., *Science* 1997, **275**, 817-820.
50. Marx, D.; Tuckerman, M. E.; Hutter, J.; Parrinello, M., *Nature* 1999, **397**, 601-604.
51. Berkelbach, T. C.; Lee, H. S.; Tuckerman, M. E., *Phys. Rev. Lett.* 2009, **103**, 238302.
52. Marx, D.; Chandra, A.; Tuckerman, M. E., *Chem. Rev.* 2010, **110**, 2174-2216.
53. Eigen, M.; Demaeyer, L., *P. Roy. Soc. Lond. A. Mat.* 1958, **247**, 505-533.
54. Eigen, M., *Angew. Chem. Int. Ed.* 1963, **75**, 489-508.
55. Zundel, G., *Adv. Chem. Phys.* 2000, **111**, 1-217.
56. von Grotthuss, C. J. D., *Ann. Chim.* 1806, **58**, 54-74.
57. Agmon, N., *Chem. Phys. Lett.* 1995, **244**, 456-462.
58. Marx, D., *ChemPhysChem* 2006, **7**, 1848-1870.
59. Lapid, H.; Agmon, N.; Petersen, M. K.; Voth, G. A., *J. Chem. Phys.* 2005, **122**, 014506.
60. Dellago, C.; Naor, M. M.; Hummer, G., *Phys. Rev. Lett.* 2003, **90**, 105902.
61. Chen, J.; Li, X. Z.; Zhang, Q. F.; Michaelides, A.; Wang, E. G., *Phys. Chem. Chem. Phys.* 2013, **15**, 6344-6349.
62. Brewer, M. L.; Schmitt, U. W.; Voth, G. A., *Biophys. J.* 2001, **80**, 1691-1702.
63. Kresse, G.; Hafner, J., *Phys. Rev. B* 1993, **47**, 558-561.
64. Kresse, G.; Hafner, J., *Phys. Rev. B* 1994, **49**, 14251-14269.
65. Kresse, G.; Furthmuller, J., *Phys. Rev. B* 1996, **54**, 11169-11186.
66. Kresse, G.; Furthmuller, J., *Comput. Mater. Sci.* 1996, **6**, 15-50.
67. Blochl, P. E., *Phys. Rev. B* 1994, **50**, 17953-17979.
68. Kresse, G.; Joubert, D., *Phys. Rev. B* 1999, **59**, 1758-1775.
69. Perdew, J. P.; Burke, K.; Ernzerhof, M., *Phys. Rev. Lett.* 1996, **77**, 3865-3868.
70. Perdew, J. P.; Burke, K.; Ernzerhof, M., *Phys. Rev. Lett.* 1997, **78**, 1396-1396.
71. Habenicht, B. F.; Paddison, S. J.; Tuckerman, M. E., *Phys. Chem. Chem. Phys.* 2010, **12**, 8728-8732.
72. Habenicht, B. F.; Paddison, S. J.; Tuckerman, M. E., *J. Mater. Chem.* 2010, **20**, 6342-6351.
73. Habenicht, B. F.; Paddison, S. J., *J. Phys. Chem. B* 2011, **115**, 10826-10835.
74. Grossman, J. C.; Schwegler, E.; Draeger, E. W.; Gygi, F.; Galli, G., *J. Chem. Phys.* 2004, **120**, 300-311.
75. VandeVondele, J.; Mohamed, F.; Krack, M.; Hutter, J.; Sprik, M.; Parrinello, M., *J. Chem. Phys.* 2005, **122**, 014515.
76. Santra, B.; Michaelides, A.; Scheffler, M., *J. Chem. Phys.* 2009, **131**, 124509.
77. Laage, D.; Hynes, J. T., *Science* 2006, **311**, 832-835.
78. Kumar, R.; Schmidt, J. R.; Skinner, J. L., *J. Chem. Phys.* 2007, **126**, 204107.

79. Hayes, R. L.; Paddison, S. J.; Tuckerman, M. E., *J. Phys. Chem. B* 2009, **113**, 16574-16589.
80. Hayes, R. L.; Paddison, S. J.; Tuckerman, M. E., *J. Phys. Chem. A* 2011, **115**, 6112-6124.
81. Falk, M., *Canad. J. Chem.* 1980, **58**, 1495.
82. Basnayake, R.; Peterson, G. R.; Casadonte, D. J.; Korzeniewski, C., *J. Phys. Chem. B* 2006, **110**, 23938-23943.
83. Moilanen, D. E.; Piletic, I. R.; Fayer, M. D., *J. Phys. Chem. A* 2006, **110**, 9084-9088.
84. Steiner, T., *Angew. Chem. Int. Ed.* 2002, **41**, 48-76.
85. Soper, A. K., *ISRN Physical Chemistry* 2013, **2013**, 67.
86. Modig, K.; Pfrommer, B. G.; Halle, B., *Phys. Rev. Lett.* 2003, **90**.
87. Dunitz, J. D.; Taylor, R., *Chem. Eur. J.* 1997, **3**, 89-98.
88. Howard, J. A. K.; Hoy, V. J.; Ohagan, D.; Smith, G. T., *Tetrahedron* 1996, **52**, 12613-12622.
89. Dunitz, J. D., *Chembiochem* 2004, **5**, 614-621.
90. Santra, B.; Michaelides, A.; Fuchs, M.; Tkatchenko, A.; Filippi, C.; Scheffler, M., *J. Chem. Phys.* 2008, **129**.

Figure Captions

Figure 1. CNT+H_2O systems used in the present study: (a) N-14, (b) F-14, (c) N-17, and (d) F-17. The different colored spheres represent different atom types where: gray–carbon, red–oxygen, white–hydrogen, and yellow–fluorine.

Figure 2. (Outer) Contour plots of the distribution of (left) oxygen and (right) hydrogen atoms projected onto the xy-plane throughout the trajectory for: (a) N-14, (b) F-14, (c) N-17, and (d) F-17 shown on the same scale where darker colors indicate more populated regions. (Inner) Corresponding distribution functions of the axial distance of the atoms from the inner wall of the CNT.

Figure 3. Radial distribution functions for the systems of water confined in the different CNTs: (a) oxygen–oxygen and (b) oxygen–hydrogen.

Figure 4. Representative snapshots of the hydrogen bond network in the smaller nanotubes showing (left) along the CNT axis and (right) down the CNT axis for the bare (a/b) and fluorinated (c/d) systems. Hydrogen bonds are denoted by dashed lines.

Figure 5. Representative snapshots of the hydrogen bond network in the larger nanotubes showing (left) along the CNT axis and (right) down the CNT axis for the bare (a/b) and fluorinated (c/d) systems. Hydrogen bonds are denoted by dashed lines.

Figure 6. Percent of time throughout the trajectory OH···F hydrogen bonds exist versus the fraction of H_2O molecules with an OH···F bond. The middle and bottom panels show representative snapshots of F-14 and F-17, respectively, with OH···F bonds shown as dashed lines.

Figure 7. (Outer) Contour plots of the distribution of (left) oxygen and (right) hydrogen atoms projected onto the xy-plane throughout the trajectory for the systems containing an excess proton: (a) N-14, (b) F-14, (c) N-17, and (d) F-17 shown on the same scale where darker colors indicate more populated regions. (Inner) Corresponding distribution functions of the axial distance of the atoms from the inner wall of the CNT.

Figure 8. Radial distribution functions for the systems of water and an excess proton confined in the different CNTs: (a) oxygen–oxygen and (b) oxygen–hydrogen

Figure 9. Representative snapshots of the hydrogen bond network in the smaller nanotubes containing an excess proton showing (left) along the CNT axis and (right) down the CNT axis for the bare (a/b) and fluorinated (c/d) systems.

Figure 10. Representative snapshots of the hydrogen bond network in the larger nanotubes containing an excess proton showing (left) along the CNT axis and (right) down the CNT axis for the bare (a/b) and fluorinated (c/d) systems.

Figure 11. Percent of time throughout the trajectory OH···F hydrogen bonds exist versus the fraction of H_2O molecules with an OH···F bond for the fluorine CNT+H_2O+H^+ systems. The middle and bottom panels show representative snapshots of F-14 and F-17, respectively, with OH···F bonds shown as dashed lines.

Figure 12. Distribution functions $P\left(\delta, R_{O^*O}\right)$ of the proton transfer coordinate $\delta \equiv R_{O^*H^*} - R_{OH^*}$ and the distance between the corresponding oxygen atoms R_{O^*O} where H* is the most active proton (see text) for: (a) N-14, (b) F-14, (c) N-17, and (d) F-17. The distributions have been smoothed and symmetrized about $\delta = 0$ and normalized to unity.

Figure 13. Location of H* throughout the trajectory projected onto the xy-plane (left) and the three-dimensional perspective (right) for: (a) N-14, (b) F-14, (c) N-17, and (d) F-17.

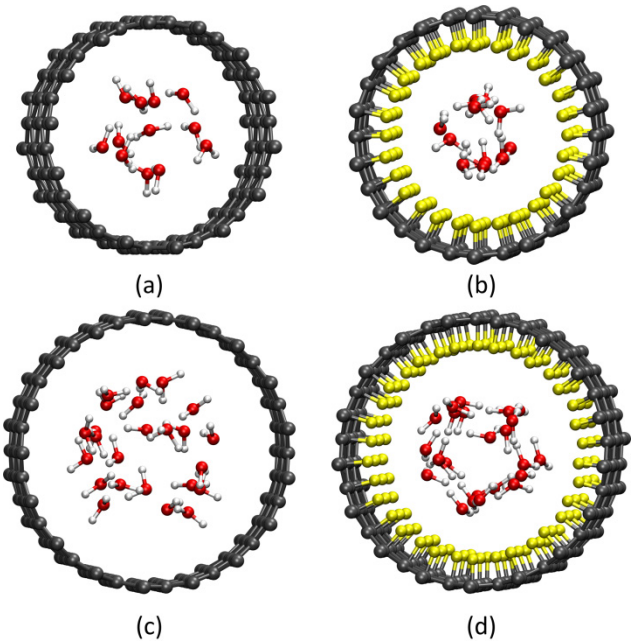

Fig. 1

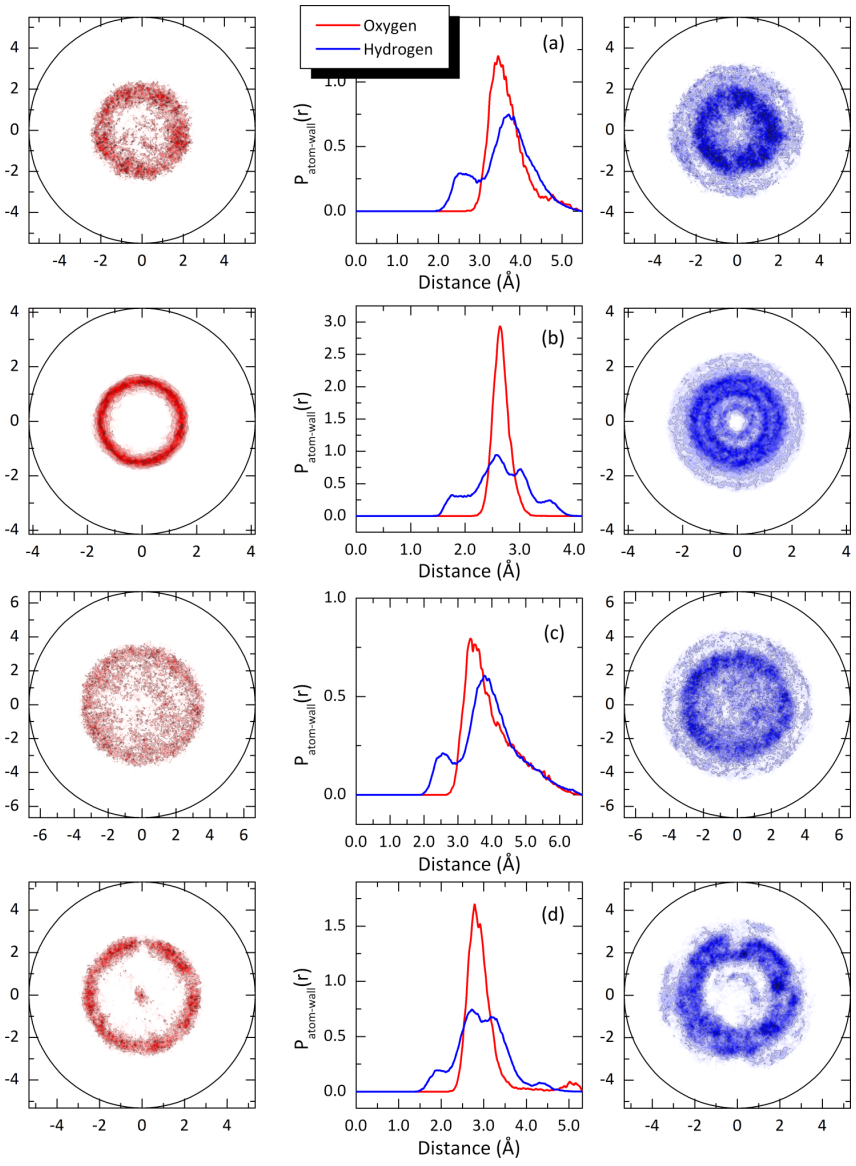

Fig. 2

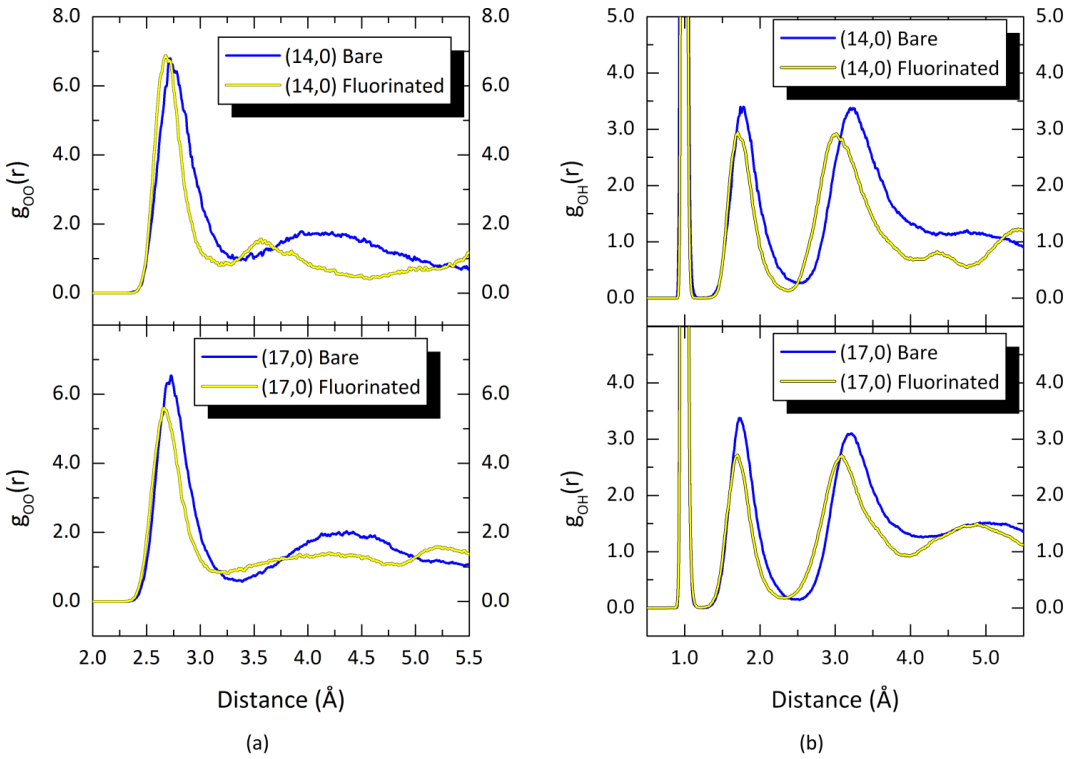
(14,0) Bare
(14,0) Fluorinated
(17,0) Bare
(17,0) Fluorinated
$g_{OO}(r)$
$g_{OH}(r)$
Distance (Å)
(a)
(b)

Fig. 3

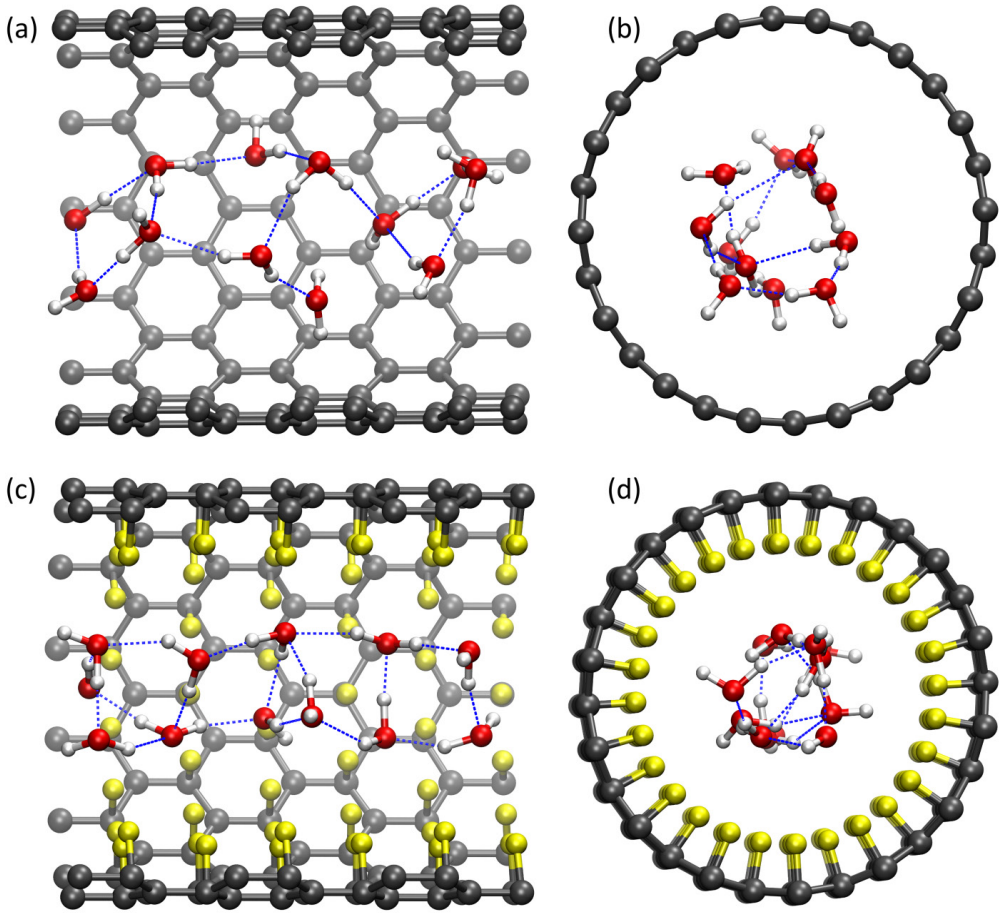

Fig. 4

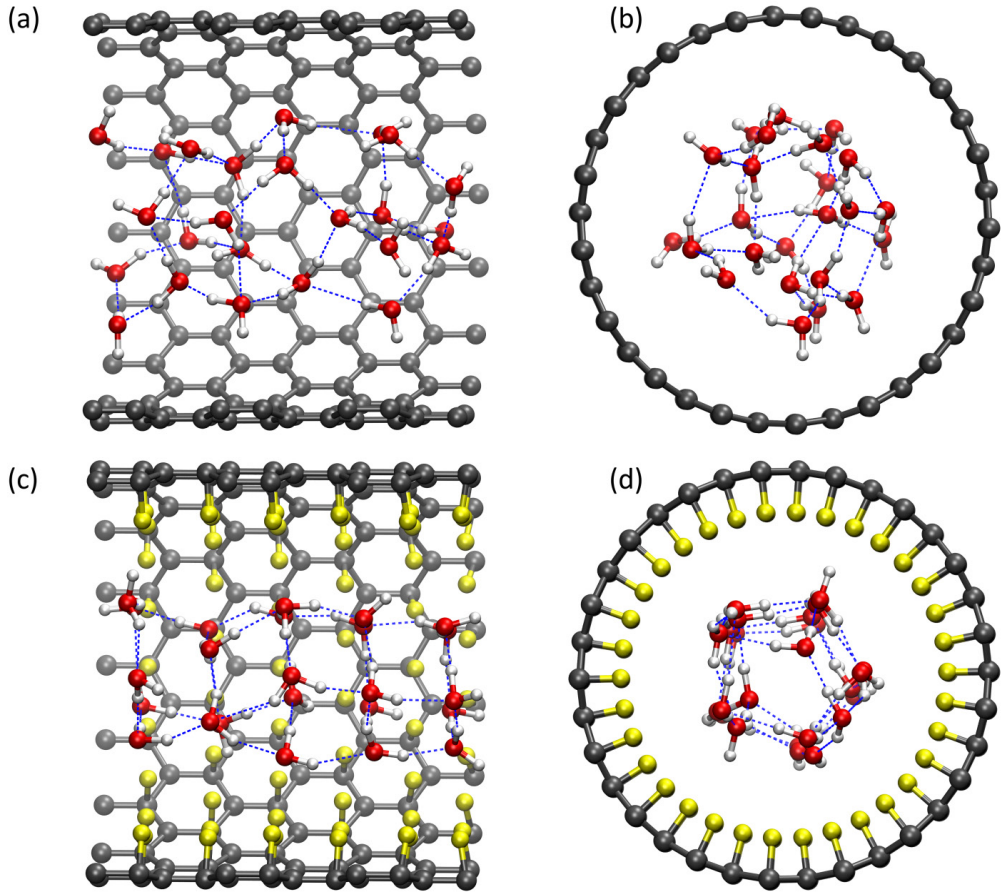

Fig. 5

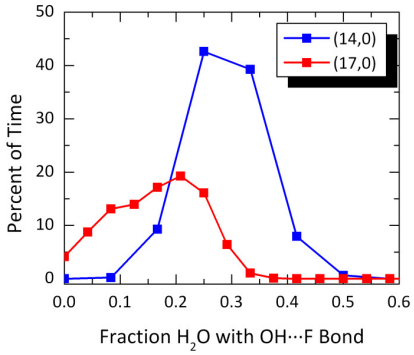
50
40
30
20
10
0
Percent of Time
(14,0)
(17,0)
0.0
0.1
0.2
0.3
0.4
0.5
0.6
Fraction H2O with OH···F Bond

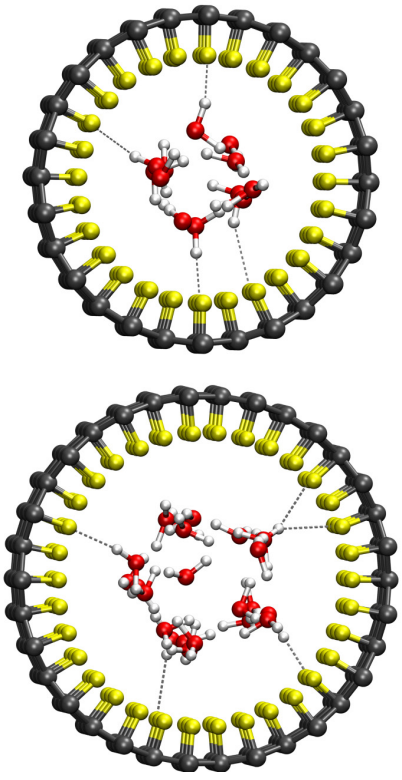

Fig. 6

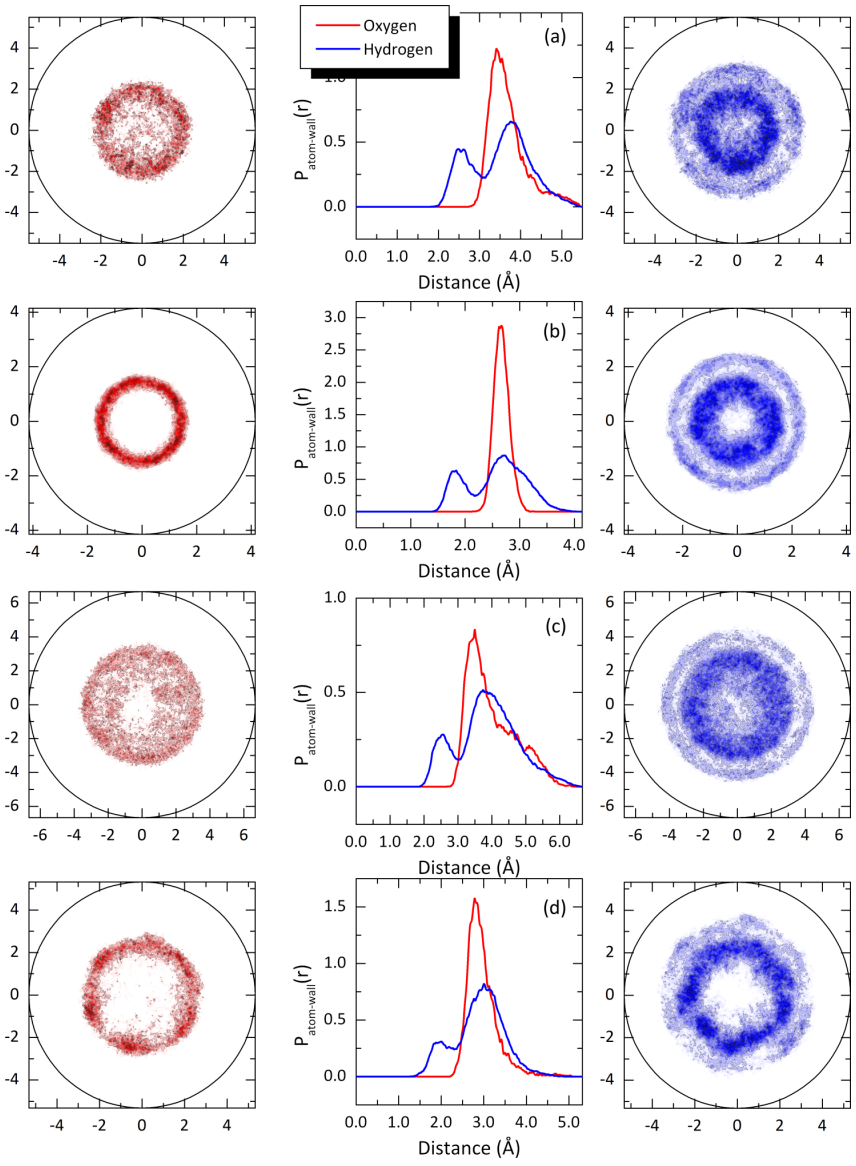

Fig. 7

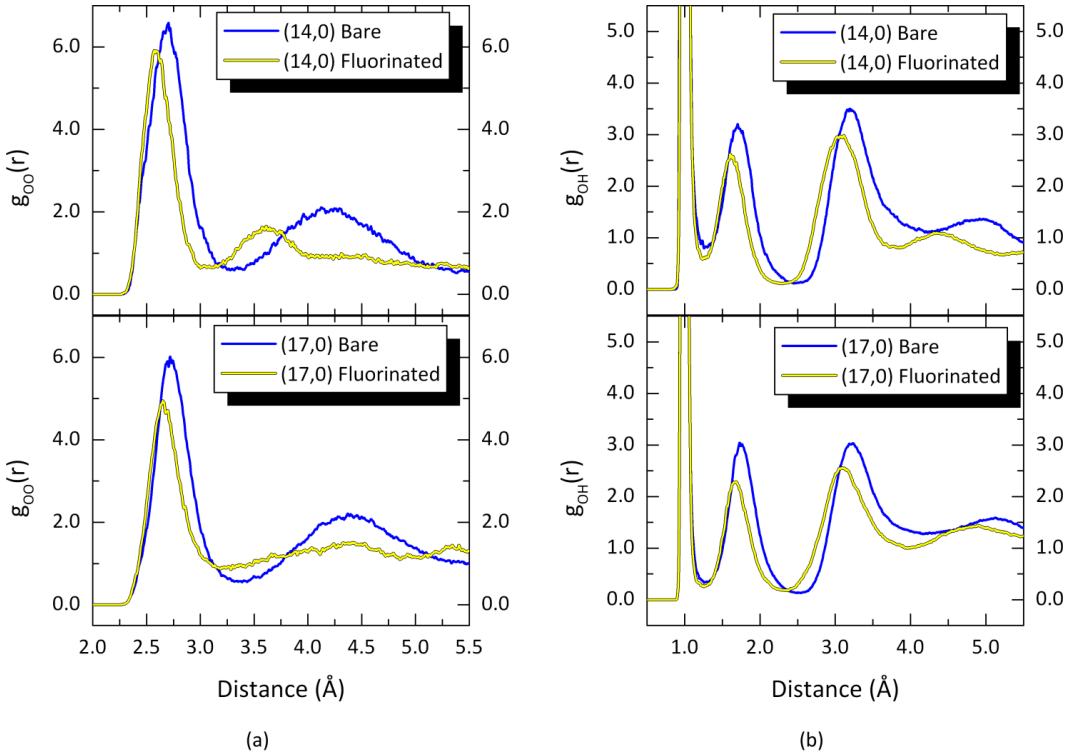
(14,0) Bare
(14,0) Fluorinated
(17,0) Bare
(17,0) Fluorinated
$g_{OO}(r)$
$g_{OH}(r)$
Distance (Å)
(a)
(b)

Fig. 8

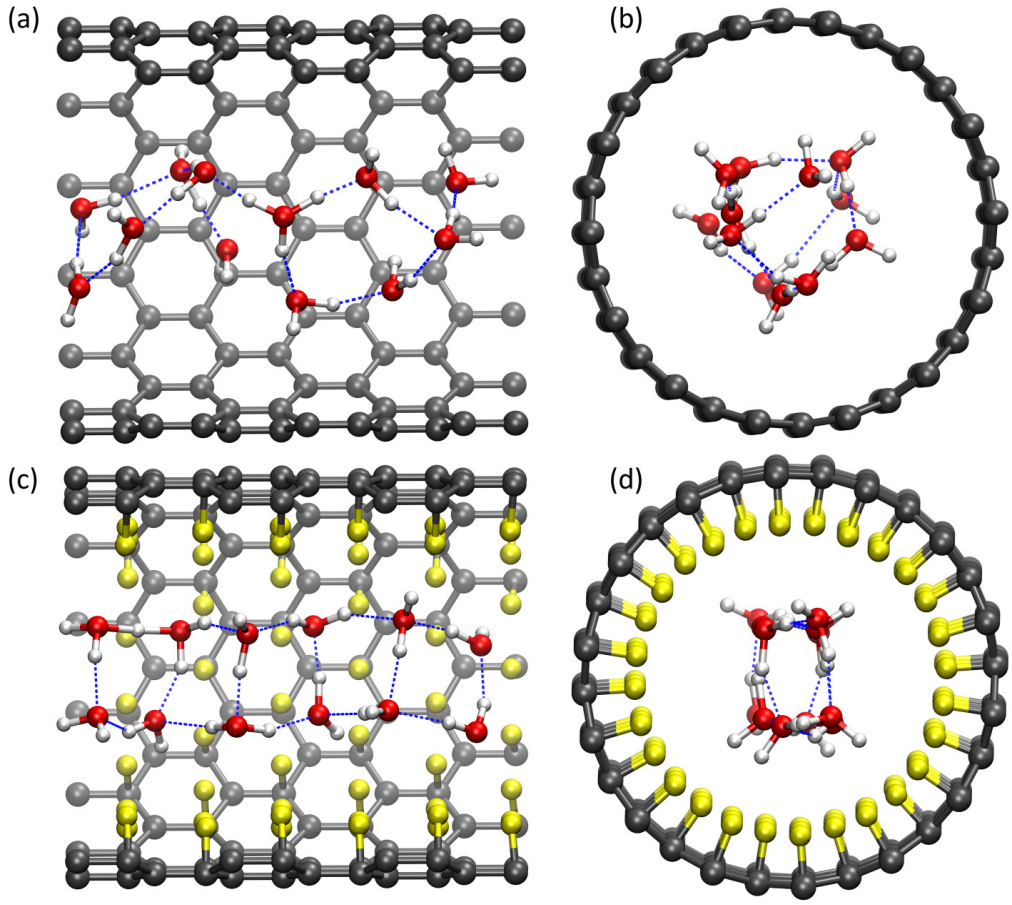

Fig. 9

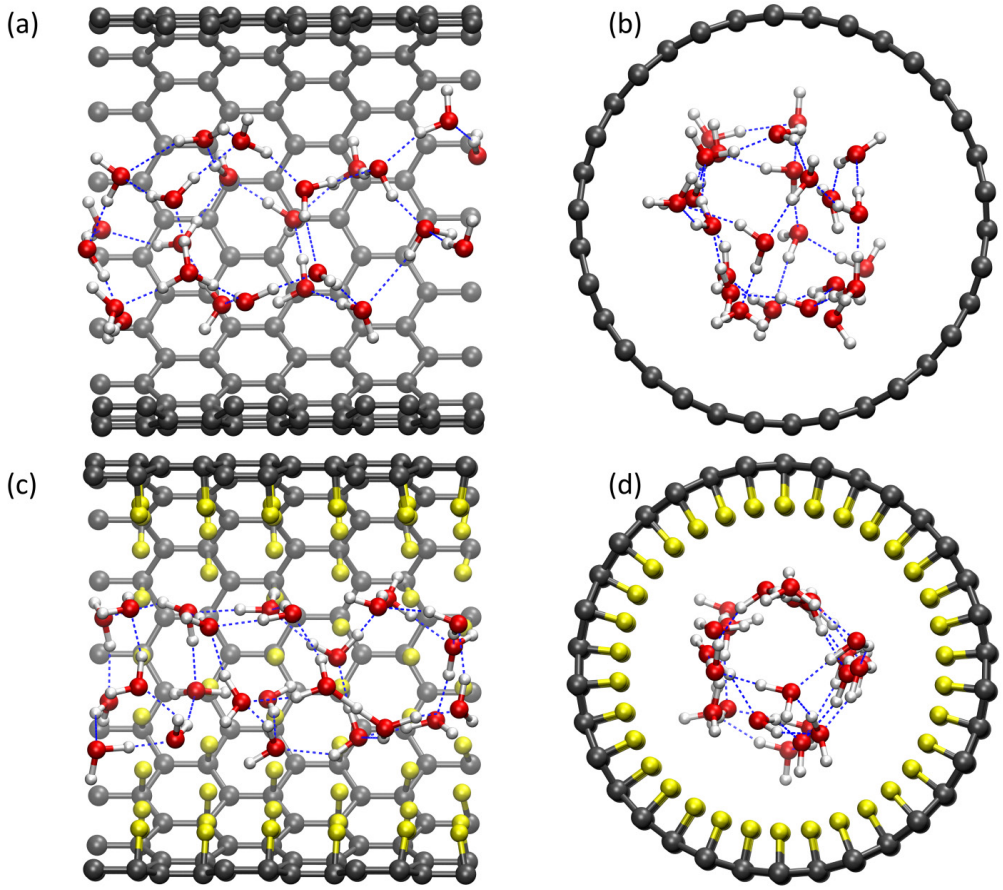

Fig. 10

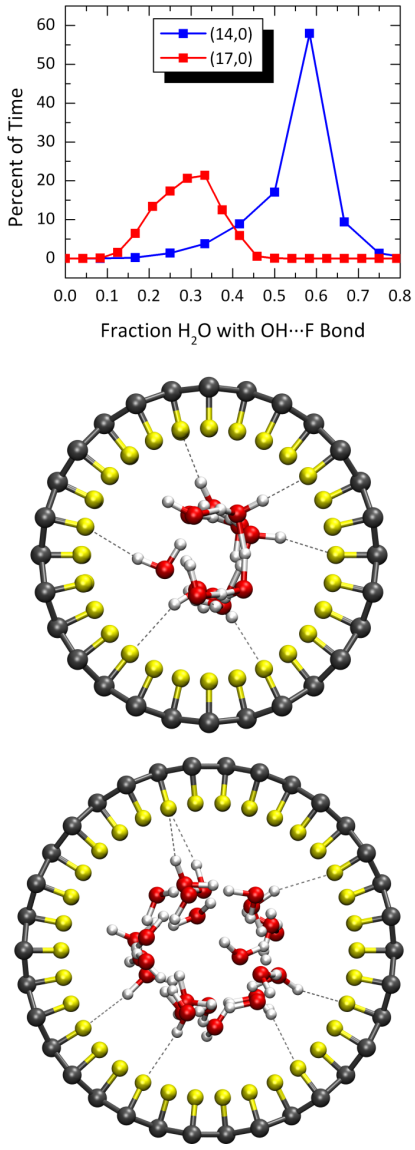
(14,0)
(17,0)
Percent of Time
Fraction H2O with OH···F Bond
0
10
20
30
40
50
60
0.0
0.1
0.2
0.3
0.4
0.5
0.6
0.7
0.8

Fig. 11

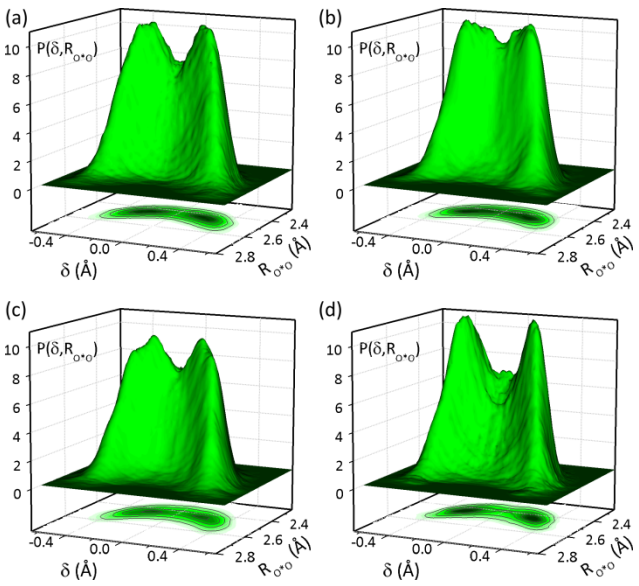

Fig. 12

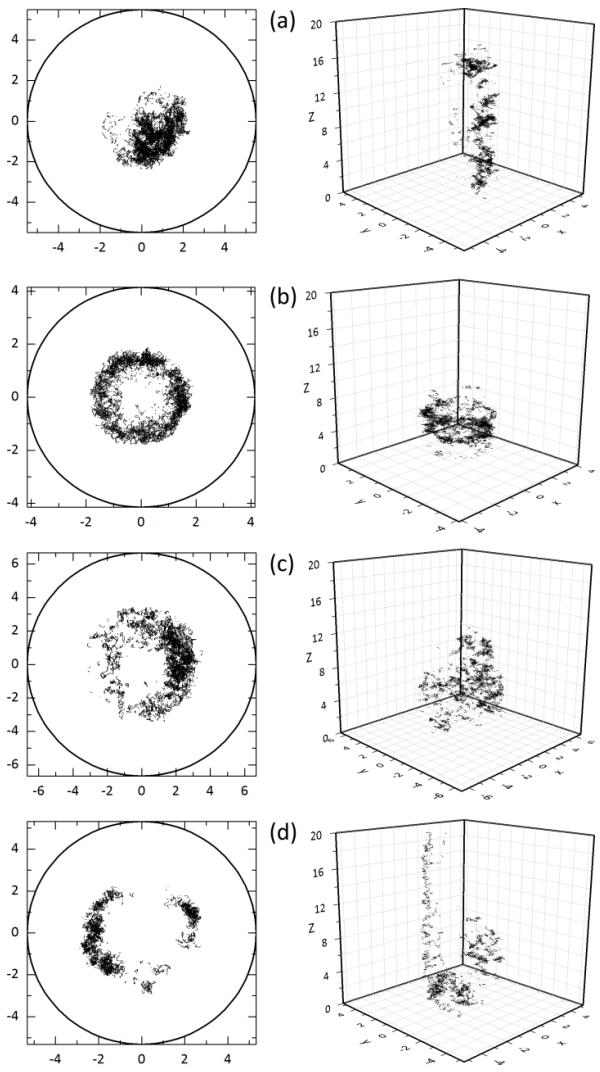

Fig. 13

Ab initio Molecular Dynamics Simulations of Aqueous Triflic Acid Confined in Carbon Nanotubes

Jeffrey K. Clark II,[†] Bradley F. Habenicht,[‡] and Stephen J. Paddison[†,*]

[†]*Department of Chemical and Biomolecular Engineering, University of Tennessee, Knoxville, TN 37996*
[‡]*School of Natural Sciences, University of California, Merced, CA 95343*

ABSTRACT

Ab initio molecular dynamics simulations were performed to investigate the effects of nanoscale confinement on the structural and dynamical properties of aqueous triflic acid (CF_3SO_3H). Single-walled carbon nanotubes (CNTs) with diameters ranging from ~11 to 14 Å were used as confinement vessels, and the inner surface of the CNT were either left bare or fluorinated to probe the influence of the confined environment on structural and dynamical properties of the water and triflic acidic. The systems were simulated at hydration levels of n = 1 – 3 H_2O/CF_3SO_3H. Proton dissociation expectedly increased with increasing hydration. Along with the level of hydration, hydrogen bond connectivity between the triflic acid molecules, both directly and via a single water molecule, played a role on proton dissociation. Direct hydrogen bonding between the CF_3SO_3H molecules, most commonly found in the larger bare CNT, also promoted interactions between water molecules allowing for greater separation of the dissociated protons from the $CF_3SO_3^-$ as the hydration level was increased. However, this also resulted in a decrease in the overall proportion of dissociated protons. The confinement dimensions altered both the hydrogen bond network and the distribution of water molecules where the H_2O in the fluorinated CNTs tended to form small clusters with less proton dissociation at n = 1 and 2 but the highest at n = 3. In the absence of nearby hydrogen bond accepting sites from H_2O or triflic acid SO_3H groups, the water molecules formed weak hydrogen bonds with the fluorine atoms. In the bare CNT systems, these involved the CF_3 groups of triflic acid and were more frequently observed when direct hydrogen bonding between CF_3SO_3H hindered potential hydrogen bonding sites. In the fluorinated tubes, interactions with the covalently bound fluorine atoms of the CNT wall dominated which appear to stabilize the hydrogen bond network. Increasing the hydration level increased the frequency of the OH···F (CNT) hydrogen bonding which was highly pronounced in the smaller fluorinated CNT indicating an influence on the confinement dimensions on these interactions.

Keywords: ab initio molecular dynamics, confinement, triflic acid, proton transfer, fuel cell

Corresponding Author

*E-mail: spaddison@utk.edu.

Submitted to PCCP. Manuscript ID: CP-ART-03-2014-001066

Introduction

Proton exchange membrane fuel cells (PEMFCs) are clean, efficient energy conversion devices that offer potential use for stationary, portable, and automotive power.[1-3] At the heart of PEMFCs is the proton-conducting polymer electrolyte, or proton exchange, membrane (PEM). The wide variety of applications for PEMFCs places demands on the membrane beyond high proton conductivity (≥ 10^{-1} Scm^{-1}) including long-term mechanical durability and high thermal and chemical stability in an oxidative environment at temperatures up to 120°C.[4-7] There are several membrane materials available that meet many of these requirements, but nearly all currently available PEMs are limited by the necessity to be highly hydrated (~95% relative humidity) to sufficiently conduct protons.[6, 8, 9] These conditions result in adverse water 'cross-over' due to electroosmotic drag and permeation and also limit the operating conditions to below 100°C (i.e., the boiling point of water) to prevent drying of the membrane.[10-12] Low temperature operation requires the use of expensive platinum or platinum-based electrocatalysts due to poor electrode reaction kinetics which are also more susceptible to poisoning from trace amounts of carbon monoxide in the hydrogen feed stream blocking the reaction sites at temperatures below 120°C degrading the fuel cell performance.[4]

The most commonly employed PEMs are perfluorosulfonic acid (PFSA) ionomers with Nafion® currently representing the industry standard. PFSA ionomers consist of a hydrophobic poly(tetrafluoroethylene) (PTFE) backbone functionalized with pendant perfluoroether side chains each terminated with a single hydrophilic sulfonic acid group. When these materials are hydrated, phase separation into hydrophilic and hydrophobic domains occurs.[11, 13] Within the aqueous domain the dissociated protons may transfer via vehicular or structural (i.e., 'Grotthuss' type) diffusion.[14-18] In bulk water, protons exist as solvated 'fluxional complexes' with Eigen ($H_9O_4^+$) and Zundel ($H_5O_2^+$) cations as idealized limiting forms,[19, 20] and proton 'shuttling' involves continuous inter-conversions between these limiting forms through transfer reactions driven by dynamical changes in the hydrogen bond network in the second and third hydration shells.[19-25] Nanoscale confinement adds additional complexity to the mechanism of proton transfer in water as the restricted environment can influence the solvation structure of the proton and the hydrogen bond network and dynamics.[26-31] The hydrophilic domains in hydrated PFSA membranes, containing the water molecules, protons, and acidic groups, are only a few nanometres in diameter which is influenced by the amount of absorbed water and specific ionomer chemistry.[32-37] Proton transport is further complicated by the heterogeneous nature of the ionomer and the presence of acidic groups,[32] and elucidation of the exact nature of proton transport in PEMs is limited by an incomplete molecular-level understanding of their hydrated morphology.[4, 11, 38-41] Nevertheless, it is accepted that, along with the level of hydration and density of acidic groups, proton transport is intimately connected to the formation and breaking of

hydrogen bonds which is difficult to resolve experimentally and multiscale modelling techniques are frequently used to probe membrane characteristics at a variety of length and time scales.[4, 42]

Insight into the effects of equivalent weight, molecular weight, and degree of hydration (i.e., H_2Os/SO_3H) on the phase separated morphology has been studied using dissipative particle dynamics (DPD) simulations.[40, 43-45] Several classical molecular dynamics (MD) simulations on hydrated PEMs have also been performed to study hydration and transport properties in systems containing thousands of atoms.[46-50] However, these simulations assume that all acidic protons are dissociated and exist as hydronium (H_3O^+) ions and cannot capture the proton hopping behaviour associated with structural diffusion. Empirical valence bond (EVB) schemes[51-54] capable of incorporating proton shuttling into classical simulations have also been used to effectively simulate proton solvation and transport in PEMs[18, 53, 55-59] but are somewhat limited in their molecular description of proton diffusion at very low levels of hydration ($\lambda \leq 3$).[60] *Ab initio* methods, which allow for the breaking and forming of covalent bonds, have also been used to study proton solvation and transfer in PEMs without the requirement of empirical parameterization or predefined states of the protons but are limited to relatively small system sizes. Static electronic structure calculations on isolated side chain fragments of PFSAs and other PEMs have shown that proton dissociation may not occur at hydration levels where $\lambda < 3$.[61-74] However, incorporating multiple side chains revealed that interactions between acidic groups through either direct hydrogen bonds or via a hydrogen bond bridge through a single water molecule or hydronium ion can enhance proton dissociation at low hydration levels.[75-80] Dynamical information can be obtained through *ab initio* molecular dynamics (AIMD) simulations, though the membranes are too complex to be fully treated with these techniques, and model systems are typically employed.[81-92]

Our previous AIMD simulations utilized carbon nanotubes (CNTs) functionalized with $-CF_2SO_3H$ groups to explore the factors that contribute to proton dynamics in PFSA ionomers a simplified confined environment.[84-86] Although the model systems are much more homogenous than true PFSA membranes, the use of CNTs provides a framework that allows for alteration of relevant parameters that may influence proton dissociation and transport such as channel size and environment, spacing of acid groups, and degree of hydration. Nanotubes with three different diameters (11.2, 13.2, and 14.1 Å) were chosen to explore the effects of the confinement dimensions, and the nanotube walls were either left bare or fluorinated to study the influence the hydrophobicity of the confined surface has on transport properties. The simulations were conducted at hydration levels of $\lambda = 1$ and 3. Systems with less separation between sulfonic acid groups resulted in increased proton dissociation but also increased the formation of trap states where a dissociated proton exists as a hydronium ion bridging two sulfonic acid groups hindering long-range proton transport. The fluorinated nanotube walls were found to provide sites that could accept weak hydrogen bonds from the water molecules which stabilized the hydrogen bond network and increased the observed proton dissociation. This is

consistent with results of IR spectroscopy studies on Nafion which showed evidence that absorbed water potentially interacts with the hydrophobic fluorocarbon backbone.[93-95] Evidence of weak hydrogen bond-like interactions was also found in AIMD simulations on hydrates of trifluoromethanesulfonic acid (triflic acid): $CF_3SO_3H(H_2O)_n$ where n = 1,2,4, and 5.[87, 88] This was found to occur when a water molecule accepted a hydrogen bond from a triflic acid SO_3H group with a CF_3 group in the near vicinity in the absence of any other water molecules or triflic acid oxygen atoms to hydrogen bond with. Limited water was also determined to increase the formation of defect structures that included two triflic acid sulfonate groups sharing a single proton and proton transfer to a single water molecule that bridge multiple sulfonate groups. Furthermore, inclusion of quantum nuclear effects via path integral techniques was found to delocalize the proton defect which increased the Zundel character of the defect structure in each of the hydrates.[87]

Here, we present the results of an extension of our previous work[84-86] using AIMD to investigate the behaviour of mobile triflic acid and water confined in single-walled CNTs of various diameters water content of n = 1 – 3 H_2O/CF_3SO_3H. The impact of the nature of the confined environment on structural properties is investigated through functionalizing the nanotube walls with fluorine atoms. This paper is organized as follows. The systems and computational methodology are first described. This is followed by presentation and discussion of the results which include hydrogen bonding and coordination numbers, connectivity of the hydrogen bond network, proton dissociation and radial distribution functions, and interactions between the water molecules and fluorine atoms. Finally, important results are summarized in the conclusions section.

Computational Methods

Ab initio molecular dynamics simulations were performed using the Vienna *Ab Initio* Simulation Package (VASP).[96-99] Core electrons were treated using the projector-augmented-wave (PAW) method.[100, 101] The Perdew–Burke–Ernzerhof (PBE) generalized gradient approximation for the exchange-correlation functional was used,[102, 103] and the electronic subsystem was sampled at the Γ-point of the first Brillouin zone with a plane wave cutoff of 400 eV. CNTs with chirality (14,0) and (17,0) were chosen as encapsulation vessels for the water molecules and triflic acid. The inner walls of the CNTs were either left bare or fluorinated to model different hydrophobic environments. The fluorine atoms were added to every next nearest neighbour carbon atom as uniformly as possible. All of the systems were simulated at water contents of n = 1 – 3 H_2O/CF_3SO_3H. The total density of triflic acid and water within the CNTs was, as close as possible, the same for all systems. This was maintained by either using nanotubes of different lengths or slightly varying the CNT carbon–carbon bond length. As addition of fluorine atoms to the CNT wall effectively reduced the accessible volume, fewer triflic acid molecules were added in the fluorinated systems. Some relevant system parameters are given in Table 1. The nomenclature used to distinguish between the different CNT systems closely follows that

of the previous work:[84-86] 14 and 17 are used for the different CNT chirality followed by 'F' or 'N' for fluorinated and nonfluorinated, and 1, 2, or 3 to designate the hydration level. For example, the (14,0) CNT system with fluorinated walls at a water content of n = 2 would read 14F2. Representative images of the systems are shown in Figure 1. As with the previous studies,[84-86] the carbon atoms of the CNT wall and the attached fluorine atoms (when applicable) were held fixed, and periodic boundary conditions were imposed with 4 Å of vacuum added in the perpendicular directions to avoid interactions with other images in the supercell. The systems were initially relaxed to their minimum energy configuration and then annealed to 600 K via repeated velocity rescaling and then returned back down to 300 K. This was followed by 3 ps simulations in the canonical ensemble and 3 ps of microcanonical MD for equilibration which were discarded. Born–Oppenheimer AIMD trajectories of up to 30 ps were generated with a time step of 0.5 fs in the microcanonical ensemble for data analysis.

Results and Discussion

Several of the analyses that follow regard hydrogen bonding between the water molecules and triflic acid molecules. In this study, a hydrogen bond was taken to exist if the oxygen–oxygen separation was less than 3.25 Å with an H–O···O angle less than 30°.[104, 105] The coordination numbers (CN) for the water molecules is defined as the average number of donating and accepting hydrogen bonds per water molecule. Figure 2 shows the average water CN based on H_2O/H_2O hydrogen bonds, H_2O/CF_3SO_3H hydrogen bonds, and the total CN for each of the systems. It should be noted that at this stage, we refer to the CNs regarding water molecules and the triflic acid SO_3H groups for ease of discussion, but these also, respectively, encompass hydrogen bonds involving Zundel and hydronium ions and triflate ($CF_3SO_3^-$) anions and will not be distinguished unless necessary. Representative snapshots of the hydrogen bonding in each system for n = 1, 2, and 3 are shown in Figures 3, 4, and 5, respectively. At n = 1, the average total H_2O CN is approximately 2 in all cases but result from different contributions from H_2O/H_2O and H_2O/CF_3SO_3H hydrogen bonds in the different systems. In the bare nanotubes, which have a slightly higher total CN, hydrogen bonding between water molecules occurs while in the fluorinated CNTs the water molecules are isolated from each other. Typical configurations in the fluorinated systems involve a water molecule donating a hydrogen bond to a CF_3SO_3H and accepting a hydrogen bond from an adjacent one with no direct interactions between the acid molecules. In the smaller CNT, this is in the form of a highly aligned hydrogen bond wire (Figure 3b) while in the larger system the pattern is less uniform. Hydrogen bonding between triflic acid molecules in the bare systems occurs regularly which promotes interactions between the water molecules at this low water content. An increase in the number of hydrogen bonds between water molecules was observed in all systems upon increasing the hydration to n = 2. The total CN also increases in all cases except 14F2 which is approximately the same as that of the lower hydration level. The typical structure in this case exhibits somewhat selective solvation of a single CF_3SO_3H by three water molecules with

the other CF_3SO_3H oriented parallel to the CNT axis only involved in one hydrogen bond with a single water molecule (Figure 4b). The average total H_2O CNs in the bare systems are each ~2.5. In the smaller CNT, the contributions are essentially split between hydrogen bonds to and from water and triflic acid molecules. A greater proportion of hydrogen bonds in the larger tube occur between water molecules with slightly less than 1 hydrogen bond per water molecule to or from a CF_3SO_3H, on average, and generally one direct hydrogen bond between triflic acid molecules. The total CN in 17F2 of ~2.25 is slightly less than 17N2, but with nearly the same CN between water molecules. The typical hydrogen bond structure contains one direct hydrogen bond between triflic acid molecules with the H_2O hydrogen bonding among themselves as well as bridging the other triflic acid oxygen atoms through two or more water molecules. At n = 3, the average H_2O–CF_3SO_3H CNs for the smaller CNTs is ~1. In 14F3, this is a result of configurations where each H_2O donates one hydrogen bond to a triflic acid molecule. In 14N3, on the other hand, this arises due to typical configurations containing two or three water molecules not hydrogen bonded to any triflic acid SO_3H groups but multiple different water molecules involved in direct hydrogen bonds to two different CF_3SO_3H effectively bridging the triflic acid molecules. In 17F3, bridging of two triflic acid molecules through one H_2O occurred frequently as well as one triflate oxygen atom accepting hydrogen bonds from two different water molecules. It was not common to find water molecules isolated from the triflic acid molecules which results in the highest H_2O–CF_3SO_3H CN of all systems at this hydration level. The highest H_2O–H_2O CN and lowest H_2O–CF_3SO_3H CN at n = 3 were found in 17N3. This indicates that the water molecules are more clustered together with rare occurrence of a water molecule involved in hydrogen bonds with multiple triflic acid SO_3H groups. At all water contents, the larger bare CNT contained strong direct hydrogen bonds between triflic acid molecules with short O···O separations that hindered accessibility of water molecules to these sites.

Along with local hydrogen bonding between neighbouring water and triflic acid molecules, the hydrogen bond network connectivity throughout the entire system is important to proton dissociation and transfer in PEMs.[32] To analyse the connectivity, a similar, but not identical, procedure of previous studies was employed.[85-88, 106, 107] An undirected graph with oxygen atoms as nodes and hydrogen bonds involving two oxygen atoms as edges was used to generate an N x N adjacency matrix, A, at each time step (where N is the total number of oxygen atoms). If a hydrogen bond existed between oxygen atoms i and j, the corresponding matrix elements A_{ij} and A_{ji} were set to 1, otherwise the matrix elements were set to 0. This differs from some of the previous studies where a directed graph was used to obtain the adjacency matrix with elements equal to 1 for hydrogen bonds donated from i and accepted by j (i.e., $A_{ij} \neq A_{ji}$). In these studies the property of adjacency matrices that element $A_{ij}^{(m)}$ of A^m gives the number of unique walks with m edges from node i to node j. Although the directionality

of hydrogen bonds plays an important role in long range proton transport,[108] the aim here is to gain additional insight into the overall hydrogen bond network structure. If a directed graph was used to map the adjacency matrix in the present study, hydronium ions, which rarely accept hydrogen bonds in these simulations, can terminate a path and defining the donor and acceptor in perfectly symmetric sharing of a proton between oxygen atoms is ambiguous. Additionally, the powers of the adjacency matrix using an undirected graph result in unwanted direct revisiting of edges leading to fictitiously long chains. Hence, a slightly difference approach is used here. A simple depth-first search algorithm was used to determine the connectivity matrix, C, whose elements C_{ij} and C_{ji} are 1 if a path of any length connected atoms i and j and 0 otherwise. This allowed for the decomposition of the entire hydrogen bond network into isolated subnetworks. Within each subnetwork a recursive branching algorithm was used to calculate the length (determined by the number of oxygen atoms) of all the chains longer than 2 that did not include a complete ring, though individual oxygen atoms that were part of a ring were initially allowed. The longest chain from each subnetwork was extracted for analysis (i.e., no chains that were branches off of the longest chain were included). All rings that did not include smaller rings were included. Further analysis was performed when rings were present by setting all elements of A_{ij} that were part of a ring to 0 and repeating the process to separate networks of rings and chains. The connectivity results are presented in Table 2 and Figures 6, 7, and 8. Snapshots of rings in systems where ring formation occurred at least 10% of the time are shown in Figures S1 and S2.

Figure 6 shows the average number of chains in each system with and without the inclusion of ring connections normalized by the number of triflic acid molecules. The rationale behind the normalization becomes evident when comparing the data at n = 1. As previously mentioned, the water molecules in the fluorinated systems at this hydration level are isolated from each other and generally form a hydrogen bond bridge between two CF_3SO_3H. The average number of chains is then dependent on and approximately determined by the number of triflic acid molecules (2 for 14F1 and 3 for 17F1). Thus, the normalization allows for a more direct comparison between systems showing approximately one chain per CF_3SO_3H in each fluorinated CNT which indicates isolated hydrogen bond networks (note that small values here indicate increased connectivity throughout the system). In the bare CNTs, the water molecules are not isolated and multiple triflic acid molecules can be bridged through multiple H_2O. This is also reflected in the average chain lengths shown in Figure 7 where the average number of water molecules in the chains is greater in the bare CNTs than in the fluorinated tubes. While the maximum length of a chain that can be formed is limited by the number of triflic acid and water molecules, the data shown for the chain length has not been normalized by the number of CF_3SO_3H for convenience of discussion and is partitioned into the type of oxygen atoms involved in the chain. The fraction of total oxygen atoms in the system per chain is also shown as a frame of reference. When the longest chain within a subnetwork terminated in a branch to both a triflic acid and water oxygen atom

(i.e., two chains with the same length but different terminating oxygen atoms) the contribution from these particular oxygen atoms to the length of the chain was divided evenly to avoid bias in the results. As no rings were observed in the fluorinated systems and were exceedingly rare in the bare tubes at this level of hydration, the results are not affected by omitting ring connections.

The average length of the chains in each system, as well as the contribution from oxygen atoms from water molecules, generally increases with increasing hydration as expected. The number of chains, however, shows less of an obvious trend. At n = 2 and 3, the number of chains per CF_3SO_3H in the smaller fluorinated tube remains equal to one indicating that the water molecules are still in separated clusters (Figures 4b and 5b) while a slight decrease in value was observed in the smaller bare tube due to increased connectivity throughout the system. Negligible ring formation was found in either of the smaller CNTs at n = 2. However, at n = 3, rings were frequently found in 14N3 with an average of 0.53 rings in the system, as shown in Figure 8a. Note that the average number of rings is not normalized because typically only one ring was present at a time in each system, with a few exceptions, so this number also gives a very close approximation to the fraction of time ring formation was observed. Omitting ring connections in 14N3 resulted in a slight drop in the number of chains and a considerable drop in the average chain length to approximately the value found at n = 2 which contains the same number of triflic acid molecules but fewer H_2O. The ring generally had the same form when present in the simulation which contained one triflate oxygen atom accepting two hydrogen bonds: one from a hydronium ion that also hydrogen bonded to a different CF_3SO_3H and the other from a neighbouring species that regularly transitioned between H_2O, H_3O^+, and $H_5O_2^+$ states (Figure S2a). Ring formation was found in each of the larger CNT systems at both n = 2 and 3 which also involved a single triflate oxygen atom receiving two hydrogen bonds from different water molecules. As previously mentioned, each of the larger systems at n = 2 contain a direct hydrogen bond between triflic acid molecules, which appears to promote ring formation at this water content. The hydrogen bonding in 17F2 has the water molecules clustered between the triflic acid molecules bridging the two together (Figure 4d) resulting in only one chain (0.5 per CF_3SO_3H in every step) when ring connections are allowed. However, the cluster forms a ring throughout approximately 26% of the trajectory, and with this hydrogen bond topography and minimal water, chains and rings do not independently exist simultaneously (Figure S1b). As such, when the oxygen atoms involved in rings are removed from the analysis, the average number of chains decreases accordingly to ~0.74 (0.34 per CF_3SO_3H) but the average chain length is negligibly impacted. The opposite was found for 17N2, which had the fewest chains per CF_3SO_3H of all systems at all hydration levels with a highly connected hydrogen bond network containing several triflate oxygen atoms accepting multiple hydrogen bonds when rings were present. Similar to 14N3, the removal of ring connections disrupts overall connectivity of the longest chain throughout the

system, but the high degree of branching in the hydrogen bond network leads to only a slight decrease in the average number of chains but with shorter lengths (Figure S1a).

The hydrogen bond networks in the larger tubes at n = 3 are well connected with fairly long chains encompassing approximately 50 and 69% of all the oxygen atoms per chain in 17F3 and 17N3, respectively, when ring connections were included. However, rings are, again, fairly common and distinctly different ring structures were commonly found in both systems. The majority of the rings in 17N3 contained one triflate oxygen atom and three or four H_2O/H_3O^+ (Figure S2b top) with two such rings occurring at the same time in ~3% of the simulation. However, in roughly 10% of the simulation rings with lengths of 9 or 10 oxygen atoms were observed that that encompassed nearly all of the water molecules (Figure S2b bottom). This led to the increase in average ring length and decrease in average number of chains when ring connections were removed while the smaller five-membered rings were responsible for the decrease in the average length of chains as with 17N2. There was less variability in the size of rings formed in 17F3 where 80% of the rings contained one triflate oxygen atom and three water molecules while the other 20% had two oxygen atoms of the same $CF_3SO_3^-$ accepting two hydrogen bonds surrounded by three H_2O/H_3O^+ on each side (Figure S2c) giving an average ring size of 4.8 oxygen atoms. The same reasoning for decreases in the number of chains and the length of chains as 17N3 when ring connections are removed can be applied to 17F3. Interestingly, the high hydrogen bond connectivity in the larger fluorinated tube occurred even though the water molecules were found in separate clusters between triflic acid/triflate molecules. Throughout the trajectory the water and triflic acid molecules were ordered in a regular fashion in what appears to be a domain mostly separated from the triflic acid CF_3 groups, shown in Figure 9, which was not observed in any other system at this hydration level. Unlike 14F3, which contained isolated water clusters that mostly formed hydrogen bonds with the triflic acid sulfonate groups from the side, water molecules in the larger fluorinated CNT were able to form hydrogen bonds from both the sides and below the triflic acid sulfonate groups due to the increased space which leads to a more uniform solvation structure. Although the overall connectivity is high, the water molecules in the clusters separated by the triflate anions in 17F3 do not interact while those in 17N3 form a well-connected channel which may impact long-range proton transfer at this hydration level.

Proton dissociation in hydrated PEMs is also known to depend on the water content. In our analysis we define five different states for the acidic protons based on the 'most active hydrogen bond' associated with each site. All protons were first assigned to their nearest neighbour oxygen atom, and the oxygen sites with either one or three nearest neighbour hydrogen atoms were located. The values of the asymmetric stretch coordinate, $\delta = R_{O_aH} - R_{O_dH}$, were then determined for each hydrogen bond associated with the oxygen atom, where R_{O_aH} and R_{O_dH} are the distances from a given

hydrogen atom to the acceptor and donor oxygen atoms in the hydrogen bond, respectively. If the nearest neighbour oxygen atom was from a triflic acid molecule, it was considered in the analysis; otherwise, the hydrogen bond with the smallest δ was used to determine the state of the proton. A proton was said to be bound if its nearest neighbour was an oxygen atom of a triflic acid molecule with $\delta \geq 0.2$ Å. If any pair had $\delta < 0.2$ Å, it was assigned one of three shared states according to the types of the oxygen atoms involved: CF_3SO_3H/CF_3SO_3H shared, CF_3SO_3H/H_2O shared, or H_2O/H_2O shared (i.e., a Zundel cation). It should be noted that the shared states between triflic acid molecules also includes sharing between triflic acid and triflate molecules, which is more commonly observed. Lastly, a hydronium (H_3O^+) state was assigned when a non-triflic acid oxygen atom had three proton neighbours with the smallest $\delta \geq 0.2$ Å. The results of the analysis for each system at all hydration levels are shown in Figure 10.

As expected, proton dissociation increases with increasing water content. At n = 1, approximately 40% dissociation was observed in the bare CNTs while in the fluorinated systems the percent dissociation was less than 20%. As mentioned earlier, each of the bare CNTs contain instances of sharing a proton between triflic acid/triflate molecules as well as interactions between water molecules, which was not observed in the fluorinated CNTs, which likely leads to the increased dissociation and the presence of Zundel cations. In 17N1, two different triflic acid molecules form direct hydrogen bonds with one triflate anion, each of which is typically in the bound state. This leads to dissociation of the proton originally associated with the triflate group forming a contact ion pair (CIP). These observations are also supported by the radial distribution function (RDF) between the triflic acid/triflate oxygen atoms and the protons shown in Figure 11a. The 17N1 RDF has the narrowest first peak of all the systems arising from the two bound protons but is followed by a clear minimum indicating less sharing of protons between triflic acid and water molecules. The first peak in the 14N1 RDF, on the other hand, is broader and occurs at a farther distance which is followed by a ridge revealing a greater tendency for sharing of protons both between triflic acid molecules and triflic acid and water molecules. In the fluorinated tubes, the first peak is shifted even farther but the distances between ~1.35-1.55 Å are less pronounced than in the bare systems suggesting that the protons are loosely bound but not fully dissociated with a much larger portion of the observed states as sharing between H_2O and CF_3SO_3H.

Increasing the hydration to n = 2 expectedly increased the degree of dissociation in all systems as well as the Zundel character of the dissociated protons. Surprisingly, ~86% dissociation was observed in 14N2 with less than 1% bound states observed, while between 45 and 55% dissociation was observed in the other systems. At this hydration level the H_2O/CF_3SO_3H CN was the highest in 14N2 and was the only system in which this CN was higher than that between water molecules (Figure 2b) indicating that the water molecules and solvated protons have a greater propensity to hydrogen bond

with multiple triflic acid molecules. As mentioned in the Introduction section that although electronic structure calculations on isolated PFSA fragments have revealed that proton dissociation may not occur at this low water content,[67, 68, 109] incorporation of multiple PFSA side chains enhances proton dissociation at low hydration levels through cooperative interactions between sulfonic acid groups and connectivity through a single water molecule.[42, 75-77, 79, 80] In each of the larger tubes, direct hydrogen bonding between triflic acid molecules lead to larger amounts of bound and shared CF_3SO_3H/CF_3SO_3H states. The dissociated proton(s), however, had greater separation from the triflic acid/triflate oxygen atoms than in 14N2 as shown in the RDF (Figure 11b) with very little instances of shared CF_3SO_3H/H_2O states. These states were quite frequent in 14F2, on the other hand, which exhibited the lowest dissociation but fewer bound states than in the larger tube. As mentioned earlier, the hydrogen bonding in this system exhibited somewhat selective solvation of one of the triflic acid molecules whose proton was generally in a dissociated state while the other acidic proton mostly rattled between triflic acid and water molecule oxygen atoms leading to a broader first peak in the RDF than in the larger systems again indicating that the protons are loosely bound but do not fully separate from the triflic acid groups. Further increasing the water content to n = 3 leads to near complete dissociation in all systems except the larger bare nanotube. Again, a hydrogen bond between triflic acid and triflate molecules led to a greater amount of bound and shared CF_3SO_3H/CF_3SO_3H states and decreases the overall proportion of dissociated protons. The average CN between water molecules and triflic acid oxygen atoms was the lowest and that between water molecules was the highest in 17N3 indicating a preference for interactions between water molecules. Indeed, hydrogen bonding from the water molecules to the oxygen atoms of the directly hydrogen bonded triflic acid/triflate molecules occurred but with average O···O and O···H distances of 2.81 and 1.87 Å, respectively, indicating weak hydrogen bonds as compared to that between water molecules which had respective distances of 2.61 and 1.58 Å. In fact, all hydrogen bonds between triflic acid/triflate and water molecules here were relatively weak when compared to the other systems as indicated in the probability distribution of δ for all O–H···O_s hydrogen bonds between the triflate and water molecules shown in Figure 12 which contains no values of $\delta \geq$ -0.3 Å with a peak at approximately -0.8 Å. Note that since all protons are dissociated aside from the one involved in the direct hydrogen bond in 17N3 and very few observed instances of CF_3SO_3H/H_2O sharing in the other systems, the distribution shown always has water molecules/solvated protons as the hydrogen bond donor in the definition of δ. The dissociated protons in 17N3 were, thus, found have the greatest separation from the triflic acid oxygen atoms (which is also reflected in the RDF of Figure 11c) and over 80% of the time at least one proton was in the solvent-separated ion pair position donating hydrogen bonds to three water molecules resembling an Eigen cation. This was also found for one proton ~60% of the time in 14N3 but the system contained several single water molecules connecting two triflic acid molecules and the other

dissociated protons remained more tightly bound as contact ion pairs. No complete separation of the protons from the triflate oxygen atoms was observed in either of the fluorinated CNTs.

Finally, we examine potential interactions between the water molecules and solvated protons with the fluorine atoms. As mentioned in the Introduction section, AIMD simulations on model PFSA systems have reported evidence of weak water–fluorine interactions to some extent similar to hydrogen bonds, though longer. Although the nature of the interactions are not entirely clear, we examine them here as weak hydrogen bonds. While the geometric criteria for weak hydrogen bonds typically allows for a wide range of hydrogen bond angles,[110] the angular cutoff in the analysis was not relaxed from that used in the hydrogen bond analysis of triflic acid and water. The hydrogen bond distance cutoff, however, was taken as an H···F length less than 2.5 Å which is slightly longer than the second minimum of the H···O RDF in bulk water of ~2.46 Å.[111] It should be noted that changing the hydrogen bond criteria did not significantly impact the results. The hydrogen bond was required to exist for longer than 5 fs to be considered in the analysis to prevent transient motions of the water molecules from affecting the results. However, if the hydrogen bond hopped between neighbouring fluorine atoms while maintaining the geometric criteria, it was still included in the determined number of O–H···F hydrogen bonds. In the bare CNTs, the only potential hydrogen bond accepting fluorine atoms come from the mobile CF_3SO_3H while in the fluorinated systems there are also the sites bound to the inner walls of the nanotube. No hydrogen bonding between a CF_3SO_3H sulfonic acid group and a fluorine atom was observed in any system, so the discussion is restricted to water molecules and solvated protons. The results for the fluorinated and bare systems are summarized in Tables 3 and 4, respectively, and Figure 13 shows the type of species involved in O–H···F hydrogen bonds. The O–H···F hydrogen bonding between water molecules and the triflic acid CF_3 groups had short lifetimes and were typically not found for multiple water molecules at any given time. In the fluorinated CNTs, these interactions were relatively rare with the most observed in 14F2 which occurred 9.2% of the time. This is likely due to the isolated water molecules and the orientation of one of the triflic acid groups (Figure 4b) leading to a lack of other available hydrogen bond acceptor sites. There was generally a greater propensity for O–H···F hydrogen bonding to the CF_3 groups in the bare CNT systems. No clear trend between the frequency of these interactions and the hydration level was found in the smaller bare tube, while in the larger system the amount of time they existed increased with hydration. One common feature observed is that all bare CNT systems that exhibited these interactions more than 15% of the time contained a direct hydrogen bond between triflic acid molecules which blocked available oxygen atoms from accepting hydrogen bonds (Figure S3). The percentage of time these O–H···F hydrogen bonds were observed in all systems is considerably higher than what was observed in our previous studies involving the CF_2 groups of CNTs functionalized with $–CF_2SO_3H$ groups[84-86]

suggesting that the additional mobility of the triflic acid groups in the present study may have an influence on these interactions.

Interactions between water and the fluorine atoms of the CNT wall were much more common than the fluorine atoms of triflic acid in the fluorinated systems, and the percent of the time at least one such O–H···F hydrogen bond existed increased as the hydration level increased with greater frequency in the smaller CNT. Representative snapshots of these interactions at all water contents are shown for the smaller and larger tubes in Figures S4 and S5, respectively. At n = 1, these were observed slightly over 60% of the time in each system with the majority of the interactions expectedly coming from water molecules in the H_2O/CF_3SO_3H shared state as it was the most prevalent at this hydration level. The previously discussed hydrogen bond topography and isolation between water molecules at this low level of hydration generally leaves multiple OH bonds not involved in a hydrogen bond with a triflic acid $–SO_3H$ group (or other water molecules) leaving them open to interact with the fluorinated walls. The average H···F and O···F distances were approximately 2.24 and 3.13 Å in each case (which was approximately the same at all hydration levels) but the average lifetimes were found to be over twice as long in the smaller CNT. Nearly all occurrences of proton dissociation as a hydronium ion in 14F1 and the majority of those in 17F1 were accompanied by an O–H···F hydrogen bond indicating the fluorine atoms might provide a means to stabilize the excess charge. As the hydration level increases, the impact of the confinement dimensions on these interactions becomes more pronounced with at least one O–H···F bond occurring 91.5 and 99.1% of the time in the smaller CNT at n = 2 and 3, respectively, compared to 68.8 and 83.3% in the larger diameter tube. The majority of the observed Zundel states and over 60% of the H_3O^+ states in 14F2 were involved in hydrogen bond interactions with the fluorinated walls which is again likely due to the absence of neighbouring stabilizing hydrogen bond accepting oxygen sites from other water or triflic acid molecules. In 17F2, however, most of these interactions involved water molecules as the protonated cations, particularly H_3O^+, were typically found to hydrogen bond with other surrounding water or triflic acid molecules as indicated by the higher average total CN than 14F2 (Figure 2b). This was observed in both systems at n = 3 where more available hydrogen bond acceptor sites from water molecules promoted interactions that delocalized the excess charge over strong hydrogen bonds with neighbouring water molecules or triflate anions.

Conclusions

Single-walled CNTs of various diameter with different surface hydrophobicity were used as encapsulation vessels for mobile triflic acid groups at water contents of n = 1 – 3 H_2O/CF_3SO_3H to investigate proton dissociation and transfer at low water content in a confined environment. Each of the different systems exhibited distinctly different hydrogen bonding between water and triflic acid molecules. At the lowest hydration level, the H_2O in the fluorinated CNTs were completely isolated from one another typically forming two hydrogen bonds with neighbouring CF_3SO_3H. This led to a

propensity for the acidic protons to be shared between water and triflic acid molecules with dissociation occurring less than 20% of the time as a hydronium ion where, in each case, interactions with the fluorinated CNT walls appear to stabilize the hydrogen bond network. Direct hydrogen bonding between triflic acid molecules in the bare CNTs at n = 1 promoted interactions between water molecules and enhanced proton dissociation. Triflic acid hydrogen bond connectivity, both directly and through a single water molecule, had a continued effect on proton dissociation at higher hydration levels. This was most pronounced in 14N2 which had several single water molecules/solvated protons bridging two triflic acid molecules through hydrogen bonds and exhibited the highest proton dissociation at this hydration level. However, this also led to multiple protons being trapped between the triflate anions with less interaction between water molecules that promotes separation of the dissociated protons from the acid groups necessary for long-range proton transport. The greatest separation of dissociated protons was found in 17N3 but at the cost of a lower overall degree of dissociation due to direct hydrogen bonding between triflic acid/triflate molecules. This also led to strong interactions between water molecules which were able to form long chains that encompassed nearly all the water molecules in the system. These direct hydrogen bonds between the acid groups were observed at all hydration levels in the larger bare CNT resulting in the highest observed CNs between water molecules at each hydration level. This may be due to the additional free volume allowing for more orientational freedom for the mobile triflic acid molecules to form strong hydrogen bonds with a triflate anion upon dissociation to stabilize the charge. Weak hydrogen bonding between the water molecules and CF_3 groups was observed in all systems when open oxygen sites were not in the vicinity. This was particularly observed in the bare CNT systems that contained direct hydrogen bonds between the acid groups, which reduced the number of available hydrogen bond acceptor sites, and short-lived OH···F interactions appeared to provide some stabilization to the hydrogen bond network. Hydrogen bonding to the fluorinated walls (when present) occurred much more frequently than to the triflic acid fluorine atoms. In both systems, the frequency of these interactions increased with increasing hydration and to a greater extent in the smaller fluorinated CNT indicating an influence of the confinement dimensions. Unlike our previous work,[84-86] the fluorine atoms did not appear to promote any particular state of the dissociated protons over those observed in the bare CNTs, aside from those at n = 1 where the isolated water molecules could not form Zundel cations. However, at n = 3, each of the bare CNT systems contained protons in the solvent-separated ion pair position surrounded by three water molecules as an Eigen cation. This was not observed in the fluorinated tubes due to the clustering of water molecules and the lack of mobility induced by the confinement dimensions and potential stabilization from the large number of OH···F interactions resulting in a fairly regular structure. It should be noted that the studies on hydrates of triflic acid[87, 88] revealed that inclusion of quantum nuclear effects through *ab initio* path integral techniques enhances the Zundel

character. As these effects are absent in the present simulations, and the systems used are highly simplified models, the results presented here should not be taken as absolute values but as a relative comparison of how the confinement dimensions and surface hydrophobicity affect hydrogen bonding and proton dissociation.

References

1. B. Smitha, S. Sridhar and A. A. Khan, *J. Membr. Sci.*, 2005, **259**, 10-26.
2. A. B. Stambouli and E. Traversa, *Renew. Sust. Energ. Rev.*, 2002, **6**, 295-304.
3. M. Granovskii, I. Dincer and M. A. Rosen, *Int. J. Hydrogen. Energ.*, 2006, **31**, 337-352.
4. K. D. Kreuer, S. J. Paddison, E. Spohr and M. Schuster, *Chem. Rev.*, 2004, **104**, 4637-4678.
5. O. Savadogo, *J. Power Sources*, 2004, **127**, 135-161.
6. M. A. Hickner, H. Ghassemi, Y. S. Kim, B. R. Einsla and J. E. McGrath, *Chem. Rev.*, 2004, **104**, 4587-4611.
7. Y. Y. Shao, G. P. Yin, Z. B. Wang and Y. Z. Gao, *J. Power Sources*, 2007, **167**, 235-242.
8. K. D. Kreuer, *ChemPhysChem*, 2002, **3**, 771-775.
9. K. D. Kreuer, *Solid State Ionics*, 1997, **97**, 1-15.
10. M. Ise, K. D. Kreuer and J. Maier, *Solid State Ionics*, 1999, **125**, 213-223.
11. K. D. Kreuer, *J. Membr. Sci.*, 2001, **185**, 29-39.
12. C. Yang, P. Costamagna, S. Srinivasan, J. Benziger and A. B. Bocarsly, *J. Power Sources*, 2001, **103**, 1-9.
13. L. Rubatat, A. L. Rollet, G. Gebel and O. Diat, *Macromolecules*, 2002, **35**, 4050-4055.
14. C. J. D. von Grotthuss, *Ann. Chim.*, 1806, **58**, 54-74.
15. M. Eikerling, A. A. Kornyshev, A. M. Kuznetsov, J. Ulstrup and S. Walbran, *J. Phys. Chem. B*, 2001, **105**, 3646-3662.
16. S. J. Paddison and R. Paul, *Phys. Chem. Chem. Phys.*, 2002, **4**, 1158-1163.
17. S. J. Paddison, R. Paul and K. D. Kreuer, *Phys. Chem. Chem. Phys.*, 2002, **4**, 1151-1157.
18. E. Spohr, P. Commer and A. A. Kornyshev, *J. Phys. Chem. B*, 2002, **106**, 10560-10569.
19. D. Marx, M. E. Tuckerman, J. Hutter and M. Parrinello, *Nature*, 1999, **397**, 601-604.
20. D. Marx, A. Chandra and M. E. Tuckerman, *Chem. Rev.*, 2010, **110**, 2174-2216.
21. N. Agmon, *Chem. Phys. Lett.*, 1995, **244**, 456-462.
22. M. E. Tuckerman, K. Laasonen, M. Sprik and M. Parrinello, *J. Phys. Chem.*, 1995, **99**, 5749-5752.
23. M. E. Tuckerman, K. Laasonen, M. Sprik and M. Parrinello, *J. Chem. Phys.*, 1995, **103**, 150-161.
24. H. Lapid, N. Agmon, M. K. Petersen and G. A. Voth, *J. Chem. Phys.*, 2005, **122**, 014506.
25. A. Chandra, M. E. Tuckerman and D. Marx, *Phys. Rev. Lett.*, 2007, **99**.
26. Z. Cao, Y. X. Peng, T. Y. Yan, S. Li, A. L. Li and G. A. Voth, *J. Am. Chem. Soc.*, 2010, **132**, 11395-11397.
27. J. C. Rasaiah, S. Garde and G. Hummer, *Annu. Rev. Phys. Chem.*, 2008, **59**, 713-740.
28. C. Dellago, M. M. Naor and G. Hummer, *Phys. Rev. Lett.*, 2003, **90**, 105902.
29. J. Kofinger, G. Hummer and C. Dellago, *Phys. Chem. Chem. Phys.*, 2011, **13**, 15403-15417.
30. J. Chen, X. Z. Li, Q. F. Zhang, A. Michaelides and E. G. Wang, *Phys. Chem. Chem. Phys.*, 2013, **15**, 6344-6349.
31. M. L. Brewer, U. W. Schmitt and G. A. Voth, *Biophys. J.*, 2001, **80**, 1691-1702.
32. S. J. Paddison, *Annu. Rev. Mater. Res.*, 2003, **33**, 289-319.
33. H. L. Lin, T. L. Yu, C. H. Huang and T. L. Lin, *J. Polym. Sci., Part B: Polym. Phys.*, 2005, **43**, 3044-3057.
34. C. H. Ma, T. L. Yu, H. L. Lin, Y. T. Huang, Y. L. Chen, U. S. Jeng, Y. H. Lai and Y. S. Sun, *Polymer*, 2009, **50**, 1764-1777.
35. G. Gebel and O. Diat, *Fuel Cells*, 2005, **5**, 261-276.
36. H. G. Haubold, T. Vad, H. Jungbluth and P. Hiller, *Electrochim. Acta*, 2001, **46**, 1559-1563.
37. W. Y. Hsu and T. D. Gierke, *J. Membr. Sci.*, 1983, **13**, 307-326.
38. K. A. Mauritz and R. B. Moore, *Chem. Rev.*, 2004, **104**, 4535-4585.
39. K. Schmidt-Rohr and Q. Chen, *Nature Mater.*, 2008, **7**, 75-83.
40. D.-S. Wu, S. J. Paddison and J. A. Elliott, *Energy Environ. Sci.*, 2008, **1**, 284-293.
41. G. Gebel, *Polymer*, 2000, **41**, 5829-5838.
42. J. A. Elliott and S. J. Paddison, *Phys. Chem. Chem. Phys.*, 2007, **9**, 2602-2618.
43. S. Yamamoto and S. A. Hyodo, *Polym. J.*, 2003, **35**, 519-527.

44. D. S. Wu, S. J. Paddison and J. A. Elliott, *Macromolecules*, 2009, **42**, 3358-3367.
45. D. S. Wu, S. J. Paddison, J. A. Elliott and S. J. Hamrock, *Langmuir*, 2010, **26**, 14308-14315.
46. A. Vishnyakov and A. V. Neimark, *J. Phys. Chem. B*, 2000, **104**, 4471-4478.
47. S. Urata, J. Irisawa, A. Takada, W. Shinoda, S. Tsuzuki and M. Mikami, *J. Phys. Chem. B*, 2005, **109**, 4269-4278.
48. S. S. Jang, V. Molinero, T. Cagin and W. A. Goddard, *J. Phys. Chem. B*, 2004, **108**, 3149-3157.
49. N. P. Blake, G. Mills and H. Metiu, *J. Phys. Chem. B*, 2007, **111**, 2490-2494.
50. I. H. Hristov, S. J. Paddison and R. Paul, *J. Phys. Chem. B*, 2008, **112**, 2937-2949.
51. T. J. F. Day, A. V. Soudackov, M. Cuma, U. W. Schmitt and G. A. Voth, *J. Chem. Phys.*, 2002, **117**, 5839-5849.
52. F. Wang and G. A. Voth, *J. Chem. Phys.*, 2005, **122**, 144105.
53. M. K. Petersen, F. Wang, N. P. Blake, H. Metiu and G. A. Voth, *J. Phys. Chem. B*, 2005, **109**, 3727-3730.
54. Y. J. Wu, H. N. Chen, F. Wang, F. Paesani and G. A. Voth, *J. Phys. Chem. B*, 2008, **112**, 467-482.
55. M. K. Petersen and G. A. Voth, *J. Phys. Chem. B*, 2006, **110**, 18594-18600.
56. E. Spohr, *Mol. Sim.*, 2004, **30**, 107-115.
57. P. Commer, C. Hartnig, D. Seeliger and E. Spohr, *Mol. Sim.*, 2004, **30**, 755-763.
58. D. Seeliger, C. Hartnig and E. Spohr, *Electrochim. Acta*, 2005, **50**, 4234-4240.
59. S. Dokmaisrijan and E. Spohr, *J. Mol. Liq.*, 2006, **129**, 92-100.
60. M. H. Eikerling and K. Malek, in *Modern Aspects of Electrochemistry, No 43*, ed. M. Schlesinger, 2009, DOI: 10.1007/978-0-387-49582-8_5, pp. 169-247.
61. S. J. Paddison, L. R. Pratt, T. Zawodzinski and D. W. Reagor, *Fluid Phase Equilib.*, 1998, **151**, 235-243.
62. S. J. Paddison and T. A. Zawodzinski Jr, *Solid State Ionics*, 1998, **113-115**, 333-340.
63. S. J. Paddison, L. R. Pratt and T. A. Zawodzinski, *J. New Mater. Electrochem. Sys.*, 1999, **2**, 183-188.
64. V. A. Glezakou, M. Dupuis and C. J. Mundy, *Phys. Chem. Chem. Phys.*, 2007, **9**, 5752-5760.
65. K. Sagarik, M. Phonyiem, C. Lao-Ngam and S. Chaiwongwattana, *Phys. Chem. Chem. Phys.*, 2008, **10**, 2098-2112.
66. M. Phonyiem, S. Chaiwongwattana, C. Lao-ngam and K. Sagarik, *Phys. Chem. Chem. Phys.*, 2011, **13**, 10923-10939.
67. C. Wang, J. K. Clark, M. Kumar and S. J. Paddison, *Solid State Ionics*, 2011, **199**, 6-13.
68. J. K. Clark, S. J. Paddison, M. Eikerling, M. Dupuis and T. A. Zawodzinski, *J. Phys. Chem. A*, 2012, **116**, 1801-1813.
69. M. Eikerling, S. J. Paddison and T. A. Zawodzinski, *J. New. Mat. Electr. Sys.*, 2002, **5**, 15-23.
70. S. J. Paddison, K. D. Kreuer and J. Maier, *Phys. Chem. Chem. Phys.*, 2006, **8**, 4530-4542.
71. C. Wang and S. J. Paddison, *Phys. Chem. Chem. Phys.*, 2010, **12**, 970-981.
72. L. Vilčiauskas, S. J. Paddison and K. D. Kreuer, *J. Phys. Chem. A*, 2009, **113**, 9193-9201.
73. S. Urata, J. Irisawa, A. Takada, S. Tsuzuki, W. Shinoda and M. Mikami, *Phys. Chem. Chem. Phys.*, 2004, **6**, 3325-3332.
74. J. K. Clark II and S. J. Paddison, *Electrochim. Acta*, 2013, **101**, 279-292.
75. S. J. Paddison and J. A. Elliott, *J. Phys. Chem. A*, 2005, **109**, 7583-7593.
76. S. J. Paddison and J. A. Elliott, *Solid State Ionics*, 2006, **177**, 2385-2390.
77. S. J. Paddison and J. A. Elliott, *Phys. Chem. Chem. Phys.*, 2006, **8**, 2193-2203.
78. S. J. Paddison and J. A. Elliott, *Solid State Ionics*, 2007, **178**, 561-567.
79. J. K. Clark and S. J. Paddison, *Solid State Ionics*, 2012, **213**, 83-91.
80. J. K. Clark II, S. J. Paddison and S. J. Hamrock, *Phys. Chem. Chem. Phys.*, 2012, **14**, 16349-16359.
81. M. Eikerling, S. J. Paddison, L. R. Pratt and T. A. Zawodzinski, *Chem. Phys. Lett.*, 2003, **368**, 108-114.
82. Y. K. Choe, E. Tsuchida, T. Ikeshoji, S. Yamakawa and S. Hyodo, *J. Phys. Chem. B*, 2008, **112**, 11586-11594.
83. Y. K. Choe, E. Tsuchida, T. Ikeshoji, S. Yamakawa and S. Hyodo, *Phys. Chem. Chem. Phys.*, 2009, **11**, 3892-3899.

84. B. F. Habenicht, S. J. Paddison and M. E. Tuckerman, *Phys. Chem. Chem. Phys.*, 2010, **12**, 8728-8732.
85. B. F. Habenicht, S. J. Paddison and M. E. Tuckerman, *J. Mater. Chem.*, 2010, **20**, 6342-6351.
86. B. F. Habenicht and S. J. Paddison, *J. Phys. Chem. B*, 2011, **115**, 10826-10835.
87. R. L. Hayes, S. J. Paddison and M. E. Tuckerman, *J. Phys. Chem. B*, 2009, **113**, 16574-16589.
88. R. L. Hayes, S. J. Paddison and M. E. Tuckerman, *J. Phys. Chem. A*, 2011, **115**, 6112-6124.
89. A. Roudgar, S. P. Narasimachary and M. Eikerling, *J. Phys. Chem. B*, 2006, **110**, 20469-20477.
90. A. Roudgar, S. P. Narasimachary and M. Eikerling, *Chem. Phys. Lett.*, 2008, **457**, 337-341.
91. S. R. Narasimachary, A. Roudgar and M. Eikerling, *Electrochim. Acta*, 2008, **53**, 6920-6927.
92. M. A. Ilhan and E. Spohr, *J. Phys.: Condens. Matter*, 2011, **23**, 234104.
93. M. Falk, *Canad. J. Chem.*, 1980, **58**, 1495.
94. R. Basnayake, G. R. Peterson, D. J. Casadonte and C. Korzeniewski, *J. Phys. Chem. B*, 2006, **110**, 23938-23943.
95. D. E. Moilanen, I. R. Piletic and M. D. Fayer, *J. Phys. Chem. A*, 2006, **110**, 9084-9088.
96. G. Kresse and J. Hafner, *Phys. Rev. B*, 1993, **47**, 558-561.
97. G. Kresse and J. Hafner, *Phys. Rev. B*, 1994, **49**, 14251-14269.
98. G. Kresse and J. Furthmuller, *Phys. Rev. B*, 1996, **54**, 11169-11186.
99. G. Kresse and J. Furthmuller, *Comput. Mater. Sci.*, 1996, **6**, 15-50.
100. P. E. Blochl, *Phys. Rev. B*, 1994, **50**, 17953-17979.
101. G. Kresse and D. Joubert, *Phys. Rev. B*, 1999, **59**, 1758-1775.
102. J. P. Perdew, K. Burke and M. Ernzerhof, *Phys. Rev. Lett.*, 1996, **77**, 3865-3868.
103. J. P. Perdew, K. Burke and M. Ernzerhof, *Phys. Rev. Lett.*, 1997, **78**, 1396-1396.
104. D. Laage and J. T. Hynes, *Science*, 2006, **311**, 832-835.
105. R. Kumar, J. R. Schmidt and J. L. Skinner, *J. Chem. Phys.*, 2007, **126**, 204107.
106. B. C. Wood and N. Marzari, *Phys. Rev. B*, 2007, **76**.
107. L. Vilčiauskas, M. E. Tuckerman, G. Bester, S. J. Paddison and K. D. Kreuer, *Nature Chemistry*, 2012, **4**, 461-466.
108. A. Hassanali, F. Giberti, J. Cuny, T. D. Kuhne and M. Parrinello, *Proc. Nat. Acad. Sci. USA*, 2013, **110**, 13723-13728.
109. S. J. Paddison, *J. New. Mat. Electr. Sys.*, 2001, **4**, 197-207.
110. T. Steiner, *Angew. Chem. Int. Ed.*, 2002, **41**, 48-76.
111. A. K. Soper, *ISRN Physical Chemistry*, 2013, **2013**, 67.

Table 1. System parameters

System	Diameter (Å)†	Length (Å)	# H_2O	# CF_3SO_3H
14N1	11.3	13.1	3	3
14N2	11.6	13.5	6	3
14N3	11.0	17.1	9	3
14F1	11.6 (8.9)	13.5	2	2
14F2	11.1 (8.4)	17.3	4	2
14F3	11.4 (8.7)	17.8	6	2
17N1	13.3	12.8	4	4
17N2	13.9	13.3	8	4
17N3	13.3	12.8	9	3
17F1	13.9 (11.2)	13.3	3	3
17F2	13.2 (10.5)	12.7	4	2
17F3	13.3 (10.6)	12.8	6	2

†Based on the CNT carbon atoms, numbers in parentheses subtract C–F bond lengths.

Table 2. Averaged connectivity data.†

System	# Chains	# Chains per CF_3SO_3H	# H_2O Oxygen Atoms	# CF_3SO_3H Oxygen Atoms	# Rings
14N1	1.98 (1.98)	0.66 (0.66)	1.36 (1.36)	1.82 (1.82)	0.0012
14N2	1.73 (1.73)	0.58 (0.58)	3.38 (3.38)	2.37 (1.82)	0.0039
14N3	1.72 (1.63)	0.57 (0.54)	4.51 (3.41)	2.63 (2.33)	0.53
14F1	1.89 (1.89)	0.94 (0.94)	1.00 (1.00)	2.00 (2.00)	-
14F2	2.00 (2.00)	1.00 (1.00)	2.00 (2.00)	1.80 (1.80)	-
14F3	2.00 (2.00)	1.00 (1.00)	2.90 (2.90)	1.95 (1.95)	0.0030
17N1	1.94 (1.94)	0.48 (0.48)	1.80 (1.80)	1.96 (1.96)	0.0026
17N2	1.32 (1.27)	0.33 (0.32)	5.53 (4.98)	2.63 (2.41)	0.29
17N3	1.23 (1.08)	0.41 (0.36)	6.45 (5.80)	2.42 (2.20)	0.33
17F1	2.91 (2.91)	0.97 (0.97)	1.00 (1.00)	2.02 (2.02)	-
17F2	1.00 (0.74)	0.50 (0.37)	3.89 (3.86)	1.85 (1.80)	0.26
17F3	1.08 (1.03)	0.54 (0.51)	5.15 (4.59)	3.06 (2.75)	0.26

†Numbers in parentheses represent values when ring connections are removed.

Table 3. O–H···F hydrogen bond data for the fluorinated systems.

System	% Time O–H···F (CNT) Exists	Average O–H···F (CNT) Life (fs)	% Time O–H···F (Triflic) Exists	Average O–H···F (Triflic) Life (fs)
14F1	64.1	127.2	2.9	21.2
14F2	91.5	54.0	9.2	35.4
14F3	99.2	137.1	3.9	27.0
17F1	63.4	58.2	0.73	20.3
17F2	68.8	70.4	4.1	22.4
17F3	83.3	116.9	6.3	36.7

Table 4. O–H···F hydrogen bond data for the bare systems.

System	% Time O–H···F (Triflic) Exists	Avg. O–H···F (Triflic) Life (fs)
14N1	29.3	53.1
14N2	7.2	26.7
14N3	14.7	31.0
17N1	16.9	41.5
17N2	18.2	40.6
17N3	25.5	36.8

Figure Captions

Figure 1. Systems used in the present study shown for n = 3: (a) 14N3, (b) 14F3, (c) 17N3, and (d) 17F3. The different coloured spheres represent different atom types where: grey–carbon, red–oxygen, white–hydrogen, yellow–fluorine, and orange–sulphur.

Figure 2. Coordination numbers of the water molecules defined by the average number of donated and accepted water/water and water/triflic acid sulfonate group hydrogen bonds for each system for: (a) n = 1, (b) n = 2, and (c) n = 3.

Figure 3. Representative snapshots of the hydrogen bond network for n = 1 for: (a) 14N1, (b) 14F1, (c) 17N1, and (d) 17F1. Hydrogen bonds are denoted by dashed lines. A portion of periodic images have been included represented by coloured rods to show the local environment. The CNT walls have been omitted for clarity.

Figure 4. Representative snapshots of the hydrogen bond network for n = 2 for: (a) 14N2, (b) 14F2, (c) 17N2, and (d) 17F2. Hydrogen bonds are denoted by dashed lines. A portion of periodic images have been included represented by coloured rods to show the local environment. The CNT walls have been omitted for clarity.

Figure 5. Representative snapshots of the hydrogen bond network for n = 3 for: (a) 14N3, (b) 14F3, (c) 17N3, and (d) 17F3. Hydrogen bonds are denoted by dashed lines. A portion of periodic images have been included represented by coloured rods to show the local environment. The CNT walls have been omitted for clarity.

Figure 6. The average number of chains per CF_3SO_3H for all CNT/triflic acid+H_2O systems: (a) including oxygen atoms that are part of rings and (b) omitting oxygen atoms involved in ring connections.

Figure 7. Average chain lengths defined by the number of oxygen atoms involved in all systems partitioned into oxygen atoms of H_2O and CF_3SO_3H: (a) with and (b) without oxygen atoms involved in ring connections. (c) and (d) show the average fraction of total oxygen atoms in the system involved per chain.

Figure 8. The data for rings showing (a) the average number of rings and (b) the average length of rings partitioned into H_2O and CF_3SO_3H oxygen atoms.

Figure 9. Snapshot down the CNT axis in 17F3 showing the water molecules in a structured domain away from the triflic acid CF_3 head groups.

Figure 10. State of the protons in each system by hydration level: (a) *n* = 1, (b) *n* = 2, and (c) *n* = 3. See text for definition of different states.

Figure 11. Radial distribution functions between the oxygen atoms of triflic acid sulfonate groups, O_S, and hydrogen atoms by hydration level: (a) *n* = 1, (b) *n* = 2, and, (c) *n* = 3.

Figure 12. Probability distribution of the asymmetric stretch coordinate, $\delta = R_{O_aH} - R_{O_dH}$, for all hydrogen bonds between water molecules and triflic acid SO_3H groups for each system at *n* = 3. In all cases at this hydration level, water molecules/solvated protons act as the hydrogen bond donor.

Figure 13. Percent time at least one OH···F hydrogen bond exists between the water molecules and/or solvated protons and (a) the fluorinated CNT walls and (b) the fluorine atoms of the mobile triflic acid groups partitioned into the types of species involved.

Figure S1. Snapshots showing ring formation in (a) 17N2 and (b) 17F2.

Figure S2. Snapshots showing ring formation in (a) 14N3, (b) 17N3 showing a 5-membered ring (top) and a 9-membered ring, and (c) 17F3 showing a 4-membered ring (top) and an 8-membered ring (bottom).

Figure S3. Snapshots of the bare CNT systems that contained OH···F hydrogen bond between water molecules and a fluorine atom of triflic acid over 15% of the time: (a) 14N1, (b) 17N1, (c) 17N2, and (d) 17N3.

Figure S4. Snapshots of hydrogen bonding to the fluorinated wall in the smaller CNT systems: (a) 14F1, (b) 14F2, and (c) 14F3.

Figure S5. Snapshots of hydrogen bonding to the fluorinated wall in the larger CNT systems: (a) 17F1, (b) 17F2, and (c) 17F3.

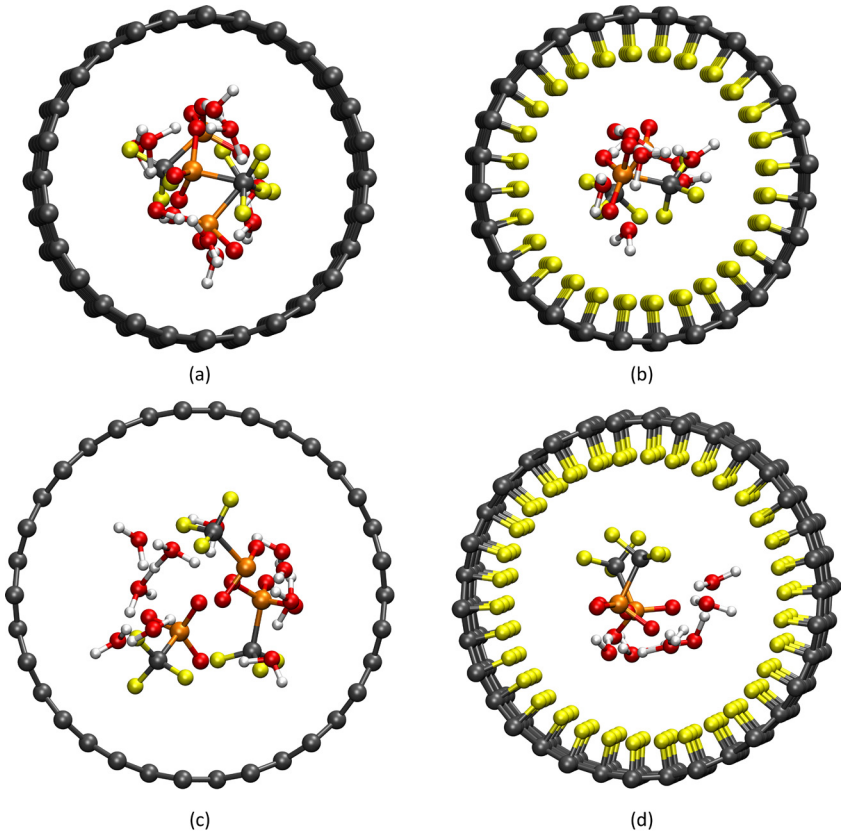

Fig. 1

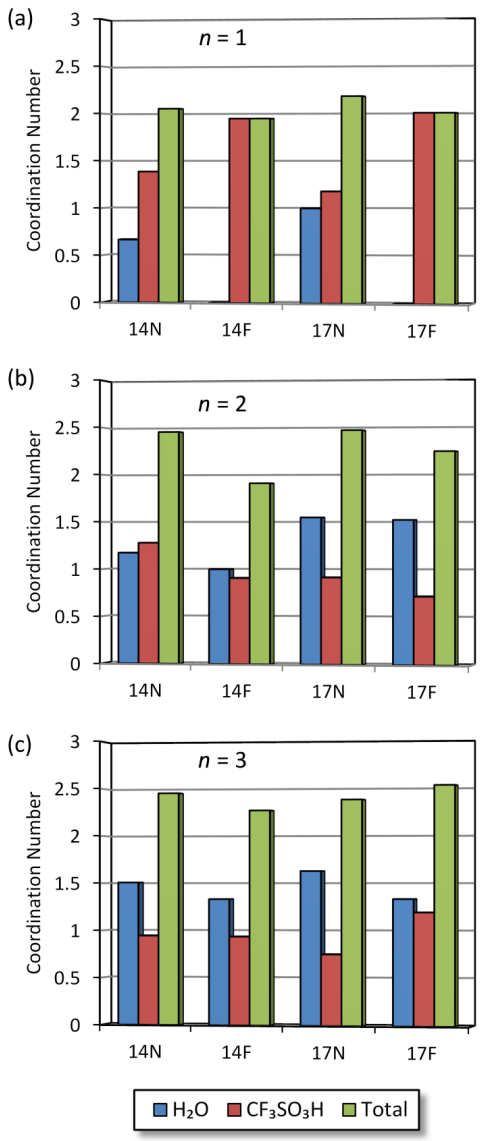
(a)
n = 1
Coordination Number
3
2.5
2
1.5
1
0.5
0
14N
14F
17N
17F
(b)
n = 2
Coordination Number
3
2.5
2
1.5
1
0.5
0
14N
14F
17N
17F
(c)
n = 3
Coordination Number
3
2.5
2
1.5
1
0.5
0
14N
14F
17N
17F
H2O
CF3SO3H
Total

Fig. 2

(a) 14N1

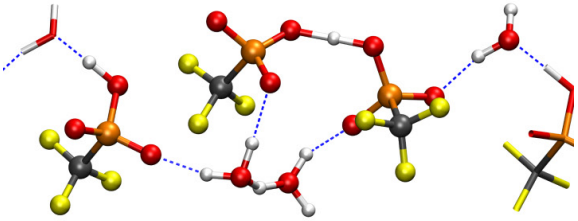

(b) 14F1

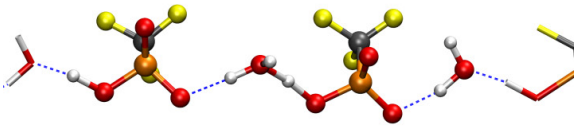

(c) 17N1

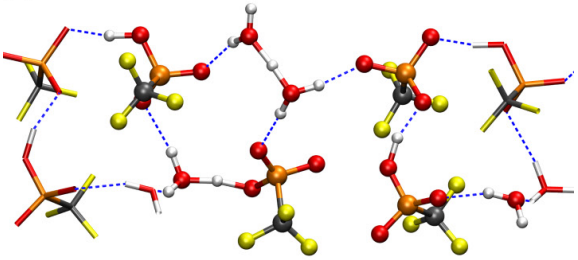

(d) 17F1

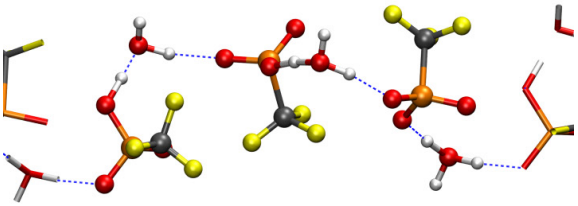

Fig. 3

(a) 14N2

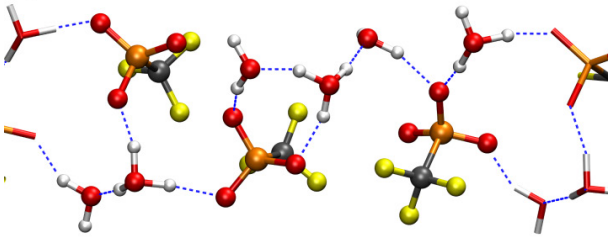

(b) 14F2

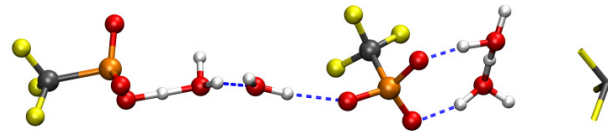

(c) 17N2

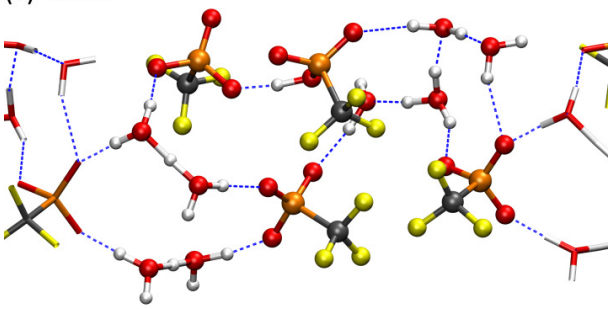

(d) 17F2

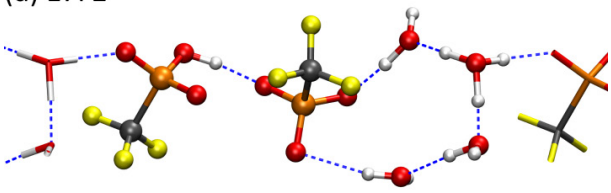

Fig. 4

(a) 14N3

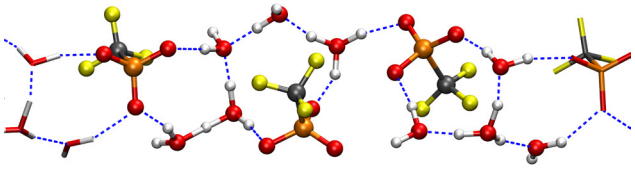

(b) 14F3

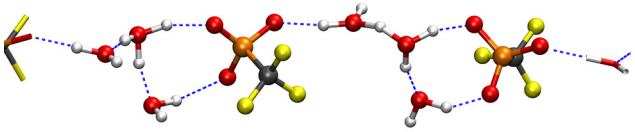

(c) 17N3

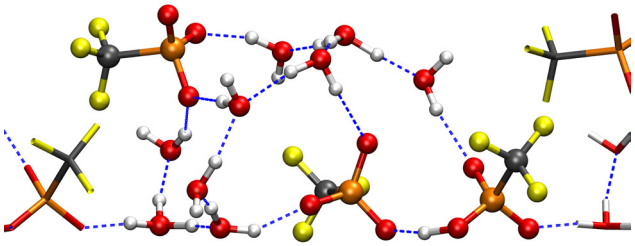

(d) 17F3

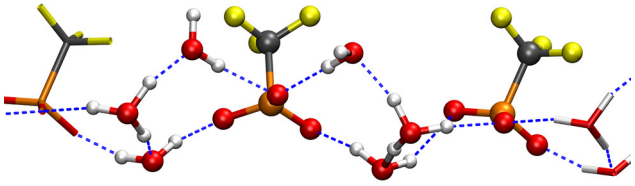

Fig. 5

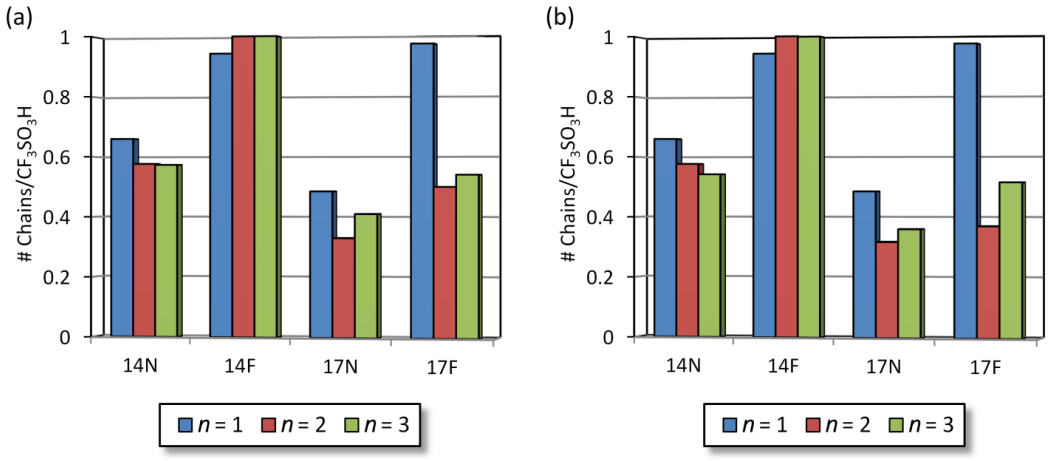

Fig. 6

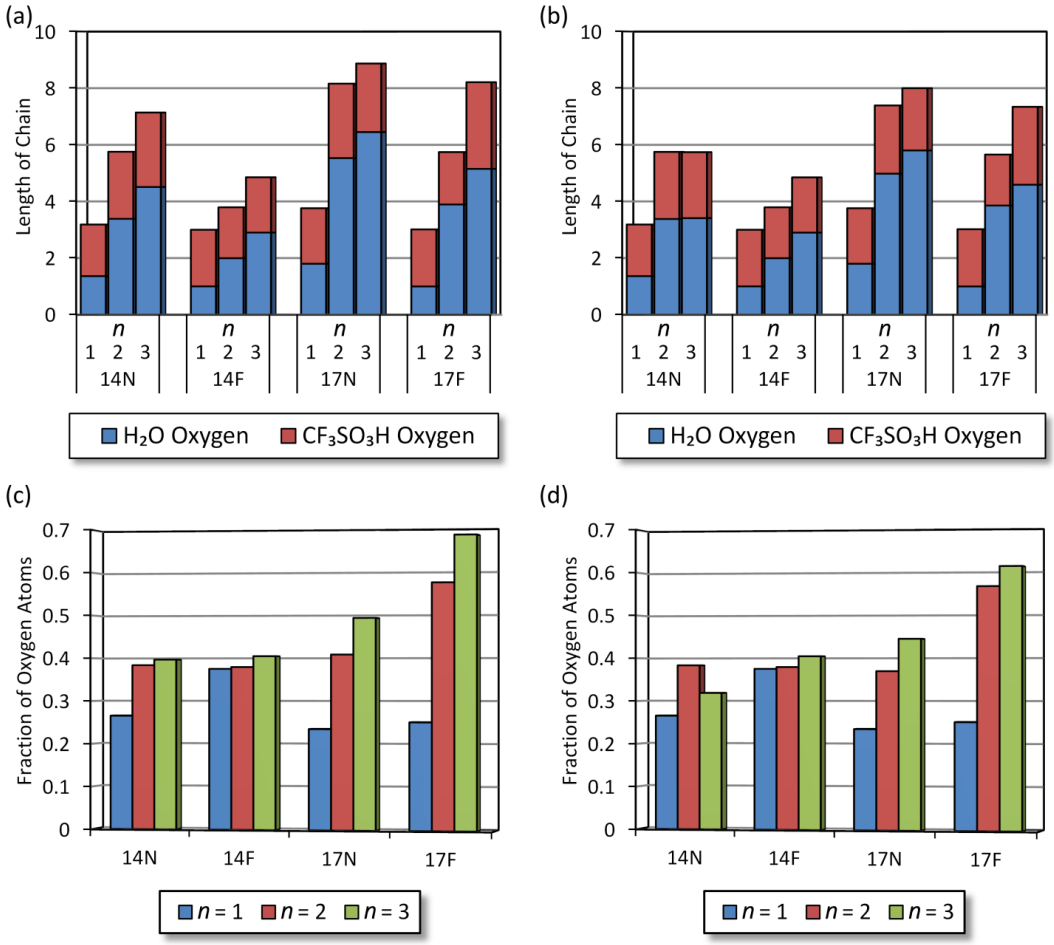
(a)
Length of Chain
10
8
6
4
2
0
n
1 2 3
14N
14F
17N
17F
H₂O Oxygen
CF₃SO₃H Oxygen
(b)
Length of Chain
H₂O Oxygen
CF₃SO₃H Oxygen
(c)
Fraction of Oxygen Atoms
0.7
0.6
0.5
0.4
0.3
0.2
0.1
0
14N
14F
17N
17F
n = 1
n = 2
n = 3
(d)
Fraction of Oxygen Atoms
n = 1
n = 2
n = 3

Fig. 7

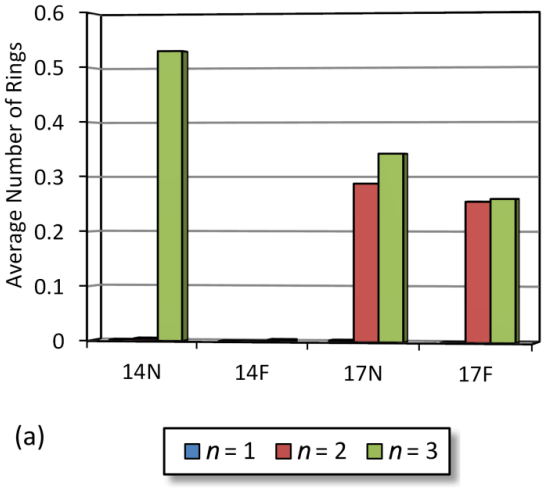
Average Number of Rings
0.6
0.5
0.4
0.3
0.2
0.1
0
14N
14F
17N
17F
(a)
n = 1
n = 2
n = 3

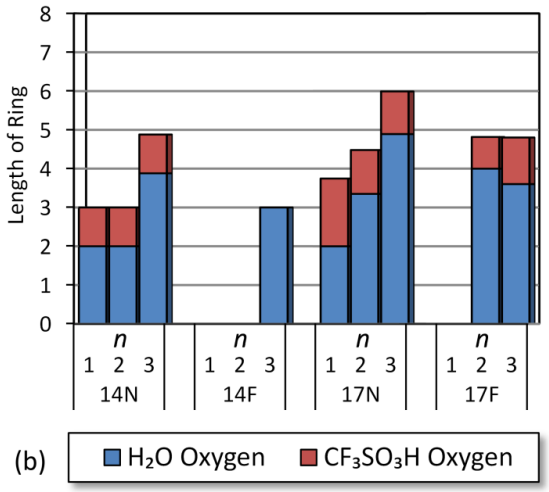
Length of Ring
8
7
6
5
4
3
2
1
0
n
1 2 3
14N
14F
17N
17F
(b)
H2O Oxygen
CF3SO3H Oxygen

Fig. 8

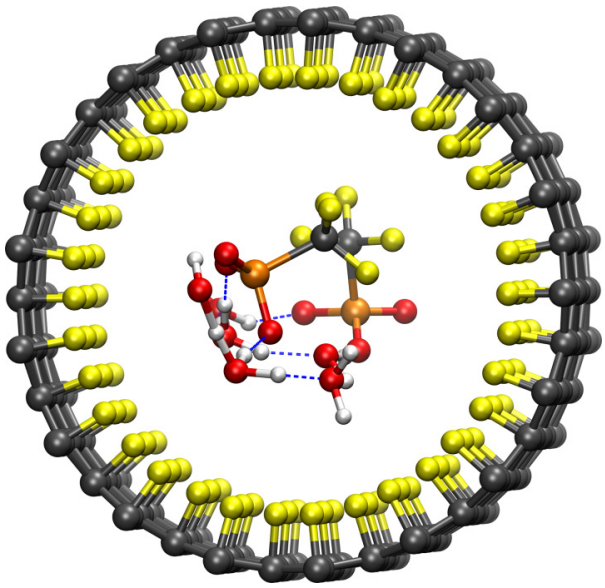

Fig. 9

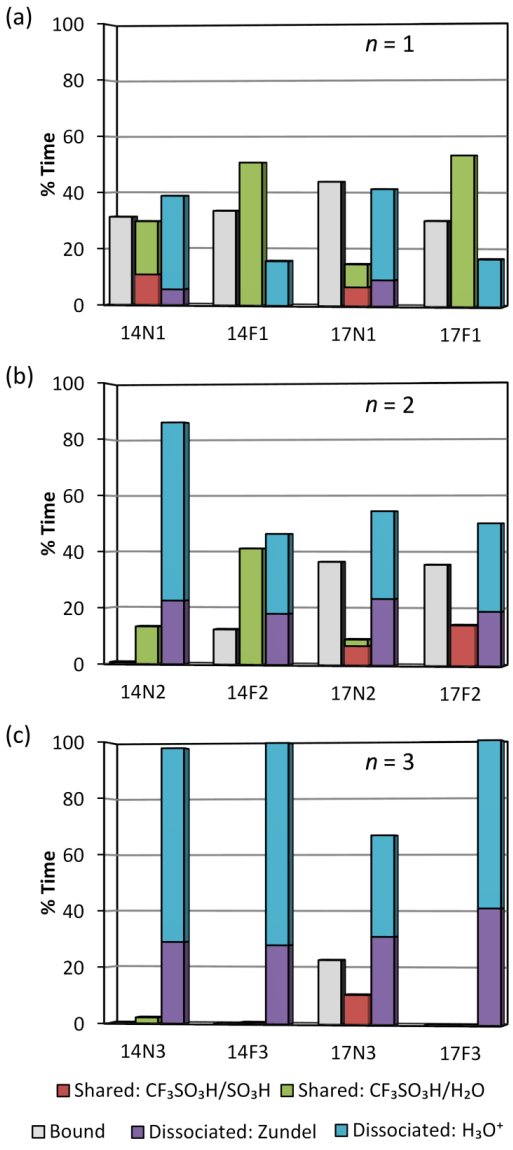
(a)
n = 1
% Time
100
80
60
40
20
0
14N1
14F1
17N1
17F1
(b)
n = 2
% Time
14N2
14F2
17N2
17F2
(c)
n = 3
% Time
14N3
14F3
17N3
17F3
Shared: CF3SO3H/SO3H
Shared: CF3SO3H/H2O
Bound
Dissociated: Zundel
Dissociated: H3O+

Fig. 10

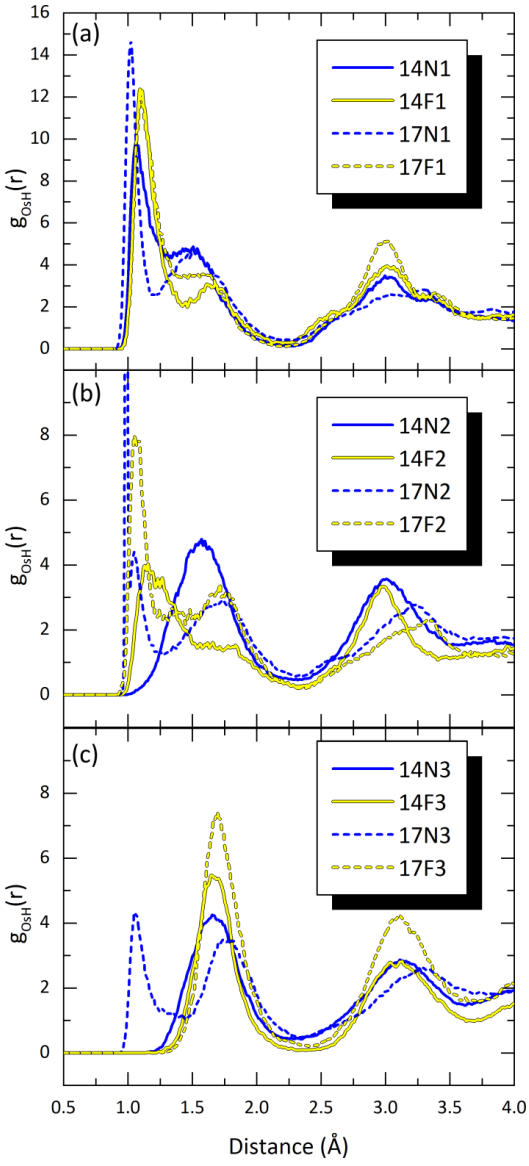
(a)
14N1
14F1
17N1
17F1
(b)
14N2
14F2
17N2
17F2
(c)
14N3
14F3
17N3
17F3
$g_{OsH}(r)$
Distance (Å)

Fig. 11

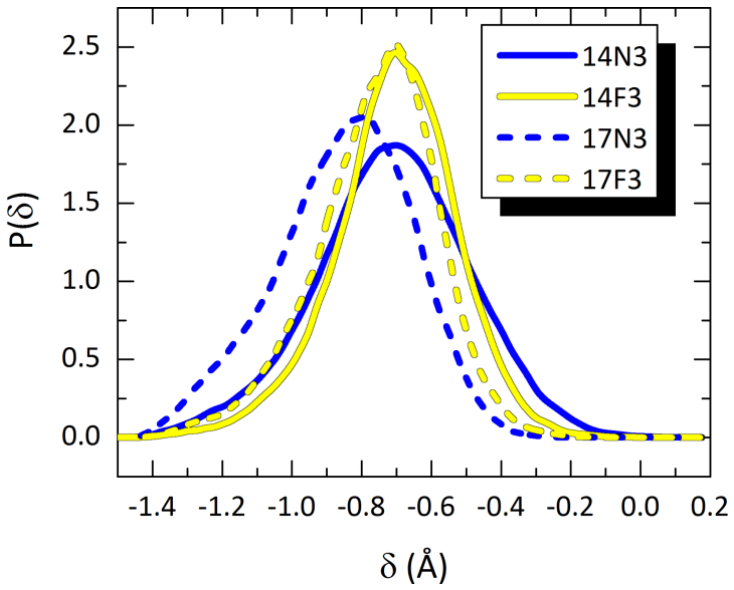
14N3
14F3
17N3
17F3
P(δ)
δ (Å)
2.5
2.0
1.5
1.0
0.5
0.0
-1.4
-1.2
-1.0
-0.8
-0.6
-0.4
-0.2
0.0
0.2

Fig. 12

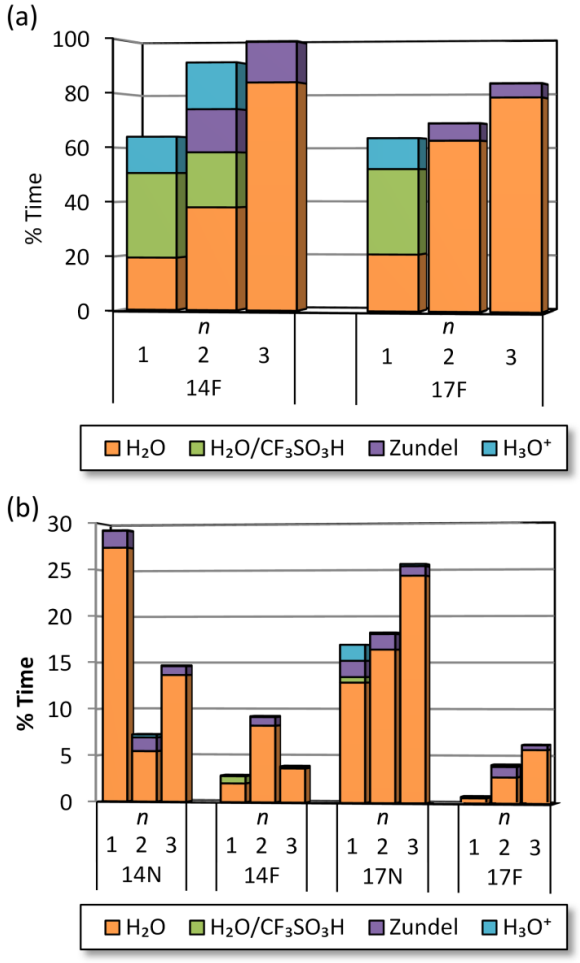
(a)
100
80
60
40
20
0
% Time
n
1 2 3
14F
1 2 3
17F
H2O
H2O/CF3SO3H
Zundel
H3O+
(b)
30
25
20
15
10
5
0
% Time
n
1 2 3
14N
1 2 3
14F
1 2 3
17N
1 2 3
17F
H2O
H2O/CF3SO3H
Zundel
H3O+

Fig. 13

(a) 17N2

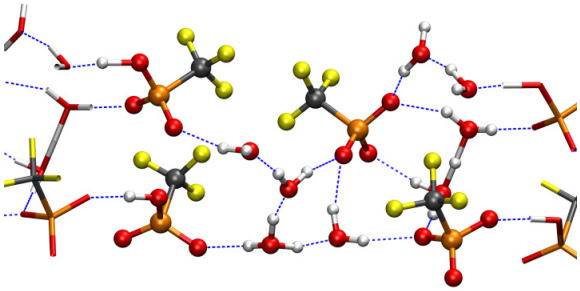

(b) 17F2

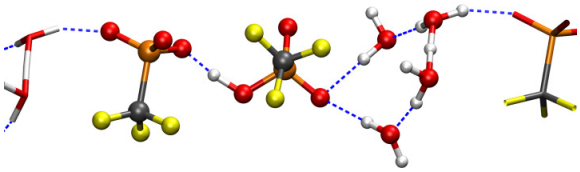

Fig. S1

(a) 14N3

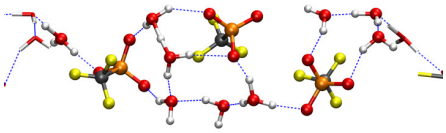

(b) 17N3

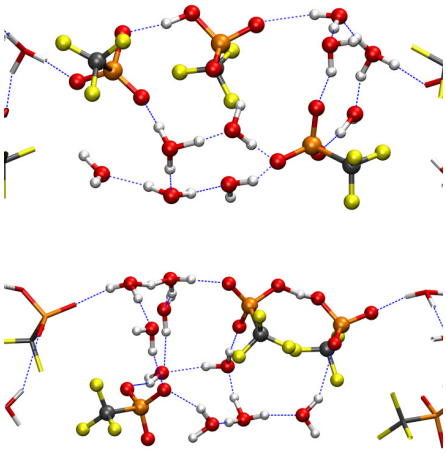

(c) 17F3

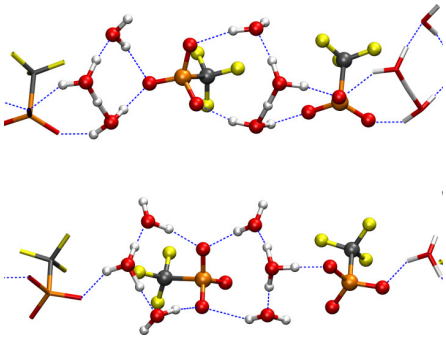

Fig. S2

(a) 14N1

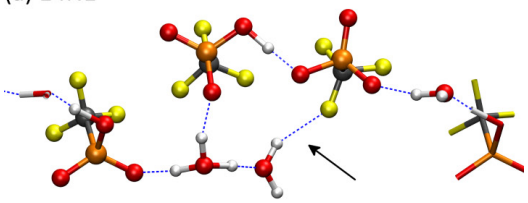

(b) 17N1

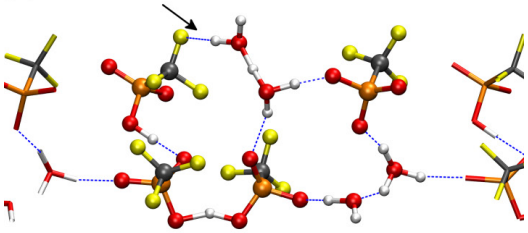

(c) 17N2

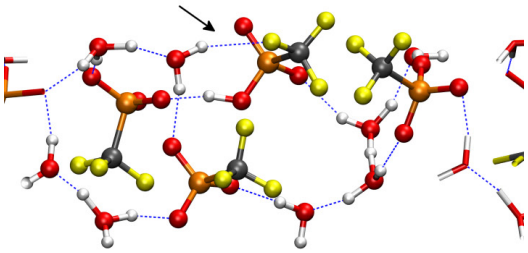

(d) 17N3

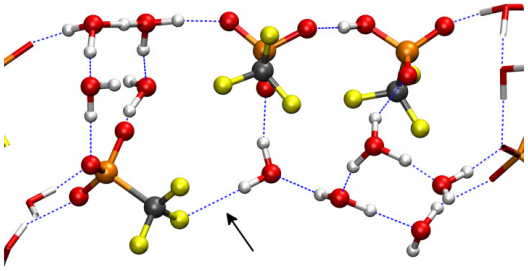

Fig. S3

(a) 14F1

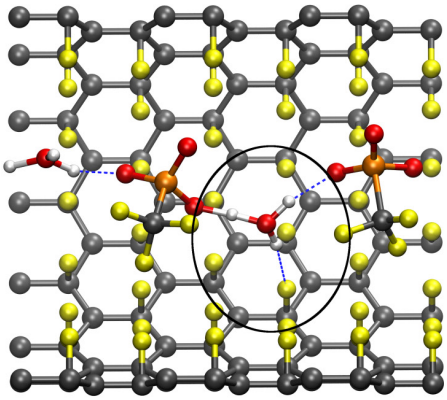

(b) 14F2

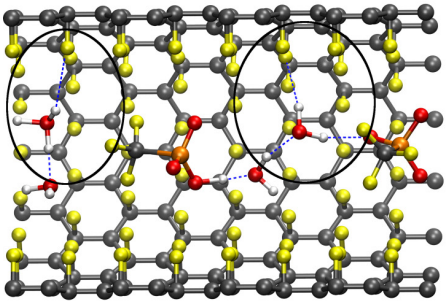

(c) 14F3

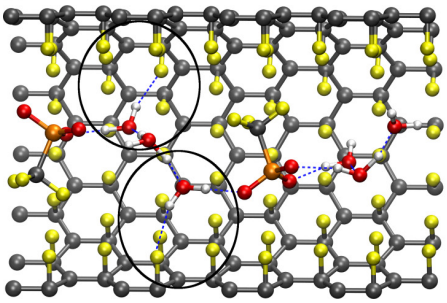

Fig. S4

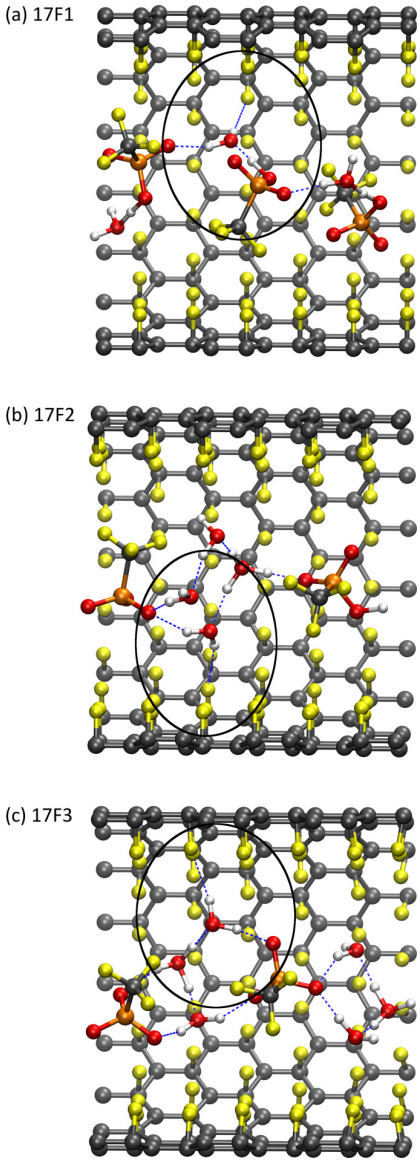

Fig. S5

Solid State Ionics 199–200 (2011) 6–13

Contents lists available at ScienceDirect

Solid State Ionics

journal homepage: www.elsevier.com/locate/ssi

An *ab initio* study of the primary hydration and proton transfer of CF_3SO_3H and $CF_3O(CF_2)_2SO_3H$: Effects of the hybrid functional and inclusion of diffuse functions

Chen Wang, Jeffrey K. Clark II, Milan Kumar, Stephen J. Paddison *

Department of Chemical and Biomolecular Engineering, University of Tennessee, Knoxville, TN 37996, USA

ARTICLE INFO

Article history:
Received 31 December 2010
Received in revised form 1 July 2011
Accepted 1 July 2011
Available online 21 August 2011

Keywords:
Perfluorosulfonic acid
Proton exchange membrane
Ionomer
Electronic structure
Proton transfer
Diffuse functions
Basis set

ABSTRACT

Electronic structures calculations were undertaken on two perfluorosulfonic acids (CF_3SO_3H and $CF_3O(CF_2)_2SO_3H$) with varying number of hydrating water molecules to assess the effects of the enhanced electron withdrawing afforded by an additional CF_2 group: the side chain of the short-side-chain (SSC) PFSA membrane. Both Becke's 3-parameter hybrid functional (B3LYP) and the extended hybrid functional (X3LYP) employing the 6-311G** split valence Gaussian basis set with and without the inclusion of diffuse functions were performed to determine the impact on proton dissociation and separation as a function of the degree of the hydration of the acids. The calculations underscore the increased acidity of $CF_3O(CF_2)_2SO_3H$ due to the enhanced electron withdrawing of the β $-CF_2-$ but did not reveal any differences in the strength of the binding of the water molecules over that computed for CF_3SO_3H. The calculated structural parameters obtained from optimized geometries of both acids with from 1 to 4 water molecules revealed that the inclusion of diffuse functions has negligible effects. Furthermore, the results obtained with the X3LYP functional were nearly identical to those obtained with the B3LYP functional.

1. Introduction

Over the past two decades, considerable interest in eliminating the overwhelming dependence on fossil fuels as an energy source has steadily increased. This has led to an intense search for clean, renewable sources of energy. One promising solution lies in the utilization of proton exchange membrane (PEM) fuel cells as efficient energy conversion devices due to their wide range of applicability and minimal environmental impact [1,2]. The PEM is critical to the operation of a fuel cell as it functions as the separator of the electrodes and reactant gases, the electrolyte, and the internal ion conductor [3]. Efficient operation of these devices thus strongly depends on the properties and functionality of the membrane electrolyte. Furthermore, the employment of PEM fuel cells in various applications (vehicular, stationary, portable) places explicit demands on the PEM, including: long-time chemical and thermal stability at temperatures up to 120 °C and good proton conductivity ($\geq 10^{-1}$ Scm^{-1}) under low humidity conditions (25–50% relative humidity) [4].

Perfluorosulfonic acid (PFSA) ionomers, such as Nafion®, are currently the most commonly used fuel cell electrolytes. PFSA membranes consist of a polytetrafluoroethylene (PTFE) backbone functionalized with pendant side chains each terminated with a single sulfonic acid (SO_3H) group. The chemical structure, properties, and functionality in PFSA and other PEMs are an ongoing area of research [3,5–14]. This work has contributed to the fundamental understanding of existing materials, as well as the development of novel materials, such as, polymers with structural and chemical variations to the polymer backbone and/or side chains and protogenic groups [15–17]. Extensive experimental testing of PEM fuel cells under relatively dry conditions will undoubtedly assist in the improvement of these materials but a molecular-level understanding of the mechanisms of proton transport is needed for the overall success of these materials. Specifically, investigation of the effects of hydration and side chain functionality on proton dissociation through the formation of contact ion pairs and separation of the proton into a solvent separated state will provide fundamental understanding that should lead to advances in the field.

Efforts using various multi-scale modeling techniques have contributed to a better understanding of morphological phenomena and chemical functionalities of PFSA membranes, as well as, molecular-level structural properties and local interactions [3,10,18]. Coarse-grained modeling methods are utilized to examine systems at long time and length scales to be representative of multiple hydrophilic domains of the material [19–23]. The morphology evolution and eventual phase separation has been examined for a variety of ionomer systems with mesoscale modeling using dissipative particle dynamics (DPD) simulations [20,24–26]. Of additional interest in mesoscale modeling is the application of self-consistent mean-field (SCMF) simulations to investigate the affect temperature and water content have on phase separation and morphology in PFSA membranes [23]. Classical molecular dynamics (MD) simulations have been utilized to study hydration and transport properties of proton exchange membranes [27–36] but on systems considerably smaller in size. Empirical valence

* Corresponding author. Tel.: +1 865 974 2026; fax: +1 865 974 7076.
E-mail address: spaddison@utk.edu (S.J. Paddison).

0167-2738/$ – see front matter © 2011 Elsevier B.V. All rights reserved.
doi:10.1016/j.ssi.2011.07.002

bond (EVB) schemes have been employed to include the structural diffusion of protons (i.e., Grotthuss hopping) and has been used for simulating solvation and transport of hydrated protons in PEMs [37,38]. On an even smaller scale, *ab initio* molecular dynamics (AIMD) simulations have been utilized to investigate proton transfer and dynamics in model systems where the positions of all the atoms are either known or set a priori [39–43].

Although various molecular mechanics methods are used to understand macroscopic properties of PEM membranes, they fail to provide a complete description of proton transport at a molecular level. Electronic structure calculations may not only be used to generate force-field parameters for molecular mechanics methods, but also help in understanding fundamental aspects in polymeric membrane materials such as structural and chemical properties of the polymeric backbone and/or side chains, and proton transfer mechanisms under minimal hydration conditions. Some of the earliest work in this area focused solely on the primary hydration in single fluorinated sulfonic acid systems [44,45]. In addition to triflic acid [46–49], other single functional acid groups were studied with electronic structure calculations, including aromatic sulfonic acids [50], sulfonyl imides [51], carboxylic acid [52], imidazole [53], phosphoric acid [54], and phosphonic acid [55]. Investigations were also undertaken on systems involving more than one acidic group including oligomeric fragments of the short side chain (SSC) PFSA membranes [56–59]. These results elucidated the important correlation between conformational changes (i.e. flexibility) of side chains and the transfer and stabilization of dissociated protons as a function of the degree of hydration and separation of the protogenic groups. For the polymeric fragments involving two pendant side chains, backbone conformation [57,58], and separation of side chains [56] are important factors impacting the dissociation and transfer of the protons. These studies of oligomeric fragments of the SSC PFSA membrane showed that the formation of a connected hydrogen bond network among the water molecules is largely dependent upon the separation of the sulfonic acid groups. It was also observed that the Zundel ion plays an important role in facilitating proton transfer in these systems. In order to simulate larger polymeric systems with multiple pendant side chains, the ONIOM method was employed [59]. This study provided insight into the effects of the conformations of the side chain and backbones have on the dissociation and separation of the protons. In an investigation of single perfluoro and aromatic (*p*-toluene) sulfonic acid systems [50], it was observed that the stability of the conjugate base (i.e. the sulfonate anion in these systems) did affect proton dissociation and separation. Recently, a computational study focusing on the consequence of introducing different functional groups on the alpha site of single phosphonic acid molecules confirmed that the trifluoromethyl acid tend to bind water molecules tighter than other substituent acids due to the stronger electron withdrawing effect [60]. However, the effect of the electron withdrawing group at the beta site to the sulfonic acid is still unclear.

In the present study, we report a quantitative comparison of proton hydration and transfer in two different PFSA acids: triflic acid (CF_3SO_3H) and its beta-site substituent acid ($CF_3O(CF_2)_2SO_3H$) (the side chain of the SSC PFSA ionomer), with from 1 to 6 hydrating water molecules. The structural parameters and binding energies per water molecule for both systems are calculated. In addition, the partial charge distribution is obtained and compared. We also assess the influence resulting from the use of different hybrid density functional theory and inclusion of augmented diffuse function basis set.

2. Computational methods

All electronic structure calculations of the ionomeric fragments were performed using the GAUSSIAN 03 suite of programs [61]. Full geometry optimizations, using conjugate gradient methods [62], were performed on both CF_3SO_3H and $CF_3O(CF_2)_2SO_3H$ initially using Hartree Fock theory with the 6-31G** split valence basis set [63] without symmetry constrains. The resulting structures were then refined through optimizations performed with density functional theory (DFT) with both Becke's 3-parameter hybrid functional (B3LYP) [64,65] and the extended hybrid functional (X3LYP) [66]. Additional optimizations were then carried out at the B3LYP/6-311G** and X3LYP/6-311G** levels of theory [67]. Finally, optimizations were performed with the inclusion of diffuse basis functions [68] at the B3LYP/6-311G**++ and X3LYP/6-311G**++ levels of theory. Subsequent to the optimization of 'dry' systems (i.e. without addition of any water molecules), water molecules were incrementally added to the optimized HF/6-31G** system at a variety of initial positions, typically four after primary hydration, and full optimization was performed using the protocol described above. It should be noted, that only the data from the optimized global minimum energy structures determined are included. Vibrational frequencies and zero point energies (ZPEs) were determined for the systems at the B3LYP/6-311G**(/6-311G**++) and the X3LYP/6-311G**(/6-311G**++) levels. The binding energies of water molecules to the ionomeric fragments were computed using both uncorrected and ZPE corrected minimum electronic energies. Additionally, partial charges distributions and electrostatic potentials for each of multi-hydrated systems were obtained according to the CHelpG scheme at these levels of theory [69]. All calculations were performed by employing the above described scheme without including the effect of a dielectric medium or solvent.

3. Results and discussion

3.1. 1–3 Water molecules

Optimized structures of both the CF_3SO_3H and $CF_3O(CF_2)_2SO_3H$ (SSC side chain) acids were obtained with the addition of water molecules as described above. Structural parameters including the O—H bond length (i.e. the distance between the oxygen of the sulfonic acid/sulfonate and the acidic proton) and the $O\cdots H\cdots OH_2$ distance (i.e. the distance between the oxygen of the sulfonic acid/sulfonate and the oxygen of the water molecule/hydronium ion) are presented in Tables 1 and 2 for the triflic acid and the SSC side chain systems, respectively. Uncorrected and ZPE corrected binding energies are presented in Tables 3 and 4 for the triflic acid and SSC side chain, respectively. The equilibrium structures of both acids without the addition of any water molecules exhibits a nearly uniform O—H bond length of 0.97 Å irrespective of the level of theory and basis set used. Upon addition of a single water molecule, this O—H bond length increased to ~1.01 Å at the B3LYP and X3LYP levels of theory with and without the implementation of the diffuse functions. A negligible difference between the results obtained for the $O\cdots H\cdots OH_2$ distance was also observed when diffuse functions were added to the basis set. The resultant fully optimized structures, shown in Figs. 1a (CF_3SO_3H) and 2a ($CF_3O(CF_2)_2SO_3H$) at the X3LYP/6-311G**++ level, exhibit the water molecule acting as both a hydrogen bond acceptor and

Table 1
Structural parameters of $CF_3SO_3H + nH_2O$[a].

n H_2O	B3LYP		X3LYP	
	r ($-SO_2O\cdots H$)	r ($-SO_2O\cdots H\cdots OH_2$)	r ($-SO_2O\cdots H$)	r ($-SO_2O\cdots H\cdots OH_2$)
0	0.97 (0.97)[b]	–	0.97 (0.97)[b]	–
1	1.01 (1.00)	2.61 (2.64)[b]	1.01 (1.00)	2.60 (2.63)[b]
2	1.05 (1.04)	2.53 (2.54)	1.05 (1.04)	2.50 (2.53)
3	1.57 (1.55)	2.56 (2.55)	1.58 (1.55)	2.55_5 (2.55)
4	1.56 (1.54)	2.56 (2.55)	1.56 (1.54)	2.56 (2.55)
4*	3.66 (3.70)	3.90 (3.93)	3.65 (3.70)	3.89 (3.92)
5	3.68 (3.70)	3.97 (3.98)	3.67 (3.69)	3.96 (3.97)
6	3.91(3.87)	4.32 (4.23)	3.91 (3.87)	4.30_5 (4.22)

[a] All reported values are in and were obtained with the 6-311G** basis set.
[b] Values in parenthesis were obtained with inclusion of diffuse functions, i.e. /6-311G**++.

Table 2
Structural parameters of $CF_3O(CF_2)_2SO_3H + nH_2O$[a].

n H_2O	B3LYP		X3LYP	
	r ($-SO_2O\cdots H$)	r ($-SO_2O\cdots H\cdots OH_2$)	r ($-SO_2O\cdots H$)	r ($-SO_2O\cdots H\cdots OH_2$)
0	0.97 (0.97)[b]	–	0.97 (0.97)[b]	–
1	1.02 (1.00)	2.60 (2.64)[b]	1.02 (1.01)	2.60 (2.63)[b]
2	1.06 (1.03)	2.50 (2.54)	1.06 (1.04)	2.49 (2.53)
3	1.58 (1.57)	2.57 (2.56)	1.58 (1.57)	2.56 (2.56)
4	1.56 (1.55)	2.56 (2.55)	1.65 (1.56)	2.62 (2.57)
4*	3.39 (3.71)	3.61 (3.93)	3.36 (3.71)	3.58 (3.92)
5	3.69 (3.81)	3.93 (4.07)	3.64 (3.74)	3.92 (4.06)
6	3.72 (3.89)	4.06 (4.20)	3.70 (3.88)	4.02 (4.19)

[a] All reported values are in and were obtained with the 6-311G** basis set.
[b] Values in parenthesis were obtained with inclusion of diffuse functions, i.e. /6-311G**++.

donor to the acid moiety in a 'ring-like' hydrogen bond network. The values for the triflic acid system are in complete agreement with prior calculations performed at the B3LYP/6-31G** level [50].

The addition of a second water molecule also resulted in nearly identical structural parameters between the two acid systems at each level of theory and basis set. Again, there was negligible difference in the structural parameters obtained with either functional, and the inclusion of diffuse functions on the basis set changes resulted in structural parameters that differed by ≤0.1 Å, a negligible amount. The fully optimized structures obtained at all levels again reveal a 'ring-like' hydrogen bond network with one water molecule accepting the hydrogen bond from the O—H of the sulfonic acid and acting as a hydrogen bond donor to the other water molecule which is also a hydrogen bond donor to a different oxygen atom of the acid group. These structures are shown in Figs. 1b and 2b for the triflic acid and SSC side chain systems at the X3LYP/6-311G**++ level, respectively. Proton dissociation was not observed to occur with either acid at this level of hydration, but the O—H bond length of the sulfonic acid group has increased to approximately 1.05 Å.

Proton dissociation is first observed, at all levels of theory tested, upon addition of a third water molecule in both the CF_3SO_3H and the $CF_3O(CF_2)_2SO_3H$ systems, as shown in Figs. 1c and 2c at the X3LYP/6-311G**++ level, respectively. The optimized structures of each system continue to show similar geometries in the region containing the sulfonate group and the water molecules/hydronium ion. Again, no differences in the structural parameters were observed with the diffuse

Table 3
Binding energies of CF_3SO_3H[a].

n H_2O	B3LYP		X3LYP	
	ΔE[b]	ΔE_{ZPE}[c]	ΔE[b]	ΔE_{ZPE}[c]
1	−16.98	−14.61	−17.79	−15.40
	(−13.11)[d]	(−10.89)[d]	(−13.84)[d]	(−11.61)[d]
2	−16.75	−14.44	−17.53	−15.22
	(−13.16)	(−10.89)	(−13.88)	(−11.62)
3	−17.54	−14.85	−18.41	−15.71
	(−13.13)	(−10.53)	(−13.92)	(−11.33)
4	−17.38	−14.77	−18.19	−15.57
	(−13.43)	(−10.90)	(−14.17)	(−11.64)
4*	−17.61	−14.99	−18.43	−15.82
	(−13.65)	(−11.13)	(−14.42)	(−11.90)
5	-17.99_5	−15.11	−18.90	−15.98 (
	(−13.15)	(−10.39)	(−13.95)	−11.18)
6	−17.88	−14.98	−18.75	−15.84
	(−13.42)	(−10.73)	(−14.19)	(−11.50)

[a] All values reported in kcal/mol obtained using the 6-311G** basis set.
[b] Binding energy based on uncorrected total electronic energies.
[c] Binding energy based on ZPE corrected total electronic energies.
[d] Values in parenthesis were obtained with the inclusion of diffuse functions, i.e. /6-311G**++.

Table 4
Binding energies of $CF_3O(CF_2)_2SO_3H$ (kcal/mol)[a].

n H_2O	B3LYP		X3LYP	
	ΔE[b]	ΔE_{ZPE}[c]	ΔE[b]	ΔE_{ZPE}[c]
1	−16.85	−14.49	−17.70	−15.32
	(−12.99)[d]	(−10.87)[d]	(−13.74)[d]	(−11.60)[d]
2	−16.38	−14.08	−17.18	−14.87
	(−12.88)	(−10.73)	(−13.61)	(−11.47)
3	−17.46	−14.78	−18.34	−15.65
	(−13.04)	(−10.48)	(−13.84)	(−11.28)
4	−17.24	−14.51	−18.56	−15.66
	(−13.46)	(−10.96)	(−13.84)	(−11.10)
4*	−17.78	−15.14	−18.61	−15.97
	(−13.69)	(−11.18)	(−14.46)	(−11.95)
5	−17.99	−15.12	−18.88	−15.99
	(−13.34)	(−10.58)	(−14.13)	(−11.37)
6	−17.72	−14.95	−18.58	−15.80
	(−13.44)	(−10.77)	(−14.21)	(−11.54)

[a] All values reported in kcal/mol obtained using the 6-311G** basis set.
[b] Binding energy based on uncorrected total electronic energies.
[c] Binding energy based on ZPE corrected total electronic energies.
[d] Values in parenthesis were obtained with the inclusion of diffuse functions, i.e. /6-311G**++.

functions or in the change of functionals. Furthermore, these parameters maintain nearly the exact same results when comparing the SSC side chain and the triflic acid systems. It is shown that two of the oxygen atoms of the sulfonate group are now involved in a hydrogen bond with two individual water molecules, and the remaining oxygen and, now, hydronium ion are involved in a contact ion pair. Furthermore, the hydronium ion is also hydrogen bonded to the two water molecules maintaining a 'ring-like' network of hydrogen bonds. Dissociation results from stabilization of excess positive charge through the hydrogen bonds and the delocalization of excess electron density due to the electron withdrawing groups attached to the sulfonate group.

Of additional interest are the results obtained for the total charge residing on the oxygen atoms in both systems (see Figs. 9 and 10). Each level of theory tested resulted in a nearly perfect agreement for this parameter upon proton dissociation. This differs from the results obtained for the fragments with the addition of one and two molecules, as well as at increasing hydration, where a noticeable difference between the charges obtained with and without the inclusion of diffuse functions was observed. The total charge on the sulfonate oxygen atoms in the SSC side chain was calculated to be less than that on the (now) triflate anion. This is actually the case for the results obtained at each level of hydration tested (excluding the 'dry' fragment); however, upon addition of three water molecules the difference becomes more apparent and continues as additional water molecules are added. This suggests that the presence of the additional electron withdrawing groups located in the beta position with respect to the sulfonate group have a nontrivial effect on the delocalization of excess electron density. Thus, the SSC side chain is presumably the stronger of the two acid moieties at least in the gas phase. It should be noted that the inclusion of diffuse functions does appear to have an effect on the ZPE corrected binding energies reported in Tables 3 and 4 for the triflic acid system and the SSC side chain system (as graphically depicted Figs. 7 and 8), respectively, upon proton dissociation. The observed trend in binding energies at this point showed little change for both systems at all levels of theory (albeit the triflic acid system with the addition of two water molecules does not exactly obey the trend, but the difference is insignificant). However, the addition of a third water molecule demonstrates a noticeable difference between calculations performed with and without diffuse functions, but no change in the trend between the two different functionals. Calculations performed with inclusion of diffuse functions showed a small decrease in the binding energy, while those without diffuse functions result in a slight increase.

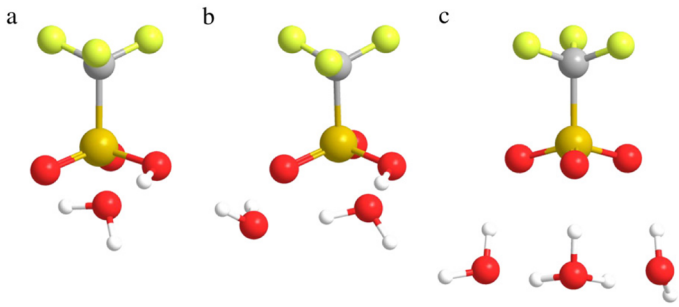

Fig. 1. Fully optimized (X3LYP/6-311G**++) global minimum energy structures of CF_3SO_3H with: (a) the addition of a single water molecule which acts as both a hydrogen bond acceptor and donor to the sulfonic acid; (b) the addition of two water molecules which further extends the 'ring-like' hydrogen bond network; and (c) the addition of three water molecules where dissociation of the proton is first observed upon formation of a contact ion pair between the hydronium ion and the triflate. The colored spheres represent different atom types in the structures where: grey—carbon, red—oxygen, yellow—fluorine, orange—sulfur, and white—hydrogen.

3.2. 4 Water molecules

The results presented for each system with the addition of four water molecules was obtained in two distinct ways. The first (designated in the data as $n=4$) follows the protocol outlined in Computational methods by simply adding an additional water molecule to the systems optimized with three water molecules. The second set (designated in the data as $n=4^*$) was obtained by completing the optimizations up to six water molecules and then removing two water molecules and then re-optimizing the structures. The 4* triflic acid system was favored by ~1 kcal/mol at each level of theory tested. This system was also favored for the SSC side chain by: 2.36 kcal/mol at the B3LYP/6-311G** level; 0.78 kcal/mol at the B3LYP/6-311G**++ level; 2.23 kcal/mol at the X3LYP/6-311G** level; and 0.88 kcal/mol at the X3LYP/6-311G**++ level (Fig. 5). The fully optimized structures for each system obtained by the two methods result are very similar. The structures obtained via the method described in Computational methods (4) are shown for the CF_3SO_3H and the $CF_3O(CF_2)_2SO_3H$ systems in Figs. 3a and 4a, while the 4* systems are shown in Figs. 3b and 4b, respectively. The structural parameters obtained in the systematic approach remain extremely similar between the systems, with little change observed between the B3LYP and X3LYP functionals with or without diffuse functions. The ZPE corrected energies calculated for these results, however, diverge from the typical trend that has been observed (see Fig. 8) in the larger SSC side chain system. The results obtained with diffuse functions appear to converge at this hydration, while those calculated in systems without diffuse functions diverge. The structural parameters in the 4* system, alternatively, vary between the SSC side chain and triflic acid systems. The parameters in the 4* SSC side chain system results in significant differences upon addition of the diffuse functions, but the differences in these values for the 4* triflic acid system remain essentially negligible. However, each level of theory tested gave qualitatively similar results. As shown, the systematically obtained structures contain a hydronium ion hydrogen bonded to two water molecules and an oxygen atom of the sulfonate group maintaining a contact ion pair. One of these water molecules is not directly hydrogen bonded to the sulfonate group; but interacts with another water molecule via a hydrogen bond creating an additional link in the 'ring-like' hydrogen bond network. The 4* system resulted in the removal of the contact ion pair as the excess proton is fully separated; the hydronium ion forms an Eigen cation as it is hydrogen bonded to three water molecules with an average O···O distance of 2.54 Å in both systems. The water molecules are also individually hydrogen bonded to different oxygen atoms of the sulfonate group. Examination of the total excess negative charge residing on the sulfonate oxygen atoms in the hypothetical system reveals a noticeable difference between the systems, as well as, differences in the levels of theories at which they are tested. As mentioned before, less total negative charge resides on the oxygen atoms of the $CF_3O(CF_2)_2SO_3H$ system than in the CF_3SO_3H system at all levels of hydration. This difference is seen to a greater extent in the 4* system.

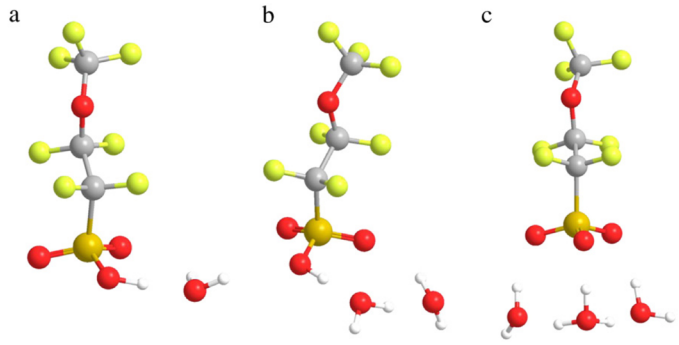

Fig. 2. Fully optimized (X3LYP/6-311G**++) global minimum energy structures of $CF_3O(CF_2)_2SO_3H$ with: (a) the addition of a single water molecule resulting in a hydrogen bond acceptor and donor as seen in the triflic acid system; (b) the addition of two water molecules continuing a 'ring-like' hydrogen bond network; (c) the addition of three water molecules where dissociation of the acidic proton is observed as a contact ion pair is formed.

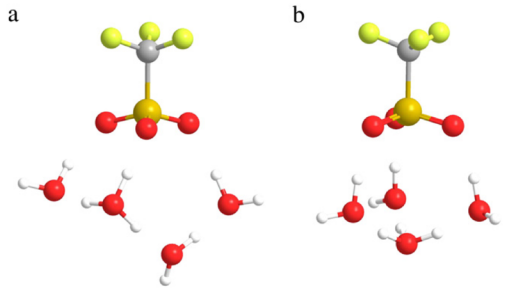

Fig. 3. Fully optimized (X3LYP/6-311G**++) global minimum energy structures of CF_3SO_3H with the addition of four explicit water molecules: (a) obtained via systematic addition of water molecules where the hydrogen bond network is expanded; (b) the 4* system was obtained by removing water molecules from a system with five water molecules (see text for explanation) where the acidic proton is in a solvent-separated state.

The calculations performed with the inclusion of diffuse functions all resulted in the 4* system representing the maximum value of excess charge on the sulfonate oxygen atoms. Not surprisingly, the 4* system also gives the maximum ZPE corrected binding energy calculated with diffuse functions as the excess negative charge results in more tightly bound water molecules to the sulfonate group. Different results are observed when diffuse functions are omitted. The total excess negative charge on the sulfonate group of the 4* system is still the maximum value found in the triflic acid system (with respect to other calculations at the same level of theory), but it does not correspond to the maximum ZPE corrected binding energy for calculations performed with either the B3LYP or the X3LYP functionals. Furthermore, calculations performed without diffuse functions on the SSC side chain for the 4* system did not result in the maximum value for the total excess negative charge on the sulfonate oxygen atoms. This suggests that the presence of the longer chain in the $CF_3O(CF_2)_2SO_3H$ system is more sensitive to the effect of diffuse functions than that observed in the CF_3SO_3H system after proton dissociation has occurred. It is known that the addition of diffuse function does not affect the neutral systems but may have a noticeable effect on ion pairs [68,70,71]. This effect can also be seen from the energetic data presented in Tables 3 and 4. The maximum binding energy difference

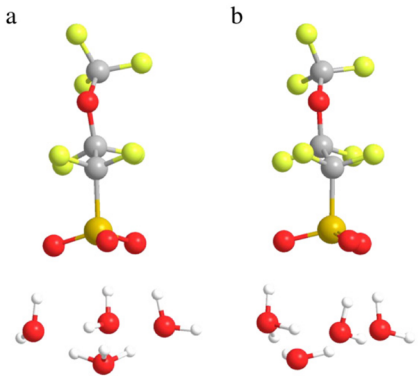

Fig. 4. Fully optimized (X3LYP/6-311G**++) global minimum energy structures of $CF_3O(CF_2)_2SO_3H$: (a) obtained via systematic addition of water molecules where the hydrogen bond network expands similarly to the triflate system; (b) the 4* system was obtained by removing water molecules from a system with five water molecules (see text for explanation) forming a contact ion pair again in a similar manner to the triflate system.

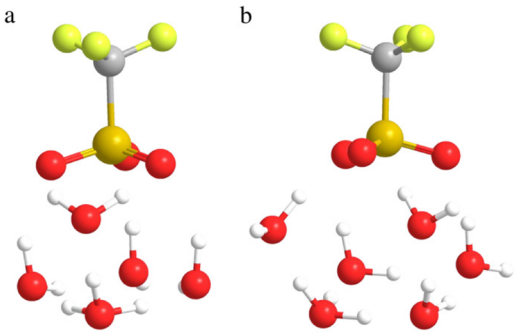

Fig. 5. Fully optimized (X3LYP/6-311G**++) global minimum energy structures of CF_3SO_3H with: (a) the addition of five water molecules where the acidic proton is no longer exists as a contact ion pair but is completely separated now as an Eigen cation as the additional water molecules fill the first hydration shell; (b) the addition of six water molecules reveals further separation of the hydrated proton from the $-SO_3^-$.

(~4.7 kcal/mol) is observed in systems where the dissociated proton moves to the next hydration shell and is stabilized by forming an Eigen cation (i.e. $n=5$). The CHelpG calculations performed at the 6-311G**++ level always gives less negative total charges of oxygen atoms for multi-hydrated systems except for systems with four water molecules (i.e. $n=4$, 4*). It is also noticed that this discrepancy observed with inclusion of diffuse functions becomes negligible for the systems with no more than three water molecules (as seen in Figs. 9 and 10).

3.3. 5 and 6 Water molecules

The addition of a fifth water molecule brings about a significant change in each system. Namely, the hydronium ion no longer exists as a contact ion pair with the sulfonate anion. Instead, an Eigen cation forms hydrogen bonded to three separate water molecules. The resultant optimized geometries at the X3LYP/6-311G**++ level for CF_3SO_3H and $CF_3O(CF_2)_2SO_3H$ are shown in Figs. 3a and 6a, respectively. This is similar to the results obtained previously with four water molecules ($n=4$*). The greater increase in the $O\cdots H\cdots OH_2$ distance indicates the complete separation of the dissociated proton from the $-SO_3^-$ due to the addition of an excess water molecule. The protonated water molecule binds slightly stronger to $CF_3O(CF_2)_2SO_3^-$ than to $CF_3SO_3^-$, which is confirmed by the smaller $O\cdots H\cdots OH_2$ separation and greater binding energies of the former (see Tables 1–4). Not surprisingly, the atomic charge distributions computed for both systems at all levels of theory encounter a noticeable increase when a fifth water molecule is added. The excess positive charge is delocalized on water molecules forming the Eigen cation. As discussed previously, the addition of electron withdrawing groups at beta positions leads to less negative charge residing on the oxygen atoms of SO_3^- (see Figs. 9 and 10). The calculations with the B3LYP and X3LYP functionals give practically identical geometries in the triflic acid systems. Specifically, both $O\cdots H$ and $O\cdots H\cdots OH_2$ distances are decreased by merely 0.01 Å with the X3LYP functional in above systems. For the $CF_3O(CF_2)_2SO_3H$ molecule, however, the $O\cdots H$ distance is shortened by over 0.05 Å when the X3LYP functional is utilized. Moreover, the addition of diffuse functions has made a significant change to $CF_3O(CF_2)_2SO_3H$, by increasing the $O\cdots H$ and $O\cdots H\cdots OH_2$ distances 0.11 Å and 0.14 Å with X3LYP, respectively. Similar to the systems with one, two, and four water molecules, the variation in the charge distribution among the different calculations becomes more pronounced with the presence of an additional electron withdrawing group.

Finally, after adding a sixth water molecule, the protonated water molecule is further separated from the sulfonate anion. Similarly, CF_3O

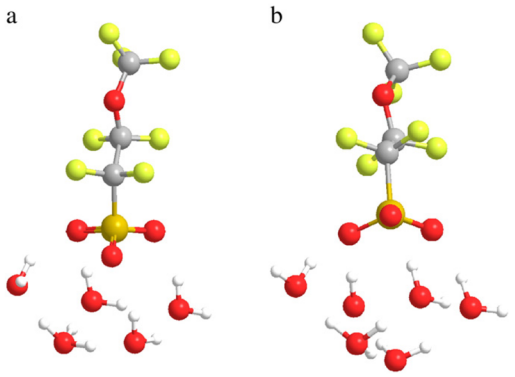

Fig. 6. Fully optimized (X3LYP/6-311G**++) global minimum energy structures of $CF_3O(CF_2)_2SO_3H$ with: (a) the addition of five water molecules showing the formation of a contact ion pair with the proton existing as an Eigen cation as the additional water molecules fill the first hydration shell; (b) the addition of six water molecules reveals further separation of the hydrated proton from the $-SO_3^-$.

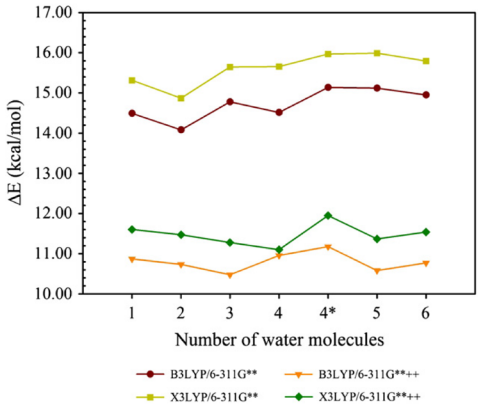

Fig. 8. ZPE corrected binding energies against the number of water molecules added for the $CF_3O(CF_2)_2SO_3H$ system. The inclusion of the diffuse functions always results in a lower magnitude of the binding energy. Also, the energy gap between systems calculated using different functionals remains relatively constant for systems both with and without diffuse functions, but this trend does deviate to a greater extent than the triflic acid system.

$(CF_2)_2SO_3^-$ brings the hydronium ion closer than $CF_3SO_3^-$ as revealed by the separation of Eigen/sulfonate ion pair listed in Tables 1 and 2. For triflic acid systems, again, the different functional methods with same basis sets give the almost indistinguishable equilibrium geometries and similar charge distributions. Nevertheless, the $CF_3O(CF_2)_2SO_3H$ molecule seems to be more sensitive to the augmented diffuse function as the O···H and O···H···OH_2 distances are both lengthened by ~0.15 Å as opposed to ~0.05 Å for triflic acid. The trends in the computed binding energy are found to be independent of the type of functional used. However, with the inclusion of diffuse functions in the basis set, the reverse trend occurs: the binding energy calculated without the diffuse functions increases after adding the sixth water molecule and decreases when diffuse functions are included.

It is important to realize that our calculations on the primary hydration of the two PFSA acids only assessed the differences of the presence of a $-CF_2-$ group located β to the sulfonic acid. Presently available PFSA membranes typically have an ether group in the side chain positioned γ to $-SO_3H$. Although we have not specifically elucidated the effects of this –O– linkage on proton hydration and transfer we can infer that this would be negligible in comparison to the electron withdrawing effects of the α and β $-CF_2-$ groups.

The present results are completely consistent with the majority of prior work examining the primary hydration and proton transfer of perfluorosulfonic acids with electronic structure calculations and BOMD simulations [44,46,47,49,50]. It should be also noted that all these theoretical results of proton dissociation with 2 or 3 water molecules and separation of the dissociated proton with a cluster consisting of 5 to 6 water molecules are in agreement with early FT-IR spectroscopy [71]. It is therefore surprising that a very recent set of electronic structure calculations of triflic acid reported qualitatively different results with dissociation and subsequent separation of the proton not occurring until after 4 and 10 water molecules were added

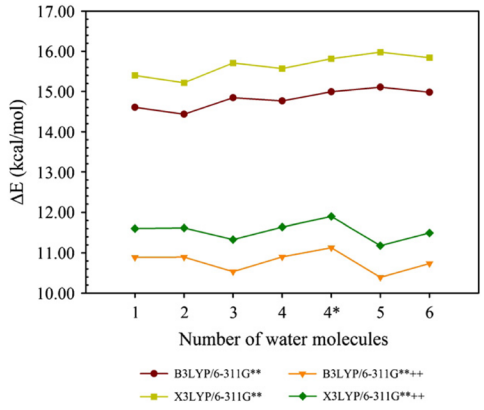

Fig. 7. ZPE corrected binding energies as a function of the number of added water molecules to CF_3SO_3H. The inclusion of the diffuse functions always results in a lower magnitude of the binding energy. Also, the energy gap between systems calculated using different functionals remains relatively constant for systems both with and without diffuse functions.

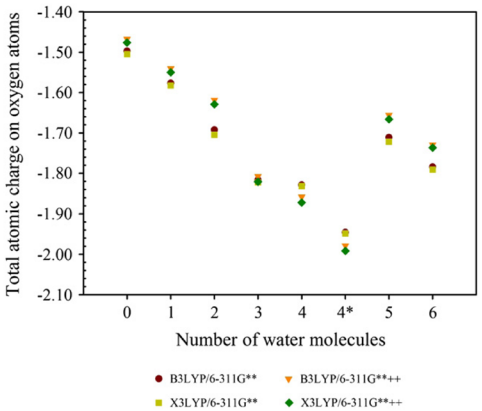

Fig. 9. Total atomic charge on the oxygen atoms of the sulfonate/sulfonic acid group in the CF_3SO_3H system as a function of water molecules added computed with the CHelpG routine of Gaussian 09.

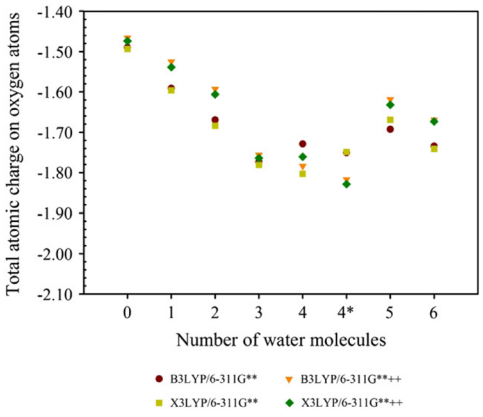

Fig. 10. Total atomic charge on the oxygen atoms of the sulfonate/sulfonic acid group in the $CF_3O(CF_2)_2SO_3H$ as a function of water molecules added system computed with the CHelpG routine of Gaussian 09.

[48]. These authors attributed this to the use of the X3LYP functional and inclusion of the diffuse functions. However, the present work clearly indicates that the difference in their results to those of others is not due to the choice of methodology.

4. Conclusions

Our study of two PFSA molecules (CF_3SO_3H and $CF_3O(CF_2)_2SO_3H$) indicates that the effects of introducing electron withdrawing groups on the beta position of the sulfonic acid is relatively minor when compare to the effects resulting from substitution at the alpha position. These effects become somewhat more significant after the self-dissociation of the proton (i.e., after three water molecules are added). The enhanced electron withdrawing group of $CF_3O(CF_2)_2SO_3H$ increases the acidity of the molecule through stabilization of the corresponding conjugate base, but does not result in significant changes to the binding of the water molecules. A comparison of the structural parameters obtained from optimized geometries of both CF_3SO_3H and $CF_3O(CF_2)_2SO_3H$ with from 1 to 4 added water molecules indicates that the inclusion of diffuse functions has negligible effects. The only discernible structural difference, however, occurs subsequent to the formation of the first hydration shell around the conjugate base (SO_3^-) where the proton was stabilized as an Eigen ion bonded to three water molecules. For both systems, the structural data obtained with the X3LYP functional is nearly identical to that with B3LYP. The X3LYP ZPE corrected binding energies indicate are approximately 0.8 kcal/mol higher than obtained with B3LYP. The slightly lower negative charge residing on the oxygen atoms of the sulfonate ion in $CF_3O(CF_2)_2SO_3H$ indicates the enhanced acidity due to the electron withdrawing effects of the $-CF_2-$ group. Thus, the acidic proton on $CF_3O(CF_2)_2SO_3H$ is more likely to dissociate from the sulfonic acid and form an Eigen ion, at least in isolated systems. The calculations for the $CF_3O(CF_2)_2SO_3H$ systems reveal that they are more sensitive to the presence of diffuse functions.

References

[1] Y.Y. Shao, G.P. Yin, Z.B. Wang, Y.Z. Gao, J. Power Sources 167 (2007) 235.
[2] M. Granovskii, I. Dincer, M.A. Rosen, Int. J. Hydrogen Energy 31 (3) (2006) 337.
[3] K.D. Kreuer, S.J. Paddison, E. Spohr, M. Schuster, Chem. Rev. 104 (2004) 4637.
[4] O. Savadogo, J. Power Sources 127 (2004) 135.
[5] M. Doyle, G. Rajendran, Handbook of Fuel Cells-Fundamentals Technology and Applications,Volume 3-Fuel Cell Technology and Applications, Wiley and Sons, Chichester, UK, 2003.
[6] K.D. Kreuer, Handbook of Fuel Cells-Fundamentals, Technology and Applications, Volume 3-Fuel Cell Technology and Applications, J. Wiley and Sons, Chichester, UK, 2003.
[7] G. Alberti, M. Casciola, Annu. Rev. Mater. Res. 33 (2003) 129.
[8] M.E. Schuster, W.H. Meyer, Annu. Rev. Mater. Res. 33 (2003) 233.
[9] J. Roziere, D.J. Jones, Annu. Rev. Mater. Res. 33 (2003) 503.
[10] S.J. Paddison, Annu. Rev. Mater. Res. 33 (2003) 289.
[11] K.A. Mauritz, R.B. Moore, Chem. Rev. 104 (2004) 4535.
[12] M.A. Hickner, H. Ghassemi, Y.S. Kim, B.R. Einsla, J.E. McGrath, Chem. Rev. 104 (2004) 4587.
[13] A. Biyikoglu, Int. J. Hydrogen Energy 30 (2005) 1181.
[14] D. Cheddie, N. Munroe, J. Power Sources 147 (2005) 72.
[15] Z.Y. Yang, R.G. Rajendran, Angew. Chem. Int. Ed. 44 (2005) 564.
[16] S.J. Hamrock, M.A. Yandrasits, Polym. Rev. 46 (2006) 219.
[17] B.R. Ezzell, W.P. Carl, W.A. Mod, The Dow Chemical Company, U.S., 1982.
[18] J.A. Elliott, S.J. Paddison, Phys. Chem. Chem. Phys. 9 (2007) 2602.
[19] K. Malek, M. Eikerling, Q.P. Wang, Z.S. Liu, S. Otsuka, K. Akizuki, M. Abe, J. Chem. Phys. 129 (2008) 204702.
[20] S. Yamamoto, S.A. Hyodo, Polym. J. 35 (2003) 519.
[21] J.T. Wescott, Y. Qi, L. Subramanian, T.W. Capehart, J. Chem. Phys. 124 (2006) 134702.
[22] D.Y. Galperin, A.R. Khokhlov, Macromol. Theory Simul. 15 (2006) 137.
[23] P.G. Khalatur, S.K. Talitskikh, A.R. Khokhlov, Macromol. Theory Simul. 11 (2002) 566.
[24] D.-S. Wu, S.J. Paddison, J.A. Elliott, Energy Environ. Sci. 1 (2008) 284.
[25] D.S. Wu, S.J. Paddison, J.A. Elliott, Macromolecules 42 (9) (2009) 3358.
[26] D.S. Wu, S.J. Paddison, J.A. Elliott, S.J. Hamrock, Langmuir 26 (2010) 14308.
[27] A. Vishnyakov, A.V. Neimark, J. Phys. Chem. B 104 (2000) 4471.
[28] S.S. Jang, V. Molinero, T. Cagin, W.A. Goddard, J. Phys. Chem. B 108 (2004) 3149.
[29] S. Urata, J. Irisawa, A. Takada, W. Shinoda, S. Tsuzuki, M. Mikami, J. Phys. Chem. B 109 (2005) 4269.
[30] S. Urata, J. Irisawa, A. Takada, W. Shinoda, S. Tsuzuki, M. Mikami, J. Phys. Chem. B 109 (2005) 17274.
[31] N.P. Blake, M.K. Petersen, G.A. Voth, H. Metiu, J. Phys. Chem. B 109 (2005) 24244.
[32] N.P. Blake, G. Mills, H. Metiu, J. Phys. Chem. B 111 (2007) 2490.
[33] A. Venkatnathan, R. Devanathan, M. Dupuis, J. Phys. Chem. B 111 (2007) 7234.
[34] R. Devanathan, A. Venkatnathan, M. Dupuis, J. Phys. Chem. B 111 (2007) 13006.
[35] I.H. Hristov, S.J. Paddison, R. Paul, J. Phys. Chem. B 112 (2008) 2937.
[36] S.T. Cui, J.W. Liu, M.E. Selvan, S.J. Paddison, D.J. Keffer, B.J. Edwards, J. Phys. Chem. B 112 (42) (2008) 13273.
[37] S. Dokmaisrijan, E. Spohr, J. Mol. Liq. 129 (2006) 92.
[38] M.K. Petersen, F. Wang, N.P. Blake, H. Metiu, G.A. Voth, J. Phys. Chem. B 109 (2005) 3727.
[39] B.F. Habenicht, S.J. Paddison, M.E. Tuckerman, Phys. Chem. Chem. Phys. 12 (2010) 8728.
[40] M. Eikerling, S.J. Paddison, L.R. Pratt, T.A. Zawodzinski, Chem. Phys. Lett. 368 (2003) 108.
[41] A. Roudgar, S.P. Narasimachary, M. Eikerling, J. Phys. Chem. B 110 (2006) 20469.
[42] R.L. Hayes, S.J. Paddison, M.E. Tuckerman, J. Phys. Chem. B 113 (2009) 16574.
[43] B.F. Habenicht, S.J. Paddison, M.E. Tuckerman, J. Mater. Chem. 20 (2010) 6342.
[44] S.J. Paddison, L.R. Pratt, T. Zawodzinski, D.W. Reagor, Fluid Phase Equilib. 151 (1998) 235.
[45] S.J. Paddison, T.A. Zawodzinski Jr., Solid State Ionics 113–115 (1998) 333.
[46] V.A. Glezakou, M. Dupuis, C.J. Mundy, Phys. Chem. Chem. Phys. 9 (43) (2007) 5752.
[47] K. Sagarik, M. Phonyiem, C. Lao-Ngam, S. Chaiwongwattana, Phys. Chem. Chem. Phys. 10 (15) (2008) 2098.
[48] M. Webber, N. Dimakis, D. Kumari, M. Fuccillo, E.S. Smotkin, Macromolecules 43 (13) (2010) 5500.
[49] M. Phonyiem, S. Chaiwongwattana, C. Lao-ngam, K. Sagarik, Phys. Chem. Chem. Phys. 13 (23) (2011) 10923.
[50] S.J. Paddison, J. New Mater. Electrochem. Syst. 4 (2001) 197.
[51] M. Eikerling, S.J. Paddison, T.A. Zawodzinski, J. New Mater. Electrochem. Syst. 5 (1) (2002) 15.
[52] S. Urata, J. Irisawa, A. Takada, S. Tsuzuki, W. Shinoda, M. Mikami, Phys. Chem. Chem. Phys. 6 (2004) 3325.
[53] S.J. Paddison, K.D. Kreuer, J. Maier, Phys. Chem. Chem. Phys. 8 (2006) 4530.
[54] L. Vilciauskas, S.J. Paddison, K.D. Kreuer, J. Phys. Chem. A 113 (2009) 9193.
[55] C. Wang, S.J. Paddison, Phys. Chem. Chem. Phys. 12 (4) (2009) 970.
[56] S.J. Paddison, J.A. Elliott, J. Phys. Chem. A 109 (2005) 7583.
[57] S.J. Paddison, J.A. Elliott, Phys. Chem. Chem. Phys. 8 (2006) 2193.
[58] S.J. Paddison, J.A. Elliott, Solid State Ionics 177 (2006) 2385.
[59] S.J. Paddison, J.A. Elliott, Solid State Ionics 178 (2007) 561.
[60] C. Wang, S.J. Paddison, Phys. Chem. Chem. Phys. 12 (2010) 970.
[61] M.J. Frisch, G.W. Trucks, H.B. Schlegel, G.E. Scuseria, M.A. Robb, J.R. Cheeseman, J.A. Montgomery, T. Vreven, K.N. Kudin, J.C. Burant, J.M. Millam, S.S. Iyengar, J. Tomasi, V. Barone, B. Mennucci, M. Cossi, G. Scalmani, N. Rega, G.A. Petersson, H. Nakatsuji, M. Hada, M. Ehara, K. Toyota, R. Fukuda, J. Hasegawa, M. Ishida, T. Nakajima, Y. Honda, O. Kitao, H. Nakai, M. Klene, X. Li, J.E. Knox, H.P. Hratchian, J.B. Cross, C. Adamo, J. Jaramillo, R. Gomperts, R.E. Stratmann, O. Yazyev, A.J. Austin, R. Cammi, C. Pomelli, J.W. Ochterski, P.Y. Ayala, K. Morokuma, G.A. Voth, P. Salvador, J.J. Dannenberg, V.G. Zakrzewski, S. Dapprich, A.D. Daniels, M.C. Strain, O. Farkas, D.K. Malick, A.D. Rabuck, K. Raghavachari, J.B. Foresman, J.V. Ortiz, Q. Cui, A.G. Baboul, S. Clifford, J. Cioslowski, B.B. Stefanov, G. Liu, A. Liashenko, P. Piskorz, I. Komaromi, R.L. Martin, D.J. Fox, T. Keith, M.A. Al-Laham, C.Y. Peng, A. Nanayakkara, M. Challacombe, P.M.W. Gill, B. Johnson, W. Chen, M.W. Wong, C. Gonzalez, J.A. Pople, Gaussian 03, Gaussian Inc., Wallingford, CT, 2004.

[62] H.B. Schlegel, J. Comput. Chem. 3 (1982) 214.
[63] Pc Harihara, J.A. Pople, Theor. Chim. Acta 28 (1973) 213.
[64] A.D. Becke, J. Chem. Phys. 98 (1993) 5648.
[65] A.D. Becke, J. Chem. Phys. 98 (1993) 1372.
[66] X. Xu, W.A. Goddard, Proc. Natl. Acad. Sci. U.S.A. 101 (9) (2004) 2673.
[67] A.D. McLean, G.S. Chandler, J. Chem. Phys. 72 (1980) 5639.
[68] T. Clark, J. Chandrasekhar, G.W. Spitznagel, P.V. Schleyer, J. Comput. Chem. 4 (3) (1983) 294.
[69] C.M. Breneman, K.B. Wiberg, J. Comput. Chem. 11 (3) (1990) 361.
[70] G.W. Spitznagel, T. Clark, P. von Ragué Schleyer, W.J. Hehre, J. Comput. Chem. 8 (8) (1987) 1109.
[71] M. Laporta, M. Pegoraro, L. Zanderighi, Phys. Chem. Chem. Phys. 1 (19) (1999) 4619.

Vita

Jeffrey Clark, II was born in Nashville, TN on August 18, 1986. He received his B.S. in chemical engineering at the University of Tennessee in 2009 during which he interned at Eastman Chemical Company and Kimberly–Clark. Following his undergraduate education, Jeffrey was granted a National Science Foundation (NSF) Integrative Education and Research Traineeship (IGERT) in the Sustainable Technology through Advanced Disciplinary Research (STAIR) graduate program at UT. He joined Dr. Stephen Paddison's research group where he primarily focused on *ab initio* molecular modeling of proton transfer in proton exchange membranes for fuel cell applications. Jeffrey received his M.S. degree in chemical engineering in May 2012. By the end of his Ph.D. studies, his work resulted in eight publications with an additional two submitted. Jeffrey intends to apply what he has gained in his experiences at UT and expand upon it in a career as a research engineer in industry.